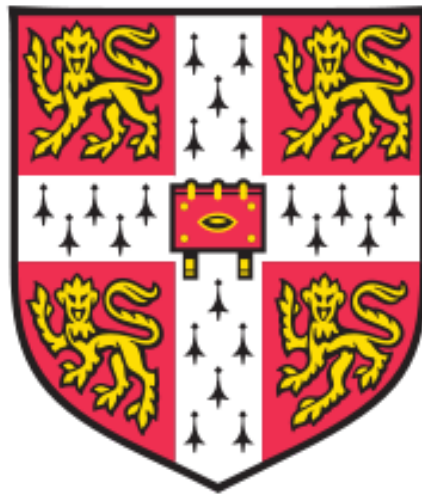


*SOIL – STRUCTURE INTERACTION FOR  
LOW DAMAGE SEISMIC ROCKING  
SYSTEMS*



**Iason Pelekis**

**St Edmund's College**

**Department of Engineering**

**University of Cambridge**

**This thesis is submitted for the degree of Doctor of  
Philosophy**

**August 2019**



*To my family, Athanasios, Vasiliki and Katerina*





UNIVERSITY OF  
CAMBRIDGE

Department of Engineering

# *SOIL – STRUCTURE INTERACTION FOR LOW DAMAGE SEISMIC ROCKING SYSTEMS*

Author: Iason Pelekis

Lead Supervisor: Dr Matthew DeJong

Advisor and Second Supervisor: Prof Gopal Madabhushi

## DECLARATION

I hereby declare this thesis is the result of my own work and includes nothing which is the outcome of work done in collaboration, except where specifically indicated in the text. It is not substantially the same as any that I have submitted, or, is being concurrently submitted for a degree or diploma or other qualification at the University of Cambridge or any other University or similar institution except as specified in the text. I further state that no substantial part of my dissertation has already been submitted, or, is being concurrently submitted for any such degree, diploma or other qualification at the University of Cambridge or any other University or similar institution except as specified in the text. The thesis contains approximately 57,200 words, 130 figures and 150 references.



## ACKNOWLEDGEMENTS

From the very beginning of this work, many people were involved by providing support, guidance and inspiration. Their continuous encouragement was of paramount importance in completing this research.

First of all, I would like to express my sincere thanks to my lead Supervisor Dr. Matthew J. DeJong. Matt's inspiration on the research of rocking structures was the ideal stimulus to orientate myself academically and pursue a PhD in the field of earthquake engineering. His expertise was critical on shaping the boundaries and core of this project. Furthermore, his supervision style, always engaging, honest and with in-depth involvement, was a real asset to my cause. I am also grateful for our discussions and fun we had in both sides of the Atlantic Ocean, including pubs, restaurants, barbeque events, conferences and other places, and for his invitation to the University of California, Berkeley. Matt has set an example to me both as a person and as an academic, and his guidance on various aspects was invaluable.

This research would not have been possible without my second Supervisor and Advisor Prof. Gopal S. P. Madabhushi. I am grateful to him for accepting me as a graduate student at the University of Cambridge initially, and then for joining forces to offer his expertise on soil-structure interaction. Gopal has always addressed my concerns about my centrifuge experiments with patience and offered significant guidance throughout this work. Especially, I would like to thank him also for his advice and feedback on matters beyond centrifuge testing and geotechnics.

Special thanks go to Frank McKenna for accommodating me with an office at the Pacific Earthquake Engineering Research Centre, Richmond, and for offering help with the OpenSees modelling. Frank has been instrumental in this work by highlighting special commands in OpenSees and providing feedback on my work. I am also very grateful to him for organizing barbecue meals and for all the fun we had in the office.

Moreover, I would like to thank my personal tutor at St Edmund's College, Dr Dirk Jongkind, for all the support with various matters while I studied in Cambridge. I am also grateful to Dr Fernando Constantino-Casas for his encouragement and our discussions over dinners at St Edmund's College.

The building models used throughout this research and the experimental campaign presented would not be possible without the critical assistance from Alistair Ross, Neil

Houghton, Mark Huntsman, Kevin Bullman, Phillip McLaren, Chris McGinnie, Mark Smith, Richard Adams, David Layfield, Kristian Pether, Martin Touhey and John Chandler. I am thankful to all of them.

Cambridge was a unique place to be for me and this is because of the people I met there, my colleagues from FIBE-CDT Cohort 1, my colleagues at the Structures and Geotechnical Research groups and my friends from St Edmund's College. I would like to thank Christiana and Marina for our extraordinary adventures, and Hannah, Petia, Bryn and Tim for a collaborative atmosphere and for having fun in various places around Cambridge. I am grateful to Anjali for her friendship and for inviting me to King's dinners, and to Irene for her tremendous support over difficult times. I would like to specially thank George for our in-depth discussions and for our many nights out, Maria for her cheerful attitude whenever we met, and Eftychia, Charis and Sinan for our technical discussions and their encouragement. Special thanks also to Srikanth for helping with my centrifuge experiments and for visiting me in Berkeley. I would also like to thank Abdul for helping me prepare and run my centrifuge experiments, and Stefan for helping with sand pouring. I am also grateful to Jad for our extensive discussions on soil-structure interaction topics. I would also like to thank Raz, Fiona and Thejesh for taking interest in my work and offering help when I needed. In addition, I would like to thank Chaitanya, Aastha, Silvia, Louis, Shub, Sohaib, Sara, Pedro and Antonis for spending numerous hours with me in and out of St Edmund's. I am also grateful to Ammar, Chris, Iria and Sam for playing tennis with me, and especially to Vanessa, and Allan and Kathleen who showed me around in San Francisco and welcomed me in Berkeley, respectively.

Many thanks also to my friends, Vangelis A., Andreas, Stelios, Orestis, Vangelis P., Lefteris, Thanos, Demetris T., Marios, Alkistis, Demetris K., Nicos T., Nicos S., who have been very supportive over the past period.

Finally, I am eternally grateful to all of my family in Greece, particularly Athanasios and Vasiliki, and in Birmingham UK, Katerina and Peter, for their constant support and encouragement in all ways possible.

## ABSTRACT

In earthquake prone areas, stakeholders now ask for low damage systems that can be easily repaired, following even earthquakes of catastrophic potential. Seismic protection of structures by means of rocking isolation is becoming increasingly popular, since allowing uplift is an inexpensive way to reduce the damage demand placed in structures. However, understanding the role of soil–structure interaction in the response of rocking systems remains a challenge. The goal of this thesis is to offer new knowledge on this field by assessing experimentally and computationally the response of rocking structures and the soil they are founded in.

For the first time, structural and foundation rocking are unified under a common experimental campaign. Two building models, designed to rock above or below their foundation level so that they can reproduce structural and foundation rocking respectively, were tested side by side in a centrifuge. The models were placed on a dry sand bed and subjected to a sequence of earthquake motions. Dense and then medium dense (loose) sand were used.

The range of rocking amplitude that is required for base isolation was quantified. Overall, it is shown that the relative density of sand does not influence structural rocking, while for foundation rocking, the change from dense to loose sand can affect the time-frequency response significantly and lead to more predictable load demands. Results also demonstrate that the rocking motion of the buildings is evident in the soil response beneath the structures, and foundation rocking causes larger dynamic differential settlements than structural rocking for a given rocking amplitude.

Within OpenSees, foundation and structural rocking were modelled using a Beam-on-a-Nonlinear-Winkler-Foundation model (BNWF). The modelling incorporated flat-slider elements for footing-soil and superstructure-footing interactions, respectively. A modified BNWF model (mBNWF) was presented that involved an uplift-dependent stiffness and viscosity transmission for both vertical and horizontal directions, and a friction-vertical force coupling. In general, the proposed modelling approach, without calibration, adequately captured the experimental response observed in centrifuge experiments. Due to its inherent dependency on initial conditions, foundation rocking was found more sensitive than structural rocking to the type of soil model and the soil properties. Finally, selecting appropriate modal damping ratios can further improve the response profile and based on these parameters a calibration scheme was proposed.



# CONTENTS

<b>LIST OF FIGURES</b> .....	<b>V</b>
<b>LIST OF TABLES</b> .....	<b>XV</b>
<b>NOMENCLATURE</b> .....	<b>XVII</b>
<b>1 INTRODUCTION</b> .....	<b>1</b>
1.1 GLOBAL CONTEXT .....	1
1.2 BACKGROUND ON ROCKING SYSTEMS .....	2
1.3 MOTIVATION.....	5
1.4 RESEARCH AIMS AND PRIMARY OBJECTIVES.....	6
1.5 OUTLINE OF THESIS .....	8
<b>2 LITERATURE REVIEW</b> .....	<b>11</b>
2.1 CATEGORIES OF ROCKING SYSTEMS .....	11
2.2 ROCKING STRUCTURES ON RIGID BASE.....	13
2.2.1 <i>Free standing rigid blocks</i> .....	13
2.2.2 <i>Rocking structures with response control from devices</i> .....	14
2.2.3 <i>Flexible superstructure rocking on rigid base</i> .....	17
2.3 ROCKING STRUCTURES ON FLEXIBLE SUPPORTS .....	19
2.3.1 <i>Rigid blocks on flexible foundation</i> .....	20
2.3.2 <i>Flexible superstructures on flexible supports</i> .....	20
2.4 ROCKING FOUNDATIONS AND SOIL – STRUCTURE INTERACTION.....	20
2.4.1 <i>Fail-safe design with soil</i> .....	21
2.4.2 <i>Effects of relative density of sand</i> .....	24
2.5 EXPERIMENTAL SOIL – ROCKING STRUCTURE INTERACTION .....	26
2.6 FINITE ELEMENT MODELLING FOR ROCKING SYSTEMS.....	29
2.6.1 <i>Modelling approaches for foundation rocking</i> .....	29
2.6.2 <i>Modelling approaches for structural rocking</i> .....	30
2.7 SUMMARY .....	32
2.7.1 <i>Research for experimental structural and foundation rocking</i> .....	35
2.7.2 <i>Research for computational structural and foundation rocking</i> .....	35
<b>3 DESIGN OF ROCKING BUILDINGS FOR CENTRIFUGE TESTING</b> .....	<b>37</b>
3.1 INTRODUCTION.....	37
3.1.1 <i>Theory of centrifuge modelling</i> .....	37

3.2	SCOPE OF THE DESIGN .....	39
3.3	DESIGN CONCEPT AND MAIN REQUIREMENTS.....	39
3.4	EXPERIMENTAL PERFORMANCE OF BRACES.....	44
3.5	DESIGN AND PERFORMANCE OF THE FOOTING – FUSE – LINKAGE SYSTEM .....	47
3.6	SYSTEM IDENTIFICATION.....	58
3.7	SUMMARY .....	60
<b>4</b>	<b>METHODOLOGY FOR CENTRIFUGE TESTING .....</b>	<b>61</b>
4.1	INTRODUCTION .....	61
4.2	EXPERIMENTAL APPARATUS .....	61
4.2.1	<i>The Turner beam centrifuge .....</i>	<i>61</i>
4.2.2	<i>Servo – hydraulic earthquake actuator .....</i>	<i>62</i>
4.2.3	<i>Automatic sand pourer .....</i>	<i>63</i>
4.2.4	<i>Equivalent shear box.....</i>	<i>64</i>
4.3	EXPERIMENTAL PROGRAMME .....	64
4.3.1	<i>Side – by – side testing on dry sand.....</i>	<i>64</i>
4.3.2	<i>Instrumentation.....</i>	<i>65</i>
4.3.3	<i>Input excitations and spectral response .....</i>	<i>67</i>
4.4	EXPERIMENTAL IDENTIFICATION OF FREQUENCY CONTENT .....	69
4.4.1	<i>Wavelet transforms for civil engineering.....</i>	<i>69</i>
4.4.2	<i>Observation of free rocking response.....</i>	<i>70</i>
4.4.3	<i>The Morse superfamily of Wavelets and the Mexican hat.....</i>	<i>72</i>
4.4.4	<i>Step by step evaluation of Wavelet Transforms .....</i>	<i>74</i>
4.5	DESIGN VALIDATION .....	80
4.6	SUMMARY .....	82
<b>5</b>	<b>SEISMIC PERFORMANCE OF ROCKING BUILDINGS.....</b>	<b>85</b>
5.1	INTRODUCTION .....	85
5.1.1	<i>Frequency content identification .....</i>	<i>85</i>
5.1.2	<i>Observed force demand .....</i>	<i>86</i>
5.1.3	<i>Extraction of shear force demand from accelerometers .....</i>	<i>88</i>
5.1.4	<i>Base isolation effect.....</i>	<i>89</i>
5.2	EFFECT OF ROCKING TYPE ON FORCE DEMAND.....	90
5.3	EFFECT OF SAND DENSITY ON FORCE DEMAND.....	93
5.3.1	<i>Evaluation of frequency content.....</i>	<i>94</i>
5.3.2	<i>Evaluation of moment-rotation response .....</i>	<i>96</i>
5.3.3	<i>Overall effect of sand density .....</i>	<i>98</i>
5.4	SUMMARY .....	102

<b>6</b>	<b>DYNAMIC BEHAVIOUR OF SOIL.....</b>	<b>105</b>
6.1	INTRODUCTION.....	105
6.2	ANALYSIS WITH WAVELET TRANSFORMS.....	105
6.2.1	<i>Low amplitude earthquake .....</i>	<i>105</i>
6.2.2	<i>Pulse response .....</i>	<i>108</i>
6.2.3	<i>Low frequency earthquake .....</i>	<i>110</i>
6.2.4	<i>Summary of wavelet analysis .....</i>	<i>111</i>
6.3	PERFORMANCE TRADE-OFFS .....	117
6.3.1	<i>Deformations below structures in loose sand .....</i>	<i>119</i>
6.4	SUMMARY .....	121
<b>7</b>	<b>FINITE ELEMENT MODELLING FOR ROCKING BUILDINGS .....</b>	<b>123</b>
7.1	INTRODUCTION.....	123
7.2	INPUT MOTION FOR COMPUTATIONAL RESPONSE.....	123
7.3	MODELLING ASSUMPTIONS.....	125
7.3.1	<i>Modelling of superstructures.....</i>	<i>125</i>
7.3.2	<i>Modelling of column-footing connection for structural rocking .....</i>	<i>126</i>
7.3.3	<i>Modelling of soil-footing interface.....</i>	<i>128</i>
7.4	INPUT FOR THE COMPUTATIONAL MODEL .....	132
7.4.1	<i>Building and soil properties.....</i>	<i>132</i>
7.4.2	<i>Mesh properties for soil.....</i>	<i>134</i>
7.4.3	<i>Algorithm, integrator and solution convergence .....</i>	<i>134</i>
7.5	VALIDATION OF COMPUTATIONAL MODEL.....	137
7.5.1	<i>Simulation with sequential excitations with default parameters.....</i>	<i>137</i>
7.5.2	<i>Response to low magnitude excitation for dense sand .....</i>	<i>138</i>
7.5.3	<i>Response to low frequency excitation for dense and loose sand.....</i>	<i>140</i>
7.5.4	<i>Response to pulse and Kobe excitations for dense sand .....</i>	<i>142</i>
7.5.5	<i>Response to historic records .....</i>	<i>144</i>
7.6	CALIBRATION BASED ON MODAL DAMPING RATIOS AND SIGNAL METRICS.....	145
7.6.1	<i>Example of response comparison with signal metrics .....</i>	<i>146</i>
7.6.2	<i>Multi-signal scheme for response comparison.....</i>	<i>148</i>
7.6.3	<i>Calibration for response to Kobe excitation for dense sand .....</i>	<i>149</i>
7.6.4	<i>Limitations of signal metrics .....</i>	<i>152</i>
7.7	SUMMARY .....	153
<b>8</b>	<b>CONCLUSIONS .....</b>	<b>157</b>
8.1	MAIN FINDINGS .....	157
8.2	RESEARCH CONTRIBUTIONS .....	160

8.3	PRACTICAL IMPLICATIONS.....	162
8.4	FUTURE RESEARCH.....	164
<b>9</b>	<b>REFERENCES.....</b>	<b>167</b>
<b>10</b>	<b>APPENDICES.....</b>	<b>177</b>
	APPENDIX A: DESIGN OF RA & RB BUILDING MODELS.....	177
	10.A.1 <i>General eigenvalue problem, sections &amp; typical buckling checks</i> .....	177
	10.A.2 <i>Load cases</i> .....	182
	10.A.3 <i>Design of braces</i> .....	183
	10.A.4 <i>Design of connections</i> .....	186
	APPENDIX B: ESSENTIAL PARTS OF BUILDING MODELS RA & RB.....	194
	APPENDIX C: ESSENTIAL PARTS OF ENERGY DISSIPATION ELEMENT.....	200
	APPENDIX D: BEHAVIOUR OF TAPERED AND NON – TAPERED BEAMS.....	202
	APPENDIX E: WAVELET TRANSFORMS WITH VARYING MORSE WAVELET.....	203
	APPENDIX F: EXPERIMENTAL RESPONSES.....	204
	APPENDIX G: COMPUTATIONAL RESPONSES.....	232

## LIST OF FIGURES

Figure 1.1: Photos of the South Rangitikei Viaduct in New Zealand. The two main piers are able to uplift and rock (a, Chen et al., 2006, and b, Palmeri & Makris, 2008).....	2
Figure 1.2: A rocking nine-story steel frame (a) and a detail of the column (b) which is allowed to uplift (Huckelbridge, 1977).....	3
Figure 1.3: Inspired by the Japanese pagodas (a, Brown, 2009), the controlled stepping mechanism of the Maison Hermes (b, left building, Renzo Piano Building Workshop 1998).....	3
Figure 1.4: A typical bridge pier of the Rion-Antirion Bridge (a) and the failure mechanism (b, Combault, Morand and Pecker, 2000).....	4
Figure 1.5: A flexible frame rocking on a rigid base.....	5
Figure 1.6: Building with rocking above the foundation level (a) and building with rocking below the foundation level (b).....	7
Figure 2.1: A rocking rigid block (a) and its amplitude ( $\theta_0$ ) dependent period (T) by Housner (b, 1963).....	13
Figure 2.2: A free-standing rocking bridge bent (a), inspired from ancient structures such as the Temple of Aphaia in Aegina, Greece (b, Makris, 2014).....	13
Figure 2.3: A dual frame rocking on a rigid level with post-tensioning and fuses yielding in shear (Ma et al., 2010).....	16
Figure 2.4: Bridge pier retrofitted with stable hysteretic BRB (a, Pollino & Bruneau 2007) and viscously damped braced frame (b, Tremblay et al. 2008).....	16
Figure 2.5: Reduction of the shear force coefficient against the slenderness of a flexible superstructure rocking on a rigid base (Meek, 1975).....	17
Figure 2.6: Time history response of a slender structure to the El Centro earthquake (a, b) and spectrum (c) for flexible structures with different slenderness ( $u_c$ is the critical displacement required for uplift, Chopra & Yim, 1985).....	18
Figure 2.7: The conventional capacity design (a) and the rocking isolation design (b, F. Gelagoti et al., 2012).....	21
Figure 2.8: A typical candidate building for centrifuge modelling (Mason et al., 2010)...	22
Figure 2.9: Structure models: (a) midrise elastic shear wall with mat foundation; (b) low rise inelastic frame structure founded on spread footings (Trombetta <i>et al.</i> , 2013).....	22

Figure 2.10: A symmetric foundation rocking dominated frame (sFRD) and a symmetric balanced designed frame (sBD) with fuses (top) and their cyclic response envelopes at different imposed drift ratios (Liu <i>et al.</i> , 2015).....	23
Figure 2.11: Elevation view of the baseline stone column-reinforced foundation-soil system (a), response comparison between the improved and unimproved cases: moment-rotation (b); settlement-rotation (c, solid circle identifies the residual location, Liu and Hutchinson, 2018).....	24
Figure 2.12: Settlement caused by cyclic rotation from cyclic and dynamic tests on a cyclic basis (Gajan <i>et al.</i> , 2005).....	25
Figure 2.13: Settlement caused by rotation on a cumulative basis (Gajan and Kutter, 2008; Deng, Kutter and Kunnath, 2012).....	25
Figure 2.14: Behaviour of two very stiff (rigid) structures on dense and loose sand (Heron, Haigh and Madabhushi, 2014).....	25
Figure 2.15: Settlement-rotation behaviour on for relative density 80% (a) and for relative density 50% (b, Heron <i>et al.</i> 2014).....	26
Figure 2.16: A small scale three storey flexible rocking frame (a) with its pad footings resting on the sand (b) and with its footings fixed on a very stiff base (c, d). The corresponding third storey acceleration responses from forced rocking are also shown (Pelekis, 2015).....	27
Figure 2.17: Vertical accelerations close to the impact point from free rocking (a), from small amplitude harmonic base excitation (b) and from high amplitude harmonic base excitation (c, Pelekis 2015). 3 and 5mm is the stroke of the harmonic excitation .....	28
Figure 2.18: Impedance models for damping ratio of a half-space of soil versus measured values extracted from free vibration tests from laboratory-scaled models (Dobry and Gazetas, 1986; NEHRP Consultants Joint Venture, 2012).....	29
Figure 2.19: Structural rocking (left) and foundation rocking (right) .....	35
Figure 3.1: The two building models, RA (left) and RB (right).....	40
Figure 3.2: Connection for partially hinged support and structural rocking, RA (a) and connection for fixed support and foundation rocking, RB (b) .....	40
Figure 3.3: Mathematica model in prototype scale (a) and final design dimensions in model scale (b) in elevation .....	43
Figure 3.4: <i>SAP2000</i> model for the prototype structure.....	43
Figure 3.5: Plan view of the buildings models RA and RB with respect to the centrifuge box.....	44

Figure 3.6: The design spectrum used for designing the structural members at the onset of uplift (CEN 2004a, damping ratio: 5%).....	44
Figure 3.7 Loaded specimens in the Instron Load Frame (a, thick walled bracing and b, thin walled bracing right).....	45
Figure 3.8: Loading protocol for the thick brace of the bottom storey (a) and similarly for the thin brace of the top storey (b) .....	46
Figure 3.9 Buckling strength and connection tensile strength for the bracing elements. Buckling limits were set conservatively in the design.....	48
Figure 3.10: A tapered plate for energy dissipation connected to the base of a rocking chimney (a, Tyler, 1978) and analogous plate with connection rod for model RA (b) .....	49
Figure 3.11: The connection rod, the fuse and strain gauged cantilevers for model RA ..	50
Figure 3.12: Tapered beam (plate) simulation with material and geometric non-linearities.....	50
Figure 3.13: Force-displacement diagram for guidance on the FE simulation .....	51
Figure 3.14: Stress-strain models for S275 adopted from Byfield <i>et al.</i> (2005) for FE predictions .....	51
Figure 3.15: Force-displacement diagram of the connection-plate subsystem for various initial angles (top) of the connection bar .....	52
Figure 3.16: Loading protocol for the top hinge in the vertical direction (a) and similarly in the horizontal direction (b) for the FE simulation .....	53
Figure 3.17: Force-displacement diagram for the vertical (shear) reaction (a) moment-displacement diagram (b) and force-displacement diagram for the axial reaction (c) at the root of the cantilever based on FE simulations.....	54
Figure 3.18: Estimation of stress magnitude under the footing and of the contact length with respect to the width of the footing under the cyclic behaviour of the fuse based on FE predictions .....	56
Figure 3.19: Loading of the plate element with the connection rod in the Instron Load Frame .....	57
Figure 3.20: The loading protocol that was used in the experiment and the FE predictions. ....	57
Figure 3.21: Deformed shape in maximum displacement (experiment-a, FE simulation-b), force vector analysis for comparison of results (c) and force-displacement diagram for the experimental result and FE prediction of the resultant root reaction parallel to the Instron vertical load (d).....	58

Figure 3.22: Obtained modal damping ratios from fixed base free vibrations.....	60
Figure 4.1: The Turner beam centrifuge in Cambridge.....	62
Figure 4.2: The Cambridge servo-hydraulic actuator (Madabhushi <i>et al.</i> , 2012).....	63
Figure 4.3: Preparation of a cylindrical sample to verify the specific density achieved with the automatic sand pourer (a) and design chart for Hostun sand (b, Chian, Stringer and Madabhushi, 2010) .....	63
Figure 4.4: Equivalent shear beam box.....	64
Figure 4.5: Cross-sectional view of the centrifuge model with overall dimensions (a) and view when fully prepared (b).....	66
Figure 4.6: Examples of instrumentation: MEMS accelerometer with special column attachment (a), piezoelectric accelerometers placed during sand pouring (b), and strain gauges attached at the bottom braces (c) .....	68
Figure 4.7: Spectral response near the soil free surface for $\zeta=5\%$ .....	69
Figure 4.8: Storey lateral accelerations and column ends vertical accelerations and their FFT (top two rows), excitation time-history with FFT (third row), and close-up at free rocking (bottom row) for model RA.....	71
Figure 4.9: The generalized Morse wavelets in time for $\gamma = 1-4$ and $\beta = 0-3$ are shown in the first four columns, while the fifth column shows the frequency domain for $\gamma = 1-4$ for the different values of $\beta$ (Lilly and Olhede, 2009).....	72
Figure 4.10: Selected wavelets and their FFTs within the time and frequency domains considered for the experiment .....	73
Figure 4.11: Time-frequency maps of different wavelet transforms for the lateral accelerations of model RA .....	75
Figure 4.12: Time-histories and time-frequency maps of the vertical accelerations at the columns ends of model RA .....	78
Figure 4.13: Close-up at the time-histories and time-frequency maps of the vertical accelerations at the columns ends of model RA.....	79
Figure 4.14: Loose sand, Test-1, Eq-4: Time-history of the axial force of the bottom braces for model RA (a) and similarly for model RB (b).....	81
Figure 4.15: Loose sand, Test-1, Eq-4: Axial load versus storey drift ratio for top storey (a) and bottom storey (b) for model RA and similarly for model RB (c, d).....	81
Figure 4.16: Loose sand, Test-1, Eq-4: Axial load versus rocking angle for top storey (a) and bottom storey (b) for model RA and similarly for model RB (c, d).....	82

Figure 5.1: Dense sand, Test-1 Eq-3: Pulse excitation (a, b), vertical acceleration response of model RA (c), storeys' time-frequency response of model RA (d-g) and similarly for model RB (h-l) .....	87
Figure 5.2: Observed force demand normalized to each building model's weight across all earthquakes for both types of sand (Tests-1, 2 Dense and Loose sand).....	88
Figure 5.3: Base shear difference with the SRSS linear elastic solution.....	89
Figure 5.4: Percentage difference of the experimental base shear with the average SRSS solution against the peak rocking angle for dense sand (left) and loose sand (right).....	90
Figure 5.5: Dense sand, Test-2 Eq-4: Lateral force demand of model RA from accelerometers and bottom braces (a), RA storey lateral response (b), RA column vertical response (c), soil and RA footing lateral response (d), and similarly for model RB (e-h)	91
Figure 5.6: Loose sand, Test-2 Eq-4: Force demand of model RA from accelerometers and bottom braces (a), RA storey lateral response (b), RA column vertical response (c), soil and RA footing lateral response (d), and similarly for model RB (e-h).....	93
Figure 5.7: Test-2 Eq-4: Input for dense sand (a) and time-frequency map (b), RA top storey response (c) and time-frequency map (d), RB top storey response (e) and time-frequency map (f), and similarly for loose sand (g-l).....	95
Figure 5.8: Restraining moment versus rocking angle for dense (left) and loose (right) sand for the Kobe excitation. Horizontal lines indicate static overturning moment.....	97
Figure 5.9: Restraining moment versus rocking angle for dense (left) and loose (right) sand for a low frequency, cyclic excitation. Horizontal lines indicate static overturning moment .....	97
Figure 5.10: Effect of the impact on the peak total external force for both storeys, for dense (left) and loose (right) sand. Fitting parameters are presented only for large peak rocking angles.....	98
Figure 5.11: Peak drift ratios against peak rocking angle for the top (a) and bottom (b) storeys for dense sand and similarly in loose sand (c, d). Low and high damage regions (LD, HD) are annotated.....	99
Figure 5.12: Loose sand, Test-1 Eq-5: Vertical acceleration response of model RA (a) and force time-history for model RA (b). Black circles are pairs of impact acceleration-force demand.....	100
Figure 5.13: Effect of the impact on the peak total external force, for dense (left) and loose (right) sand. Dashed lines indicate the slenderness values according to Table 3.2.....	101

Figure 6.1: Time history (a) and time-frequency map (b) of the excitation measured at the base of the centrifuge box.....	106
Figure 6.2: Bottom storey lateral acceleration and time-frequency map (a, b) for model RA and similarly for model RB (c, d) .....	106
Figure 6.3: Time history and time-frequency map of column vertical accelerations (a, b), time history and time-frequency map of soil vertical accelerations (c, d) for model RA and similarly for model RB (e-h) .....	107
Figure 6.4: Time history (a) and time-frequency map (b) of the excitation measured at the base of the centrifuge box.....	108
Figure 6.5: Bottom storey lateral acceleration and time-frequency map (a, b) for model RA and similarly for model RB (c, d) .....	109
Figure 6.6: Time history and time-frequency map of column vertical accelerations (a, b), time history and time-frequency map of soil vertical accelerations (c, d) for model RA and similarly for model RB (e-h) .....	110
Figure 6.7: Schematic diagram of wave propagation from structures to the soil and identified zone of influence due to dynamic soil-structure interaction .....	111
Figure 6.8: Dense sand Test-2 Eq-4: Time-frequency maps of the excitation as it propagates from the base of the centrifuge box to the bottom storey of the building models .....	112
Figure 6.9: Dense sand Test 2 EQ 4: Example of high frequency area definition (a) and cut-off frequencies $f_h$ in model scale (b) .....	114
Figure 6.10: Ratio of energy of high frequency area over the energy of the input motion wavelet transform at the surface (a), mid-height (b) and base level (c) for dense sand and similarly at loose sand (d-f) for the accelerometer arrays A and B (see Figure 6.7) .....	114
Figure 6.11: Relative ratio of high frequency energy (a), high frequency energy ratio with respect to the input motion (b), low frequency energy ratio with respect to the input motion (c) and total energy ratio with respect to the input motion (d) for dense sand for each pair of vertical accelerometers ( $j = 1, 2$ , Figure 6.7) below building RA and RB....	116
Figure 6.12: Relative ratio of high frequency energy (a), high frequency energy ratio with respect to the input motion (b), low frequency energy ratio with respect to the input motion (c) and total energy ratio with respect to the input motion (d) for loose sand for each pair of vertical accelerometers ( $j = 1, 2$ , Figure 6.7) below building RA and RB....	117

Figure 6.13: Test 2 EQ 3: 50 Hz pulse excitation (a), rocking amplitude (b) and soil vertical differential displacement (c) for models RA and RB for dense sand, and the equivalent results for loose sand (d-f).....	118
Figure 6.14: Relationship between maximum normalized soil differential displacement and maximum rocking angle for models RA and RB for dense (a) and loose sand (b) ..	119
Figure 6.15: Loose sand Test 2 EQ 2: Restraining moment versus rocking angle for model RA (a), foundation moment vs foundation rotation for model RA (b) and restraining moment versus rocking angle for model RB (c) for an Imperial Valley excitation .....	120
Figure 6.16: Loose sand Test 2 EQ 4: Restraining moment versus rocking angle for model RA (a), foundation moment vs foundation rotation for model RA (b) and restraining moment versus rocking angle for model RB (c) for a low frequency cyclic excitation ..	120
Figure 7.1: Loose sand Test-2 Eq-4: Time-history and wavelet transform of acceleration at base of centrifuge box (a, b), at surface below RA (c, d), between the buildings (e, f), below RB (g, h) and lateral side of the centrifuge box (i, j). See also Figure 4.5a for sensor location .....	124
Figure 7.2: Basic element discretization (a) and refined configuration (b) for model RA (see Figure 7.3 for soil-footing-column detail) .....	126
Figure 7.3: Modelling of an RA footing (a) and an RB footing (b) for structural and foundation rocking, respectively, with the mBNWF model, and typical application of the BNWF model for an RB footing (c) (Raychowdhury and Hutchinson, 2009).....	127
Figure 7.4: The friction-gap element <i>flatSliderBearing</i> (a) with a force-displacement law relating the sliding and axial responses (b) (Schellenberg, 2014).....	127
Figure 7.5: Dense sand, Test-1 Eq-6: Trajectory of column ends of model RA as obtained by using inclined friction-gap elements .....	128
Figure 7.6: Typical behaviour of the elements of the BNWF model with material laws as defined by Raychowdhury and Hutchinson (2009).....	128
Figure 7.7: Loose sand, Test-1 Eq-5: Sequence of displacements for model RB when the BNWF model (a-f) and the mBNWF models are used (g-l).....	129
Figure 7.8: Loose sand, Test-1 Eq-4: Footing forces with respect to building rocking angle when the BNWF model is employed (a) and similarly when the proposed modified model is employed (b) for RA.....	131
Figure 7.9: Loose sand, Test-1 Eq-5: Footing forces with respect to building rocking angle when the BNWF model is employed (a) and similarly when the proposed modified model is employed (b) for RB.....	131

Figure 7.10: Loose sand, Test-1 Eq-5: Interaction diagrams for the forces below the left and right footings below models RA and RB when the BNWF model (a) and the mBNWF model (b) are used .....	132
Figure 7.11: Loose sand, Test-1 Eq-5: Lateral relative displacement of the end node of the left column for model RB (see instrument BFH1 in Figure 4.5).....	132
Figure 7.12: Loose sand, Test-1 Eq-1: Bottom storey acceleration (a) and rocking angle (b) for model RA for different combinations of $\beta, \gamma$ .....	135
Figure 7.13: Effect of time step on the numerical response of model RA (a-e) and similarly for model RB (e-h).....	136
Figure 7.14: Summary of footing residual rotations for different output frequencies for dense sand (a) and loose sand (b).....	136
Figure 7.15: Dense sand, Test-0 Eq-6: Top storey acceleration (a) and rocking angle (b) for model RA when the excitation and response are treated separately, and similarly for model RB (c, d).....	138
Figure 7.16: Dense sand, Test-0 Eq-4: Top storey (a), bottom storey (b), rocking angle (c) and left column experimental and numerical responses (d) for default set of parameters for model RA and similarly for model RB (e-h). Time-frequency maps of the vertical accelerations at columns are also included.....	139
Figure 7.17: Dense sand, Test-0 Eq-6: Top storey (a), bottom storey (b), rocking angle (c) and left column experimental and numerical responses (d) for default set of parameters for model RA and similarly for experimental and calibrated numerical response (e-h) .....	140
Figure 7.18: Test-2 Eq-4: Top storey accelerations (a) and rocking angle (b) responses for experimental and numerical simulations using default modelling parameters for model RA in dense sand (a, b), in loose sand (c, d), and for dense sand with calibrated damping parameters (e-f): $(\zeta_1, \zeta_2) = (0.04, 0.06)$ .....	141
Figure 7.19: Test-2, Eq-4: Top storey accelerations and rocking angles for experimental and numerical simulations using default modelling parameters for model RB in dense sand (a, b) and similarly in loose sand (c, d) .....	142
Figure 7.20: Dense sand, Test-2, Eq-1: Top storey (a) and rocking angle (b) experimental and numerical responses for default set of parameters for model RA and similarly for model RB (c, d).....	143

Figure 7.21: Dense sand, Test-2, Eq-3: Top storey (a) and rocking angle (b) experimental and numerical responses for default set of parameters for model RA and similarly for model RB (c, d).....	143
Figure 7.22: Peak drift ratios against peak rocking angle for the top and bottom storeys for RA and RB for dense sand (a, b) and similarly for loose sand (c, d).....	145
Figure 7.23: Loose sand Test-1 Eq-3: Lateral acceleration response for top storey for model RA for $(\zeta_1, \zeta_2) = (0.02, 0.04)$ (a) and for $(\zeta_1, \zeta_2) = (0.03, 0.07)$ (b) and similarly for Test-1 Eq-1 for $(\zeta_1, \zeta_2) = (0.06, 0.03)$ (c) and $(\zeta_1, \zeta_2) = (0.07, 0.07)$ (d) .....	148
Figure 7.24: Dense sand, Test-2, Eq-1: Top storey (a), bottom storey (b) and rocking angle (c) experimental and numerical responses for model RA for typical set of modal damping ratios and similarly for optimum modal damping rations (d-f) .....	149
Figure 7.25: Dense sand, Test-2, Eq-1: Top storey (a), bottom storey (b) and rocking angle (c) experimental and numerical responses for model RB for typical set of modal damping ratios and similarly for optimum modal damping rations (d-f) .....	150
Figure 7.26: Contour plot of the <b>RWTC</b> score for each test for model RA in dense sand (a-c) and similarly for model RB (e-g). Circles without dots in their centre indicate analyses that did not converge.....	151
Figure 7.27: Contour plot of the of the <b>RWTC</b> global score for each test for model RA in loose sand (a, b) and similarly for model RB (e, f). Circles without dots in their centre indicate analyses that did not converge.....	152
Figure 7.28: Dense sand, Test-1, Eq-6: Top storey (a, d), bottom storey (b, e) and rocking angle (c, f) experimental and numerical responses for model RB for two different sets of modal damping ratios .....	153
Figure 10.1: Static approach in the half frame (hence, forces are factored with $\frac{1}{2}$ ) for estimating the loadings due to extreme rotation.....	182
Figure 10.2: Slot connection for the column to the footing.....	188
Figure 10.3: Connection of the PETG bracing element to the aluminium volume (bottom) and typical shear mode failure (top) .....	189
Figure 10.4: Connection of bracing element to the column.....	191
Figure 10.5: Seismic bending moment diagram (top) and connection of the column to the slab (bottom) .....	192
Figure 10.6: Detail of the aluminium part for the connection of top storey bracing.....	193
Figure 10.7: Force–displacement diagram for equal volume beams in bending.....	202

Figure 10.8: Dense sand, Test-1 Eq-3: Top storey lateral acceleration response of model RA and time-frequency maps for different values of the  $\beta$ ,  $\gamma$  parameters of the Morse wavelet.....203

Figure 10.9: Dense sand, Test-2 Eq-4: Top storey lateral acceleration response of model RA and time-frequency maps for different values of the  $\beta$ ,  $\gamma$  parameters of the Morse wavelet.....203

## LIST OF TABLES

Table 2.1: Categories of rocking structures according to their characteristic source of energy dissipation .....	12
Table 2.2: Attributes, experimental validation and original development purpose of common BNWF models and of the proposed model. Arrows indicate vertical and horizontal directions .....	31
Table 2.3: Summary of the literature review for rocking structures on rigid base.....	33
Table 2.4: Summary of the literature review for rocking structures on flexible supports .....	34
Table 2.5: Summary of the literature review for rocking foundations and soil -structure interaction.....	34
Table 2.6: Contributions from this thesis .....	36
Table 3.1 Scaling laws for centrifuge testing (Madabhushi, 2017) .....	38
Table 3.2: Design properties of the two rocking building models, RA and RB.....	42
Table 3.3: Summary of selected results from cyclic and monotonic tests.....	47
Table 3.4: Strain rates for bracing elements in prototype and model scales.....	49
Table 3.5: Summary of system identification .....	59
Table 4.1: Overview of experimental sets conducted in centrifuge conditions.....	64
Table 4.2: Programme with soil and input motion characteristics of the experimental set IP03 (Dense sand) and IP04 (Loose sand).....	67
Table 7.1: Input properties with default values (in prototype scale) .....	134
Table 10.1: Selection of steel bolts (EC9, Table 8.1, Table 8.5, (8.9) & (8.17)) .....	186
Table 10.2: Properties and analytic equations.....	202



# NOMENCLATURE

$\alpha$	Angle of slenderness for a rocking building model
$\alpha$	Contact length of footing
$a_c$	Acceleration generated from centrifuge at the radial direction
$\beta, \gamma$	Constants controlling the number of oscillations and the family of a Morse wavelet, respectively (Chapters 4-6), and Newmark integration constants (Section 7.4.3)
$\gamma$	Shear strain of soil
$\gamma$	Soil unit weight (Section 7.4.1)
$\delta$	Free end forced displacement from the FE simulation of the fuse element
$\varepsilon_b$	Strain to the buckling load
$\dot{\varepsilon}_b$	Strain rate to the buckling load
$\zeta_x, \zeta_y$	Damping ratios for radiation damping in the horizontal and vertical directions respectively
$\zeta_1, \zeta_2$	Modal damping ratios for the first and second mode, respectively
$\theta, \theta$	Rocking angle
$\mu$	Coefficient of friction for a system with aluminium surfaces
$\nu$	Poisson's ratio of soil
$\pi$	Ratio of a circle's circumference to its diameter
$\rho_{y,h}$	Normalized value of $E_{y,h}$ to $E_{y,tot}$
$\sigma_y$	Yield stress of steel S275
$\sigma'_m$	Mean principal effective stress
$\sigma_1, \sigma_2, \sigma_3$	End stresses for stress profile under a footing
$\tau$	Auxiliary variable for time integration
$\varphi'$	Friction angle of sand
$\varphi'_{crit}$	Friction angle of sand at critical state
$\varphi_1, \varphi_2$	Shape of first mode and second mode, respectively
$\psi_{\beta,\gamma}$	A Morse wavelet based on the values $\beta, \gamma$
$\omega$	Angular velocity of centrifuge (Chapter 3) and circular frequency (Chapters 4-6)
$\Delta d$	Transient differential settlement as obtained from the vertical accelerometers below the footings of a rocking building model
ag	Design ground acceleration (EC8)
$b$	Width of footing
$c$	Cohesion of soil
<b>c</b>	Damping matrix for a rocking building model
$c_x, c_y$	Radiation damping in the horizontal and verticals direction, respectively
$c_{x,i}, c_{y,i}$	Radiation damping in the horizontal and vertical directions, respectively, calculated according to Gazetas (1991)
$e$	Base of natural logarithm, void ratio of sand (Chapter 7)
$f$	Frequency
$f_c$	Cut-off frequency for wavelet transform coherence
$f_h$	Cut-off frequency specifying area of wavelet transform with high frequency content
$f_{o,c}$	Centrifuge sampling frequency at model scale
$f_o$	Solution and output sampling frequency of computational response
$f_u$	Upper frequency limit for integration of wavelet transforms across frequency
<b>g</b>	Earth's gravity acceleration
$h$	Height of footing

$i$	Unit imaginary number (Chapter 4), depth of soil accelerations in centrifuge box (Chapter 6), type of response considered when comparing experimental and computational response match
$j$	Refers to the position of the accelerometer measuring vertical acceleration below each footing of each rocking building, $j = 1$ left footing, $j = 2$ right footing
$l$	Length of a footing
$l_e/b$	Spring spacing ratio
mBNWF	Modified Beam-on-nonlinear-Winkler-Foundation model
$m$	Refers to mode number ( $m = 1$ , first mode, $m = 2$ , second mode)
$m_n$	Lumped mass of slab $n$
$\mathbf{m}$	Lumped mass matrix for a rocking building model
$m(\gamma)$	Shear strain dependent parameter for calculation of calculation of $G_{max}$
$n$	Definition for slabs of the rocking building models, $n = 1$ bottom slab and $n = 2$ top slab
$p_a$	Atmospheric pressure
$q$	Behaviour factor (EC8)
$q$	Pressure at the footing's surface due to static loading
$r$	Radius of centrifuge
$r_{x,h,i}$	Normalized value of high frequency contribution on signal energy from wavelet transform of soil acceleration at depth $i$ in the lateral direction to the signal energy from wavelet transform of the input motion
$r_y$	Normalized value of $E_{y,tot}$ to the signal energy from wavelet transform of the input motion
$r_{y,h}$	Normalized value of $E_{y,h}$ to the signal energy from wavelet transform of the input motion
$r_{y,l}$	Normalized value of $E_{y,l}$ to the signal energy from wavelet transform of the input motion
$s$	Scale parameter for wavelet transforms
$t$	Time
$u_{r,n}$	Relative displacement at the slab $n$
$u_{t,n}$	Total displacement at the slab $n$
$x$	Example signal
$A(\gamma)$	Shear strain dependant parameter for calculation of calculation of $G_{max}$
$B$	Semi-width of the superstructure of a rocking building model
BNWF	Beam-on-nonlinear-Winkler-Foundation model
$CoD$	Coefficient of determination
$D_r$	Relative density of sand
$E$	Young's modulus for PETG referring to the value obtained from axial tests
$E_{x,h,i}$	Signal energy with high frequency components from wavelet transform of soil acceleration at depth $i$ in the lateral direction
$E_{x,i}$	Multiple of signal energy from wavelet transform of soil acceleration at depth $i$ in the lateral direction
$E_{y,h}$	Energy with high frequency components from wavelet transforms of vertical accelerations in the soil below the footings of a rocking building model
$E_{y,l}$	Energy with low frequency components from wavelet transforms of vertical accelerations in the soil below the footings of a rocking building model
$E_{y,tot}$	Total energy from wavelet transforms of vertical accelerations in the soil below the footings of a rocking building model
$F_{E,n,x}$	External force of slab $n$ in lateral direction
$F_{E,x}$	Total external force in lateral direction
$F_{D,n}$	Storey damping force with reference to slab $n$
$F_p$	Vertical reaction of the fuse element at the root

$F_{S,n}$	Storey shear forces with reference to slab $n$
FFT	Fast Fourier transform
$FoS$	Factor of safety for vertical loading for a footing
$G_{max}$	Maximum shear modulus of soil
$G_0$	Initial shear modulus of soil
$H_n$	Building elevation of the slab $n$
$K$	Constant based on the void ratio for calculation of $G_{max}$
$M_m$	Modal mass with reference to mode $m$
$M_p$	Moment reaction of the fuse element at the root
$N_g$	Multiple of Earth's gravity acceleration $g$
$N_p$	Horizontal force reaction of the fuse element at the root
$N_R$	Tie rod force
$N_s$	Frictional resistance from soil
$R^2$	Coefficient of determination of fitted trends to sets of data points
RA	Building model rocking above its foundation level and representing structural rocking
RB	Building model rocking below its foundation level and representing foundation rocking
$PRC$	Periodogram based coherence
$Q$	Horizontal load distribution factor
$R_{CoD},$ $R_{PRC},$ $R_{WTC}$	Values of $CoD, PRC, WTC$ normalised to their maximum values, respectively.
$R_e$	Definition of end length of a footing
$R_k$	Definition of end stiffness intensity
$R_{WTC,i}$	Main signal match indicator
$S$	Factor for soil type (EC8)
$S_a$	Spectral acceleration (EC8)
$SC_{Eq}$	Average score of signal matching for a sequential excitation $Eq$
$SC_T$	Global score of a test $T$ with sequential excitations
SDoF	Single-degree of freedom system
S/N	Signal to noise ratio
$T_1$	First mode
$W$	Wavelet transform
$W$	Weight of a rocking building model
$W_F$	Weight of a footing
$W_{x,i}$	Wavelet transform of soil acceleration at depth $i$ for the lateral direction
$W_{y,j}$	Wavelet transform of soil acceleration at position $j$ for vertical direction
$WTC$	Wavelet transform coherence
2DoF	Two-degree of freedom system



# 1 INTRODUCTION

## 1.1 Global context

Earthquake engineering has developed tremendously over the last decades. Experiences from previous earthquakes and extensive research at the global scale have led to the establishment of successful practices for protecting human lives from catastrophic collapse of buildings. This success comes from a basic recognition of the earthquake engineering community, that to ensure a building survives an earthquake, large amounts of damage may be necessary, to allow the earthquake's energy to be dissipated by the building. In addition, some buildings are more important than others (for example a hospital versus a warehouse) so acceptable performance levels must be associated with the importance of a building (Hamburger *et al.*, 2012). Nevertheless, in earthquakes of large magnitude the design approach of damage tolerance may result in unsatisfactory performance of buildings in terms of repairing costs, downtime and business disruption, despite protecting human lives effectively. Consequently, stakeholders in the built environment and infrastructure increasingly ask for structures that are readily repairable after major earthquakes. An example is the catastrophic Christchurch earthquake in New Zealand, which led building owners and managers to opt for increased seismic performance and damage mitigation technologies to avoid disruption, economic losses and dependence on insurance in future earthquakes (Marquis *et al.*, 2015). In Chile's 2010 earthquake, although the majority of building stock performed well, it was concluded that "*efforts still need be made for better construction practices*", while the economic losses reached a third of the country's gross domestic product (Franco and Siembieda, 2010). It is therefore clear that the design objectives are becoming more advanced, taking into account the economic and social implications of earthquake events.

In response to these constantly evolving requirements, earthquake engineering is transitioning from allowing damage in ductile buildings to systems which are isolated from the ground motion, either through large bearings, or by the allowance of sliding or uplifting. Uplifting systems are becoming increasingly popular because they avoid being excited by mobilizing a negative stiffness upon uplift, effectively resulting in uncoupling from an earthquake motion. It is thus the scope of this research to examine uplifting, or rocking systems as a means of base isolation.

## 1.2 Background on rocking systems

Modern structures that can rock on their base are in fact rare around the world, since the philosophy of rocking is radically different to the philosophy of most design guidelines. The first modern structure, and probably the most frequently referred to, that was built as a rocking system was the South Rangitikei Viaduct in New Zealand in 1981 (Figure 1.1).

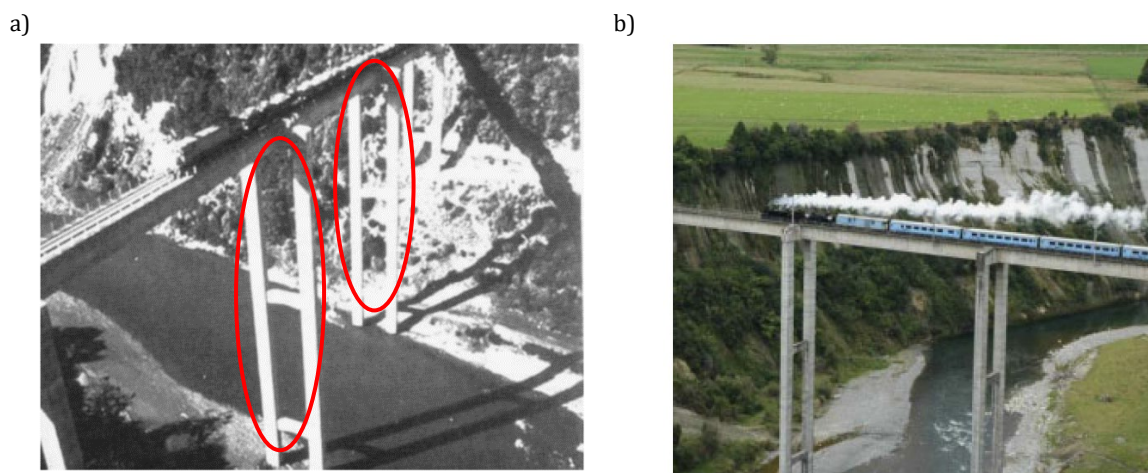


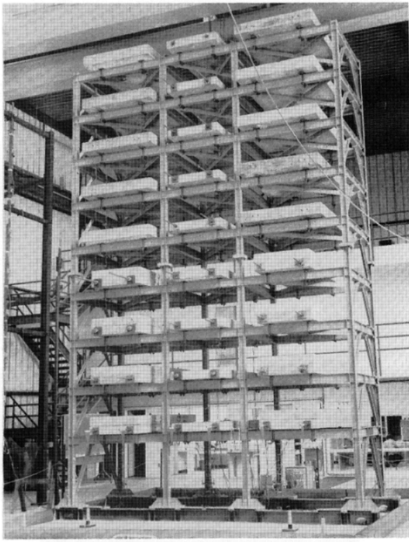
**Figure 1.1: Photos of the South Rangitikei Viaduct in New Zealand. The two main piers are able to uplift and rock (a, Chen *et al.*, 2006, and b, Palmeri & Makris, 2008)**

This structure exemplifies the philosophy of a rocking mechanism for seismic protection, because in the transverse direction the two central and slenderest piers are allowed to step. Each column of the pier alternatively uplifts and separates from the pile cap under earthquake excitation (Chen *et al.*, 2006).

Even before the South Rangitikei Viaduct, researchers focused on major experiments investigating the rocking response of nearly full-scale buildings under ground shaking. Such an example is the shaking table test of a nine story building in Berkeley (Huckelbridge, 1977). As Figure 1.2 shows, the columns of the frame are allowed to uplift from the foundation beam while they are connected to a flexural plate to ensure they do not step out of the foundation. Pads are also used to accommodate the impact of the

column when it returns to the foundation beam. Another example, inspired by the ancient Japanese structures, is the Maison Hermes in Tokyo, the columns of which are allowed to step in a controlled way by installing dampers on the interface between foundation and column (Figure 1.3, Piano, 1998; Brown, 2009).

a)



b)

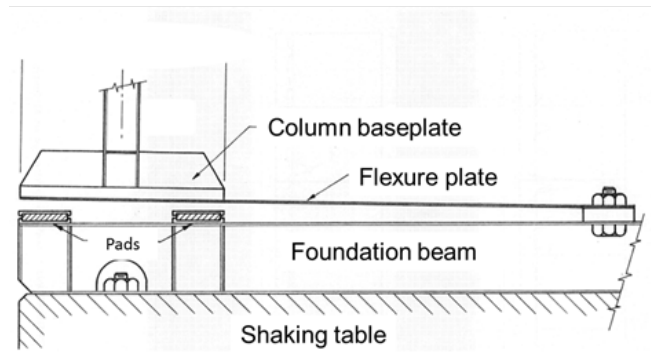
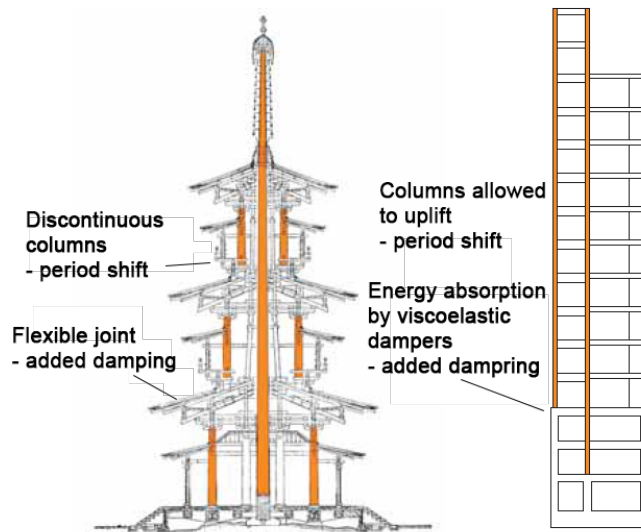


**Figure 1.2: A rocking nine-story steel frame (a) and a detail of the column (b) which is allowed to uplift (Huckelbridge, 1977)**

a)



b)



**Figure 1.3: Inspired by the Japanese pagodas (a, Brown, 2009), the controlled stepping mechanism of the Maison Hermes (b, left building, Renzo Piano Building Workshop 1998)**

The above examples could be termed as structural rocking. However, there is also a growing consensus that soil could serve as an energy dissipating base, on top of which foundations are allowed to uplift, rock and even slide. An example of this design philosophy is the bridge pier of the Rion-Antirion Bridge (Figure 1.4) in Greece (Combault, Morand and Pecker, 2000).

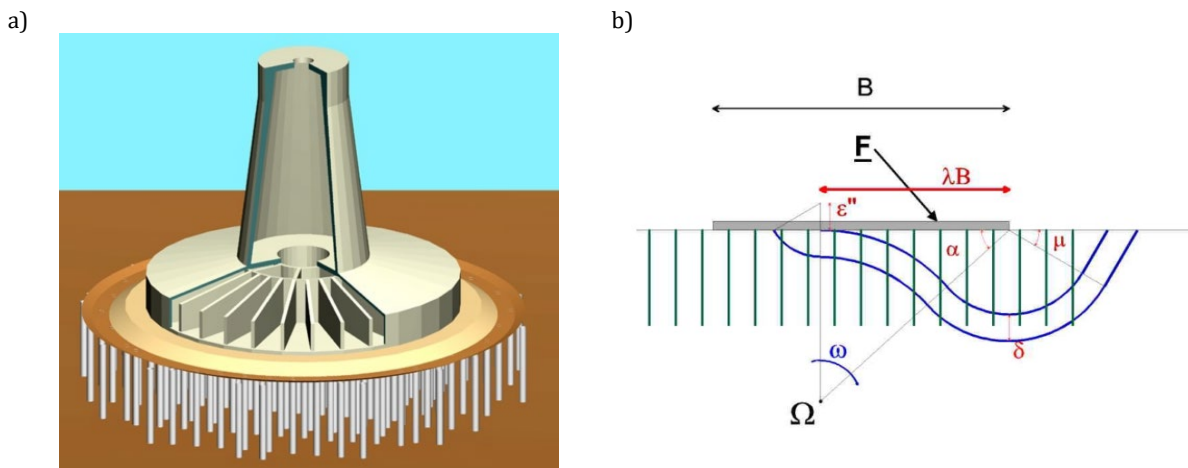


**Figure 1.4: A typical bridge pier of the Rion-Antirion Bridge (a) and the failure mechanism (b, Combault, Morand and Pecker, 2000)**

In general, rocking takes place once the lateral force required to cause uplift of the one side of a frame, has developed as a result of an earthquake motion. Allowing for uplift limits the internal forces induced to the superstructure since there is no connection to the foundation to provide tensional resistance to the uplifting superstructure. During uplift of the one side, the structure is practically supported by a limited area on the other side and vibrates at the same time (Figure 1.5). Meanwhile, the self-weight acts as a restoring force to return the frame to its initial position. The frame may then continue to rock back and forth, effectively protecting its attached superstructure from experiencing internal damage, while some of the ground motion energy is dissipated in the form of impacts between the foundation and the superstructure during the re-centring process. The uplifting sequence continues until the earthquake terminates and the rocking and structural vibration are damped out. There are many variations of the example described above. For example, the restoring force can be enhanced by post-tensioned cables that run along the height of the structure (see Section 2.2.2). The energy dissipation capability can also be enhanced with the addition of special fuses. However, adding fuses that are too stiff and strong can actually attract more energy, reducing the benefit of pure rocking motion.

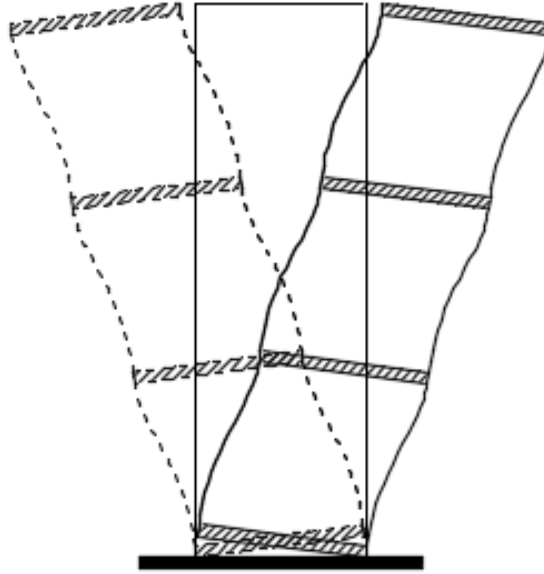


**Figure 1.5: A flexible frame rocking on a rigid base**

Limiting the internal forces due to the uplift results in smaller sections with less material. Therefore, rocking systems can be part of a sustainable future, in which not only economical structures are built, but fewer resources could be spent in retrofitting. Of course, this potential would only be realized if rocking systems were used extensively. At this time they are not, as they have not been fully understood and reliable design guidelines do not exist.

### 1.3 Motivation

Accelerations of rocking systems mainly develop from two sources. The first source is the direct ground shaking which excites the superstructure as seismic waves propagate from the soil to the structure. The second source that contributes to the acceleration demand is the impact caused by the superstructure on the foundation (Figure 1.5). Being able to predict the acceleration demands accurately considering the soil-structure interaction (SSI) is vital if alternative design methods are to be established. Such methods would depart from the traditional design approaches of highly ductile structures that experience high damage under major ground accelerations; most of the time it is not feasible or cost effective to repair such damage (Iwata et al. 2005; Tremblay et al. 2008; Ruiz-garcía & Negrete-Manriquez 2011 and references therein). However, it is not clear which type of rocking would be more repairable and reliable. Foundation rocking would potentially

require excavation or underpinning to restore a tilted or settled structure, although this type of rocking can result in dissipating a significant amount of energy (Gajan and Saravanathiiban, 2011). Structural fuses in a structural rocking system need to be designed properly and would require maintenance. Therefore, understanding the way rocking accelerations develop and the relative benefits of different rocking systems on soil would equip practicing engineers with confidence to use rocking isolation practically, and would reduce the cost of building and repairing the next generation of earthquake resistant structures.

#### 1.4 Research aims and primary objectives

The research aim of this thesis is to offer new knowledge on rocking systems and their behaviour so that the concepts of rocking isolation are deeply understood and implemented in the future infrastructure and built environment. In particular, the aim is to better understand the soil-structure interaction of rocking systems, quantify the benefits in different types of rocking (i.e. structural and foundation rocking) and finally identify the most beneficial type with reference to the location of the stepping mechanism (i.e. above or below the foundation level).

The main idea therefore, is to integrate the effect of the soil in the acceleration demand of flexible building models which can separate from their foundation or the ground. Hence, for this thesis the primary objectives are:

- 1) *To experimentally quantify the demand that rocking systems experience during their motion, including soil-structure interaction effects as well as the effect of impact at the interface of the superstructure with the foundation (structural rocking) or the interface of the foundation with the soil due to rocking (foundation rocking). More specifically, the demand is defined as local forces such as element loadings and global forces such as base shear and restraining moment, and deformations such as local building and soil accelerations, rocking rotation and differential settlements.*
- 2) *To develop and evaluate a computational tool that involves footing-superstructure interaction for buildings with structural rocking, as well as soil-structure interaction for buildings with foundation rocking.*

To meet the first objective, a research campaign utilizing centrifuge modelling is at the core of this research. The testing quantifies the benefits of allowing rocking in the structure versus allowing rocking on the soil. Building models designed to rock above their foundation level were compared against others that rock below their foundation level (Figure 1.6). Centrifuge modelling was used because it provides realistic stress-strain responses of the model materials, such as the foundation soil. A variety of excitations, including real earthquakes, were used. The centrifuge rocking foundation tests are the first that include SSI effects for multi-storey rocking frames on spread footings (Figure 1.6b). Moreover, the centrifuge structural rocking tests are the first that include a stepping mechanism, an elastic superstructure and SSI effects (Figure 1.6a).

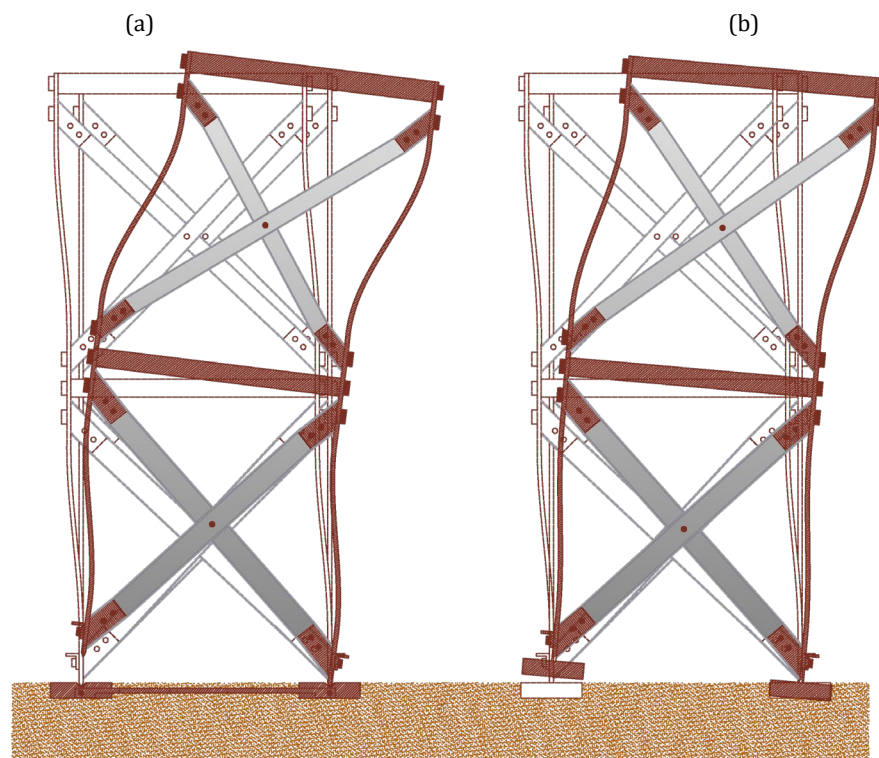


**Figure 1.6: Building with rocking above the foundation level (a) and building with rocking below the foundation level (b)**

To meet the second objective, a new computational model for rocking structures is presented. The proposed computational model is the first to account for total loss of contact for a footing using a Beam-on-nonlinear-Winkler-Foundation model (Figure 1.6b). It also provides a unique representation of a slot connection that acts as a shear key depending on the contact state between two structural elements. (Figure 1.6a). The aim of the modelling is to provide a computational tool, validated with experimental data, to

assess the seismic performance of structures that are intended to uplift, rock and use energy dissipation from soil when excited by a ground motion.

## 1.5 Outline of thesis

In Chapter 2, a literature review is provided, categorized according to the most common types of rocking systems. In addition, a review of the computational tools available to model rocking systems and soil-footing problems is presented. The chapter concludes with the introduction of the two rocking systems considered throughout the thesis.

In Chapter 3, the design of two rocking building models is described. The design of critical elements such as the braces of the models and the structural fuses is presented, including experimental validation of their performance. The system identification with 1g experiments is also presented.

The methodology for centrifuge testing is introduced in Chapter 4. This includes the data acquisition system and the positioning of the models in the centrifuge box. Moreover, the input excitations are presented, and their characteristics are discussed. Throughout this research, the wavelet transforms of the experimentally (and computationally) generated signals were calculated to study the evolution of frequency content in time. Therefore, Chapter 4 also includes a calibration process for the wavelet transform procedure employed.

In Chapter 5, the seismic performance of the rocking buildings is discussed. First, the base isolation effect is presented and quantified. Next, the interaction between a rocking superstructure and its supporting medium is discussed. The chapter concludes with the effect of sand density on the force demand for the structures.

The behaviour of soil below rocking structures is examined in Chapter 6. Soil behaviour is evaluated by measurement of wave propagation through the soil during full contact conditions and during impacts when rocking occurs. Transient settlements of the soil are also considered in conjunction with the rocking amplitude to identify performance trade-offs.

Chapter 7 presents the computational modelling of the two types of rocking buildings. Comparison to experimental data is presented to identify whether key types of response can be satisfactorily captured. A new, comprehensive Beam-on-non-linear-Winkler-Foundation model is used to address the soil-structure interaction. Moreover, special elements are proposed to model partial hinges that allow uplift for structural rocking. To

assist the comparison between experimental and computational responses, a criterion based on wavelet transform coherency is presented.

Finally, Chapter 8 summarises the conclusions. The relative benefits between structural and foundation rocking are presented, and based on these, some practical implications are discussed. Finally, additional research to further the understanding of rocking systems is suggested.



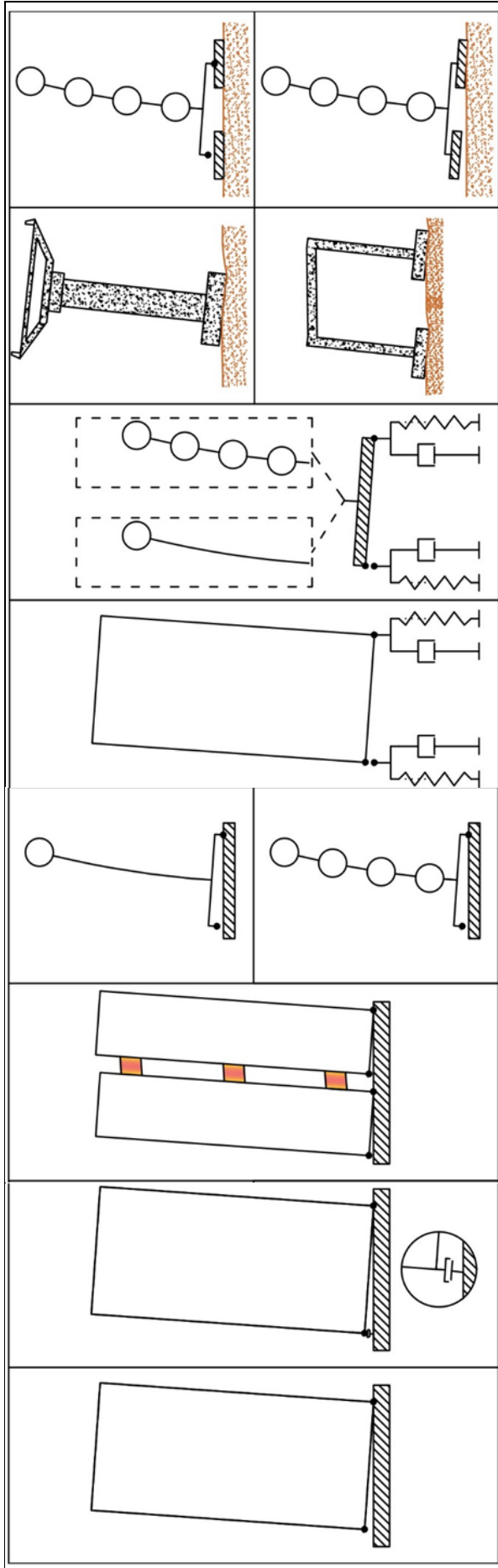
# 2 LITERATURE REVIEW

## 2.1 Categories of rocking systems

It is useful to categorise structural systems based on the source of energy dissipation they are accompanied with. Firstly, plastic hinges (fuses) are designed to dissipate energy in structural elements mainly in beam ends and at the base of vertical elements for a typical structure designed under the conventional design philosophy of the capacity rule, while it is expected that the soil undergoes small settlements. Within the soil-structure interaction (SSI) regime, a second design philosophy is recognized according to which, energy is dissipated by the non-linear behaviour of the soil, while the structure then rocks on the soil surface remaining nearly rigid. Finally, in rocking structures that separate from their base, energy is dissipated from the consequent impacts of the superstructure to its base, and therefore a type of fuse action is introduced by the uplift at the interface of rocking. The above categories can be mixed, and it is possible to have fuse action in both the soil and the superstructure of a system or between the superstructure and its base.

These categories are further discretized considering sources of damping that are frequently encountered (Table 2.1). Structures which rock above the foundation level are reviewed (Section 2.2 & Section 2.3, structural rocking), followed by a review of structures rocking below their foundation level (Section 2.4, foundation rocking). A structural rocking system on rigid base and then on dry sand is briefly discussed in Section 2.5. Section 2.6 presents computational tools for the response of rocking structures. Section 2.7 highlights conceptual additions to the structural and foundation rocking systems which form the core of the experimental campaign throughout Chapters 3 -6. It also introduces new modelling approaches that are used in Chapter 7 for predicting their rocking response.

Table 2.1: Categories of rocking structures according to their characteristic source of energy dissipation



Source of energy dissipation	Typical rocking		Mixed rocking & simple models for SSI		Rocking in SSI/Mixed SSI & beam hinging	Two new rocking systems	
	\$2.2.1	\$2.2.2	\$2.2.3	\$2.3.1	\$2.3.2	\$2.4.1	\$2.5, \$2.7
	Impact	Impact Additional viscous or hysteretic absorbers	Impact Viscous superstructure	Impact Viscous (soil)	Impact Viscous superstructure & soil	Radiation Soil fuse Plastic hinging in frame	Impact Viscous superstructure Base structural/soil fuse

## 2.2 Rocking structures on rigid base

### 2.2.1 Free standing rigid blocks

Housner (1963) examined the survival of tall slender structures by introducing essentially for the first time the rigid block rocking on a rigid base model (Figure 2.1). It was shown that the free vibration period of the rocking block is amplitude and geometry dependent. The rigid block model is the most appropriate choice for rocking isolation of bridge piers as concluded by Makris (2014). This is because the heavier the deck, the more stable is a rocking frame consisting of the deck as a free-standing beam on top of rocking columns which are not connected to the ground. This is essentially an identical configuration to ancient free-standing structures (Figure 2.2).

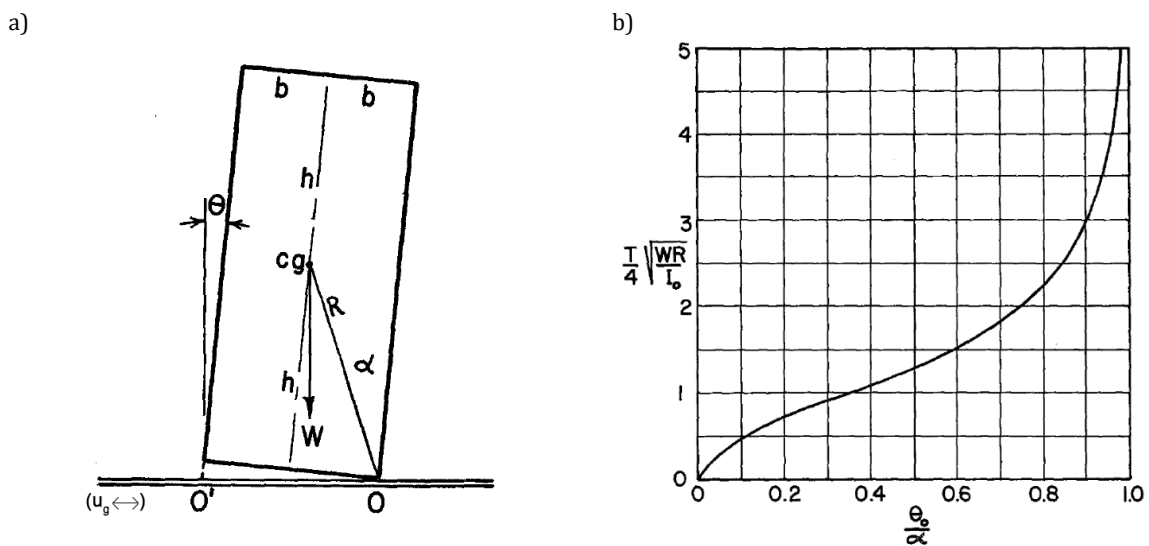


Figure 2.1: A rocking rigid block (a) and its amplitude ( $\theta_0$ ) dependent period ( $T$ ) by Housner (b, 1963)

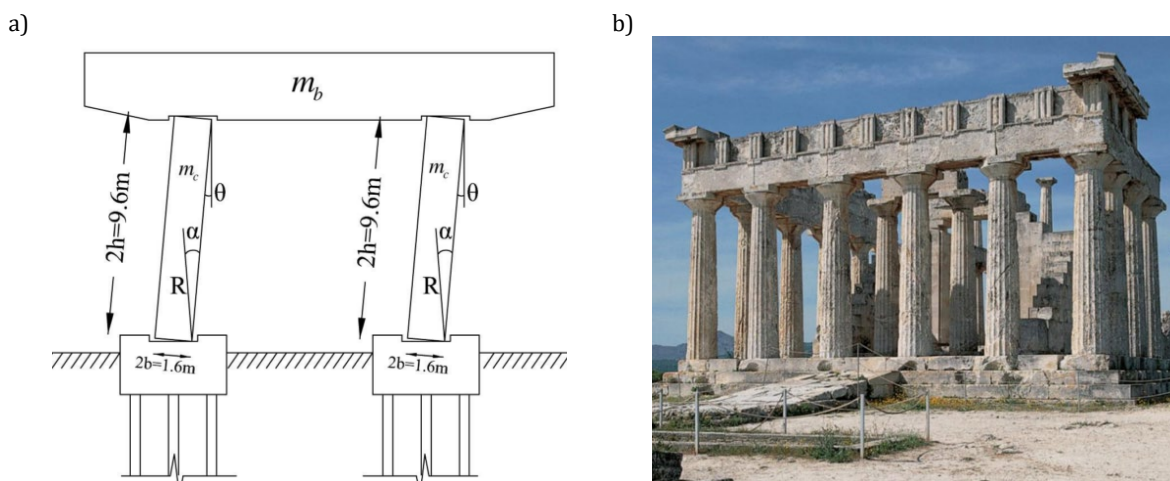


Figure 2.2: A free-standing rocking bridge bent (a), inspired from ancient structures such as the Temple of Aphaia in Aegina, Greece (b, Makris, 2014)

Priestley et al. (1978) argued that the response spectra for flexural vibrations could be used for rocking structures. However, Makris & Konstantinidis (2003) have shown methodologies that rely fully on the flexural SDoF, are not correct since a rigid block and a flexural SDoF have fundamental differences (F. Gelagoti *et al.*, 2012). An example of such difference is the additional amplitude dependency of the oscillation period of the rocking block (Figure 2.1) as opposed to the fixed base SDoF, the period of which depends only on mass and stiffness and is irrelevant of its geometry.

Plaut et al. (1996) extended Housner's work numerically, validating the tendency of larger blocks to be less likely to overturn than smaller, geometrically similar blocks. In other words, this can be explained by considering the dynamic equilibrium for a rocking rectangular block (Figure 2.1). The seismic demand and seismic resistance are the left and right-hand side terms respectively of the following equation.

$$\begin{aligned}
 -\ddot{u}_g(t)R\cos(a - \theta(t)) &= \left(\frac{4}{3}\right)R^2\ddot{\theta}(t) + gR\sin(a - \theta(t)), & \theta > 0 \\
 -\ddot{u}_g(t)R\cos(-a - \theta(t)) &= \left(\frac{4}{3}\right)R^2\ddot{\theta}(t) + gR\sin(-a - \theta(t)), & \theta < 0
 \end{aligned}
 \tag{2.1}$$

The size  $R$  of the block dominates the seismic resistance as the dimensions of the block increase resulting in greater stability for larger blocks (Makris, 2014).

The dependency of the rocking amplitude and overturning of a rocking rigid block on various characteristics of the ground motion has been studied extensively. Housner (1963) indicated that the duration of strong ground motion is important for rocking amplification. Later on, DeJong (2012) showed that when the rotational velocity and ground acceleration are out of phase, then rocking amplification can occur, provided that the ground motion is a down-chirp signal (i.e. a signal with decreasing frequency). However, this rocking resonance waveform is unlikely to be a real ground motion. Finally, following studies showing rocking is sensitive to the velocity characteristics of a ground motion, it has been shown that the cumulative absolute velocity, defined as the time integral of the absolute ground acceleration that exceeds the minimum acceleration to cause uplift, correlates well with the rocking demand (see Giouvanidis and Dimitrakopoulos, 2018, and references therein).

## 2.2.2 Rocking structures with response control from devices

This category is about rigid blocks or elastic frames that are equipped with devices primarily for mitigation of response amplitude and enhanced stability against

overturning. These devices are usually dampers that can be viscous (linear or non-linear) or hysteretic (fuses). To enhance re-centring, post tensioning with tendons has been proposed (Figure 2.3). Combinations of these elements are frequently encountered in experimental, analytical and design studies, on the assumption of a rigid base regarding the rocking interface.

The use of special devices as fuses was likely first conceived by Kelly et al. (1972) who suggested the separation of the load carrying system from the energy dissipation system in a single structure. The first such application is the South Rangitikei Viaduct (1971), the piers of which can step and are equipped with hysteretic dampers between their ends and the foundation (Makris, 2018). Other early applications include installation of tapered steel plates at the base of a rocking chimney (Sharpe and Skinner, 1983) and the Dunedin bridge piers (Tyler, 1978). Beck & Skinner (1974) showed that such designs can significantly reduce the number of steps and magnitude of displacements which may build up as a result of the main swaying motion in combination with the lateral flexibility of the pier, under a strong ground motion. More recently, the cyclic non-linear bending behaviour of tapered plates has been found to be represented well by the Bouc-Wen model (Acikgoz, Argyle and DeJong, 2014).

Dimitrakopoulos & DeJong (2011) found that as the base additional viscous damping increases, the range of excitation frequencies required to overturn a rocking block is reduced. It was also shown that use of non-linear viscous dampers does not guarantee the stability of rigid blocks as opposed to linear viscous dampers (Dimitrakopoulos and DeJong, 2012). Although in general it is expected that adding viscous or hysteretic damping will result in smaller rocking amplitude, it is still possible that during an excitation marginally higher rotations can occur from the undamped case. However, these amplitudes are still tolerable from a design point of view (Makris and Aghagholizadeh, 2019). Tremblay et al. (2008) showed that available computational tools can predict well the response of rocking frames with viscous dampers at their base (Figure 2.4b).

Rocking walls or rocking frames as part of a superstructure on rigid base have received great attention with a focus on how to supplement additional damping. Ajrab et al. (2004) used tendons and energy dissipation devices to control the rocking behaviour of a shear wall as part of a model frame. It was observed that an equivalent viscous damping of 20% can be achieved using this type of control. Ma et al. (2010) developed a new structural system which integrates rocking action with response control from replaceable structural fuses mounted on a frame (Figure 2.3). They experimentally verified essential

performance characteristics (self-centring, column base rocking, and damage control and reusability). A more broad review on the experimental performance of this category's systems can be found in Hajjar et al. (2013).

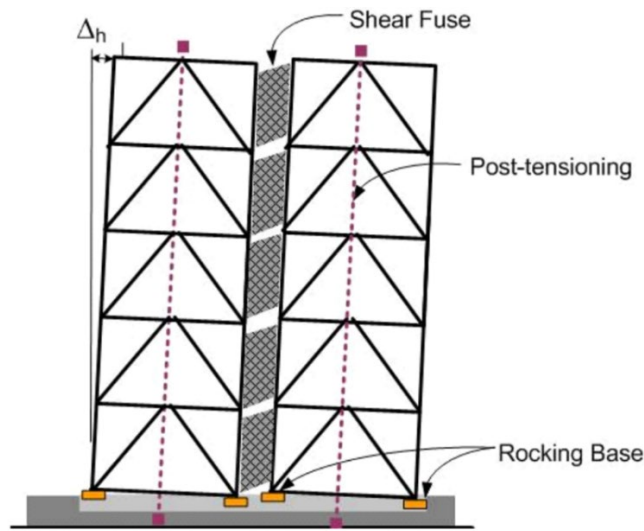


**Figure 2.3: A dual frame rocking on a rigid level with post-tensioning and fuses yielding in shear (Ma et al., 2010)**

Apart from shearing and bending, a fuse action can be provided also from axial deformation. For instance, Pollino & Bruneau (2007) proposed retrofitting a bridge pier installing buckling restrained members (BRB) at the base of the pier (Figure 2.4a). They considered a conservative capacity-based approach to ensure controlled rocking with high ductility and self-centring.

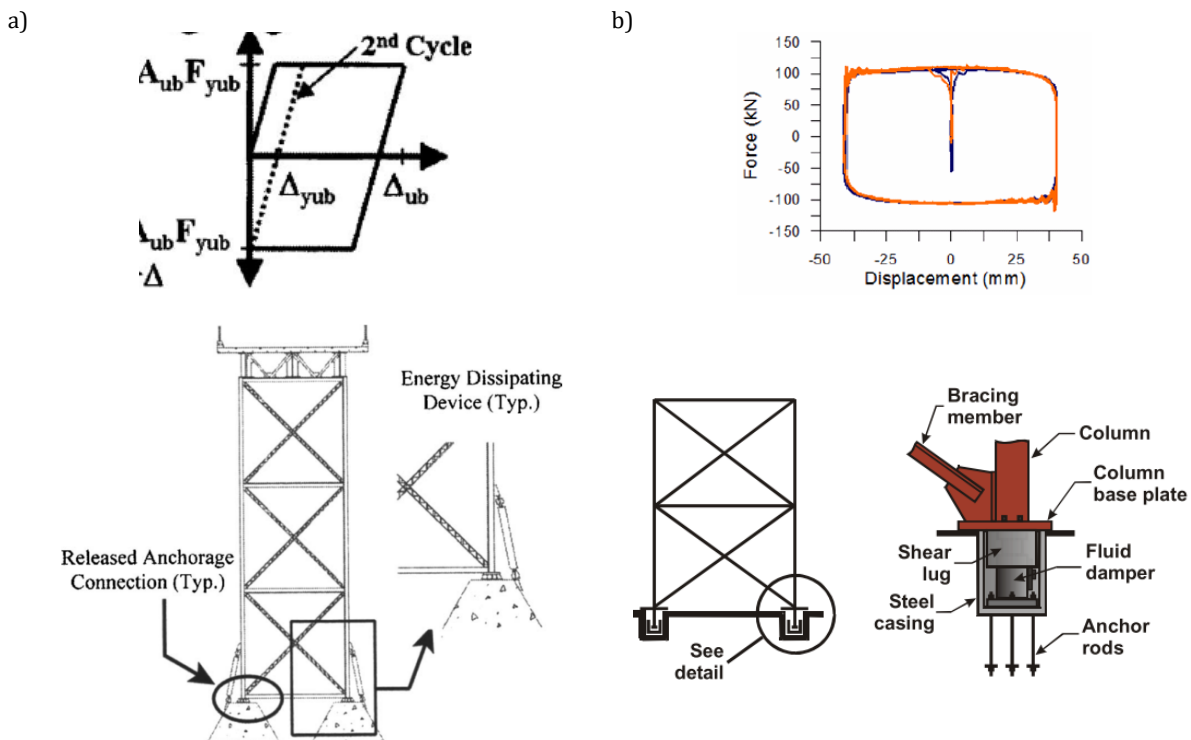


**Figure 2.4: Bridge pier retrofitting with stable hysteretic BRB (a, Pollino & Bruneau 2007) and viscously damped braced frame (b, Tremblay et al. 2008)**

Regarding the addition of tendons, it is generally established that they do not lead to enhanced re-centring. Owing to their stiffness, tendons can store energy, which can be released resulting in increased rotational velocities, snapping and eventually overturning (Makris and Zhang, 2001; Dimitrakopoulos and DeJong, 2012).

Alternative to the installation of damping devices, additional energy dissipation can be provided by considering a rocking interface with a special material. El Gawady et al. (2011) showed that by using a rubber layer in the interface of rocking, a faster energy dissipation can be achieved in the response of rigid blocks as opposed to using timber or concrete instead. Finally, very recently, inerters have been proposed to control rocking response. These devices provide additional inertia to the rigid block and therefore increase its seismic resistance without altering its geometry. The response of an inerter is proportional to the relative acceleration between two nodes (see Makris (2017) and references therein for details). Generally, inerters can reduce rocking demands in terms of rotation and acceleration, but regarding stability, some unprotected blocks that would not overturn, may still not survive the ground motion when an inerter is added (Thiers-Moggia and Málaga-Chuquitaype, 2018).

### 2.2.3 Flexible superstructure rocking on rigid base

Meek (1975) showed the potential of rocking isolation in a flexible SDoF. The slenderer the superstructure the larger the reduction in shear force, while the stockier the superstructure the more the response resembles that of a fixed base SDoF with little or no reduction in shear force (Figure 2.5).

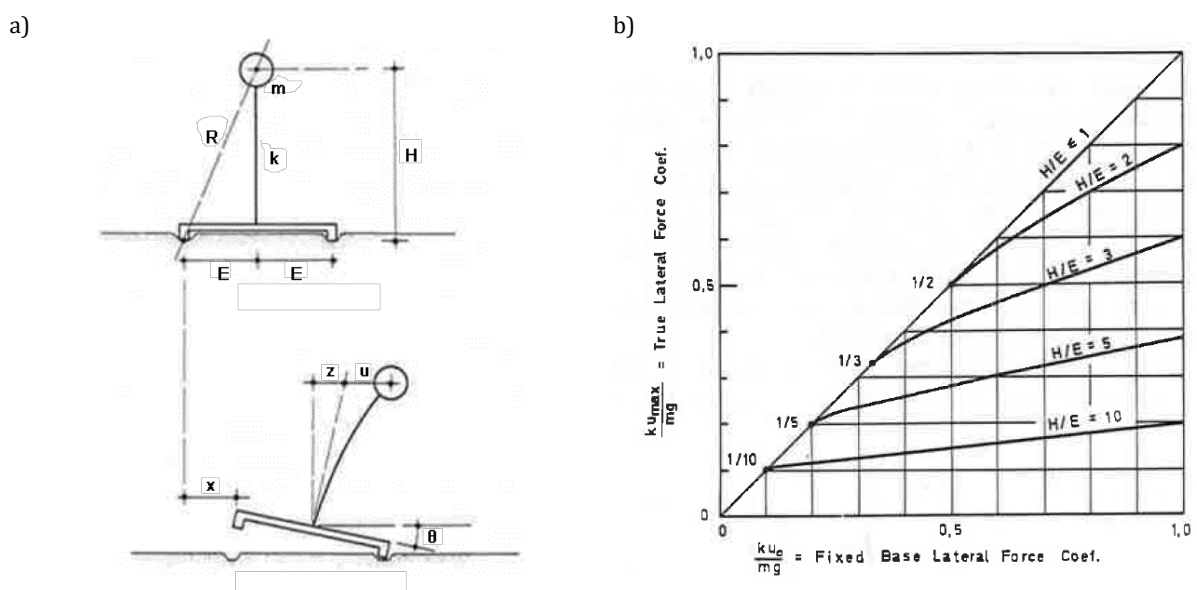


**Figure 2.5: Reduction of the shear force coefficient against the slenderness of a flexible superstructure rocking on a rigid base (Meek, 1975)**

Chen et al. (2006) showed that for rocking of a flexible bridge pier, the stronger the earthquake intensity (in terms of PGA), the more efficient is the rocking design. This is because once the critical load to cause uplift is exceeded, then rocking occurs with a constant angular acceleration, preventing any additional horizontal acceleration increase, compared to the fixed base case.

To estimate the internal loading developed in flexible rocking structures, Chopra & Yim (1985) devised a simplified approach which included the SDoF pseudo-acceleration spectrum. When rocking starts, the structural deformation is measured from onset of uplift and for only the first cycle the peak response can be written as a function of the response estimated in the response spectrum for a fixed base SDoF (spectral displacement) and the superstructure geometry. Then from the response spectrum, the base shear can be easily calculated (Figure 2.6).

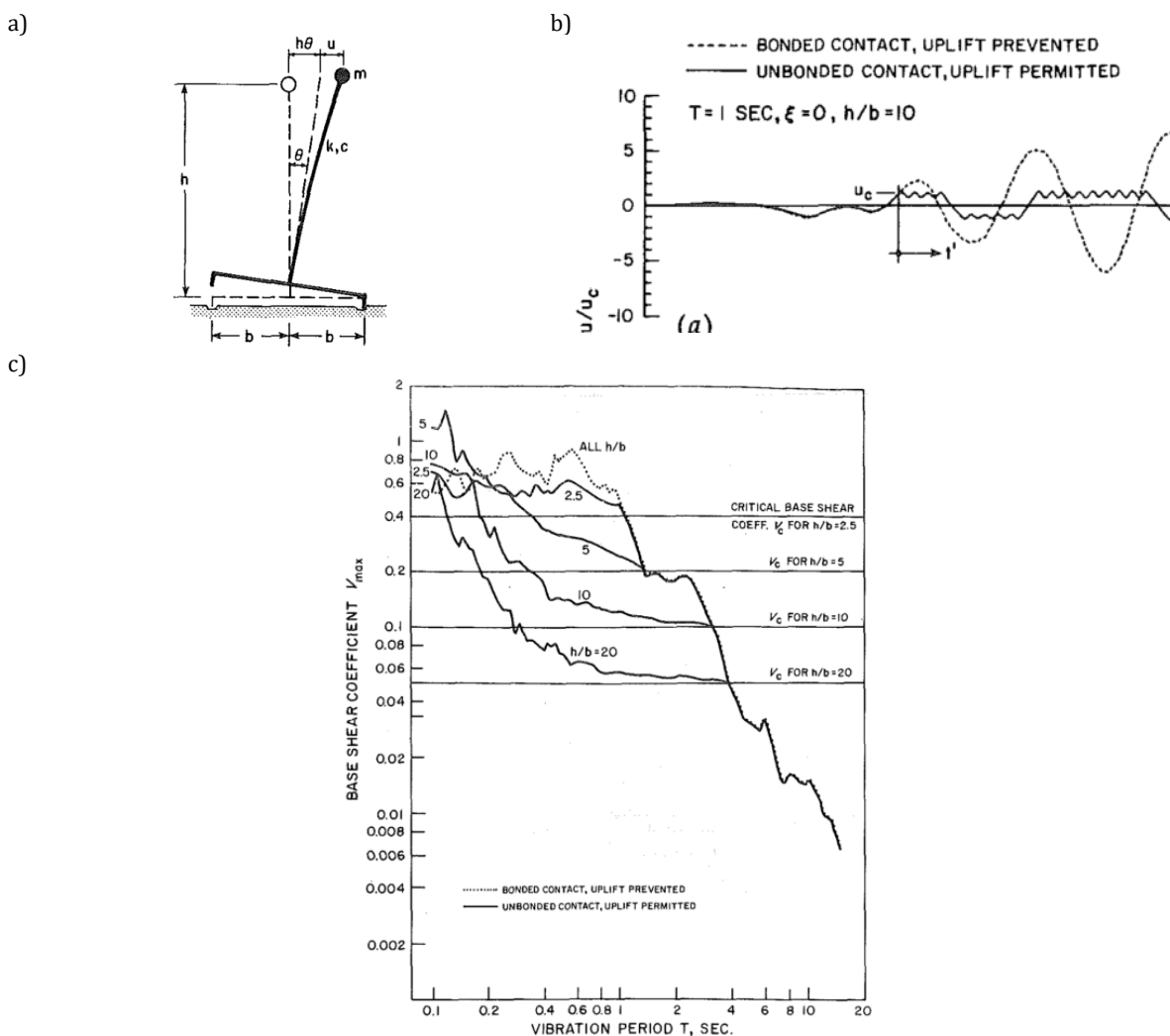


**Figure 2.6: Time history response of a slender structure to the El Centro earthquake (a, b) and spectrum (c) for flexible structures with different slenderness ( $u_c$  is the critical displacement required for uplift, Chopra & Yim, 1985)**

Regarding the parameter that causes more severe structural deformations, Psycharis (1991) concluded that this is the ratio of the superstructure natural period to the excitation period. When this ratio is very small or very large, then under harmonic excitation, uplift does not reduce the structural deformation and hence it is not beneficial. When the ratio is close to unity the deformation reduction is maximum.

Acikgoz & DeJong (2012) investigated the stability of flexible rocking systems. It was shown that the frequency range that causes overturning after one impact shortens when the ratio flexibility/scale increases. They also showed that very flexible structures might survive toppling provided they can sustain very large structural deformations, while stiffer systems become unstable. Most importantly, it was found that resonance at the uplifted state caused by high frequency excitation can increase both the structural deformation and rocking amplitude. Following this work, Giouvanidis and Dimitrakopoulos (2017) showed that the post-impact state of a flexural rocking oscillator in terms of bouncing, rocking or full contact depends on the flexural deformation at the instance of impact.

Furthermore, Acikgoz and DeJong (2013) identified coherent velocity pulses hidden in earthquake records as a major cause for large rocking motion. Following a similarity in terms of maximum rocking angle obtained either directly from records or equivalent hidden pulses, their analysis demonstrated that the parameters controlling the pulse shape can affect significantly the rocking amplitude.

In summary, the distinct interaction between elasticity and rigid body motion in rocking forms a huge motivation of this dissertation (Acikgoz and DeJong, 2016; Acikgoz *et al.*, 2016), as estimating the acceleration demands accurately has not been achieved on the one hand and on the other, using a soil base instead of a rigid one might lead to a more predictable response.

### 2.3 Rocking structures on flexible supports

In this study, by mentioning flexible supports, viscoelastic spring properties are assumed to model soil contact with a rocking superstructure at two discrete points only. The properties are considered for vertical vibrations only and no effect of horizontal flexibility is considered<sup>1</sup>. Viscoelastic springs form the very first approach to simulate soil interaction with stepping of superstructures and this is because they are very simple

---

<sup>1</sup> More about flexible supports in two directions can be found in other studies (Psycharis and Jennings, 1985) in which a more complex response of the rocking block is described, including fly-off.

conceptually as opposed to non-linear properties which are complicated (Psycharis & Jennings, 1983, and references therein, see also Table 2.1).

### 2.3.1 Rigid blocks on flexible foundation

Palmeri & Makris (2008) concluded that as the angle of block slenderness decreases, the smaller is the effect of flexibility, damping and coefficient of restitution of the foundation to the block response. They also concluded that as the foundation stiffness increases dramatically, the peak rotation changes slightly. While Palmeri & Makris (2008) formed and solved the non-linear equations of motion taking into account the conservation of momentum at the impacts, including the effects from the viscoelastic springs, Ma & Butterworth (2012) approached rocking response differently. They firstly considered a general expression of the non-linear restoring force which later identified using a pushover analysis. This static approach describes the response as initially being linear until the point which uplift occurs and the rigid structure leaves the one spring while starts rotating about the other. After identifying the static non-linear behaviour, they implemented it to determine the dynamic rocking response. Their results matched well previous experimental data.

### 2.3.2 Flexible superstructures on flexible supports

Psycharis (1983) and Yim & Chopra (1985) simulated numerically the response of multi-storey rocking frames on springs representing the soil. They separately concluded that the first mode period elongates the most after lift-off while the higher modes are not affected by rocking. This contradicts the case of the rigid foundation, in which the natural frequency of a flexible structure increases while rocking takes place (Acikgoz and DeJong, 2012). Furthermore, Acikgoz & DeJong (2016) showed that the second mode can interact with the rocking motion and the second mode frequency increases too for rigid base conditions. Wiebe et al. (2013) have proposed multiple force-limiting mechanisms to prevent increase of internal loading along the height due to the excitation of higher modes. Overall, the flexibility of supports can have a significant effect on the response of flexible rocking structures and in simulations, this also pivots about the modelling assumptions such as the coupling of modes with rocking. Regarding the viscous damping offered by the superstructure, Acikgoz and DeJong (2012) showed that during uplift an increased value of that is achieved based on the superstructure's dimensions.

## 2.4 Rocking foundations and soil – structure interaction

The distinct lengthening of a structure's first modal period founded on soft soil was also reflected in the study of Veletsos & Meek (1974). For typical structures which are not

allowed to uplift and rock, there have been published many guidelines such as that from NEHRP Consultants Joint Venture (2012) and explain SSI in full extent. Rocking in SSI terms describes the partial detachment of a footing or a mat foundation rather the stepping action above the foundation as in the previous case of Section 2.3.

### 2.4.1 Fail-safe design with soil

SSI is a widely addressed topic because the non-linear behaviour of soil can be used as a fuse against ground shaking. When this behaviour is combined with initiation of uplifting of the foundation then the superstructure “benefits” as concluded by Gazetas & Apostolou (2004). One such benefit is the dissipation of energy induced by the earthquake motion and Gajan & Kutter (2008) showed experimentally that footings that rock on soil can dissipate energy with a damping ratio of 20%.

Such continuously emerging findings have led to consider whole frames rigidly connected to their shallow footings, which rock on a soil experiencing a non-linear behaviour without fuse action in the base of columns as it would normally be designated. Instead, the fuse action is directed in the form of plastic hinging only in the frame’s beams and in the soil (Figure 2.7). This is the case of Gelagoti et al. (2012) who carried out a finite element analysis of a frame in an effort to quantify the overturning demands, following the work on overturning of rigid blocks and flexible stepping structures. It was concluded that the number of motion cycles with amplitude larger than that causing uplift plays a role in the toppling potential of an earthquake, a conclusion which refreshes the build-up of a motion over time as mentioned by Housner (1963).

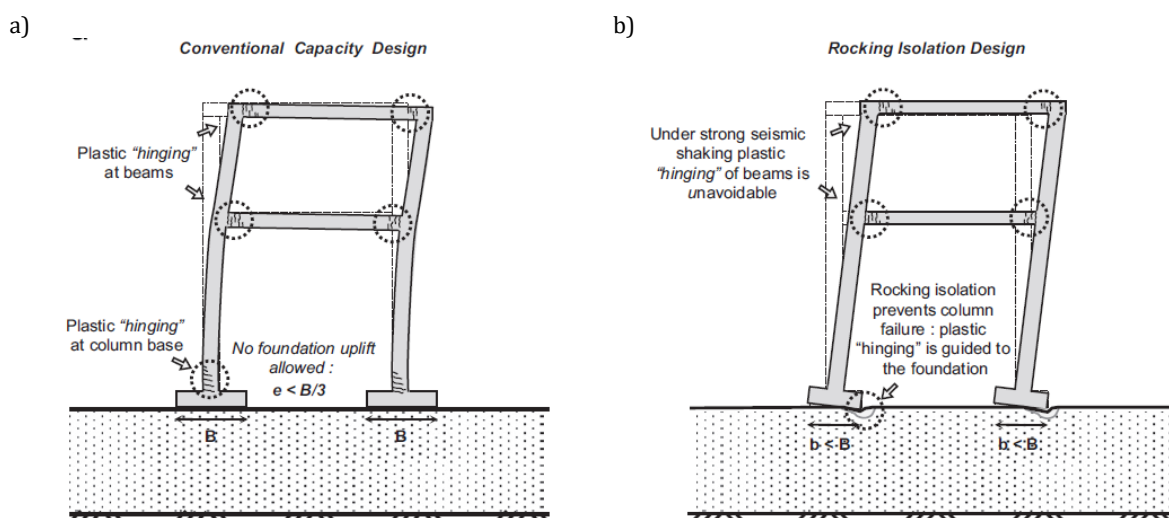


**Figure 2.7: The conventional capacity design (a) and the rocking isolation design (b, F. Gelagoti et al., 2012)**

For centrifuge testing, the conceptual structures are considered as non-ductile reinforced concrete (RC) buildings with typical shapes (e.g. rectangular) and with moment resistant

connections and shear walls (Mason et al. 2010, Figure 2.8). Regarding the foundation, it is modelled as rigid representing a prototype building which has a reinforced concrete raft. Since in reality the dominant shaking frequency is between 1 Hz and 2 Hz, many typical low-rise and mid-rise buildings (5 storeys) may likely respond with resonance. Therefore, candidate prototype structures for centrifuge have a natural frequency of 1 Hz to ensure that the centrifuge experiment will replicate realistic dynamic response (Heron, 2013). Rocking bridge piers are modelled assuming a nearly rigid body behaviour once rocking begins (Deng, Kutter and Kunnath, 2012; Loli *et al.*, 2014). Overall, the main concept in modelling of structures in centrifuge is to consider key mechanisms that are of interest in dynamic behaviour (e. g. mode of response, fundamental period, yield strength, yield drift, bearing pressure, foundation stiffness) with a limited number of degrees of freedom (Trombetta et al. 2014; Heron 2013, Figure 2.9).

Non-ductile reinforced concrete frame buildings: with or without shear walls; 5 to 10 stories; no basement; circa 1940 to 1970.

Building Shape	Structural System	Stories	Foundation	$T_1^{Fixed}$ (sec)
Rectangular	Dual (Moment Frame + Wall)	5	Spread Footings	0.6

Figure 2.8: A typical candidate building for centrifuge modelling (Mason et al., 2010)

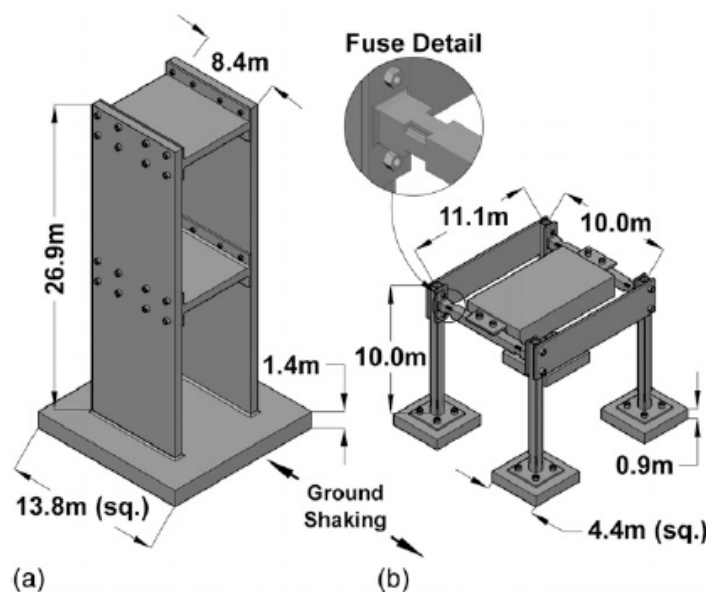
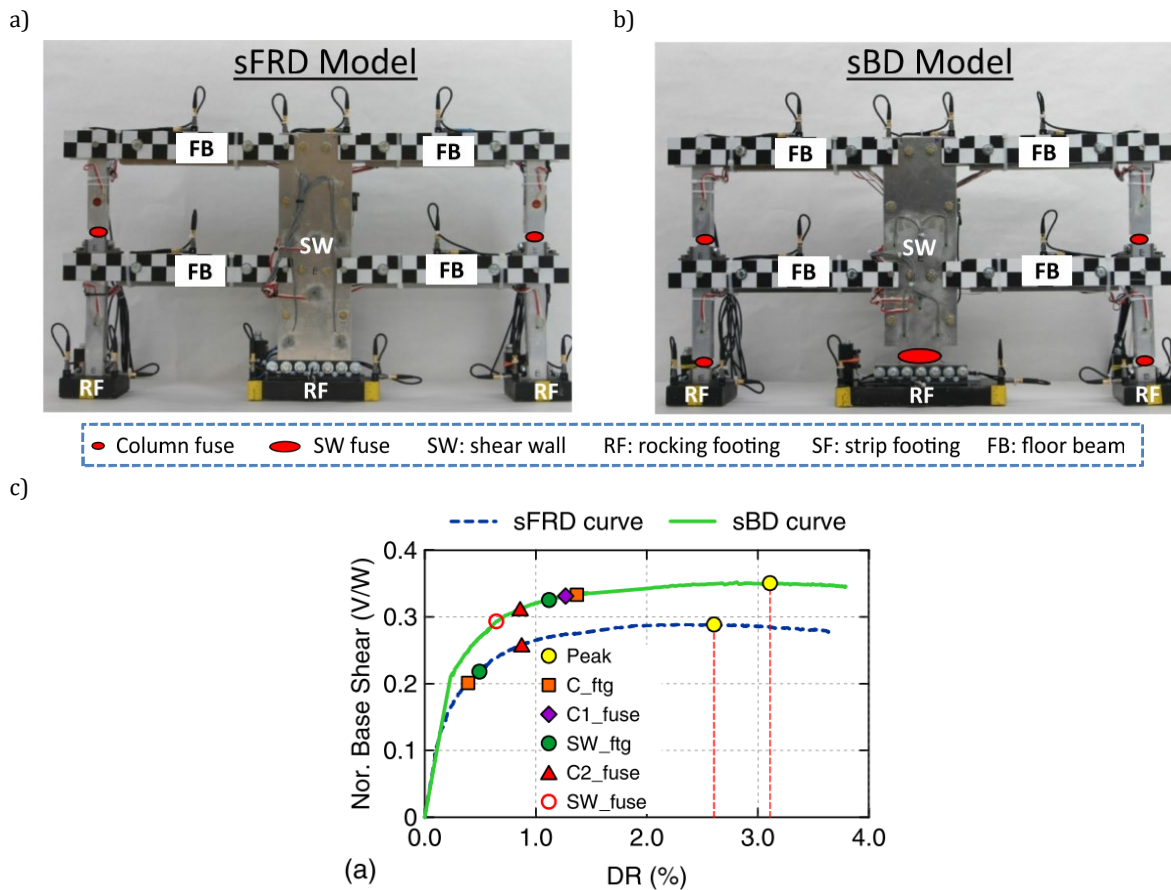


Figure 2.9: Structure models: (a) midrise elastic shear wall with mat foundation; (b) low rise inelastic frame structure founded on spread footings (Trombetta *et al.*, 2013)



**Figure 2.10: A symmetric foundation rocking dominated frame (sFRD) and a symmetric balanced designed frame (sBD) with fuses (top) and their cyclic response envelopes at different imposed drift ratios (Liu *et al.*, 2015)**

Liu *et al.* (2015) subjected frames with plastic hinging and rocking footings to cyclic loading in centrifuge and concluded that different types of rocking foundation frames can have a similarly ductile behaviour despite their differently allocated structural fuses (Figure 2.10c). However, some systems might re-centre better than others after the end of the imposed excitation, thus experiencing smaller residual drifts. This study shows that ultimately the combinations of mixed rocking systems with plastic yielding of soil and yielding structural elements can be numerous but with trade-offs in performance.

All the aforementioned findings confirm the potential of soil in governing the fail-safe design and raise the question whether capacity design regulations should be re-evaluated. Rocking on energy dissipating soil is very promising, since it can enhance the structure's resilience against aftershocks as it was shown by Loli *et al.* (2014). They tested a rocking bridge pier in consequent earthquakes, and it was shown that survival (in terms of not toppling) is achievable while for the same sequence of motion the conventionally designed pier experiences at least twice as large drifts. However, a conventionally designed pier settles very little compared to a rocking pier. In fact, excessive settlements

from rocking is the main reason of not fully adopting yet a change in the capacity design philosophy which would utilize the fuse action offered by the plastic yielding of the soil.

To tackle excessive settlement of rocking foundations, soil improvement can be used (see Ko et al., 2019, and references therein). For instance, installation of stone columns (granular columns, gravel drains or aggregate piers) into soft soils can stiffen and reinforce soil below a rocking footing (Figure 2.11a). Specifically, a pair of stone columns can increase moment capacity by 80% and reduce residual settlement by 64%. However, the energy dissipated by the improved case is reduced to 35% compared to the unimproved case, suggesting a trade-off between different performance characteristics (moment capacity, settlement, energy dissipation, Figure 2.11b, c, Liu and Hutchinson, 2018).

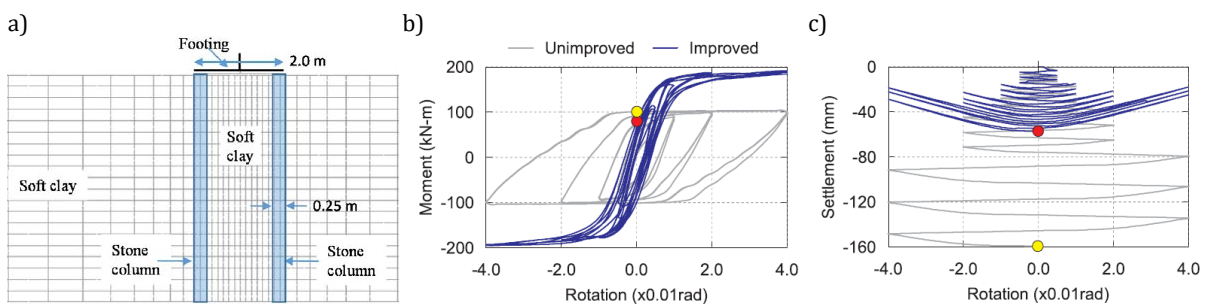


**Figure 2.11: Elevation view of the baseline stone column-reinforced foundation-soil system (a), response comparison between the improved and unimproved cases: moment-rotation (b); settlement-rotation (c, solid circle identifies the residual location, Liu and Hutchinson, 2018)**

#### 2.4.2 Effects of relative density of sand

Little information on rocking foundations with loose sand is available (Deng, Kutter and Kunnath, 2012) and this is also evident from Table 5-2 of the NIST report on soil-structure interaction (NEHRP Consultants Joint Venture, 2012). A reason to explain that is a dense sand can be used to have clear hysteretic behaviour for rocking footings, minimizing settlements at the same time (Liu *et al.*, 2015).

Generally, a high relative density of sand allows a clear rocking behaviour with small settlements and large rotations for rigid footings on sand. This is partially evident either implicitly by considering the settlement-rotation against the safety factor or contact ratio of footings or explicitly against the relative density (Figure 2.12-Figure 2.15). The settlements generally increase as the factor of safety, which is a function of relative density, decreases, while the amplitude of rotation increases implying a stable rocking behaviour on the surface of sand on a per cycle basis (Figure 2.12). If a cumulative basis

is used, the trend is similar, recalling that the contact ratio is a similar value to the safety factor and thus, it is the same way connected to the relative density (Figure 2.13).

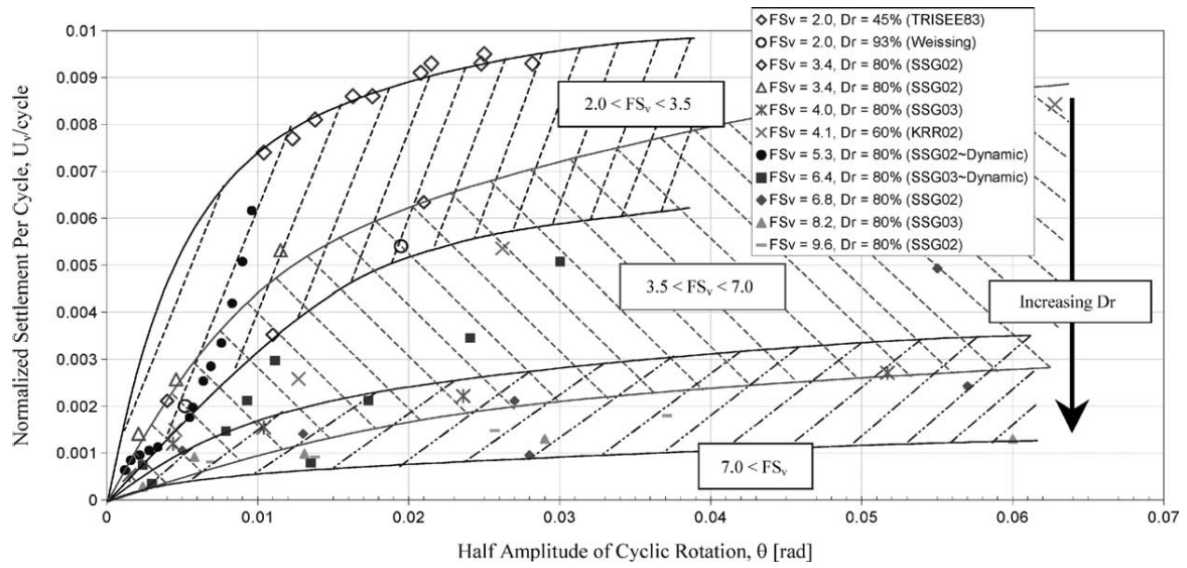


Figure 2.12: Settlement caused by cyclic rotation from cyclic and dynamic tests on a cyclic basis (Gajan *et al.*, 2005)

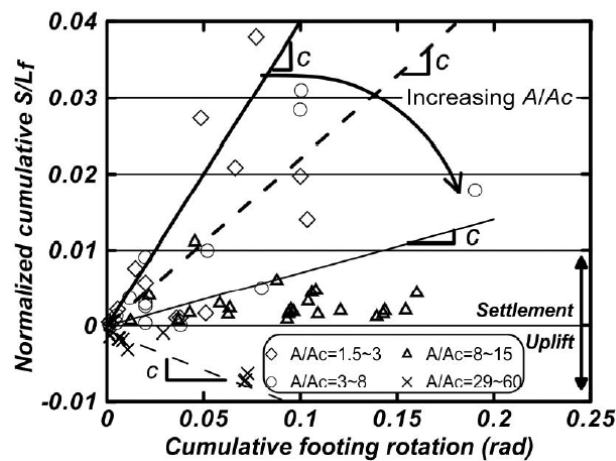


Figure 2.13: Settlement caused by rotation on a cumulative basis (Gajan and Kutter, 2008; Deng, Kutter and Kunnath, 2012)

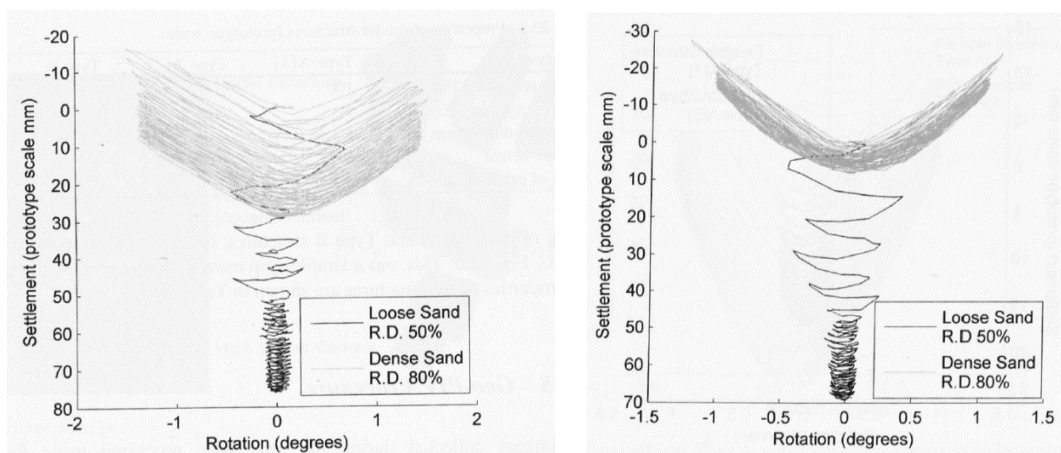
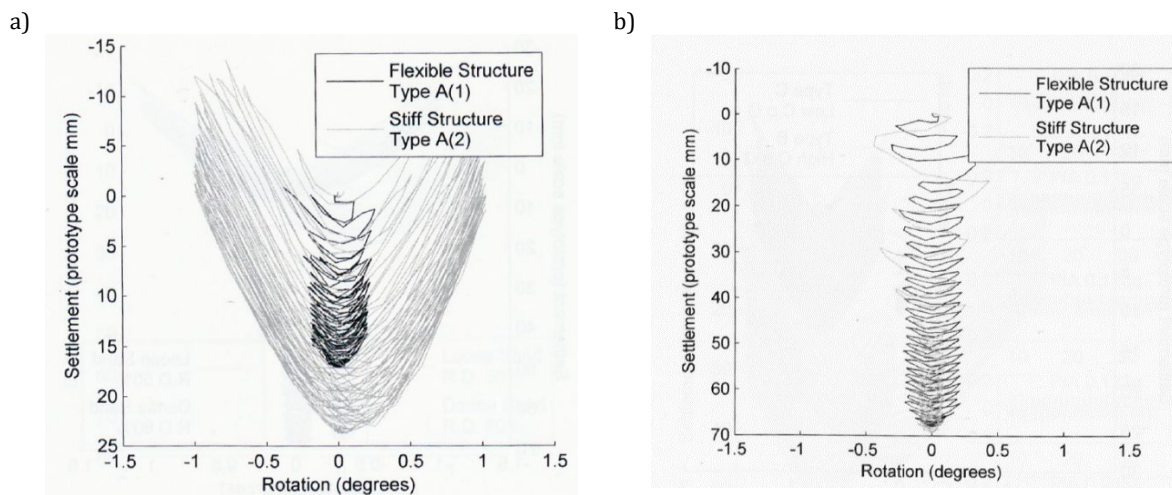


Figure 2.14: Behaviour of two very stiff (rigid) structures on dense and loose sand (Heron, Haigh and Madabhushi, 2014)

An explicit example is shown in Figure 2.14, where the steady behaviour of the mat foundation of rigid structures in the dense sand is clear throughout the shaking. However, the steady behaviour develops in the loose sand only after a large settlement has occurred. The previous trends appear to develop only when the superstructure connected to the footing is rigid. In flexible structures energy is transferred to the superstructure in the form of bending action and rocking behaviour develops with a small amplitude of rotation when the sand is relatively dense. If the sand is loose, both flexible and stiff structures will rock with a small rotation amplitude and they will have the same large settlement. This is because loose sand dissipates large amounts of energy (Heron, 2013) by excessive yielding and thus can dominate the response regardless of the superstructure's flexibility (Figure 2.15).



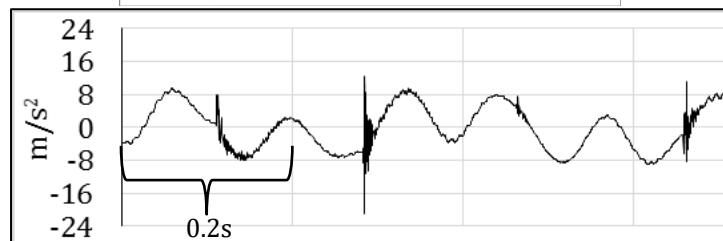
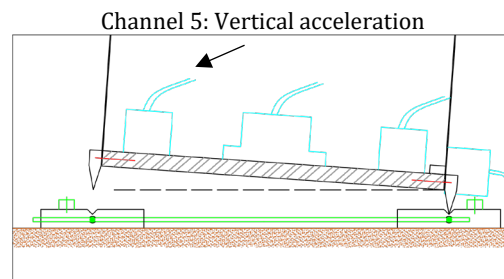
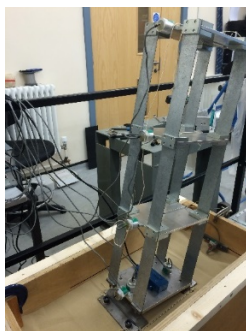
**Figure 2.15: Settlement-rotation behaviour on for relative density 80% (a) and for relative density 50% (b, Heron *et al.* 2014)**

## 2.5 Experimental soil – rocking structure interaction

Most studies are consistently limited to reproducing certain rocking systems which do not integrate the soil and structural characteristics at their full extent. An experimental pilot study addressing the effects of soil on a rocking structure stepping on pad footings (i.e. soil-rocking structure interaction) was conducted in Cambridge (Pelekis, 2015). This study forms the natural continuation of the analytical modelling efforts of Psycharis (1983) and Yim & Chopra (1985) to include soil springs and of the experimental and analytical study of Acikgoz (2014) on the interaction of (structural) vibration modes with rocking. The experiments involved free and forced rocking of a flexible three storey building on soil and on a very stiff base (Figure 2.16). It was observed that *“a layer of sand can diminish fast the transient terms from excited vibration modes due to impact, in the*

acceleration demands of a rocking superstructure. In contrast, a stiff base can lead the vibration modes to being excited for a longer period and with a continuously stronger profile". In addition, it was observed that the "magnitudes of the vertical accelerations caused by the impacts of the rocking superstructure on its footings resting on a sand layer are considerable lower than those when the footings are fixed on a stiff base" (Figure 2.17). These findings are an additional motivation to further explore the soil-rocking structure interaction, as they essentially mean that if rocking structures are to be the next generation of earthquake resistant structures, then the effects of soil need to be understood in depth and then implemented in new design guidelines.

a)



b)

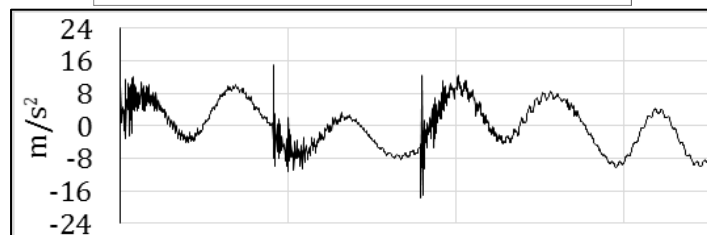
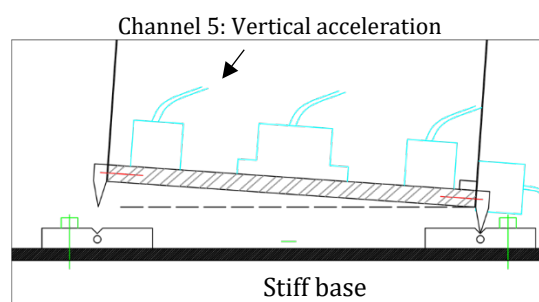
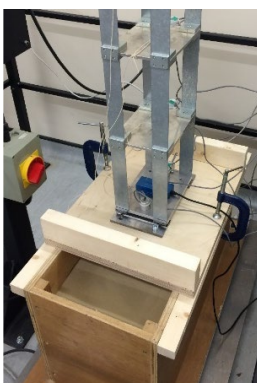
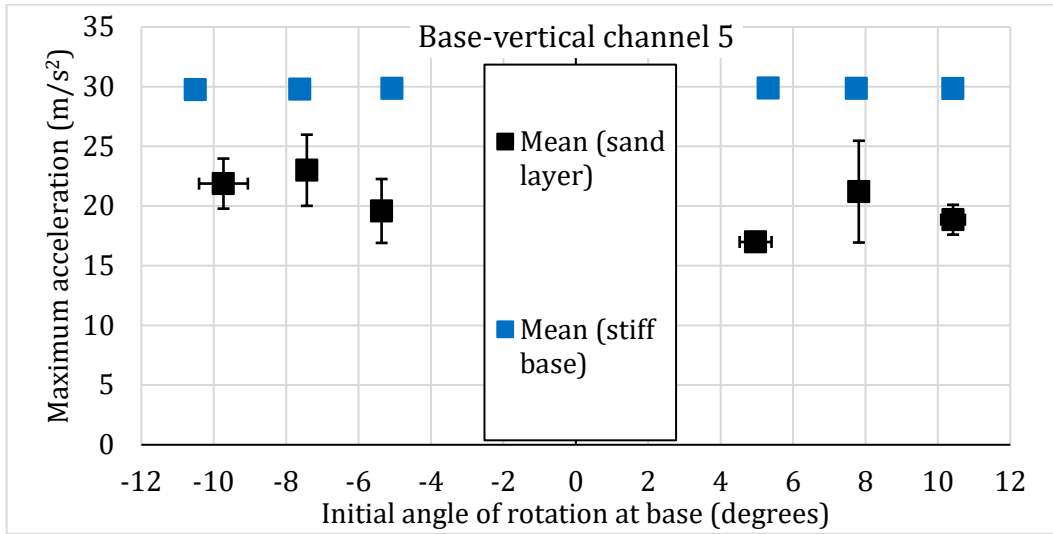
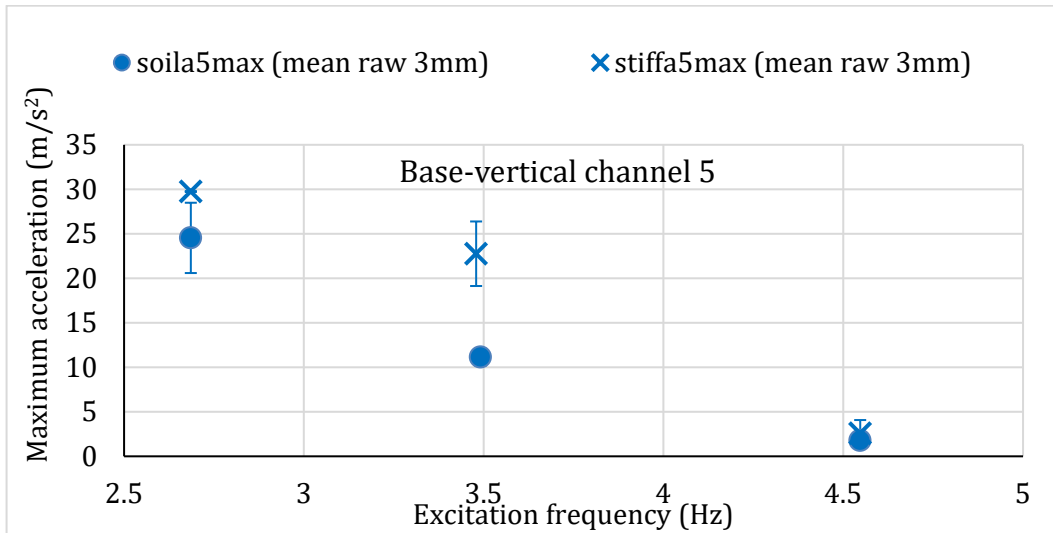


**Figure 2.16: A small scale three storey flexible rocking frame (a) with its pad footings resting on the sand (b) and with its footings fixed on a very stiff base (c, d). The corresponding third storey acceleration responses from forced rocking are also shown (Pelekis, 2015)**

a)



b)



c)

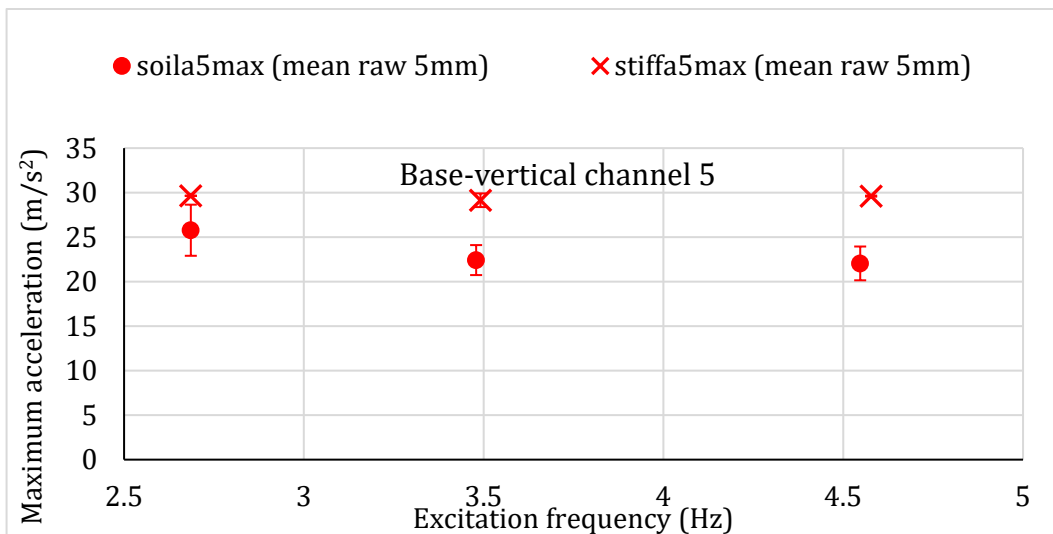
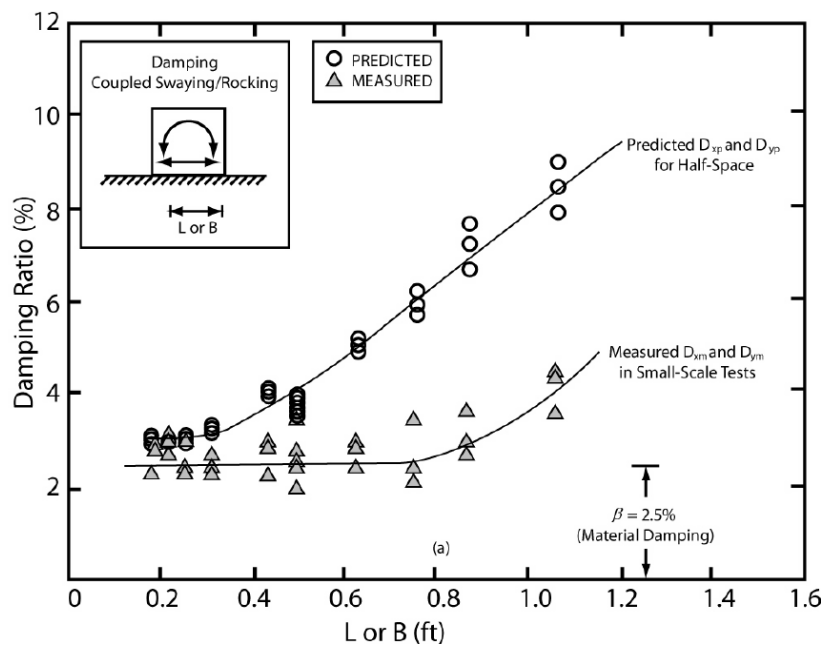


Figure 2.17: Vertical accelerations close to the impact point from free rocking (a), from small amplitude harmonic base excitation (b) and from high amplitude harmonic base excitation (c, Pelekis 2015). 3 and 5mm is the stroke of the harmonic excitation

A limitation of this study was the small-scale physical modelling that was based on. Although the different interaction mechanisms for the two different base conditions were clearly observed, the behaviour of soil was not deemed realistic. This is because under small body forces, such as those generated in 1g small scale experiments, the stress gradients along the soil depth do not correspond to the real scale values. This means that the soil is significantly less stressed than it would have been and therefore it is prone to adopt a not so realistic behaviour. Furthermore, considering that small footings (in small scale tests) provide less damping than the corresponding theoretical models would predict (Dobry & Gazetas 1986; NEHRP Consultants Joint Venture 2012, Figure 2.18), the damping was also not considered to have been developed realistically.



**Figure 2.18: Impedance models for damping ratio of a half-space of soil versus measured values extracted from free vibration tests from laboratory-scaled models (Dobry and Gazetas, 1986; NEHRP Consultants Joint Venture, 2012)**

## 2.6 Finite element modelling for rocking systems

### 2.6.1 Modelling approaches for foundation rocking

Three main approaches are available for computational modelling of foundation rocking (NEHRP Consultants Joint Venture, 2012). The first approach is to use continuum models with constitutive law for soil which can describe sufficiently the stress-strain response anywhere within the soil domain. This approach is followed when complicated phenomena are of interest. Such applications are blast-induced ground vibrations (Lu and Wang, 2006), combined failure mechanism with yielding in both the superstructure and

the founding soil (Anastasopoulos *et al.*, 2010; F Gelagoti *et al.*, 2012) determining the total energy dissipated from the full soil domain for buildings with very large foundations (Sinha *et al.*, 2017). For a list of soil models for this approach see (Pisanò and Jeremić, 2014). The second approach describes the behaviour of a soil-footing system that uses a constitutive law to link footing displacements with forces that develop in the soil-footing interface. Hence, a macro-element is formed between the footing and a rigid boundary (see Gajan and Kutter, 2009; Figini, Paolucci and Chatzigogos, 2012; Heron, Haigh and Madabhushi, 2015; Lu, Marshall and Hajirasouliha, 2016, for some example macro-elements and applications). A common limitation of the two approaches is that numerous material parameters are required, and the properties cannot always be connected directly to physical soil properties. On the contrary, a third approach involving a Beam-on-a-Nonlinear-Winkler-Foundation (BNWF) requires fewer parameters, and can be implemented relatively quickly to predict response trends. This dissertation focuses on the third approach.

Ideally, a BNWF model will consist of elements which can detect uplift, remove stiffness and viscous damping in all directions when uplift occurs (i.e. forces drop to zero), provide a sufficiently accurate nonlinear material law with appropriate strength and damping characteristics and allow for easy calibration based on soil properties. Historically, all these attributes have never been combined before (Table 2.2). Early efforts (Taylor, Barlett and Wiessing, 1980) showed that vertical springs can be used to capture uplift of the footing and yielding of the soil. However, for a flexible rocking structure, a BNWF model can affect significantly the first mode (Chopra and Yim, 1985). Wotherspoon and Pender (2010) focused on different stiffness distributions across the footings of a two-bay portal frame. By using springs with stiffness dependant on uplift for all directions, they examined the force distribution between extreme and central columns. However, their model was limited since material non-linearities were not considered. Raychowdhury and Hutchinson (2009) used constitutive laws calibrated against centrifuge experiments with rocking footings to describe more accurately the nonlinear response of soil in both the vertical and horizontal directions. An important addition of their model was the inclusion of a passive resistance component for embedded footings, alongside a spring for sliding resistance.

## 2.6.2 Modelling approaches for structural rocking

Modelling a rocking superstructure on a rigid surface typically involves the creation of partial hinges at the support points. This type of hinge allows pivoting of the

superstructure about a corner point, and then switching the hinge to the opposite corner point to allow rocking in the opposite direction. Upon contact, the stiffness and damping provided by the support during the impact can significantly affect the subsequent response. Generally, an inelastic impact allows a rigid block to maintain a continuous rocking response where rotation alternates between two support points (Housner, 1963), whereas an elastic impact can lead to bouncing or rebound.

**Table 2.2: Attributes, experimental validation and original development purpose of common BNWF models and of the proposed model. Arrows indicate vertical and horizontal directions**

Attributes		(Taylor, Barlett and Wiessing, 1980)	(Chopra and Yim, 1985)	(Raychowdhury and Hutchinson, 2009)	(Wotherspoon and Pender, 2010)	Proposed model
Uplift dependent	stiffness transmission	↕	↕	↕	↔ ↕	↔ ↕
	viscosity transmission	×	↕	↕	↔ ↕	↔ ↕
Material's constitutive law	linear elastic soil	✓	✓	✓	✓	✓
	non-linear soil	✓	×	✓	×	✓
	friction/vertical force coupling	×	×	×	×	✓
Experimental validation		✓	×	✓	×	✓
Purpose of model development		Replicate behaviour of a rocking footing	Effect of rocking in higher modes	Capture moment rotation and settlement behaviour	Examine distribution of footing forces in two-bay portal frame	Capture total loss of contact with soil and replicate superstructure response

Within a finite element environment with linear elements between nodes, the most common way to model contact is to use gap elements that have a very large finite stiffness in compression and zero stiffness in tension (Ma *et al.*, 2010; Eatherton *et al.*, 2014). Normally, the gap elements are placed in pairs along the vertical and horizontal directions. To account for damping during the impact, a viscous damper either in parallel (Schau and Johannes, 2014) or in series with the stiffness of the gap element can be used. However, if in series (creating a Maxwell element), the damper leads to a stiffness matrix with zero stiffness elements, which results in equilibrium problems under gravity loading. To avoid this shortcoming, a parallel spring-damper element in series with a gap element can be used. This configuration was used by Ma, Butterworth and Davidson (2005) along with additionally support masses, to mimic Housner's plastic impact model and ensure continuous rocking response about two corner points. Moreover, nonlinear constitutive

laws can be calibrated to account for an appropriate stiffness and damping to replicate instantaneous energy loss, an approach effectively applied in pounding of large-scale structures (Muthukumar and DesRoches, 2006). Alternatively, numerical dissipation can be used by appropriately tuning the Hilbert-Hughes-Taylor (HHT) and Newmark time integration methods (Vassiliou, Mackie and Stojadinović, 2017). If numerical convergence is difficult to achieve when an impact occurs, a nonlinear (displacement-dependent) stiffness (Acikgoz and DeJong, 2016) can be used.

## 2.7 Summary

A summary of the literature review is presented in Table 2.3 - Table 2.5. Overall, experimental studies on structural rocking do not take into full account the presence of the soil and *vice versa* for the studies on the foundation rocking, where the interaction of structural flexibility with the rocking motion is neglected. Additionally, foundation rocking refers only to mat foundations rather spread footings below the superstructure and the stepping mechanism for such configurations is unexplored.

**Table 2.3: Summary of the literature review for rocking structures on rigid base**

Type of superstructure	Type of supports: Rigid base		
	Study	Approach	Contribution
Rigid block	(Housner, 1963)	Analytical	Introduction of rocking and size-frequency effect
	(Priestley, Evison and Carr, 1978)	Analytical	Iterative method to predict response using flexural vibrator response spectrum
	(Spanos and Koh, 1984)	Analytical	Conditions for symmetric and asymmetric rocking under harmonic excitation
	(Plaut, Fielder and Virgin, 1996)	Analytical	Overturning behaviour is fractal
	(Makris and Konstantinidis, 2003)	Analytical	Introduction of rocking spectrum
	(DeJong, 2012)	Analytical	Down-chirp signal as ground motion causes rocking resonance
	(Makris, 2014)	Analytical	Re-interpretation of Housner's model: Size dominates the seismic resistance
	(Giouvanidis and Dimitrakopoulos, 2018)	Analytical	High correlation between rocking demand and velocity characteristics of ground motion
Response controlled	(Kelly, Skinner and Heine, 1972; Beck and Skinner, 1974; Tyler, 1978; Sharpe and Skinner, 1983)	Analytical/ Experimental/ Design	Control with hysteretic dampers can reduce rocking steps
	(Makris and Zhang, 2001; Dimitrakopoulos and DeJong, 2011, 2012; Makris and Aghagholizadeh, 2019) (Tremblay <i>et al.</i> , 2008)	Analytical/ Experimental/ Computational	Tendons store energy that sometimes can lead to additional excitation for rocking Linear viscous dampers guarantee rocking stability Damping reduces rocking amplitude in most cases (although a marginally higher amplitude than the undamped case, but design tolerable, can still occur)  Computational tools can predict well the damped rocking response
	(Ajrab, Pekcan and Mander, 2004; Ma <i>et al.</i> , 2010; Hajjar <i>et al.</i> , 2013)	Experimental	Performance assessment of rocking superstructures
	(Pollino and Bruneau, 2007)	Design /Experimental	Design example using buckling restrained braces
	(Acikgoz, Argyle and DeJong, 2014)	Analytical	Bouc-Wen model for hysteretic dampers used alongside equations for rocking
	(El Gawady <i>et al.</i> , 2011; Thiers-Moggia and Málaga-Chuquitaype, 2018)	Experimental/ Analytical	Soft interface reduces steps of free rocking Inerters can reduce rocking amplitude, but do not necessarily improve stability
Flexible superstructure	(Meek, 1975) (Chopra and Yim, 1985)	Analytical	Rocking response spectrum: For natural periods (0.2-4 s), the slender the superstructure, the larger the reduction in shear force demand
	(Clough and Huckelbridge, 1977; Huckelbridge, 1977)	Experimental/ Computational	Verification of load demand reduction with large scale rocking buildings
	(Psycharis, 1991)	Analytical	The flexural displacement reduces the most when an excitation with resonant period occurs. Away from that, uplift is not beneficial. Excitation strength and slenderness have a much smaller effect.
	(Chen <i>et al.</i> , 2006)	Analytical /Experimental	Efficiency in base isolation is more evident as the earthquake intensity (PGA) increases. Analytical tools predicted well experimental time-histories
			Uplifted resonance increases demand of structural and rocking deformations

**Table 2.3 (continued)**

	(Acikgoz and DeJong, 2012)	Analytical	Flexible structures rocking are more stable than stiffer structures
	(Acikgoz and DeJong, 2013)	Analytical	Velocity pulses can cause significant rocking Framework for linking pulse shape parameters to rocking amplitude
	(Acikgoz and DeJong, 2016; Acikgoz <i>et al.</i> , 2016)	Analytical/ Experimental	Validation of mathematical model to capture rocking response including key response characteristics such as frequency shift
	(Giouvanidis and Dimitrakopoulos, 2017)	Analytical	Flexural vibration governs post-impact response

**Table 2.4: Summary of the literature review for rocking structures on flexible supports**

Type of superstructure	Type of supports: Flexible		
	Study	Approach	Contribution
Rigid block	(Psycharis and Jennings, 1983)	Analytical	Viscoelastic springs for soil representation can adequately model energy loss due to impact
	(Palmeri and Makris, 2008)	Analytical	The response of slender blocks depends little on the soil properties (stiffness, damping)
	(Ma and Butterworth, 2010)	Analytical	Derivation of static backbone curve and use in dynamic analysis
Flexible superstructure	(Psycharis, 1983; Yim and Chopra, 1984, 1985)	Analytical	Soil-structure interaction leads to a reduction of the fundamental frequency while higher mode frequencies are not affected  For load demands, the effect of foundation flexibility and uplift can be considered only for the first mode
Shallow footings-slots and linear elastic superstructure	Chapter 4	Experimental	Observations on frequency evolution at free rocking on soil
	Chapter 5	Experimental	Assessment of base isolation effect and base shear demand-impact acceleration relationship
	Chapter 7	Computational	Slot representation with special friction-gap elements

**Table 2.5: Summary of the literature review for rocking foundations and soil -structure interaction**

Type of soil-foundation system	Rocking foundations and soil-structure interaction		
	Study	Approach	Contribution
Single footing or mat foundation	(Gazetas and Apostolou, 2004)	Computational	A rocking footing's behaviour depends on the soil deformability and the footing's vertical load
	(Gajan and Kutter, 2008)	Experimental	Rocking foundations have a very ductile mechanism, significant energy dissipation and re-centring because of uplift and gap-closure
	(Loli <i>et al.</i> , 2014)	Experimental	Sinking response prevents real implementation
	(Liu and Hutchinson, 2018; Ko <i>et al.</i> , 2019)	Experimental	Soil improvement for optimum design of rocking foundations
Additional structural hinging	(Mason <i>et al.</i> , 2010)	Experimental	Advanced modelling of rocking systems for centrifuge testing
	(Deng, Kutter and Kunnath, 2012)	Experimental	Enhanced tendency of re-centring for rocking piers pinned to bridge deck
	(F. Gelagoti <i>et al.</i> , 2012)	Analytical	Systematic investigation of toppling potential
	(Liu <i>et al.</i> , 2015)	Experimental/ Computational	Tools to design systems with parallel structural and soil fuse action
No structural hinging	(Heron, 2013)	Experimental	Structural stiffness and sand density can dictate the rocking response

### 2.7.1 Research for experimental structural and foundation rocking

To unveil the relative benefits of different stepping mechanisms, and ultimately compare the foundation rocking against structural rocking, two new rocking systems are proposed (Figure 2.19). If a linear elastic flexible building frame rocks above its foundation (structural rocking), then it detaches from its footings and steps on them during rocking. The footings rest on soil and can carry additional energy dissipating devices. In general, however, energy would be dissipated, by impacts during stepping and radiation in the soil. If a linear elastic flexible building frame rocks below its foundations (foundation rocking), then it does not detach from its footings, which might experience local uplift. In this case, the soil is the main energy dissipater as it is expected to undergo large deformations. These systems formed the core of this research campaign, as their interaction with soil is rather unexplored and therefore more knowledge is required to be well understood. Table 2.6 shows the contributions produced as a result of this research.

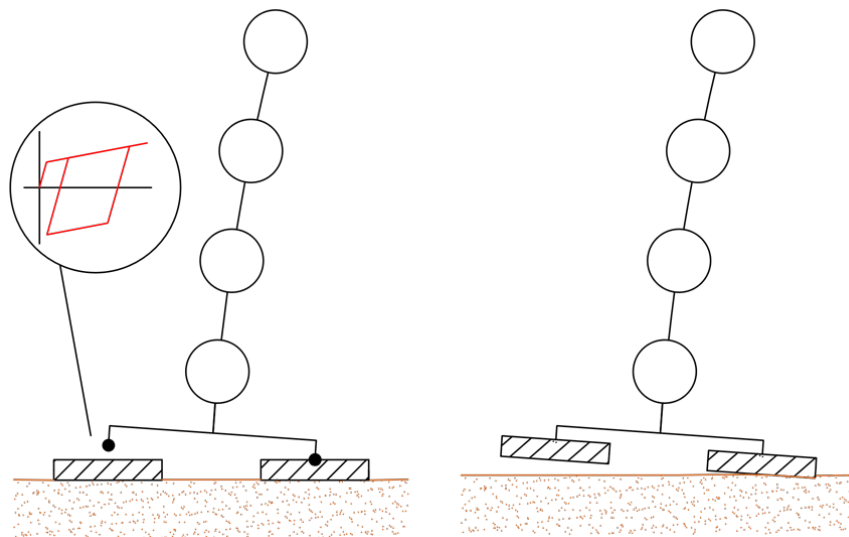


**Figure 2.19: Structural rocking (left) and foundation rocking (right)**

### 2.7.2 Research for computational structural and foundation rocking

The BNWF model of this dissertation is a modified version of Raychowdhury and Hutchinson (2009) and merges all previous attributes (Table 2.2). Specifically, uplift dependent horizontal stiffness and damping are added, along with the coupling of friction with vertical force at the surface of the footing. This upgrade can capture potential total loss of contact between spread footings and the soil when the building uplifts and rocks (foundation rocking). In addition, it provides viscosity in all directions, and thus can capture radiation effects at contact establishment either between soil and footings (foundation rocking) or between superstructure and footings (structural rocking). Within

the OpenSees environment this is achieved by replacing the gap elements below the footings with friction-gap elements (Schellenberg, 2014). It is demonstrated that this model not only can provide a realistic foundation behaviour in general, but also can sufficiently reproduce the superstructure’s rocking response as a result of the direct ground shaking, as well as the impacts that occur at the interface of rocking, either below or above the foundation level.

**Table 2.6: Contributions from this thesis**

Chapter	Contribution	Area
3, 4	New rocking building specimens for centrifuge testing Methodology for use of wavelet transforms for advanced signal processing	Building design Experimental setup Post-processing tools
5	Investigation of effect of sand density and excitation frequency on rocking response and load demand	Experimental building performance
6	Investigation of trade-off between rocking rotation demand and differential settlements Identification of zone of influence in the soil domain due to interaction with rocking buildings	Experimental soil performance
7	Modification of existing BNWF model for comprehensive modelling of soil-structure interaction Modelling of footing-superstructure interaction mimicking shear key function Calibration scheme based on wavelet transform coherency	Computational modelling

# 3 DESIGN OF ROCKING BUILDINGS FOR CENTRIFUGE TESTING

## 3.1 Introduction

Following the need for realistic stress-strain development in soil when rocking systems are subjected to ground excitations, the basics of centrifuge modelling are introduced in this Chapter. Next, the design of two rocking building models to be subjected in ground excitations within increased gravity is presented, along with the design of special components. The chapter concludes with the system identification of the building models.

### 3.1.1 Theory of centrifuge modelling

The potential of centrifuge modelling to produce a complete mechanical and loading similarity with prototype conditions (physical modelling) was exploited for the first time back in 1930's (see for instance Pokrovsky & Fedorov, 1936). However, Eduard Philips in 1869 recognized first the importance of the self-weight body forces in various applications and stressed the need for centrifuge, so that stress similarity is achieved between a prototype and model structures of the same material (Craig, 1995). The concept of centrifuge testing has evolved over the last century so that now is considered a well-documented physical modelling approach to geotechnical problems. In principle, centrifuge modelling is when a  $1/N_g$  scale model of prototype is subjected to a gravitational field of  $N_g$  times the magnitude of earth's gravity. Scaling laws have been derived so that the stress similarity is preserved between a prototype and its model (Schofield, 1981, Table 3.1).

**Table 3.1 Scaling laws for centrifuge testing (Madabhushi, 2017)**

Parameter	Scaling law model/prototype	Parameter	Scaling law model/prototype
Length	$1/N_g$	Bending moment	$1/N_g^3$
Area	$1/N_g^2$	Energy	$1/N_g^3$
Volume	$1/N_g^3$	Time	$1/N_g$
Mass	$1/N_g^3$	Frequency	$N_g$
Stress	1	Displacement	$1/N_g$
Strain	1	Velocity	1
Force	$1/N_g^2$	Acceleration	$N_g$

Centrifuge testing falls in the category of small scale experiments. Small scale testing is useful for reproducing a very large and complex problem, which would be expensive and time consuming to test numerous times. It is limited though, as the stress or strain levels that develop are significantly smaller than in a real case. This has significant implications for materials that behave highly non-linearly, such as the soil, as a rather linear behaviour develops under small strains, rather a non-linear one. The radial acceleration field of the centrifuge can be chosen to shift the stress level enough, so that the non-linear behaviour develops and thus the testing replicates realistically a large-scale problem. The high stress level arises from the body weight, since in centrifuge conditions a mass is heavier than in earth's gravity.

The increase in stress level is paired with scaling down the dimensions of a prototype, but the size of the soil particles remains the same. This means that a smaller number of particles surrounds the scaled specimen compared to the number of particles surrounding the prototype. As long as a prototype is not over-scaled and sufficient number of particles surround a model, the soil can still be treated as a continuum just as in theoretical soil mechanics and numerical approximations. Therefore, centrifuge modelling does not compromise the stress-strain behaviour of the soil due to particle size effects (Madabhushi, 2017).

A radial acceleration field can be generated by spinning a large beam in a special facility. The radial acceleration can be determined from the uniform circular motion equation ( $a_c = r\omega^2$ ). The centrifugal acceleration can be matched to the chosen scaling level  $N_g$  so that

$$\begin{cases} a_c = r\omega^2 \\ a_c = N_g g \end{cases} \Rightarrow N_g g = r\omega^2 \quad (3.1)$$

However, it is obvious from Eq. (3.1) that the acceleration level  $a_c$  varies along the radius  $r$  of the spinning arm. This essentially means that very tall models (for instance, very tall buildings on soils with large depth) are subjected at different acceleration levels along

their height. As a result, the parts closer to the centrifuge centre are under-stressed and the parts further away from the centrifuge centre are over-stressed when compared to their prototype conditions. The error due to that is 1.3% in Cambridge, since the Turner beam (see Chapter 4) has a radius to the swinging platform of 4.125 m. This large radius also eliminates errors from variations of the gravitational field parallel to the swinging platform. Generally, the larger the centrifuge radius, the smaller the errors from the radial gravity field.

## 3.2 Scope of the design

A series of centrifuge experiments was conducted as a method to meet the objective of this research. The tests consisted of two very similar building models on dry sand being subjected to earthquake loading, in the Turner beam centrifuge, Cambridge. The design of the models and their parts (Appendices A-C) had to meet a series of requirements, so that rocking behaviour could be obvious and could therefore be observed and captured without other significant events taking place (e.g. severe collapse of the models). The two models represent two different types of buildings rocking on soil.

First, the main design of the experimental models is introduced, including their definitions. The models have a system of braces as a primary mechanism to resist lateral loads prior uplift and its design and experimental verification of that is explained next. An energy dissipation component was designed additionally for the one of the two models and its design and experimental verification of that is explained too. Finally, the models once manufactured in the Workshop of the Department of Engineering, were subjected to free vibrations as a means for system identification.

## 3.3 Design concept and main requirements

Two building models were designed for testing in the artificial gravitational environment of the Cambridge centrifuge beam (Figure 3.1). In the tests presented later the model scale is  $N_g = 33$ . One model represents structural rocking, and the other model represents foundation rocking. Structural rocking is expected to occur to the model *rocking above* its foundation level (hereafter named RA, Figure 3.2a) while foundation rocking is expected to occur to the model *rocking below* its foundation level (hereafter named RB, Figure 3.2b). While not in rocking action and assuming the soil surface as rigid, the RA and RB models essentially correspond to a hinged base frame and a fixed base frame, respectively. The purpose of this distinction is to highlight the existence of a different type of interface (top surface of footings or soil) that links to a specific type of rocking. The dynamic

properties of the building models (Table 3.2) were designed to be the same as much as possible for a straight comparison of the experimental responses. To avoid masking the rocking performance of the models with out-of-interest events, the structural members were designed to remain linearly elastic throughout the experiment. Therefore, the main design requirements were:

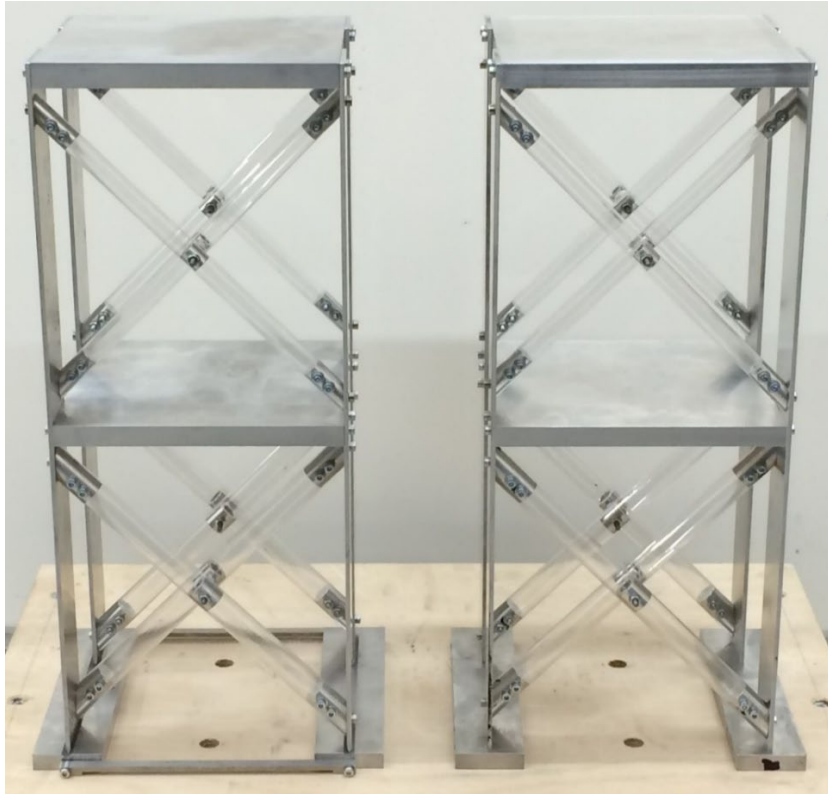


**Figure 3.1: The two building models, RA (left) and RB (right)**

a)



b)



**Figure 3.2: Connection for partially hinged support and structural rocking, RA (a) and connection for fixed support and foundation rocking, RB (b)**

1. Buckling of all members must be prevented
2. Material yielding of all members and their connections must be prevented
3. Excessive settlements in the soil should be prevented before the firing of an earthquake in the centrifuge, which is typical for real buildings under only gravitational loads. Therefore, the static pressure should be 50 - 100 kPa.

4. To ensure higher modes will not be suppressed, a mass participation of below 95% would be desirable for the first mode. This would allow to study effects from higher modes on the rocking response.
5. The distance between the footings should be larger than two times the width of a single footing, to avoid a foundation response that resembles that of a mat foundation.

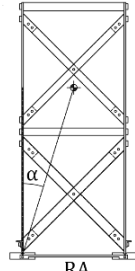
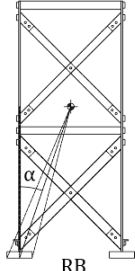
The two models represent 3-4 storey buildings with shallow, spread footings. Initially, the buildings were discretised as shear frames with two slab masses and had a set of columns resisting gravity loads and a set of braces resisting lateral loads. A 2DoF parametric eigenvalue problem was solved in *Mathematica* and then materials and member dimensions that provide stiffness and are not prone to buckling were estimated, based on the first mode only (Figure 3.3a, Appendix A.1). After trying different sets of materials and sections, aluminium slabs, columns and footings and PETG<sup>1</sup> braces were chosen. The software *SAP2000* was used to verify the vibration modes and periods of the model frame in prototype, and later, in model scale. The *SAP2000* model involved beam-column and shell elements (with distributed mass), pin connections for the braces and fixed connections for the other elements (Figure 3.4). With this model, the first two lateral modal shapes were approximated during full contact. For a 2DoF system simplification of the building models, these modal shapes are not orthogonal and hence only indicative.

The columns' thickness was designed to be sufficient to carry gravity loads but to contribute very little in the lateral stiffness. As a result, the fixity of the columns with the footings did not govern the lateral stiffness, which was then tuned in conjunction with the two slab masses to achieve a typical period of 0.6-0.7 s in prototype scale. Table 3.2 shows the storey lumped masses, which include the mass of slabs along with half of the columns and braces above and below the given storey. Note that an identical lumped mass for both the first and the second storeys was achieved by modifying the slab thicknesses (Figure 3.3b, Appendix A.1). The geometry of the two models was the same, however the mass of the footings fixed to the superstructure of the model RB cause it to have a different rocking slenderness than RA. Furthermore, the slenderness of RB is also dependent on an assumed point of rotation of its footings; assuming rotation occurs about the outer edge of the footing causes minimum slenderness, while assuming a rotation point at the centre of the footing causes a larger slenderness (see Table 3.2).

---

<sup>1</sup> PETG is Polyethylene Terephthalate Glycol

**Table 3.2: Design properties of the two rocking building models, RA and RB**

Properties	RB		RA	
	Model scale	Prototype scale	Model scale	Prototype scale
First mode period (prototype 2DoF shear model, <i>Mathematica</i> )	Not modelled	0.7 s	Not modelled	
First mode design period (Prototype model, <i>SAP2000</i> )	(0.019 s) (53 Hz)	0.66 s	(0.02 s) (50 Hz)	0.7 s
2DoF mode shapes (Prototype model, <i>SAP2000</i> )	$\varphi_1^T = (1 \quad 0.38)$ $\varphi_2^T = (-0.39 \quad 1)$		$\varphi_1^T = (1 \quad 0.45)$ $\varphi_2^T = (-0.47 \quad 1)$	
Total mass of uplifting parts	2.4 kg	86 metric tonnes	2.1 kg	75 metric tonnes
Top storey design stiffness	0.24 MN/m	7.9 MN/m	0.24 MN/m	7.9 MN/m
Bottom storey design stiffness	0.50 MN/m	16.5 MN/m	0.48 MN/m	15.9 MN/m
Friction angle $\varphi'_{crit}$ (Shepley, 2013)	33°			
Factor of safety for vertical loading for initial design	$FoS = 2.3$ , Design Approach 1/2 of EC7			
Storey lumped mass	0.83 kg (30 metric tonnes, prototype scale)			
Slenderness ratio, $\tan(\alpha)$ for a distributed mass configuration	Internal point: 0.25  Middle point: 0.34  External point: 0.42	0.30		
				

Regarding the footings, a design factor of safety for vertical loading  $FoS = 2.3$  was initially specified using Design Approach 1/2 of EC7, which is typical for the type of buildings considered here and with a static bearing pressure of approximately 80 kPa used below each footing. In addition, the proposed design allows both buildings to be tested simultaneously on the same centrifuge box with enough space from the boundaries and each other (Figure 3.5). Placing adjacent buildings too close might trigger the structure–soil–structure interaction which amplifies force demands in adjacent buildings (Trombetta *et al.*, 2013). To minimize effects from this interaction, the distance from the face of footings was larger than two times the width of a single footing. This distance was also adapted as a design requirement for each individual model to avoid triggering a mat foundation response, which is not within the research interest of this study.

Overall, this design was chosen to ensure that the pre-uplift response is as similar as possible for the models and enables direct comparison between structural and foundation rocking. With a typical natural period of the first mode of 0.7 s, the design was carried out in prototype scale (Appendix A). After that, the required performance of the various members was verified experimentally in model scale.

Two load cases were considered (Appendix A.2). These consist of the case at which the models are at the onset of uplift and the case at which the maximum rocking angle is achieved before toppling, that is the slenderness angle. For the first load case, the shape

of the acceleration spectrum of the EC8 was used (type 1) assuming linear elastic response (Figure 3.6, CEN 2004).

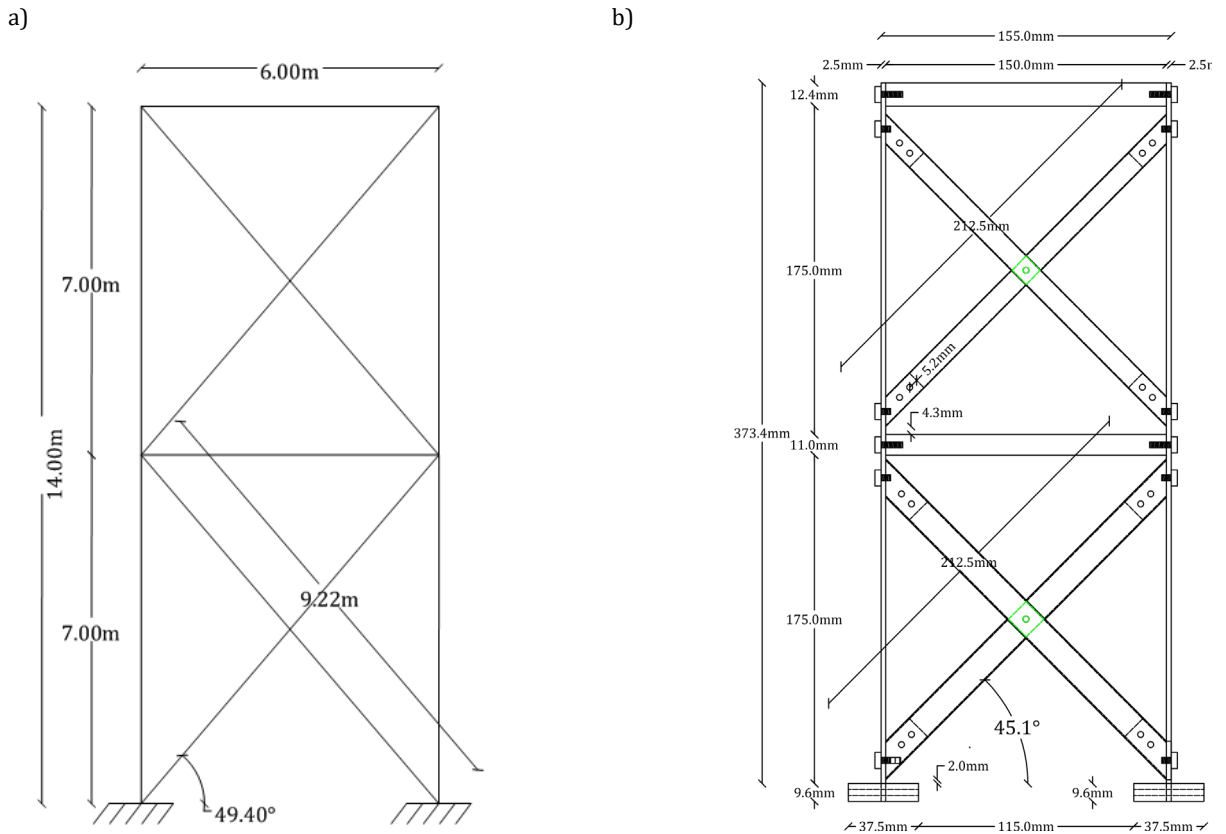


**Figure 3.3: Mathematica model in prototype scale (a) and final design dimensions in model scale (b) in elevation**

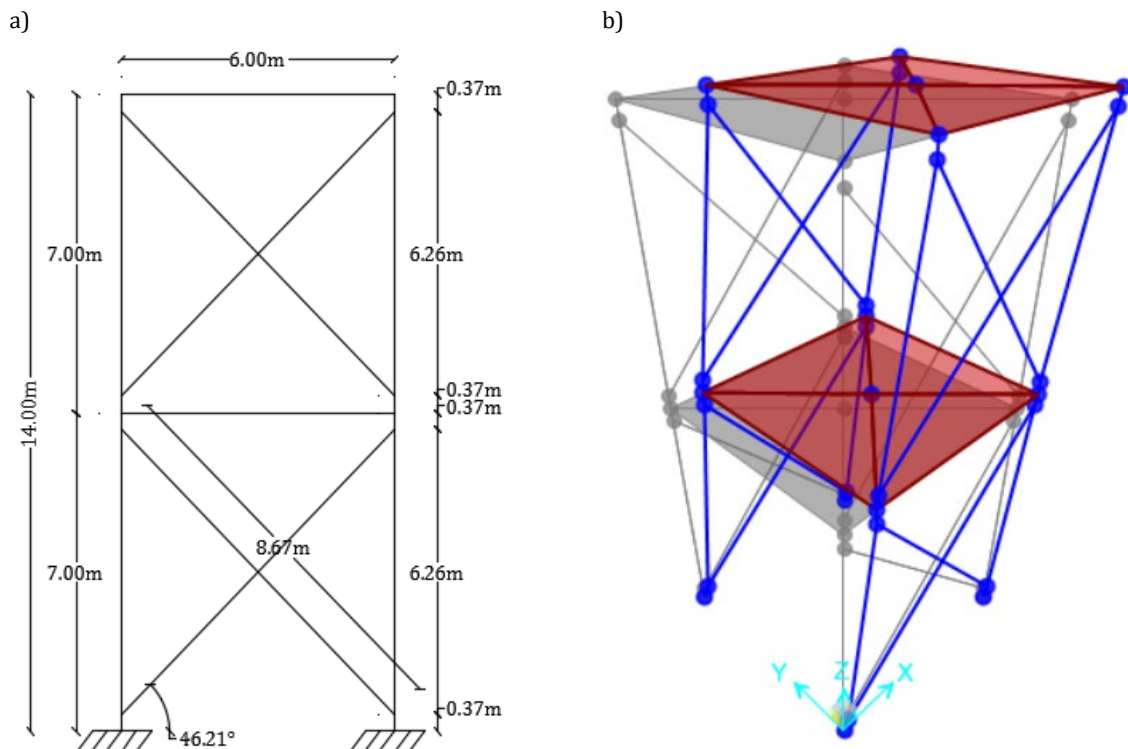


**Figure 3.4: SAP2000 model for the prototype structure**

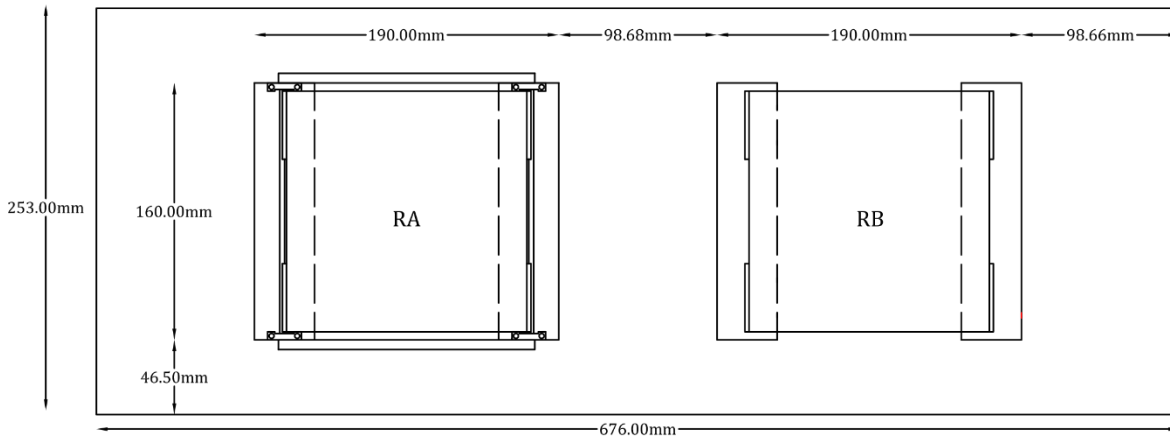


**Figure 3.5: Plan view of the buildings models RA and RB with respect to the centrifuge box**

When rocking action develops, the weight of the structure is transferred to the soil mainly from the columns of the one side. These columns are subjected to increased compressional forces due to this redistribution of loading. The shear force in the columns is capped by rocking and the maximum shear load should not be larger than the value at the onset of uplift. Based on this, the frame was assigned a tilted position with an angle equal to the slenderness angle and was constrained at the top and free at its base, where the shear and weight reaction are applied as external loads to the column ends. This is a simplistic way to estimate internal loads, avoiding time-consuming non-linear dynamic analysis for uplift and rocking. Part of the design process with respect to these two load cases is in Appendices A and B.

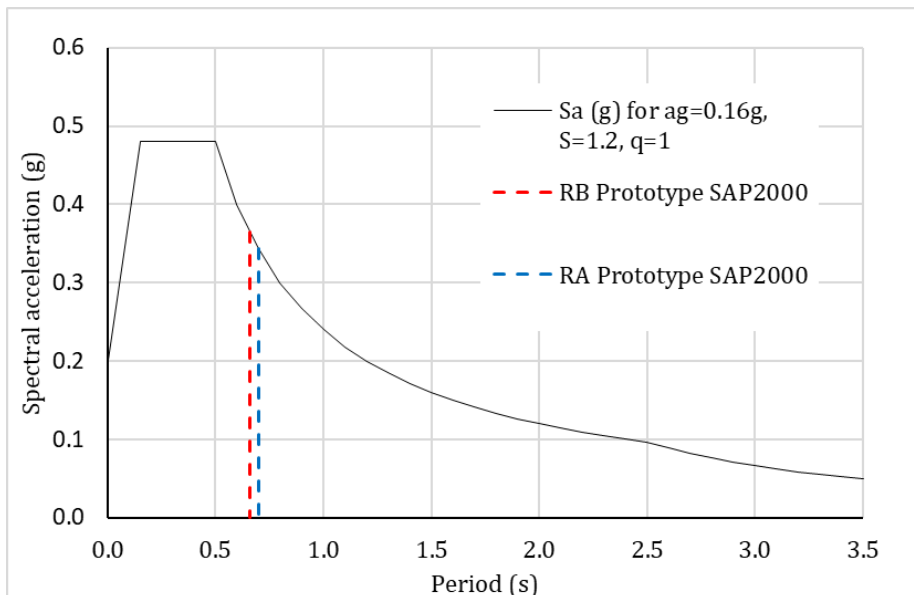


**Figure 3.6: The design spectrum used for designing the structural members at the onset of uplift (CEN 2004a, damping ratio: 5%)**

### 3.4 Experimental performance of braces

The design of the braces is available in Appendix A.3. The design ensures that the bracing elements will not experience buckling or material failure and that their connections

remain intact throughout the experiment, while the provided stiffness satisfies the tuning of the period as described in the main design. The bracing material is the polyester PETG, a derivative from poly(ethylene terephthalate) (PET), produced after the partial addition of cyclohexane-1,4 – dimethanol and is typically used for plastic sheet or where high-clarity parts are required (Via and Stretching, 2011; Focke *et al.*, 2016). A key characteristic of the building models is that the bottom storey has thick walled PETG tube braces, while the top storey has thin walled PETG tube braces instead.

To verify the design, a series of experiments was carried out. Figure 3.7 shows two of the specimens loaded in the Instron Load Frame. A loading protocol has to be chosen and the FEMA 461 (2007) is selected here which was developed for non-structural elements, but “*is also applicable to drift sensitive structural components*” (Krawinkler, 2009). Since the bracing system is drift sensitive, the loading protocol is applicable. The most critical failure is element buckling and this was chosen to be the ultimate point for the FEMA 461

a)



b)

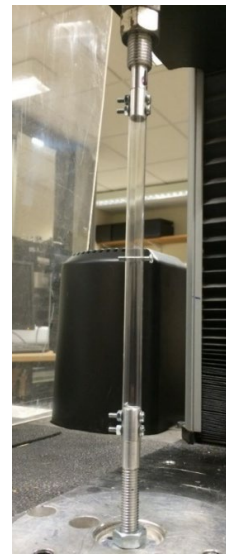


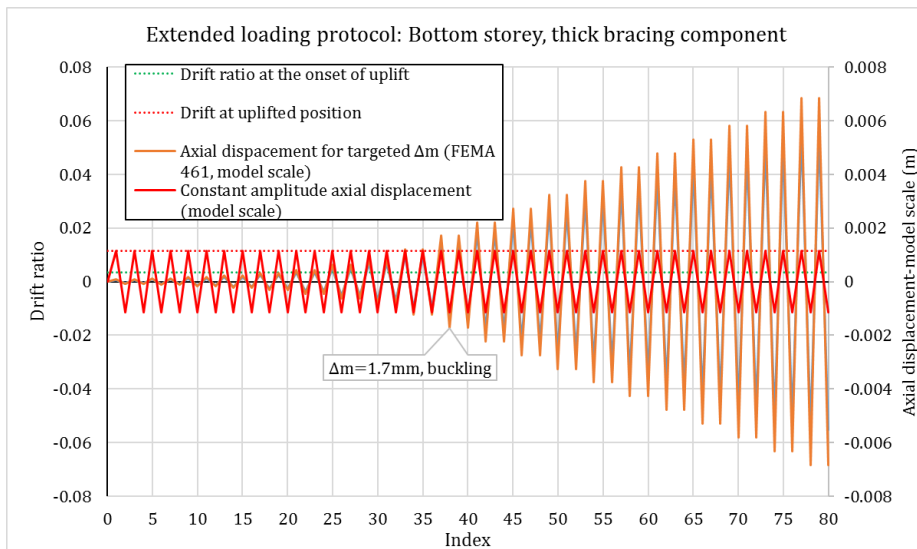
**Figure 3.7 Loaded specimens in the Instron Load Frame (a, thick walled bracing and b, thin walled bracing right)**

loading protocol which has a varying amplitude (Figure 3.8). A second loading protocol with a constant amplitude slightly smaller than the one corresponding to buckling was used too, as to eliminate any concerns on stiffness degradation at over 100 cycles (Figure 3.8). Table 3.3 summarizes the results of selected experiments as shown throughout Figure 3.9. Overall, the experiments verified that the design is adequate for the braces for the two load cases that were described in Section 3.2 and for the natural frequency of the building models. Based on the elastic modulus  $E$  measured (Table 3.3), for the top storeys the prototype scale design lateral stiffness is 7.9 MN/m with 85% provided by the braces.

For the bottom storeys, the same figures account for 15.9 MN/m and 98% for RA, while for RB 16.5 MN/m and 85%.

There was a very wide range of frequencies to test, implying that strain rate effects that enhance the strength and stiffness of the specimen might develop. Indeed, Table 3.4 shows that due to the centrifuge scaling laws, the strain rate increases. This would effectively mean that under centrifuge conditions the natural frequency of the structure would increase due to the rate enhancement of the stiffness. However, it can be assumed that strain rate effects on the performance of the PETG members are negligible for this material (Dupaix and Boyce, 2005).

a)



b)

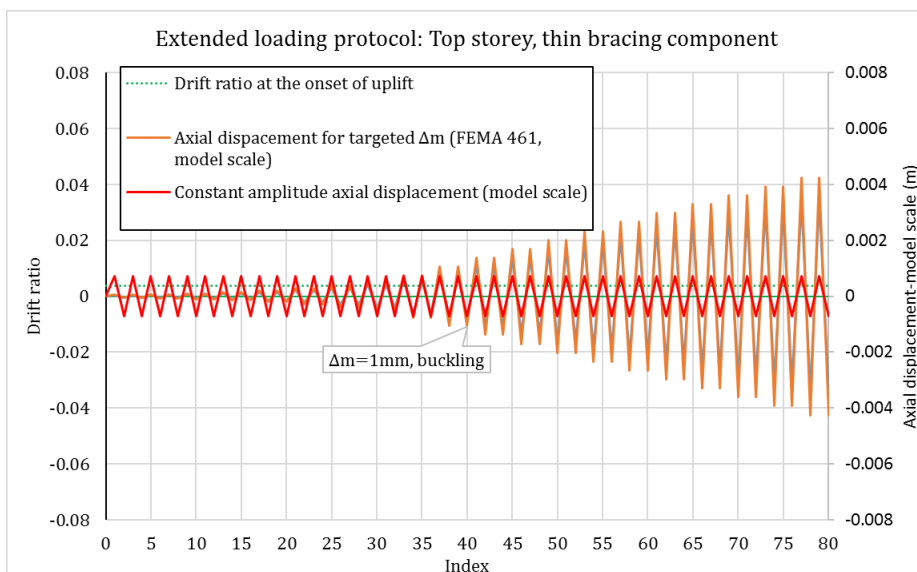


**Figure 3.8: Loading protocol for the thick brace of the bottom storey (a) and similarly for the thin brace of the top storey (b)**

### 3.5 Design and performance of the footing – fuse – linkage system

The building model RA can be upgraded for additional energy dissipation with a specially designed plate element (Figure 3.10, Appendix C). The plate element can yield and deform plastically due to bending from cyclic loading. This type of device is called “fuse”, because it absorbs the energy that would otherwise damage severely a building and is replaceable (see Section 2.2.2). A fuse is attached in each footing for the RA model. Each fuse is also attached to the bottom of the columns with an additional linkage. To attach the plate to the RA building model, a rod and linkage cantilevers are used, a design similar to that of the rocking chimney (Tyler, 1978, Figure 3.10, Figure 3.11). When the RA model uplifts and then rocks, the plate deforms in bending and dissipates energy due to hysteresis.

**Table 3.3: Summary of selected results from cyclic and monotonic tests**

Specimen code	Description	Displacement rate (mm/s)	Stiffness K (N/m)	Clear length of PETG specimen (m)	Nominal E (Design E=2.00E+09 Pa)	Design connection strength or design buckling load +/- (N)	Experimental buckling load or experimental connection strength +/- (N)
tcsctrial	Thick tube, constant amplitude	2.3	235500	0.1877	1.84E+09		
tcsc1	Thick tube, constant amplitude	2.3	226600	0.1877	1.77E+09		
tcfc	Thick tube, constant amplitude	7.5	250400	0.1877	1.95E+09		
tdsc1	Thin tube, constant amplitude	2.3	127200	0.1877	2.30E+09		
tdsv	Thin tube, varying amplitude	0.05-4.04	119800	0.1877	2.17E+09	245.6	221.0
tdfc1	Thin tube, constant amplitude	7.9	130000	0.1877	2.35E+09		
tcfte	Thick tube, fast tensional loading	7.5	246225	0.1877	1.92E+09	450.0	481.0
tcfbu	Thick tube, fast compressional loading	7.5	243616	0.1877	1.90E+09	-387.5	-654.2
tdfbu	Thin tube, fast compressional loading	7.5	127548	0.1877	2.31E+09	-103.8	-276.6

Average E (Pa)	2.06E+09
----------------	----------

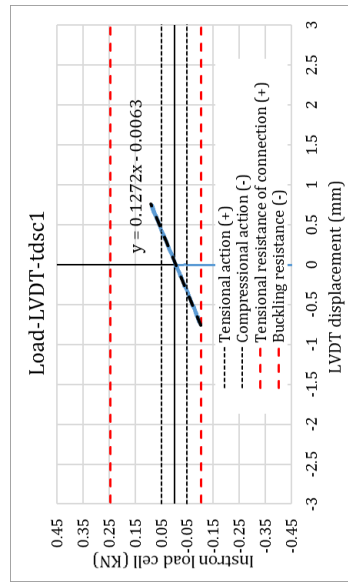
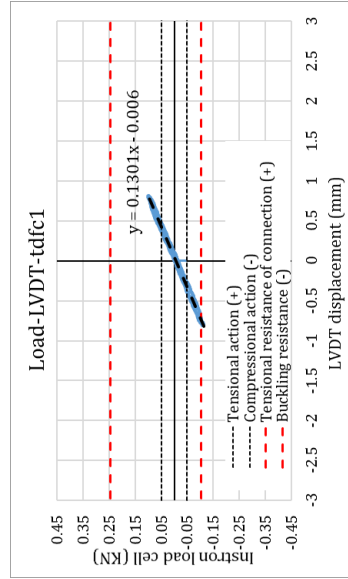
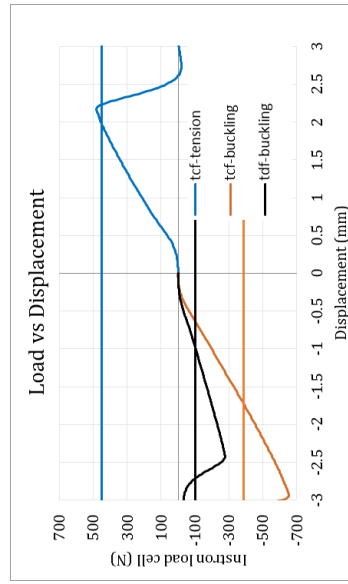
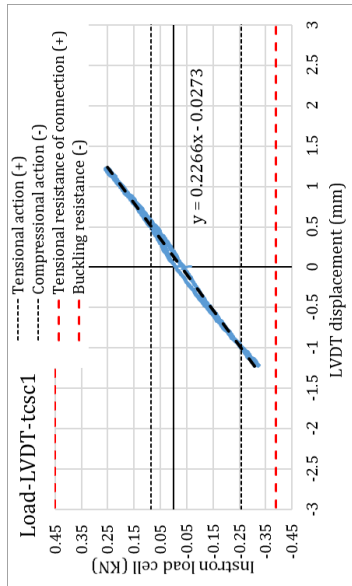
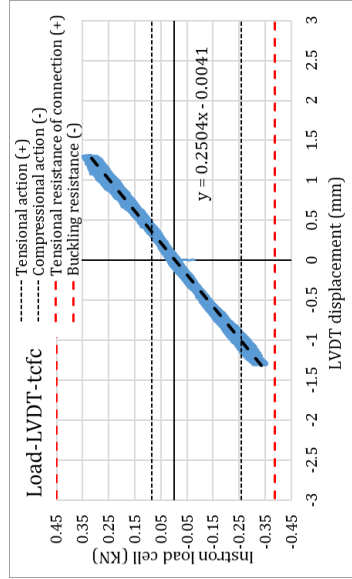
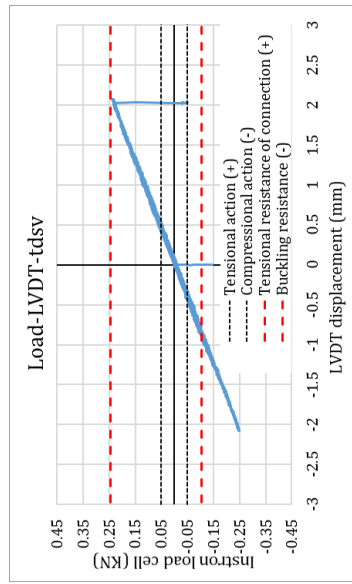
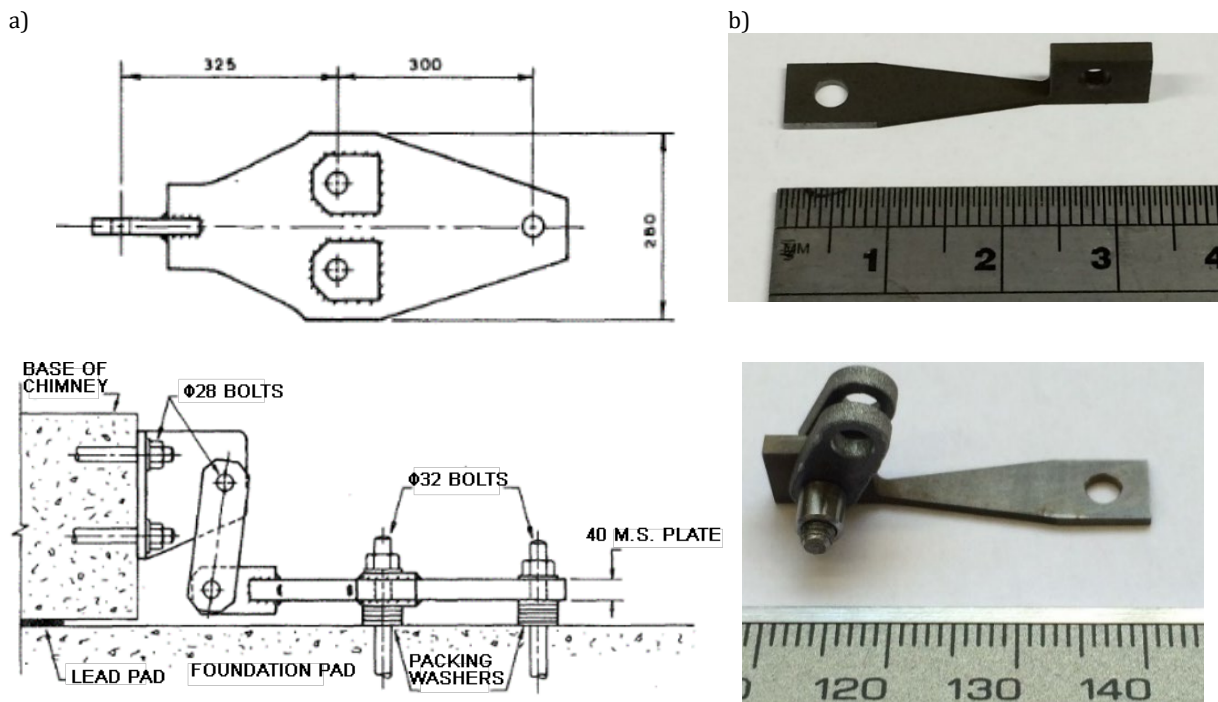


Figure 3.9 Buckling strength and connection tensile strength for the bracing elements. Buckling limits were set conservatively in the design

**Table 3.4: Strain rates for bracing elements in prototype and model scales**

Bracing element	Strain to the buckling load $\epsilon_b$	Strain rate - prototype scale (1/s) $\dot{\epsilon}_b = \frac{\epsilon_b}{T_1/4}$	Strain rate - model scale (1/s) $\dot{\epsilon}_b = \left(\frac{\epsilon_b}{T_1/4}\right) \cdot N_g$
Bottom storey, thick walled tube	0.08	0.05	1.65
Top storey, thin walled tube	0.005	0.03	1.01

The key design requirements of the fuse are two. The first one is that the fuse should yield relatively easily so that the weight of the footing that is attached on can work as an anchor. By considering this, the possibility the fuse drags the footing upwards during the uplift is minimized. The second requirement is to ensure that the anchoring will be effective even for a  $\pm 25\%$  rocking amplitude, which is considered very large for typical structures. This ensures that even for a severe earthquake in the centrifuge the fuse can continue functioning.



**Figure 3.10: A tapered plate for energy dissipation connected to the base of a rocking chimney (a, Tyler, 1978) and analogous plate with connection rod for model RA (b)**

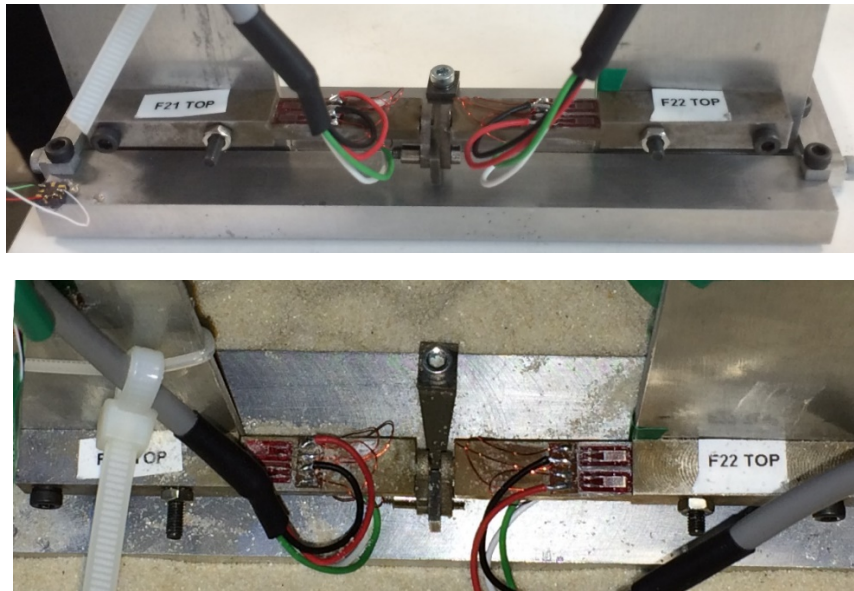


**Figure 3.11: The connection rod, the fuse and strain gauged cantilevers for model RA**

The design takes place in three steps. First, the shape of the plate is chosen to be a thin tapered S275 part. This decision for a tapered shape is based on real fuse elements (Tyler, 1978) and a tapered plate can be shown to dissipate more energy compared to a non-tapered beam (Appendix D). The main reason for this advantage is that a tapered plate yields uniformly over its length when bending develops. By considering an elastic-perfectly plastic model for S275, an elastoplastic solution for the force-displacement diagram can be derived (Appendix D). This solution is used as a guide for a finite element (FE) solution with *Abaqus*. In later FE simulations, the plate has an extended shape to partially mimic the final design. The simulation is compared against the analytic solution (Figure 3.12, Figure 3.13). For small displacements the responses match, but for larger displacements the FE simulation predicts a stiffness enhancement due to the development of tensional loading. This is expected as solutions for non-tapered beams analysed with large deflection theory exhibit same trends (Yu and Zhang, 1995). Strain hardening is also used in a later simulation (Figure 3.13), with a material model shown in Figure 3.14.

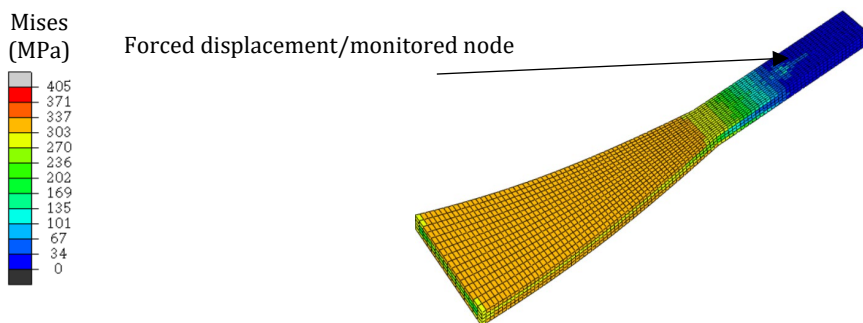


**Figure 3.12: Tapered beam (plate) simulation with material and geometric non-linearities**

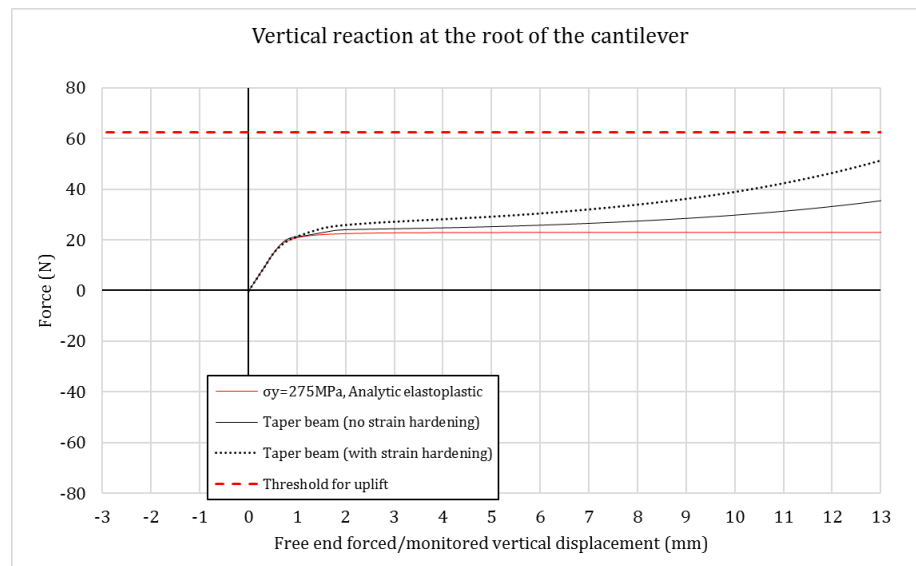


**Figure 3.13: Force-displacement diagram for guidance on the FE simulation**

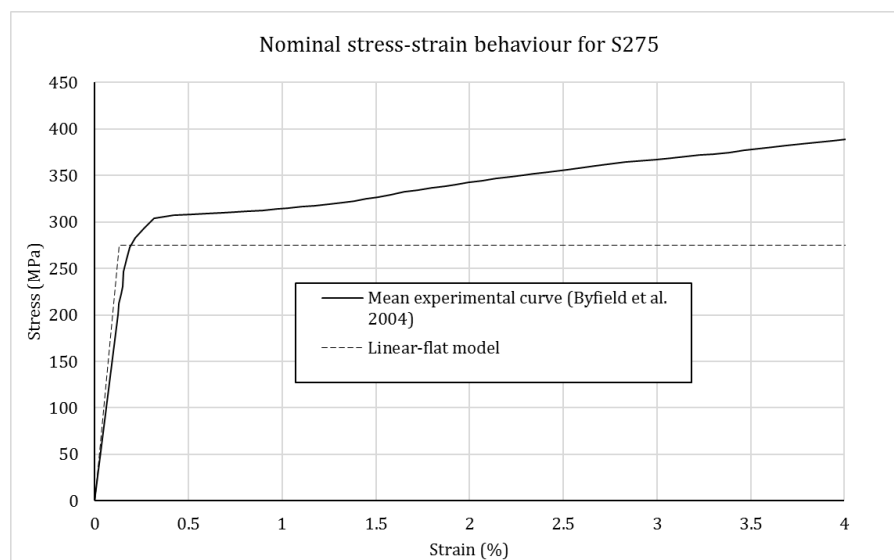


**Figure 3.14: Stress-strain models for S275 adopted from Byfield *et al.* (2005) for FE predictions**

After this validation, in the second step the FE model is extended to incorporate a rod which connects the plate element to the columns of the building model (Figure 3.10b). The design question is at which initial angle of the rod, the fuse can deform with a plateau force as much as possible, not only due to the material non-linearity but also due to the membrane force which potentially can be used in favour of sustaining the plateau. Figure 3.15 shows the force displacement behaviour for various angles when the fuse deforms due to an applied displacement on the top hinge, which according to the different kinematics and rod shape of each initial angle, corresponds to a rocking envelope of +25% to 100%. The force at the plateau of the fuse is compared with the weight of the footing in centrifuge conditions. If the plateau force crosses the weight of the footing, then the fuse

will drag the footing and the rocking behaviour of the RA model will be similar to that of the RB model. Therefore, based on the graph of Figure 3.15, an angle of  $30^\circ$  is considered as appropriate, as for a large part of the rocking amplitude the footing can work as an anchor. The selected configuration was modelled further by applying a cyclic displacement path for the horizontal and vertical direction of the top hinge (Figure 3.16). The cyclic responses of the root reactions are shown in Figure 3.17.

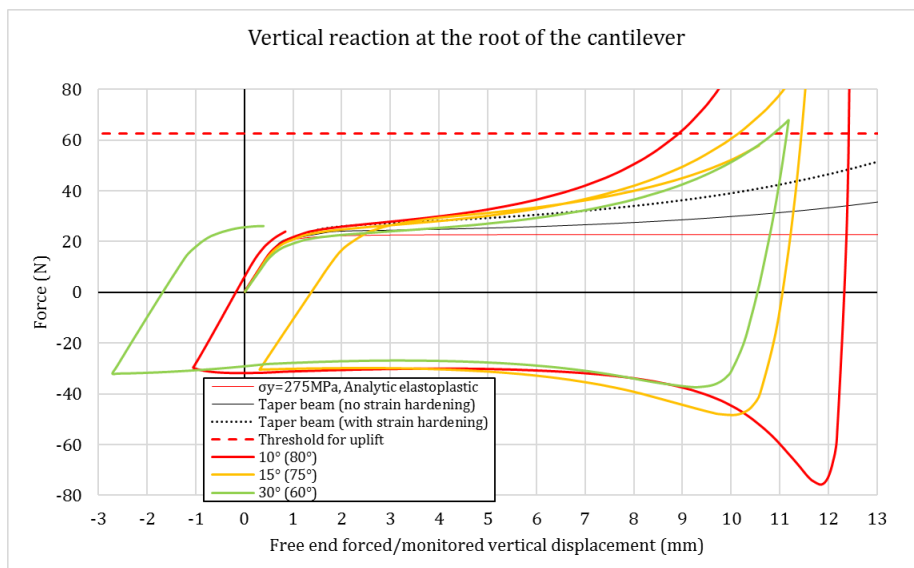
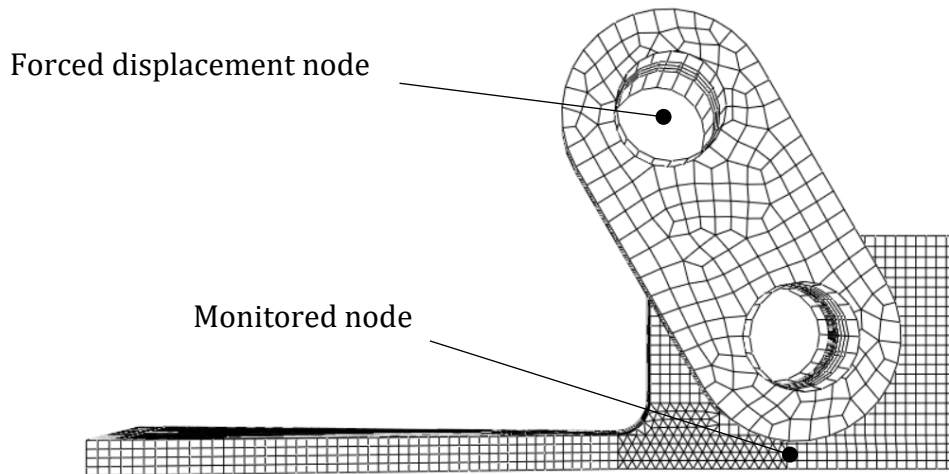
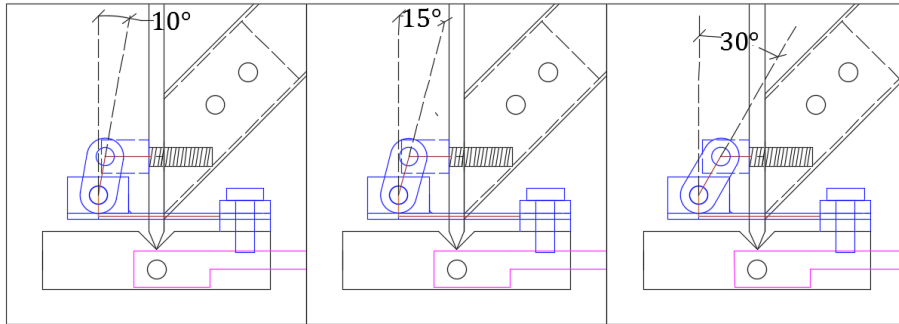
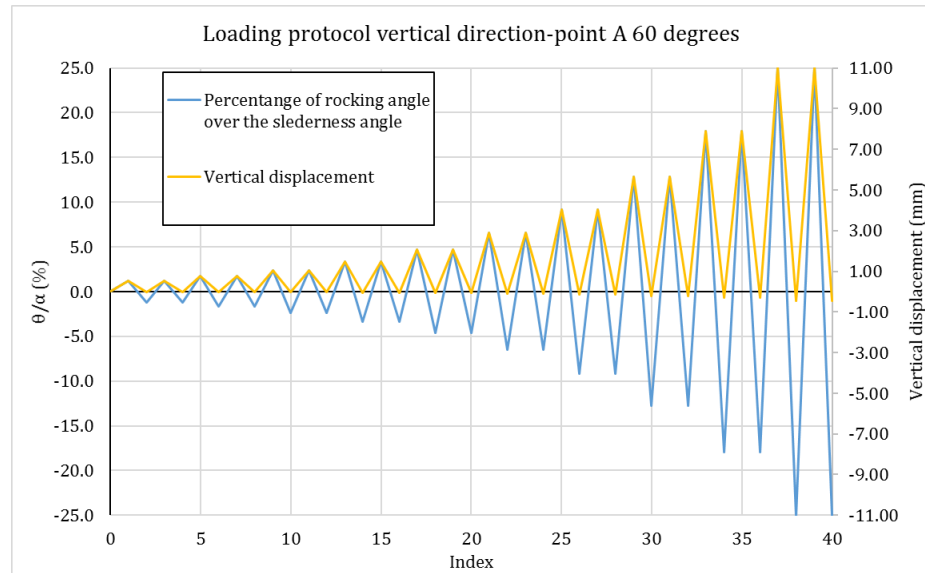


**Figure 3.15: Force-displacement diagram of the connection-plate subsystem for various initial angles (top) of the connection bar**

a)



b)

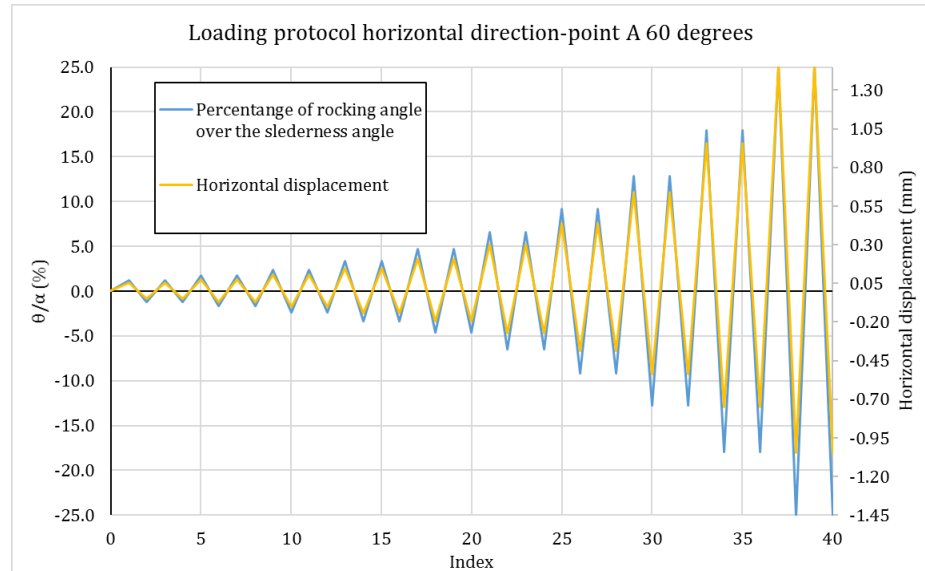


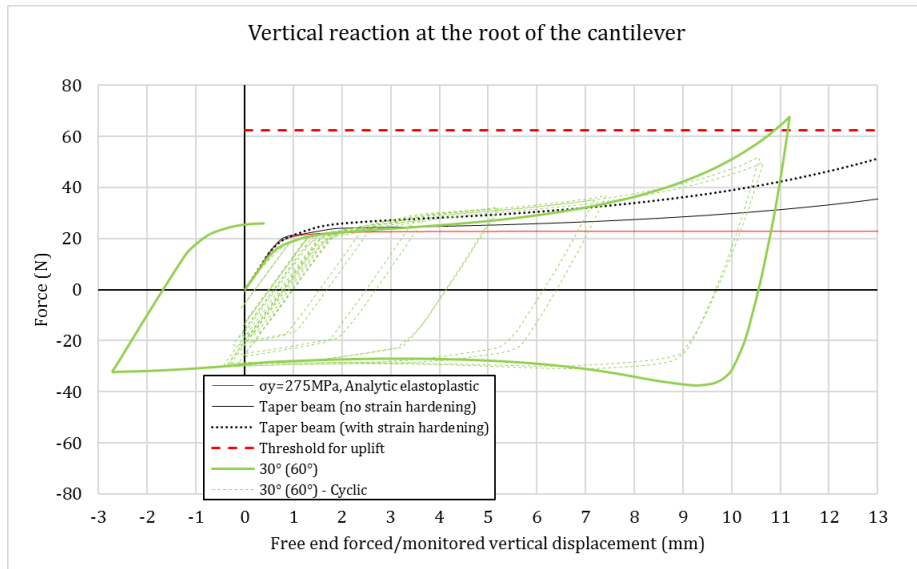
**Figure 3.16: Loading protocol for the top hinge in the vertical direction (a) and similarly in the horizontal direction (b) for the FE simulation**

Estimations on the contact length that remains between the footing and the soil surface during the uplift are also carried out, by considering equilibrium of the footing (Figure 3.18a). The equilibrium requires all three reactions from the root of the fuse cantilever to be applied as actions on the footing. The frictional force and the resistance provided by the tie rod are included in the predictions.

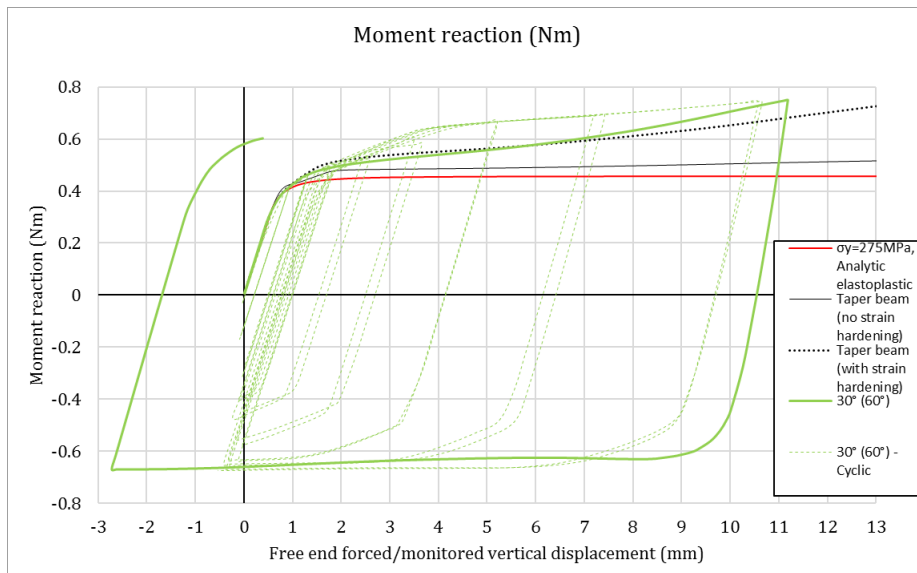
More specifically, the equations used to describe the contact length variation are two. For full contact conditions and assuming a trapezoidal distribution, Eq 3.2 describing vertical force equilibrium can be used (Figure 3.18a):

$$bl(\sigma_1 + \frac{\sigma_2}{2}) = W_F - F_p(\delta) \quad (3.2)$$

a)



b)



c)

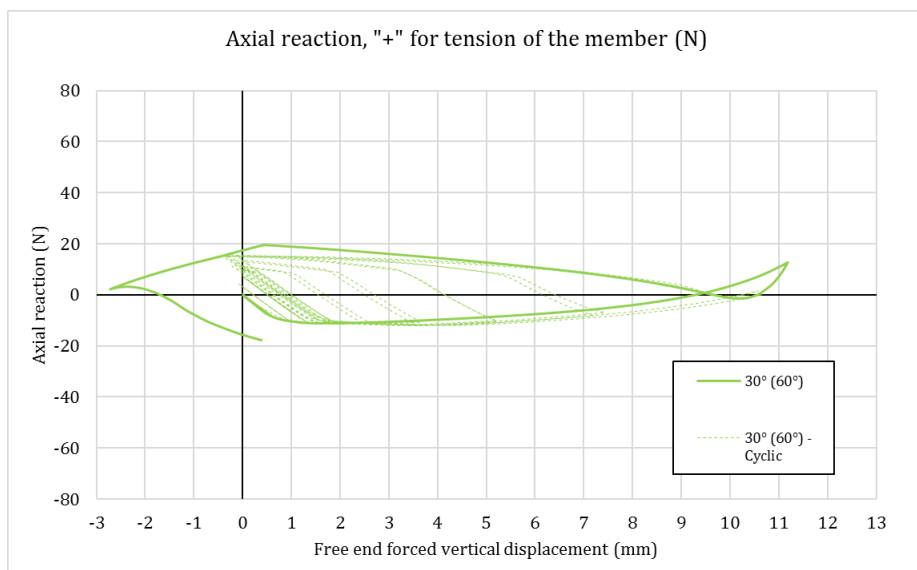


**Figure 3.17: Force-displacement diagram for the vertical (shear) reaction (a) moment-displacement diagram (b) and force-displacement diagram for the axial reaction (c) at the root of the cantilever based on FE simulations**

where  $W_F$  is the footing's weight and  $F_p(\delta)$  is the vertical reaction of the fuse element at the root, obtained as a function of the free end forced displacement  $\delta$  from the FE simulation. In addition, using moment equilibrium about point O yields:

$$\frac{b^2 l}{12}(\sigma_2 - \sigma_1) = M_p(\delta) - xF_p(\delta) - yN_p(\delta) - \frac{1}{2}(h - y)N_s \quad (3.3)$$

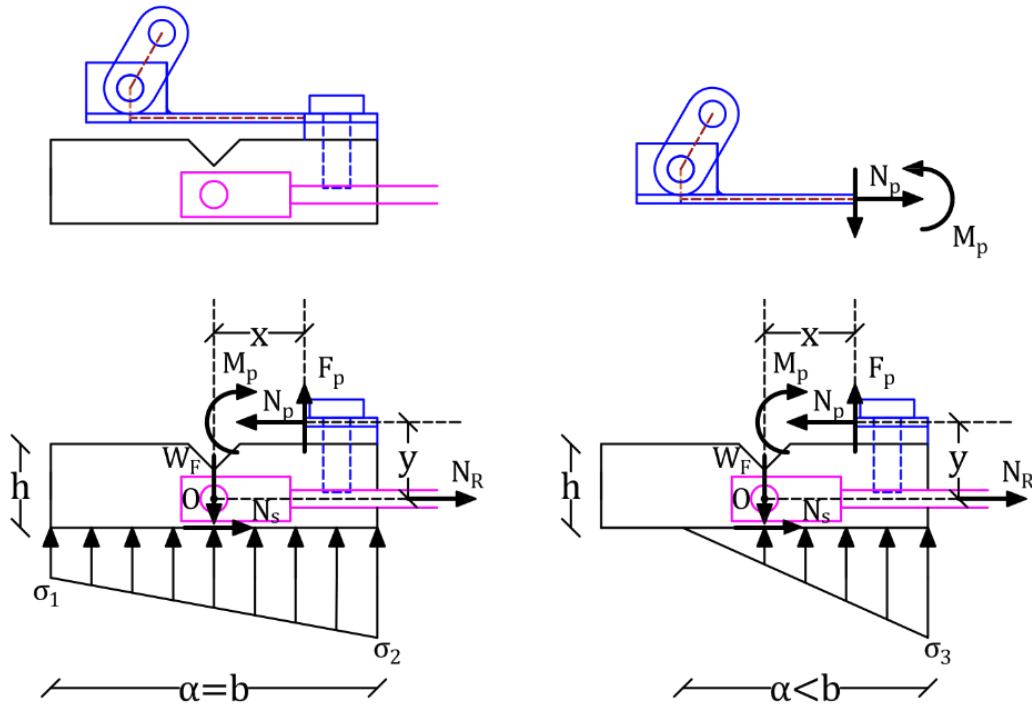
with  $M_p(\delta), N_p(\delta)$  the moment and horizontal force reactions of the fuse element at the root, obtained similarly as  $F_p(\delta)$ . For the frictional resistance of the soil  $N_s = qN_p$  where  $q$  is a factor which is assumed to be 0.5, meaning that the frictional resistance of the soil on the footing being on the side of the uplift receives 50% of the fuse horizontal reaction. The rest of this load is assumed to be transferred to the other footing via the tie rod force  $N_r$ . Eq. 3.2, 3.3 can then be used to solve for  $\sigma_1(\delta), \sigma_2(\delta)$ .

Similarly, when in partial contact and assuming a triangular stress distribution Eq. 3.2, 3.3 can be used repeatedly to solve for the unknown pair  $\sigma_3, a$ , with  $\sigma_3(\delta)$  the peak stress and  $a(\delta)$  the contact length, using the same assumptions for the horizontal load transfer. When the contact length reduces from the value of the full contact length ( $a < b$ ), then  $\sigma_1(\delta) = 0, \sigma_2 = \sigma_3(\delta)$ . When  $a = b$  then  $\sigma_1(\delta), \sigma_2(\delta)$  describe the stress profile, and  $\sigma_3(\delta)$  is not applicable.

Figure 3.18b suggests that the selected orientation of the fuse does not compromise the anchoring provided by the footing because  $\sigma_3(\delta)$  is never below or equal to zero when  $a < b$ .

In the third step, the final design was validated experimentally in the Instron Load Frame. The subsystem of the plate element with the connection rod were tested in an inclination such that the applied displacement in the FE model is mimicked (Figure 3.19). The derived displacement protocol is based on kinematics and corresponds to a  $\pm 25\%$  of rocking amplitude. This value is set as the ultimate point for the FEMA 461 loading protocol which is adopted here too (Figure 3.20). To perform the validation, the vertical and horizontal reactions from the FE model are analysed in the direction parallel to the vertical load of the Instron Load Frame. The plateau force can be easily validated although there is clearly a stiffness mismatch in the results (Figure 3.21). This is most probably due to a slack of the top hinge in the testing machine, as it was found that the stiffness of the bar in the top hinge is so large that the whole stiffness of the system reduces practically to the stiffness of the fuse. To manufacture a perfect hinge at this small scale is rather challenging and thus, slacks are expected in the fuse system in the centrifuge.

a)



b)

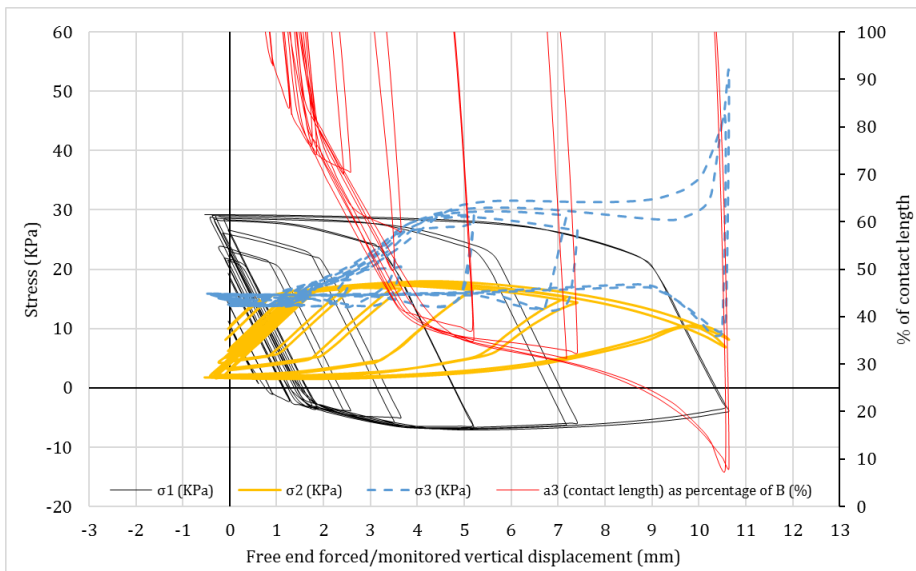
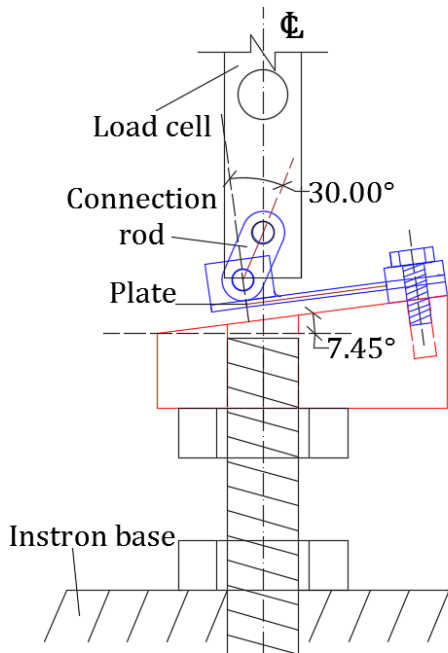


**Figure 3.18: Estimation of stress magnitude under the footing and of the contact length with respect to the width of the footing under the cyclic behaviour of the fuse based on FE predictions**

a)



b)

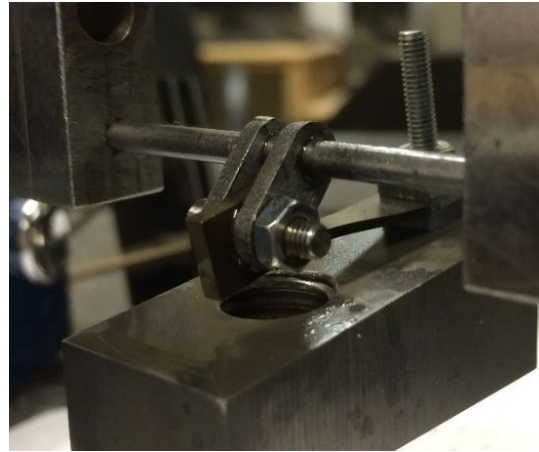


**Figure 3.19: Loading of the plate element with the connection rod in the Instron Load Frame**

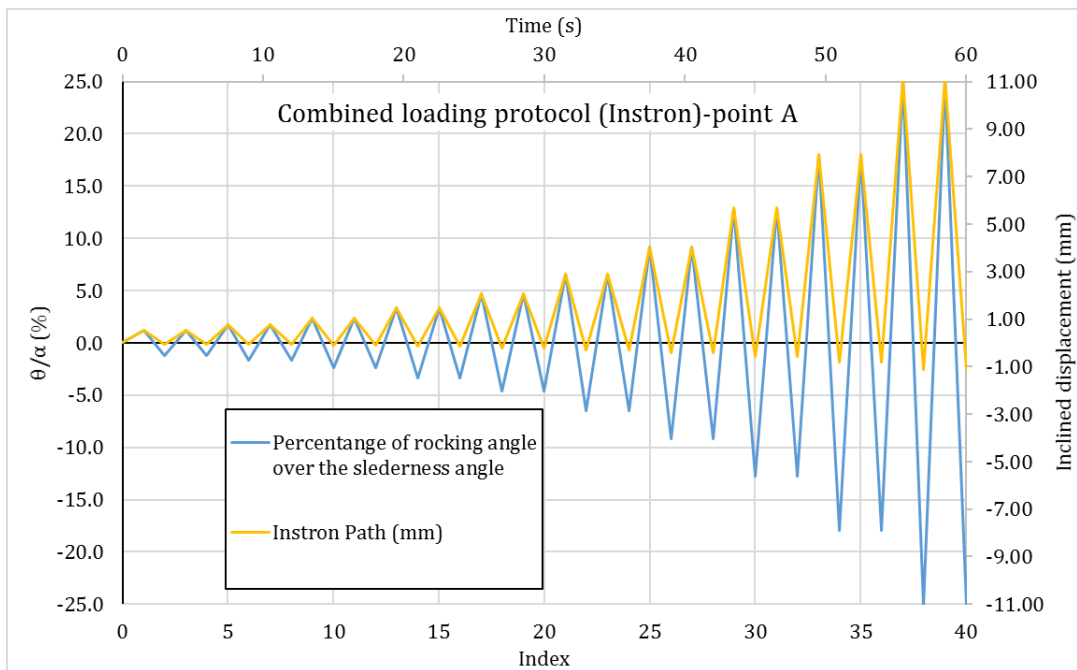


**Figure 3.20: The loading protocol that was used in the experiment and the FE predictions.**

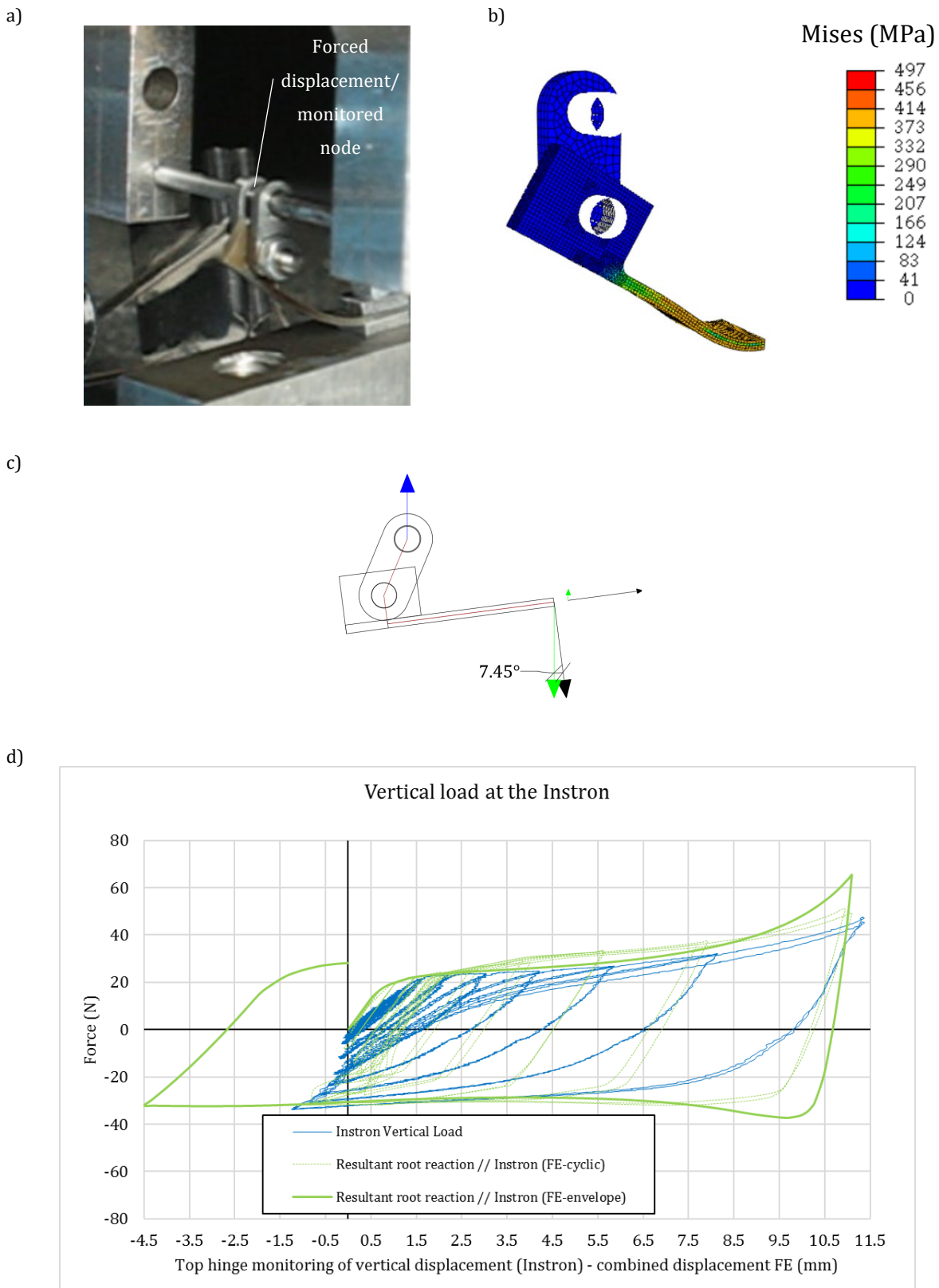


**Figure 3.21: Deformed shape in maximum displacement (experiment-a, FE simulation-b), force vector analysis for comparison of results (c) and force-displacement diagram for the experimental result and FE prediction of the resultant root reaction parallel to the Instron vertical load (d)**

### 3.6 System identification

The natural frequencies and modal damping ratios were measured experimentally by exciting the building models (Table 3.5). To measure the natural frequency in fixed base

conditions and before the centrifuge testing, the storeys and the base were excited by lateral impact and excitation by uplift and rocking was used too. Selected free vibration traces were used after the excitations to extract the natural frequencies and the modal damping ratios. The damping measured in this case refers only to the energy dissipated by the structural components.

From the free vibration traces following the earthquake excitations in the centrifuge, same natural frequencies were obtained for both models (see Sections 5.1, 5.3). Table 3.5 shows that only in the case of the first mode for model RA, a smaller frequency is obtained before the centrifuge tests. This can be perhaps attributed to geometric imperfections for the lengths of the RA columns. A slightly shorter column for instance will not establish full contact during the vibration and thus the natural frequency will be smaller when compared to a perfectly hinged model.

**Table 3.5: Summary of system identification**

Properties	RB		RA	
	Model scale	Prototype scale	Model scale	Prototype scale
First mode frequency (fixed base)	53 Hz	1.6 Hz	46 Hz	1.4 Hz
Second mode frequency (fixed base)	147 Hz	4.5 Hz	136 Hz	4.1 Hz
First mode frequency (in centrifuge)	53 Hz	1.6 Hz	50 Hz	1.5 Hz
Second mode frequency (in centrifuge)	147 Hz	4.5 Hz	136 Hz	4.1 Hz
Modal damping ratios $\zeta_1, \zeta_2$ (fixed base)	0.0208, 0.0057		0.0053, 0.0066	

To estimate the modal damping ratios  $\zeta_1, \zeta_2$  in fixed base conditions, the free vibration traces were filtered to isolate the vibration modes and then, the logarithmic decay was applied to each of them. Figure 3.22 indicates a difference between the first modal damping ratios for the RA building model (hinged) and the RB model (fixed). This can be partially explained by considering the difference in the base conditions. Since the columns of the RB are rigidly connected in the footings, material and frictional damping can be assumed to be provided by the footings and their connection respectively. On the contrary, the RA model cannot develop additional damping from its footings, simply because it rests on them and this also perhaps explains the reduced scattering compared to the RB model.

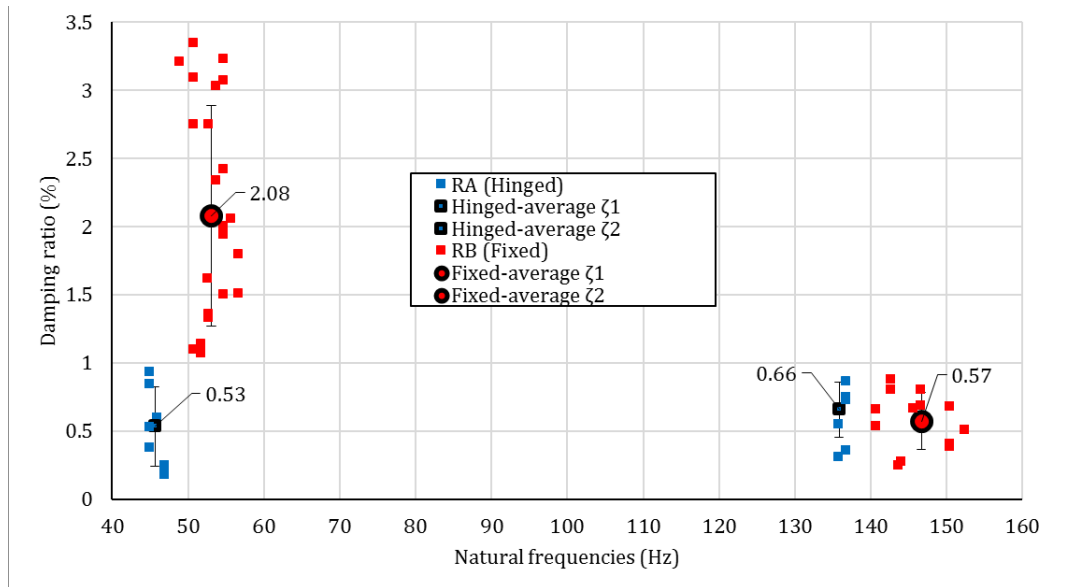


**Figure 3.22: Obtained modal damping ratios from fixed base free vibrations**

### 3.7 Summary

A structural design, particular to achieving similar properties between buildings with different types of rocking, was presented. The design involved braces that carry lateral loads at the pre-uplift stage of the response. For structural rocking, a fuse element was designed too. The performance of these special components was assessed experimentally and was found adequate for the purposes of this research. Overall, the two buildings, one rocking above the foundation level (RA), and the other rocking below the foundation level (RB), represent structural and foundation rocking respectively. Their characteristics refer to typical prototype scale buildings and hence they can be used as the main specimens for centrifuge testing.

# 4 METHODOLOGY FOR CENTRIFUGE TESTING

## 4.1 Introduction

This chapter builds on the system identification of the building models and the performance of their components in 1g conditions, by introducing the experimental equipment and program of the centrifuge campaign. Next, a signal processing tool is presented, the so-called wavelet transform. This tool enables the visualization of frequency evolution over time and is particularly useful for rocking response, since that contains highly mixed content over small periods of time. A calibration procedure for this tool is performed based on free rocking response as observed in a specific centrifuge test. Finally, the design of the buildings is validated in hyper gravity with specific examples from centrifuge testing (Pelekis *et al.*, 2018a).

## 4.2 Experimental apparatus

### 4.2.1 The Turner beam centrifuge

The Turner beam in the Schofield Centre (Figure 4.1) was used for geotechnical centrifuge operations. This is a 150 g-ton machine with a radius of 4.125m. The Turner beam is designed to rotate about its central axis in a horizontal level. At the one end of the beam, the container with the specimen and the equipment rest in a swing, whereas at the other end a package with the same weight is attached to ensure balance. While the beam develops an angular acceleration, the swings at both ends are pushed outwards and eventually lift due to the centrifugal force. At the same time the beam is in tension, and

also bends due to the earth's gravitational field. The bending effects are negligible compared to the tensional action.

#### 4.2.2 Servo – hydraulic earthquake actuator

To produce earthquake motions in a centrifuge environment is a very challenging task, since very high accelerations are required to be achieved in a very small amount of time.



**Figure 4.1: The Turner beam centrifuge in Cambridge**

Madabhushi et al. (2012) designed and manufactured an actuator which is operated by controlling the flow of oil (Figure 4.2). The innovative design tackles challenges from both gravitational fields resulting in pressure demands of 280 bar. This is a large pressure but comparable to other typical servo-hydraulic actuators, such as the MTS 506.00 which was used for 1g shaking tests operating at 210 psi (DeJong, 2009). This actuator can receive input in the form of real earthquake motions, harmonic motions and pulses and this why was selected for the series of excitations presented later.

More specifically, the main parts of the actuator are an external power pack, a servo-valve, a hydraulic system and a local oil storage system. To generate the shaking of the centrifuge model mounted on the actuator, the required amount of energy is stored in hydraulic oil pressurised at the power pack, located outside the centrifuge chamber. From there, the hydraulic system delivers the pressurised oil to the servo-valve of the actuator, which is mounted on the centrifuge swing. An electric signal proportional to the desired displacement time-history then controls the flow rate in the servo-valve. The change in the flow rate achieves the motion of the actuator and thus the earthquake is generated. To ensure the earthquake demand for high flow rate, the oil is first stored in accumulators next to the actuator (locally) and at the end of the earthquake is stored again in a separate local accumulator. Finally, a return pump delivers it back to the power pack which houses units to cool and heat the oil so as to maintain appropriate levels of viscosity. This process can then be repeated for additional earthquakes.



Maximum displacement	$\pm 10$ mm
Useful frequency range	20 – 100 Hz
Operational temperature	18 – 35 °C
High flow pressure	300 bar

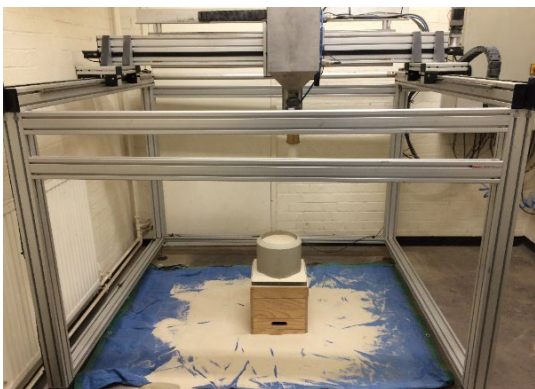
**Figure 4.2: The Cambridge servo-hydraulic actuator (Madabhushi *et al.*, 2012)**

Generally, the use of an actuator might trigger vibrations of the centrifuge arm while in flight, since the frequency content of the fired motion might match the natural frequencies of the centrifuge arm. Mason *et al.* (2010) have proposed filtering out potential resonant frequencies to avoid exciting the centrifuge arm while in flight.

#### 4.2.3 Automatic sand pourer

Advances in control engineering have allowed to manufacture a sand pourer which replicates the manual methods of pouring (Madabhushi, Houghton and Haigh, 2006). Its automation allows for consistency in the drop height and more importantly in covering uniformly the area of interest with sand of the required density. The basic principle of operation is that the machine hopper moves in a 3D space according to the commands of an operator to a desktop PC. The operator can run commands for pausing and continuing the pouring so that instruments can be placed in the soil model or to reload the hopper. Prior the preparation of a soil model for centrifuge testing, small samples are used to verify that the used nozzle and drop height can result in the desired specific density and it is possible to create a chart for multiple relative densities (Figure 4.3).

a)



b)

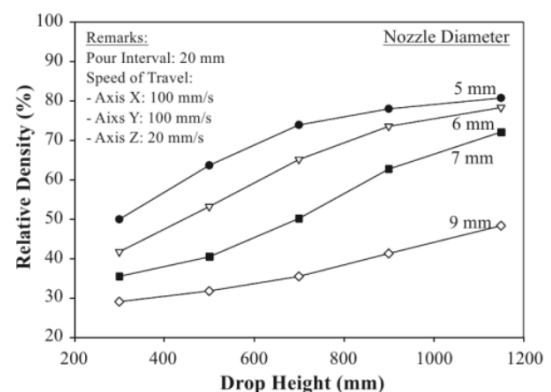


**Figure 4.3: Preparation of a cylindrical sample to verify the specific density achieved with the automatic sand pourer (a) and design chart for Hostun sand (b, Chian, Stringer and Madabhushi, 2010)**

#### 4.2.4 Equivalent shear box

In dynamic centrifuge testing, waves are generated in the soil and propagate in its mass as a result of the earthquake actuator. It is essential to avoid reflections on the boundaries of the centrifuge box as these can amplify and contaminate the waves generated originally by shaking. To avoid boundary effects, Brennan & Madabhushi (2002) designed a box made of a series of stacked metal rings joined with rubber layers in between (Figure 4.4). The design allows for a close match of the soil' stiffness with the stiffness of the box. This represents a prototype scenario according to which the waves propagate freely in a soil space of uniform properties. This is ideal for comparisons of analytical and experimental data and this is why it was used.



**Figure 4.4: Equivalent shear beam box**

**Table 4.1: Overview of experimental sets conducted in centrifuge conditions**

EXPERIMENTAL SET	BUILDING MODELS	SOIL TYPE	EXCITATION TYPE	CRITICAL INSTRUMENT MALFUNCTION
IP01	RA and RB	Dry dense sand	Multi-cyclic	YES
	RA w fuse and RB			
IP02	RA and RB	Dry loose sand	Multi-cyclic	YES
	RA w fuse and RB			
IP03	RA w fuse and RB	Dry dense sand	Single-, multi-cyclic and real records	NO
	RA and RB			
IP04	RA w fuse and RB	Dry loose sand	Single-, multi-cyclic and real records	NO
	RA and RB			

### 4.3 Experimental programme

#### 4.3.1 Side – by – side testing on dry sand

The two building models were placed side by side on dry sand and were subjected to a series of earthquake motions (Figure 4.5). This configuration ensures that the input motion induced from the actuator is the same and that any later comparisons of seismic performance can be straightforward. Overall, four experimental sets were carried out

(Table 4.1). The first two experimental sets (IP01 and IP02) were conducted with different densities of sand. During IP01 and IP02 there was critical instrument malfunction, so a comparison was not possible and therefore these tests are not discussed here (Pelekis, Madabhushi and DeJong, 2017). Similarly, experimental sets IP03 and IP04 were conducted in different sand densities and these form the core of the experimental analysis in Chapters 5, 6 (Table 4.2). Specifically for these experimental sets, dry, dense, Hostun HN31 sand ( $D_r = 96\%$ ) was used for IP03, while a relatively looser dry sand ( $D_r = 58\%$ ) of the same type was used for IP04. Throughout the dissertation, the two different densities of sand are referred to as "loose" and "dense" to indicate the relative densities, while limited reference to "IP03" and "IP04" is provided after this section.

### 4.3.2 Instrumentation

The response of the building models and the soil were monitored by using accelerometers in the horizontal and vertical direction (Figure 4.5). The building models were instrumented with Micro-Electro-Mechanical System (MEMS) accelerometers (MEMS) of type ADXL 193 with a built-in filter with a nominal cut-off frequency of 400 Hz (Figure 4.6a). The accelerometers embedded in the soil were of piezoelectric type DJB A23 (Figure 4.6b) and their operating frequency is between 1 – 10 kHz. For these piezoelectric accelerometers, frequencies below 10 Hz are not registered uniformly compared to the rest of the frequency band, which in addition is limited due to instrument resonance starting beyond 1 kHz. Furthermore, sources of noise were detected at 1.5 kHz and 3 kHz during both on and off testing time. Therefore, it is reasonable to define an operating frequency of the piezoelectric accelerometers of 15 – 1000 Hz, which also sufficiently covers the operating frequency range of the servo hydraulic shaker employed for generating earthquakes. The difference of frequency ranges of the two types of accelerometers means that any potential frequency content over 400 Hz in the buildings' response might appear only in the soil.

Finally, strain gauges were attached to the braces of the top and bottom storeys and only on the one side of the building to obtain internal loads directly (Figure 4.6c). These were connected with a half bridge configuration and measured the axial deformations of the braces. The design of the bolted connections of the braces to the columns allowed to remove and re-attach the former in their original position. While off the building models, the strain gauges of the braces were calibrated with weights.

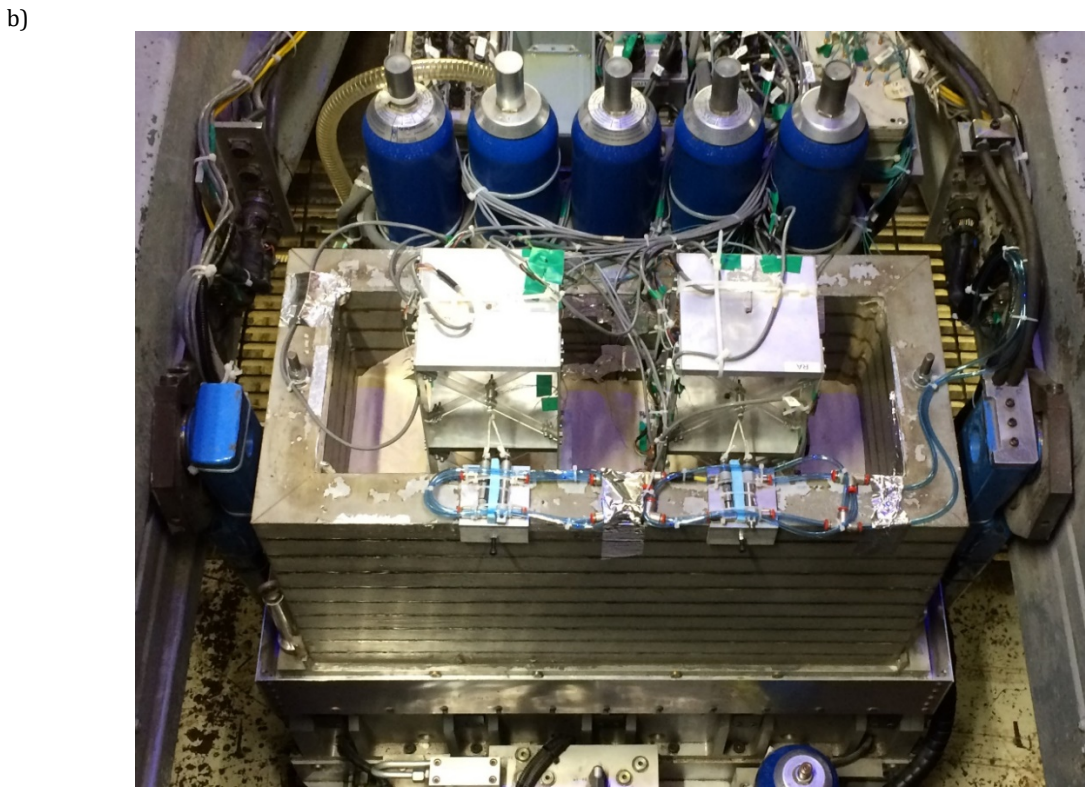
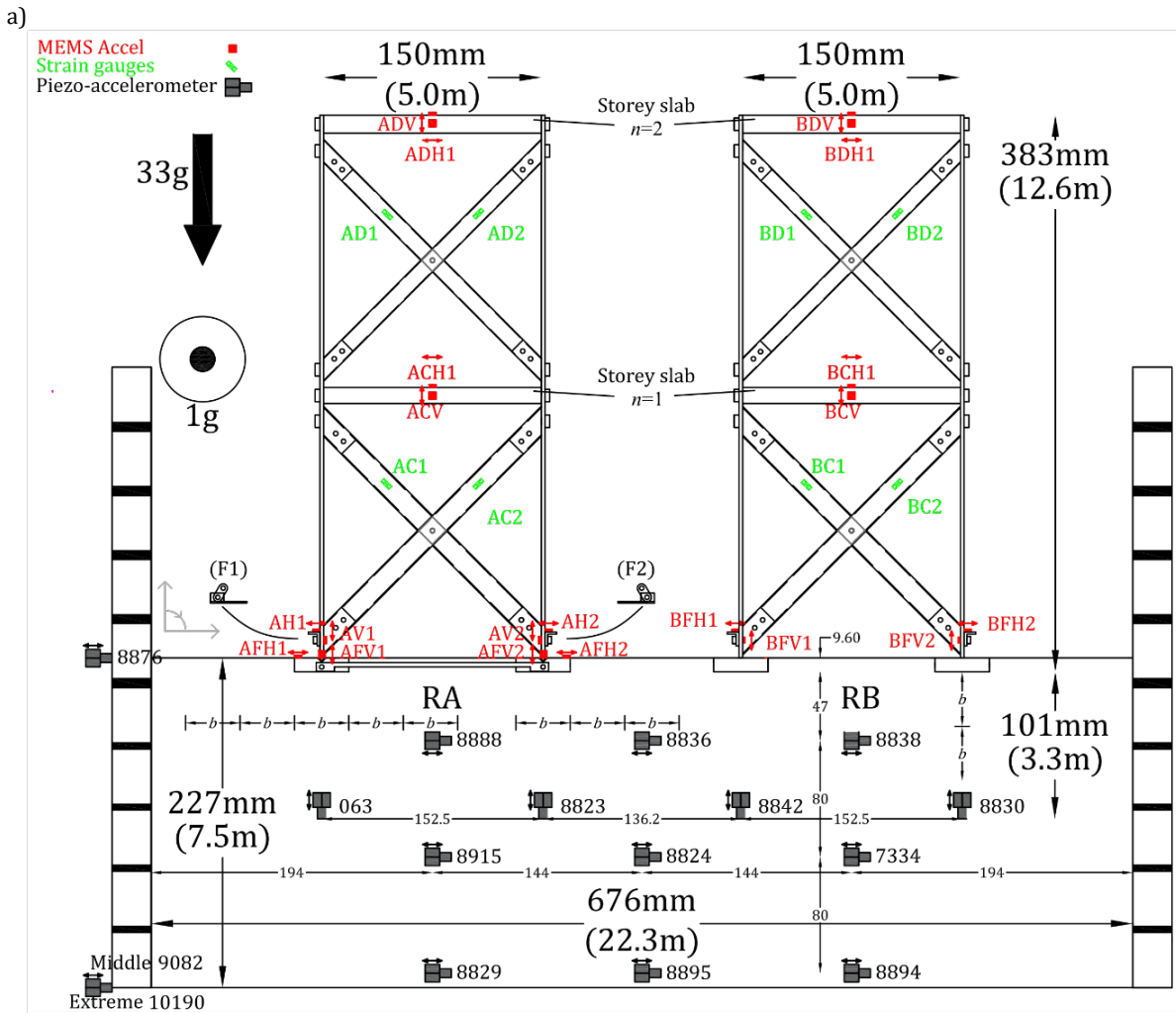


Figure 4.5: Cross-sectional view of the centrifuge model with overall dimensions (a) and view when fully prepared (b)

**Table 4.2: Programme with soil and input motion characteristics of the experimental set IP03 (Dense sand) and IP04 (Loose sand)**

EXPERIMENTAL SET (RELATIVE DENSITY)	TEST (FLIGHT#, RA FUSES)	SEQUENCE & INPUT MOTION*		Max Acc of	Max Acc of	PGA*** (g)	PGA (g)	
				input** (g) Model scale	input (g) Prototype scale	Model scale	Prototype scale	
DENSE SAND ( $D_r = 96\%$ )	TEST-0 (FLIGHT-0, ON)	EQ-1	0.1: Kobe	10.21	0.31	13.82	0.42	
		EQ-2	0.2: 50 Hz Pulse	9.41	0.29	14.06	0.43	
		EQ-3	0.3: 30 Hz Pulse	6.84	0.21	10.07	0.31	
		EQ-4	0.4: 50 Hz Cyclic	1.26	0.04	1.81	0.05	
		EQ-5	0.5: 50 Hz Cyclic	6.93	0.21	8.27	0.25	
		EQ-6	0.6: 30 Hz Cyclic	7.10	0.22	11.60	0.35	
	TEST-1 (FLIGHT-1, ON)	EQ-1	1.1: Kobe	10.04	0.30	13.85	0.42	
		EQ-2	1.2: Imperial Valley	2.50	0.08	3.51	0.11	
		EQ-3	1.3 50 Hz Pulse	11.57	0.35	16.86	0.51	
		EQ-4	1.4: 30 Hz Cyclic	7.20	0.21	9.94	0.30	
		EQ-5	1.5: Hz Cyclic	9.31	0.28	13.08	0.40	
	TEST-2 (FLIGHT-2, OFF)	EQ-1	2.1: Kobe	9.49	0.29	13.68	0.42	
		EQ-2	2.2: Imperial Valley	2.52	0.08	3.68	0.11	
		EQ-3	2.3: 50 Hz Pulse	11.41	0.34	16.67	0.51	
		EQ-4	2.4: 30 Hz Cyclic	7.25	0.22	10.83	0.33	
		EQ-5	2.4: 50 Hz Cyclic	11.74	0.36	17.09	0.52	
	LOOSE SAND ( $D_r = 58\%$ )	TEST-1 (FLIGHT-3, ON)	EQ-1	1.1: Kobe	8.68	0.26	10.68	0.32
			EQ-2	1.2: Imperial Valley	2.45	0.07	3.00	0.09
EQ-3			1.3: 50 Hz Pulse	10.15	0.31	15.47	0.47	
EQ-4			1.4: 30 Hz Cyclic	6.92	0.21	10.24	0.31	
EQ-5			1.5: 50 Hz Cyclic	11.02	0.33	16.08	0.49	
EQ-6			1.6: 30 Hz Pulse	6.74	0.20	10.24	0.31	
TEST-2 (FLIGHT-4, OFF)		EQ-1	2.1: Kobe	9.18	0.28	10.86	0.33	
		EQ-2	2.2: Imperial Valley	2.36	0.07	2.79	0.08	
		EQ-3	2.3: 50 Hz Pulse	10.83	0.33	15.38	0.47	
		EQ-4	2.4: 30 Hz Cyclic	7.03	0.21	9.15	0.28	
		EQ-5	2.5: 50 Hz Cyclic	11.02	0.33	15.78	0.48	
		EQ-6	2.6: 30 Hz Pulse	7.04	0.21	9.58	0.29	

\*Note: Model scale frequencies 50 Hz and 30 Hz correspond to prototype scale periods 0.66 and 1.10 respectively.

\*\* Max Acc represents the maximum acceleration of the input ground motion as recorded at the base of the centrifuge box (sensor 10190).

\*\*\*PGA is the maximum acceleration recorded at the free surface of the soil in between the two building models (sensor 8836).

### 4.3.3 Input excitations and spectral response

Results from the main experimental sets of dense and loose sand are discussed throughout the dissertation; each experimental set involved more than one centrifuge flight and each flight involved a series of earthquake excitations (Table 4.2). The input motions used during each flight included a combination of real earthquake records and single- and multi-cycle input motions of a nominal frequency (Table 4.2, Figure 4.7).

The philosophy behind the selection of the earthquake input motions is to examine the response of the models for a variety of scenarios. Single- and multi-cyclic motions with a frequency close to the buildings' natural frequency were selected to cause uplift following resonance in full contact conditions. Rocking structures are also known to be vulnerable to low frequency excitations, and especially pulse excitations, so single- and multi-cyclic excitations with a relatively lower frequency were used too. Similarly, a record of the Kobe 1995 earthquake was chosen because it contains a distinct pulse. The Imperial

Valley record has a very high frequency content over many cycles, so it was used to test the buildings' response on a different scenario than the other excitations. The resulting Imperial Valley motion was of lower amplitude than expected and therefore, it rather caused a full contact response with small amplitude. First, motions that are not expected to cause small deformations in the soil and the buildings were used such as the pulses or small amplitude motions, and then the cyclic motions were used which are expected to cause cumulative and thus larger deformations.

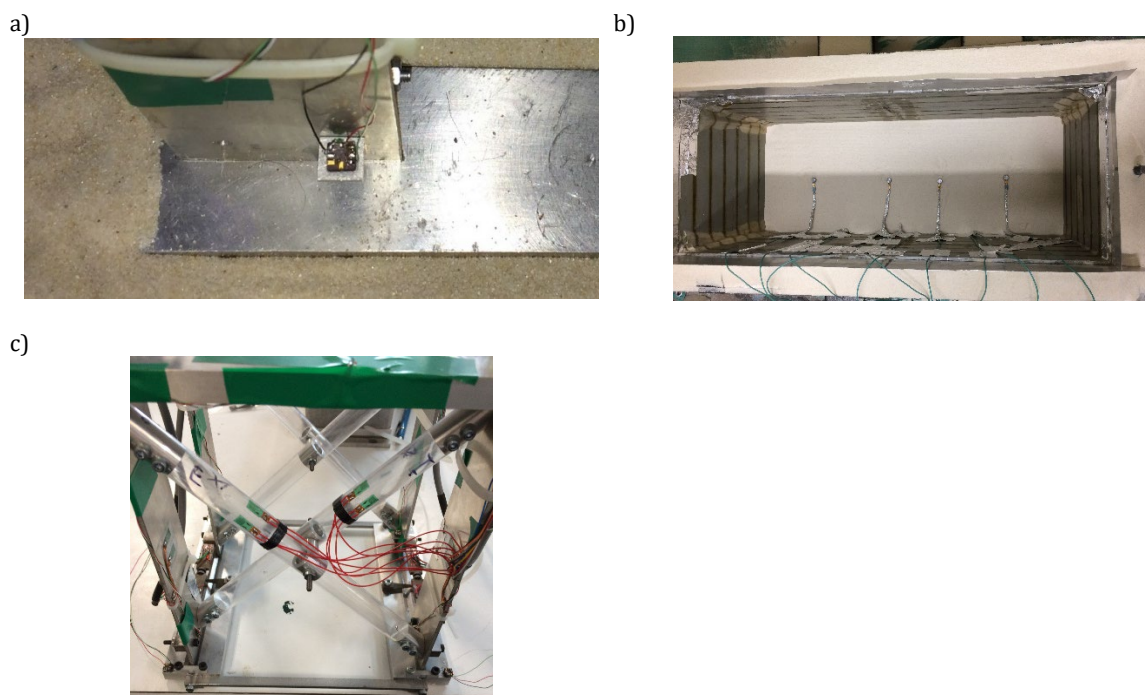


**Figure 4.6: Examples of instrumentation: MEMS accelerometer with special column attachment (a), piezoelectric accelerometers placed during sand pouring (b), and strain gauges attached at the bottom braces (c)**

The accelerometer embedded close to the surface between the two models (sensor 8836, Figure 4.5a) was used as the soil free (near) surface for the PGA (Table 4.2) and the response spectra (Figure 4.7). For most cases where the same input excitations were used, the PGA values and response spectra were found to be similar both in terms of spectral magnitude and frequency range of practical interest (0-3 Hz, prototype scale). The cases with a discrepancy in spectral magnitude (particularly the Imperial Valley records and 50 Hz cyclic excitations in dense sand) can be explained by a difference in the shaker's actual input (not shown) rather than any alteration from soil amplification/attenuation. Table 4.2 also shows that there is some amplification of the motion in terms of the maximum input accelerations compared to measured PGA (see for

instance Test-0 Eq-1). This can potentially be attributed to the soil medium and some feedback from the building models. The latter is investigated in Chapter 6.

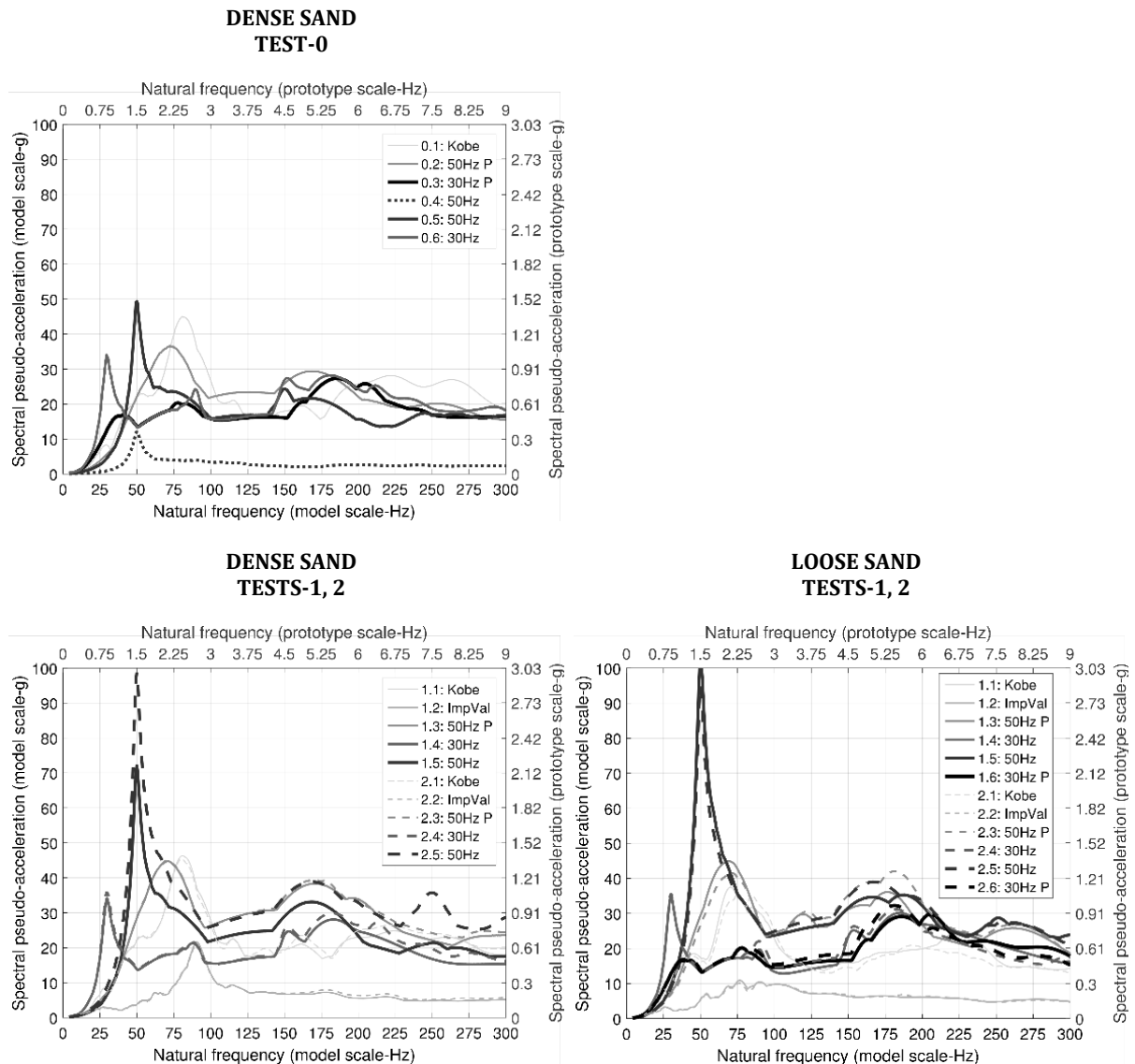


Figure 4.7: Spectral response near the soil free surface for  $\zeta=5\%$

## 4.4 Experimental identification of frequency content

### 4.4.1 Wavelet transforms for civil engineering

Wavelet transforms were used to identify the frequency content throughout the dynamic response (Pelekis *et al.*, 2018). With Fourier analysis, a signal can be broken down to multiple stationary sinusoids of infinite duration with varying frequencies, but a wavelet transform involves wavelets with both varying duration and frequency for the signal decomposition. This type of analysis is useful to investigate time-varying frequency response, and has been used in the civil engineering context, for example, to interpret vibrations in buildings caused by nearby trains or vehicles (D. E. Newland, 1994; D.E. Newland, 1994), or to identify hidden pulses in earthquake records (Vassiliou and Makris,

2011). Additionally, wavelet transforms have been found to clearly indicate suppression of driving frequency content in upper layers of soil during liquefaction (Haigh *et al.*, 2002). More recently, wavelet transforms were used to indicate excitation of higher modes in bridge response with translational and rotational components of ground motion (Sextos, Mylonakis and Mylona, 2015). All these applications have in common the non-stationarity of the signals examined, i.e. signals where the frequency content of which changes locally in time due to a specific event. Since severe ground shaking can cause the structure to switch between being in full contact with the ground and rocking, the wavelet transform is a useful tool to detect changes in frequency content due to dynamic response transition.

#### 4.4.2 Observation of free rocking response

In this section, a test with a single excitation pulse of a nominal, low frequency of 30 Hz is discussed. Figure 4.8 shows the time history of the lateral and vertical accelerations of model RA, along with the input acceleration at the base of the centrifuge box and its frequency content. The FFT of the input acceleration indicated that the dominant excitation frequency was slightly off from the specified 30 Hz (as a result of the actuator), to a higher value of 40 Hz, yet this was below the first mode frequencies of the structures. The readings from the vertical accelerometers indicate that sequential uplift occurred at either side of model RA, demonstrating rocking motion. The trace of the storey accelerations is characterized by initially small, high frequency oscillations superimposed on low frequency oscillations, before rocking ceases and a full contact, free vibration response occurred.

A close-up of this response from 5.62 - 5.66 s is shown in Figure 4.8d to highlight the rocking response. The input acceleration was nearly zero for the duration examined here. The vertical column acceleration plot shows that the left column of the model RA oscillated vertically while it was not in contact with the footing, while the right column experienced a near zero acceleration while it was in contact with the footing and was the rotation point for rocking, and then the trend reversed. The higher frequency oscillations of storey accelerations can also be seen more clearly in Figure 4.8, superimposed on the larger low frequency component of the rocking response which dominated the signal over that time. Essentially, this close-up indicates that the type of response that occurred was a full cycle of free rocking. Following this response, possibly due to the large damping provided by the soil, a full contact response developed with free flexural vibration.

To explore the frequency content of the response, the FFTs of the lateral storey accelerations and the vertical acceleration of the column bases are also shown (Figure

4.8a-c). There is significant energy concentrated at the low end of the spectrum for the lateral accelerations which is attributed to the excitation's frequency content and the first natural frequency for full contact free vibration response. For the bottom storey acceleration, there are two distinct frequency peaks, namely, at 136 Hz and at 125 Hz. The former frequency comes from the second mode hinged base response towards the end of the record, superimposed on the first mode. For the top storey, the 124 Hz frequency appears suppressed, while the 136 Hz is as profound as in the bottom storey. Due to the inherent nature of the FFT, it is difficult to evaluate the dominance of the various frequencies during different times of the response. To achieve this, the frequency content of this response is examined using the wavelet transform in the next section.

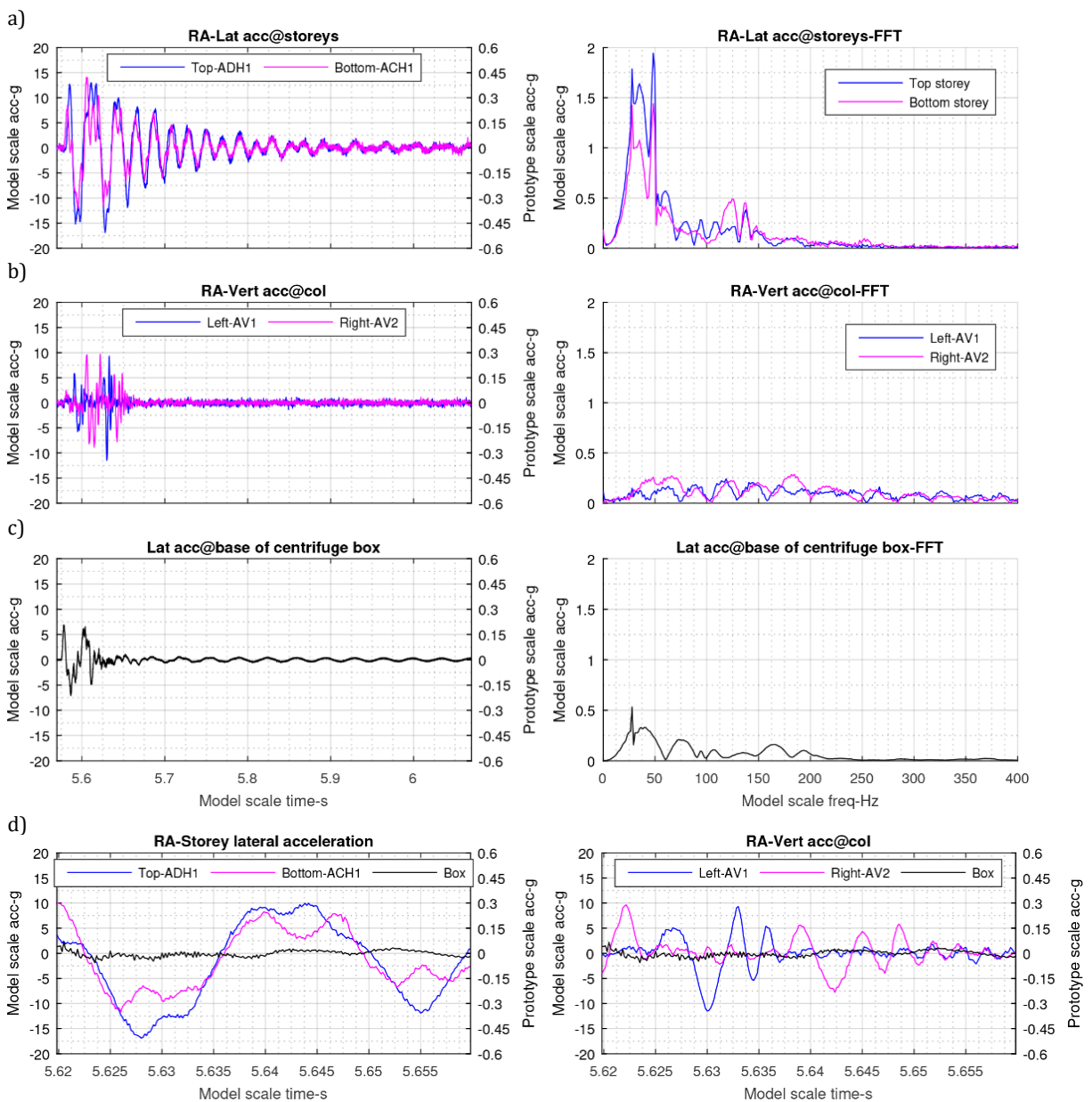


**Figure 4.8: Storey lateral accelerations and column ends vertical accelerations and their FFT (top two rows), excitation time-history with FFT (third row), and close-up at free rocking (bottom row) for model RA**

### 4.4.3 The Morse superfamily of Wavelets and the Mexican hat

The wavelets employed for the time-frequency analysis were the Morse superfamily using an online available package (Lilly, 2017), and the Mexican hat as provided by MATLAB (Misiti *et al.*, 2015; The MathWorks Inc, 2015). The Morse superfamily has complex wavelets and is characterized by the so-called time-frequency bandwidth product  $\beta\gamma$  which controls the shape of the employed wavelet with respect to the desired discretisation in time and frequency. In generalized form, the Morse wavelet can be defined in the time domain as (Lilly and Olhede, 2009):

$$\psi_{\beta,\gamma}(t) = \frac{1}{\pi} \int_0^\infty \left(\frac{e\gamma}{\beta}\right)^{\beta/\gamma} \omega^\beta e^{-\omega^\gamma} e^{i\omega t} d\omega \quad (4.1)$$

where  $t$  and  $\omega$  represent the time and circular frequency, respectively. Then the Morse wavelet transform  $W(t, s)$  of a signal  $x(t)$  is defined as:

$$W(t, s) = \int_{-\infty}^\infty \frac{1}{s} \psi_{\beta,\gamma}\left(\frac{\tau - t}{s}\right) x(\tau) d\tau \quad (4.2)$$

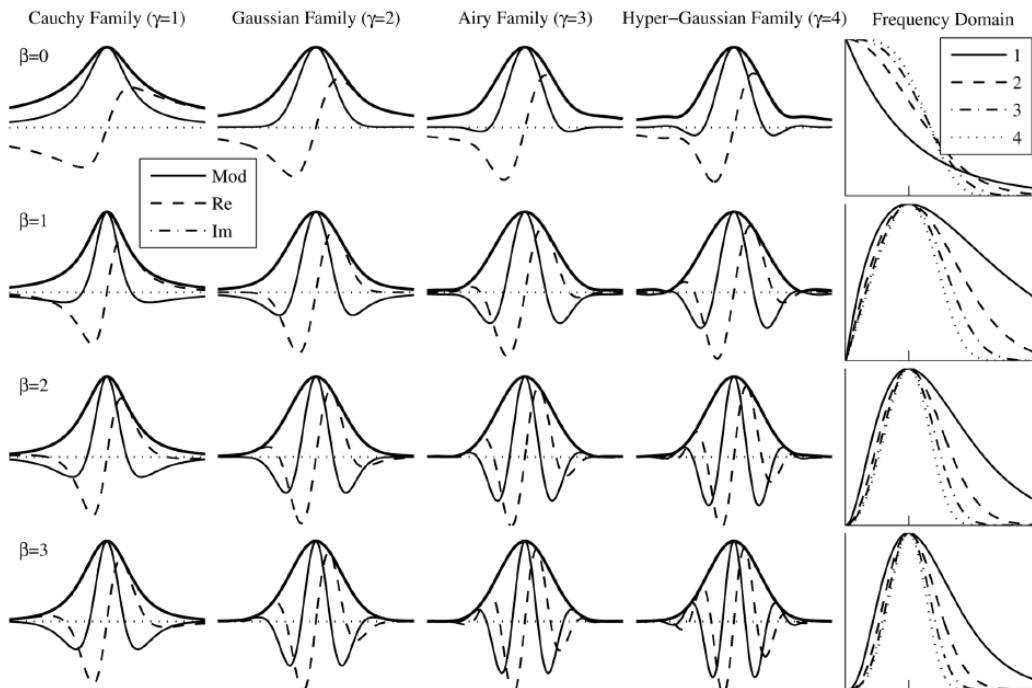


**Figure 4.9: The generalized Morse wavelets in time for  $\gamma = 1-4$  and  $\beta = 0-3$  are shown in the first four columns, while the fifth column shows the frequency domain for  $\gamma = 1-4$  for the different values of  $\beta$  (Lilly and Olhede, 2009)**

where the over-dash indicates the complex conjugate, and  $s$  a scale parameter which is a function of  $\omega$ . The parameters  $\beta, \gamma$  tune the wavelet's shape. More specifically, the number of oscillations of the chosen wavelet is controlled by the parameter  $\beta$ , while  $\gamma$  refers to the sub-family of wavelets. For  $\gamma = 2$ , the Morse wavelet reduces to the (complex) "Derivative of Gaussian" (DoG) type of wavelet (Lilly and Olhede, 2010), while for  $\gamma = 3$  the Airy family

of wavelets is obtained (Lilly and Olhede, 2012). Figure 4.9 shows the different shapes obtained for different values of the parameters  $\beta$ ,  $\gamma$  (Lilly and Olhede, 2009). Generally,  $\gamma = 3$  results in a zero-skewness wavelet about the frequency axis, while the higher the value of  $\beta$  the lower the discretisation in the frequency domain. A very large value of  $\beta$  will result in a wavelet with too many oscillations, which may lead to difficulty capturing responses with very few cycles at a given frequency. In this case, the resulting time-frequency map is an extension of the Fourier spectrum across any point in time. Evidently, the values of

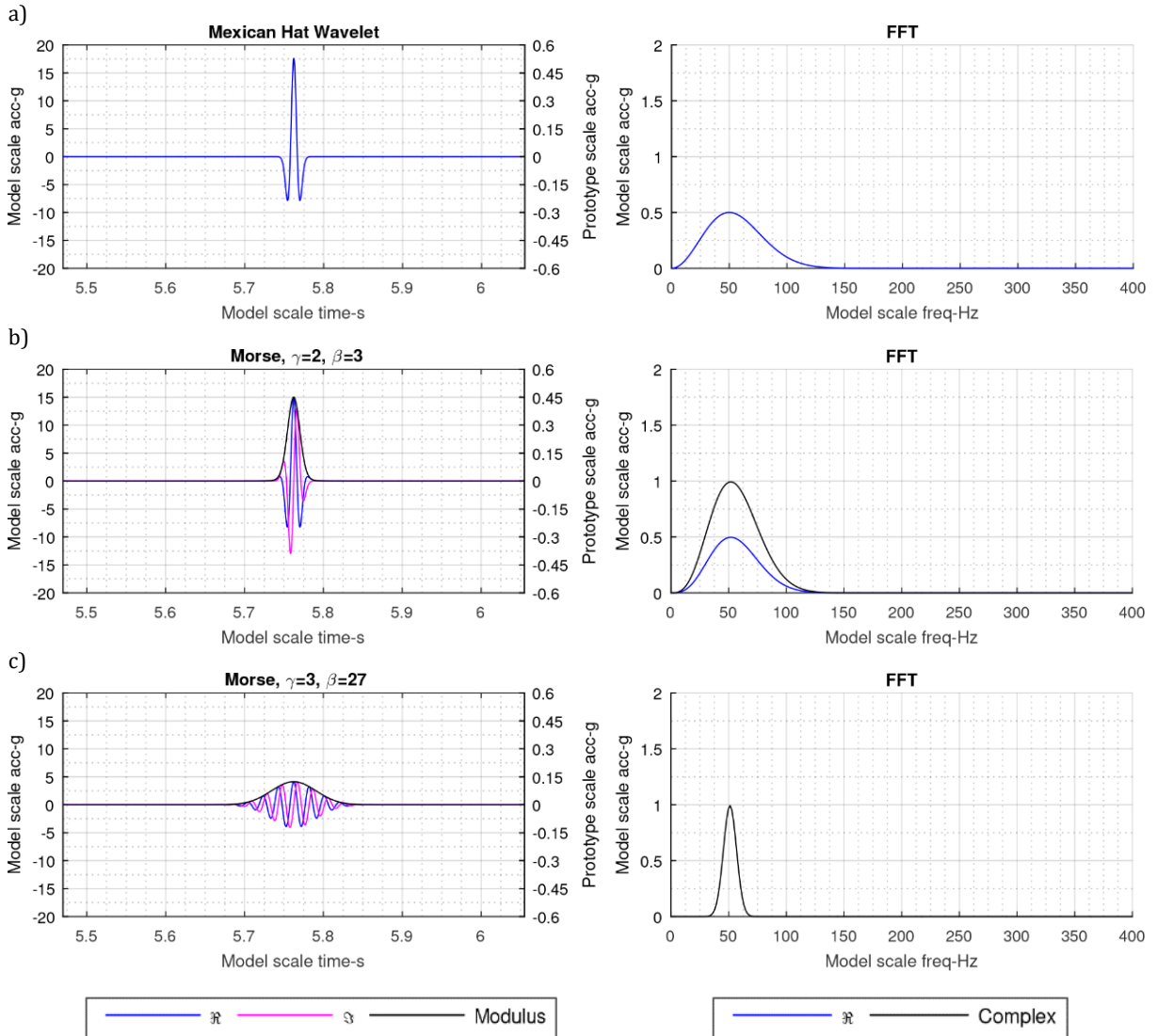


**Figure 4.10: Selected wavelets and their FFTs within the time and frequency domains considered for the experiment**

$\beta$ ,  $\gamma$  depend on the desired application and a calibration of these parameters for a signal might lead to poor results for another. The Mexican hat was chosen as a starting point for this analysis because it is a frequently used wavelet. It is however limited to only having a real part and no imaginary part is present, therefore no information on the phase is provided. This is why it is traditionally used along with other, complex wavelets, such as also the frequently used Morlet wavelet. However, the Morlet wavelet does not comply

strictly to the wavelet criteria, for instance for analysis close to very low frequencies, a zero-frequency component can emerge. For this reason, as a next step to employ a complex wavelet, a Morse wavelet was chosen resembling the Mexican hat (alternatively, a complex version of the Mexican hat can be created according to the method of Addison, Watson and Feng, 2002).

Figure 4.10 shows the selected Morse wavelets and the Mexican hat wavelet used in this section. The plotted wavelets represent accelerations and have been tuned to produce a peak over a frequency of 50 Hz when the FFT is applied to them. When compared to a Morse wavelet of  $\gamma = 2$  and  $\beta = 3$ , which is of a very similar shape, the Mexican hat has a nearly identical frequency response with the real part of the Morse wavelet. However, for the latter, when its imaginary part is considered the amplitude under the frequency of interest is double, indicating a better localization in the time domain. As a final step, another Morse wavelet was considered with more oscillations under the modulus envelope, because greater degree of frequency localisation is achieved with this configuration (Addison 2017). Therefore, if  $\gamma = 3$  and  $\beta = 27$  then respectively, a symmetric sharp shape is obtained in the frequency domain and the number of oscillations in the wavelet is larger compared to the previous two wavelets as shown in Figure 4.10. Due to this configuration, the 50 Hz frequency can be captured more clearly in time, and as it will be shown later no severe loss of time localisation occurred when implementing the transform with this wavelet. To mitigate boundary effects from the transformation with wavelets, a reverse boundary condition was used which mirrors the signal but with a sign reversal. The weighting function was the  $1/s$  which is generally recommended for oscillatory signals (Lilly and Olhede, 2010). However, the cone of influence was not identified in this analysis.

#### 4.4.4 Step by step evaluation of Wavelet Transforms

The wavelet transform was used to examine both filtered and unfiltered signals of the lateral storey accelerations (Figure 4.11a). For the filtered signals, a Butterworth bandpass filter (2nd order, forward/backward inclusive) with a range of 54 – 250 Hz was applied. The low order filtering allowed to de-amplify only slightly the low frequencies developing from the shaker and the building's rocking and free vibration response, so that the higher frequencies under examination are shown with larger clarity. First, the filtered response of the storey accelerations was considered with the Mexican hat wavelet, which produced very similar results to the Morse wavelet with  $\gamma = 2$  and  $\beta = 3$ . Subsequently, the Morse wavelet of  $\gamma = 3$  and  $\beta = 27$  is considered (Appendix E).

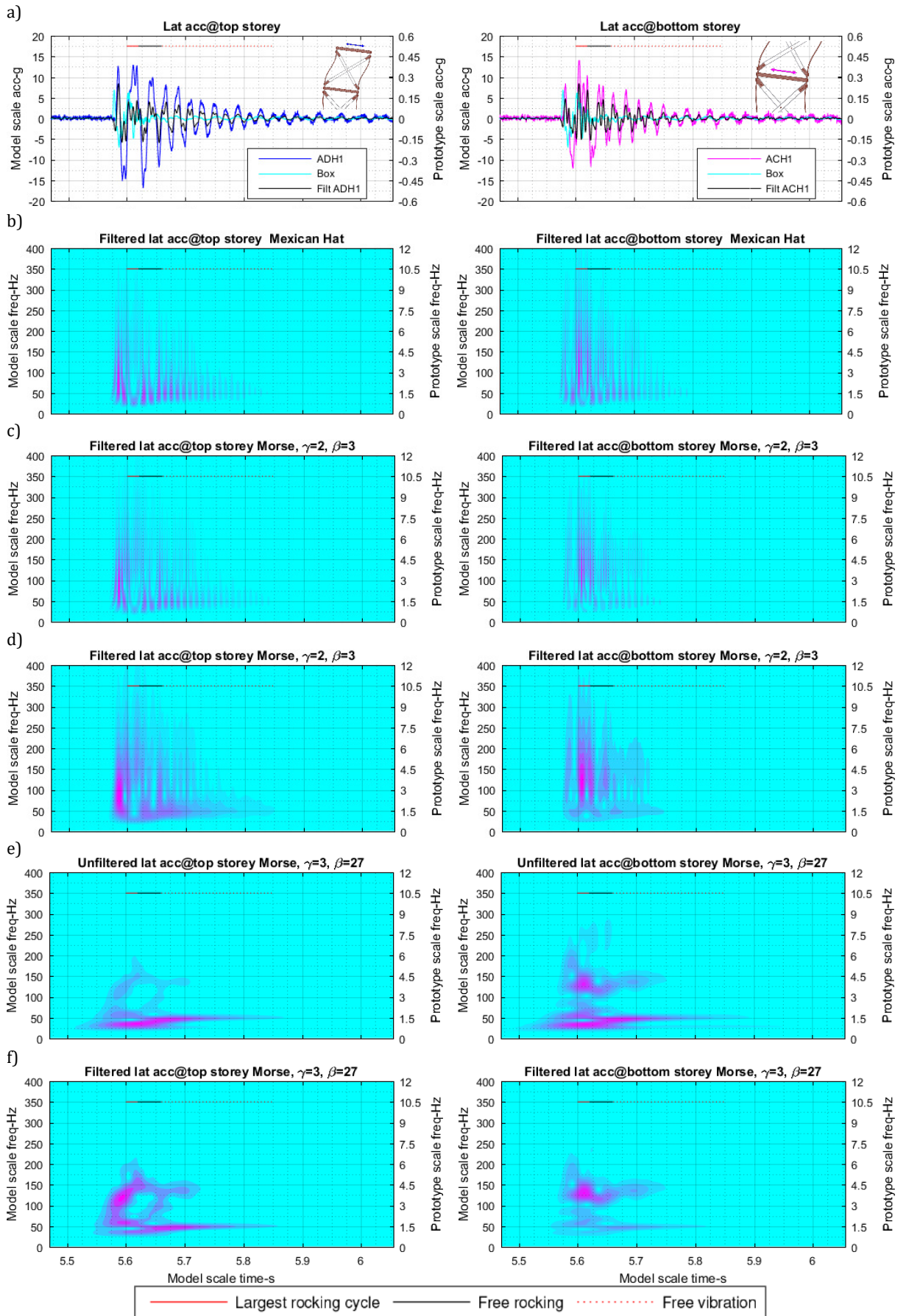


**Figure 4.11: Time-frequency maps of different wavelet transforms for the lateral accelerations of model RA**

Figure 4.11b-f shows the time-frequency maps for the top and bottom accelerations including an additional legend (bottom of figure) to highlight the different behaviours at different times during the response, including: i) the largest uplift cycle of rocking (red line), ii) free rocking after the input excitation ceased (black line), and iii) free vibration in full contact with the footings. The transforms for the top and bottom storey accelerations with the Mexican hat wavelet (Figure 4.11b) show a trend with two distinct characteristics, namely a discontinuity across the time domain and a leakage across the frequency domain. The former is because of the absence of the imaginary part while the latter is due to two reasons. The first is the broadband behaviour as visualized by applying the FFT on the wavelet (Figure 4.10a) and the second is the existence of the actual higher frequency content in the response. A mixing of the leakage artefact with the actual higher frequency content can be seen clearly for example, towards the end of the top storey free rocking, while for the bottom storey during the free vibration part ( $t = 5.7$  s). It can be concluded that the standard Mexican hat wavelet is not suitable in this case, as on the one hand its discontinuity provides an obscure map where mode transition is difficult to track in time and on the other hand, the merging of the leakage with the high frequency content prevents visualizing any high frequencies clearly.

The transform maps with the complex Morse wavelet with  $\gamma = 2$  and  $\beta = 3$  are considered next. The similarity of this wavelet with the Mexican hat is due to the same low cycle shape in the time domain and the similarity was also shown in terms of their frequency behaviour in Figure 4.10. The real part of the Morse wavelet transform (Figure 4.11c) is nearly identical to the Mexican hat transform (Figure 4.11b). However, considering both the real and the imaginary part of the Morse wavelet transform provides more useful results (Figure 4.11d). The continuity of the transform results is significantly improved; the plots clearly indicate the development of high frequency content during both the largest rocking cycle (during ground excitation) and the free rocking (after ground acceleration ceases) in both storey accelerations. However, at the beginning of the response of the top storey ( $t = 5.575$ s) a broadband frequency response is indicated from 50 Hz to 150 Hz, with a central peak at 100 Hz, although the FFT suggests a series of peaks instead. Therefore, this is considered as a leakage artefact, again possibly emerging from lower frequencies. Similarly, a leakage artefact appears at the free vibration part of the bottom storey acceleration between the two vibration modes of the structure ( $t = 5.7$  s). This behaviour is again attributed to the low number of cycles of the chosen Morse

wavelet, which results in a broadband frequency response (Figure 4.10b) and therefore further improvement is required to avoid leakage to higher frequencies.

Finally, the transform with the Morse wavelet of  $\gamma = 3$  and  $\beta = 27$  is considered (Figure 4.11e, f), with this complex wavelet exhibiting many more oscillations and a sharper frequency response (Figure 4.10c). For this transform, a more distinct ridge path without leakage to higher frequencies is obtained. For the top storey, the unfiltered data indicates that a lower frequency peak between 35-40 Hz first dominates as uplift occurs almost immediately after the ground motion commences at about  $t = 5.58$  s, and rocking occurs. This rocking frequency then increases as the rocking motion dies out (as expected as the natural rocking frequency increases with smaller rocking angle). At about  $t = 5.67$  s, the rocking has nearly ceased, and the response is dominated by the full contact first mode frequency of approximately 50 Hz. This ridge slowly dies out as the vibration ceases. The plot of the filtered top storey data amplifies the higher frequency response by filtering out the low frequency. The filtered data indicates an initial peak at approximately 120 Hz when the response commences, and the ridge line then increases in frequency to about 150 Hz at  $t = 5.62$  s. This shift is difficult to interpret as it involves a few rocking cycles. Finally, after rocking ceases at about  $t = 5.67$  s, the data indicates a clear higher frequency peak at about 135 Hz, which is clear evidence of the full contact second mode. As expected, the second mode damps out more quickly than the first. For the bottom storey lateral accelerations, the unfiltered results again indicate the dominance of the rocking response and show how this transitions to a full contact vibration response at about 50 Hz. However, the amplitude of the higher frequency response (compared to the low frequency response) is relatively larger than what was observed for the top storey. In particular, a very clear and dominant peak occurs in the top story filtered data at approximately 130 Hz, at about  $t = 5.61$  s. This clear peak occurs during the largest rocking cycle, caused by large vibrations that are clearly evident in the filtered response (Figure 4.11a). These vibrations must then be associated with the uplifted vibration mode, and likely induced by the previous impact. The exact frequency of this mode is difficult to distinguish in the results, as it appears to shift as impacts occur and very short rocking cycles continue in each direction, but the results do clearly indicate that this mode is significantly excited during rocking.

Figure 4.12 shows the wavelet transform results for the vertical accelerations at the ends of the columns. Different values of  $\beta$  were considered (i.e. wavelets with different number of oscillations) while  $\gamma = 3$  throughout this investigation. It is seen that a high value of  $\beta =$

40 results in low frequency peaks leaking across time, while the same occurs for a low value of  $\beta = 20$  in the frequency domain. Comparing the results for the left and right columns, large vibrations alternate between the two columns, and clearly indicate when a given column is not in contact with the footing. The frequency of the vibration is difficult to distinguish because the peak spans across a very large range of frequencies and this is potentially due to broad band excitation at impact, but the dominant frequency also seems to shift very quickly to higher frequencies (Figure 4.13). The high frequency leakage was evident for all different values of  $\beta$  suggesting that its existence is due to the signals

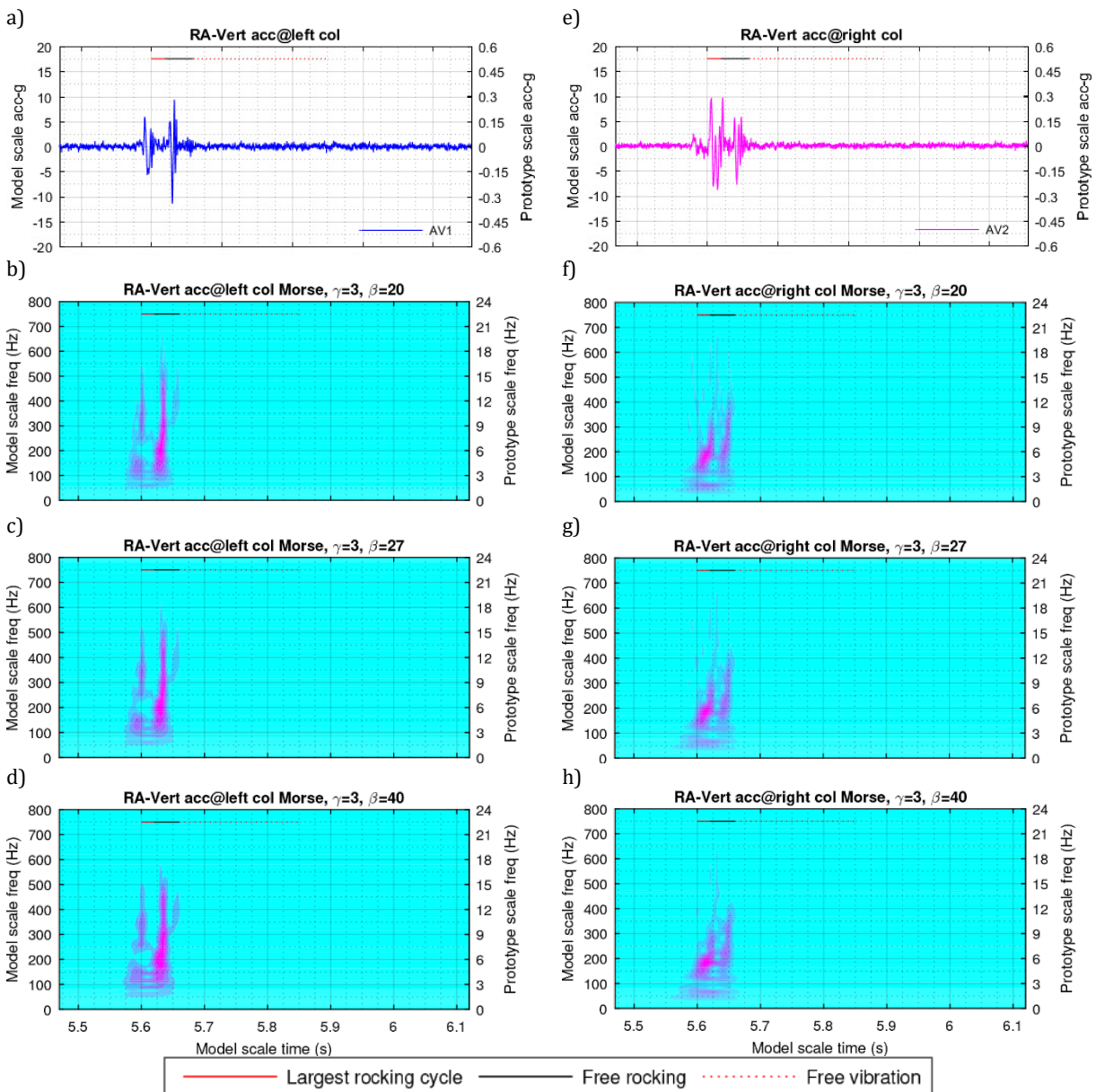


**Figure 4.12: Time-histories and time-frequency maps of the vertical accelerations at the columns ends of model RA**

examined rather than the nature of the wavelets interacting with these. In addition, considering that the cut-off frequency of the MEMS accelerometers is 400 Hz with an upper limit of 440 Hz (Analogue Devices Inc, 2010), it is difficult to distinguish the

dynamic response from any other noisy source occurring at such high frequencies after the accelerometer's filtering, but across time it is indicated that no other source exists. For the right column results, it is surprising that the dominant frequency during the largest rocking cycle (at about  $t = 5.61$  s) is much higher than the approximately 130 Hz evident in the bottom story data. However, there is still evidence of some response in the 130 Hz region, which could be indicative of weak coupling between the vertical column acceleration and the lateral storey acceleration.

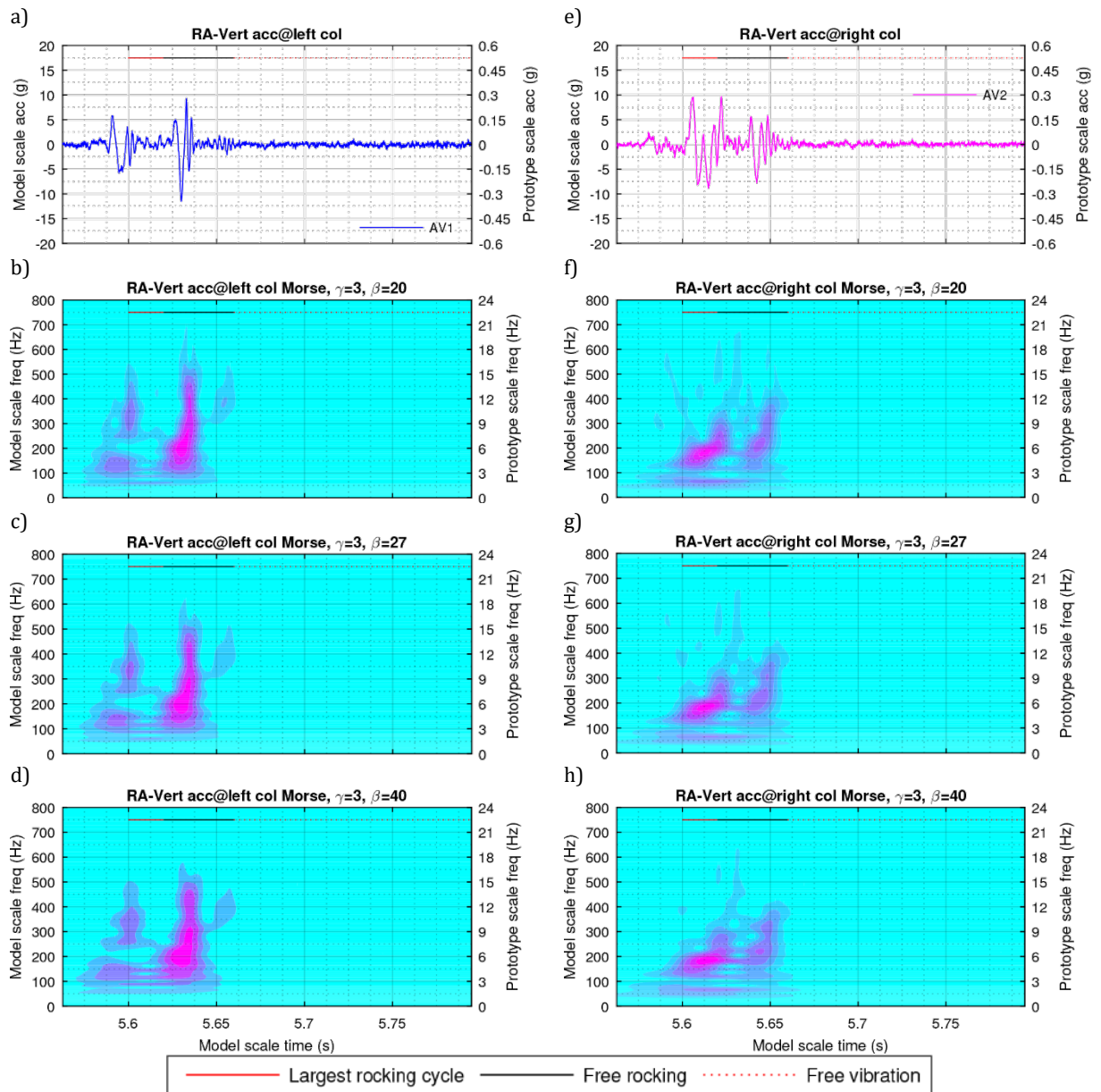


**Figure 4.13: Close-up at the time-histories and time-frequency maps of the vertical accelerations at the column ends of model RA**

Overall, the results clearly indicate that significant excitation of vibration modes during rocking occurred. Considering that the frequency content is significantly higher than the natural frequency of the structure at the first mode (50 Hz), this finding agrees with the experimental findings for free rocking of flexible structures on a rigid base (Acikgoz and DeJong, 2016). Consequently, having a soft base as in the form of dense sand here is not sufficient to suppress the significant excitation of these higher modes.

## 4.5 Design validation

The measured axial force of the braces is useful to assess their stiffness and strength throughout the rocking response in the centrifuge (see Figure 4.14 for bottom braces as an example). It was observed that offset values of loading occurred at the beginning and end of a given earthquake for both models across all tests. These offsets were taken into account sequentially for a following earthquake. Since the time-history response is well within the boundaries set by the linear elastic performance under cyclic testing (Figure 3.9), it was concluded that these offsets were not due to plastic deformation. Their existence was the result of a new state of equilibrium for the soil-structures.

The axial load response of the braces was plotted against the obtained storey drift ratios from the MEMS accelerometers, including the load offsets (Figure 4.15). To obtain the interstorey drift ratios, the MEMS accelerometers placed at the building slabs and column ends were used (Figure 4.5a). When large rocking develops, the rotational acceleration  $\ddot{\theta}$  of the building needs to be considered (Acikgoz, 2014). This is defined as:

$$\ddot{\theta} = \frac{AV1 - AV2}{2B} \quad (4.3)$$

for example for model RA, where  $B$  is the semi-width of superstructure and  $AV1$ ,  $AV2$  are the vertical accelerations measured at left and right columns respectively (Figure 4.5a). The storey drifts are then obtained by the following equation:

$$u_{r,n+1} - u_{r,n} = \int \int (MEMS_{n+1} - MEMS_n) - (H_{n+1} - H_n) \ddot{\theta} dt dt \quad (4.4)$$

where  $n = 0, 1$ , with the elevations  $H_n$  considered as the column bottom ends ( $n = 0$ ), the bottom slab ( $n = 1$ ), and the top slab ( $n = 2$ ). The storey drift ratios are defined as the storey drift over the storey height.

Generally, the centrifuge response of model RB matched the design stiffness for both storey bracings. Regarding model RA, there was a mismatch of stiffness in the bottom

braces only, due to the cross sections being smaller than the nominal dimensions and this trend was found in other tests too, yet the response remained linear elastic. Overall, any non-linear effects from the superstructures of the models RA and RB were minimal.

**LOOSE SAND TEST-1 EQ-4**

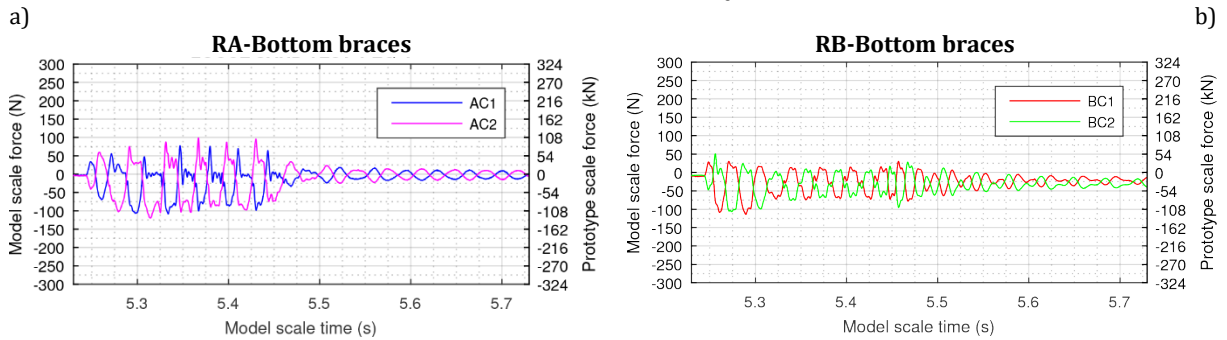


**Figure 4.14: Loose sand, Test-1, Eq-4: Time-history of the axial force of the bottom braces for model RA (a) and similarly for model RB (b)**

**LOOSE SAND TEST-1 EQ-4**

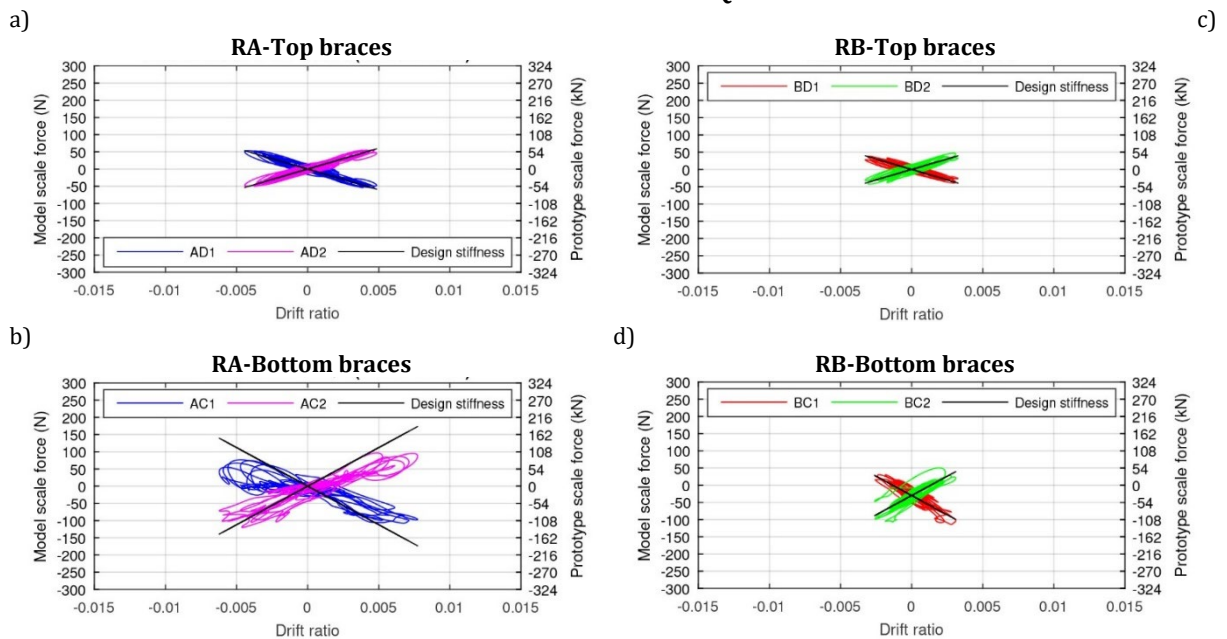


**Figure 4.15: Loose sand, Test-1, Eq-4: Axial load versus storey drift ratio for top storey (a) and bottom storey (b) for model RA and similarly for model RB (c, d)**

Therefore, any type of rocking and soil deformation were the only potential non-linear phenomena to develop and be observed clearly, as planned from the initial design of the building models.

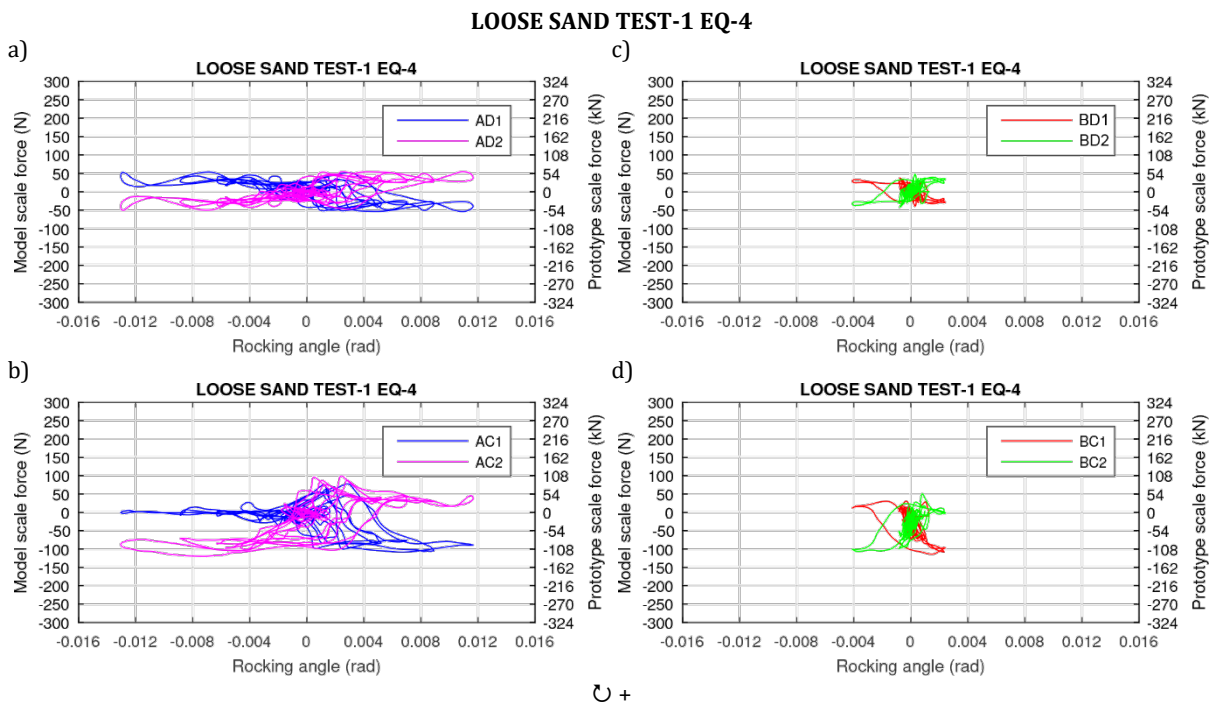


**Figure 4.16: Loose sand, Test-1, Eq-4: Axial load versus rocking angle for top storey (a) and bottom storey (b) for model RA and similarly for model RB (c, d)**

Finally, plotting the axial load response of the braces and the rocking angle  $\theta$  verifies the development of rocking action in the centrifuge (Figure 4.16). For instance, for loose sand in Test-1 and Eq-4 as the rotation develops the axial load of the braces for RA tends to zero. This trend is not very clear for RB, but this test is discussed in more detail in Chapter 5.

## 4.6 Summary

This chapter presented the experimental apparatus of the centrifuge campaign with two types of building models, one for structural rocking and another for foundation rocking. For the experimental setup, the building models were placed side to side, so that the tests can provide a uniform basis for comparison regarding the input motion and the soil conditions. A detailed instrumentation was used, involving strain gauges for direct load measurement and accelerometers embedded in the soil and attached on the building models. For the input excitations, single- and multi- cyclic motions and historic records were used, and their spectral content was presented.

Using wavelet transforms of the acceleration signals obtained during the centrifuge testing, the evolution of frequency content over time can be observed. Since this procedure depends on the various characteristics of the so-called “mother wavelet”, a calibration procedure was performed. Overall, this signal processing tool allowed to

observe the shift in frequency response over time during rocking and is used over Chapters 5 and 6.

Finally, the design of the building models was validated in centrifuge conditions. First, expressions that utilize the measurements of the accelerations were combined with load measurements from the strain gauges. It was shown that no strength or stiffness degradation occurred as the story drifts of the buildings increased. Most importantly, it was shown that when rotation of the superstructure increases, then the load of the braces reduces, thus confirming the rocking of the building specimens upon ground excitation in centrifuge conditions.



# 5 SEISMIC PERFORMANCE OF ROCKING BUILDINGS

## 5.1 Introduction

Structural rocking has been predominantly studied on the assumption of a rigid base, or viscoelastic springs. For the design scenario that the columns of a building are detailed at their base such they can pivot about a point on their foundations, the effect of soil, including the effects near the vicinity of the impact points, have not yet been explored. On the other hand, foundation rocking predominately refers to structures rocking below their foundation level. However, the rocking of discrete footings in a similar step mechanism to structural rocking has not been studied before, and in situations where a mat foundation is not appropriate this type of system could be a useful alternative. Therefore, this Chapter (Pelekis *et al.*, 2018) addresses rocking above and below the foundation to both reveal the characteristics of structural and foundation rocking and compare them. Chapters 3, 4 presented the building models RA and RB, the experimental program they were subjected to, and tools to analyse their frequency-time response. To provide new insights regarding the seismic performance of the rocking models, an extensive time-frequency study is conducted, along with a derivation of the force and moment demands. This Chapter parametrises the types of sand and rocking mechanisms to draw similarities and differences between the various cases.

### 5.1.1 Frequency content identification

The changing frequency content of the response with time was evaluated using continuous wavelet transforms for both buildings, with Morse wavelets as the mother wavelets. An application of wavelet transform was presented in Chapter 4 for model RA,

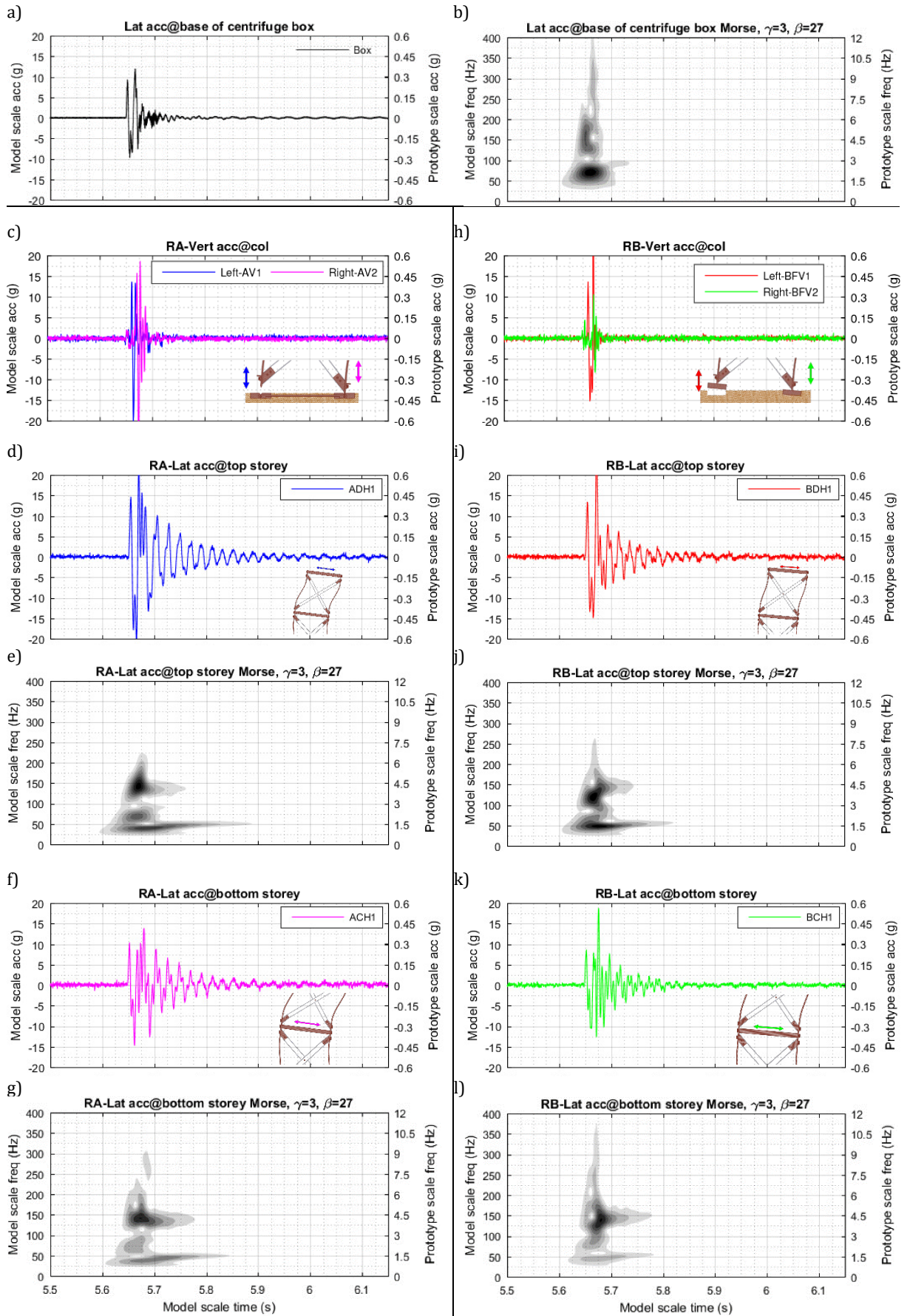
along with a calibration process. This section presents and compares directly the pulse response and the relevant frequency content of both models.

Figure 5.1 (see also Appendix F) shows example time-frequency maps of the storey response of models RA and RB, along with the input excitation at the base of the centrifuge box (sensor 9082, Figure 4.5a) from the nominal 50 Hz pulse record in dense sand (Test-1 Eq-3). As also visualized in the linear elastic response spectra (Figure 4.7), the principle excitation frequency was approximately 70 Hz, higher than the nominal value of 50 Hz specified, and with appreciable higher frequency content between 100-400 Hz also present (Figure 5.1a, b). The storey accelerations of both buildings are characterized by an initial large duration cycle with clear higher frequency oscillations (Figure 5.1d, f, i, k), while at the same time uplift occurred as evidenced by the vertical accelerometers placed at the column bases (Figure 5.1c, h). After some initial rocking, the structure regains full contact with the soil and the motion slowly damps out, providing a full-contact free vibration trace.

At the onset of the excitation, the time-frequency maps of the storey accelerations (Figure 5.1e, j, g, l) reveal a high-frequency response locally in time, along with a lower frequency component that continues throughout the response. The clear peaks in the higher frequency range (>100 Hz) occur predominantly during the very brief rocking response ( $t = 5.65-5.67$  s) and provide clear evidence of vibration during rocking (uplift), after which the higher frequency oscillation damps out much quicker than the lower frequency response. The peak frequency content in the higher frequency range (>100 Hz) appears to be at a slightly lower frequency for RB than for RA. Meanwhile, in the lower frequency range (<60 Hz), the peak frequency response for RA is initially at about 35 Hz during rocking, and then increases to the first mode natural frequency of approximately 50 Hz during the full contact free vibration stage. The initial rocking frequency is not fixed, but dependent on amplitude of the rocking response. For RB, the lower frequency during this initial rocking stage is barely evident in the time-frequency plots; it appears the single rocking cycle has a smaller amplitude, and thus a higher natural frequency ( $\sim 50$  Hz for RB compared to  $\sim 35$  Hz for RA), and thus the rocking phase is not clearly distinguishable from the full contact natural frequency in the time-frequency plots.

### 5.1.2 Observed force demand

The total lateral accelerations  $\ddot{u}_{t,n}$  recorded at the storey slabs ( $n = 1, 2$ , Figure 4.5a) were used to extract the lateral external forces  $F_{E,n,x}$  developed on the storey slabs because of both the ground motion and the subsequent rocking motion, and consequently the total



**Figure 5.1: Dense sand, Test-1 Eq-3: Pulse excitation (a, b), vertical acceleration response of model RA (c), storeys' time-frequency response of model RA (d-g) and similarly for model RB (h-l)**

external force,  $F_{E,x}$  is  $F_{E,x} = \sum_{n=1}^2 F_{E,n,x} = \sum_{n=1}^2 m_n \ddot{u}_{t,n}$ . The peak value of the total external force was normalized with reference to each building's weight and plotted for each input motion for both types of sand (Figure 5.2). Generally, the low frequency excitation caused larger force demands, whereas the Imperial Valley excitation resulted in a full contact response and the smallest force demand. In addition, the added fuse had no significant effect on RA's force demand (see Appendix F). In all earthquakes and regardless of the type of the sand, model RA resulted in a larger external force demand than model RB. The effect of sand density on the force demand was frequency dependent. For excitations with larger high frequency content (Imperial Valley) and the 50 Hz excitations, loose sand resulted in a larger force demand than dense sand for RA. On the contrary, for excitations with a larger low frequency content, such as Kobe and the 30 Hz cyclic and pulse motions, dense sand resulted in larger force demand than loose sand for RA. Regarding RB, a mixed trend is observed, but the difference was larger for the low frequency excitation of 30 Hz compared to the other excitations.

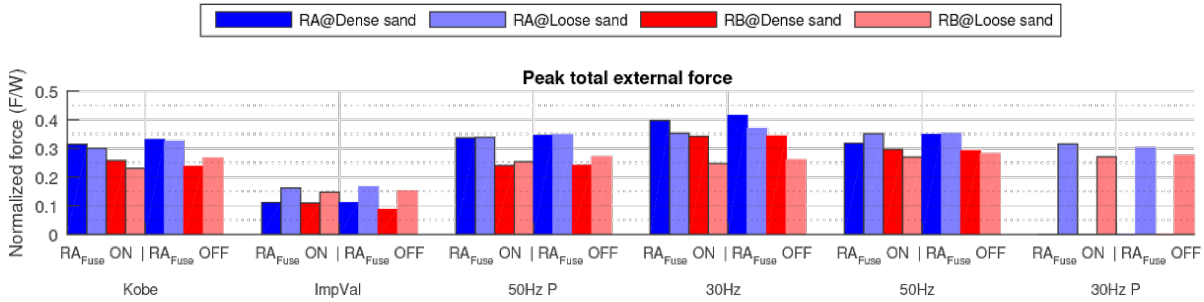


**Figure 5.2: Observed force demand normalized to each building model's weight across all earthquakes for both types of sand (Tests-1, 2 Dense and Loose sand)**

### 5.1.3 Extraction of shear force demand from accelerometers

To extract the shear force demand for each storey, the superstructure damping was first approximated. Specifically, the discretization of the models to 2DoF in full contact conditions was used. A classic damping matrix based on the modal characteristics of this configuration is shown in Eq. (5.1) (Chopra, 2007). The modal damping ratios refer to the damping as obtained from full contact free flexural vibration tests on each model before the loading in the centrifuge beam (Section 3.6). These values are only representative and were difficult to measure with accuracy. The storey damping forces  $\underline{F}_D$  were evaluated as

$$\underline{F}_D = \underline{c}\dot{\underline{u}}_r \Rightarrow \begin{Bmatrix} F_{D,1} \\ F_{D,2} \end{Bmatrix} = \mathbf{m} \left( \sum_{m=1}^2 \frac{2\zeta_m \omega_m}{M_m} \underline{\varphi}_m \underline{\varphi}_m^T \right) \mathbf{m} \begin{Bmatrix} \dot{u}_{r,1} \\ \dot{u}_{r,2} \end{Bmatrix} \quad (5.1)$$

Therefore, the storey shear forces  $F_{S,n}$  were obtained as  $F_{S,2} = -F_{E,2,x} - F_{D,2}$ ,  $F_{S,1} = -F_{E,1,x} - F_{D,1} + F_{D,2} + F_{S,2}$ . The amplitude of the damping forces was found to be very

small compared to the external forces, therefore the trend from the external forces developed due to ground shaking and rocking was also reflected in the shear forces.

### 5.1.4 Base isolation effect

After extracting the storey shear forces, the base isolation effect was investigated with reference to a fixed base linear elastic solution of the base shear value (Figure 5.3). The input considered was the excitation as recorded below each building model (accelerometers 8888 and 8838, Figure 4.5a). The linear elastic solution to the base shear was obtained using the SRSS method and the response spectra for each earthquake, which was obtained for different values of damping corresponding to the two first lateral modes of the structure (as identified in the free vibration traces of the building models during centrifuge testing). The variation in response due to the damping estimate is shown in Figure 5.3 in the form of error bars representing one standard deviation away from the mean value. The largest difference to the SRSS base shear (Figure 5.3) was, for both building models, at the 50 Hz cyclic and pulse records; the large standard deviation occurred due to the sharp peak in the response spectra of these motions.

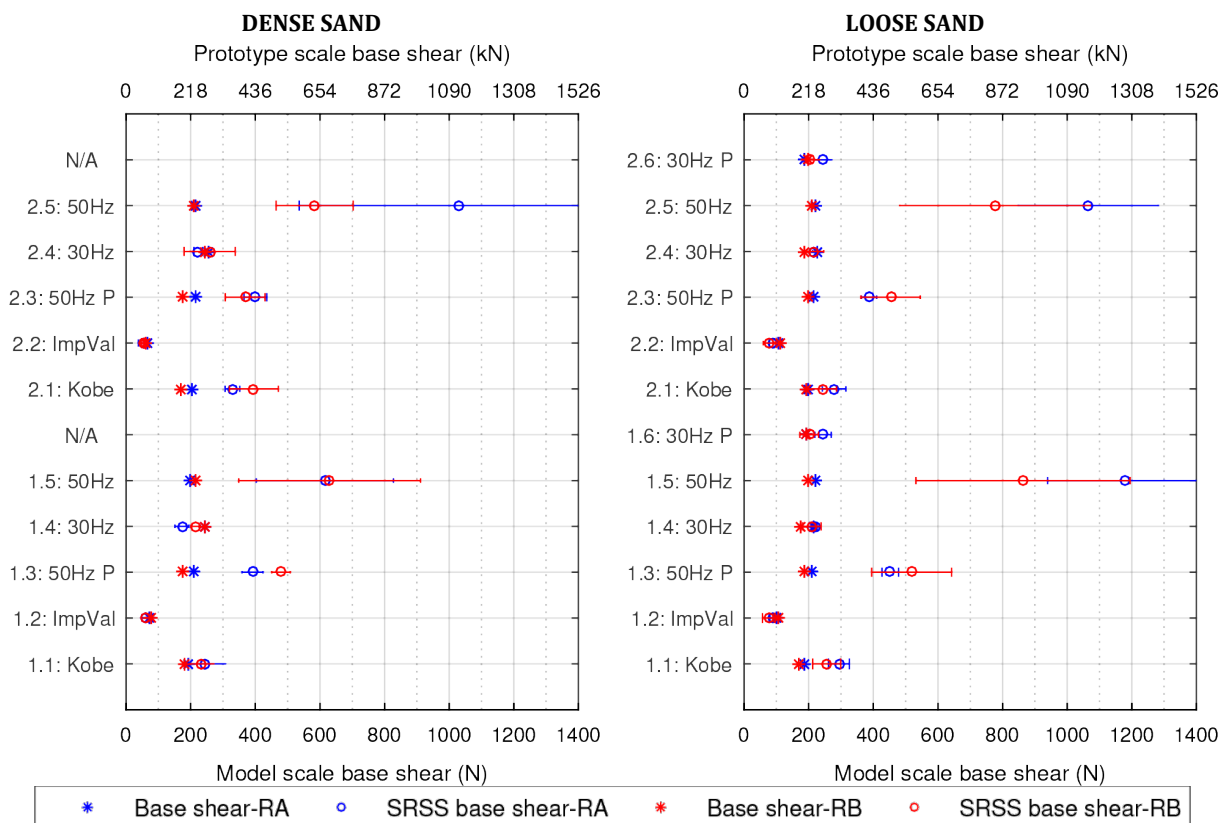


**Figure 5.3: Base shear difference with the SRSS linear elastic solution**

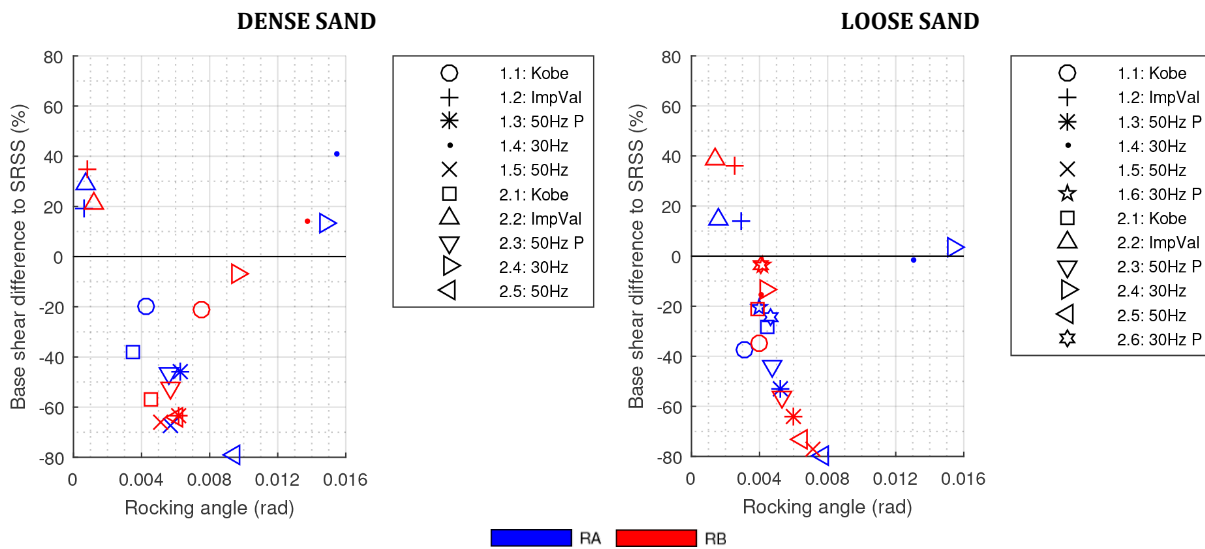


**Figure 5.4: Percentage difference of the experimental base shear with the average SRSS solution against the peak rocking angle for dense sand (left) and loose sand (right)**

The Kobe excitation also generally showed an appreciable reduction in base shear compared to the linear elastic solution. Regarding the Imperial Valley excitations, the linear elastic solution produced base shear values smaller than those observed in the centrifuge, suggesting that structural damping in the centrifuge testing might be underestimated in this case. In general, the isolation effect is achieved for both types of rocking when the peak rocking angle (Eq. (4.3)) is above approximately 0.4%, which in prototype scale corresponds to 20mm of uplift (Figure 5.4).

## 5.2 Effect of rocking type on force demand

To examine the effect of the impacts generated at the interface of rocking (either above or below the foundation level), the force demand, the storey lateral raw accelerations, the vertical raw accelerations at the column ends and the excitation below each building are closely examined in Figure 5.5a-h; the selected dataset is part of the low frequency (30 Hz) excitation in dense sand (Test-2 Eq-4). The force demand is shown in terms of total external force (Figure 5.5a, e) as calculated from the raw lateral storey accelerations (Figure 5.5b, f). In addition, a portion of the base shear force obtained by the strain gauges at the bottom storey is also plotted to examine any profile discrepancies between different instruments (i.e. MEMS accelerometers and strain gauges, Figure 5.5a). Since only the front side of the building models was strain gauged, the base shear of the braces was close to 50% of the actual value of the total base shear (half of the total external force and with an opposite sign is also plotted). The base sign convention is such that a deformed shape towards the right of the models would produce a positive shear force. Impact can be recognized at the time when a vertical acceleration rises sharply, while the

counterpart accelerometer shows an acceleration increase shortly after (Figure 5.5c). The local maxima of the total external force and example impact have been marked in Figure 5.5a, e and Figure 5.5c, g, respectively.

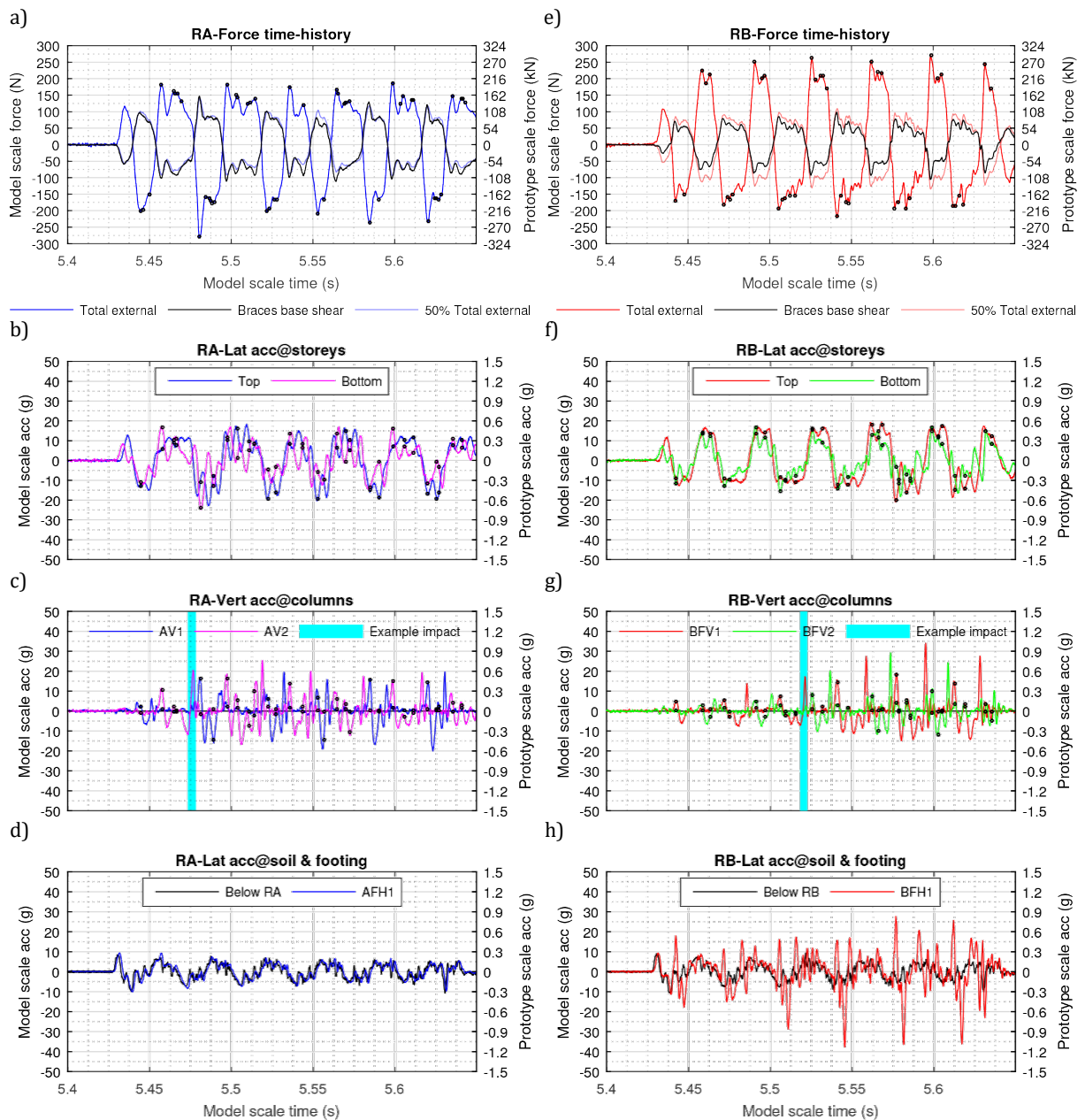


**Figure 5.5: Dense sand, Test-2 Eq-4: Lateral force demand of model RA from accelerometers and bottom braces (a), RA storey lateral response (b), RA column vertical response (c), soil and RA footing lateral response (d), and similarly for model RB (e-h)**

Regarding model RA, when the impact occurs, the external force has a zero crossing, indicating that the structure passes through the initial zero deflection state (Figure 5.5a). The rising part of the inertial force develops after its zero crossing with a peak value corresponding to a local maximum of the vertical acceleration immediately after the impact point (Figure 5.5c). Therefore, the local maxima of the force demand are related with the rocking motion as indicated with the smooth vertical accelerations, following the

impacts generated at the contact points. This essentially means that, for rocking on dry dense sand, impact excites the superstructure and increases the total external force demand. This confirms previous experimental and analytical research for flexible structures rocking on a rigid base (Acikgoz and DeJong, 2016, 2018; Acikgoz *et al.*, 2016). Finally, note that the horizontal accelerations of the foundations of model RA followed very closely the excitation below its footings (Figure 5.5d), meaning that no sliding occurred.

Comparing the total external force time-histories for models RA and RB, the latter experienced a smaller maximum total external force (Figure 5.5e). During the first half of the response, small impacts occurred at the ends of the columns, while during the second half impact accelerations of larger amplitude developed (Figure 5.5g). This response suggests that following the very small duration of fixed base response initially, a weak form of foundation rocking took place, with the footings not losing much contact with the soil. Subsequently, the impacts became larger and caused more distinguishable higher mode oscillations. Note that the RB model has a lower centre of gravity because of its attached footings, so the static force required to cause uplift depends on the specific point of rotation for RB (Table 3.2). From a static point of view, a high force demand for RB would mean rotation about a pivot point close to the foundation's external edge or would indicate a high rotational stiffness from a pre-yielding soil with a pivot point close to the footing's centre or potential further inward. In fact, the time-histories of RB suggest that, similar to RA, large post-peak force maxima occur after impacts, in parallel with rocking motion. The maximum force demand of RB corresponds to static rotation about the centre of the footing, which results in a slenderness ratio of 0.34 (264 N). However, considering the force demand caused by impact at re-centring, the actual effective slenderness falls between 0.34 and 0.25 (264 N to 199 N), indicating that the rotation develops about a point within the inner half of the footing. The extent of soil yielding cannot be determined from these results alone, but the results do indicate that some soil yielding appears to be likely.

Finally, comparison of the footing lateral accelerations (Figure 5.5d, h) provides clear evidence of uplift of the RB footings, and potential hammering during uplift. While model RA showed a lateral acceleration footing profile that matches the soil exactly, the RB lateral footing accelerations are very different from the soil. More specifically, large lateral oscillations occurred at the left footing of RB when that footing has uplifted, i.e. after impact and subsequent rotation about the right footing.

### 5.3 Effect of sand density on force demand

The response from the low frequency (30 Hz) excitation on the loose sand is shown in Figure 5.6. The response of model RA is generally very similar to the dense sand case. In contrast, model RB behaved differently in loose sand compared to dense sand. Similar to

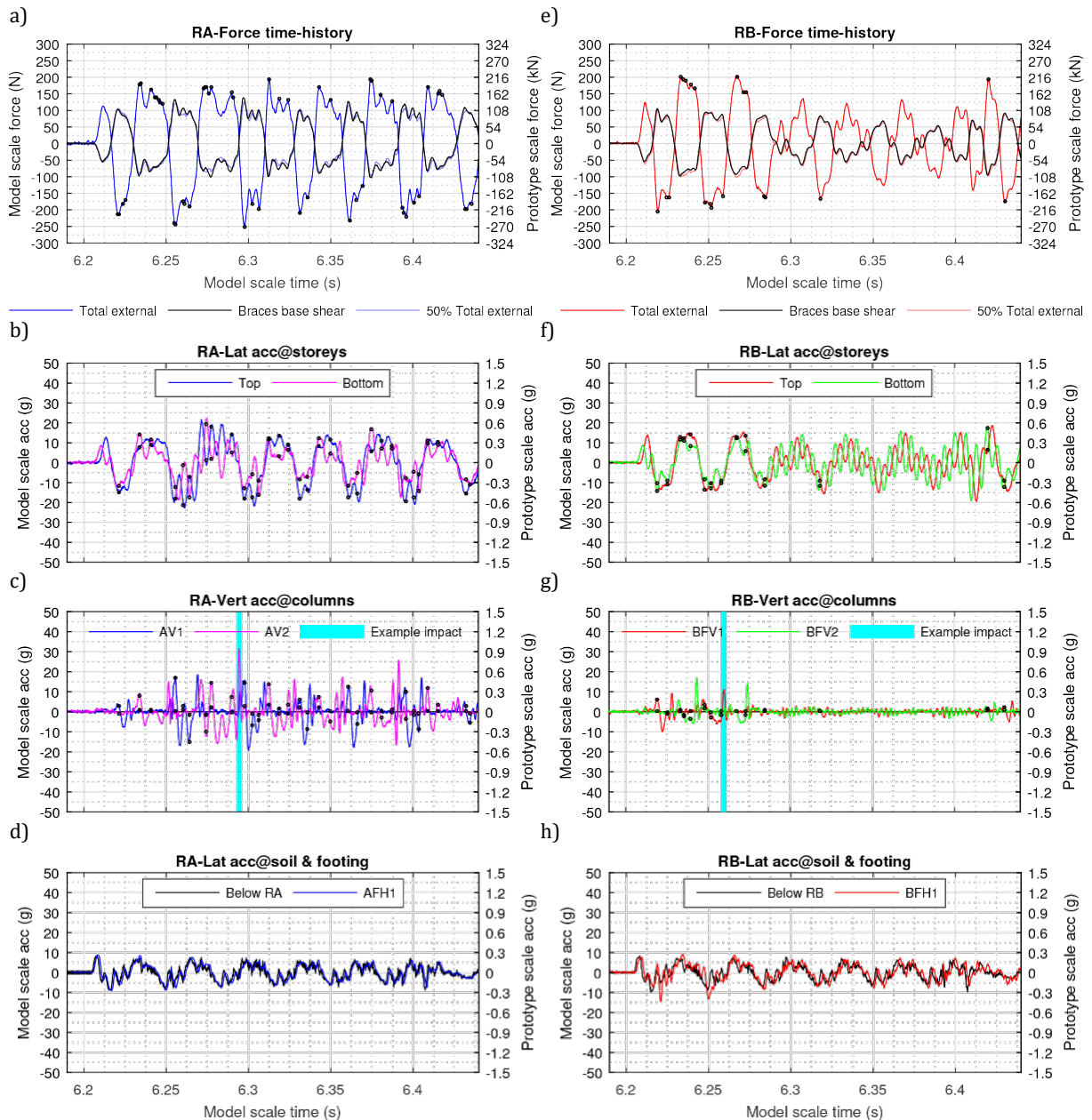


**Figure 5.6: Loose sand, Test-2 Eq-4: Force demand of model RA from accelerometers and bottom braces (a), RA storey lateral response (b), RA column vertical response (c), soil and RA footing lateral response (d), and similarly for model RB (e-h)**

the first half of the response in dense sand (Figure 5.6e-h), small, sharp impacts indicate that rocking of the footings on the soil took place immediately after the initial full-contact response. However, unlike the dense sand case, rocking was suppressed significantly after a few cycles, changing the lateral acceleration profiles (Figure 5.6) and reducing the total force demand (Figure 5.6e). The suppression of rocking is also confirmed by the lateral acceleration of the RB footing, which matches the response of the soil below nearly exactly

after uplift ceases at about 6.25 s (Figure 5.6h). The above changes suggest a transition from a rocking response to a nearly full contact response with an appreciable higher mode contribution (as indicated by Figure 5.6). This suggests that more soil yielding occurred for loose sand; the extent of soil yielding or rounding of the soil surface beneath the footings (Gajan *et al.*, 2005) could not be measured directly. Visual inspection after the test showed no major differences between start and end of the centrifuge flight. In contrast, for dense sand the gradual increase over time of the vertical accelerations can be attributed to a densifying soil which becomes gradually stiffer. Overall, for the RB model, the soil density governed the transition from rocking with small impacts to either a full contact response with associated soil yielding (loose sand) or to rocking with progressively larger impacts (dense sand).

### 5.3.1 Evaluation of frequency content

Because the sand density can govern the type of response for foundation rocking, while having very little effect on the building performance for structural rocking, visualization of the change in frequency content with time can provide further insights of the response. Wavelet transforms using the Morse wavelet with  $\gamma = 3$  and  $\beta = 27$  were applied (Lilly, 2017) for the storey lateral accelerations and the excitation as recorded at the base of the centrifuge box. The selection of the specific wavelet transform was investigated previously (Section 4.4).

Only the time-frequency maps of the top storey accelerations are discussed and presented (Figure 5.7) for brevity. The time frequency maps of the input (Figure 5.7a, b, g, h) are very similar in both the time and frequency domain. Higher harmonics of the dominant low frequency input are also observed. The response of model RA was governed by the low frequency component of the excitation, indicating that a quasi-steady-state rocking response occurred at the excitation frequency. In the higher frequency range, prominent peaks in the wavelet transform are evident during some rocking cycles. The frequency of the uplifted vibration response matches the high frequency content of the excitation. However, theoretically the higher mode response should be largely uncoupled from horizontal excitation input. It was not possible to confirm that, since some even higher frequency content might not have been captured due to the 400 Hz built-in filter of the MEMS accelerometers used here. Thus, this large high frequency response during uplift is

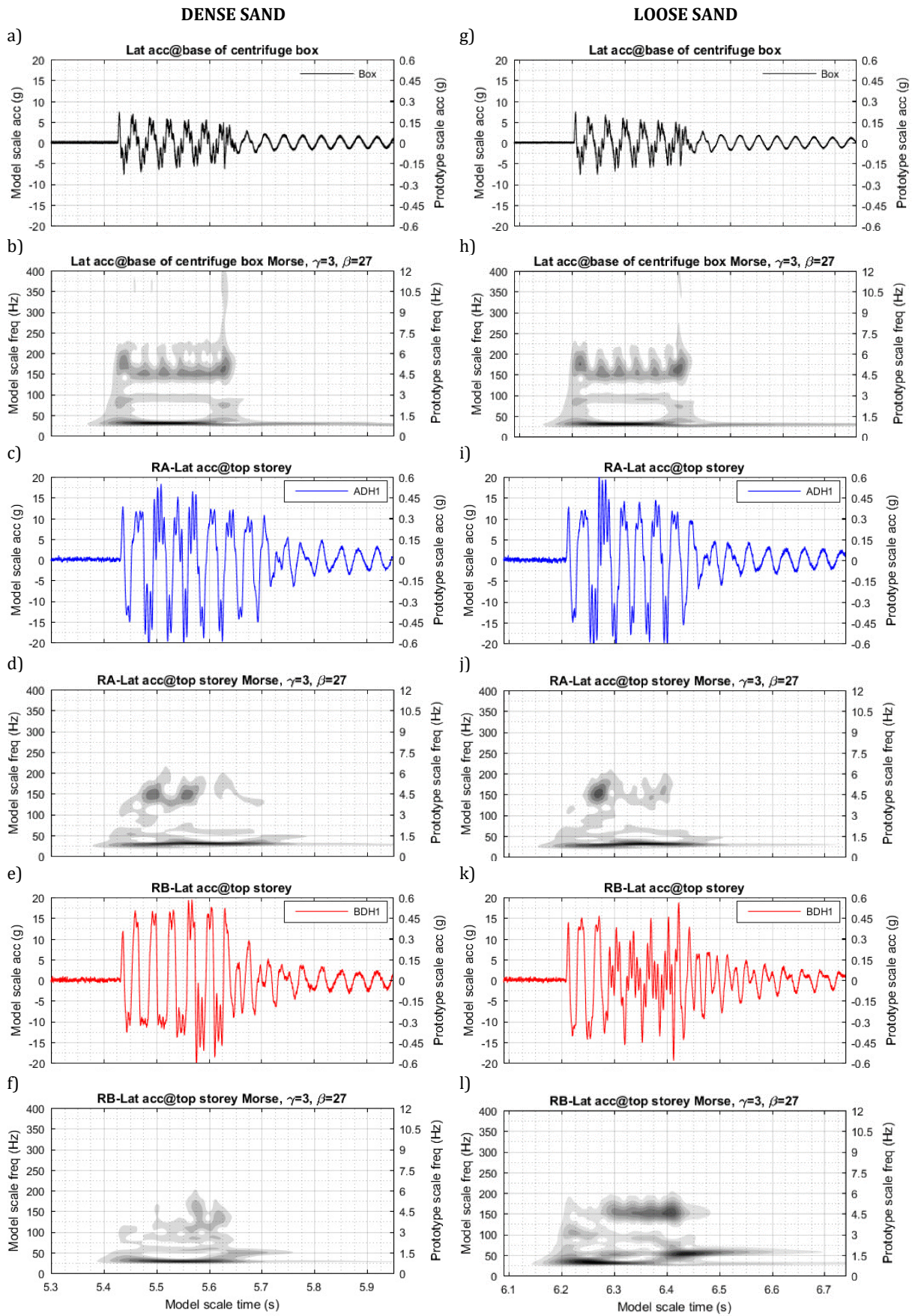


**Figure 5.7: Test-2 Eq-4: Input for dense sand (a) and time-frequency map (b), RA top storey response (c) and time-frequency map (d), RB top storey response (e) and time-frequency map (f), and similarly for loose sand (g-l)**

likely caused by a combination of lateral excitation at approximately 150 Hz, combined with excitation of the uplifted vibration modes caused by impact. Overall, only minor differences can be observed between dense and loose sand (Figure 5.7c, d, Figure 5.7i,j).

On the other hand, the quantitative change in the response profile of model RB for different sand densities (Figure 5.7e, k) is also reflected in the frequency content (Figure 5.7f, l). In dense sand, model RB exhibited foundation rocking with local high frequency excitation during some rocking cycles, similar to the model RA response. On the contrary, in loose sand, initial foundation rocking with very weak high frequency response was converted to a full contact response which enabled significant high frequency excitation caused by the input excitation. The end of the main excitation then caused abrupt transition to a clear free vibration response of the first mode.

### 5.3.2 Evaluation of moment-rotation response

The effect of sand density on the building response can also be visualized by comparing the restraining moment-rocking angle response of the two building models. Here, the restraining moment for model RA is the moment acting on the top surface of its footings, while for model RB, the restraining moment is presented at the soil surface. Figure 5.8 and 5.9 present the moment-rotation response for the Kobe excitation and the 30 Hz excitation, respectively. Both figures exhibit a typical moment rotation response for a rocking structure, where the maximum moment is capped by the static moment that causes uplift, indicated by the solid horizontal line in the figures. However, for model RA, the static overturning moment was more significantly exceeded; this is again the result of the higher frequency excitation superposed on the rocking response. For model RB, the static moment is shown with respect to a point of rotation about the middle of the bottom surface of the footings. The restraining moment of model RB was generally within these limits, which again suggests that the effective rotation point may be slightly inward from the centre of the footing.

Regarding the Kobe excitation, which has a large but short duration low-frequency content, a single main cycle of rocking is induced for both RA tests and for the RB test on dense sand (Figure 5.8). Meanwhile, for the RB test on loose sand, a smoother rotation response is observed with an increased number of large rotation responses. This curve is representative of rotations due to soil deformations, but some uplift of the rocking foundations also occurred. Meanwhile, the 30 Hz excitation exhibits numerous cycles of large rocking amplitude. As in the previous section, for model RA no effect of sand density is evident. Moreover, for dense sand the cyclic response of model RB was similar to that

of RA, though of smaller rocking amplitude. On the contrary, in loose sand, the cyclic response of model RB was smoother and of considerably smaller amplitude.

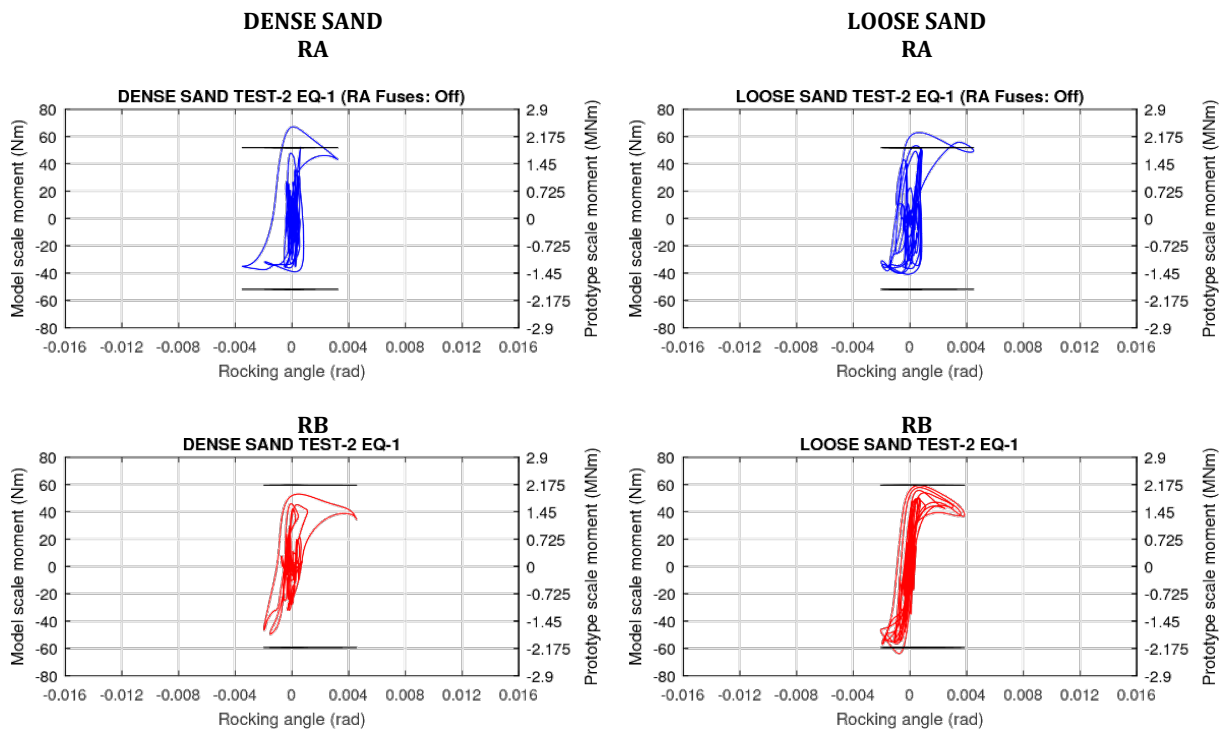


**Figure 5.8: Restraining moment versus rocking angle for dense (left) and loose (right) sand for the Kobe excitation. Horizontal lines indicate static overturning moment**

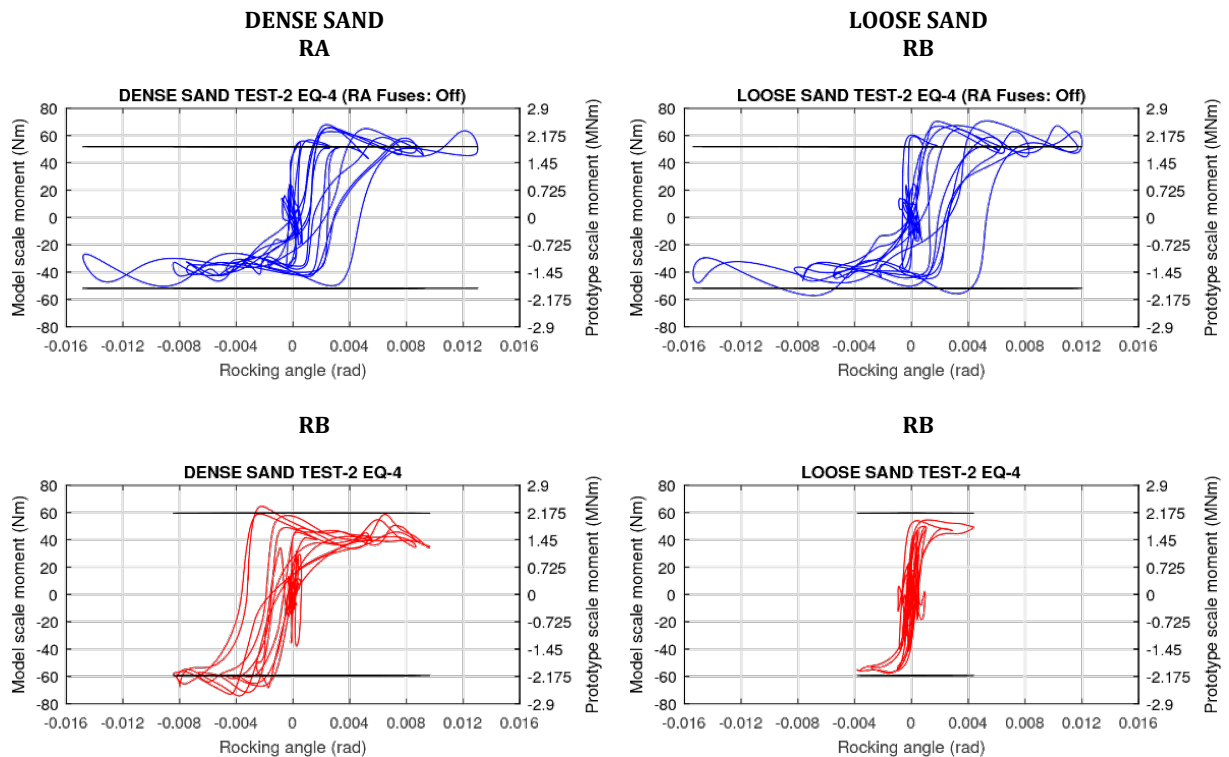


**Figure 5.9: Restraining moment versus rocking angle for dense (left) and loose (right) sand for a low frequency, cyclic excitation. Horizontal lines indicate static overturning moment**

Overall, for small rocking amplitude, the models perform the same. In general, this means that it is impractical to distinguish actual uplift of the superstructure (model RA) or a local dynamic settlement of the footings (model RB), which again would result in an apparent rocking motion, as far as building response is concerned. For large rotations, uplift of the superstructure (including the footings for model RB) was the typical mechanism, with expected static limits being exceeded because of higher frequency excitation caused by direct excitation from the harmonics of the input, in combination with impacts and hammering action of the footings on the soil.

### 5.3.3 Overall effect of sand density

The effect of sand density on the response is further evaluated by plotting the peak force demand against the peak rocking angle for each input excitation (Figure 5.10). The peak values do not necessarily occur at the same instance in the time-history; however, they can provide general insight into the trends forming with respect to the relative density of the sand. Fitting with piecewise lines for full contact and rocking conditions indicates that

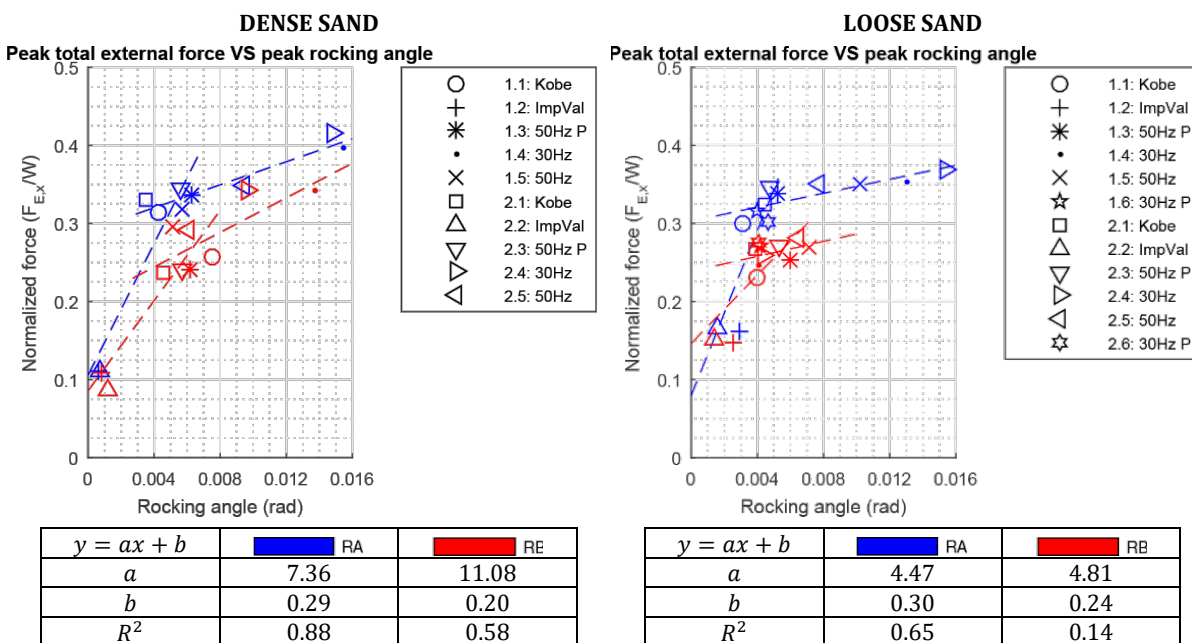


**Figure 5.10: Effect of the impact on the peak total external force for both storeys, for dense (left) and loose (right) sand. Fitting parameters are presented only for large peak rocking angles**

for an excitation in dense sand, a large rocking angle is associated with an increasing total force demand for both RA and RB. The reason for this correlation could be that larger rocking angles cause larger impacts and therefore larger high frequency response, or that larger rocking angles allow increased higher mode excitation by the high frequency ground motion input. The prior hypothesis seems more plausible. Next, the slope

difference in loose sand for model RA indicates that a very large peak rocking angle leads to a smaller increase of force demand for loose sand. This suggests that either the impact again causes less excitation of the high frequency uplifted vibration mode, or that the loose soil filters the high frequency excitation input more than the dense soil. Finally, for model RB, loose sand did not allow large rotations to occur, thus a cluster of points is created with the same force demand. This indicates that soil deformations caused energy dissipation that both decreased the rotation and high frequency response.

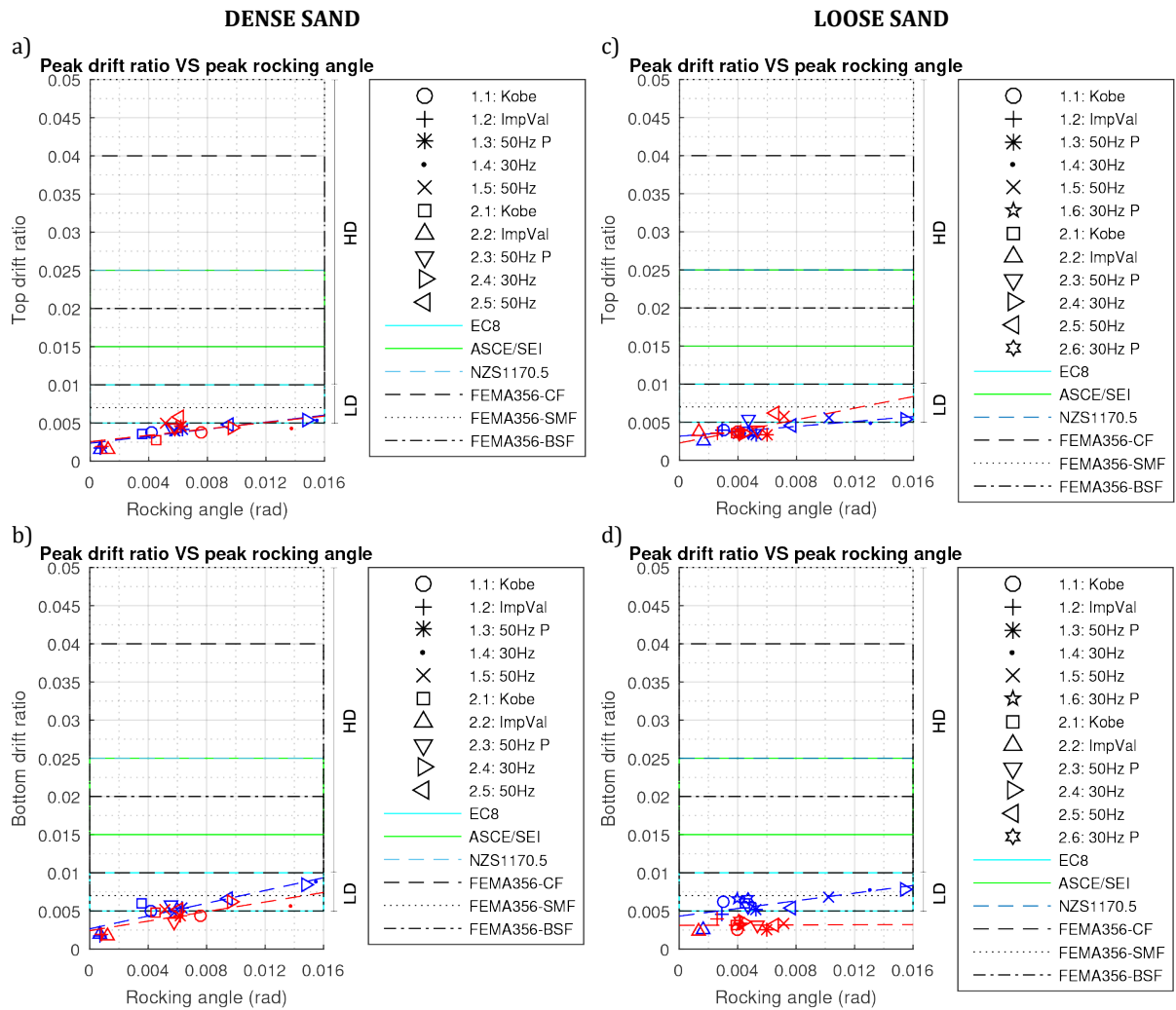


**Figure 5.11: Peak drift ratios against peak rocking angle for the top (a) and bottom (b) storeys for dense sand and similarly in loose sand (c, d). Low and high damage regions (LD, HD) are annotated.**

The data in Figure 5.4 and 5.10 can be re-interpreted by considering a damage approach that incorporates the peak storey drift ratios against the peak rocking angle (Figure 5.11). In dense sand, increasing trends are obtained for both storeys indicating an additional excitation due to large rocking for both buildings. For RA, the trends are the same between dense and loose sand for both stories, while for RB lower drift demands than RA are noted for the bottom storey and no dependence on the peak rocking angle is evident. This

indicates that loose sand can reduce expected drifts for foundation rocking and thus may reduce damage in the superstructure. Limits for storey drift ratios from code provisions are presented. The obtained drift ratios from rocking are within an annotated lower damage region. This region is the damage limitation state for Eurocode 8 (CEN, 2004), while also the FEMA356 thresholds for immediate occupancy cover this region (these are only additional here because they refer to vertical elements and not strictly to storey drifts, ASCE, 2000). Clearly, the obtained drifts also satisfy higher levels of drifts (NZS1170.5:2004, 2004; ASCE/SEI, 2017). In any case, since code drift limits are associated with inelastic response of fixed base buildings whereas the building models used here are linear elastic with rocking response, this comparison is only indicative.

Next, the local effect of sand density on the impact excitation at the rocking interface is considered more directly by extracting the acceleration as associated with an impact spike and relating that to the maximum force immediately following. For example, an impact is identified in the vertical acceleration at the base of the columns (Figure 5.12a, slightly before  $t = 4.85\text{s}$ ) and associated with the following local peak in the total external force time history (Figure 5.12, black circle slightly after  $t = 4.85\text{s}$ ). Figure 5.13 plots the extracted external force versus the impact acceleration for impacting at either left or right side, for both buildings and across both types of the relative density of sand and all earthquake excitations.

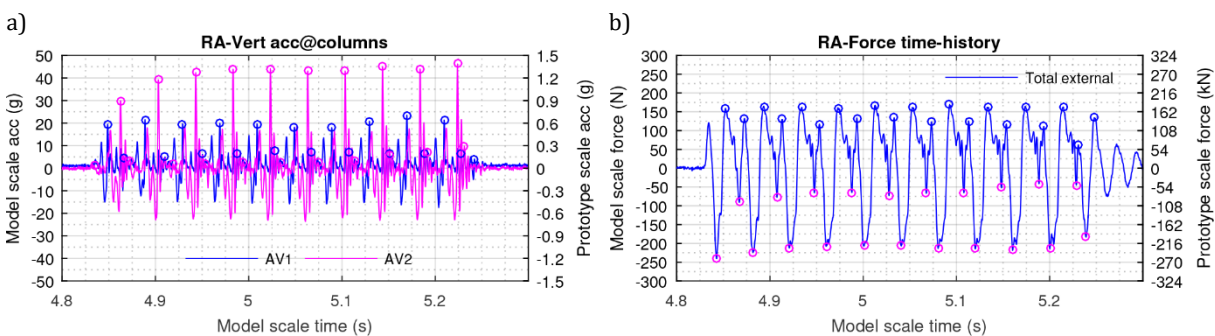


**Figure 5.12: Loose sand, Test-1 Eq-5: Vertical acceleration response of model RA (a) and force time-history for model RA (b). Black circles are pairs of impact acceleration-force demand**

For dense sand, the behaviour of model RA appears again similar to that of RB. More specifically, large scattering appears for both models, however this is even larger for RB. In general, different earthquake excitations create different clusters of points in the graph. This means that on the one hand the impact-peak force response is dependent on the excitation (frequency content, amplitude, phase difference) and at the same time can randomly vary locally. For instance, it is important to note that for all 50 Hz excitations of model RA, an asymmetric steady-state rocking response was observed, with large impact

accelerations followed by small local maxima of force demand (Figure 5.12). This steady-state response requires further investigation, but clearly results in a system where the global rocking response governs the force demand rather than the excitation by impact, thus causing a different trend than what is observed for other excitations. Regarding model RB, the randomness appears to be more extended for the individual data clusters. This is again attributed to the difference between having a known and discrete two-point rotation system (RA) with little uncertainty as to where the re-centring occurs, as opposed to a finite area interface of rocking and increased soil deformations.

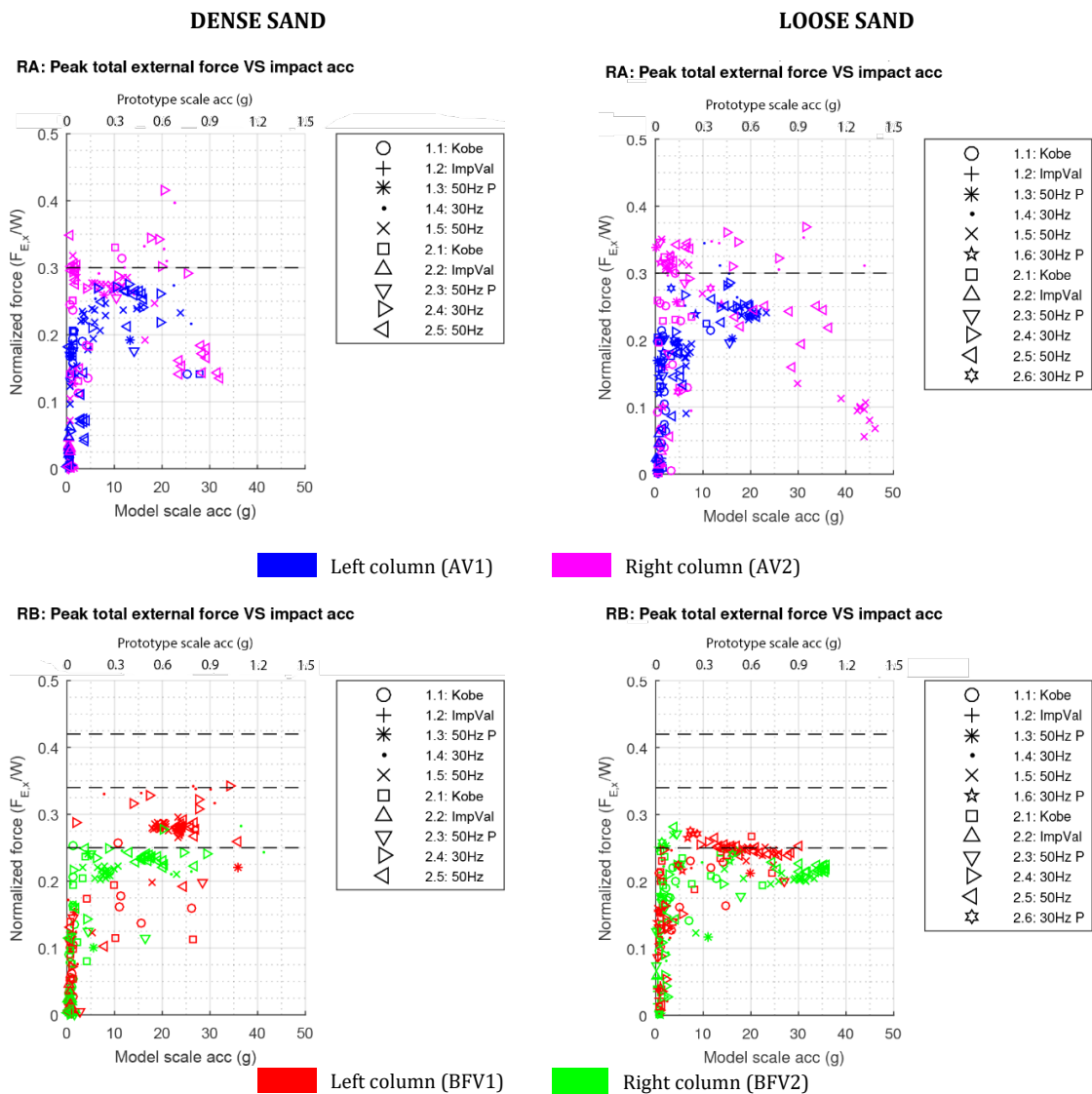


**Figure 5.13: Effect of the impact on the peak total external force, for dense (left) and loose (right) sand. Dashed lines indicate the slenderness values according to Table 3.2**

For loose sand the behaviour of model RA appears to have a similar degree of scattering with the dense sand case. The slenderness limit of RA simply indicates the impact-induced force demand component as an addition to a static force demand for uplift. This again indicates that structural rocking is relatively unaffected by the change of relative density. On the contrary, the scattering of model RB appears reduced between dense and loose

sand, and a force demand plateau forms for large impacts close to the minimum slenderness limit (0.25).

This general and local behaviour of RB is explained by recalling that its footings impose additional stress due to the building's rotation while rocking, which in conditions of loose sand can lead quickly to yielding and a stiffness reduction below the footing. The difference of pre-yielding soil stiffness below the footing due to change of sand density might not mean significant reduction of the impact amplitude, as this is similar for RB across both dense and loose sand, but it may prevent the development of a large impact-induced structural deformation (and hence a large force demand) by allowing a soil settlement instead. If an impact induced force demand is considered, then the actual slenderness value is smaller than 0.25, suggesting that the point of rotation in loose sand might be even further than the internal edge of the footing. In addition, when soil settlement is activated, the response does not involve large values of the peak rocking angle anymore for RB. For RA, soil yielding is essentially eliminated. Further increase of rocking rotations would not increase the soil pressure further, so would not increase soil yielding. However, increased rotations could increase impact forces, which could cause some soil yielding at impact for very large rotations.

## 5.4 Summary

This paper compares the seismic behaviour between two building models resting on dry sand and allowed to uplift and subsequently indulge in two different types of rocking action. Structural rocking, defined as rocking where a building uplifts and rocks above its foundation level, was represented by a building model with no connections to its footings. On the other hand, foundation rocking, where a building is allowed to rock below its foundation level, was represented by a dynamically similar building model which had fixed column-footing connections. Sequential earthquake excitations were run with the two building models tested side by side in centrifuge conditions, with both low and high relative densities of dry sand considered. Evaluation of the seismic response of the two building models led to the following conclusions:

- The base isolation effect, quantified measuring the experimental base shear and comparing to a linear elastic solution (response spectrum), was very significant for excitations with frequency content close to the fundamental natural frequency of the structures. For low frequency excitations, there was no clear benefit of

rocking compared to the fixed base linear response; both exhibited similar force demands. This was attributed to large rotations with large impacts causing additional force demand for both structural and foundation rocking. For low magnitude excitations, no significant uplift occurred.

- The weight-normalized magnitude of the maximum total base shear force developed because of the ground excitation and the intrinsic rocking mechanisms was consistently, though not extensively, larger in structural rocking for either type of sand. This finding was attributed to two effects. First, the foundation rocking model was effectively more slender because the effective rotation point moved away from the footing edge due to soil deformation, which decreased the static lateral force demand. Second, the structural rocking model experienced larger higher frequency vibration response, which was likely caused by increased impact excitation due to the two-point rocking mechanism as opposed to the partial contact mechanism in foundation rocking.
- For structural rocking, the sand density did not have a significant effect on the response. Limited evidence suggests only that the sand density might have a minor influence on higher frequency vibrations caused by impact. On the contrary, foundation rocking is inherently dependant on the soil conditions. This was more profound during the low frequency excitations where loose sand ceased rocking and led to full contact response with evidence of significant soil deformations and smaller storey drift demands.

In general, these results demonstrate both structural rocking and foundation rocking provide effective base isolation, and highlight some trade-offs between these systems. However, the critical effect of foundation settlements caused by foundation rocking is not addressed here because it could not be measured directly in the tests. By visual inspection at the footprints, similar total and differential settlements were observed for both buildings and these were relatively small. The wider implications of this comparison are associated with the potential uncertainty of the soil properties often encountered in practice, and the relative importance of residual settlements. Structural rocking presents a similar behaviour across different densities of sand with potentially smaller residual settlements, reducing uncertainty related to soil deformations. Foundation rocking on loose sand reduces the effects of rocking impact, while increasing soil yielding (energy dissipation) and moderately decreasing force demand.



# 6 DYNAMIC BEHAVIOUR OF SOIL

## 6.1 Introduction

While the previous Chapter focused on the seismic performance of the building models, this Chapter (Pelekis *et al.*, 2018b) presents results that quantify the relative differences in building and soil deformation amplitudes. These results are then used to evaluate the importance of the damping provided by each system during rocking action. In addition, the raw dynamic behaviour of soil below each rocking structure was analysed by using wavelet transforms to explore the propagation of waves through the soil resulting from the impacts generated during the re-centring process, and the fluctuation of vertical pressure due to the loads induced on the foundation during lateral swaying.

## 6.2 Analysis with wavelet transforms

The frequency response of the soil and building models was analysed across time with wavelet transforms using the Morse wavelet with  $\gamma = 3$  and  $\beta = 27$ , similarly to Chapter 5. In general, the building response can be broken into three parts, which are common between the two building models. The first is a very short duration of full contact response, the second a potential uplifting or rocking response, and finally a mixture between free rocking and full contact free vibration. Based on this distinction, the evolution of frequencies in the soil is examined due to soil-structure interaction.

### 6.2.1 Low amplitude earthquake

Firing of a small amplitude earthquake can provide insights for the overall mechanisms of soil-structure interaction, with a focus on the small deformation, mostly full contact behaviour. In this section, results from a small amplitude excitation with a basic

### DENSE SAND TEST-0 EQ-4

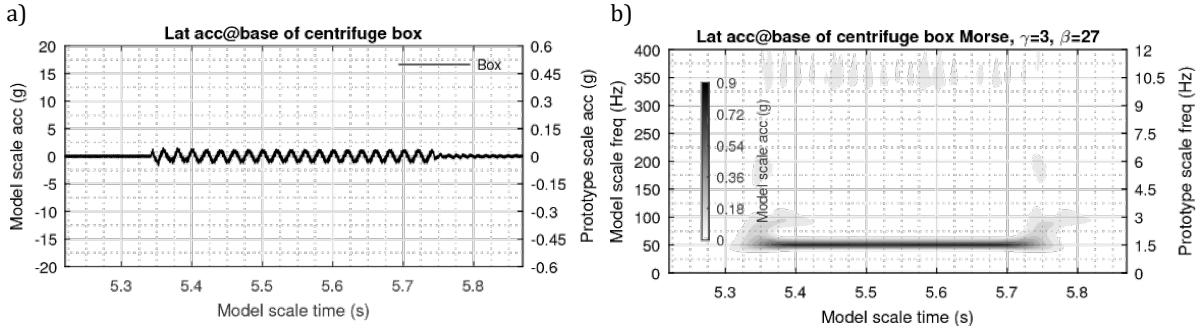


**Figure 6.1: Time history (a) and time-frequency map (b) of the excitation measured at the base of the centrifuge box**

### DENSE SAND TEST-0 EQ-4

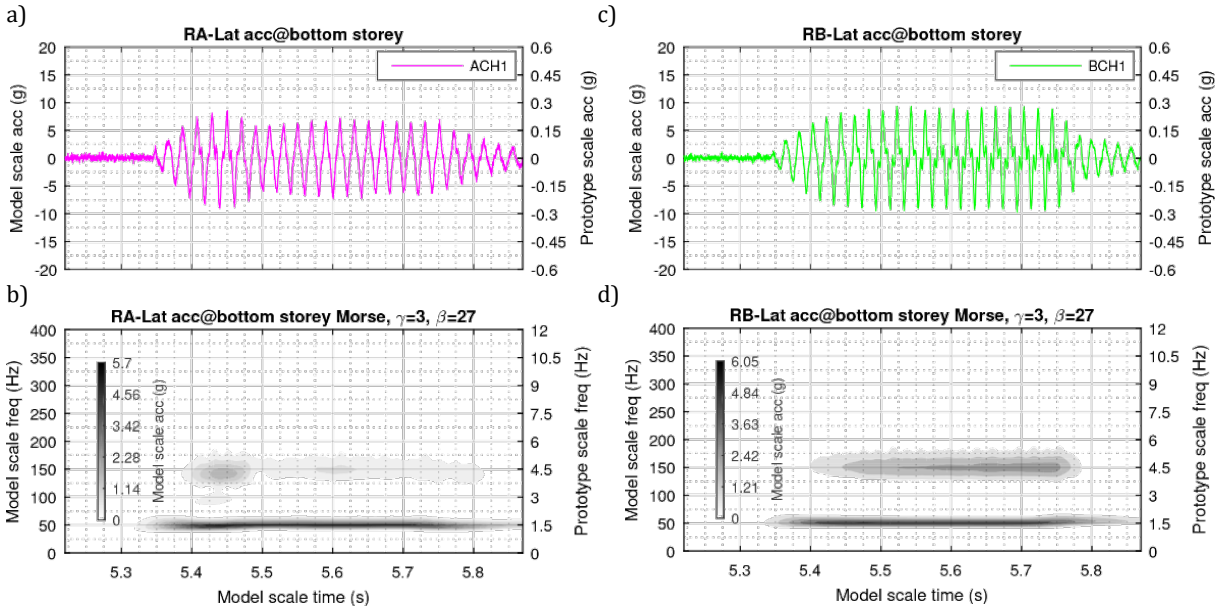


**Figure 6.2: Bottom storey lateral acceleration and time-frequency map (a, b) for model RA and similarly for model RB (c, d)**

component of 50 Hz (Figure 6.1a, b), which provides a near-resonant input, are discussed (Figure 6.2). The time history response of model RA (Figure 6.2a), is characterized initially by an increasing amplitude response at time  $t = 5.35 - 5.50$  s, followed by a dissipation and a further amplitude increase. This is expected since model RA has a nearly identical natural frequency with the excitation, therefore the initial response represents resonance being developed over time (Figure 6.2b). At a critical point, there will be enough external force to induce uplift. Evidence of uplift is shown in the form of the three distinct disturbances in the column vertical acceleration measurements (Figure 6.3a), which indicate impact and correspond to the resulting broadband frequency excitation (vertical strips) in the time-frequency plots. In contrast, no uplift occurred for model RB (Figure 6.2c, 6.3e). The time-frequency maps of the two buildings' lateral accelerations (Figure 6.2b, d) reveal the main driving frequency at approximately 50 Hz; higher modes of response at approximately 137 and 150 Hz for RA, RB respectively also developed.

DENSE SAND TEST-0 EQ-4

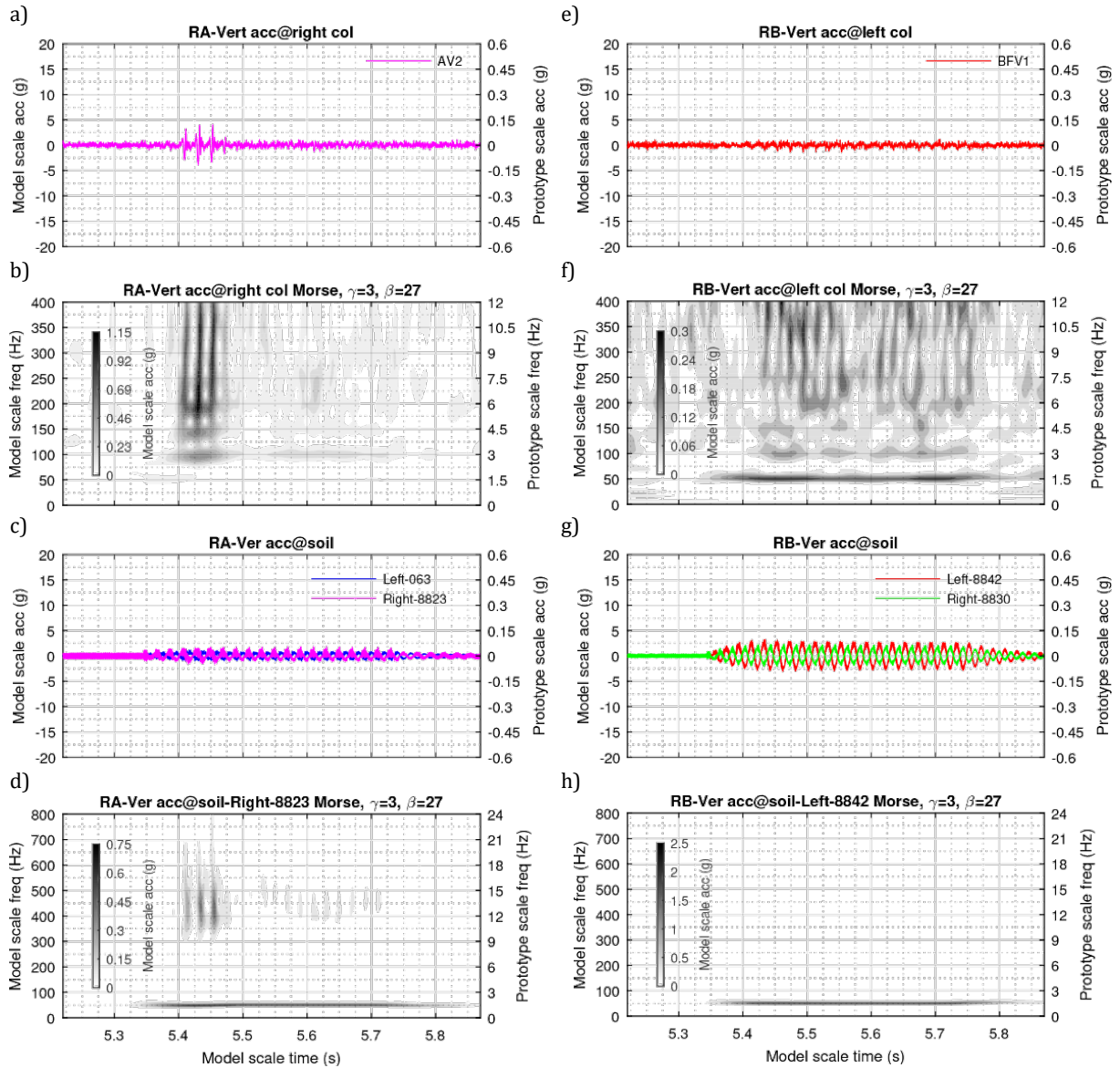


**Figure 6.3: Time history and time-frequency map of column vertical accelerations (a, b), time history and time-frequency map of soil vertical accelerations (c, d) for model RA and similarly for model RB (e-h)**

Model RB does not show any distinct spike in the vertical acceleration to suggest the development of uplift causing large impacts (Figure 6.3e). However, a clear 50 Hz component is seen on the time-frequency map for the left vertical acceleration of model RB (Figure 6.3f) which, although practically absent in RA for the right column (Figure 6.3b), was also found in the time-frequency map of the left column (not shown here). This means that small vertical motion of the footings occurred in RA and RB, with very small uplift of the column only in a few instances for RA. Therefore, even under a small excitation, small vertical excitation of each footing can still occur.

Furthermore, the vertical accelerations of the soil below the footings presented in Figure 6.3c, g show a clear steady-state response, with the response being more profound for model RB. The out of phase profile observed suggests that the vertical excitation of the

footings was actually a weak form of rocking for both building models. Considering also that the vertical accelerations on the footings are so small to be practically buried in noise ( $S/N \ll 5$ , Figure 6.3e), the indications from all the vertical accelerations show a significant amplification due to the building models loading the soil, although a small vertical component may have developed by the shaker as well (Hughes and Madabhushi, 2018). More specifically, model RA clearly transmitted the high frequency content close to 400 Hz (Figure 6.3d), due to uplifting and impacting behaviour, whereas in contrast model RB transmitted only the 50 Hz component (Figure 6.3h). This behaviour essentially means that, overall, even under a small earthquake, structural and foundation rocking can activate the vertical deformation of the soil well below the surface.

### 6.2.2 Pulse response

Next, the interaction caused by a pulse excitation is considered, to examine whether the free, full contact vibration affects soil well below surface level. Figure 6.4 shows the low frequency pulse excitation and its time-frequency map. As also shown in Figure 4.7, the driving frequency content is slightly off from the specified 30 Hz, to a higher value of approximately 40 Hz, and is accompanied by some strong high frequency content. The acceleration profiles from the vertical accelerometers (Figure 6.6a, e) suggest that sequential uplift occurred, and consequently rocking, for both building models.

High frequency content developed for the two models during the driven rocking, which is very close to their second mode frequency respectively (Figure 6.5a, c). By the end of the excitation, model RA already switched to full contact free vibration response with both modes participating (Figure 6.5b), although the second mode was damped faster. On the contrary, in model RB the second mode free vibration is not clearly evident (Figure 6.5d).

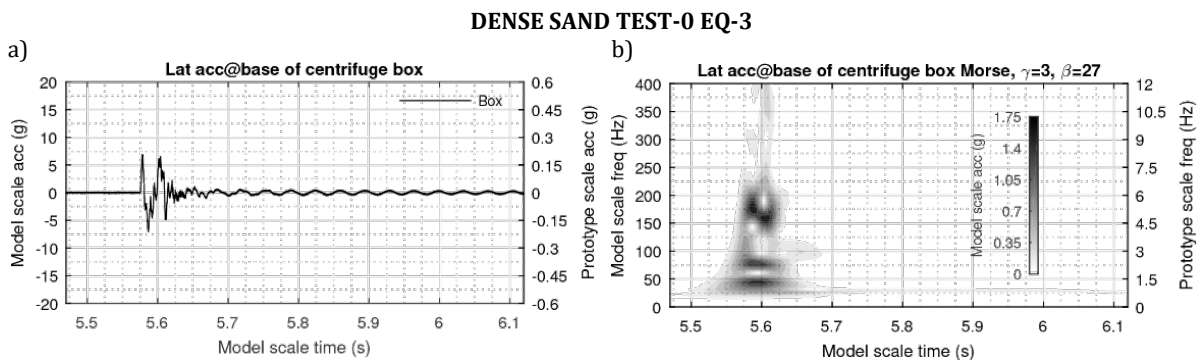


**Figure 6.4: Time history (a) and time-frequency map (b) of the excitation measured at the base of the centrifuge box**

### DENSE SAND TEST-0 EQ-3

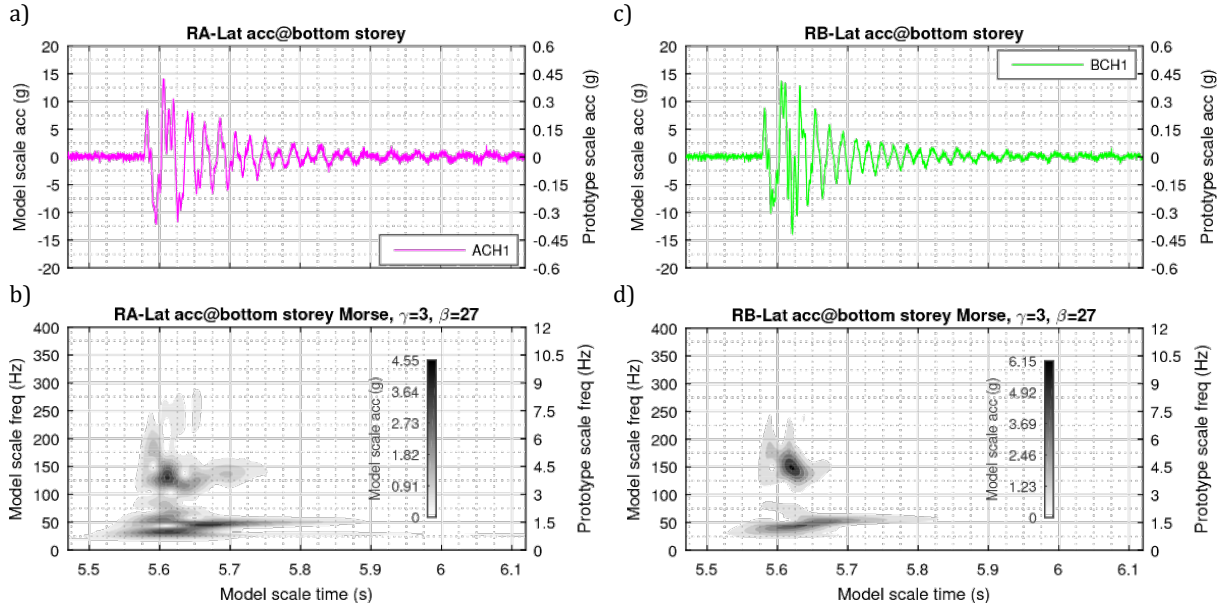


**Figure 6.5: Bottom storey lateral acceleration and time-frequency map (a, b) for model RA and similarly for model RB (c, d)**

The time frequency maps (Figure 6.6b, f) of the buildings' vertical accelerations show ripples of high frequency content exactly at the time when vertical oscillation occurred as indicated by the vertical acceleration time histories (Figure 6.6a, e). Furthermore, the vertical acceleration below each footing of each model (Figure 6.6c, g) show out of phase profiles for both buildings while the response is larger below model RB. Very clear high frequency oscillations are also evident, and these were not observed in Section 3.1. The time frequency maps of the soil (Figure 6.6d, h) show that the low frequency ( $< \sim 60$  Hz) vertical response in the soil is similar to the response developed by the buildings (Figure 6.5b, d); the shift in response from  $\sim 40$  Hz to  $\sim 50$  Hz is observed in both. In addition, ripples spanning from 300 Hz to 800 Hz (Figure 6.6d, h) developed with their time instance matching the ripples in the time-frequency maps (Figure 6.6b, f), and also the time histories, (Figure 6.6a, e) of the vertical accelerometers on the building columns. Considering that this very high frequency content matches timewise the uplift, its existence can be attributed to the hammering action of either the column knives on the footings for model RA, or of the footings' bottom surface on the soil for model RB, during rocking. Therefore, it is concluded here that soil can register the free vibration lateral motion of the buildings in the form of vertical motion and similarly, repeating the conclusion of the previous section, it can also register the impacts and their broad frequency response.

### DENSE SAND TEST-0 EQ-3

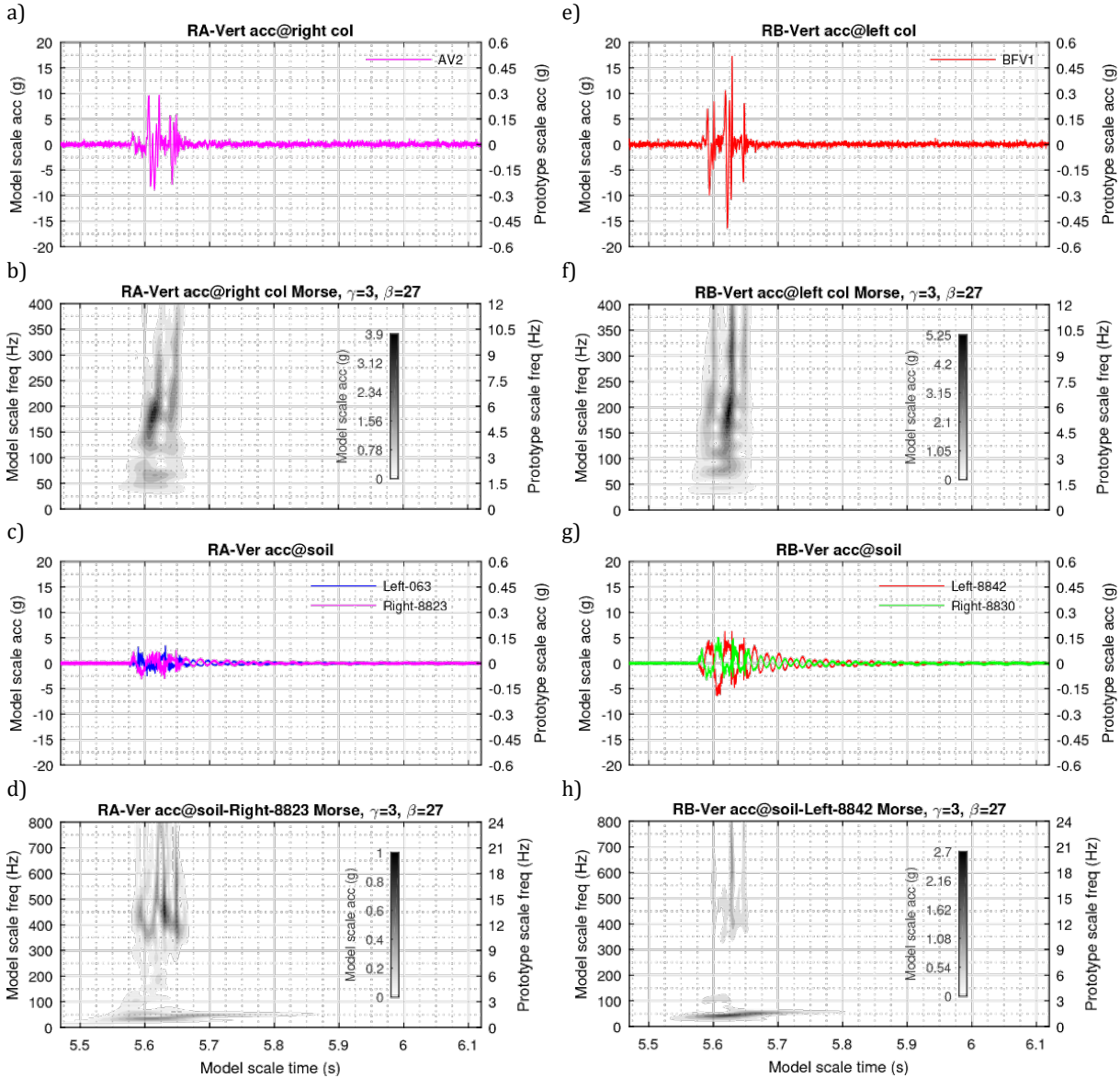


**Figure 6.6: Time history and time-frequency map of column vertical accelerations (a, b), time history and time-frequency map of soil vertical accelerations (c, d) for model RA and similarly for model RB (e-h)**

### 6.2.3 Low frequency earthquake

The low frequency cyclic excitation of 30 Hz is considered (Figure 5.7a) as an example to study the lateral response of the soil. It is convenient to define arrays A, B, C that correspond to the vertical line of accelerometers below RA, RB and in between, respectively (Figure 6.7). Each array is formed by three instruments for the lateral soil accelerations, at the surface ( $i = 1$ ), at the mid-height ( $i = 2$ ) and at the base level ( $i = 3$ ). The metal base of the centrifuge box ( $i = 4$ ) is considered as the bedrock.

The time-frequency maps of the lateral soil accelerations are shown in Figure 6.8. The main low frequency component along with the higher harmonics of the shaker (up to

about 200 Hz) are similar without major differences in amplitude across the horizontal direction  $x$  of the soil domain and up to the surface. The time-frequency maps of the lateral accelerations at the soil surface show additional very high frequency content ( $\sim 300 - 800$  Hz), which appears very weak in the mid-height and is absent at the time frequency maps of the base level (not shown here). The same very high frequency content is also found in the vertical soil accelerations below the footings, which was previously found to be the result of the buildings rocking (Sections 6.2.1, 6.2.2). Therefore, rocking of the buildings affects the lateral response of the soil and consequently, a zone of influence can be defined (based on the presented arrangement of accelerometers, Figure 6.7), extending from the surface down to the mid-height of the centrifuge box (depth  $\approx 3.4b$ ).

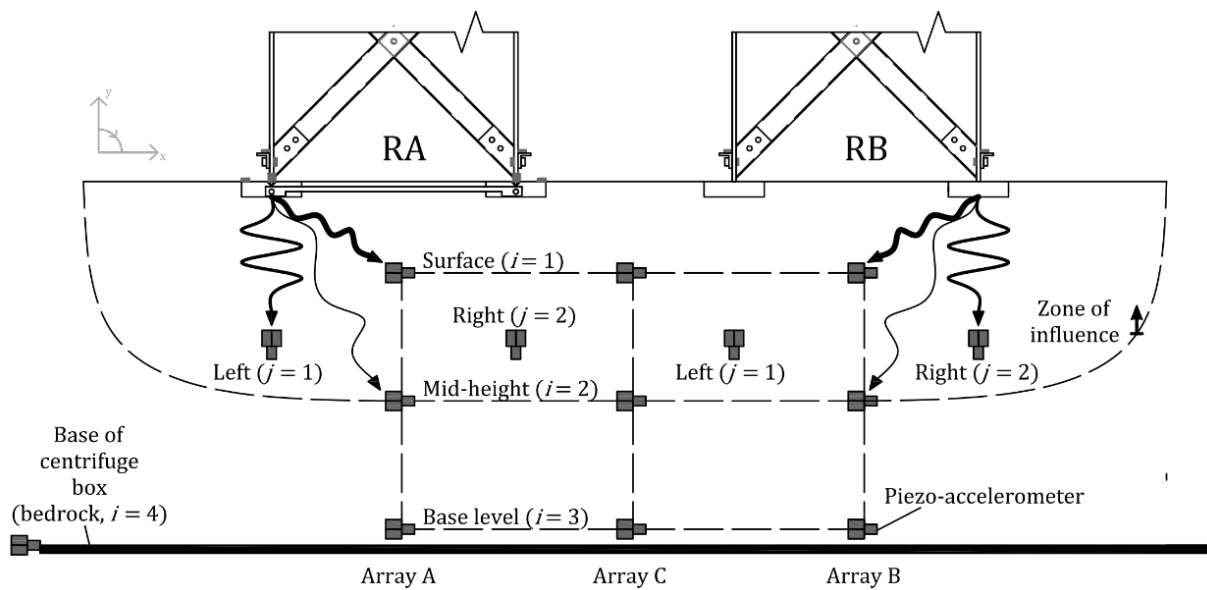


**Figure 6.7: Schematic diagram of wave propagation from structures to the soil and identified zone of influence due to dynamic soil-structure interaction**

#### 6.2.4 Summary of wavelet analysis

To provide insights across all the earthquake excitations, the relation between the signal energy (calculated from the wavelet transforms) and the peak rocking angle was used. As opposed to other signal intensity measures such as the Arias intensity, the use of wavelet

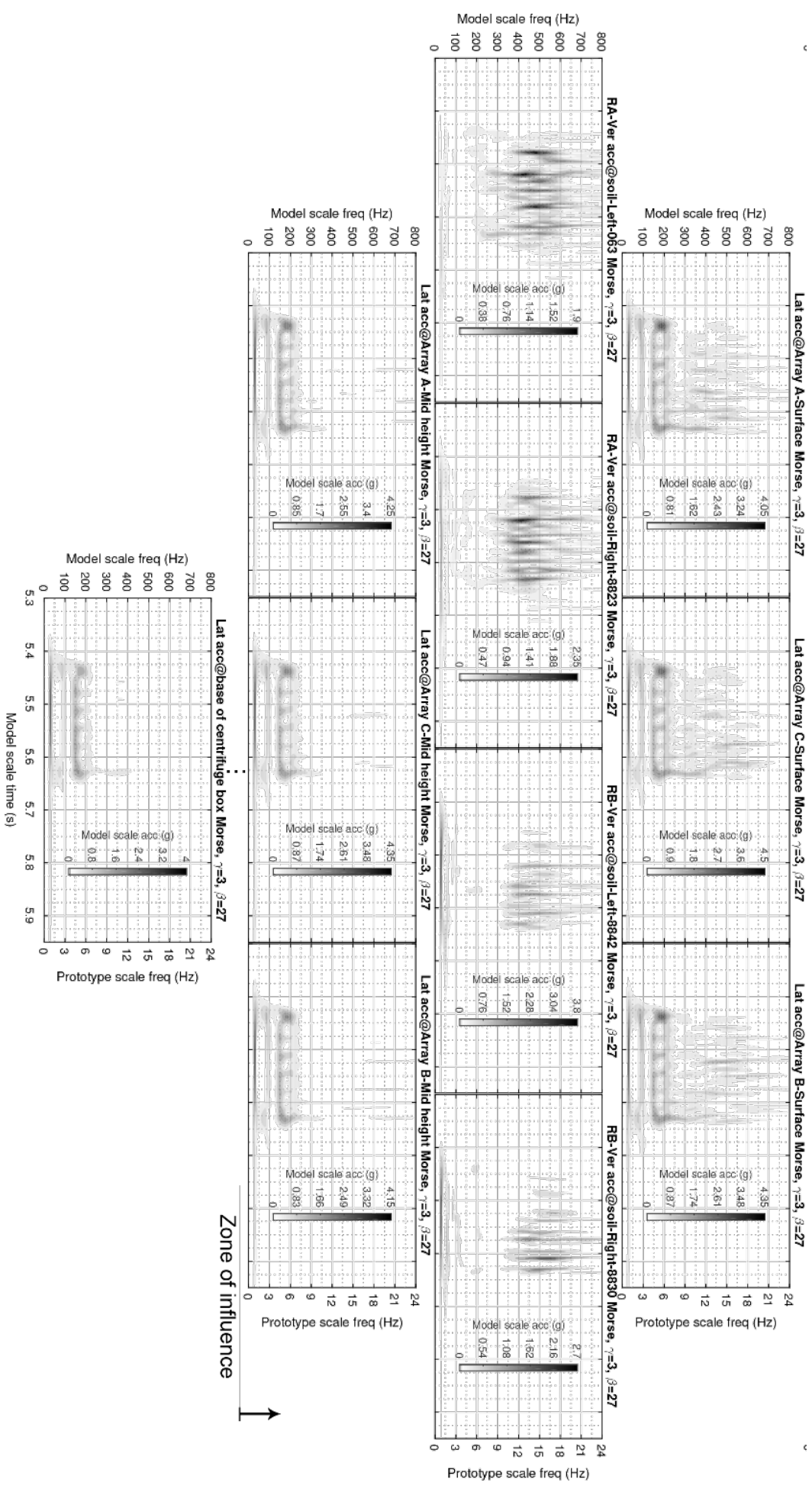


Figure 6.8: Dense sand Test-2 Eq-4: Time-frequency maps of the excitation as it propagates from the base of the centrifuge box to the bottom storey of the building models

transforms to extract signal energy allows the breakdown of the time-frequency domain to individual parts. Generally, a multiple of the signal energy from the wavelet transform can be defined as (Addison, 2017):

$$E_{x,i} = \int_{-\infty}^{\infty} \int_0^{\infty} |W_{x,i}(t,f)|^2 df dt, \quad i = 1,2,3,4 \quad (6.1)$$

where  $|W_{x,i}(t,f)|^2$  is the energy density of the wavelet transform  $W_{x,i}(t,f)$  in the horizontal direction  $x$ , for the soil depth  $i$ , across the frequency domain  $f$  and time domain  $t$ . An upper frequency limit  $f_u = 1$  kHz was used. Next, a high and a low frequency area were defined for each earthquake test by specifying a cut-off frequency  $f_h$  (Figure 6.9a, b) which is used to obtain the signal energy  $E_{x,h,i}$  from the high frequency components of a wavelet transform:

$$E_{x,h,i} = \int_{-\infty}^{\infty} \int_{f_h}^{f_u} |W_{x,i}(t,f)|^2 df dt, \quad i = 1, 2, 3, 4 \quad (6.2)$$

A normalized value  $r_{x,h,i}$  of this energy contribution can then be defined by using the total signal energy from the wavelet transform of the input motion at the base of the centrifuge box ( $i = 4$ ) as a normalizing constant:

$$r_{x,h,i} = \frac{E_{x,h,i}}{E_{x,4}} \quad (6.3)$$

Figure 6.10 plots the ratio  $r_{x,h,i}$  for all soil depths ( $i = [1, 3]$ ) against the peak rocking angle of each building. In dense sand (Figure 6.10a), high frequency content in the lateral soil accelerations increases with the peak rocking angle, with this being more profound in the soil directly below the buildings and at a distance of about  $1.3b$ , where  $b$  is the footing width. This means that the more a building is allowed to rock, the larger will be the scattering of energy in the soil during the re-centring process due to impact. A relatively small difference is found between the two types of rocking models on dense sand. In the loose sand case (Figure 6.10b), there was no correlation between energy ratio and peak rocking angle. This may be due to plastic soil deformations occurring below left and right footings in alternate half cycles, limiting the peak rotation in the building but at the expense of some differential settlements. This is explained in more detail in Section 6.3. In any case, Figure 6.10 shows that the scattering of energy developed up to the distance of about  $3.4b$  below the footings creating a zone of influence up to that point, while it was even smaller at the base of the centrifuge box and at a distance of about  $5.5b$  away (Figure 6.7).

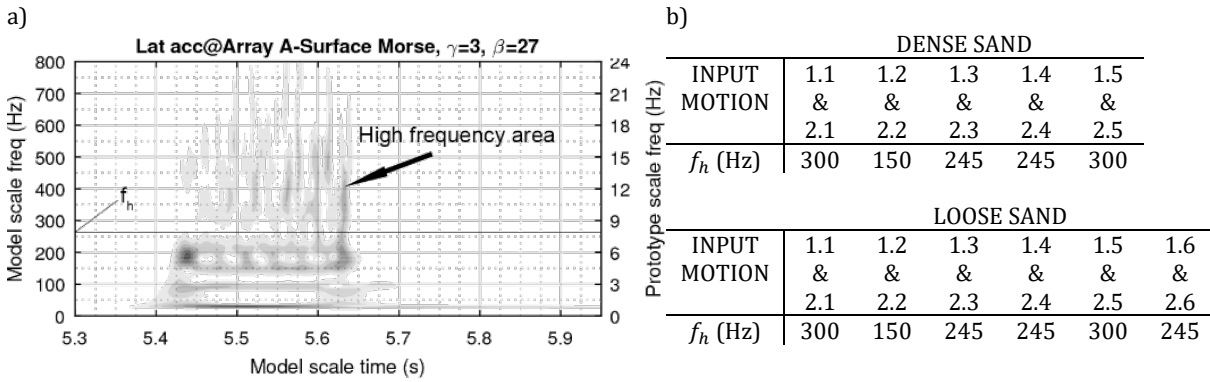


**Figure 6.9: Dense sand Test 2 EQ 4: Example of high frequency area definition (a) and cut-off frequencies  $f_h$  in model scale (b)**

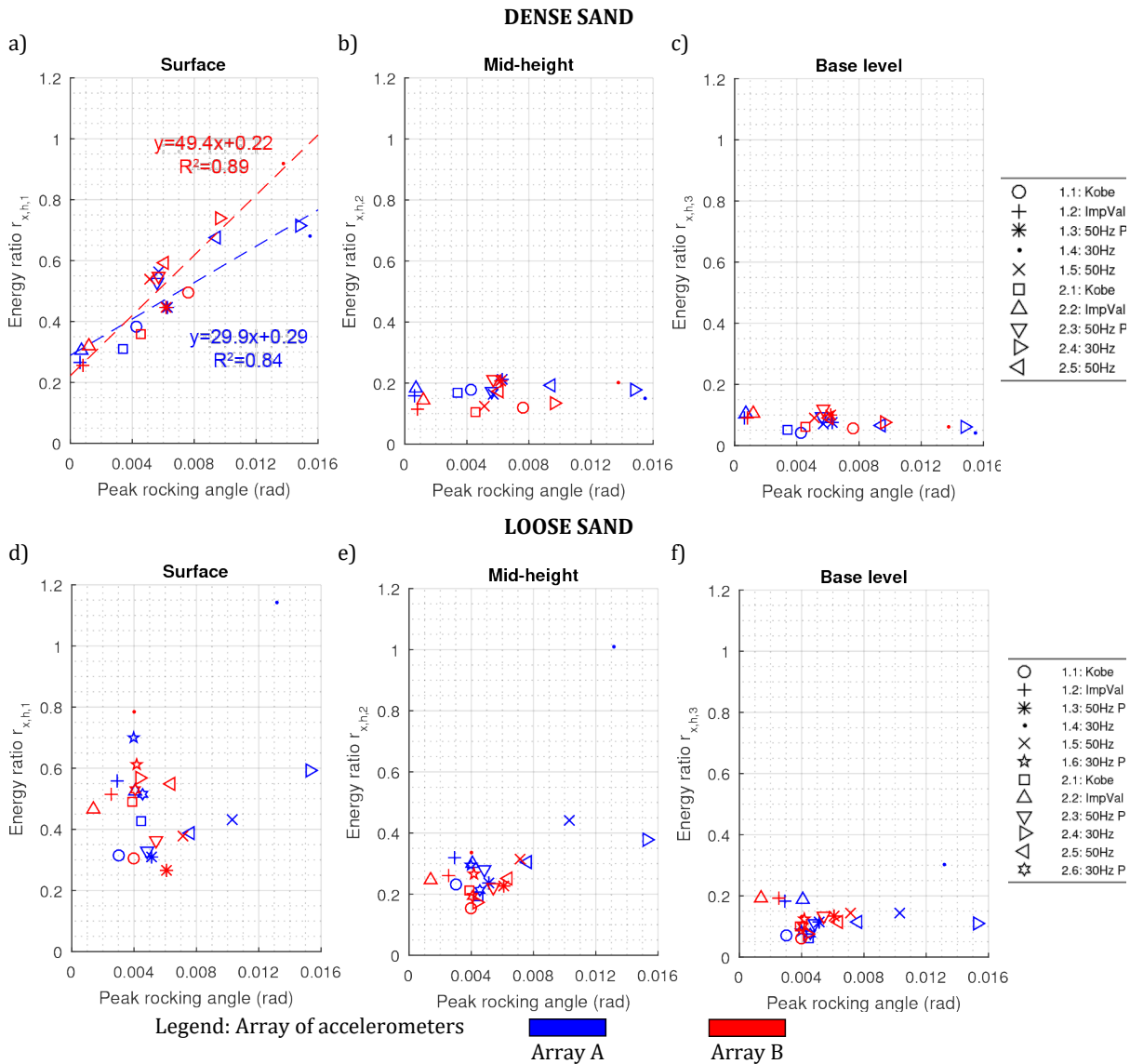


**Figure 6.10: Ratio of energy of high frequency area over the energy of the input motion wavelet transform at the surface (a), mid-height (b) and base level (c) for dense sand and similarly at loose sand (d-f) for the accelerometer arrays A and B (see Figure 6.7)**

For the wavelet transforms of the vertical soil accelerations below each pair of footings and at depth of  $2.2b$ , the total, high, and low frequency signal energies are calculated by using the equations below:

$$E_{y,tot} = \sum_{j=1}^2 \int_{-\infty}^{\infty} \int_0^{f_u} |W_{y,j}(t, f)|^2 df dt, \quad E_{y,h} = \sum_{j=1}^2 \int_{-\infty}^{\infty} \int_{f_h}^{f_u} |W_{y,j}(t, f)|^2 df dt, \quad (6.4)$$

$$E_{y,l} = \sum_{j=1}^2 \int_{-\infty}^{\infty} \int_0^{f_h} |W_{y,j}(t, f)|^2 df dt$$

where  $|W_{y,j}(t, f)|^2$  is the energy density of the wavelet transform  $W_{y,j}(t, f)$  in the vertical direction  $y$  and with  $j = 1, 2$  referring to the left and right vertical accelerometers below each building (Figure 6.7). In this case, the cut-off frequency  $f_h$  was set to a value slightly larger than the second mode frequency for each building. Normalised versions of these signal energy contributions can be defined as:

$$r_y = \frac{E_{y,tot}}{E_{x,4}}, \quad r_{y,h} = \frac{E_{y,h}}{E_{x,4}}, \quad r_{y,l} = \frac{E_{y,l}}{E_{x,4}}, \quad \rho_{y,h} = \frac{E_{y,h}}{E_{y,tot}} \quad (6.5)$$

with  $r_y, r_{y,h}, r_{y,l}$  representing normalisation to the signal energy  $E_{x,4}$  of the input motion and  $\rho_{y,h}$  representing normalisation to the total energy of signals, from left and right vertical accelerometers in the soil and below a building.

Figure 6.11a-d shows these ratios for the case of dense sand. Figure 6.11a shows that high frequency energy is  $\sim 90\%$  of the total energy below RA, while the same figure accounts for  $\sim 80\%$  below model RB, suggesting that high frequency content from impacts are more significant in the soil for structural rocking;  $\rho_{y,h}$  is not significantly dependent on the peak rocking angle, above a minimum rocking threshold, for either rocking type. When the normalisation to the input energy is considered (Figure 6.11b-d), both buildings exhibited a clear dependence on the peak rocking angle. In general, the signal energy of RB was larger than RA for all cases (high frequency, low frequency, and total energy). This can be explained by the rotational motion of the RB footings imposing additional load on the soil, causing more vertical movement beneath. Overall, in dense sand there is a clear dependence of the soil vertical response on the impacts for both types of rocking (Figure 6.11d).

In loose sand and for model RB, high frequency content participation is well correlated to the maximum rocking angle (Figure 6.12a). In addition, the larger the maximum rocking angle RB experiences, the larger the high frequency energy while the smaller the low

frequency energy (Figure 6.12b, c). As a result, no overall correlation exists between the total energy and the maximum rocking angle (Figure 6.12d). Reduction of the low frequency energy with increasing rocking amplitude in RB on loose sand can mean a drop of soil stiffness below the supporting footing experiencing partial contact during rocking. For the soil below model RA, Figure 6.12b-d shows generally weak correlations to the maximum rocking angle suggesting that soil is not affected excessively by structural rocking.

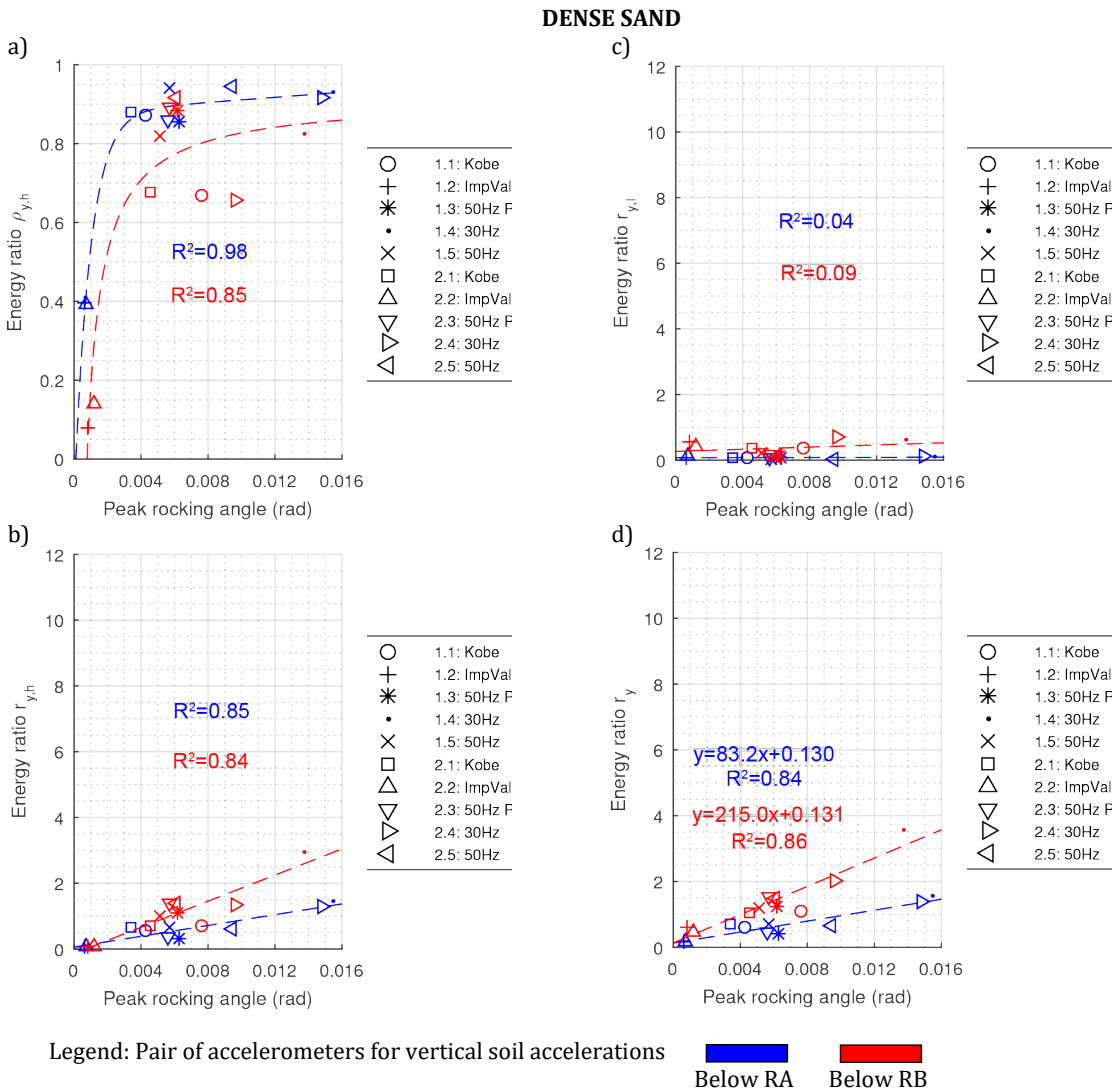


**Figure 6.11: Relative ratio of high frequency energy (a), high frequency energy ratio with respect to the input motion (b), low frequency energy ratio with respect to the input motion (c) and total energy ratio with respect to the input motion (d) for dense sand for each pair of vertical accelerometers ( $j = 1, 2$ , Figure 6.7) below building RA and RB**

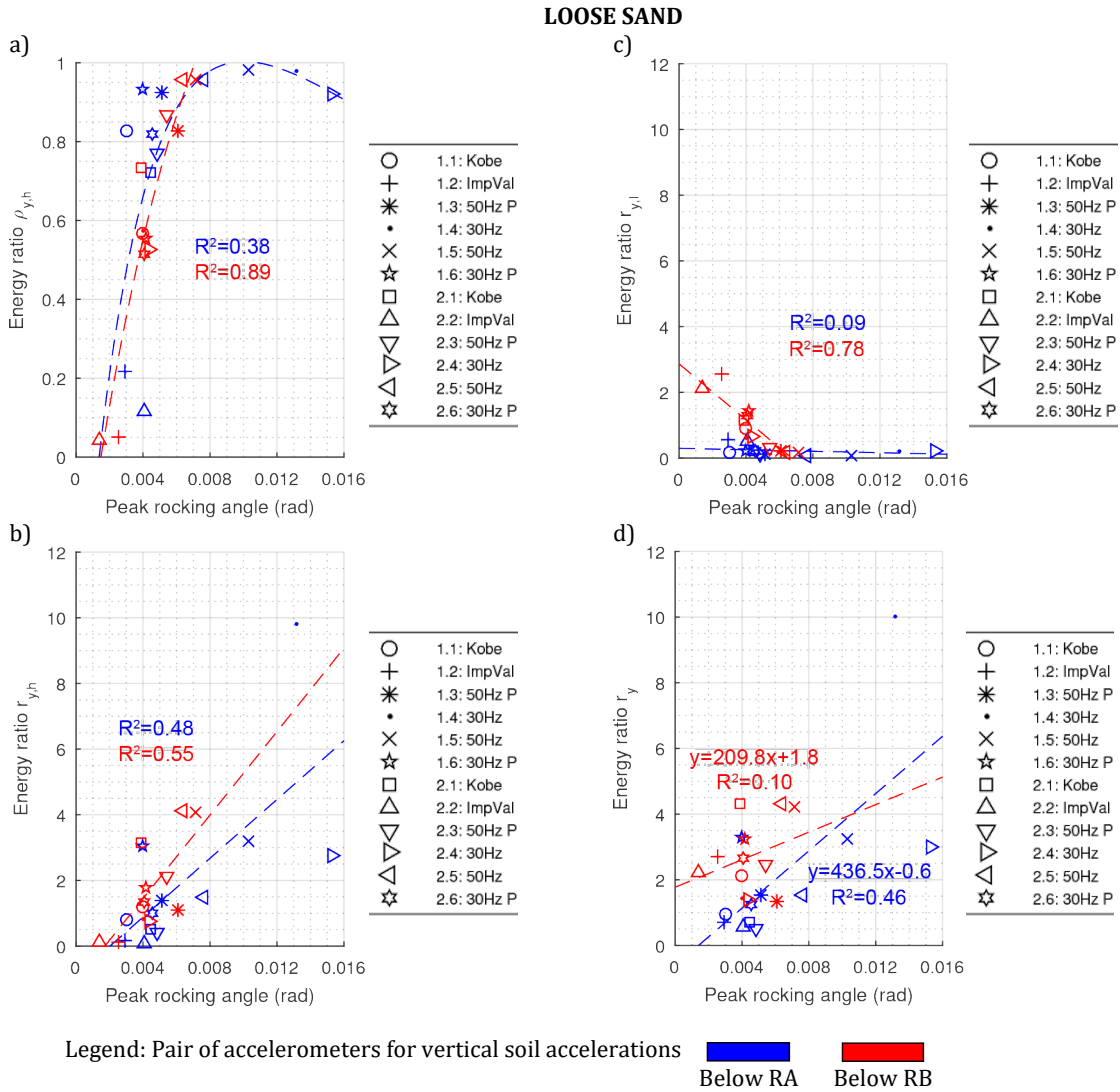


**Figure 6.12: Relative ratio of high frequency energy (a), high frequency energy ratio with respect to the input motion (b), low frequency energy ratio with respect to the input motion (c) and total energy ratio with respect to the input motion (d) for loose sand for each pair of vertical accelerometers ( $j = 1, 2$ , Figure 6.7) below building RA and RB**

### 6.3 Performance trade-offs

The relative deformations in terms of building rocking angle  $\theta$  and soil vertical differential displacement  $\Delta d$  below each pair of footings were compared for the two building models. Both deformation values were extracted by using double integration of the obtained accelerations and therefore are baseline-corrected and without any residual values. A pulse excitation is shown in Figure 6.13a, d and the resulting deformation time-histories are shown in Figure 6.13b-f. It is observed that between dense and loose sand, the two building models have at most the same rocking amplitude, but soil deformation is larger for RB throughout the time-histories. Regarding residual settlements, at the end of the centrifuge flights these were found to be very small by visual inspection and similar for the two models.

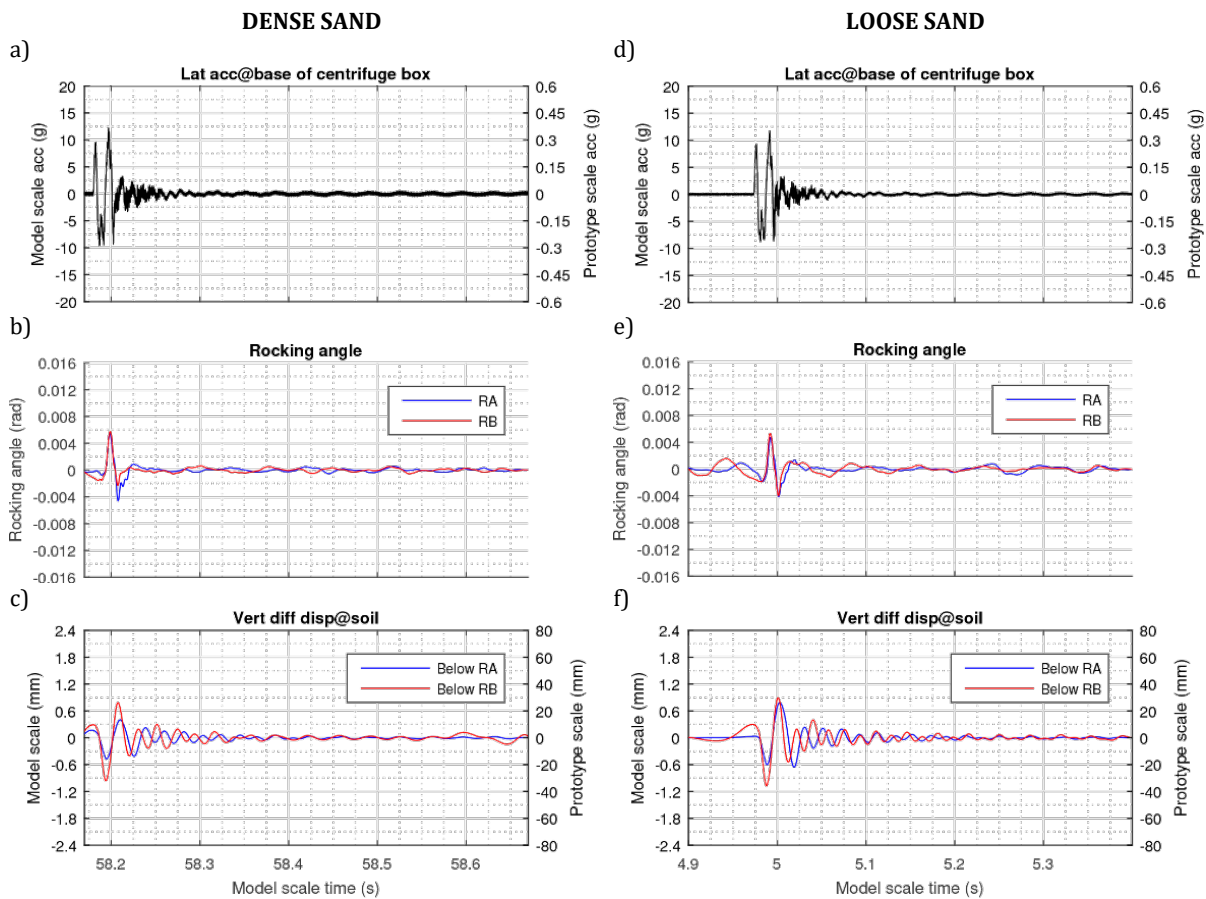


**Figure 6.13: Test 2 EQ 3: 50 Hz pulse excitation (a), rocking amplitude (b) and soil vertical differential displacement (c) for models RA and RB for dense sand, and the equivalent results for loose sand (d-f)**

Next, the maxima of these deformations ( $\Delta d$  now normalised by the footing width  $b$ ) from all the excitations are compared in Figure 6.14. A fitting of the data is also shown, only to highlight relative differences between the two buildings across the different soil densities. The trends suggest that for any given building rocking amplitude RB will result in larger soil transient differential settlements compared to those of RA across both sand densities. Sand density does not affect as much the mechanism for structural rocking; the slope of the linear trend in loose sand is only half the slope in dense sand. In loose sand, foundation rocking can increase soil vertical differential displacements without development of large rocking angles. Considering that structural rocking was found to result in a higher force demand due to the additional excitation caused by impacts (Chapter 5), and that foundation rocking results in larger soil transient differential settlements, clearly a performance trade-off between force demand and soil settlements is created when the two types of rocking are compared from a design point of view.

The relative difference regarding soil differential settlements between the two models can be expected. The reason stems from the difference of their footings' behaviour. While the footing beneath model RA is primarily expected to move in the vertical direction

because of the partial hinge connection, model RB imposes additional rotation which is similar to the building's rotation. As a result, a larger volume of soil may be disturbed which can explain a larger relative displacement below RB's pair of footings in general.

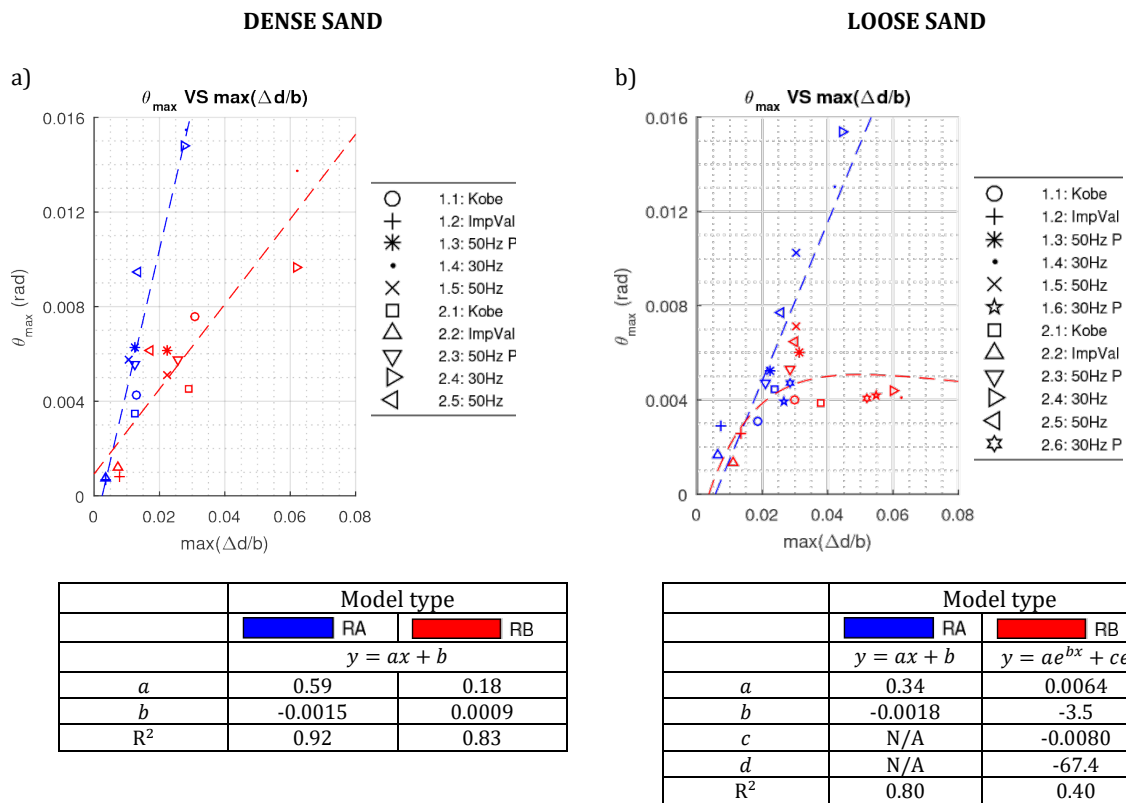


**Figure 6.14: Relationship between maximum normalized soil differential displacement and maximum rocking angle for models RA and RB for dense (a) and loose sand (b)**

### 6.3.1 Deformations below structures in loose sand

Furthermore, the response of soil locally below the footings of each building is investigated by plotting the rocking angle against restraining moment. The latter is defined as the result of rotational inertial and overturning moments. In addition, for model RA, the total moment acting on the bottom surface of the footings was plotted against the foundation rotation, which is defined here as the transient differential settlement between the two RA footings as obtained by the vertical accelerations of those and is normalised with the building's width. This additional graph is essential to examine the soil response since the pair of footings of model RA will impose different deformations on the soil as opposed to the pair of footings directly connected on RB.

For a small earthquake with a full contact response, the soil below each model performs the same. Specifically, Figure 6.15a, c shows that the restraining moment of both models fluctuates on the vertical axis between the static uplift limits and so does the foundation moment for model RA (Figure 6.15b). This means that no large plastic deformations nor excessive yielding of the soil occurred. When a larger earthquake is considered, the soil

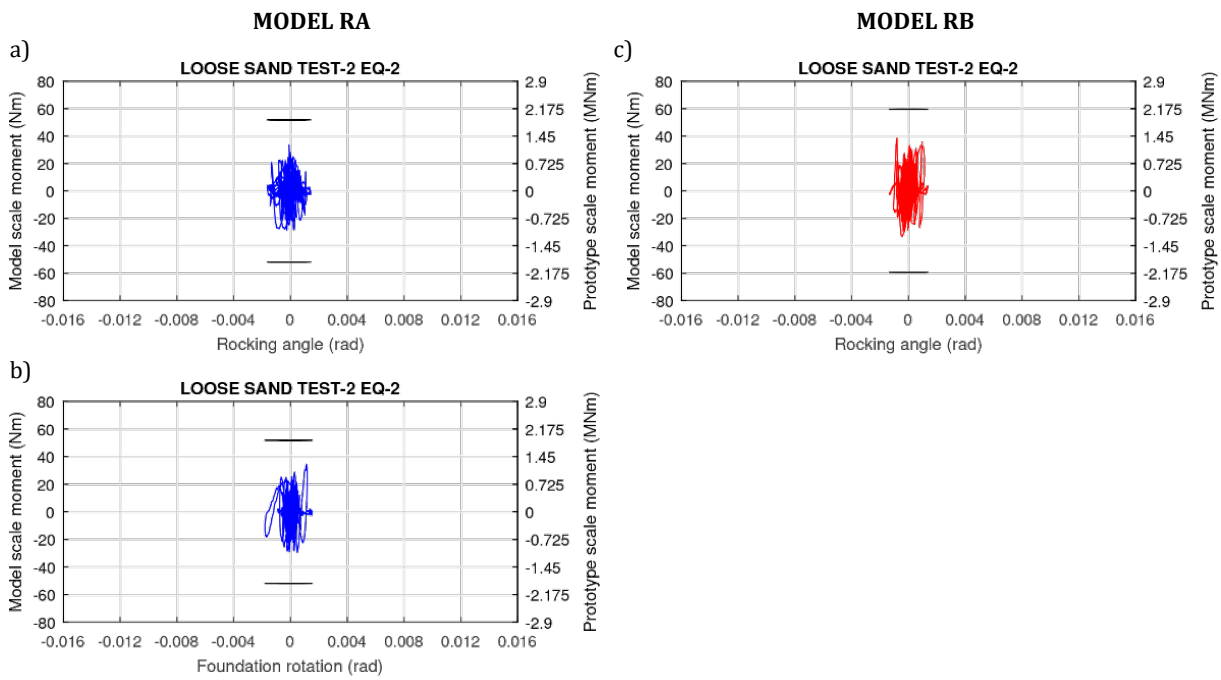


**Figure 6.15: Loose sand Test 2 EQ 2: Restraining moment versus rocking angle for model RA (a), foundation moment vs foundation rotation for model RA (b) and restraining moment versus rocking angle for model RB (c) for an Imperial Valley excitation**

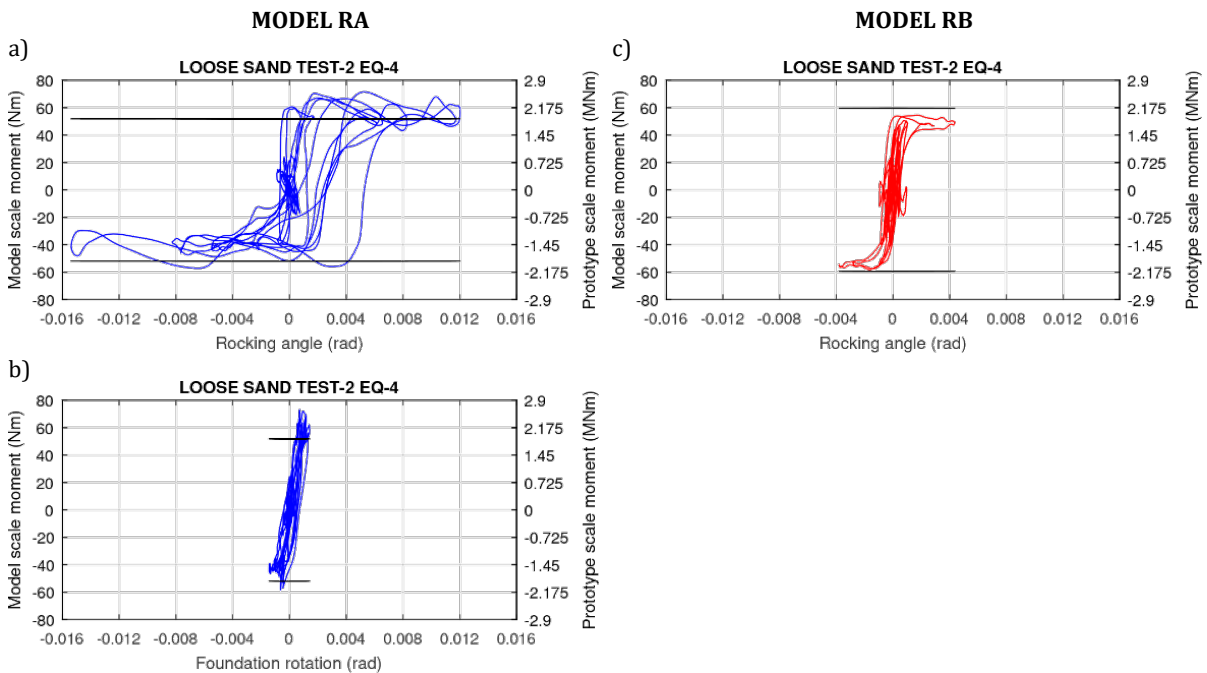


**Figure 6.16: Loose sand Test 2 EQ 4: Restraining moment versus rocking angle for model RA (a), foundation moment vs foundation rotation for model RA (b) and restraining moment versus rocking angle for model RB (c) for a low frequency cyclic excitation**

response below each building's foundation is expected to be different. Figure 6.16a, c (Chapter 5) shows that model RA sustained large rocking angles with a long plateau of the moment, while model RB developed smaller building rotations. It is difficult to evaluate the extent of energy dissipation in Figure 6.16a due to the rotation being a result of a double integration scheme. However, Figure 6.16b suggests that RA dissipated relatively

little energy during rocking, since the rotation of model RA's foundation system indicates no plastic deformation. Meanwhile, for model RB, Figure 6.16c shows some rounding of the loops that indicate some energy dissipation because of rocking. Therefore, the results indicate, as expected, that model RA experienced a smaller plastic response than model RB, and structural rocking exhibited smaller soil settlements and damping compared to foundation rocking.

## 6.4 Summary

The transfer of impact forces to the soil, either because of the contact establishment between a column and a footing (structural rocking) or between the footing and the soil (foundation rocking), was identified by post-processing recorded vertical and lateral soil and building accelerations. The wavelet transforms of these signals were examined along with the maximum rocking angle of each building across all excitations. This methodology allowed temporal tracking and separation of the high frequency content due to impact and the low frequency content resulting from interstory building deformations. By calculating the energy corresponding to each type of frequency content, correlations were drawn between rocking amplitude and energy transfer to the soil due to impact. Acceleration time-histories were also used to derive building rocking angles and the foundation rotation angles, so that the moment-foundation rotation plots can be compared for both types of buildings. This methodology led to the following conclusions:

- Soil acceleration measurements register the changes in vertical bearing pressure of the buildings as they oscillate following an input ground motion. The measurements also register high amplitude rocking in the form of high frequency response due to impacts.
- At a depth of about 1.3 times the footing's width, the high frequency excitation due to rocking, measured in the form of lateral soil accelerations, is similar for structural and foundation rocking in dense sand.
- At a depth of about 2.2 times the footing's width, the vertical soil response below the building with structural rocking was dominated by the high frequency response caused by impacts. Below the building with foundation rocking, the vertical soil response was larger across the entire frequency spectrum but was relatively less dominated by the high frequency component.
- Based on the lateral acceleration measurements, the high frequency excitation caused by impact was only evident up to 3.4 times the footing's width, which indicates the length scale of the zone of influence for soil-structure interaction.

- The foundation system for structural rocking does not impose large deformations on the soil, while in foundation rocking larger soil deformations are expected as these can be directly associated with the rocking angle of the building.
- Foundation rocking causes larger transient differential settlements in the soil than structural rocking in dense sand for a known rocking amplitude. In loose sand, foundation rocking can increase soil differential settlements even without development of large rocking amplitudes. Finally, dynamic differential settlements from structural rocking are practically similar for the different densities of sand considered here.

# 7 FINITE ELEMENT MODELLING FOR ROCKING BUILDINGS

## 7.1 Introduction

The previous Chapters focused on the experimental performance of the buildings rocking above (RA) or below their foundation (RB) and their founding soil. This Chapter (Pelekis *et al.*, 2019) addresses the computational modelling of these buildings. Within the OpenSees framework, foundation and structural rocking were modelled using a Beam-on-a-Nonlinear-Winkler-Foundation model (BNWF) combined with flat-slider elements for footing-soil and for superstructure-footing interactions, respectively. Flat-slider elements were also used and modified to improve the existing BNWF model. The modified BNWF model (mBNWF) involves an uplift dependent stiffness and viscosity transmission for both vertical and horizontal directions and a friction/vertical force coupling. The proposed computational model was used to simulate the set of centrifuge tests involving both structural rocking and foundation rocking with sequential excitations. In addition, a methodology based on signal metrics is introduced to compare parametric versions of a computational signal with its experimental counterpart.

## 7.2 Input motion for computational response

The series of tests described in Table 4.2 are simulated within the OpenSees environment. The input motions of Table 4.2 were described in OpenSees by using the accelerations measurements from the external surfaces of the centrifuge box and the soil surfaces.

Figure 7.1 shows recorded accelerations at these different locations, along with the corresponding wavelet transforms. Generally, in computational simulations compared to

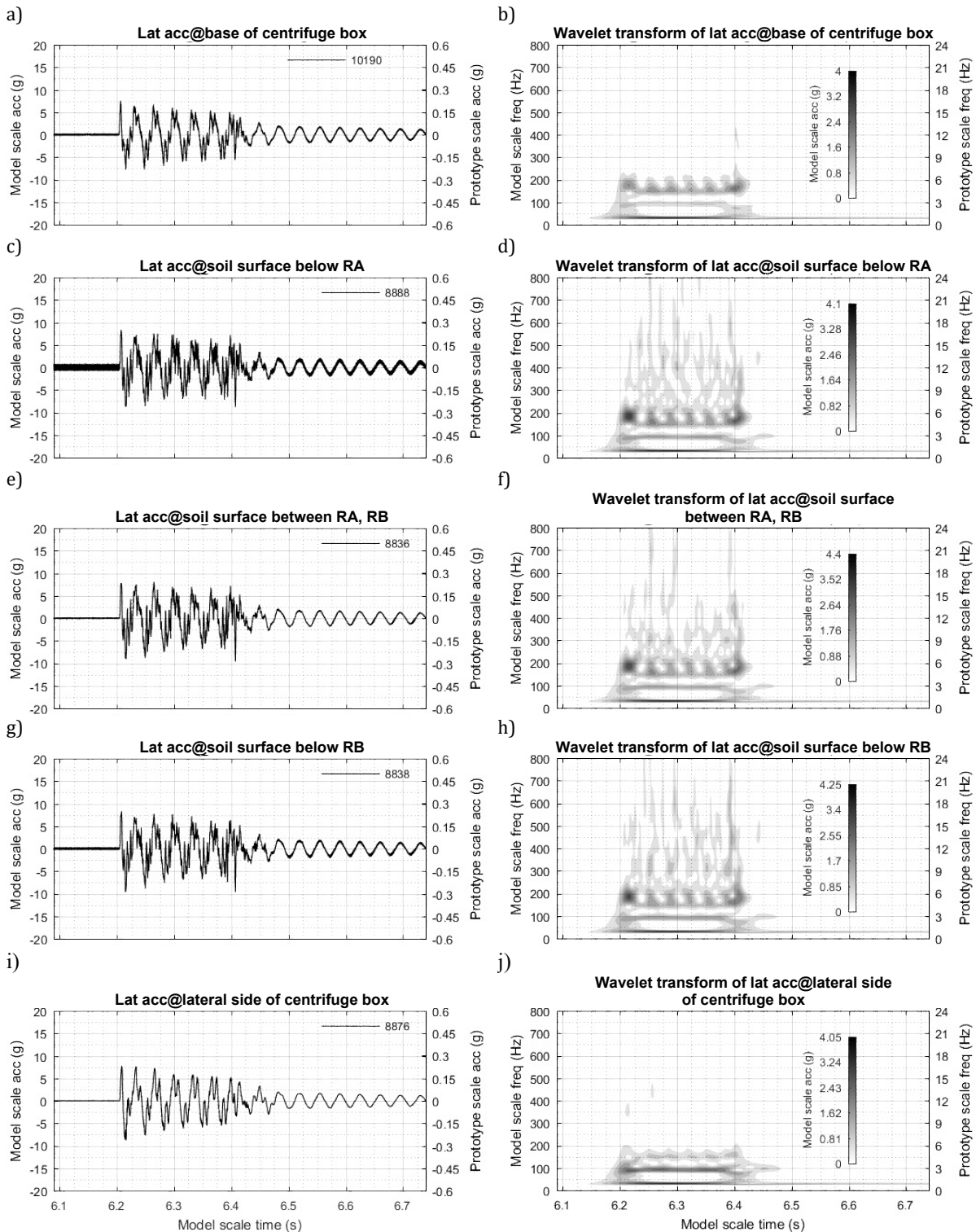


**Figure 7.1: Loose sand Test-2 Eq-4: Time-history and wavelet transform of acceleration at base of centrifuge box (a, b), at surface below RA (c, d), between the buildings (e, f), below RB (g, h) and lateral side of the centrifuge box (i, j). See also Figure 4.5a for sensor location**

centrifuge tests, it is typical to assume the free field acceleration as the input motion at the base of the soil springs (see for example Boulanger *et al.*, 1999). However, in this case, recordings from the free field accelerometer between the two rocking buildings contain

high frequency contamination (Figure 7.1e, f). This high frequency content is similar in the recordings from accelerometers directly below the buildings (Figure 7.1c, d, g, h), and was found to be the result of impacts caused by rocking (see Chapter 7). Therefore, the buildings influenced the typical candidate acceleration for input motion for computational modelling, and for this reason the accelerations recorded on the outside lateral surface of the centrifuge box (Figure 7.1i, j) were instead used. This record preserves the main low frequency components of the input motion (Figure 7.1a, b), while the high frequency components are not present. In addition, to avoid artificial excitation from any electrical noise present in the signal, a low pass filter was used with a cut-off frequency of 500 Hz.

### 7.3 Modelling assumptions

Prototype scale was used to model the buildings and the soil in the OpenSees environment. The full mass and stiffness were modelled in a 2D plane for the building and plane strain conditions are assumed for the soil. Each building type was modelled separately with non-linear dynamic analyses. Throughout the chapter, results from both single excitation and sequential excitations are discussed. The initial conditions in either case were specified as zero tilting and settlements, although using experimental values of these could significantly improve the computational response (Knappett, Madden and Caucis, 2015). Prior to the dynamic analysis, a nonlinear static analysis was carried out considering only the self-weight of the buildings. The fuses were also modelled but are not discussed here (see Appendix G for an example simulation).

#### 7.3.1 Modelling of superstructures

Linear elastic beam/column elements were used, located at the centrelines of the structural components and discretised to allow a more realistic wave propagation from impacts (Figure 7.2). A lumped mass matrix was used which, for the specified element discretisation, distributes the frame mass in close intervals near the impact point and the structure. The values of the first two natural frequencies of the model were similar to experimental measurements, when considering soil stiffness. To account for the small difference between the experimental and computational frequencies, rotational springs at the connections between the columns and the slabs were calibrated iteratively, while

the connections between the columns and the bracing members were assumed rigid. Finally, the weight of each element was applied uniformly across the element.

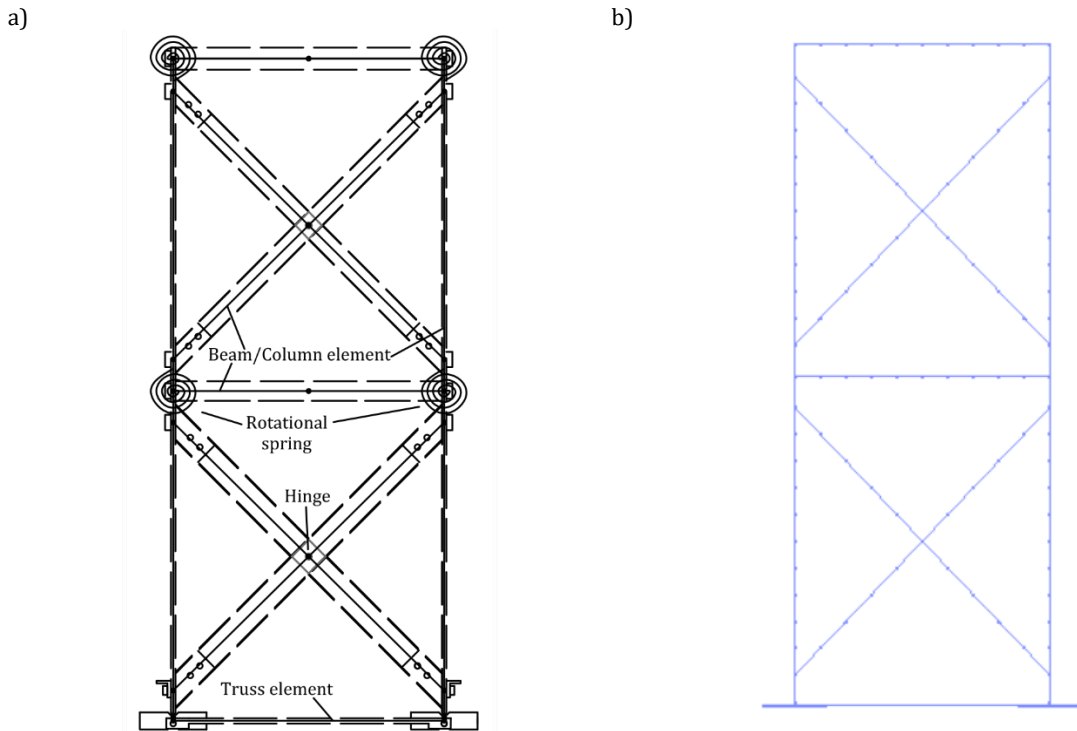
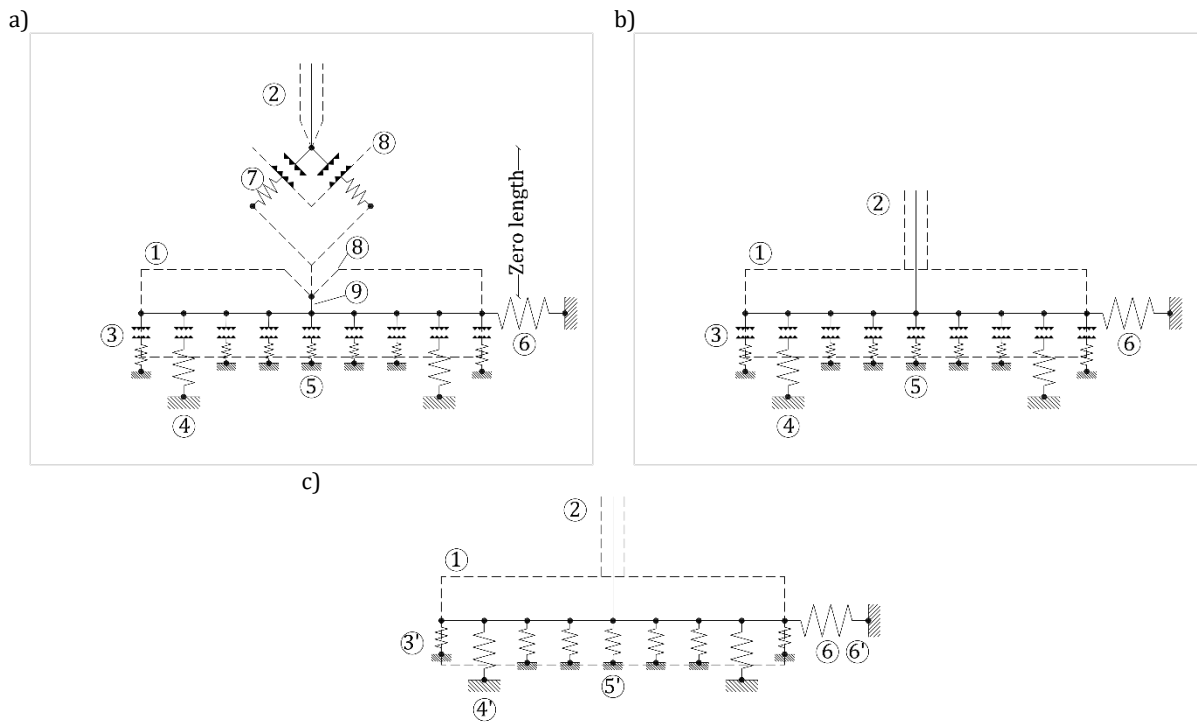


**Figure 7.2: Basic element discretization (a) and refined configuration (b) for model RA (see Figure 7.3 for soil-footing-column detail)**

### 7.3.2 Modelling of column-footing connection for structural rocking

To model the contact interface between an RA footing and a column, friction-gap elements were used (Figure 7.3a). This type of element (*flatSliderBearing* element in OpenSees, developed by A. Schellenberg, Figure 7.4) represents a bearing with a flat surface for sliding and allows for uplift. Its main use is for base isolation with sliding (Schellenberg *et al.*, 2013; Konstantinidis and Nikfar, 2015; Sachdeva, Chakraborty and Ray-Chaudhuri, 2018). In this case, the friction-gap elements were used in pairs and in an inclined position, which is identical to the shape of the footing slot (groove) in each RA footing. This allows to mimic the shape of the physical slot of the RA footing and therefore helps capture any potential sliding of the column end nodes along the slot's surface. The main input parameters are the shearing stiffness and spring stiffness for the axial direction. No rotational stiffness was assigned in the element to prevent linking and constraining the rotation of the column ends with the footing. Simulating uplift is achieved by assigning a no-tension criterion for the axial direction. The order of magnitude of the sliding and axial stiffnesses was estimated iteratively so that reasonable natural frequencies are obtained, and that the numerical solution is stable. In addition, a coefficient of friction of  $\mu = 0.43$  was specified, which is the mean value of static and kinetic coefficients of friction for

systems with sliding surfaces made of aluminium (Davis, 1997). Overall, by using the proposed configuration, the local re-centring capability of the column ends can develop. A typical example of the trajectory of the column ends shows that the latter always remain within the RA footing slot (Figure 7.5). Thus, the infinitely long sliding planes extending outwards of the footing slot as a result of the elements inherent configuration (Figure 7.4a) do not interfere with the column end trajectory. Additionally, recalling that a semi-arc trajectory would form if the building model was perfectly rigid, it is clear that the column flexibility influences the trajectory.



Key: (1) Footing, (2) Column, (3)-(5) Zero length friction-gap elements (*flatSliderBearing*), (3')-(5') Zero length vertical resistance spring (6) Zero length passive resistance spring, (6') Zero length sliding resistance spring (7) 45° inclined friction-gap element, (8) Plane of sliding (9) Rigid offset

**Figure 7.3: Modelling of an RA footing (a) and an RB footing (b) for structural and foundation rocking, respectively, with the mBNWF model, and typical application of the BNWF model for an RB footing (c) (Raychowdhury and Hutchinson, 2009)**

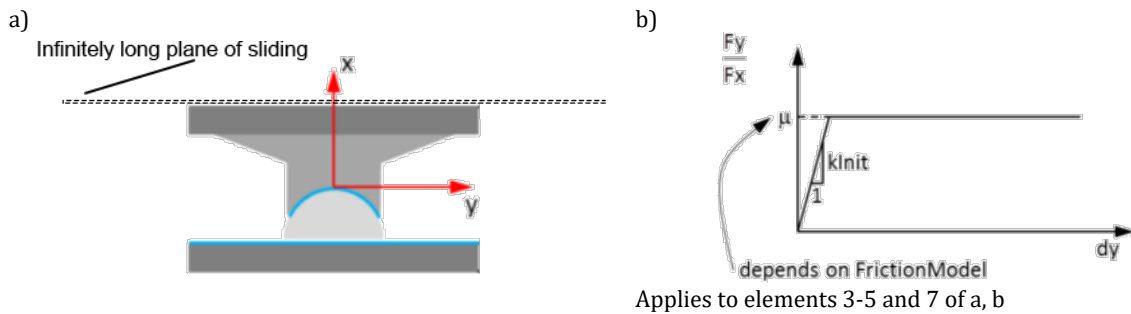


**Figure 7.4: The friction-gap element *flatSliderBearing* (a) with a force-displacement law relating the sliding and axial responses (b) (Schellenberg, 2014)**

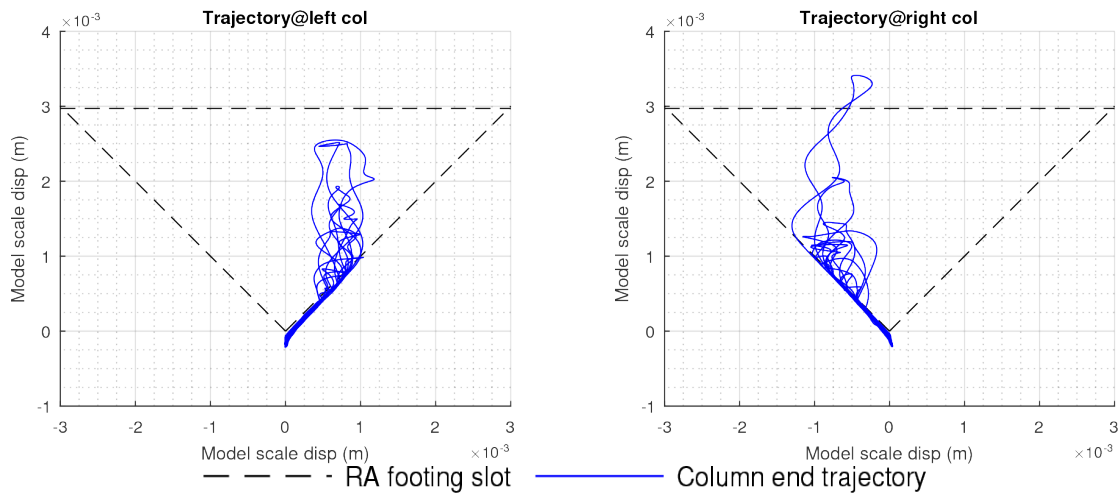
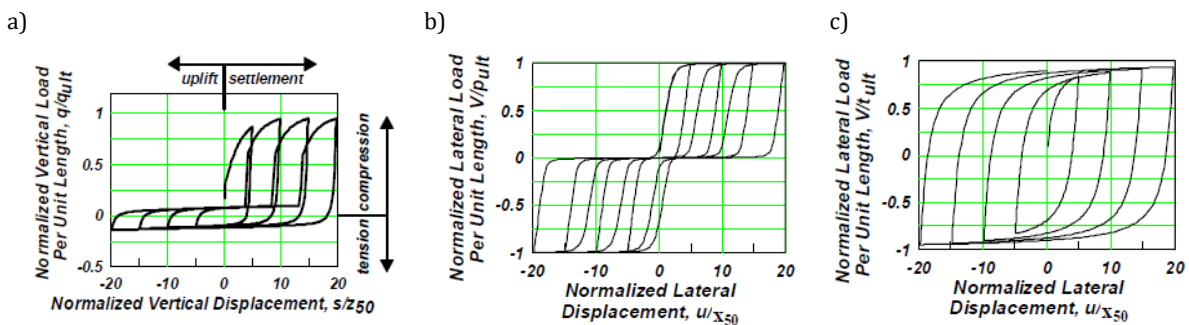


**Figure 7.5: Dense sand, Test-1 Eq-6: Trajectory of column ends of model RA as obtained by using inclined friction-gap elements**



Applies to elements 3-5, 3'-5' of Figure 7.3

Applies to element 6 of Figure 7.3

Applies to element 6' of Figure 7.3c

**Figure 7.6: Typical behaviour of the elements of the BNWF model with material laws as defined by Raychowdhury and Hutchinson (2009)**

### 7.3.3 Modelling of soil-footing interface

To model the interface between the soil and footings the BNWF model (Figure 7.3c) was used initially, while it was modified later and the modified version (mBNWF, Figure 7.3a, b) was used in all the analyses presented here. In its original configuration, the BNWF model distributes a group of vertical springs below the footing to capture vertical and rotational resistance of the soil. In addition, two lateral springs are placed in parallel at the one end of the footing to capture sliding and passive resistances. The constitutive law for all the springs was derived initially by Boulanger et al., (1999) after performing tests on piles and was later calibrated (Raychowdhury and Hutchinson, 2009) against shallow foundation tests. The vertical springs have an asymmetric hysteretic response and allow compression to develop nonlinearly up to a capacity limit, while a reduced or zero strength can develop in tension (Figure 7.6a). The linear elastic stiffness can be derived using typical equations (Gazetas, 1991), while Terzaghi's bearing capacity equation is used for the ultimate capacity. For the horizontal direction, the sliding spring is assigned the lateral soil stiffness, while a capacity based on a Mohr-Coulomb criterion is assigned

(Figure 7.6c). The capacity of the passive resistance spring (Figure 7.6b) is determined using a passive earth pressure coefficient assuming a linearly varying earth pressure distribution. For further details on the equations describing the backbone curves of the vertical and horizontal springs see Raychowdhury (2008). Vertical stiffness and capacity are distributed according to the selected number of springs and their area of influence below the foundation. Stiffer springs can be placed at the ends of the footings to represent the initial stress concentration near the footing edges (Figure 7.3). Radiation damping in the vertical direction is distributed uniformly across the number of springs, while in the lateral direction it is placed in parallel with the horizontal spring for sliding. A limitation of the original configuration of the BNWF model is that the sliding resistance is always present, which limits the lateral motion of the footing nodes (Figure 7.7a-f). This behaviour can be acceptable for footings that always maintain partial contact with the

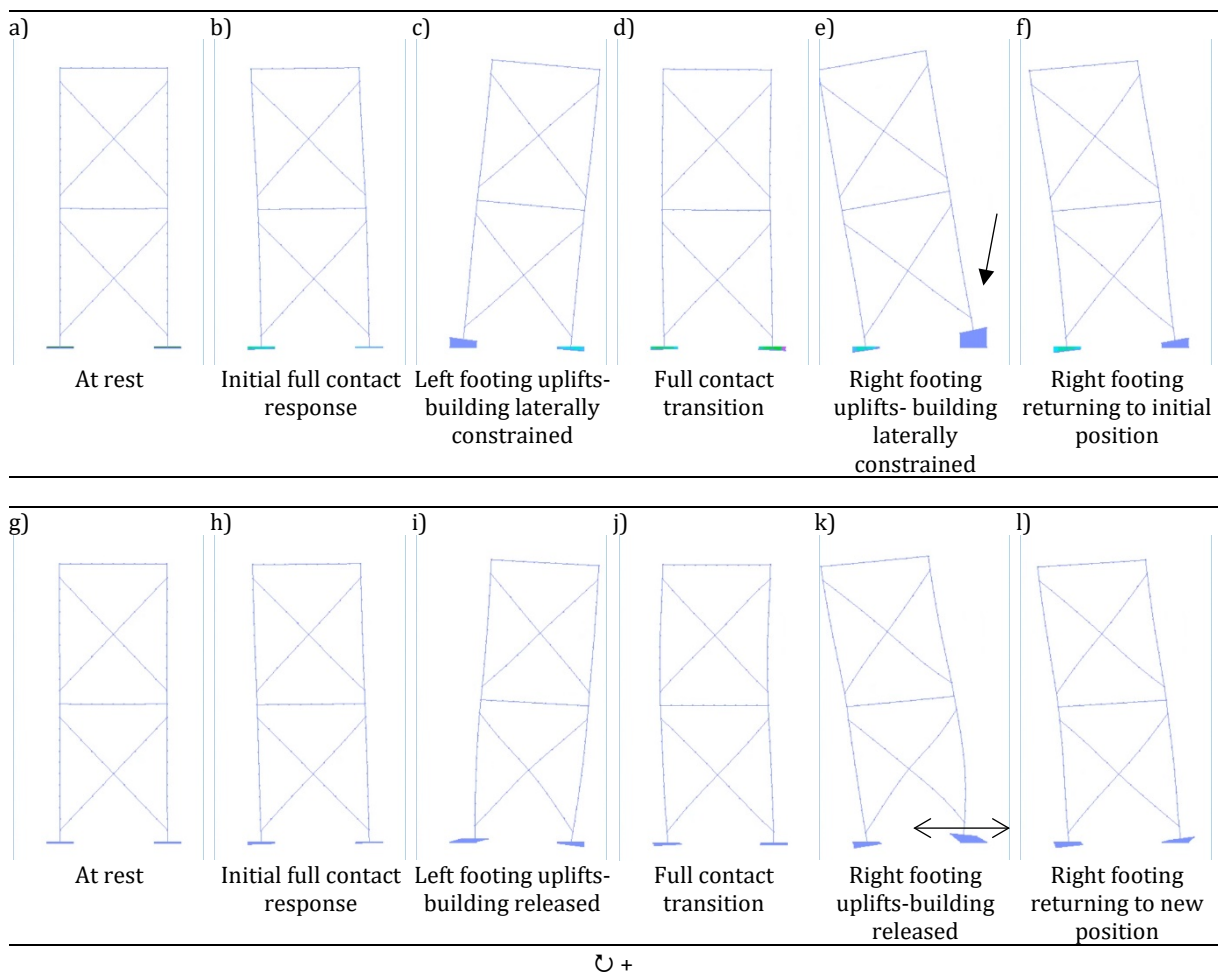


**Figure 7.7: Loose sand, Test-1 Eq-5: Sequence of displacements for model RB when the BNWF model (a-f) and the mBNWF models are used (g-l)**

soil, or generally for single-footing structures. However, when the entire footing loses contact with the soil, the sliding resistance should be zero and the footing should be free to move laterally. Here, this type of response would be expected primarily for the RB

model. To account for this behaviour (Figure 7.7g-l), the *flatSliderBearing* is employed which allows for the development of vertical and horizontal forces only when the soil springs are compressed. In the axial direction, the constitutive law from the BNWF model is used to account for the vertical and rotational resistance of the soil. For the sliding direction, the stiffness (Gazetas, 1991) can be distributed in a fashion similar to the vertical stiffness according to the BNWF model. Recalling that this element is capable of assigning a failure criterion of the Coulomb type, each horizontal force from each individual bearing can be linked to the axial (vertical) force with a friction coefficient. In this case, a friction coefficient for dry sand was used. A limitation of the *flatSliderBearing* is that there is no entry for a viscosity coefficient in the sliding direction which could be used to account for radiation damping laterally. Therefore, the source code of the *flatSliderBearing* was modified so that the sliding force is represented with both a stiffness and a viscosity coefficient. This allowed to distribute radiation damping uniformly in the lateral direction, similarly to the vertical direction.

A typical response of the soil total forces against the rocking angle for each building is shown in Figure 7.8, 7.9. The total force in each direction is the total of all the forces of the elements below the footing while the rocking angle is the rotation of the bottom story slab. For the RA and RB left footings, the vertical soil forces are quantitatively different although they share the same trend with respect to the rocking angle. For RA, the vertical soil force returns to the footing's self-weight upon uplift, whereas for RB it diminishes to zero, as expected when the buildings rotate clockwise. However, when the BNWF model is considered for RB, a substantial non-zero lateral force develops even though, for the same clockwise rotations, the vertical force is zero. The same behaviour applies for RA with the constant vertical force indicating loss of contact between the superstructure and the footing. Similar observations were made for the right-hand column footing. In contrast, when the mBNWF model is used the lateral forces drop to zero as the loss of contact occurs during the clockwise rotation. The above behaviour is summarised in an interaction diagram for the vertical and horizontal forces and it is verified that the footing behaviour locally is quite different for the two cases (Figure 7.10). This means that when earthquake scenarios with multiple excitations in series are considered (see Table 4.2), then errors from insufficient modelling of the local footing behaviour may lead to unrealistic response downstream. This error in terms of residual displacements can be significant, not only between the two computational responses (Figure 7.11a, b), but also between the numerical and the experimental responses (Figure 7.11a). If we high-pass

filter the response at 10 Hz, we can remove the residual displacements, and compare directly to the displacements derived from the experimental tests. Figure 7.11b shows that the mBNWF model (after high-pass filtering) can better capture the response.

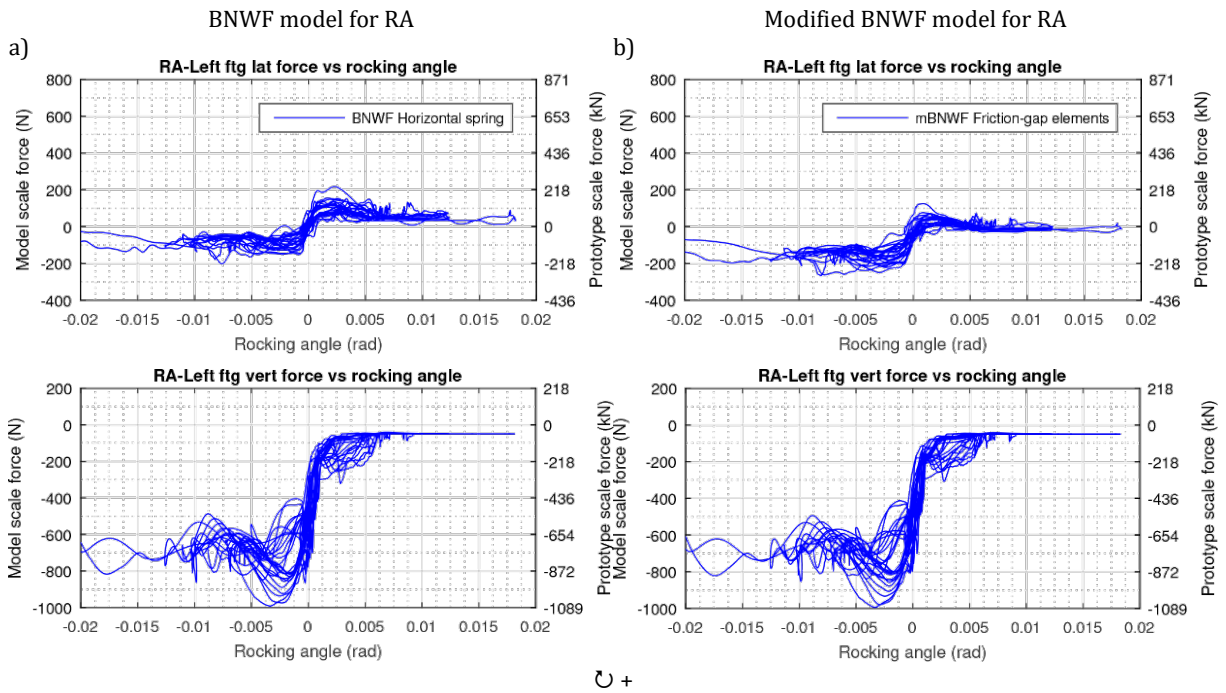


**Figure 7.8: Loose sand, Test-1 Eq-4: Footing forces with respect to building rocking angle when the BNWF model is employed (a) and similarly when the proposed modified model is employed (b) for RA**

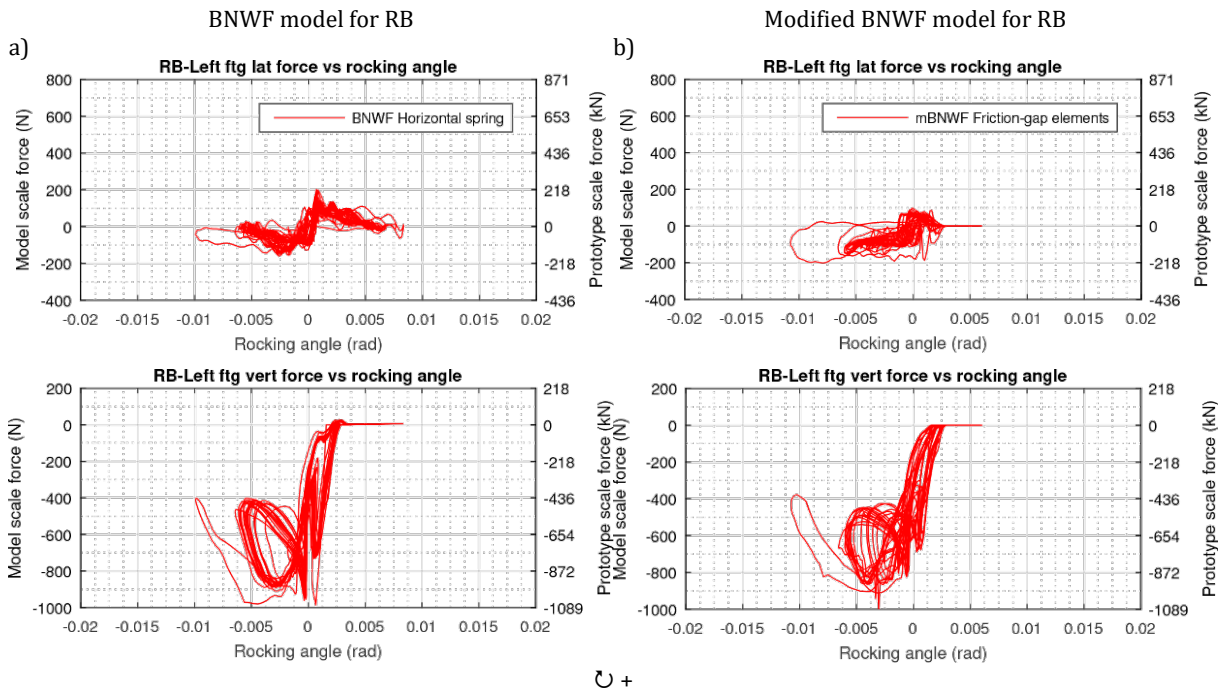


**Figure 7.9: Loose sand, Test-1 Eq-5: Footing forces with respect to building rocking angle when the BNWF model is employed (a) and similarly when the proposed modified model is employed (b) for RB**

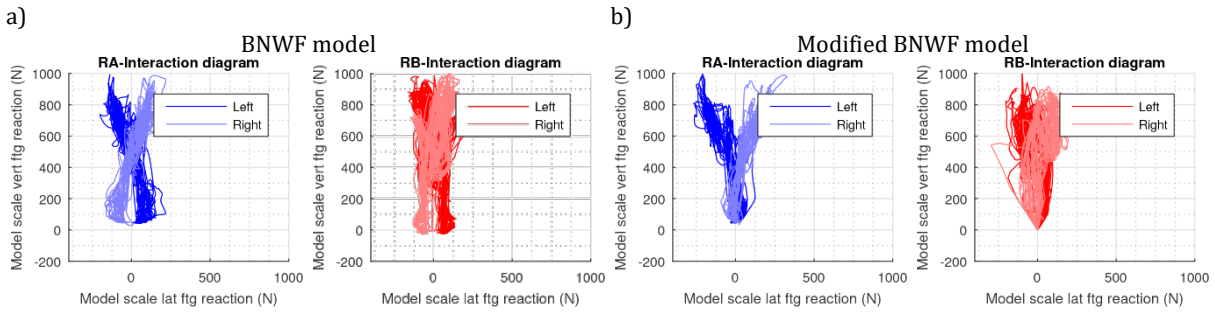


**Figure 7.10: Loose sand, Test-1 Eq-5: Interaction diagrams for the forces below the left and right footings below models RA and RB when the BNWF model (a) and the mBNWF model (b) are used**

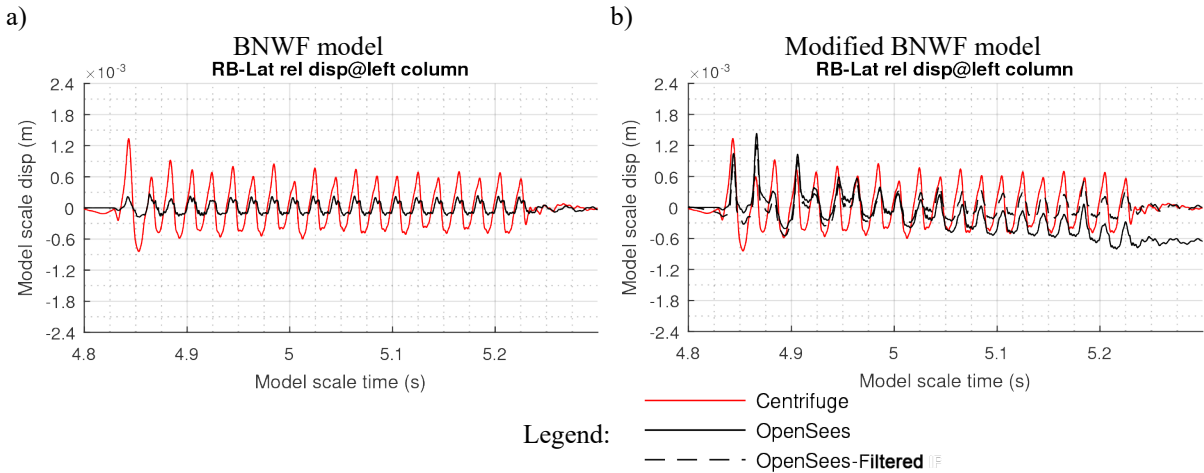


**Figure 7.11: Loose sand, Test-1 Eq-5: Lateral relative displacement of the end node of the left column for model RB (see instrument BFH1 in Figure 4.5)**

## 7.4 Input for the computational model

### 7.4.1 Building and soil properties

Most building properties were directly specified to match the centrifuge model. The main additional properties influencing the response of the superstructure are the modal damping ratios used to create the Rayleigh damping matrix (Table 3.5). The effect of these properties is further investigated in Section 7.6.

For the soil, the BNWF model requires as input an initial value of the soil's shear modulus  $G_0$  to derive the stiffness of the spring elements in the linear elastic range of their deformation. The value of  $G_0$  may be set equal to the maximum shear modulus  $G_{max}$  which for a given depth and void ratio depends on the stress level. When experimental or field measurements are not provided, Eq. (7.1) can be used to empirically estimate  $G_{max}$  (Seed and Idriss, 1970; Kramer, 1996):

$$G_{max} = 1000 \cdot K \cdot (\sigma'_m)^{0.5} \quad (7.1)$$

where  $K$  is a constant based on the void ratio  $e$  and  $\sigma'_m$  is the mean principal effective stress in lb/ft<sup>2</sup>. Eq. (7.2) provides a recently modified expression of Eq. (7.1), considering a large number of datasets from literature (Oztoprak and Bolton, 2013):

$$G_{max} = \frac{A(\gamma) \cdot p_a}{(1 + e)^3} \cdot \left( \frac{\sigma'_m}{p_a} \right)^{m(\gamma)} \quad (7.2)$$

where  $A(\gamma)$  and  $m(\gamma)$  are dependent on the shear strain  $\gamma$  and  $p_a$  is the atmospheric pressure. A representative value for  $\sigma'_m$  referring to the soil beneath the footing can be estimated based on Eq. (7.3) (Perkins and Madson, 2000; Deng, Kutter and Kunnath, 2012):

$$\sigma'_m = \frac{1}{6} \left( 0.52 - 0.04 \frac{l}{b} \right) q \quad (7.3)$$

where  $l$  and  $b$  are the footing's length and width respectively, and  $q$  the pressure at the footing's surface due to static loading. Alternatively, the mean principal effective stress can be calculated explicitly based on a depth below the footing, but there is no clear consensus on defining that depth, meaning differences can be substantial. For instance, in dense sand when  $\sigma'_m$  is calculated at a depth of  $1.3b$  assuming a linear elastic half-space, then  $\sigma'_m = 34$  kPa, as opposed to  $\sigma'_m = 3.8$  kPa when using Eq. (7.3). Regarding  $G_{max}$ , assuming very small strains ( $\gamma = 0.0001\%$ ) then Eq. (7.1), (7.2) produce the same result. Overall, using Eq. (7.1), (7.3) and assuming very small initial strains,  $G_{max}$  is 30 and 22 MPa for the dense and loose sands respectively and these values are adopted for  $G_0$ .

The vertical capacity of each spring is a fraction of the footing's bearing capacity based on the tributary area below each spring as specified by the BNWF model. The capacity is dependent on a friction angle, which in this case is selected as the critical state friction angle. This means that the deformation history of the sand or its dilation behaviour are not considered, rather a shear deformation large enough to lead directly to the critical state is implicitly assumed.

Next, the dashpot coefficients for radiation damping in the horizontal ( $c_x$ ) and vertical ( $c_y$ ) directions were specified following the methodology proposed by Gazetas, (1991). Based on this methodology, a nominal excitation frequency (mean value of the main low frequencies found in all excitations) was chosen to calculate the ratio of shear wave velocity to frequency, upon which vertical and horizontal radiation damping depends. When considering the resulting damping ratios  $\zeta_x$ ,  $\zeta_y$  for these translational modes of response, these fall within the expected range of values (Gazetas, 1991) for the mass and soil stiffness of the buildings considered here.

## 7.4.2 Mesh properties for soil

According to the BNWF model, the end length ( $R_e$ ), end stiffness intensity ( $R_k$ ) and spring spacing ( $l_e/b$ ) ratios need to be determined as input parameters. In this case,  $R_e = 0.15$  which is very close to the  $1/6$  recommended by ATC-40, (1996). For  $R_k$ , a value of  $\sim 8.7$  is recommended by ATC-40, (1996), while for the specific footing dimensions a value of  $\sim 2.3$  is obtained according to Harden et al., (2005). Generally, a high value results in smaller settlements while the moment demand on the footing is not affected (Raychowdhury, 2008). A value of  $R_k = 6$  was selected. Finally, for  $l_e/b = 0.02$  the number of elements below the footing is 69, which results in a very fine mesh and can satisfactorily capture settlement and moment demands (Raychowdhury, 2008).

**Table 7.1: Input properties with default values (in prototype scale)**

a) Soil properties	Soil Type		b) Soil mesh properties	
	Dense sand	Loose sand	End length ratio $R_e$	Stiffness intensity ratio $R_k$
	Default value:		Spring spacing $l_e/b$	0.02
Cohesion $c$ (kPa)	0			
Friction angle $\phi'$ ( $^\circ$ )	33.0 (Shepley, 2013)			
Soil unit weight $\gamma$ (kN/m $^3$ )	16.3	15.0		
Shear modulus $G_0$ (MPa)	30.0	22.0		
Poisson's ratio $\nu$	0.375			
Damping coeff. and ratio, $c_{x,i}$ (Ns/m) and $\zeta_x$	1.75x10 $^6$ , 0.22	1.44x10 $^6$ , 0.21		
Damping coeff. and ratio, $c_{y,i}$ (Ns/m) and $\zeta_y$	2.78x10 $^6$ , 0.63	2.29x10 $^6$ , 0.61		

## 7.4.3 Algorithm, integrator and solution convergence

The finite element model is characterised by two main types of expected response. The superstructure is expected to remain linear elastic throughout rocking and in full contact conditions, while the soil springs are expected to undergo material nonlinearity. This model is similar to a model for a dynamic progressive collapse simulation where nonlinearity is expected at the neighbourhood of the column removal, while the rest is expected to remain linear. For this reason, the Krylov-Newton algorithm was selected which has been shown to accelerate convergence in this type of simulation (Scott and Fenves, 2010).

Typically, in rigid base conditions, large impact forces are expected to develop causing many iterations for convergence if force increment vectors are used as convergence criteria. Therefore, convergence criteria based on displacement increments can lead to a smaller number of iterations (Kosbab, 2010). In this case, the soil springs are soft, and the impact forces should be capped due to the soil's nonlinearity. To ensure this, an energy convergence criterion, which depends on both displacements and forces, was specified (tolerance of  $1 \times 10^{-7}$ ).

The effect of the solution integrator and the time step were investigated using default values for input (Table 7.1). Using a Newmark scheme with  $\beta = 0.8$  and  $\gamma = 1$  a highly dissipated solution is returned, while for  $\beta = 0.25$  and  $\gamma = 0.5$  a computational solution with no numerical damping is obtained (Figure 7.12). The differences are obvious in the storey accelerations in terms of the frequency content, but no significant difference exists for the rocking angle. The former scheme would be preferable for rigid base conditions, since artificial damping usually assists in achieving convergence in contact problems involving gap elements impacting rigid boundaries. Since the BNWF springs employed here are soft and involve a viscosity coefficient to account for radiation damping, there is no justification to use artificial damping, although some convergence problems at the contact establishment still occurred. To resolve these convergence issues, the time step was reduced temporarily until convergence was achieved, and it was then restored to the initially specified value.

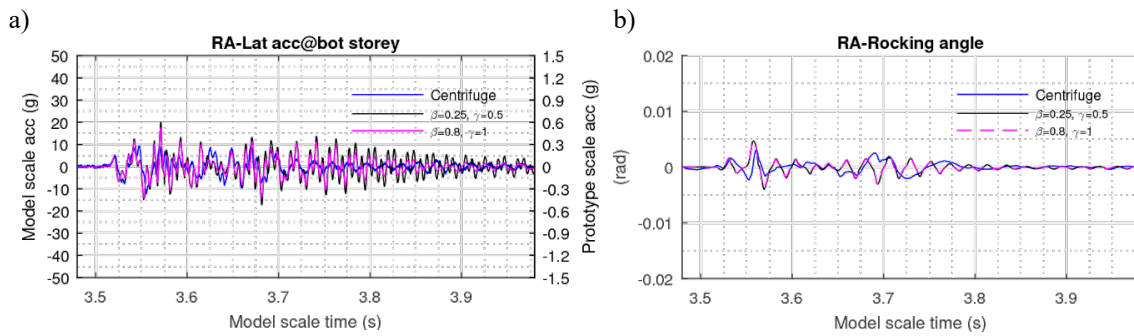


**Figure 7.12: Loose sand, Test-1 Eq-1: Bottom storey acceleration (a) and rocking angle (b) for model RA for different combinations of  $\beta, \gamma$**

The effect of the time step was investigated for  $\beta = 0.25$  and  $\gamma = 0.5$ . The numerical responses for an output frequency (inverse of time step) of  $f_{o,c} = 6$  kHz (equal to the centrifuge sampling frequency at model scale) and for multiple values  $f_o$  of  $f_{o,c}$  were simulated considering each excitation separately. The time step was consecutively reduced, and the individual residual rotation of the footings were compared until they converged. The residual rotations were used for evaluation because on the one hand the footings are the only source of nonlinearity due to soil springs (and the sliding plane for RA) and on the other, their rotations are dependent on the horizontal and vertical displacements. This reduced the number of degrees of freedom to monitor and compare. All obtained responses match reasonably well the centrifuge response (Figure 7.13). Model RA appears to be sensitive during the transition period from rocking to full contact response, with high frequency content manifesting without convergence in the storey accelerations (Figure 7.13c). In addition, the footing response changes significantly for

the first two output frequencies. On the contrary, the top storey acceleration of model RB appears to converge relatively faster (Figure 7.13a). For these motions,  $f_o/f_{o,c} = 3$  was determined to be appropriate. Figure 7.14 can be interpreted as a guide when various single records are considered in an analysis; RA can have a reduced output frequency with  $f_o/f_{o,c} = 1$  for most records. For model RB  $f_o/f_{o,c} = 3$  is appropriate except for the Imperial Valley excitations which impose small rotations on the RB footings, so  $f_o/f_{o,c} = 1$  can be used.

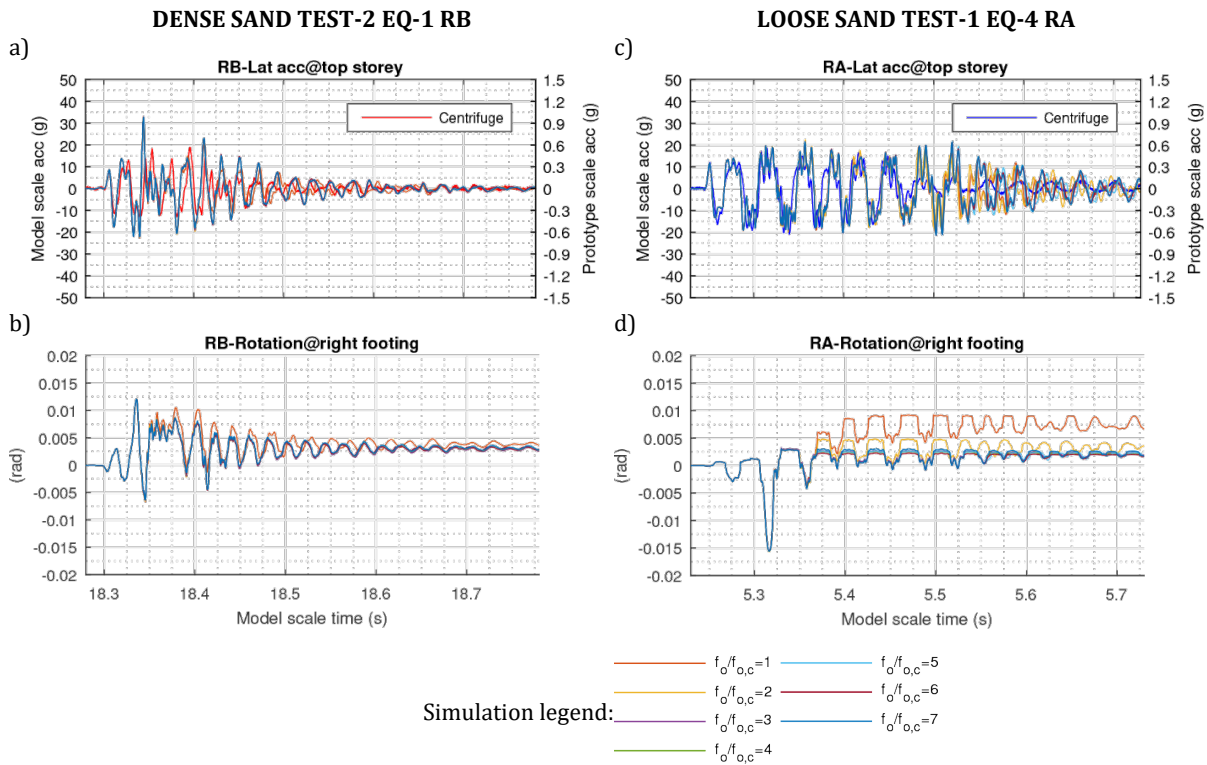


**Figure 7.13: Effect of time step on the numerical response of model RA (a-e) and similarly for model RB (e-h)**

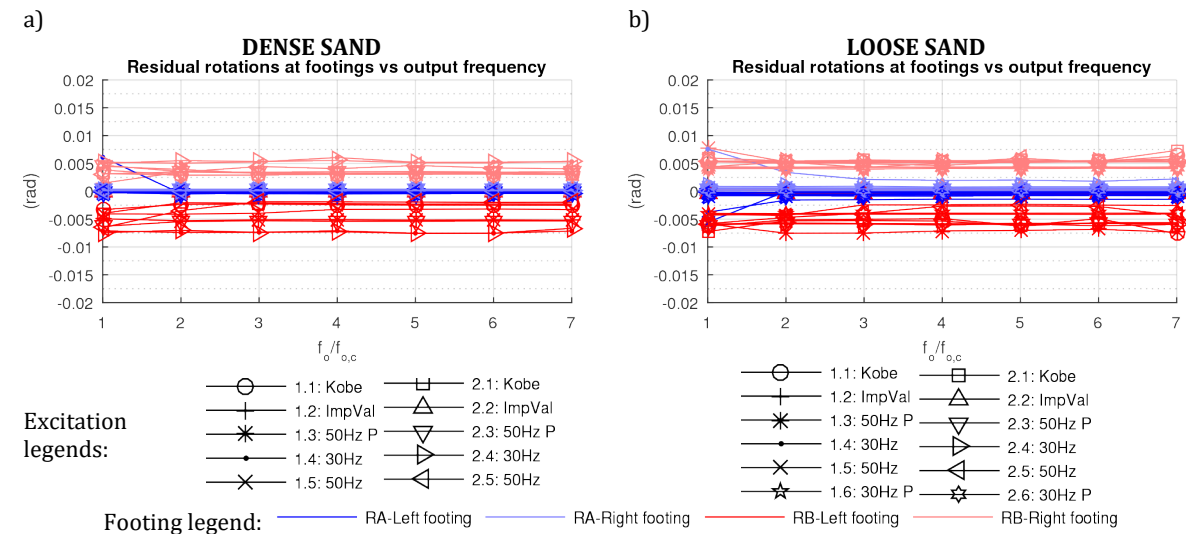


**Figure 7.14: Summary of footing residual rotations for different output frequencies for dense sand (a) and loose sand (b)**

## 7.5 Validation of computational model

### 7.5.1 Simulation with sequential excitations with default parameters

The goal of the validation is to assess whether the computational model can predict key features of the mechanisms observed in the centrifuge. More specifically, it is of interest to predict the uplifting and rocking part of the buildings' response and to provide a reasonable prediction of the amplitude of the demand, in the form of storey accelerations and rocking amplitude. Similarly, it is important to predict the part of response with full contact or a transition from full contact to rocking and *vice versa*. Note that to limit the amount of output, all responses were generated for  $f_o/f_{o,c} = 2$ , except for model RB in Test-0 of dense sand where  $f_o/f_{o,c} = 3$ .

Each centrifuge flight/test (Table 4.2) was simulated separately, by applying the excitations in series (see Appendix G). After each excitation, zero padding was used to allow the response of the building to dissipate before the start of a new excitation. The default set of parameters was used for each building (Table 7.1). For model RB, comparison of Figure 7.15c, d with Figure 7.17e, h shows that if an excitation is treated separately (i.e. without the effect of initial conditions caused from a previous excitation), then a qualitative difference of rocking to no rocking can develop. One reason for this difference can certainly be the effect of the initial conditions from previous excitations. More specifically, when the input excitation is a single excitation then the initial conditions are those created only by the gravity loading. In sequential excitations used as input, the initial conditions vary from analysis to analysis, as some residual deformations develop at the end of an excitation. Although the actual initial conditions before an excitation were not available in the centrifuge tests and thus were not used in the computational model, this comparison indicates that cumulative deformations from excitation to excitation can have a difference in the response and may ultimately result in a significantly improved response prediction. For model RA, there was no qualitative difference when considering an excitation and the response in a single analysis (see Figure 7.15a, b with Figure 7.17a, d). This indicates that model RA is less dependent on the performance of the soil springs and the initial conditions compared to RB, and this is expected considering their different column/footing connections. Specifically, the local deformations of the soil below the footings can distort the building frame into a new equilibrium which favours a qualitative difference in response to subsequent excitations.

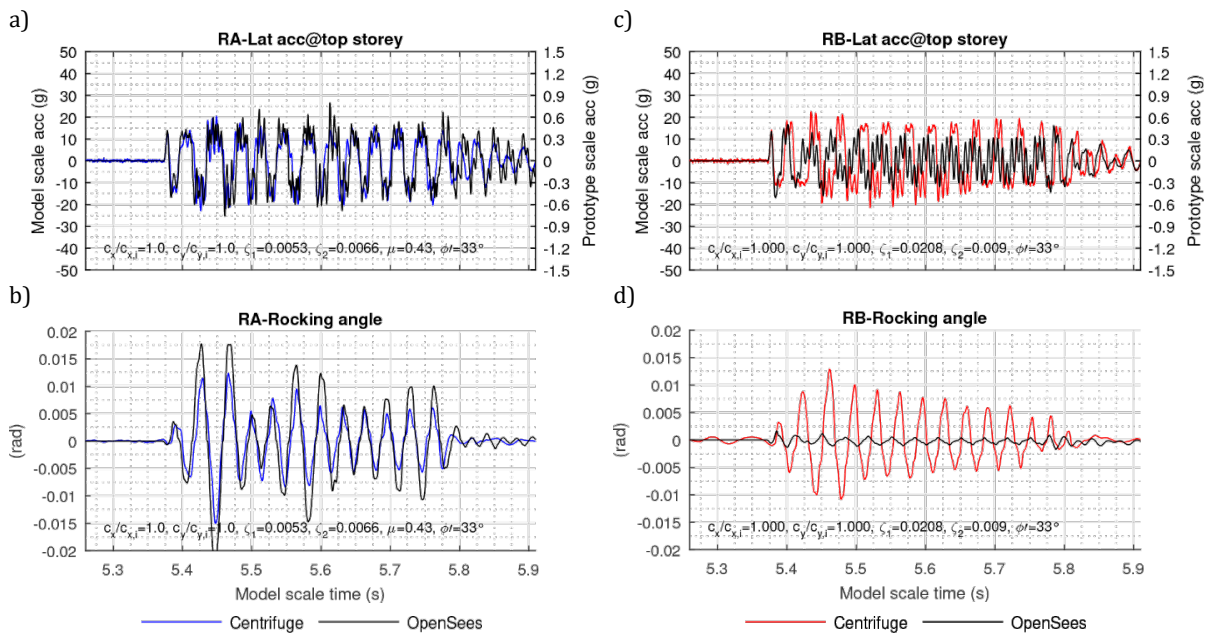


**Figure 7.15: Dense sand, Test-0 Eq-6: Top storey acceleration (a) and rocking angle (b) for model RA when the excitation and response are treated separately, and similarly for model RB (c, d)**

## 7.5.2 Response to low magnitude excitation for dense sand

Test-0, Eq-4 on dense sand is considered here to reveal insights for a small amplitude excitation where full contact response is mostly expected. During this test, model RA responded indeed mostly in full contact except for minor uplift and rocking as a result of the resonant excitation ( $t = 5.45\text{s} - 5.5\text{s}$ ). The default computational model reproduces the experimental trace of lateral accelerations reasonably well, although with slightly larger fluctuations of the rocking angle than observed in the experimental response (Figure 7.16a-d). However, the high frequency flexural vibrations in Figure 7.16b developed between  $t = 5.5\text{s} - 5.6\text{s}$  suggest further rocking. Comparing the time-frequency map of the numerical vertical acceleration of the left column (Figure 7.16c) with the experimental counterpart (Figure 6.3b) verifies the uplifting and rocking of the superstructure of the numerical model RA.

For model RB, the computational response partially matches the experimental response (Figure 7.16e-h). The bottom storey response is underpredicted by the computational model, although the rest of the indicators provide a good estimation of response amplitude. It is clear also, that the computational response is driven by one frequency, whereas a higher mode participation is evident in the experimental response. The partial match of responses suggests that more damping is provided overall by the model than necessary. The computational profile of the rocking angle shows that foundation rocking occurred but without uplift of the footings (Figure 7.16g, h). In addition, no strong high frequency content is detected in the time frequency map of Figure 7.16g which further

verifies the continuous contact of the footings with the soil. Recalling also that the rotations of the RB footings can deform the structural frame and therefore affect the bottom storey response directly (Figure 7.7g-l), it is possible that the damping provided by the soil springs is overestimated for this low amplitude excitation, causing smaller bottom storey accelerations to develop. Figure 7.16f also suggests that higher modes might have been over-damped in the computational model, either by the specified Rayleigh damping or the damping provided by the soil springs.

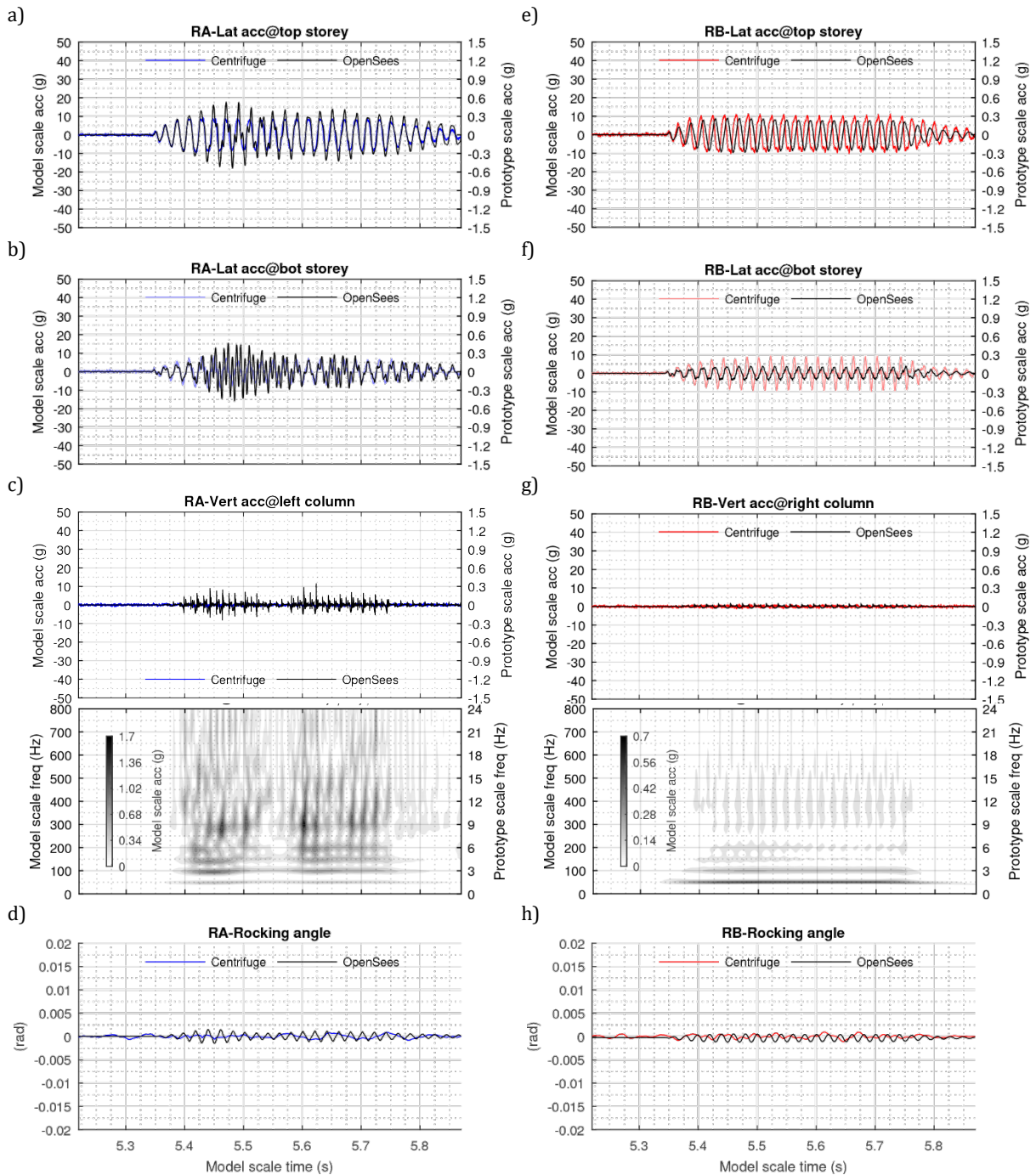


**Figure 7.16: Dense sand, Test-0 Eq-4: Top storey (a), bottom storey (b), rocking angle (c) and left column experimental and numerical responses (d) for default set of parameters for model RA and similarly for model RB (e-h). Time-frequency maps of the vertical accelerations at columns are also included**

### 7.5.3 Response to low frequency excitation for dense and loose sand

A clear rocking response occurred during Test-0, Eq-6 of dense sand for both types of buildings. For model RA, the default computational response is very similar to the experimental. First, uplifting of the superstructure is verified by the similarity of the vertical accelerations at the column end, indicating rocking of the superstructure as observed in the experiment (Figure 7.17c, d). The characteristic trace of rocking in the lateral accelerations is evident throughout the response, and only the final transition to full contact is not as accurately predicted (Figure 7.17a, b). For a similar excitation on

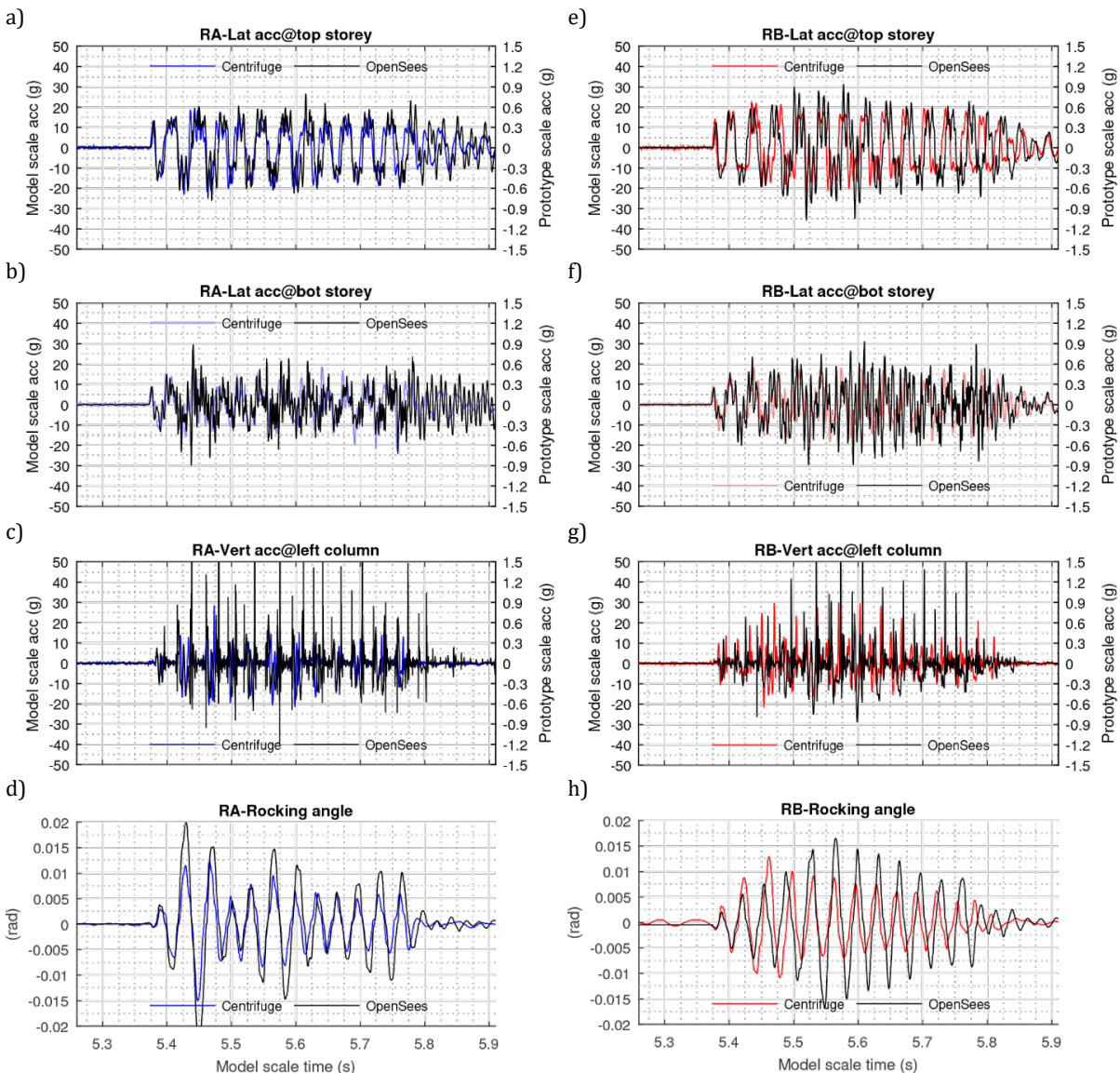


**Figure 7.17: Dense sand, Test-0 Eq-6: Top storey (a), bottom storey (b), rocking angle (c) and left column experimental and numerical responses (d) for default set of parameters for model RA and similarly for experimental and calibrated numerical response (e-h)**

dense sand, Test-2, Eq-4, it can be seen that rocking is over-predicted by the model, and is also predicted to continue longer than observed in the experiment (Figure 7.18a, b).

Clearly in this case, the default damping parameters are less satisfactory, but adjusting the modal damping ratios can result in capturing all phases of the response quite well (Figure 7.18e, f and see Section 7.6). A similar type of response was predicted in loose sand (Figure 7.18c, d). This indicates that the computational model of RA is not sensitive to the different properties of the soil model used here with respect to dense and loose sand. In any case, considering the small amplitude of the excitation during the second half of the response (Figure 7.1i, j), rocking should be expected to cease in the computational model, but it is possible that the phase difference between the excitation and the impact sequence is such that enough energy is input to sustain rocking in a steady state mode (Spanos and Koh, 1984; DeJong, 2012).

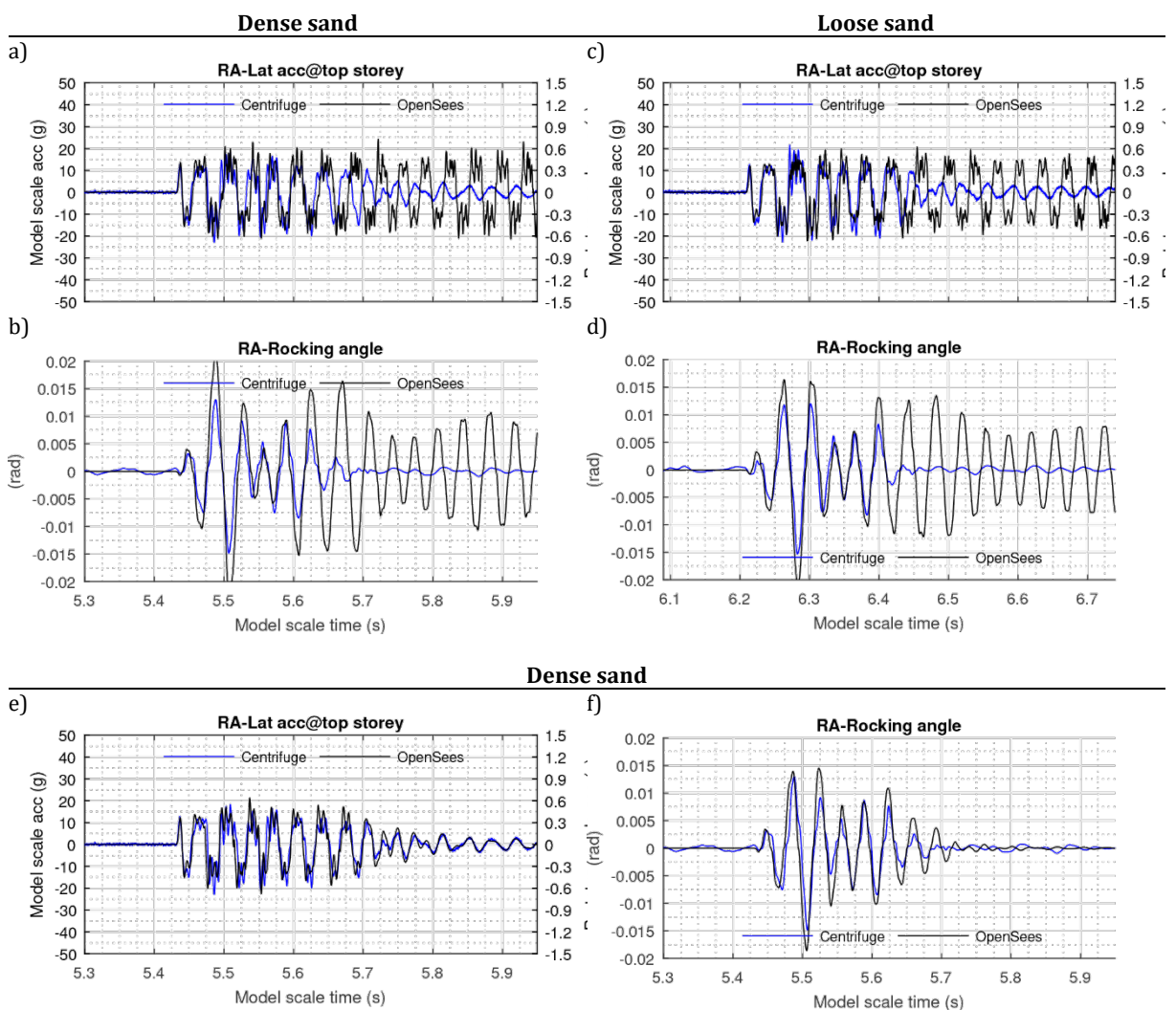


**Figure 7.18: Test-2 Eq-4: Top storey accelerations (a) and rocking angle (b) responses for experimental and numerical simulations using default modelling parameters for model RA in dense sand (a, b), in loose sand (c, d), and for dense sand with calibrated damping parameters (e-f):  $(\zeta_1, \zeta_2) = (0.04, 0.06)$**

Regarding model RB, the computational response also has a similar profile to the experimental response. For the storey accelerations, an underestimation of damping is evident in higher frequency oscillations during uplift (Figure 7.17e, f). The acceleration

spikes of the computational response show that rocking has occurred as a result of the footings fully detaching from the soil and then impacting and rocking locally (Figure 7.17g). The resulting response of the building's rotation suggests that the mBNWF model can provide a similar profile to the experimental one, but amplitude differences might still occur due to limited damping provided for large excitations (Figure 7.17h). Similarly, good predictions were calculated for similar excitations on dense sand, where first continuous rocking developed for a long period before full contact response developed (Figure 7.19a, b). During a similar excitation in loose sand, RB switched to full contact conditions early and the model employed here is shown to capture this change reasonably well (Figure 7.19c, d). This means that the computational model of RB is sensitive to the different properties of the soil model used here, as opposed to that of model RA.

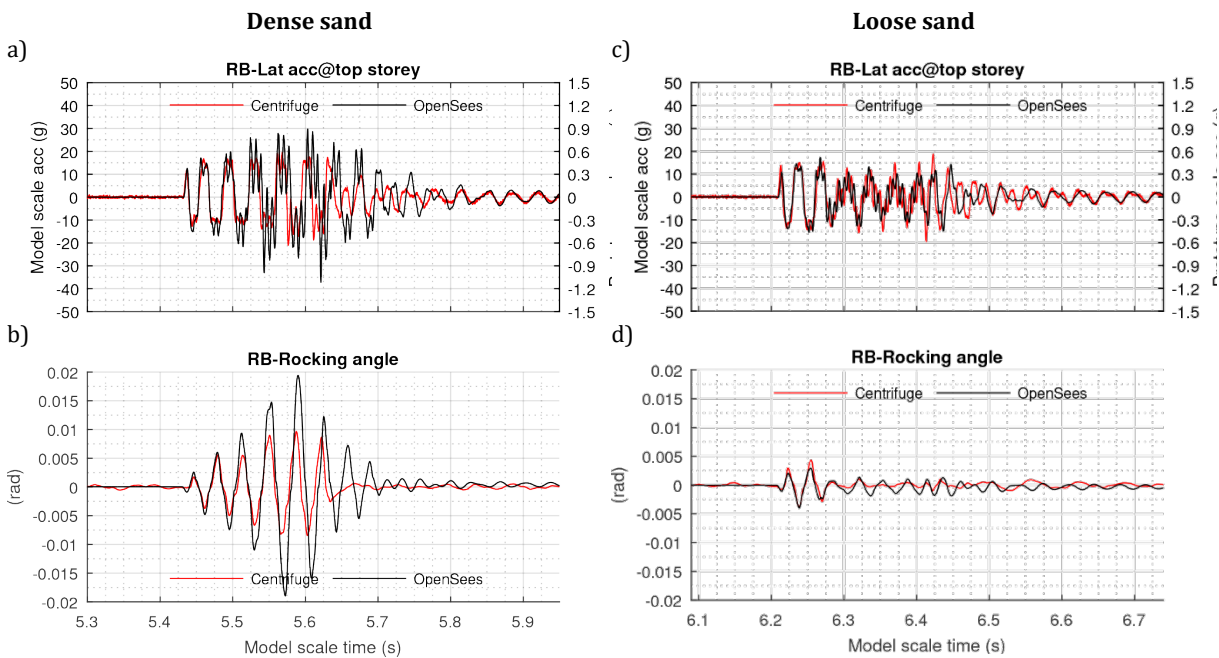


**Figure 7.19: Test-2, Eq-4: Top storey accelerations and rocking angles for experimental and numerical simulations using default modelling parameters for model RB in dense sand (a, b) and similarly in loose sand (c, d)**

#### 7.5.4 Response to pulse and Kobe excitations for dense sand

The response to Kobe excitation is considered here to assess the performance of the computational models when a steady state mode is unlikely to be established (Figure 7.20). During the experiment, both models responded initially with a cycle of rocking, followed by a short duration of full contact, and then with additional rocking of a smaller amplitude. The computational models of RA and RB predict reasonably well this type of response.

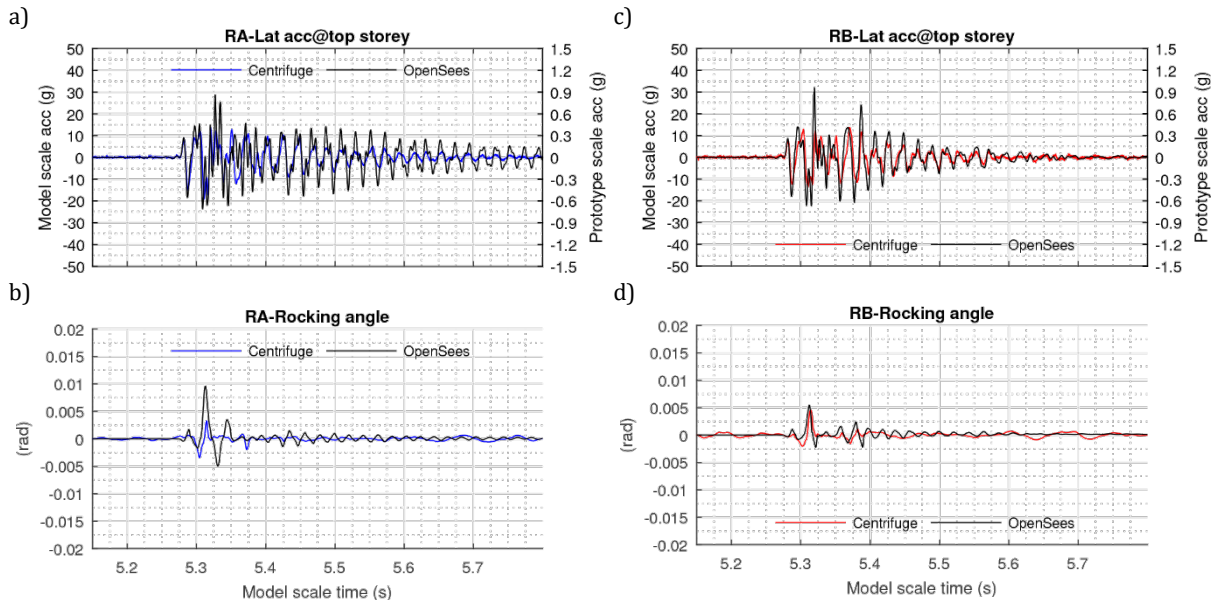


**Figure 7.20: Dense sand, Test-2, Eq-1: Top storey (a) and rocking angle (b) experimental and numerical responses for default set of parameters for model RA and similarly for model RB (c, d)**

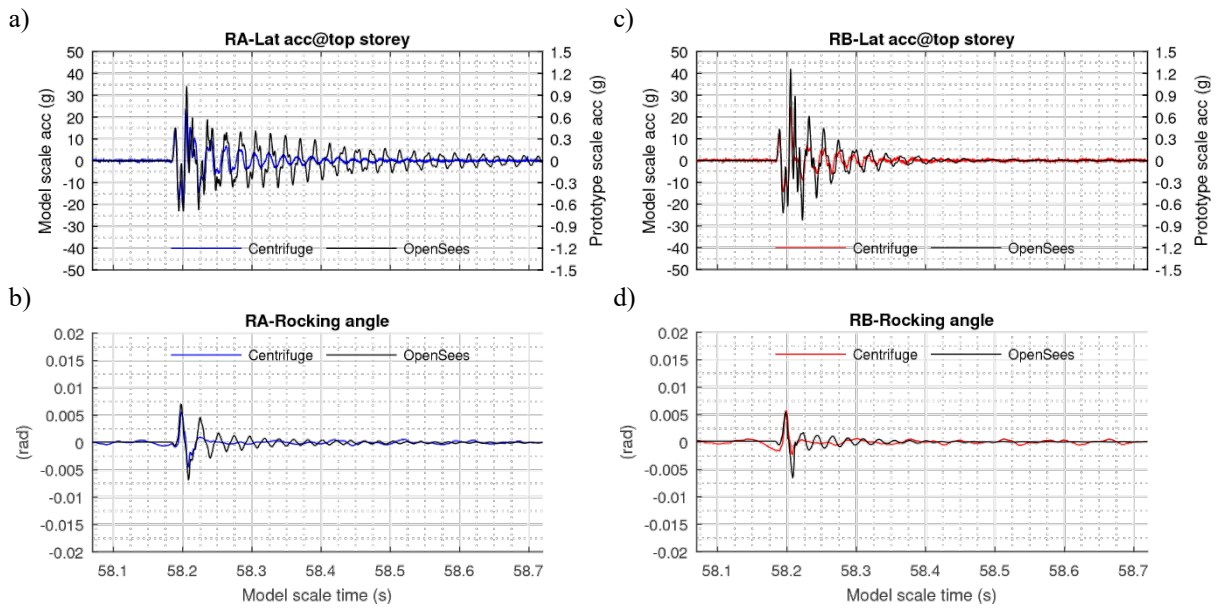


**Figure 7.21: Dense sand, Test-2, Eq-3: Top storey (a) and rocking angle (b) experimental and numerical responses for default set of parameters for model RA and similarly for model RB (c, d)**

The response to a pulse is considered additionally to examine the amplitude decay at the free vibration during full contact. During the experiment, the pulse led to a single cycle of

rocking followed directly by full contact response, whereas the computational models indicate free rocking for many cycles (Figure 7.21). Regarding the experimental response, it is reasonable to consider that the soil below the footings might have experienced some dilation due to mobilized plastic strains. The mBNWF model ignores this and considers only a single value for the bearing capacity and the friction angle, effectively assuming an elastic-perfectly plastic relationship between shear strains and stresses. This can explain why following a large response, the computational model is limited in capturing the subsequent small amplitude response.

### 7.5.5 Response to historic records

The capability of the computational models to capture the features of the experimental responses allows to further investigate the rocking response more broadly. This analysis involved a suite of 49 records consisting of three subgroups, namely far-field records and near field records with and without pulses as summarized in the ATC-63 project (Kircher, Haselton and Deierlein, 2006). This is a comprehensive suite of records involving both high and low frequency ground excitations that can result from full contact response to large uplift for the rocking buildings considered here. The performance is assessed from a damage perspective incorporating the peak drift ratios against the peak rocking angle (Figure 7.22). As expected, very small rotations are associated with very small drifts, indicating a nearly full contact response equivalent for the building models under small amplitude earthquakes. Relatively large rotations ( $>0.05$  rad) occurred but these were more frequent for the RA model. These rotations were found to be associated with larger drift demands indicating the capability of the model to predict the interaction between flexibility and rocking either because of the impact at re-centering or the additional excitation due to the rotational motion of the superstructures. Practically, this effect is the same across dense and loose sand for RA and RB. For small rotations ( $<0.03$  rad), model RB experienced marginally lower drifts than RA but for the rest of the range ( $>0.03$  rad) this trend inversed, suggesting a mechanism change in the response of RB. This could possibly be attributed to the variation of the point of contact of the RB footings causing a change in the effective slenderness of the RB model, but that would require further investigation. Overall, the computational models provided reasonable predictions in terms of drift and rotation demand which are consistent with the corresponding experimental observations for small rocking angles ( $<0.03$  rad, Figure 5.11). For the drift

ratios, again these were found small compared to code provisions, but this comparison is only indicative.

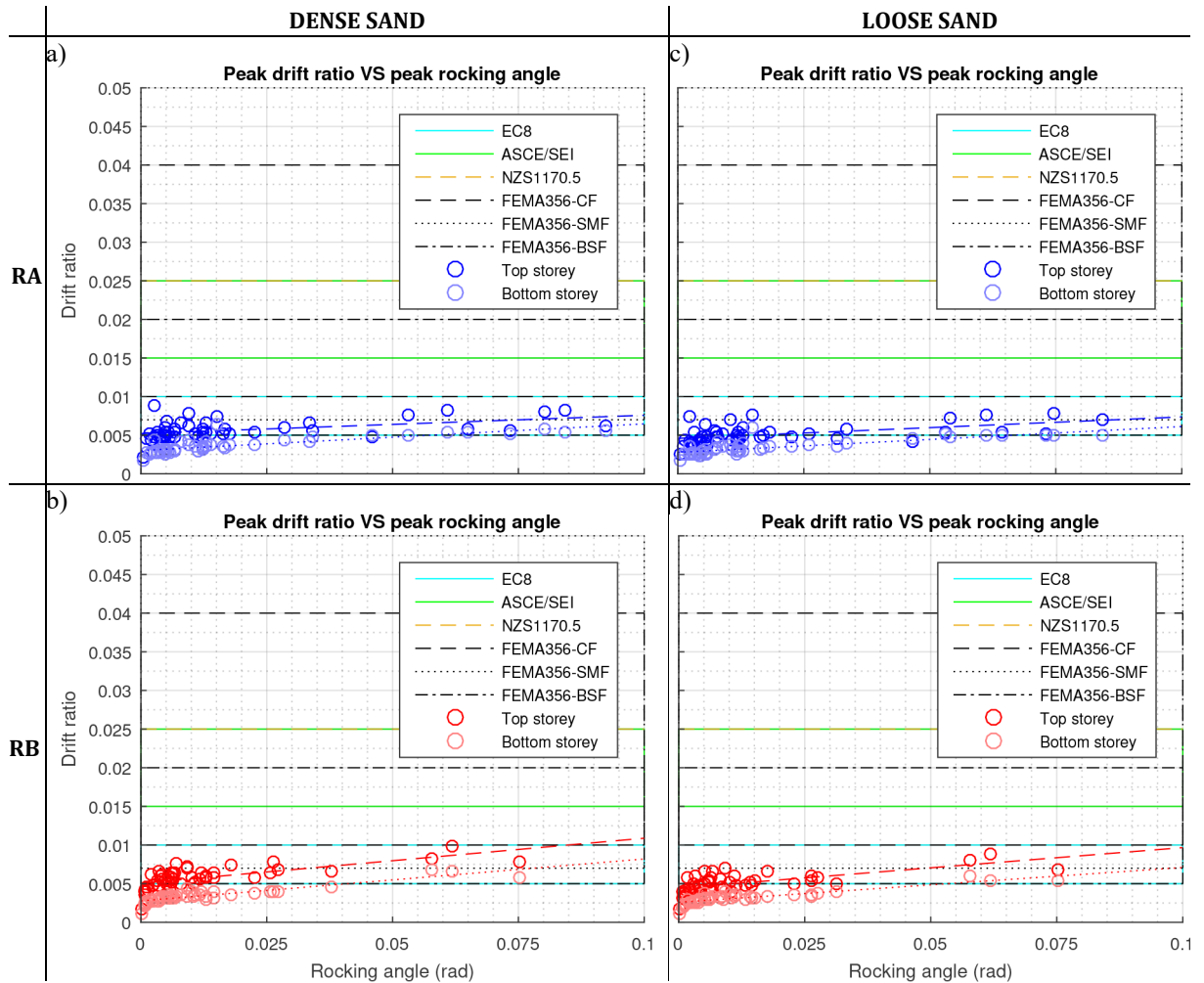


**Figure 7.22: Peak drift ratios against peak rocking angle for the top and bottom storeys for RA and RB for dense sand (a, b) and similarly for loose sand (c, d).**

## 7.6 Calibration based on modal damping ratios and signal metrics

A parametric study was conducted to assess the effect of superstructure’s modal damping ratios  $\zeta_1$ ,  $\zeta_2$  on the computational response of models RA and RB. This is an attempt to calibrate the analysis by using only two variables. This will allow to consider the effect of other variables which were not experimentally available, or the soil model does not consider in detail. For instance, these involve the coefficient of friction  $\mu$  for model RA, and the soil’s friction angle and stiffness regarding both models.

A two-dimensional grid in the range of 0.01 to 0.07 was specified for  $\zeta_1$ ,  $\zeta_2$  for both building models, which is acceptable for most buildings. The measured structural damping (Table 3.5) was also included in the grid as the default case.

To assess the effectiveness of different values of  $\zeta_1$ ,  $\zeta_2$  resulting in capturing well the experimental response, a methodology is required for signal comparison. In general,

comparison of signals can be conducted by using common metrics, such as the coefficient of determination (*CoD*) and a periodogram based coherence (*PRC*). For rocking buildings, a frequency match over time between experimental and computational responses is of the main interest, since this would validate the rocking mechanism of the computational model. Therefore, the wavelet transform which captures the frequency evolution, can also be used and more specifically, the wavelet transform coherence (*WTC*) can be considered as a tool to compare signals.

### 7.6.1 Example of response comparison with signal metrics

This comparison refers only to one signal, while a scheme for comparison considering multiple signals is presented next (Section 7.6.2). The single-signal comparison is useful because it allows the evaluation of the performance of these three metrics (*CoD*, *PRC*, *WTC*).

The coefficient of determination is defined as:

$$CoD = \left[ \left( \frac{1}{N-1} \right) \sum_{i=1}^N \left( \frac{h_i - \mu_h}{\sigma_h} \right) \left( \frac{g_i - \mu_g}{\sigma_g} \right) \right]^2 \quad (7.4)$$

where  $N$  is the number of samples  $i$  of the signals  $h, g$  and  $\mu_h, \mu_g$  and  $\sigma_h, \sigma_g$  are their mean and standard deviations respectively.

Next, the coherence based on the periodograms of the signals  $h, g$  is defined as a function of the frequency  $f$  as:

$$PRC(f) = \frac{|P_{hg}(f)|^2}{P_{hh}(f)P_{gg}(f)} \quad (7.5)$$

where  $P_{hh}, P_{gg}$  are the power spectral densities of signals  $h$  and  $g$  respectively, and  $P_{hg}$  the cross power spectral density. The spectral power densities are calculated first with an averaging window across multiple segments of the signals. This results in the PRC taking values between 0 and 1 (Cauchy-Schwartz inequality), otherwise the trivial result of 1 is always obtained. Here, the Welch's overlapped averaged periodogram method was used.

Finally, the wavelet transform based coherence is defined as a function of the frequency  $f$  and time  $t$  as:

$$WTC(t, f) = \frac{|\langle \bar{W}_h(t, f) W_g(t, f) \rangle|^2}{\langle |W_h(t, f)|^2 \rangle \langle |W_g(t, f)|^2 \rangle} \quad (7.6)$$

where  $W_x(t, f)$  is the transform of a signal  $x$ . In Eq. (7.6),  $\langle \cdot \rangle$  is a smoothing operator which ensures that  $WTC$  takes values between 0 and 1 (Cauchy-Schwartz inequality), a procedure equivalent for the calculation of the power spectral density in Eq. (7.5). The smoothing operator preferred here is a multiple of the average in both time and frequency domains due to its simplicity, although it is unclear what smoothing option would be most appropriate (Torrence C. and Compo G., 1998). Note that in this case Eq. (7.6) reduces directly to the typical Cauchy-Schwartz-Hölder inequality for two dimensional complex functions (Bahri and Ashino, 2017). This means that  $WTC$  is a constant in the time-frequency plane. To preserve value consistency with Eq. (7.4) and (7.6),  $PRC$  is approximated also by a multiple of its average value on the frequency range  $0 - f_c$ , where  $f_c$  is a cut-off frequency equal to 400 Hz based on the frequency response of the MEMS accelerometers. The wavelet transforms were also considered at the same frequency range.

The signal metric for a computational response resulting from a selection of  $\zeta_1, \zeta_2$  can now be normalized with respect to the maximum value obtained from a computational response within the batch of computational responses of the assigned grid, so that a value of 100% would indicate the best match according to this metric. Therefore, the response match indicators are now defined as:

$$R_{CoD}(\zeta_1, \zeta_2) = \frac{CoD(\zeta_1, \zeta_2)}{\max(CoD(\zeta_1, \zeta_2))} \quad (a)$$

$$R_{PRC}(\zeta_1, \zeta_2) = \frac{PRC(\zeta_1, \zeta_2)}{\max(PRC(\zeta_1, \zeta_2))} \quad (b) \quad (7.7)$$

$$R_{WTC}(\zeta_1, \zeta_2) = \frac{WTC(\zeta_1, \zeta_2)}{\max(WTC(\zeta_1, \zeta_2))} \quad (c)$$

Figure 7.23 shows computational responses of the top storey of model RA when different pairs of modal damping ratios  $\zeta_1, \zeta_2$  are used. Both responses capture reasonably well the initial part where some rocking has developed as a result of a pulse excitation. However, the free vibration traces are different and for larger  $\zeta_1, \zeta_2$  a better match is achieved (Figure 7.23b). When using the response match indicators  $R_{PRC}, R_{CoD}$  the lightly damped response is scored higher than the damped response (Figure 7.23a). On the contrary,  $R_{WTC}$  predicts well the match since it scores higher the damped response (Figure 7.23b). In addition,  $R_{WTC}$  scores higher a computational response with a peak closer to the experimental peak. This is evident when Figures 7.24a, b are compared, and the effectiveness of the  $R_{WTC}$  is also somewhat evident when comparing the responses from the Kobe excitation (Figure 7.23c, d). Although the two computational responses seem

identical,  $R_{PRC}$ ,  $R_{COD}$  underscore the computational response with the peak closer to the experimental one (Figure 7.23d).

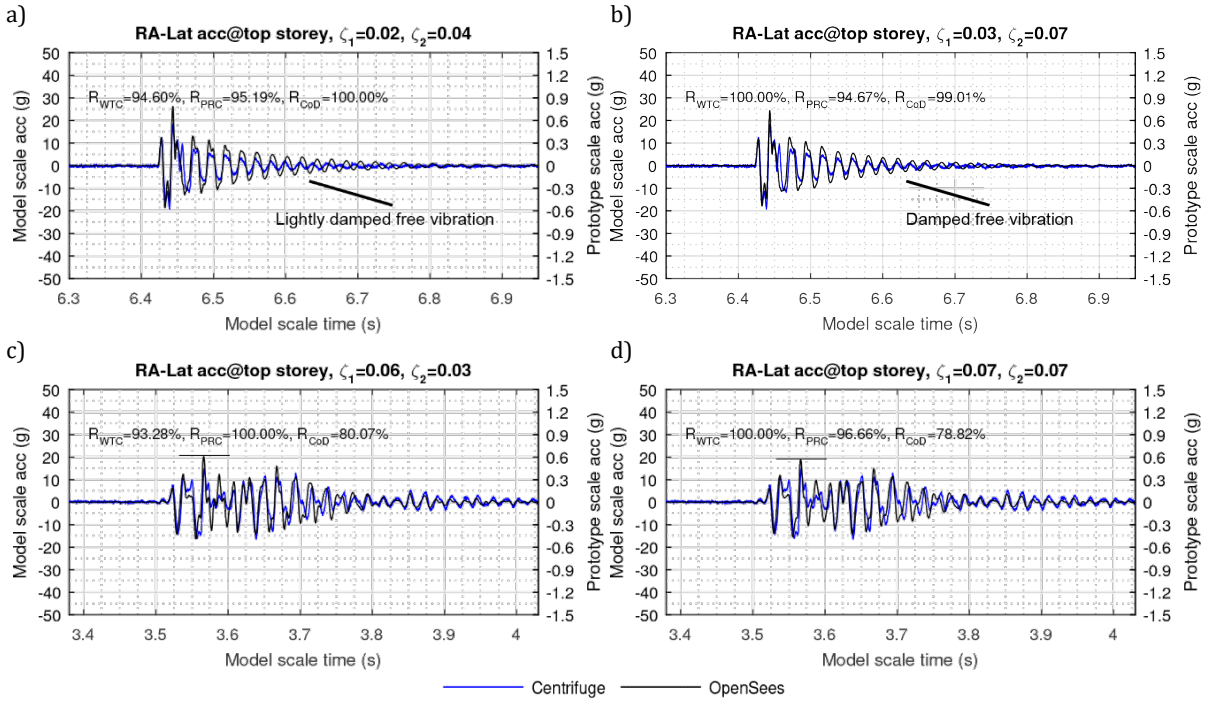


**Figure 7.23: Loose sand Test-1 Eq-3: Lateral acceleration response for top storey for model RA for  $(\zeta_1, \zeta_2) = (0.02, 0.04)$  (a) and for  $(\zeta_1, \zeta_2) = (0.03, 0.07)$  (b) and similarly for Test-1 Eq-1 for  $(\zeta_1, \zeta_2) = (0.06, 0.03)$  (c) and  $(\zeta_1, \zeta_2) = (0.07, 0.07)$  (d)**

For the parametric studies on a multi-signal scheme in the following section, the  $R_{WTC}$  is preferred as a signal match indicator for batch processing, since it was found it is more consistent. Note however, that using different smoothing functions for both the WTC and PRC might result in match indicators with different effectiveness.

### 7.6.2 Multi-signal scheme for response comparison

To assess the similarity of the computational response with the experimental response, the signal match indicator  $R_{WTC}$  is employed. The top and bottom storey accelerations and the rocking angle are considered as three main signal match indicators ( $R_{WTC, i}, i = 1, 2, 3$ ) and an average score is produced for each sequential excitation  $Eq$ :

$$SC_{Eq}(\zeta_1, \zeta_2) = \frac{\sum_{i=1}^3 w_i R_{WTC, i}(\zeta_1, \zeta_2)}{\sum_{i=1}^3 w_i} \quad (7.8)$$

Next, a global score of a test  $T$  with sequential excitations from  $Eq = 1$  to  $Eq = Eq_{max}$  can be defined as:

$$R_{WTC} \equiv SC_T(\zeta_1, \zeta_2) = \frac{\sum_{Eq=1}^{Eq=Eq_{max}} q_{Eq} SC_{Eq}(\zeta_1, \zeta_2)}{\sum_{Eq=1}^{Eq=Eq_{max}} q_{Eq}} \quad (7.9)$$

In Eq. (7.8), (7.9)  $w_i$  and  $q_{Eq}$  are weights which can be used as different than 1.0 to represent the importance of a specific signal and the importance of a specific earthquake, respectively. For simplicity, these are set as 1.0, and the term  $R_{WTC}$  is adopted again in Eq. (7.9). Its maximum value indicates the pair of  $\zeta_1, \zeta_2$  that leads to the computational response that can capture best the experimental response across all sequential excitations  $Eq$  of a test  $T$  on average, based on equal weighting of the top and bottom storey accelerations and the rocking angle.

### 7.6.3 Calibration for response to Kobe excitation for dense sand

Figures 7.20, and 7.21 showed a relatively good match of the behaviour for the default values of  $\zeta_1, \zeta_2$ , but now the wavelet transform coherency is considered to improve the match. Figures 7.25 and 7.26 show the obtained response and its evaluation with the WTC when  $(\zeta_1, \zeta_2) = (0.02, 0.02)$  and when the optimum values  $(\zeta_1, \zeta_2) = (0.04, 0.06)$  for model RA are used. Both cases show a very good match, but the latter prevents the development of high frequency response, which is more evident at the second storey acceleration. A small improvement in the peak rocking amplitude is evident too (Figure 7.24), while similar improvements are overall noticeable for model RB (Figure 7.25).

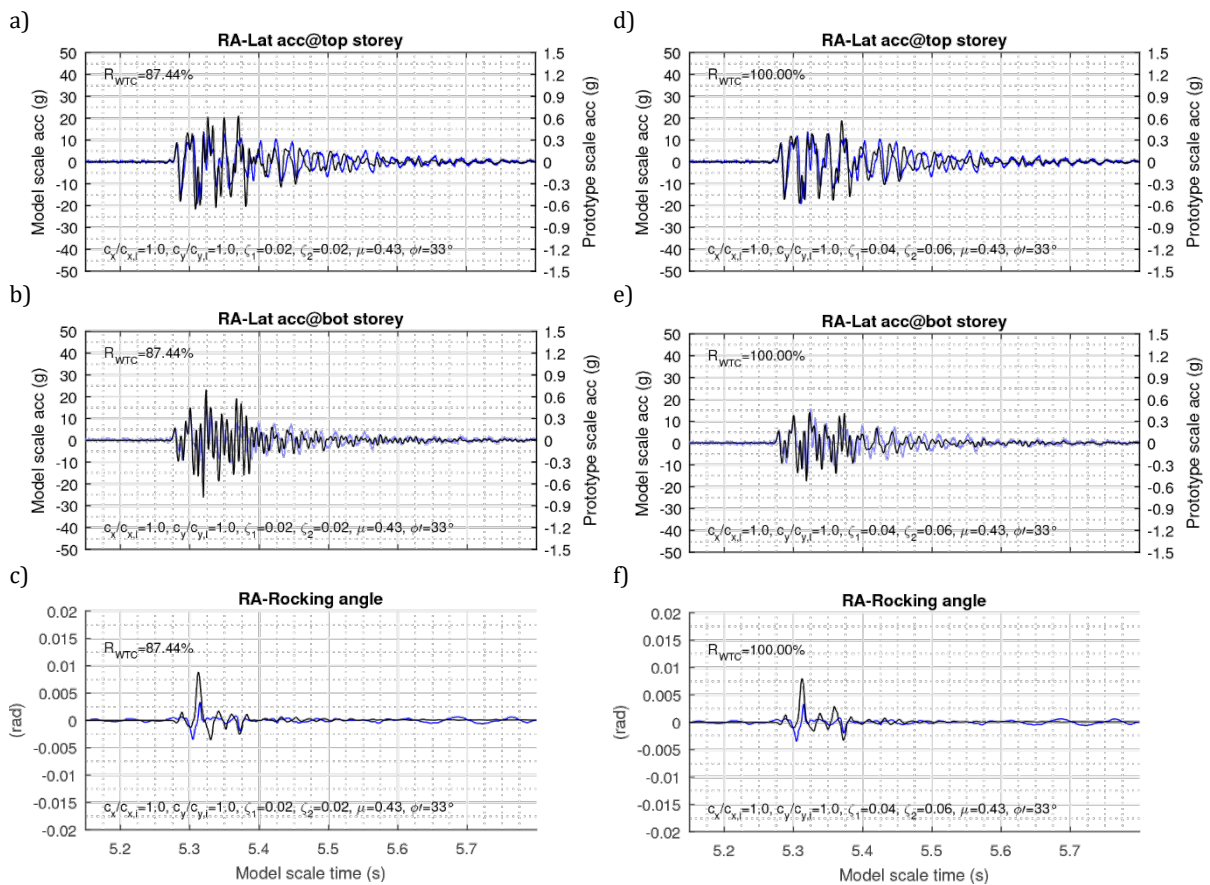


**Figure 7.24: Dense sand, Test-2, Eq-1: Top storey (a), bottom storey (b) and rocking angle (c) experimental and numerical responses for model RA for typical set of modal damping ratios and similarly for optimum modal damping ratios (d-f)**

However, the overall match can come at the cost of a new mismatch locally in some cases, as for instance before the end of the rocking angle response for RA (Figure 7.24f). Since this mismatch does not cause a new maximum value, this result is acceptable as an optimum solution.

For all the different computational responses, a contour plot can be created showing the  $R_{WTC}$  score over the grid of  $\zeta_1, \zeta_2$  (Figure 7.26, Figure 7.27). It is observed that for model RA values in the space of  $(0.03 - 0.07) \times (0.03 - 0.07)$  yield a similar match between 85 - 100%; the contours indicate small variation over that space, and this is repeated across all tests for the case of dense sand (Figure 7.26a-c). In loose sand, the same space is now  $(0.03 - 0.05) \times (0.03 - 0.07)$  for both tests. For model RB, a clear trend is difficult to establish across the tests with dense sand (Figure 7.26d-f), whereas in loose sand a similarity exists between the two tests.

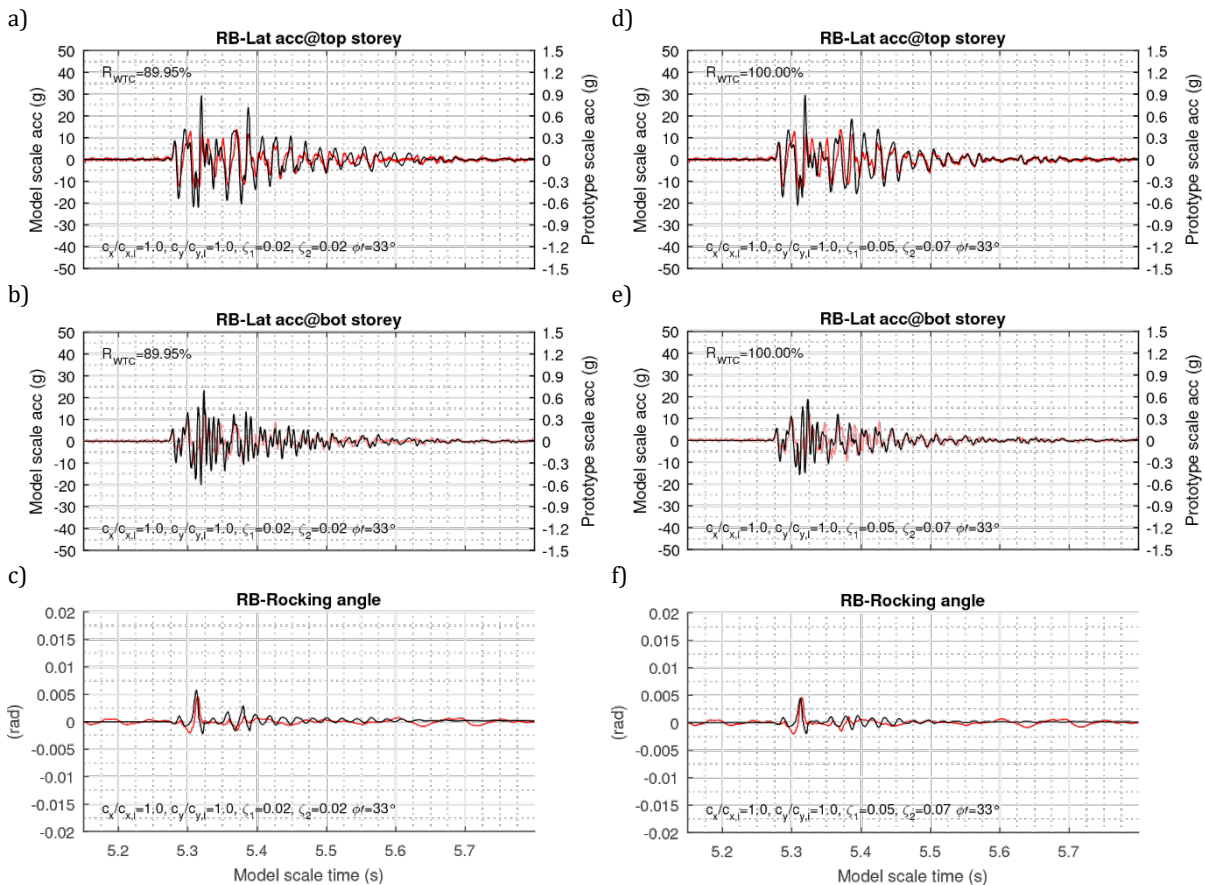


**Figure 7.25: Dense sand, Test-2, Eq-1: Top storey (a), bottom storey (b) and rocking angle (c) experimental and numerical responses for model RB for typical set of modal damping ratios and similarly for optimum modal damping ratios (d-f)**

Recalling that the excitation sequence is different from Test-0 to Tests-1, 2 for dense sand (Table 4.2) and the different soil conditions between dense and loose sand, the results indicate that the response of model RA can be sufficiently described independently for all

these cases, and a variety of damping levels  $\zeta_1, \zeta_2$  are acceptable as long as these fall within the space of  $(0.03 - 0.05) \times (0.03 - 0.07)$ . This highlights the relatively low sensitivity of the proposed modelling approach for structural rocking to the modal damping ratios when soil is involved.

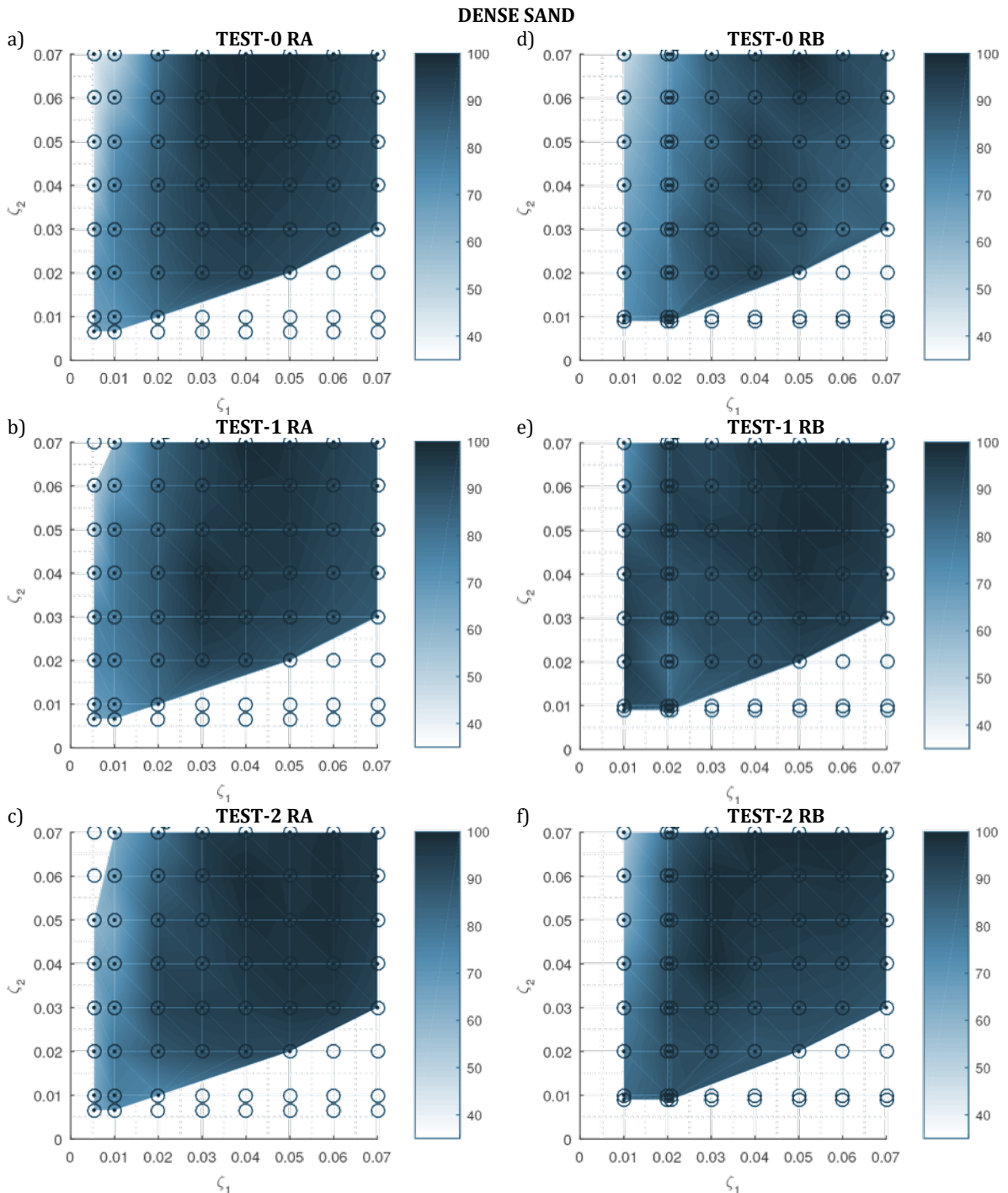


**Figure 7.26: Contour plot of the  $R_{WTC}$  score for each test for model RA in dense sand (a-c) and similarly for model RB (e-g). Circles without dots in their centre indicate analyses that did not converge**

Model RB appears to be sensitive to the excitation sequence in dense sand and the same values of  $\zeta_1, \zeta_2$  can lead to very different scores across the tests (e.g.  $R_{WTC}(0.02, 0.05) \approx$

70%, Figure 7.26d, and  $R_{WTC}(0.02, 0.05) \approx 90\%$ , Figure 7.26e). In loose sand, the space  $(0.05 - 0.07) \times (0.03 - 0.07)$  provides similar high scores of matching across both tests. The difference of trends between dense and loose sand further suggests that the computational response for foundation rocking is dominated more by the soil deformations, rather the assigned superstructure properties such as the modal damping ratios. Again, recalling that model RB utilizes its footings for rocking with fixed column-footing connections, this interpretation is plausible.

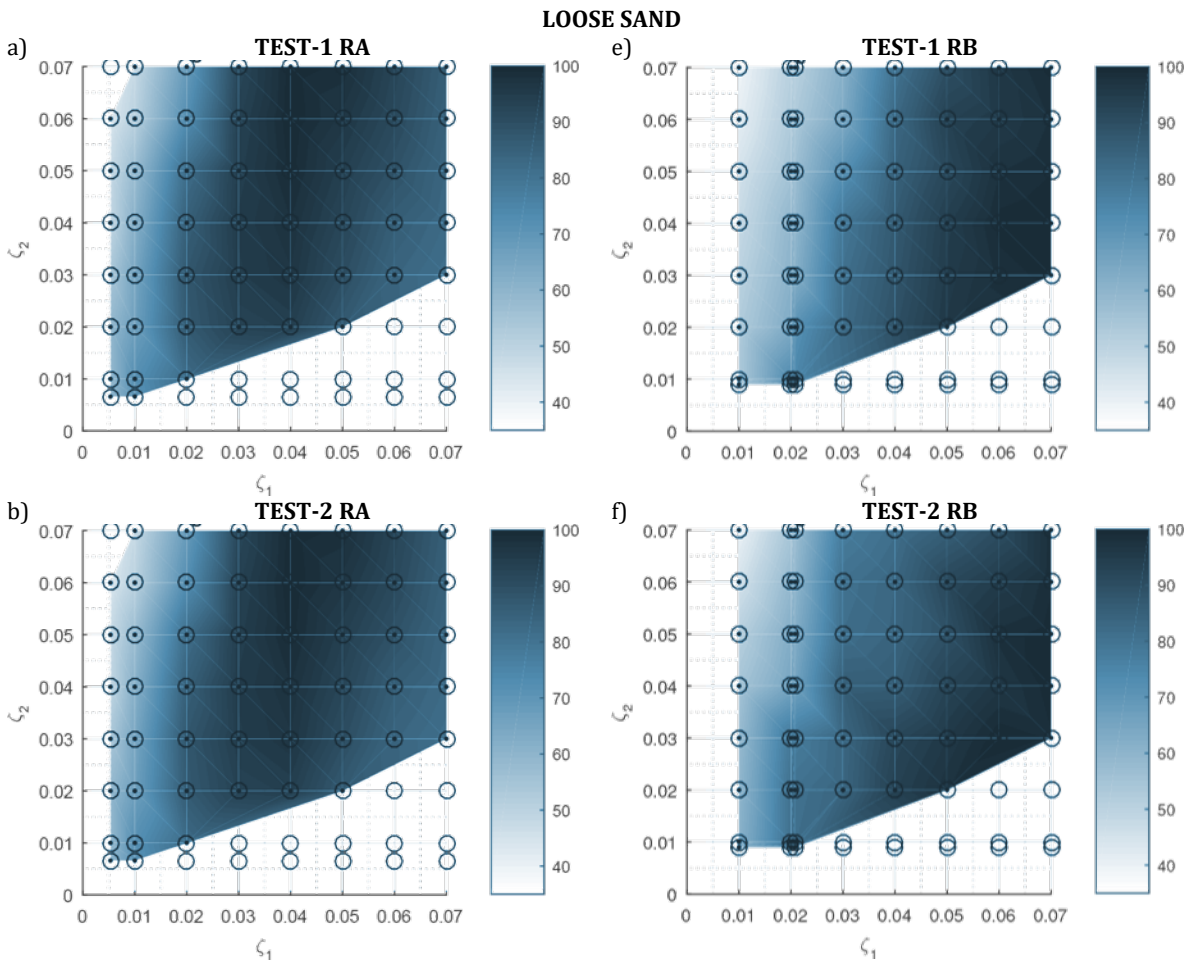


**Figure 7.27: Contour plot of the of the  $R_{WTC}$  global score for each test for model RA in loose sand (a, b) and similarly for model RB (e, f). Circles without dots in their centre indicate analyses that did not converge**

#### 7.6.4 Limitations of signal metrics

While the previous sections quantified the sensitivity of models RA and RB to the modal damping ratios using the wavelet transform coherency as a criterion of response comparison, this section shows that this method might not always function consistently. For example, the method was not consistent when no rocking or partial rocking occurred as a result of an overdamped model RB. Figure 7.28 shows that overall a response with partial rocking is underscored on average compared to a no rocking response. Since in

this case the experimental response was continuous rocking, the higher score should be attributed to the computational response with partial rocking. Regarding the rocking angle (Figure 7.28c, f) and the bottom storey acceleration response (Figure 7.28b, e), expected values of the  $R_{WTC,i}$  are obtained; partial rocking is scored higher, although with a minimal difference. However, the top storey acceleration response which indicates no rocking reverses this comparison (Figure 7.28a, d). It seems that the high frequency content of the no rocking response matches better the corresponding high frequency parts of the experimental response, so that this match is scored higher. It is evident that improvement of this method is necessary to achieve more consistent results.

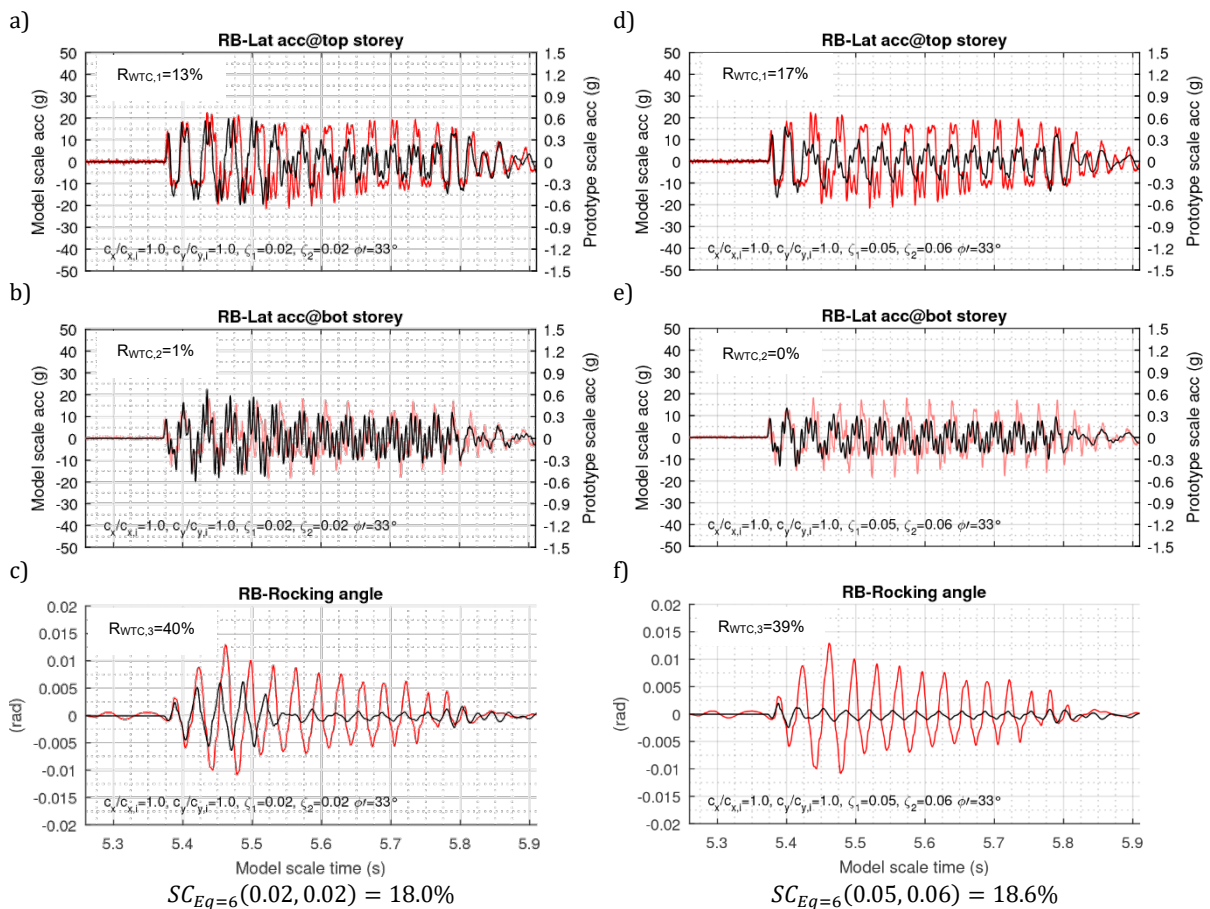


**Figure 7.28: Dense sand, Test-1, Eq-6: Top storey (a, d), bottom storey (b, e) and rocking angle (c, f) experimental and numerical responses for model RB for two different sets of modal damping ratios**

## 7.7 Summary

In this Chapter, an approach to computationally model the response of flexible buildings with structural and foundation rocking that were previously subjected in centrifuge testing was presented. The modelling approach involved both the soil-structure interaction (SSI) developing below the footings of the building models, but also the superstructure-footing interaction for structural rocking. For SSI, the Beam-on-a-

Nonlinear-Foundation model (BNWF) was selected and modified within the OpenSees framework using the *flatsliderBearing* element (mBNWF). The same element was used also to model partial hinges for structural rocking, and specifically to replicate footing slots that act as shear keys. The final objective was to predict key response features, such as rocking response, full contact response and the transition between these across time. This effort led to the following conclusions:

- Modification of the existing BNWF model allowed for a realistic development of the vertical and horizontal forces below a footing. For sequential earthquake excitations, this is very important, since residual deformations can significantly affect the response to subsequent excitations.
- Effects from sequential excitations (i.e. cumulative deformations used as initial conditions for subsequent analyses) can lead to a qualitative difference in the response from rocking to no rocking. This difference was significant for the building with foundation rocking, whereas structural rocking was found relatively insensitive regarding this effect.
- The mBNWF model predicted reasonably well different types of response for both structural and foundation rocking. More specifically, the modelling of the building with the foundation rocking captured the rocking and no rocking response for the dense and loose sand cases respectively. This allowed to use the model for assessment with a broad suite of real records, which indicated that storey drift demand can be within a serviceability limit state, but this can come at the cost of very large rocking angles.
- The simple nature of the mBNWF model is an advantage as on the one hand a relatively small number of model parameters is required to produce realistic responses for buildings with foundation and structural rocking. On the other hand, effects such as soil dilation cannot be modelled and in situations where a large variation of shear strain can occur, for example in transitioning from large rocking to full contact response, a more sophisticated modelling approach might be more appropriate.
- It was shown that by selecting appropriate modal damping ratios a better match between experimental and computational responses can be achieved. In pursuit of calibrating the computational models for an optimum match between computational and experimental response, it was shown that structural rocking is

not very sensitive to the selection of modal damping ratios. In contrast, foundation rocking is more dependent on the earthquake excitation sequence and therefore a specific set of modal damping ratios might not necessarily lead to the best match.

- The criterion for a best match was based on the wavelet transform coherency between an experimental response and its computational counterpart. Although this criterion was found to consistently score higher rocking responses that follow closely the profile of the experimental rocking response, when no rocking responses were generated as a result of a poor calibrated model, these were not underscored. Therefore, this approach requires further investigation.



# 8 CONCLUSIONS

## 8.1 Main findings

The main objectives of this thesis, as stated in Chapter 1, are:

- 1) *To experimentally quantify the demand that rocking systems experience during their motion, including soil-structure interaction effects as well as the effect of impact at the interface of the superstructure with the foundation (structural rocking) or the interface of the foundation with the soil due to rocking (foundation rocking). More specifically, the demand was defined as local forces such as element loadings and global forces such as base shear and restraining moment, and deformations such as local building and soil accelerations, rocking rotation and differential settlements.*
  
- 2) *To develop and evaluate a computational tool that involves footing-superstructure interaction for buildings with structural rocking, as well as soil-structure interaction for buildings with foundation rocking.*

Therefore, this research focused on the experimental earthquake response of two types of rocking buildings and the soil behaviour beneath. A computational tool regarding the prediction of their rocking response was presented and validated against experimental data. The main findings are:

- Structural and foundation rocking implemented for dynamically similar buildings led to a similar base isolation effect. This effect was maximum when the buildings were excited at their resonant frequency, which is consistent with previous analytical models. Moreover, low frequency excitations were the most detrimental,

causing the highest load demand for structural rocking across both sand densities. While this was also true for foundation rocking, loose sand caused generally a lower force demand in low frequency excitations by preventing the development of rocking after the initial cycle of excitation and forcing a full contact response.

- More specifically, structural rocking resulted in higher load demand compared to foundation rocking. This was almost consistently the case when both weight-normalised and non-normalised base shear values were compared. For loose sand, a shift of the pivot point to the interior of the foundation rocking building caused smaller force demand than in dense sand. Due to loose sand conditions (low stiffness), the additional excitation of the superstructure caused by impacting the soil at re-centring was not evident. On the contrary, for dense sand, some additional excitation was evident generally resulting in higher load demand, although with an increase in variability of response. A similar degree of variability was found for structural rocking for both dense and loose sand cases. The similarity of the variability in the load demand between all of the different types of rocking for the dense sand case, and the similarity of the variability in the load demand between the different types of sand for structural rocking, suggest that structural and foundation rocking are tautological depending on the soil conditions.
- The amplitude of the vertical acceleration close to the columns following re-centring (impact acceleration) was similar across both buildings, which indicates that for the range of densities considered here the area of the contact interface (i.e. finite area for a footing on a soil or point contact for column on a footing) did not play a role. Upon full contact establishment at re-centring, the energy dissipation mechanism is activated in a similar fashion: temporarily and with a vertical push of the footings downwards. Beyond that point in time, the different footing-column connectivity of each rocking building will result in a different behaviour of the soil.
- A performance trade-off was evident when considering the maximum rocking amplitude against the maximum differential settlement. For the same rocking angle, differential settlements were much larger for foundation rocking. The sand density did not affect the demand in rocking amplitude or differential settlements for structural rocking; similar values were noted for dense and loose sand. In contrast, foundation rocking in loose sand resulted in a mixed trend, in which small

rocking amplitudes can be achieved for large high differential settlements and large rocking amplitudes are linked to small differential settlements.

- In all excitations, a free rocking response only developed from the pulse excitation with low frequency for the building with structural rocking. This allowed observation of the temporal shift in frequency response which has been clearly demonstrated with various analytical and experimental models, but had not previously been experimentally observed with soil present. However, the absence of free rocking for the rest of the centrifuge tests, which represent prototype buildings of 3-4 storeys high, suggests that free rocking is unlikely to occur. Rather, due to the presence of soil, a direct switch from rocking to full contact vibration response is more probable for buildings of this type. This further suggests that damping from hysteretic response of soil (for both structural and foundation rocking) is significantly larger than the damping associated with impacts at a rigid base, which often result in many cycles of free rocking.
- The wave propagation caused by the buildings rocking on the soil was assessed based on wavelet transforms. It was shown that high frequency content generated either from the impacts at the footing-column interface or from the soil footing-interface are clearly evident in acceleration measurements close to the surface, and up to a depth of about 3.4 times the footing width. This observation was used to define a zone of influence that shows that soil participates not only locally below the footings, but also at much larger depths.
- The sequence of input excitations was critical in the evaluation of the computational models. For foundation rocking, it was found that different computational responses are obtained when an excitation is used alone and when the experimental sequence of excitation is used instead. Particularly, for low frequency excitations, the computational response changed from no rocking to the experimentally observed rocking when sequential input was used. This suggests that buildings with foundation rocking may be sensitive to residual deformations acting as initial conditions for a subsequent excitation. In contrast, structural rocking was not sensitive to the earthquake sequence, confirming that it is less dependent on the soil behaviour. By directly employing measured or derived parameters, without any additional calibration, the rocking, full contact and transition between the two types of response were satisfactorily captured for both buildings.

## 8.2 Research contributions

The above findings are the result of a centrifuge campaign with unique features. This experimental process required the design and assembly of two building models, which were particularly designed to represent prototype structures while addressing the physical constraints of the experimental setup. A large volume of experimental data was generated with instruments attached to the building models and embedded in the soil. For the post-processing, all time-histories were transformed in a time-frequency domain. More specifically,

- *Experimental data:* A large dataset comparing highly detailed buildings with structural and foundation rocking in centrifuge conditions was produced. This involved single- and multi-cyclic excitations but also historic earthquake records. Different sand densities were considered, and tests were repeated. This is a one of a kind dataset that not only provides experimental evidence to improve understanding of the effects of soil-structure interaction on rocking structures, but also provides a valuable resource for other earthquake engineers and computational modelers.
- *Design of two types of rocking buildings for one-to-one comparison in centrifuge conditions:* A procedure was presented on how to achieve a building design which provides a uniform basis for comparison between structural and foundation rocking. The use of braces in conjunction with a minimum column thickness allowed for a common distribution of stiffness across the height of the buildings resulting eventually in buildings with similar natural frequencies. This led to a common pre-uplift full-contact response at the initial part of an excitation, whereas the different rocking mechanisms could be observed easily after that point.
- *Prototype braces and connections for provision of lateral stiffness in centrifuge conditions:* To ensure the buildings have realistic natural frequencies and that the superstructures remain linear elastic, so as to prevent any material nonlinearities to mask the rocking response, hollow circular plastic members were selected for braces. To ensure that the system braces and connections have no strength or stiffness degradation, an experimental assessment was performed based on procedures for components subjected to cyclic loading. The design allowed for portable braces which could be removed and calibrated axially with hanging weights, before placed into position again.

- *Step by step calibration for wavelet transforms*: The resulting time-frequency map of a wavelet transform depends on the so-called mother wavelet which interacts with the signal (wavelet transform) and eventually extracts the frequency evolution across time. To understand the relative limitations between different mother wavelets, a pulse response was considered from the building with structural rocking, since it contained highly mixed frequency content. The proposed calibration procedure resulted in an appropriately tuned Morse wavelet eventually resulting in clear time-frequency maps. Similar calibration procedures with more than one type of mother wavelet can be used for signals with different oscillation characteristics.
- *Systematic wavelet transform analysis*: To provide insights into the feedback effect from the buildings to the soil, analysis with wavelet transforms was implemented, including batch processing of an extensive amount of data. While this tool provides information in the frequency-time domain in the form of a varying two-dimensional complex function, it is difficult to interpret the wavelet transforms of multiple signals quickly. Using the energy of wavelet transforms as a key characteristic non-varying value which is unique to each different signal, comparisons across all generated time-histories could be made.
- *Column-footing interaction for physical and computational modelling of structural rocking*: To enable structural rocking in the physical building model, a triangular slot was designed to allow the column simply to rest on the footing. Upon excitation, the column would uplift freely. After contact establishment, the slot acts as a shear key. To simulate that in an FE environment with line-elements, friction-gap elements were used in pairs and in a configuration copying the physical geometry of the slot. Overall, this approach paves the way forward for considering similar designs for structural rocking buildings, as on the one hand a clear stepping mechanism is obtained, and on the other hand modelling of that can be quickly implemented.
- *Footing-soil interaction elements for computational modelling of soil-structure interaction*: Winkler foundation models are popular owing to the limited number of physical properties they require for implementation within a FE environment, as opposed to macro-elements and detailed constitutive laws. This is the first time a fully comprehensive Beam-on-Nonlinear-Winkler-Foundation (BNWF) model is presented. The model allows for full or partial loss of contact for a footing with

simultaneous reductions in vertical and horizontal forces due to uplift. The resistance in shear is determined based on Coulomb friction. For stiffness and damping in the translational directions, the Gazetas equations are used. In addition, non-linear force-displacement laws calibrated against previous centrifuge experiments are used for the springs providing the vertical resistance. As a result, the model can provide a realistic response from a kinematics point of view, producing also realistic residual footing displacements, which are critical for simulations with sequential excitations.

### 8.3 Practical implications

An overarching objective of this thesis is to bring together the two schools of thought in rocking (structural versus foundation), often encountered separately in literature during the last 60 years, and examine the relative benefits and weaknesses. To achieve this, for the first time, two highly detailed building models founded on soil were tested to sequential earthquake excitations in centrifuge conditions. Each building model represented structural and foundation rocking respectively, while their design ensured realistic structural properties when scaled back to their equivalent prototypes. Therefore, this research provides a unique basis to understand the practical implications associated with the different types of rocking isolation.

Generally, design for rocking response as an isolation mechanism would be justifiable provided the seismic performance is better to that of the conventional fixed-base ductile design. Within the context of performance-based design, modern design codes specify limits on storey drift demand, since storey drift is commonly accepted as a damage proxy for ductile structures. These limits are with respect to a serviceability limit state and an ultimate limit state, which essentially represent a low damage region and a high damage region, respectively. Moreover, it is expected that little or no damage occurs for small and frequent earthquakes while large damage is expected for large and rare earthquakes. The design and response of the building models followed closely this concept. Specifically, when the excitation is small (serviceability limit state), rocking reduces practically to a full contact response with very low drift demand for both buildings. When the rocking angle increases as a result of a large excitation (or an excitation with low frequency content), then the drift demand on the two buildings increases too. Even for the largest rocking angle noted ( $\approx 0.016$  rad or 8 cm of uplift for a prototype), which here can be interpreted as an ultimate limit state, the associated drift demand falls within typical

serviceability limits. Moreover, when even larger rocking angles were noted from the computational analysis with the modified BNWF model and a broad suite of earthquake records, the obtained drifts were still in the low damage region. Recalling that the building models used here have linear elastic superstructures as opposed to real buildings that have minimum ductility requirements for preserving general structural robustness, the obtained drifts are indicative. However, with regards to performance-based design, this research overall suggests that design for rocking is a good alternative when significant reduction of storey drifts becomes an important design parameter.

Moreover, this research shows that structural rocking is less sensitive to the soil conditions, while foundation rocking is more sensitive, as expected, due to the fixed footing-column connection. Consequently, the ultimate selection of the type of rocking implemented in a design for seismic isolation would depend not just on the storey drift demand but also on acceptable settlements. Most importantly, the maximum rocking angle, or equivalently the maximum uplift, may govern the design decision between structural and foundation rocking. This research suggests that in loose sand foundation rocking can result in a maximum rocking angle significantly smaller than that of structural rocking (up to about 50%), while practically the associated soil differential displacement is marginally larger for the former (about 6% of the footing width, or 7.5 cm in prototype scale). Dense sand favours structural rocking because while the maximum rocking angle can be the same practically for the two cases, the corresponding soil differential displacement of structural rocking can be up to a third of that of foundation rocking. Overall, structural rocking can lead to a better performance in dense sand, while this holds true for foundation rocking in loose sand instead. In any case, all maximum values of soil differential displacement (up to about 6% of the footing width) would be acceptable for an ultimate limit state. However, more research is needed to define the limit states for rocking buildings in terms of maximum rocking angle.

Moreover, it is useful to consider various scenarios with additional design constraints before selecting the appropriate type of rocking. For instance, when the soil properties are difficult to characterize with confidence, then opting for structural rocking would be appropriate since any variation on the soil properties have a smaller effect on the rocking response. Moreover, when rapid post-earthquake repair is of paramount importance (e.g. slender piers supporting bridge deck) then again structural rocking has advantages and can be combined with a damper that can be easily replaced. This design would require special consideration of the foundation-damper system. Generally, the partial hinge

connection necessary for structural rocking poses a challenge. Stress concentration at impact might cause local damage. However, a variety of special structural details have been proposed to protect the elements at the rocking interface. Furthermore, excessive sliding of the columns might lead to dislocation of the superstructure, so acceptable horizontal displacements need to be defined, while also the local-recentring mechanisms of the columns need always function properly.

On the other hand, foundation rocking is a convenient solution when retrofitting structures that have undersized footings, allowing the foundations to rock and take advantage of the energy dissipation from the soil, rather than increasing the capacity of the foundations. Generally, foundation rocking for a new building may also be more plausible to implement in practice, as the special detailing required at the structural rocking interface is avoided.

Assessing in-depth which type of rocking would be more appropriate is beyond the scope of this work, which would also depend on an extensive cost/benefit analysis. Ultimately, however, based on this research, the design of any of the two types of rocking systems would hinge on the serviceability and ultimate state deformations (soil settlements and building rotations) and the base shear demand resulting from the ground excitation and any additional excitation from impact at re-centring. Finally, to further harness the benefits of rocking systems, more research is required, as discussed in the following section.

## 8.4 Future research

With regards to the work presented in this thesis, suggestions are provided for further research:

- *Improved design of fuses for structural rocking in centrifuge testing:* Fuse elements were placed between the footing and the column for the building with structural rocking. The objective of this elements was to dissipate energy through plastic deformation in order to limit the rocking amplitude. While these elements deformed plastically, their contribution in mitigating the rocking amplitude was minimal. This was primarily because the design capacity was constrained by the weight of the individual footings, essentially acting as anchors. Considering the plateau of the restoring moment of the building, this capacity was a negligible contribution in the overall restoring moment. Therefore, exploring different

scenarios with the same building model for structural rocking, but with heavier footings and larger fuse capacity could provide more insights about the role of dampers in mitigating rocking and the distribution of energy dissipation between soil and dampers.

- *Structural rocking on a rigid base in centrifuge conditions:* To further explore the effect of soil in the rocking response of realistic buildings, a comparison to the typical rigid base case would be suitable. While many analytical and experimental models have addressed the rigid base case, it would be the first time this is addressed in centrifuge conditions. This would provide a better view of the extent to which impacts during re-centring can excite the superstructure. Then, comparing the rigid base and soil base responses would more directly quantify the energy dissipation for each case.
- *Advanced instrumentation:* To provide a better understanding of the development of residual deformations, and thus accommodate the industry need for more guidance on rocking systems, the absolute foundation movements should be directly measured and be combined with measurements from load cells. This would allow more direct assessment of permanent tilts of the superstructure due to differential settlements of the footings, which could be important from a serviceability point of view.
- *Different types of soil could be considered:* Studying rocking on liquefiable soil might provide different views on load and deformation demand for the two types of rocking buildings considered here. Similarly, buildings with pad foundations on clayey soils may be of interest.
- *Parametric study on building scale and soil properties based on computational model:* Since the computational model presented here produced reasonably good matches with the experimental data, it can be used for other structural configurations and soil properties. In particular, to further explore the interaction between elasticity and rocking, multi-storey building frames could be modelled. This would highlight further the effect of higher modes on the acceleration demand and could be linked to different values of soil properties such as stiffness and friction angle for various scenarios. For example, desirable soil properties may be defined such that specific superstructure acceleration limits are established for building serviceability.

- *Signal metrics for calibration of computational models:* It was shown that in some cases, when different modal damping ratios are used to create the Rayleigh matrix in a computational model, then a better prediction is calculated. To prioritize between different pairs of modal damping ratios that provide different computational responses, the wavelet transform coherency was proposed as an optimization function. When there is a large similarity between the frequency contents evolving over time for two different signals, then this term can be reduced to a high value indicating a relatively good match between the two signals. This technique was suitable in this case, because the signals examined were accelerations with frequency content that varied significantly over time. However, it is possible that this method might not consistently lead to an optimum set of parameters for the best match. Therefore, other signal metrics, such as the coefficient of correlation or the periodogram coherency, could be used in conjunction with the wavelet transform coherency and improve the calibration process.

# 9 REFERENCES

- Acikgoz, M. S. (2014) *Seismic assessment of flexible rocking structures*. University of Cambridge. PhD Thesis.
- Acikgoz, S., Argyle, A. and DeJong, M. J. (2014) 'The role of supplemental damping in limiting forces and displacements in a rocking structure', *Proceedings of the 2nd European Conference on Earthquake Engineering and Seismology*, pp. 1–12.
- Acikgoz, S. and DeJong, M. J. (2012) 'The interaction of elasticity and rocking in flexible structures allowed to uplift', *Earthquake Engineering & Structural Dynamics*, 41(11), pp. 2177–2194.
- Acikgoz, S. and DeJong, M. J. (2013) 'The rocking response of large flexible structures to earthquakes', *Bulletin of Earthquake Engineering*, 12(2), pp. 875–908.
- Acikgoz, S. and DeJong, M. J. (2016) 'Analytical modelling of multi-mass flexible rocking structures', *Earthquake Engineering & Structural Dynamics*, 45(13), pp. 2103–2122.
- Acikgoz, S. and DeJong, M. J. (2018) 'A simple model to quantify rocking isolation', *Bulletin of the New Zealand Society for Earthquake Engineering*, 51(1), pp. 12–22.
- Acikgoz, S., Ma, Q., Palermo, A. and DeJong, M. J. (2016) 'Experimental Identification of the Dynamic Characteristics of a Flexible Rocking Structure', *Journal of Earthquake Engineering*, 20(8), pp. 1199–1221.
- Addison, P. S. (2017) *The illustrated wavelet transform handbook: introductory theory and applications in science, engineering, medicine and finance*. Second. CRC Press.
- Addison, P. S., Watson, J. N. and Feng, T. (2002) 'Low-Oscillation Complex Wavelets', *Journal of Sound and Vibration*, 254(4), pp. 773–762.
- Ajrab, J. J., Pekcan, G. and Mander, J. B. (2004) 'Rocking wall-frame structures with supplemental tendon systems', *Journal of Structural Engineering*, 130(6), pp. 895–903.
- Analogue Devices Inc (2010) 'Single-Axis, High-g, iMEMS® Accelerometers ADXL193'.
- Anastasopoulos, I., Gazetas, G., Loli, M., Apostolou, M. and Gerolymos, N. (2010) 'Soil failure can be used for seismic protection of structures', *Bulletin of Earthquake Engineering*, 8(2), pp. 309–326.
- ASCE/SEI (2017) *Minimum Design Loads and Associated Criteria for Buildings and Other*

*Structures.*

ASCE (2000) *FEMA 356 Prestandard and Commentary for the Seismic Rehabilitation of Building*.

ATC-40 (1996) *Seismic Evaluation and Retrofit of Concrete Buildings*. Redwood City, California.

Bahri, M. and Ashino, R. (2017) 'A Variation on Uncertainty Principle and Logarithmic Uncertainty Principle for Continuous Quaternion Wavelet Transforms', *Abstract and Applied Analysis*, 2017, pp. 1–11.

Beck, J. L. and Skinner, R. I. (1974) 'The seismic Response of a Reinforced Concrete Bridge Pier Designed To Step', *Earthquake Engineering and Structural Dynamics*, 2(4), pp. 343–358.

Boulanger, R. W., Curras, C. J., Kutter, B. L., Wilson, D. W. and Abghari, A. (1999) 'Seismic Soil-Pile-Structure Interaction Experiments and Analyses', *Journal of Geotechnical and Geoenvironmental Engineering*, 125(9), pp. 750–759.

Brennan, A. J. and Madabhushi, S. P. G. (2002) 'Design and performance of a new deep model container for dynamic centrifuge testing', in *The International Conference on Physical Modelling in Geotechnics*, pp. 183–188.

Brown, D. J. (ed.) (2009) *The Arup Journal*. London: Corporate Communications Group.

Byfield, M. P., Davies, J. M. and Dhanalakshmi, M. (2005) 'Calculation of the strain hardening behaviour of steel structures based on mill tests', *Journal of Constructional Steel Research*, 61(2), pp. 133–150.

CEN (2004) 'Eurocode 8: Design of structures for earthquake resistance Part 1: General rules, seismic actions and rules for buildings'.

CEN (2009) 'Eurocode 9: Design of aluminium structures - Part 1-1: General structural rules'.

Chen, Y. H., Liao, W. H., Lee, C. L. and Wang, Y. P. (2006) 'Seismic isolation of viaduct piers by means of a rocking mechanism', *Earthquake Engineering and Structural Dynamics*, 35(6), pp. 713–736.

Chian, S. C., Stringer, M. E. and Madabhushi, S. P. G. (2010) 'Use of automatic sand pourer for loose sand models', in *7th International Conference on Physical Modelling in Geotechnics*. Zurich, Switzerland: Balkema.

Chopra, A. K. (2007) *Dynamics of Structures*. Berkeley.

Chopra, A. K. and Yim, S. C. -S. (1985) 'Simplified earthquake analysis of structures with foundation uplift', *Journal of Structural Engineering*, 111(4), pp. 906–930.

Clough, R. W. and Huckelbridge, A. A. (1977) *Preliminary experimental study of seismic uplift of a steel frame*. Berkeley.

Combault, J., Morand, P. and Pecker, A. (2000) 'Structural response of the Rion-Antirion Bridge', *Proceedings 12th World Conference on Earthquake Engineering*, pp. 1–8.

Craig, W. H. (1995) 'Geotechnical centrifuges: past, present and future', in Taylor, R. N. (ed.) *Geotechnical Centrifuge Technology*. London: CRC Press, pp. 1–18.

Davis, J. R. (1997) 'Coefficients of Friction', in *Concise Metals Engineering Data Book*. ASM International, pp. 190–199.

- DeJong, M. (2009) *Seismic assessment strategies for masonry structures*. Massachusetts Institute of Technology.
- DeJong, M. J. (2012) 'Amplification of Rocking Due to Horizontal Ground Motion', *Earthquake Spectra*, 28(4), pp. 1405–1421.
- Deng, L., Kutter, B. L. and Kunnath, S. K. (2012) 'Centrifuge modeling of bridge systems designed for rocking foundations', *Journal of Geotechnical and Geoenvironmental Engineering*, 138(March), pp. 335–344.
- Dimitrakopoulos, E. G. and DeJong, M. J. (2011) 'Seismic overturning of damped rocking structures', in Papadrakakis, M., Fragiadakis, M., and Plevris, V. (eds) *III ECCOMAS Thematic Conference on Computational Methods in Structural Dynamics and Earthquake Engineering*. Corfu.
- Dimitrakopoulos, E. G. and DeJong, M. J. (2012) 'Overturning of Retrofitted Rocking Structures under Pulse-Type Excitations', *Journal of Engineering Mechanics*, 138, pp. 963–972.
- Dobry, R. and Gazetas, G. (1986) 'Dynamic response of arbitrarily shaped foundations', *Journal of Geotechnical Engineering*, 112(2), pp. 109–135. doi: 10.1061/(ASCE)0733-9410(1986)112:2(136).
- Dupaix, R. B. and Boyce, M. C. (2005) 'Finite strain behavior of poly (ethylene terephthalate) (PET) and poly (ethylene terephthalate)-glycol (PETG)', *Polymer*, 46, pp. 4827–4838.
- Eatherton, M. R., Ma, X., Krawinkler, H., Deierlein, G. G. and Hajjar, J. F. (2014) 'Quasi-Static Cyclic Behavior of Controlled Rocking Steel Frames', *Journal of Structural Engineering*, 140(11), p. 04014083.
- FEMA (2007) 'FEMA 461 - Interim testing protocols for determining the seismic performance characteristics of structural and nonstructural components'.
- Figini, R., Paolucci, R. and Chatzigogos, C. T. (2012) 'A macro-element model for non-linear soil-shallow foundation-structure interaction under seismic loads: theoretical development and experimental validation on large scale tests', *Earthquake Engineering and Structural Dynamics*, 41, pp. 475–493.
- Focke, W. W., Joseph, S., Grimbeek, J., Summers, G. J., Focke, W. W., Joseph, S., Grimbeek, J., Summers, G. J. and Kretzschmar, B. (2016) 'Mechanical properties of ternary blends of ABS + HIPS + PETG', 2559(January).
- Franco, G. and Siembieda, W. (2010) 'Chile's 2010 M8.8 earthquake and tsunami: Initial observations on resilience', *Journal of Disaster Research*, 5(5), pp. 577–590.
- Gajan, S. and Kutter, B. L. (2008) 'Capacity, settlement, and energy dissipation of shallow footings subjected to rocking', *Journal of Geotechnical and Geoenvironmental Engineering*, 134(8), pp. 1129–1141.
- Gajan, S. and Kutter, B. L. (2009) 'Contact Interface Model for Shallow Foundations Subjected to Combined Cyclic Loading', *Journal of Geotechnical and Geoenvironmental Engineering*, 135(March), pp. 407–419.
- Gajan, S., Kutter, B. L., Phalen, J. D., Hutchinson, T. C. and Martin, G. R. (2005) 'Centrifuge modeling of load-deformation behavior of rocking shallow foundations', *Soil Dynamics and Earthquake Engineering*, 25(7–10), pp. 773–783.
- Gajan, S. and Saravanathiiban, D. S. (2011) 'Modeling of energy dissipation in structural

devices and foundation soil during seismic loading', *Soil Dynamics and Earthquake Engineering*. Elsevier, 31(8), pp. 1106–1122. doi: 10.1016/j.soildyn.2011.02.006.

El Gawady, M. A., Ma, Q., Buteerworth, J. W. and Ingham, J. (2011) 'Effects of interface material on the performance of free rocking blocks', *Earthquake Engineering & Structural Dynamics*, 40, pp. 375–392. doi: 10.1002/eqe.

Gazetas, G. (1991) *Foundation Engineering Handbook*. Edited by H. Fang. New York.

Gazetas, G. and Apostolou, M. (2004) 'Nonlinear soil – structure interaction: Foundation uplifting and soil yielding', *Proceedings Third UJNR Workshop on Soil-Structure Interaction*. Menlo Park, California, USA, (1), pp. 1–16.

Gelagoti, F., Kourkoulis, R., Anastasopoulos, I. and Gazetas, G. (2012) 'Rocking-isolated frame structures: Margins of safety against toppling collapse and simplified design approach', *Soil Dynamics and Earthquake Engineering*. Elsevier, 32(1), pp. 87–102.

Gelagoti, F., Kourkoulis, R., Anastasopoulos, I. and Gazetas, G. (2012) 'Rocking isolation of low-rise frame structures founded on isolated footings', *Earthquake Engineering and Structural Dynamics*, 41, pp. 1177–1197.

Giouvanidis, A. I. and Dimitrakopoulos, E. G. (2017) *Nonsmooth dynamic analysis of sticking impacts in rocking structures*, *Bulletin of Earthquake Engineering*. Springer Netherlands.

Giouvanidis, A. I. and Dimitrakopoulos, E. G. (2018) 'Rocking amplification and strong-motion duration', *Earthquake Engineering & Structural Dynamics*, 47, pp. 2094–2116.

Haigh, S. K., Teymur, B., Madabhusi, S. P. G. and Newland, D. E. (2002) 'Applications of wavelet analysis to the investigation of the dynamic behaviour of geotechnical structures', *Soil Dynamics and Earthquake Engineering*, 22(9–12), pp. 995–1005.

Hajjar, J. F., Sesen, H. A., Jampole, E. and Wetherbee, A. (2013) *A synopsis of sustainable structural systems with rocking, self centering, and articulated energy-dissipating fuses*. Boston.

Hamburger, R. O., Rojahn, C., Heintz, J. A. and Mahoney, M. G. (2012) 'FEMA P58: Next-Generation Building Seismic Performance Assessment Methodology', in *15th World Conference on Earthquake Engineering*.

Harden, C., Hutchinson, T., Martin, G. R. and Kutter, B. L. (2005) *Numerical Modeling of the Nonlinear Cyclic Response of Shallow Foundations*.

Heron, C., Haigh, S. and Madabhusi, G. (2014) 'Susceptibility of shallow foundation to rocking and sliding movements during seismic loading', in Ansal, A. (ed.) *Geotechnical, geological and earthquake engineering*, pp. 407–424.

Heron, C. M. (2013) *The dynamic soil structure interaction of shallow foundations on dry sand beds*.

Heron, C. M., Haigh, S. K. and Madabhusi, S. P. G. (2015) 'A new macro-element model encapsulating the dynamic moment–rotation behaviour of raft foundations', *Géotechnique*, 65(5), pp. 442–451.

Housner, G. W. (1963) 'The behaviour of inverted pendulum structures during earthquakes', *Bulletin of Seismological Society of America*, 53(2), pp. 403–417.

Huckelbridge, A. A. (1977) *Earthquake simulation tests of a nine story steel frame with columns allowed to uplift*. Berkeley.

- Hughes, F. E. and Madabhushi, S. P. G. (2018) 'The importance of vertical acceleration in liquefied soils', in *9th International Conference on Physical Modelling in Geotechnics*. London.
- Iwata, Y., Sugimoto, H. and Kuwamura, H. (2005) 'Reparability limit of steel structural buildings based on the actual data of the Hyogoken-Nanbu Earthquake', in *38th Joint Meeting of the Panel on Wind and Seismic Effects*. Gaithersburg, MD.
- Kelly, J. M., Skinner, R. I. and Heine, A. J. (1972) 'Mechanisms of energy absorption in special devices for use in earthquake resistant structures.', *Bulletin of the New Zealand Society for Earthquake Engineering*, 5(3), pp. 63–73.
- Kircher, C. A., Haselton, C. B. and Deierlein, G. G. (2006) *Overview of Ground Motions, ATC-63 Project*. Berkeley, CA. Available at: <http://people.duke.edu/~hpgavin/cee541/ATC63-readme.html>.
- Knappett, J. a., Madden, P. and Caucis, K. (2015) 'Seismic structure–soil–structure interaction between pairs of adjacent building structures', *Géotechnique*, 65(5), pp. 429–441.
- Ko, K.-W., Ha, J.-G., Park, H.-J. and Kim, D.-S. (2019) 'Centrifuge Modeling of Improved Design for Rocking Foundation Using Short Piles', *Journal of Geotechnical and Geoenvironmental Engineering*, 145(8).
- Konstantinidis, D. and Nikfar, F. (2015) 'Seismic response of sliding equipment and contents in base-isolated buildings subjected to broadband ground motions', *Earthquake Engineering & Structural Dynamics*, 44, pp. 865–867.
- Kosbab, B. D. (2010) *Seismic performance evaluation of port container cranes allowed to uplift*. Georgia Institute of Technology.
- Kramer, S. L. (1996) 'Geotechnical Earthquake Engineering'. Prentice Hall.
- Krawinkler, H. (2009) 'Loading histories for cyclic tests in support of performance assessment of structural components', in *Third international conference in experimental earthquake engineering*. Stanford, CA.
- Lilly, J. M. (2017) 'jLab: A data analysis package for Matlab'.
- Lilly, J. M. and Olhede, S. C. (2009) 'Higher-Order Properties of Analytic Wavelets', *IEEE Transactions on signal processing*, 57(1), pp. 146–160.
- Lilly, J. M. and Olhede, S. C. (2010) 'On the analytic wavelet transform', *IEEE Transactions on Information Theory*, 56(8), pp. 4135–4156.
- Lilly, J. M. and Olhede, S. C. (2012) 'Generalized Morse Wavelets as a Superfamily of Analytic Wavelets', *IEEE Transactions on Signal Processing*, 60(11), pp. 6036–6041.
- Liu, W. and Hutchinson, T. C. (2018) 'Numerical investigation of stone columns as a method for improving the performance of rocking foundation systems', *Soil Dynamics and Earthquake Engineering*. Elsevier Ltd, 106, pp. 60–69.
- Liu, W., Hutchinson, T. C., Gavras, A. G., Kutter, B. L. and Hakhmaneshi, M. (2015) 'Seismic Behaviour of Frame-Wall-Rocking Foundation Systems. I: Test Program and Slow Cyclic Results', *Journal of Structural Engineering*, 141(12), p. 04015059.
- Loli, M., Knappett, J. A., Brown, M. J., Anastasopoulos, I. and Gazetas, G. (2014) 'Centrifuge modeling of rocking-isolated inelastic RC bridge piers', *Earthquake Engineering & Structural Dynamics*, 43, pp. 2341–2359.

- Lu, Y., Marshall, A. M. and Hajirasouliha, I. (2016) 'A simplified Nonlinear Sway-Rocking model for evaluation of seismic response of structures on shallow foundations', *Soil Dynamics and Earthquake Engineering*. Elsevier, 81, pp. 14–26.
- Lu, Y. and Wang, Z. (2006) 'Characterization of structural effects from above-ground explosion using coupled numerical simulation', *Computers and Structures*, 84, pp. 1729–1742.
- Ma, Q. T. and Butterworth, J. W. (2010) 'Simplified expressions for modelling rigid rocking structures on two-spring foundations', in *Bulletin of the New Zealand Society for Earthquake Engineering*.
- Ma, Q. T., Butterworth, J. W. and Davidson, B. J. (2005) 'Modelling rocking structures using standard finite elements', *2005 NZSEE Conference*, (20), pp. 1–8.
- Ma, X., Deierlein, G., Eatherton, M., Krawinkler, H., Hajjar, J., Takeuchi, T., Kasai, K., Midorikawa, M. and Hikino, T. (2010) 'Large-scale shaking table tests of steel braced frame with controlled rocking and energy dissipating fuses', in *Proceedings of the 9th U.S. National and 10th Canadian Conference on Earthquake Engineering*. Toronto, Ontario, Canada.
- Madabhushi, G. (2017) *Centrifuge Modelling for Civil Engineers*. CRC Press.
- Madabhushi, S. P. ., Houghton, N. E. and Haigh, S. K. (2006) 'A new automatic sand pourer for model preparation at University of Cambridge', in *6th International Conference on Physical Modelling in Geotechnics*. Hong Kong.
- Madabhushi, S. P. G., Haigh, S. K., Houghton, N. E. and Gould, E. (2012) 'Development of a servo-hydraulic earthquake actuator for the Cambridge Turner beam centrifuge', *International Journal of Physical Modelling in Geotechnics*, 12(2), pp. 77–88.
- Makris, N. (2014) 'A half-century of rocking isolation', *Earthquakes and Structures*, 7(6), pp. 1187–1221.
- Makris, N. (2017) 'Basic Response Functions of Simple Inertioelastic and Inertoviscous Models', *Journal of Engineering Mechanics*, 143(11).
- Makris, N. (2018) 'Seismic isolation: Early history', *Earthquake Engineering & Structural Dynamics*, 48(2), pp. 269–283.
- Makris, N. and Aghagholizadeh, M. (2019) 'Effect of Supplemental Hysteretic and Viscous Damping on Rocking Response of Effect of Supplemental Hysteretic and Viscous Damping on Rocking Response of Free-Standing Columns', *Journal of Engineering Mechanics*, 145(5).
- Makris, N. and Konstantinidis, D. (2003) 'The rocking spectrum and the limitations of practical design methodologies', *Earthquake Engineering and Structural Dynamics*, 32(2), pp. 265–289.
- Makris, N. and Zhang, J. (2001) 'Rocking Response of Anchored Blocks under Pulse-Type Motions', *Journal of Engineering Mechanics*, 127(5).
- Marquis, F., Kim, J. J., Elwood, K. J. and Chang, S. E. (2015) 'Understanding post-earthquake decisions on multi-storey concrete buildings in Christchurch, New Zealand', *Bulletin of Earthquake Engineering*.
- Mason, H. B., Kutter, B. L., Bray, J. D., Wilson, D. W. and Choy, B. Y. (2010) 'Earthquake motion selection and calibration for use in a geotechnical centrifuge', in *7th International Conference on Physical Modelling in Geotechnics*. Zurich, Switzerland.

- Mason, H. B., Trombetta, N. W., Gille, N. W., Lund, J. N., Zupan, J. D., Puangnak, H., Choy, B. Y., Chen, Z., Bolisetti, C., Bray, J. D., Hutchinson, T. C., Fiegel, G. L., Kutter, B. L. and Whittaker, A. S. (2010) *Seismic performance assessment in dense urban environments: centrifuge data report for HBM02*.
- Meek, J. W. (1975) 'Effects of foundation tipping on dynamic response', *Journal of Structural Division*, 101(7), pp. 1297–1311.
- Misiti, M., Misiti, Y., Oppenheim, G. and Poggi, J.-M. (2015) 'Wavelet Toolbox (TM) User's Guide'.
- Muthukumar, S. and DesRoches, R. (2006) 'A Hertz contact model with non-linear damping for pounding simulation', *Earthquake Engineering and Structural Dynamics*, 35, pp. 811–828.
- NEHRP Consultants Joint Venture (2012) *Soil-structure interaction for building structures*.
- Newland, D. E. (1994) 'Wavelet Analysis of Vibration: Part 1-Theory', *Journal of Vibration and Acoustics*, 4(116), pp. 409–416.
- Newland, D.E. (1994) 'Wavelet Analysis of Vibration: Part 2-Wavelet Maps', *Journal of Vibration and Acoustics*, 4(114), pp. 417–425.
- NZS1170.5:2004 (2004) *Structural design actions. Part 5: Earthquake actions - New Zealand*.
- Oztoprak, S. and Bolton, M. D. (2013) 'Stiffness of sands through a laboratory test database', *Geotechnique*, 63(1), pp. 54–70.
- Palmeri, A. and Makris, N. (2008) 'Response analysis of rigid structures rocking on viscoelastic foundation', *Earthquake Engineering and Structural Dynamics*, 37, pp. 1039–1063.
- Pelekis, I. (2015) *Soil-structure interaction for low damage seismic rocking systems*. University of Cambridge. MRes Dissertation.
- Pelekis, I., Madabhushi, G. S. P. and DeJong, M. (2018) 'Experimental identification of frequency content for a rocking structure on dense sand', in *16th European Conference on Earthquake Engineering*. Thessaloniki, Greece.
- Pelekis, I., Madabhushi, G. S. P. and DeJong, M. J. (2017) 'A Centrifuge Investigation of two different Soil-Structure Systems with Rocking and Sliding on Dense Sand', in Papadrakakis, M. and Fragiadakis, M. (eds) *6th ECCOMAS Thematic Conference on Computational Methods in Structural Dynamics and Earthquake Engineering*. Rhodes Island, Greece, pp. 15–17.
- Pelekis, I., Madabhushi, G. S. P. and DeJong, M. J. (2018a) 'Modelling of Rocking Structures in a Centrifuge', in *9th International Conference on Physical Modelling in Geotechnics*. London, United Kingdom.
- Pelekis, I., Madabhushi, G. S. P. and DeJong, M. J. (2018b) 'Soil behaviour beneath buildings with structural and foundation rocking', *Soil Dynamics and Earthquake Engineering*, 123, pp. 48–63.
- Pelekis, I., Madabhushi, S. P. G. and DeJong, M. J. (2018) 'Seismic performance of buildings with structural and foundation rocking in centrifuge testing', *Earthquake Engineering and Structural Dynamics*, 47(12), pp. 2390–2409.
- Pelekis, I., McKenna, F., Madabhushi, G. S. P. and DeJong, M. (2019) 'Finite element

- modelling of buildings with structural and foundation rocking on dry sand', *Earthquake Engineering and Structural Dynamics*. Available at: In review.
- Perkins, S. W. and Madson, C. R. (2000) 'Bearing Capacity of Shallow Foundations on Sand: A Relative Density Approach', *Journal of Geotechnical and Geoenvironmental Engineering*, 126(6), pp. 0521–0530.
- Piano, R. (1998) *Maison Hermes, Renzo Piano Building Workshop*. Available at: <http://www.rpbw.com/project/2/maison-hermes/>.
- Pisanò, F. and Jeremić, B. (2014) 'Simulating stiffness degradation and damping in soils via a simple visco-elastic – plastic model', *Soil Dynamics and Earthquake Engineering*, 63, pp. 98–109.
- Plaut, R. H., Fielder, W. T. and Virgin, L. N. (1996) 'Fractal behavior of an asymmetric rigid block overturning due to harmonic motion of a tilted foundation', *Chaos, Solitons & Fractals*, 7(2), pp. 177–196.
- Pokrovsky, G. I. and Fedorov, I. S. (1936) 'Studies of soil pressures and soil deformations by means of a centrifuge', in *Proceedings of the First International Conference ISSMFE*. Harvard, p. 70.
- Pollino, M. and Bruneau, M. (2007) 'Seismic retrofit of bridge steel truss piers using a controlled rocking approach', *Journal of Bridge Engineering*, 12(5), pp. 600–610.
- Priestley, M. J. N., Evison, R. J. and Carr, a. J. (1978) 'Seismic response of structures free to rock on their foundations', *Bulletin of the New Zealand Society for Earthquake Engineering*, 11(3), pp. 141–150.
- Psycharis, I. N. (1983) 'Dynamics of flexible systems with partial lift-off', *Earthquake Engineering & Structural Dynamics*, 11(4), pp. 501–521.
- Psycharis, I. N. (1991) 'Effect of base uplift on dynamic response of SDOF structures', *Journal of Structural Engineering*, 117(3), pp. 733–754.
- Psycharis, I. N. and Jennings, C. (1985) 'Uphrow of objects due to horizontal impulse excitation', *Bulletin of Seismological Society of America*, 75(2), pp. 543–561.
- Psycharis, I. N. and Jennings, P. C. (1983) 'Rocking of slender rigid bodies allowed to uplift', *Earthquake Engineering and Structural Dynamics*, 11(1), pp. 57–76.
- Raychowdhury, P. (2008) *Nonlinear Winkler-based Shallow Foundation Model for Performance Assessment of Seismically Loaded Structures*. UC San Diego.
- Raychowdhury, P. and Hutchinson, T. C. (2009) 'Performance evaluation of a nonlinear Winkler-based shallow foundation model using centrifuge test results', *Earthquake Engineering and Structural Dynamics*, 38, pp. 679–698.
- Ruiz-garcía, J. and Negrete-Manriquez, J. C. (2011) 'Evaluation of drift demands in existing steel frames under as-recorded far-field and near-fault mainshock-aftershock seismic sequences', *Engineering Structures*. Elsevier Ltd, 33(2), pp. 621–634.
- Sachdeva, G., Chakraborty, S. and Ray-Chaudhuri, S. (2018) 'Seismic response control of a structure isolated by flat sliding bearing and nonlinear restoring spring: Experimental study for performance evaluation', *Engineering Structures*. Elsevier, 159, pp. 1–13.
- Schau, H. and Johannes, M. (2014) 'Numerical analysis of rocking of unanchored bodies subjected to seismic load using Finite Element analyses', in Cunha, A., Caetano, E., Ribeiro, P., and Müller, G. (eds) *Proceedings of the 9th Interantional Conference on Structural*

*Dynamics, EURO DYN*. Porto, Portugal, pp. 373–380.

Schellenberg, A. (2014) *Flat Slider Bearing Element*. Available at: [http://opensees.berkeley.edu/wiki/index.php/Flat\\_Slider\\_Bearing\\_Element](http://opensees.berkeley.edu/wiki/index.php/Flat_Slider_Bearing_Element).

Schellenberg, A., Maffei, J., Telleen, K. and Ward, R. (2013) 'Structural analysis and application of wind loads to solar arrays', *Journal of Wind Engineering and Industrial Aerodynamics*. Elsevier, 123, pp. 261–272.

Schofield, A. N. (1981) 'Dynamic and Earthquake Geotechnical Centrifuge Modelling'.

Scott, M. H. and Fenves, G. L. (2010) 'Krylov Subspace Accelerated Newton Algorithm: Application to Dynamic Progressive Collapse Simulation of Frames', *Journal of Structural Engineering*, 136(May), pp. 473–480.

Seed, H. B. and Idriss, I. M. (1970) *Soil Moduli and Damping Factors for Dynamic Analysis*, *Earthquake Engineering Research Center*.

Sextos, A. G., Mylonakis, G. E. and Mylona, E. V. (2015) 'Rotational excitation of bridges supported on pile groups in soft or liquefiable soil deposits', *Computers and Structures*. Elsevier Ltd, 155, pp. 54–66.

Sharpe, R. D. and Skinner, R. I. (1983) 'The seismic design of an industrial chimney with rocking base', *Bulletin of the New Zealand National Society for Earthquake Engineering*, 16(2), pp. 98–106.

Shepley, P. (2013) *Water injection to assist pile jacking*. University of Cambridge. PhD Thesis.

Sinha, S. K., Feng, Y., Yang, H., Wang, H., Nebojsa, O., David, B. M. and Boris, J. (2017) '3D Non-Linear Modeling and Its Effects in Earthquake Soil-Structure Interaction', in *Transactions, SMiRT-24*. Busan, Korea.

Spanos, P. D. and Koh, A.-S. (1984) 'Rocking of Rigid Blocks due to Harmonic Shaking', *Journal of Engineering Mechanics*, 110(11), pp. 1627–1642.

Taylor, P. W., Barlett, P. E. and Wiessing, P. R. (1980) 'Foundation Rocking under Earthquake Loading', *Le Mouvement des Semelles dans les Tremblements de Terre*, pp. 313–322.

The MathWorks Inc (2015) 'MATLAB and Wavelet Toolbox Release 2015b'.

Thiers-Moggia, R. and Málaga-Chuquitaype, C. (2018) 'Seismic protection of rocking structures with inerters', *Earthquake Engineering & Structural Dynamics*, 48(5), pp. 528–547. doi: 10.1002/eqe.3147.

Torrence C. and Compo G. (1998) 'A practical guide to wavelet analysis.', *Bulletin of the American Meteorological Society*, 79 (1), pp. 61--78.

Tremblay, R., Poirier, L., Bouaanani, N., Leclerc, M., Rene, V., Fronteddu, L. and Rivest, S. (2008) 'Innovative Viscously Damped Rocking Braced Steel Frames', in *The 14th World Conference on Earthquake Engineering (14 WCEE), October 12-17*. Beijing, China.

Trombetta, N. W., Asce, S. M., Mason, H. B., Asce, M., Hutchinson, T. C., Zupan, J. D., Bray, J. D., Asce, F. and Kutter, B. L. (2014) 'Nonlinear soil-foundation-structure and structure-soil-structure interaction: Centrifuge test observations', (1), p. 04013057.

Trombetta, N. W., Mason, H. B., Chen, Z., Hutchinson, T. C., Bray, J. D. and Kutter, B. L. (2013) 'Nonlinear dynamic foundation and frame structure response observed in geotechnical centrifuge experiments', *Soil Dynamics and Earthquake Engineering*.

Elsevier, 50, pp. 117–133.

Tyler, R. G. (1978) 'Tapered steel energy dissipators for earthquake resistant structures', *Bulletin of the New Zealand National Society for Earthquake Engineering*, 11(4).

Vassiliou, M. . and Makris, N. (2011) 'Estimating Time Scales and Length Scales in Pulselike Earthquake Acceleration Records with Wavelet Analysis', *Bulletin of the Seismological Society of America*, 2(101), pp. 596–618.

Vassiliou, M. F., Mackie, K. R. and Stojadinović, B. (2017) 'A finite element model for seismic response analysis of deformable rocking frames', *Earthquake Engineering & Structural Dynamics*, 46(3), pp. 447–466.

Veletsos, A. S. and Meek, J. W. (1974) 'Dynamic behaviour of building-foundation systems', *Earthquake Engineering & Structural Dynamics*, 3(January), pp. 121–138.

Via, I. and Stretching, U. (2011) 'Superior tensile extensibility of PETG/PC amorphous blends', 29(1), pp. 125–132.

Wiebe, L., Christopoulos, C., Tremblay, R. and Leclerc, M. (2013) 'Mechanisms to limit higher mode effects in a controlled rocking steel frame. 1: Concept, modelling, and low-amplitude shake table testing', *Earthquake Engineering & Structural Dynamics*, 42, pp. 1053–1068.

Wotherspoon, L. and Pender, M. (2010) 'Effect of Uplift Modelling on the Seismic Response of Shallow Foundations', in *Interantional Conferences on Recent Advances in Geotechnical Earthquake Engineering and Soil Dynamics*. Missouri.

Yim, S. C.-S. and Chopra, A. K. (1984) 'Dynamics of Structures on Two Spring Foundation Allowed to Uplift', *Journal of Engineering Mechanics*, 110(7), pp. 1124–1146.

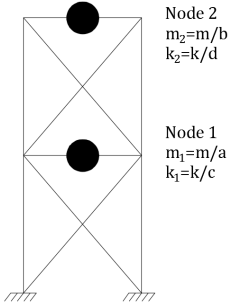
Yim, S. C.-S. and Chopra, A. K. (1985) 'Simplified earthquake analysis of multistory structures with foundation uplift', I(12), pp. 2708–2731.

Yu, T. X. and Zhang, L. C. (1995) *Plastic bending: Theory and applications*.

# 10 APPENDICES

## Appendix A: Design of RA & RB building models

### 10.A.1 General eigenvalue problem, sections & typical buckling checks

<p><math>S_A = a_g 2.5 \cdot 1.2 \cdot 0.5 / T_1 = 3.15 m/s^2, T_1 = 0.7 s</math></p> <p>Solving for the half-frame and from the sketch</p> $\begin{vmatrix} \frac{k}{d} - \omega^2 \frac{m}{b} & -\frac{k}{d} \\ -\frac{k}{d} & \frac{k}{d} + \frac{k}{c} - \omega^2 \frac{m}{a} \end{vmatrix} = 0 \Rightarrow$ <p><math>k = k(m, a, b, c, d, T_1 = 0.7 s) = k(m, a, b, c, d) \quad (1)</math></p>	<p>Solve <math>k</math> with respect to the first period and as a function of <math>m, a, b, c, d</math></p>  <p>Node 2 <math>m_2 = m/b</math> <math>k_2 = k/d</math></p> <p>Node 1 <math>m_1 = m/a</math> <math>k_1 = k/c</math></p>
$\frac{k}{c} = \frac{2 \cdot 12 E_c I_c}{L_c^3} + 2 \frac{E_b A_b}{L_b} \cos(\theta)^2 \quad (2)$ <p><math>E_c</math>: Young's Modulus for columns  <math>I_c</math>: Moment of inertia of column's section  <math>L_c</math>: Clear length of column  <math>E_b</math>: Young's Modulus for bracing members  <math>A_b</math>: Area of bracing's cross section  <math>L_b</math>: Length of bracing's member  <math>\theta</math>: Angle of rotation of a bracing member</p>	<p>Stiffness <math>k/c</math> is provided from columns and braces</p>
$\frac{k}{c} = \frac{2 \cdot 12 E_c I_c}{L_c^3} + 2 \frac{L_e^2 P_c}{L_b r_c^2 \pi^2} \cos(\theta)^2 \Rightarrow$	<p>Replacing in (2) <math>E_b</math> with Euler's buckling load</p>

<p><math>P_c</math>: buckling load of a bracing member in <math>c</math> stiffness  <math>L_e = 0.75l_b</math>, 0.75: Assuming a semi – fixed bracing  <math>r_c</math>: radius of gyration for the bracing in the <math>c</math> stiffness  Similarly, <math>P_d = P_d(m, a, b, c, d)</math>  <math>r_d</math>: radius of gyration for the bracing in the <math>d</math> stiffness</p>	<p>expression and solving with respect to that yields (3)</p>
<p><math>E_c = 70GPa</math>, (aluminium), <math>I_c = 0.10^3 \cdot 1.2/12m^4</math>,  <math>L_c = 7m</math>, (a rectangular section bending at its weak axis)</p>	<p>Selection of column properties</p>
<p>Bracing: A thick circular hollow section in the <math>c</math> stiffness and a thin circular hollow section in the <math>d</math> stiffness made of PETG</p> <p><math>E_b = 2GPa</math>, (PETG)  <math>D_c^{ext} = 0.0145m</math>, (1/40 scaled)  <math>D_c^{int} = 0.0134m</math>, (1/40 scaled)  <math>D_d^{ext} = 0.0113m</math>, (1/40 scaled)  <math>D_d^{int} = 0.0107m</math>, (1/40 scaled)  <math>l_b = \sqrt{(6^2 + 7^2)} = 9.22m</math>, <math>l_e = 0.75l_b = 6.91m</math></p>	<p>Selection of properties of braces</p> <p>External and internal diameters of available PETG sections online</p>
<p>If in mode 1, <math>\varphi_2 = 1</math>, then</p> $\varphi_1 = \frac{\frac{k}{d} - \left(\frac{2\pi}{T}\right)^2 \frac{m}{b}}{\frac{k}{d}} = \varphi_1(m, a, b, c, d)$ <p>This results in having</p> <p><math>M = M(m, a, b, c, d)</math>, <math>L = L(m, a, b, c, d)</math>  <math>\Gamma = \Gamma(m, a, b, c, d)</math>, <math>f_2 = f_2(m, a, b, c, d)</math>  <math>f_1 = f_1(m, a, b, c, d)</math>, <math>V = f_2 + f_1 = V(m, a, b, c, d)</math></p>	<p>For simplicity, only mode 1 is considered</p>

$N_c = \frac{\frac{V}{2} - \frac{12E_c I_c}{L_c^3} \frac{V}{c}}{\frac{\sqrt{2}}{2}} = N_c(m, a, b, c, d)$ <p>Similarly,</p> $N_d = \frac{\frac{f_2}{2} - \frac{12E_c I_c}{L_c^3} \frac{f_2}{d}}{\frac{\sqrt{2}}{2}} = N_d(m, a, b, c, d)$	<p>Using equilibrium</p> <p>Axial force in one of the two bracing members in the c storey.</p> <p>Axial force in one of the two bracing members in the d storey</p>
<p>The area of a bracing member is connected to a varying stiffness as:</p> $A_{bc} = \frac{\frac{k}{c} - \frac{2 \cdot 12E_c I_c}{L_c^3}}{2 \frac{E_b}{L_b} \cos(\theta)^2} = A_{bc}(m, a, b, c, d)$ $A_{bd} = \frac{\frac{k}{d} - \frac{2 \cdot 12E_c I_c}{L_c^3}}{2 \frac{E_b}{L_b} \cos(\theta)^2} = A_{bd}(m, a, b, c, d)$	
<p>Part of the third requirement to be satisfied: No buckling in the bracing. If <math>a = b = c = 1</math>, then the supplied stiffness from the selected sections should lead to a <math>d</math> and <math>m</math> such that the axial force in the bracing is not too large and smaller than the buckling load which is inherently predetermined from the member slenderness. The following set of inequality and equation(s) was solved in <i>Mathematica</i>:</p> $\left\{ \begin{array}{l} P_c(m, 1, 1, 1, d) \geq 1.5N_c(m, 1, 1, 1, d) \\ \frac{\pi}{4} \left( \frac{40D_c^{ext}}{2} \right)^4 - \frac{\pi}{4} \left( \frac{40D_c^{int}}{2} \right)^4 = r_c^2 A_{bc}(m, 1, 1, 1, d) \\ \frac{\pi}{4} \left( \frac{40D_d^{ext}}{2} \right)^4 - \frac{\pi}{4} \left( \frac{40D_d^{int}}{2} \right)^4 = r_c^2 A_{bd}(m, 1, 1, 1, d) \end{array} \right\}$	<p>A factor of safety at least 1.5 against member buckling</p>

<p>The two latter equations simply ensure and verify that  <math>I_c = r_c^2 A_{bc}</math> &amp; <math>I_d = r_d^2 A_{bd}</math></p> <p>The solution was found to be <math>m = 26595.1kg</math> and <math>d = 2.14</math>.</p> <p>In this case <math>N_c(26595.1,1,1,1,2.14) = 101.4KN</math> and  <math>N_d(26595.1,1,1,1,2.14) = 67.0KN</math>, whereas</p> $P_c(26595.1,1,1,1,2.14) = \frac{\pi^2 E_b I_b}{L_e^2} =$ $= \frac{\pi^2 \cdot 2000000 \cdot \left[ \frac{\pi}{4} \left( \frac{40 \cdot 0.0145}{2} \right)^4 - \frac{\pi}{4} \left( \frac{40 \cdot 0.0134}{2} \right)^4 \right]}{(0.75 \cdot \sqrt{6^2 + 7^2})^2}$ $= 620.7KN \geq 1.5N_c$ <p>Similarly,</p> $P_d(26595.1,1,1,1,2.14)$ $= \frac{\pi^2 \cdot 2000000 \cdot \left[ \frac{\pi}{4} \left( \frac{40 \cdot 0.0113}{2} \right)^4 - \frac{\pi}{4} \left( \frac{40 \cdot 0.0107}{2} \right)^4 \right]}{(0.75 \cdot \sqrt{6^2 + 7^2})^2}$ $= 165.9KN \approx 2.5N_d$	<p>Member buckling check in bracing</p> <p>Check in the <math>c</math> storey (bottom)</p> <p>Check in the <math>d</math> storey (top)</p>
<p>For <math>m = 26595.1kg</math> the half-mass of the total frame would be</p> $HalfMass(m, a, b, c, d) = \frac{m}{a} + \frac{m}{b} =$ $= \frac{26595.1}{1} + \frac{26595.1}{1} = 53190.2kg$ <p>And the total mass of the frame would be</p> $TotalMass = 2 \cdot 53190.2 = 106380.4kg$ <p>The static pressure on an assumed striped footing would be</p> $\sigma_{st} = \frac{2gHalfMass(26595.1,1,1,1,2.14)}{2((L_{cw} + 0.4)L_c/4)}$	<p>Check on static pressure of soil</p> <p>Acceptable for the 3<sup>rd</sup> requirement</p>

$= \frac{2 \cdot 9.81 \cdot 53190.2}{2((6 + 0.4) 6/4)} = 54.4KPa$	
<p>Following the eigenvalue problem, the mass participation of the first mode would be</p> $\mathcal{M} = \mathcal{M}(m, a, b, c, d) = \frac{\Gamma \cdot L}{HalfMass} \cdot 100$ $= \mathcal{M}(26595.1, 1, 1, 1, 2.14) = 84.1\%$	<p>Check on mass participation</p>
<p>Design of slabs</p> <p>For <math>m = 26595.1kg</math> and taking into account the mass of columns and bracings being lumped at the storeys, the dimensions of the slab can be determined.</p> <p>More specifically:</p> <p><math>TM</math> = total mass of complete frame in model scale</p> <p><math>TM_{ts}</math> = total mass of top slab in model scale</p> <p><math>TM_{bs}</math> = total mass of bottom slab in model scale</p> <p><math>e_{ts}</math> = top storey columns and bracings mass</p> <p><math>e_{bs}</math> = bottom storey columns and bracing mass</p> <p><math>t_{ts}</math> = thickness of top slab in model scale</p> <p><math>t_{bs}</math> = thickness of bottom slab in model scale</p> $TM = \frac{2HalfMass(26595.1, 1, 1, 1, 2.14)}{G^3} = \frac{2 \cdot 53190.2}{40^3}$ $= 1.66Kg$ $TM_{ts} = \frac{TM}{2} - \frac{e_{ts}}{2} = 0.75Kg$ $TM_{bs} = \frac{TM}{2} - \frac{e_{ts}}{2} - \frac{e_{bs}}{2} = 0.67Kg$ $t_{ts} = \frac{TM_{ts}}{\frac{6}{G} \frac{6}{G} \cdot 2700} = 0.0124m$ $t_{bs} = \frac{TM_{bs}}{\frac{6}{G} \frac{6}{G} \cdot 2700} = 0.0110m$	<p>The slabs are considered rigid</p> <p><math>G = 40</math></p> <p>The column's width increased from 1.2m to 1.7m to accommodate both bracing sections, but that will have little difference on the shear model for a column width of 1.2m.</p>

### 10.A.2 Load cases

Two load cases are considered here. The first ( $G + E, a_g = 0.16g, T_1 = 0.66s, S_A = 3.56m/s^2$ ) is slightly before the onset of uplift and *SAP2000* is used to define the spectral response based on the SRSS method. The second is at the angle of maximum rotation which is assumed as the angle of slenderness of the building based on its geometry and mass distribution. To estimate the loading in that case a static approach was used with *SAP2000* ("Uplift, static", SU case). The bottom storey is considered fixed at the top ends of the columns while the total gravity load is applied at the end of the supporting column. The total resultant seismic shear from the *E* case is also applied at the end of the same column (Figure 10.1).

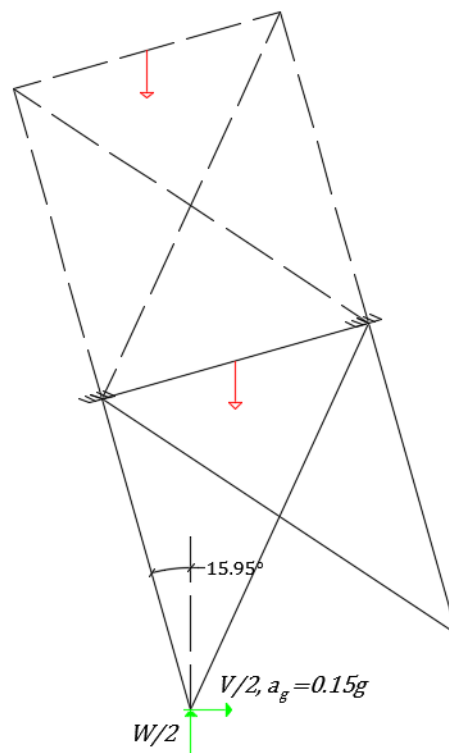


**Figure 10.1: Static approach in the half frame (hence, forces are factored with  $\frac{1}{2}$ ) for estimating the loadings due to extreme rotation**

Half of the frame was modelled. Therefore, the force from gravity is

$$9.81 \frac{TotalMass}{2} = 9.81 \cdot \frac{106380.4}{2} = 521.8KN \rightarrow \frac{W}{2}$$

The above expression simply means that the total weight of the frame from its mass is applied on the two corner columns that touch the ground surface and each of them takes the half of that load. The half load is used in *SAP2000*, since only one bay is modelled.

Similarly, the seismic force would be ( $a_g = 0.15g$ )



Load Case	$N_{Ed}^{Compression}$ (KN)	$N_{Ed}^{Tension}$ (KN)
G+E/s HB (RA)	-137	137
G+E/s FB (RB)	-122	122
Uplift, static (SU)	-412	N/A

Tensional resistance

$$N_{T,Rd} = \frac{A_{net}f_0}{1.1} = \frac{0.029 \cdot 50000}{1.1} = 1318KN > N_{Ed}^{Tension}$$

$$= 121KN$$

Compressional resistance

$$N_{C,Rd} \approx N_{T,Rd} > N_{Ed}^{Compression} = 412KN$$

Member flexural buckling:

$$N_{b,Rd} = \frac{\pi^2 EI}{L_e^2} = \frac{\pi^2 \cdot 2000000 \cdot \left[ \frac{\pi}{4} \left( \frac{40 \cdot 0.0145}{2} \right)^4 - \frac{\pi}{4} \left( \frac{40 \cdot 0.0134}{2} \right)^4 \right]}{(0.75 \cdot \sqrt{6^2 + 7^2})^2}$$

$$= 620KN > N_{Ed}^{Compression} = 412KN$$

Local buckling of thickness:

$$N_{b,Rd} = \frac{EA_{net}}{\sqrt{3(1-\nu^2)}} \frac{t}{r} \cdot 0.6 = \frac{0.6EA_{net}}{\sqrt{3(1-\nu^2)}} \frac{\frac{D_c^{ext} - D_c^{int}}{2}}{\frac{D_c^{ext} + D_c^{int}}{4}} = \frac{0.6 \cdot 2000 \cdot 0.029}{\sqrt{3(1-0.33^2)}} \frac{0.00056}{0.006975} = 1708KN > N_{Ed}^{Compression}$$

$$= 412KN$$

Bracing of top (d) story:

Gross Area:

$$D_d^{ext} = 0.0113m, (1/40 \text{ scaled})$$

$$D_d^{int} = 0.0107m, (1/40 \text{ scaled})$$

Eurocode 3 Part 1.6, buckling stress

0.6 is a factor for very long tubular shell structures, EC3 1.6 Annex D D1.2.1 (D10)

$$d = \frac{0.208}{40} = 5.2mm$$

(scaled)

$$A_g = \pi \left( \frac{40 \cdot 0.0113}{2} \right)^2 - \pi \left( \frac{40 \cdot 0.0107}{2} \right)^2 = 0.0166m^2$$

Net Area:

Assume a hole of a diameter of  $d = 0.208m$  for a pin connection, two holes in total, diametrically opposite,

$$A_{net} \approx A_g - 2 \cdot 0.208 \cdot \frac{40(0.0113 - 0.0107)}{2} = 0.0116m^2$$

Load Case	$N_{Ed}^{Compression}$ (KN)	$N_{Ed}^{Tension}$ (KN)
G+E/s HB (RA)	-75	75
G+E/s FB (RB)	-80	80
Uplift, static (SU)	N/A	N/A

Tensional resistance:

$$N_{T,Rd} = \frac{A_{net} f_0}{1.1} = \frac{0.0116 \cdot 50000}{1.1} = 527KN > N_{Ed}^{Tension} = 75$$

Compressional resistance:

$$N_{C,Rd} \approx N_{T,Rd} > N_{Ed}^{Compression} = 75KN$$

Member flexural buckling:

$$N_{b,Rd} = \frac{\pi^2 EI}{L_e^2} = \frac{\pi^2 \cdot 2000000 \cdot \left[ \frac{\pi}{4} \left( \frac{40 \cdot 0.0113}{2} \right)^4 - \frac{\pi}{4} \left( \frac{40 \cdot 0.0107}{2} \right)^4 \right]}{(0.75 \cdot \sqrt{6^2 + 7^2})^2} = 166KN > N_{Ed}^c = 75KN$$

Local buckling of thickness:

Eurocode 3 Part 1.6, buckling stress

0.6 is a factor for very long tubular shell structures,

EC3 1.6 Annex D D1.2.1 (D10)

$$N_{b,Rd} = \frac{EA_{net}}{\sqrt{3(1-\nu^2)}} \frac{t}{r} \cdot 0.6 = \frac{0.6EA_{net}}{\sqrt{3(1-\nu^2)}} \frac{D_d^{ext} - D_d^{int}}{2} =$$

$$\frac{0.6 \cdot 2000 \cdot 0.0166}{\sqrt{3(1-0.33^2)}} \frac{0.0003}{0.0055} = 664KN > N_{Ed}^{Compression}$$

$$= 75KN$$

### 10.A.4 Design of connections

Steel bolts will be used (Table 10.1, CEN 2009).

**Table 10.1: Selection of steel bolts (EC9, Table 8.1, Table 8.5, (8.9) & (8.17))**

Bolt Class	$f_{yb}$ (MPa)	$f_{ub}$ (MPa)	$a_v$	$\gamma_{M2}$	Scaled	Scaled	Scaled	Scaled	Prototype ( $\cdot G^2$ )	Prototype ( $\cdot G^2$ )
					$d$ (m)	$A$ (m <sup>2</sup> )	$F_{v,Rd}$ (N)	$F_{t,Rd}$ (N)	$F_{v,Rd}$ (KN)	$F_{t,Rd}$ (KN)
4.6	240	400	0.6	1.25	0.003	7.07E-06	2261	2035	3617	3256
4.8	320	400	0.5	1.25	0.003	7.07E-06	2261	2035	3617	3256
5.6	300	500	0.6	1.25	0.003	7.07E-06	2826	2543	4522	4069
5.8	400	500	0.5	1.25	0.003	7.07E-06	2826	2543	4522	4069
6.8	480	600	0.5	1.25	0.003	7.07E-06	3391	3052	5426	4883
8.8	640	800	0.6	1.25	0.003	7.07E-06	4522	4069	7235	6511
10.9	900	1000	0.5	1.25	0.003	7.07E-06	5652	5087	9043	8139

Slot for column in the footing (Figure 10.2):	EC9-1-1 8.5.1															
$\varepsilon = 0.98, d_0 = d + 0.1 = 3.1mm \approx 3mm,$																
$t = 2.5mm$ (scaled), $f_u = 300MPa$																
Minimum and maximum spacing for a compression member	Table 8.2 Columns 1, 2 & 5															
<table border="1"> <thead> <tr> <th>Distances &amp; Spacings (mm) (scaled)</th> <th>Minimum (mm)</th> <th>Maximum (mm)</th> </tr> </thead> <tbody> <tr> <td><math>e_1 = 3.25</math></td> <td><math>1.2d_0 = 1.2 \cdot 3 = 3.6</math></td> <td><math>12t = 12 \cdot 2.5 = 30</math></td> </tr> <tr> <td><math>e_2 = 8.74</math></td> <td><math>1.2d_0 = 1.2 \cdot 3 = 3.6</math></td> <td><math>12t = 12 \cdot 2.5 = 30</math></td> </tr> <tr> <td><math>p_1 = 13.95</math></td> <td><math>2.2d_0 = 2.2 \cdot 3 = 6.6</math></td> <td><math>14t = 14 \cdot 2.5 = 36</math></td> </tr> <tr> <td><math>p_2 = 18.82</math></td> <td><math>2.4d_0 = 2.4 \cdot 3 = 7.2</math></td> <td><math>14t = 14 \cdot 2.5 = 36</math></td> </tr> </tbody> </table>	Distances & Spacings (mm) (scaled)	Minimum (mm)	Maximum (mm)	$e_1 = 3.25$	$1.2d_0 = 1.2 \cdot 3 = 3.6$	$12t = 12 \cdot 2.5 = 30$	$e_2 = 8.74$	$1.2d_0 = 1.2 \cdot 3 = 3.6$	$12t = 12 \cdot 2.5 = 30$	$p_1 = 13.95$	$2.2d_0 = 2.2 \cdot 3 = 6.6$	$14t = 14 \cdot 2.5 = 36$	$p_2 = 18.82$	$2.4d_0 = 2.4 \cdot 3 = 7.2$	$14t = 14 \cdot 2.5 = 36$	
Distances & Spacings (mm) (scaled)	Minimum (mm)	Maximum (mm)														
$e_1 = 3.25$	$1.2d_0 = 1.2 \cdot 3 = 3.6$	$12t = 12 \cdot 2.5 = 30$														
$e_2 = 8.74$	$1.2d_0 = 1.2 \cdot 3 = 3.6$	$12t = 12 \cdot 2.5 = 30$														
$p_1 = 13.95$	$2.2d_0 = 2.2 \cdot 3 = 6.6$	$14t = 14 \cdot 2.5 = 36$														
$p_2 = 18.82$	$2.4d_0 = 2.4 \cdot 3 = 7.2$	$14t = 14 \cdot 2.5 = 36$														

$$\frac{p_1}{t} = \frac{G \cdot 13.95}{G \cdot 2.5} = 5.58 < 9\epsilon$$

= 9 · 0.98 = 8.82, local buckling between the fasteners need not to be checked

Table 8.2 note 2)

Shear failure in bolts (Figure 10.2)

Axial load from the column	$N_{Ed}$
$a_g = 0.16g$	-639KN
Uplift, static (SU)	-419KN

Shear force considered,  $F_{v,Ed} = |N_{Ed}| = 639KN$

For two 10.9M3 bolts (model scale, Table 10.1) with 4 shear planes in total, that would be  $F_{v,Rd} = 4 \cdot 9043 = 36172KN > 639KN$  (prototype) (scale 400N)

Material: silver steel, 280MPa->1400N- per slot (model)

Bearing failure in the aluminium column (plate)

$$F_{b,Rd} = \frac{k_1 a_b f_u dt}{\gamma_{M2}}$$

Calculation of  $a_b, f_{ub}/f_u = 1000/300 = 3.33$

End bolts:  $a_d = e_1/3d_0 = 3.25/3 \cdot 3 = 0.36$

Inner bolt:  $a_d = (p_1/3d_0) - 0.25 = (13.95/3 \cdot 3) - 0.25$

= 1.3

Edge bolts:  $(2.8 \cdot \frac{e_2}{d_0}) - 1.7 = (2.8 \cdot \frac{8.74}{3}) - 1.7 = 6.45 \rightarrow 2.5$

Inner bolts:  $(1.4 \cdot \frac{p_2}{d_0}) - 1.7 = (1.4 \cdot \frac{18.82}{3}) - 1.7 = 7.08 \rightarrow 2.5$

For simplicity,  $a_b = \min(0.66, 1.3, 3.33, 1), k_1 = 2.5,$

$$F_{b,Rd} = 0.8 \frac{k_1 a_b f_u dt}{\gamma_{M2}}$$

Table 8.5

(8.11)-(8.16)

(8.12)

(8.13)

(8.14)

(8.15)

(8.16)



For two 10.9M3 bolts (model scale) with 2x2 shear planes in total, that would be  $F_{v,Rd} = 4 \cdot 9043KN$  (prototype)

Bearing capacity of PETG circular hollow section:

It is assumed that the contact stress due to tension is distributed in the hole of the tubular PETG section as if the bracing member was a plate element. In this case, the expression for a pin connection could be used from EC9-1-1.

Four holes will be used in total:

$$F_{b,Rd} = \frac{1.5tdf_{0,min}}{\gamma_{M1}}, f_{0,min} = f_0^{PETG} \approx 50MPa$$

$$F_{b,Rd}^{c \text{ bracing}} = 4 \frac{1.5 \cdot 0.00055 \cdot 0.003 \cdot 50000 \cdot G^2}{1.1} = 720KN$$

> 137KN

$$F_{b,Rd}^{d \text{ bracing}} = 4 \frac{1.5 \cdot 0.0003 \cdot 0.003 \cdot 50000 \cdot G^2}{1.1} = 393KN$$

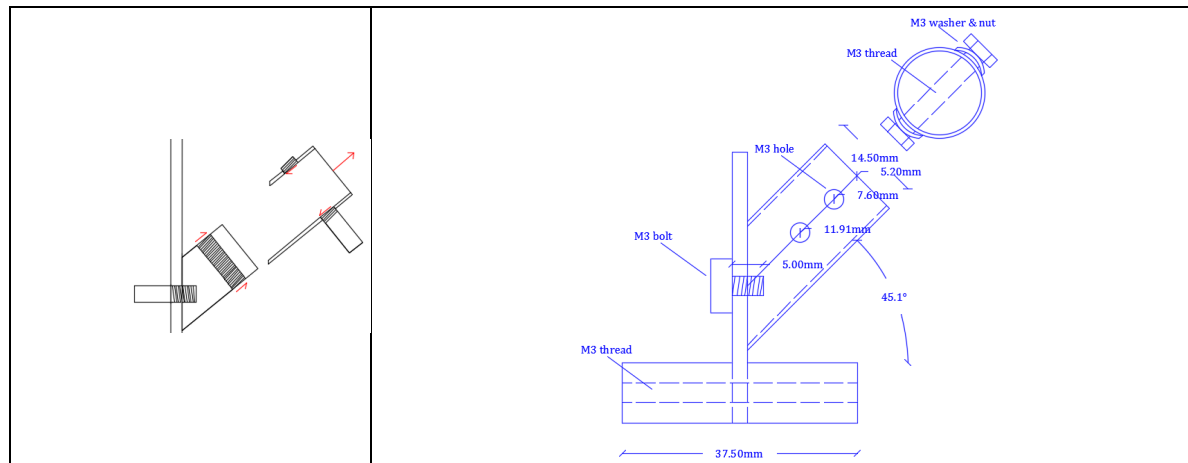
> 75KN

Table 8.7

$t$ , thickness of tube section

Table 8.7

Consider  $\gamma_{M1} = \gamma_{M1}^{PETG} = 1.1$



**Figure 10.3: Connection of the PETG bracing element to the aluminium volume (bottom) and typical shear mode failure (top)**

Mode of failure in the bracing: block tearing for fastening

$$V_{eff,1,Rd} = \frac{f_u A_{nt}}{\gamma_{M2}} + \frac{f_0 A_{nv}}{\sqrt{3}\gamma_{M1}}, f_u = f_0 = f_0^{PETG} \approx 50MPa$$

Bottom c bracing

$$A_{nt} \approx 2dt = 2 \cdot 0.003 \cdot 0.00055 \cdot G^2 = 0.00528m^2$$

EC9 8.5.2.2 (1) & (2),

Figure 8.5-1

Eq 8.1



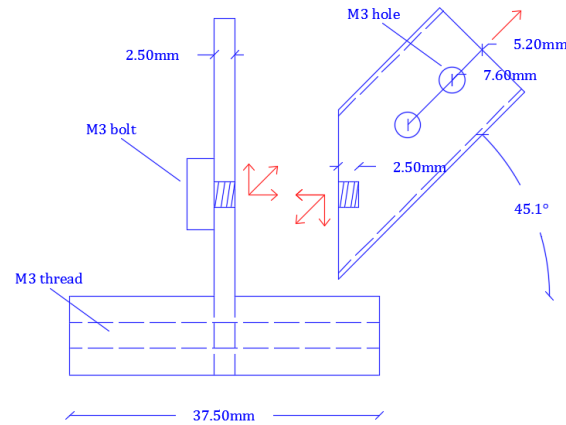


**Figure 10.4: Connection of bracing element to the column**

The height of the slab is  $0.011m$  (scaled). Two bolts of 10.9M3 are used in the mid-height of the slab. The bolts are subjected to the seismic and gravitational shear and to moment which is only seismic (the gravitational moment is negligible). The bolts resist the tensional part of that moment while the compressional is resisted by the column in the contact point (Figure 10.5).

$$T = \frac{M_{z,Ed}^{Top\ column} + M_{z,Ed}^{Bottom\ column}}{\frac{h_s}{2}} = \frac{54 + 51}{G \frac{0.011}{2}} = 477kN$$

For two 10.9M3 bolts (model scale), the total tensional force would be  $F_{t,Rd} = 8139 + 8139 = 16278kN$  (prototype). Additionally, the connection experiences shear loading from the gravity and seismic forces. The total shear force on the connection would be:

$$V_G = \frac{2 \cdot Half\ Mass\ of\ the\ slab}{4} \cdot 9.81 = \frac{2 \cdot 26595.1}{4} \cdot 9.81 = 130kN$$

$$V_E = \frac{M_i - M_j}{L_{slab}} = \frac{54 + 51 - (-(54 + 51))}{6} = 35kN$$

$$V_{total} = V_G + V_E = 165kN < F_{v,Rd} = 2 \cdot 9043kN$$

Interaction of shear and tension

$$\frac{F_{v,Ed}}{F_{v,Rd}} + \frac{F_{t,Ed}}{1.4F_{t,Rd}} = \frac{165}{2 \cdot 9043} + \frac{477}{1.4 \cdot 2 \cdot 8139} \ll 1$$

Connection of column to slab

$$G = 40$$

$M = M_j = M_i$  refers to the bending moment developing in the halfslab, at its ends

Two bolts with one shear plane each

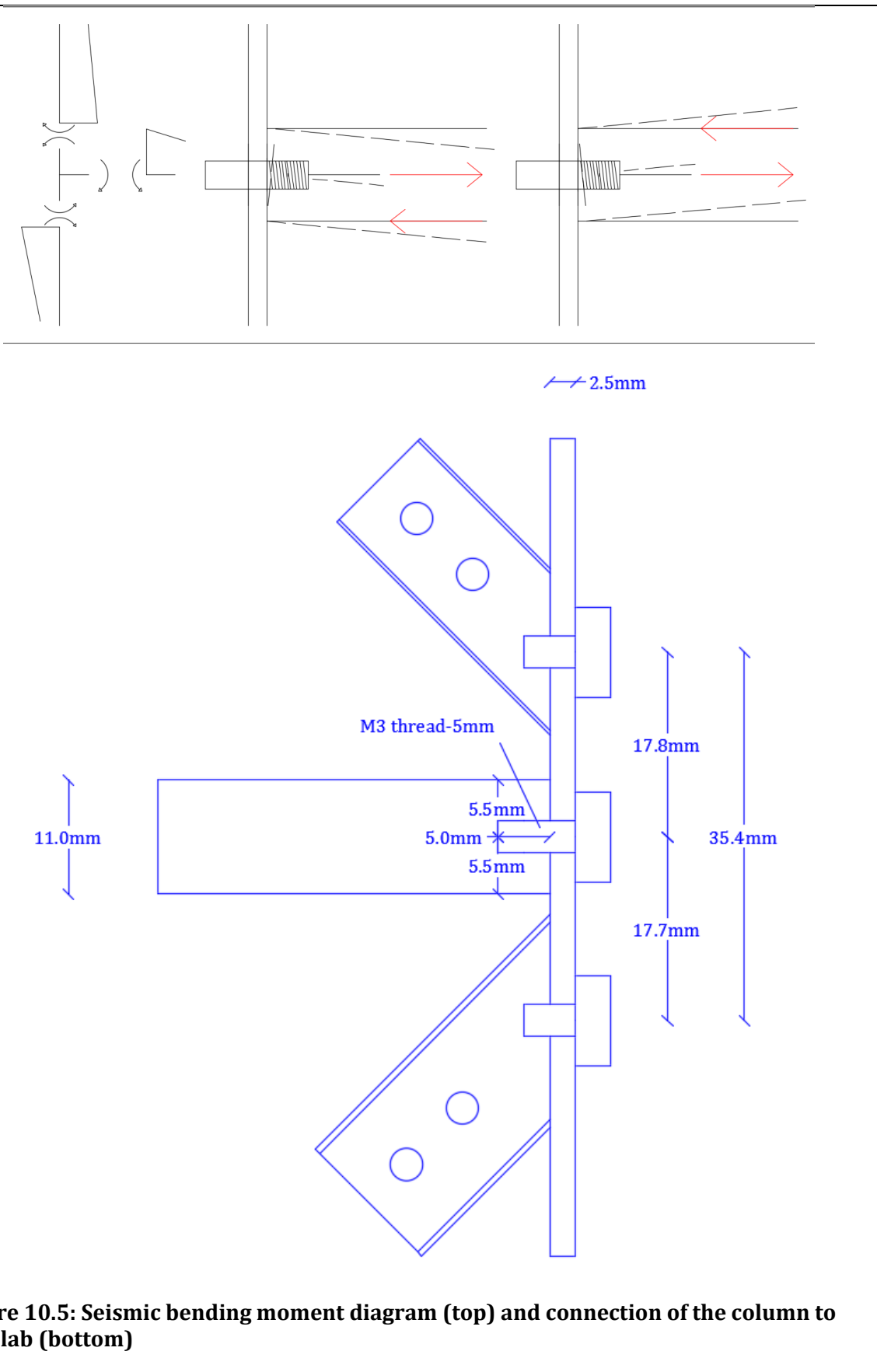


**Figure 10.5: Seismic bending moment diagram (top) and connection of the column to the slab (bottom)**

Aluminum fillet for connection of the braces:

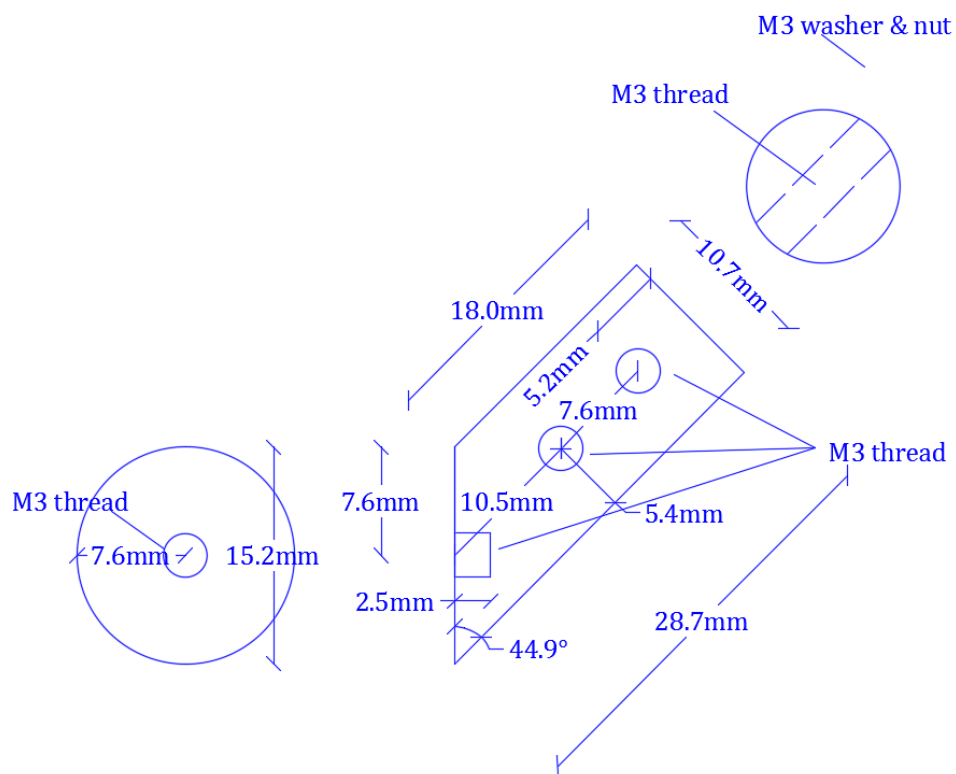
The mass of the aluminium volume, assuming there are no threads, is:

$$2700 \cdot \frac{1}{2} \cdot (0.018 + 0.0287) \cdot \frac{0.0107^2 \cdot 3.14}{4} \cdot G^3 = 362Kg \approx 1\% \text{ of Total Mass}$$

Mass of bolts

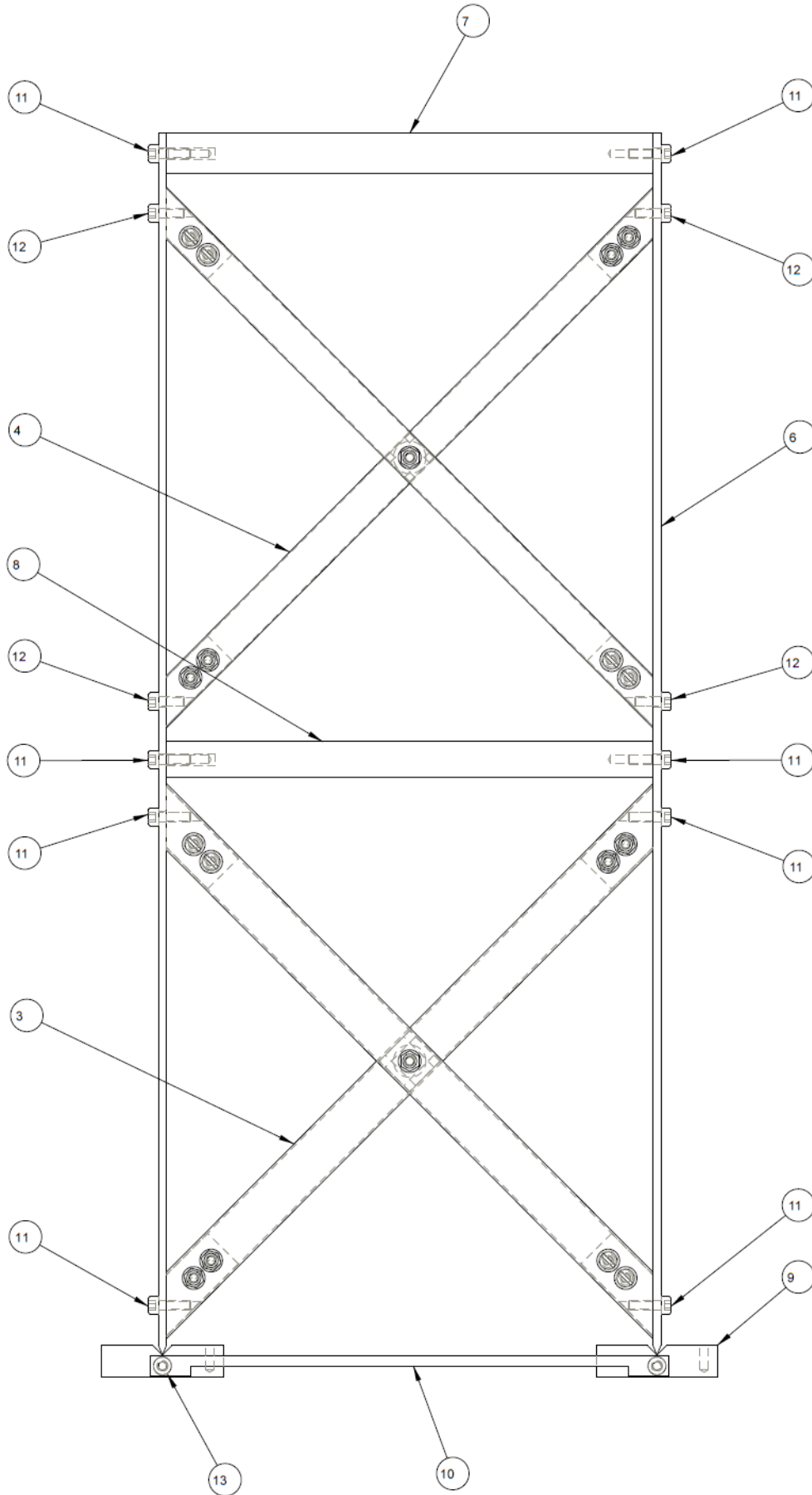
$$3 \cdot 7800 \cdot 0.0107 \cdot \frac{0.003^2 \cdot 3.14}{4} \cdot G^3 = 113Kg$$

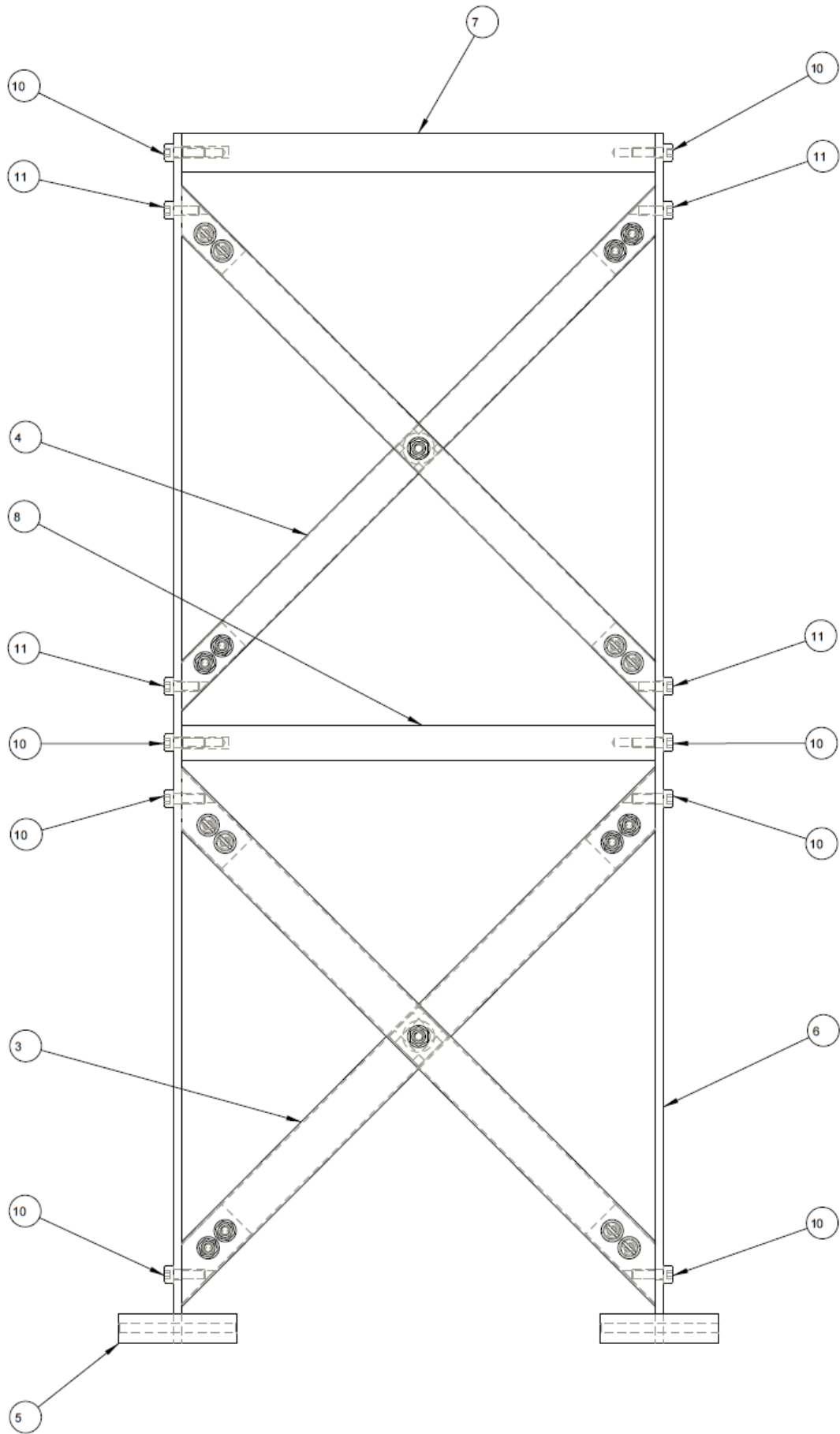
Due to the large cross section of the aluminium volume, it will resist easily the compressional and tensional forces from the PETG bracing.

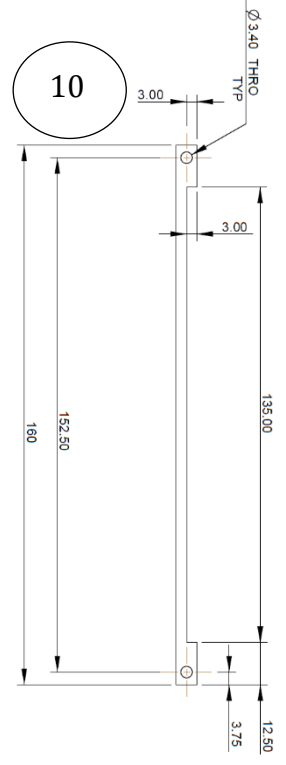
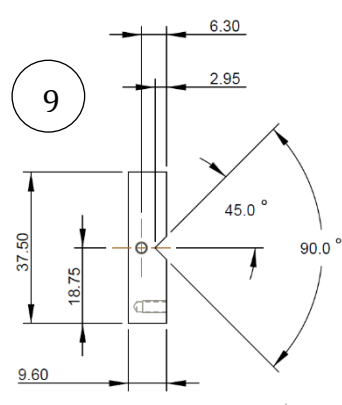
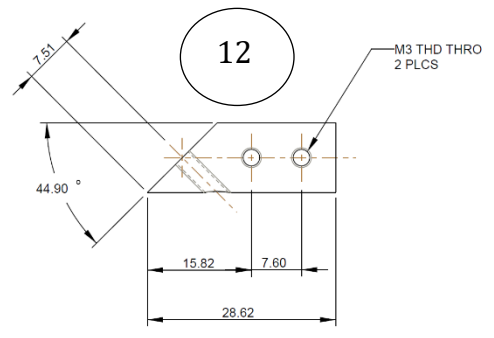
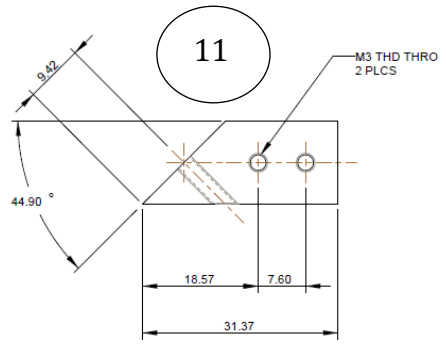
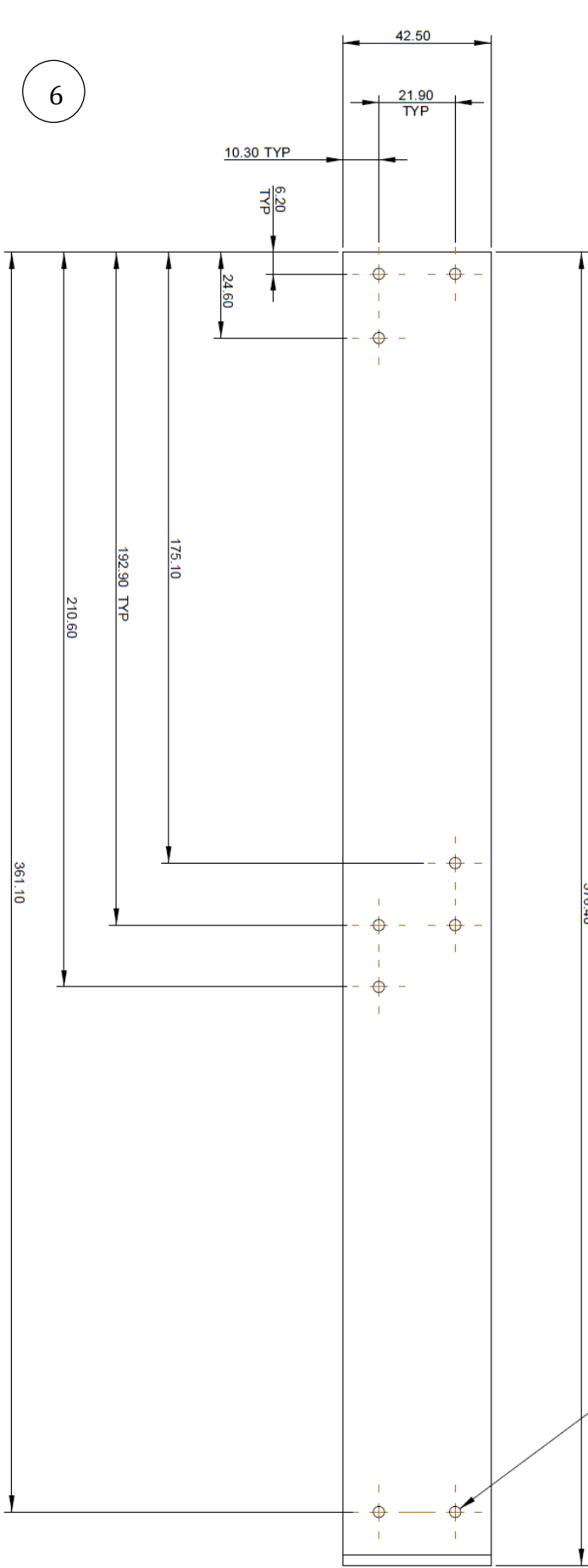


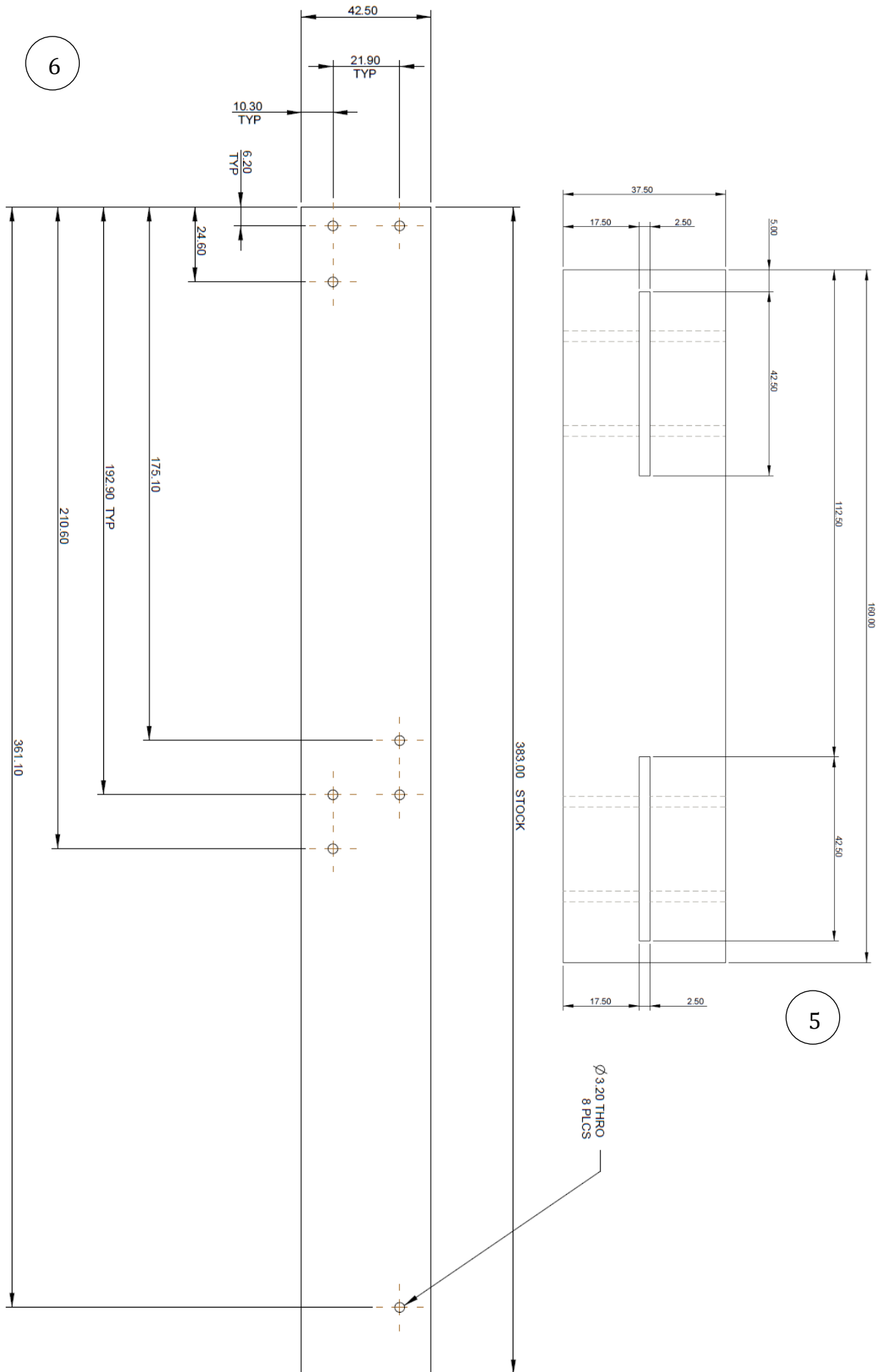
**Figure 10.6: Detail of the aluminium part for the connection of top storey bracing**

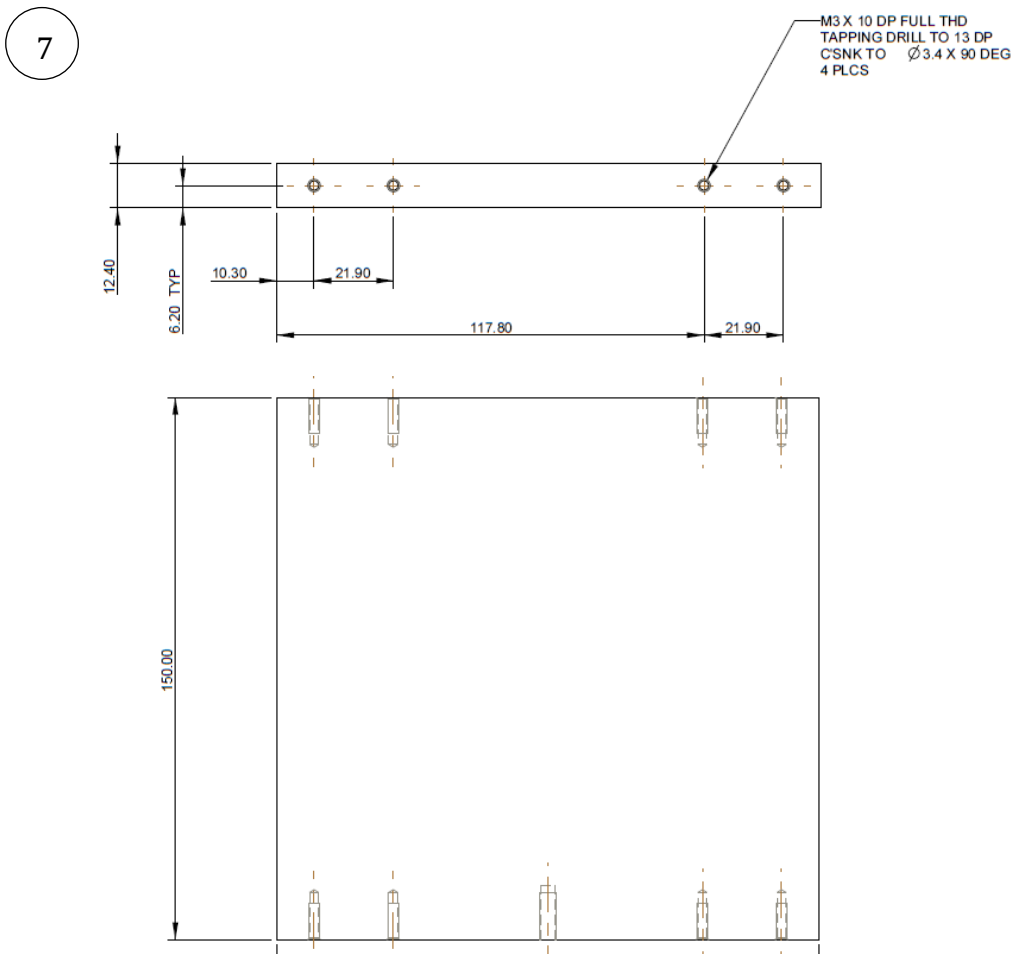
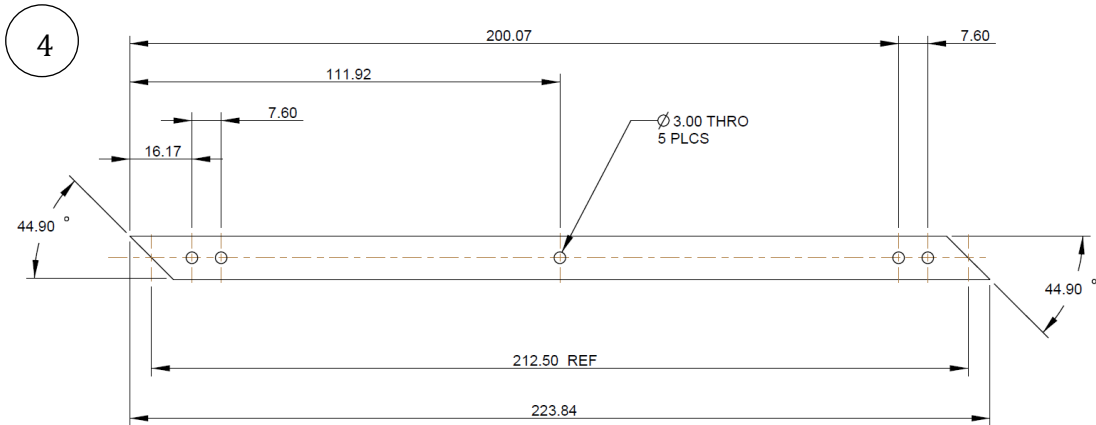
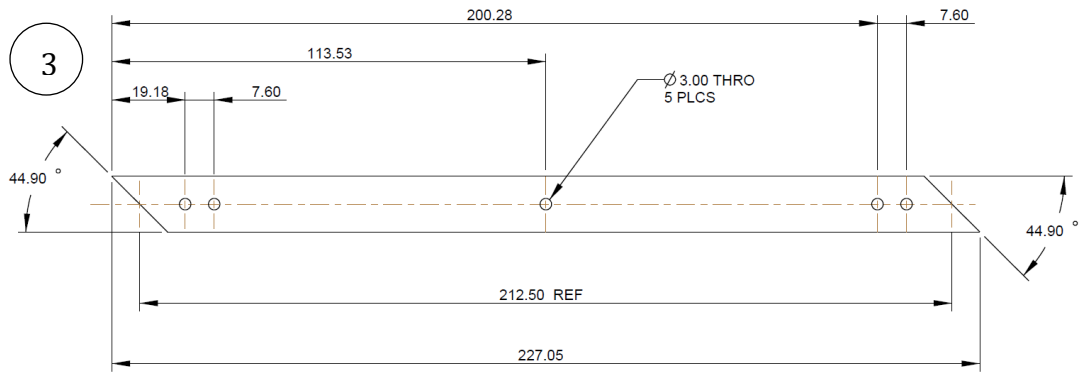
## Appendix B: Essential parts of building models RA & RB



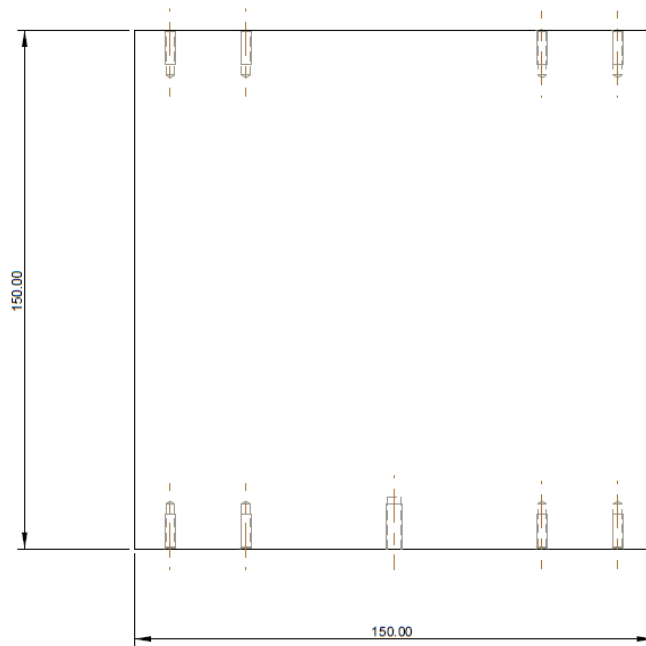
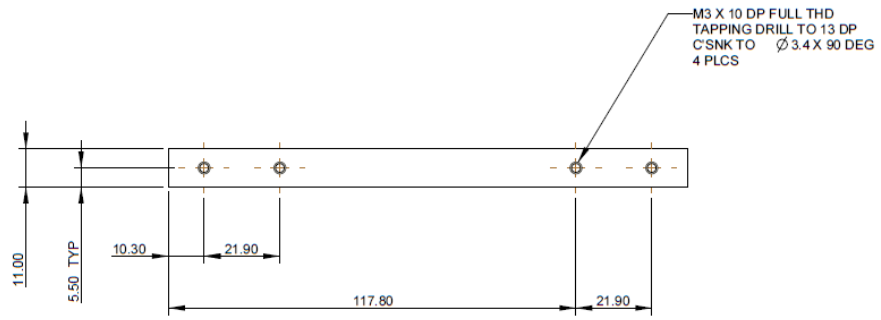




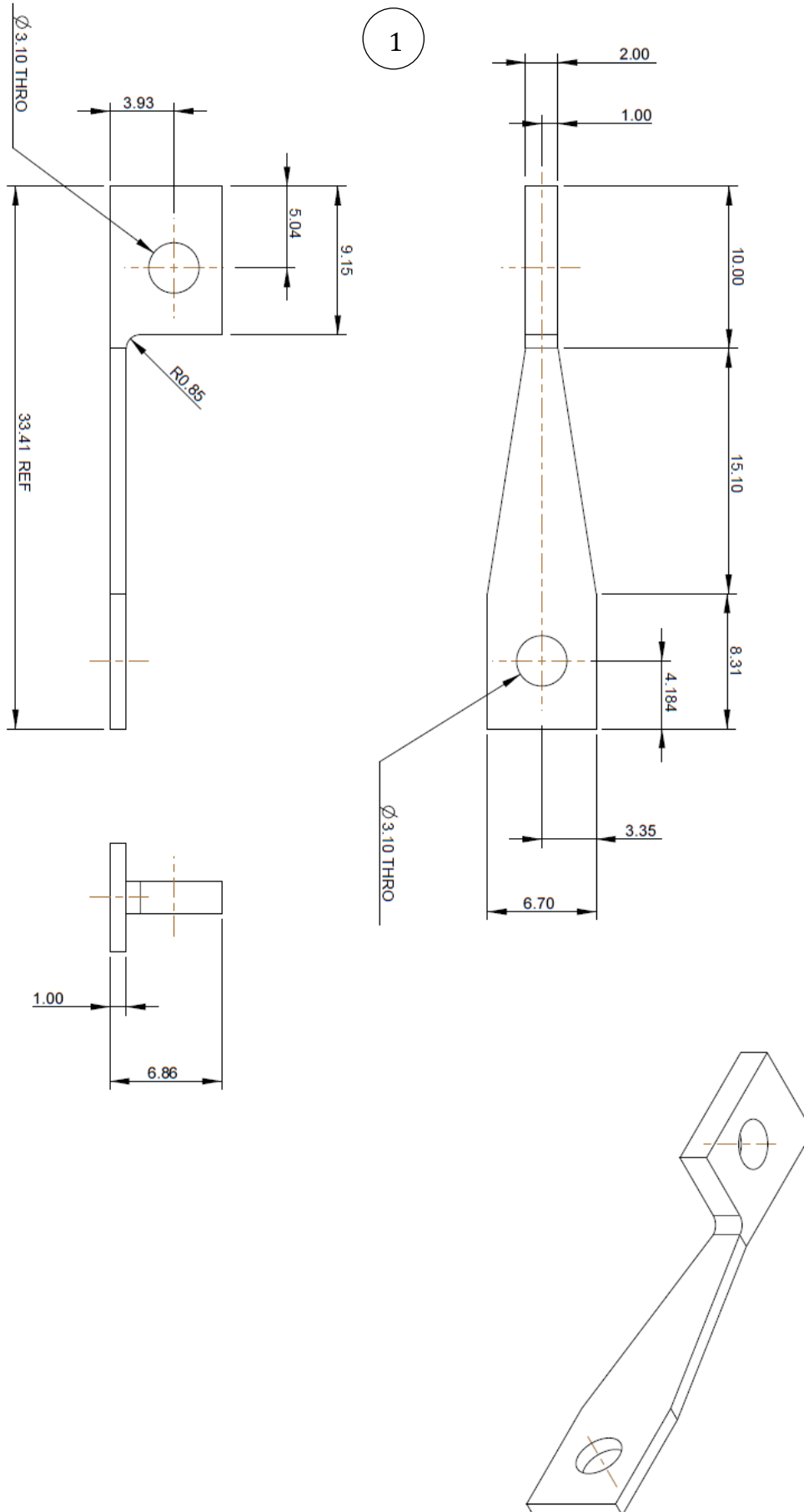


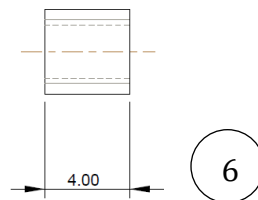
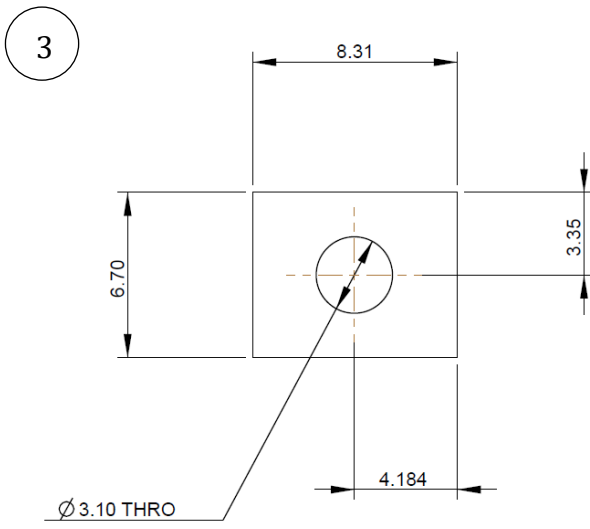
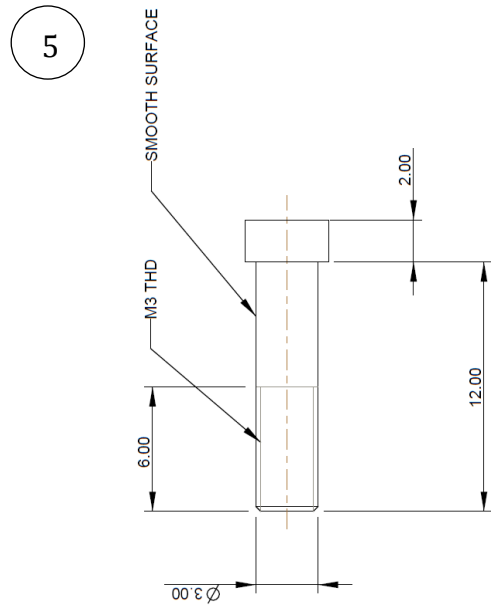
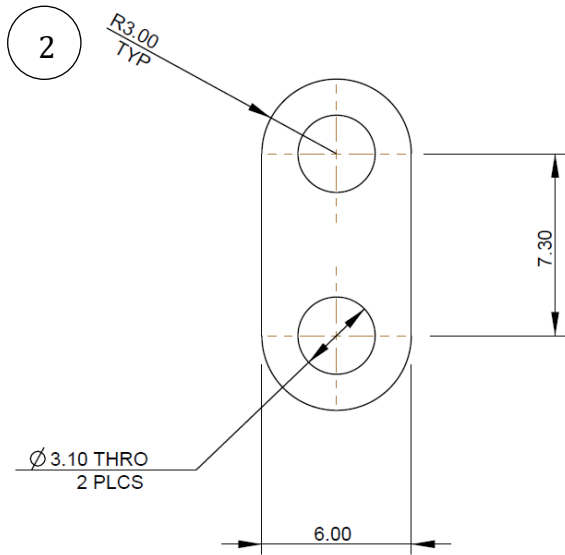


8



# Appendix C: Essential parts of energy dissipation element





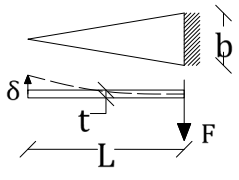
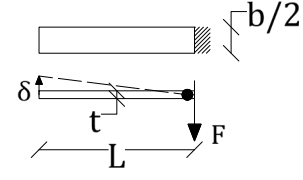
## Appendix D: Behaviour of tapered and non – tapered beams

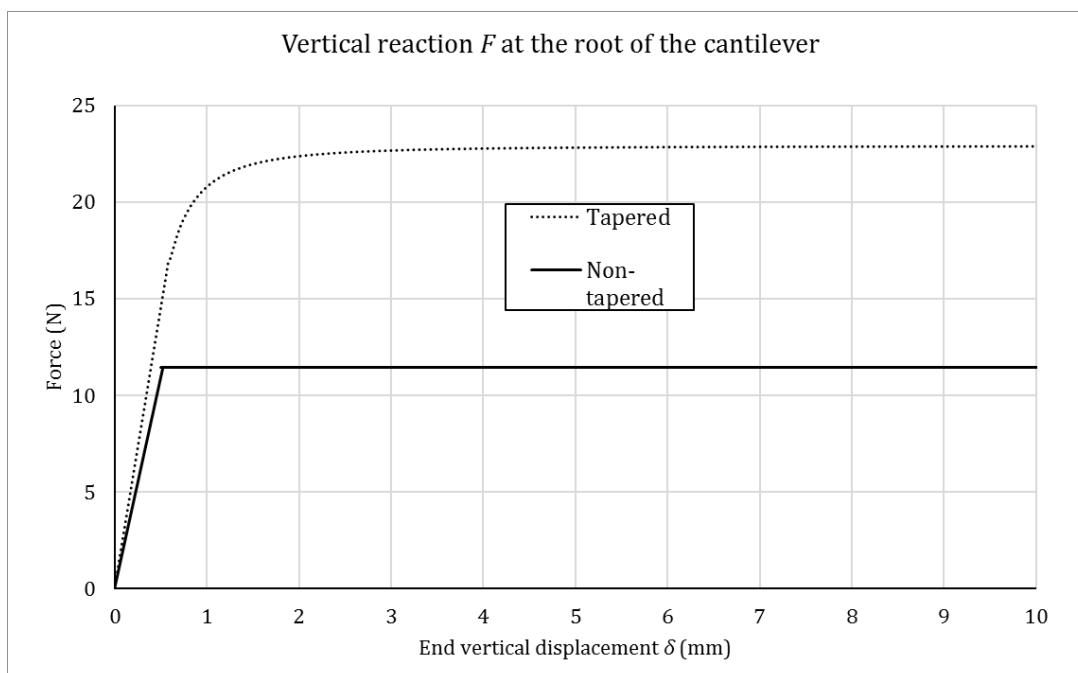
The areas under the force-displacement curve of equal volume tapered and non-tapered beams show the former can absorb more energy (Table 10.2, Figure 10.7).

**Table 10.2: Properties and analytic equations**

$E$ (GPa)	$\sigma_y$ (MPa)	$L$ (mm)	$b$ (mm)	$t$ (mm)
210	275	20	6.7	1

	
<p>Constant non-zero curvature,  <math>k_y = 2\sigma_y/Et</math> (uniform yielding)</p>	<p>Discretized plastic hinge model</p>
$F(\delta) =$	
$= \begin{cases} \frac{Et^3 b \delta}{6L^3}, & \delta \leq \delta_y \\ \frac{t^2 b \sigma_y}{6L} \left( \frac{3}{2} - \frac{1}{2} \left( \frac{k_y}{\frac{2\delta}{L^2}} \right)^2 \right), & \delta > \delta_y \end{cases}$	$F(\delta) = \begin{cases} \frac{Et^3 (b/2) \delta}{4L^3}, & \delta \leq \delta_y \\ \frac{t^2 (b/2) \sigma_y}{4L}, & \delta > \delta_y \end{cases}$



**Figure 10.7: Force–displacement diagram for equal volume beams in bending**

# Appendix E: Wavelet transforms with varying Morse wavelet

## DENSE SAND TEST-1 EQ-3

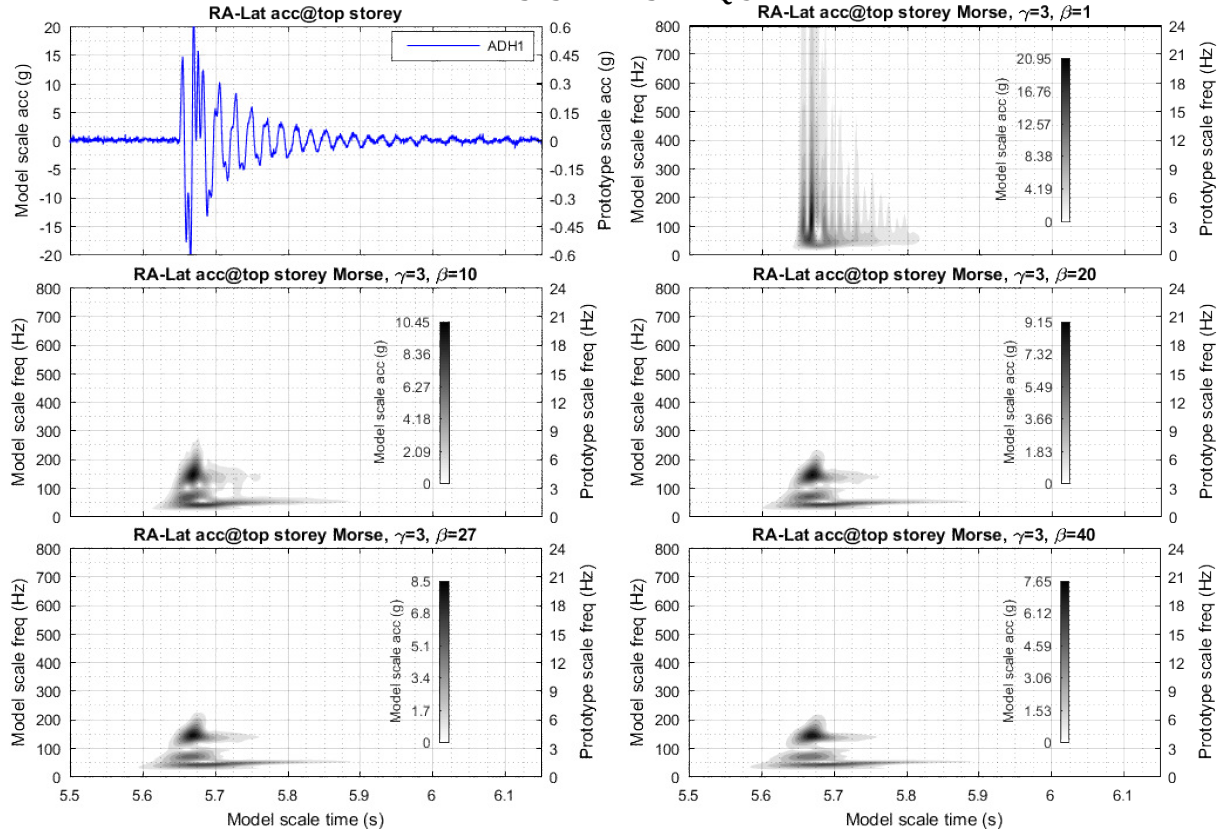


**Figure 10.8: Dense sand, Test-1 Eq-3: Top storey lateral acceleration response of model RA and time-frequency maps for different values of the  $\beta$ ,  $\gamma$  parameters of the Morse wavelet**

## DENSE SAND TEST-2 EQ-4

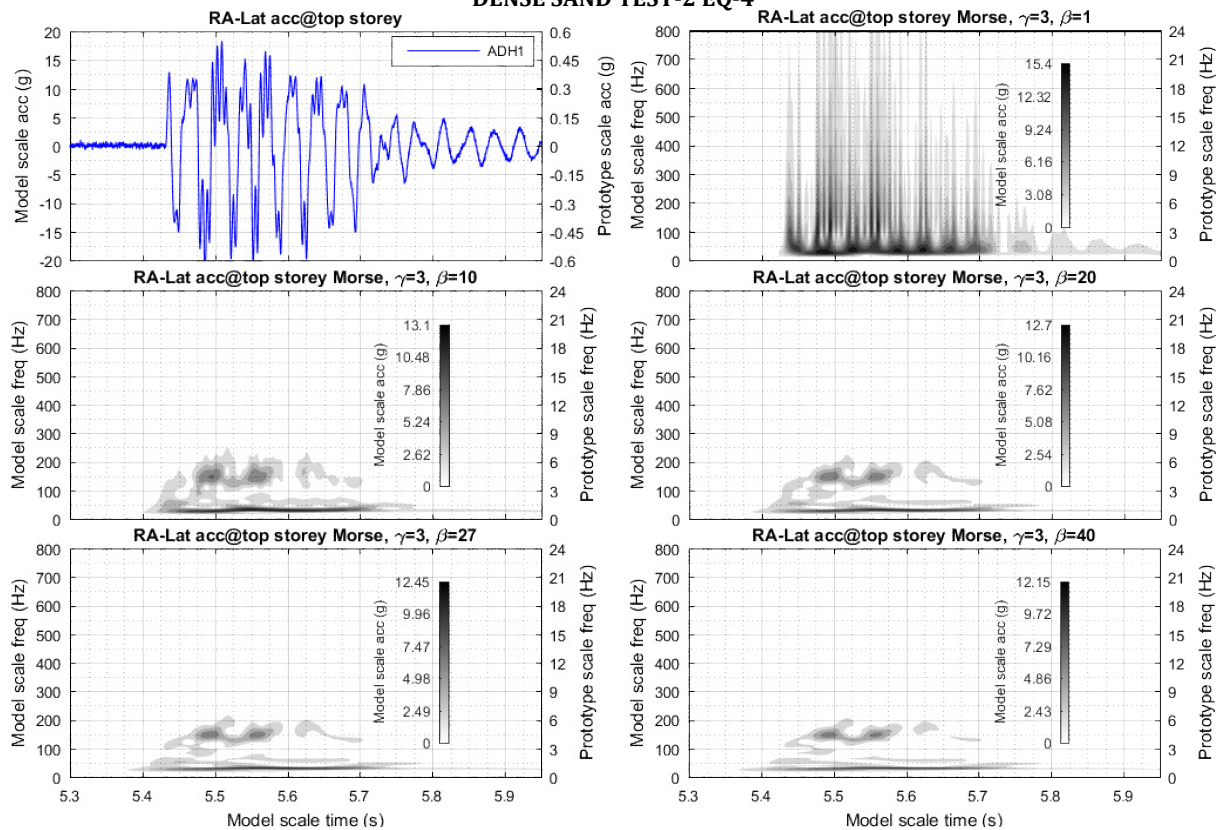
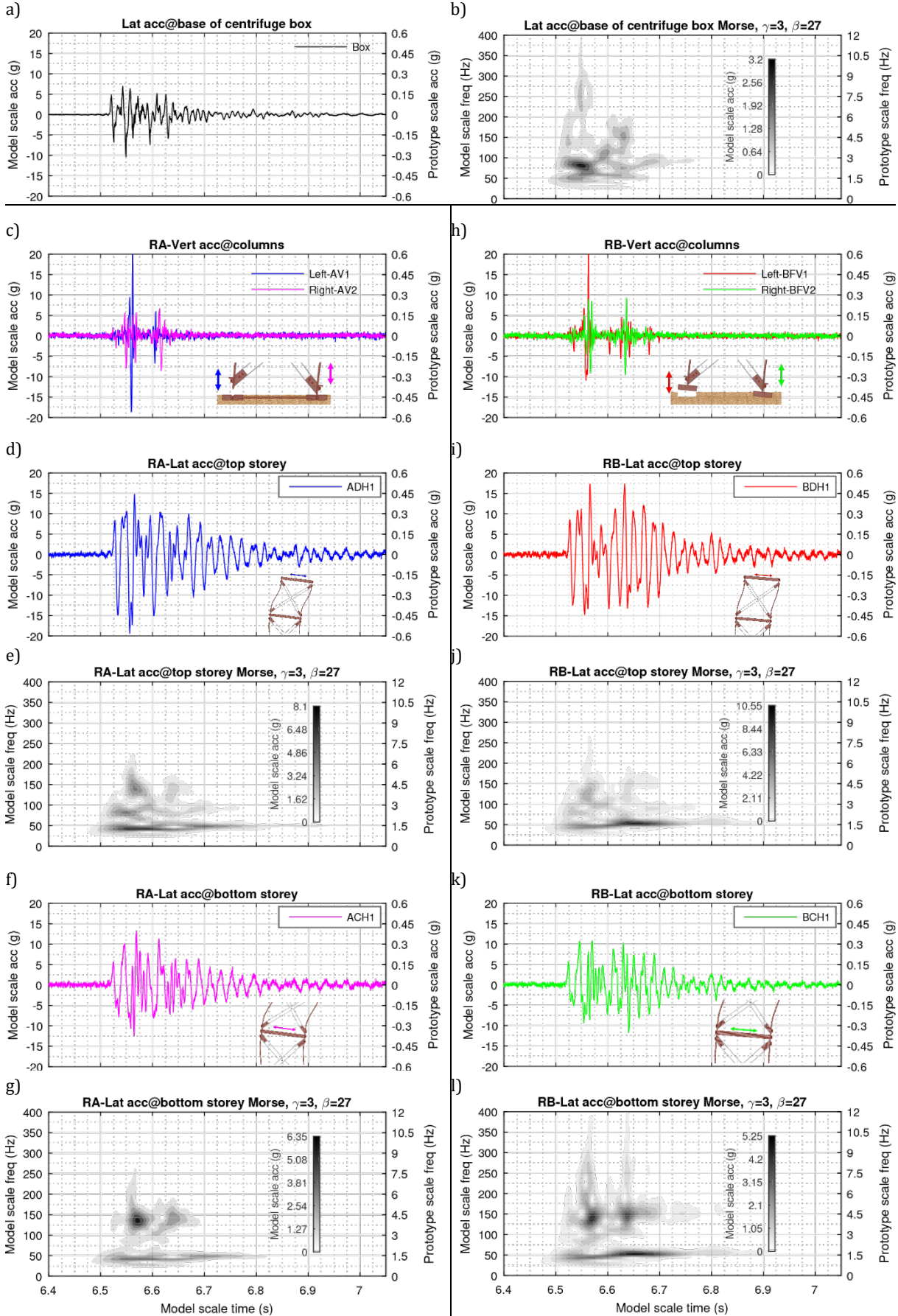
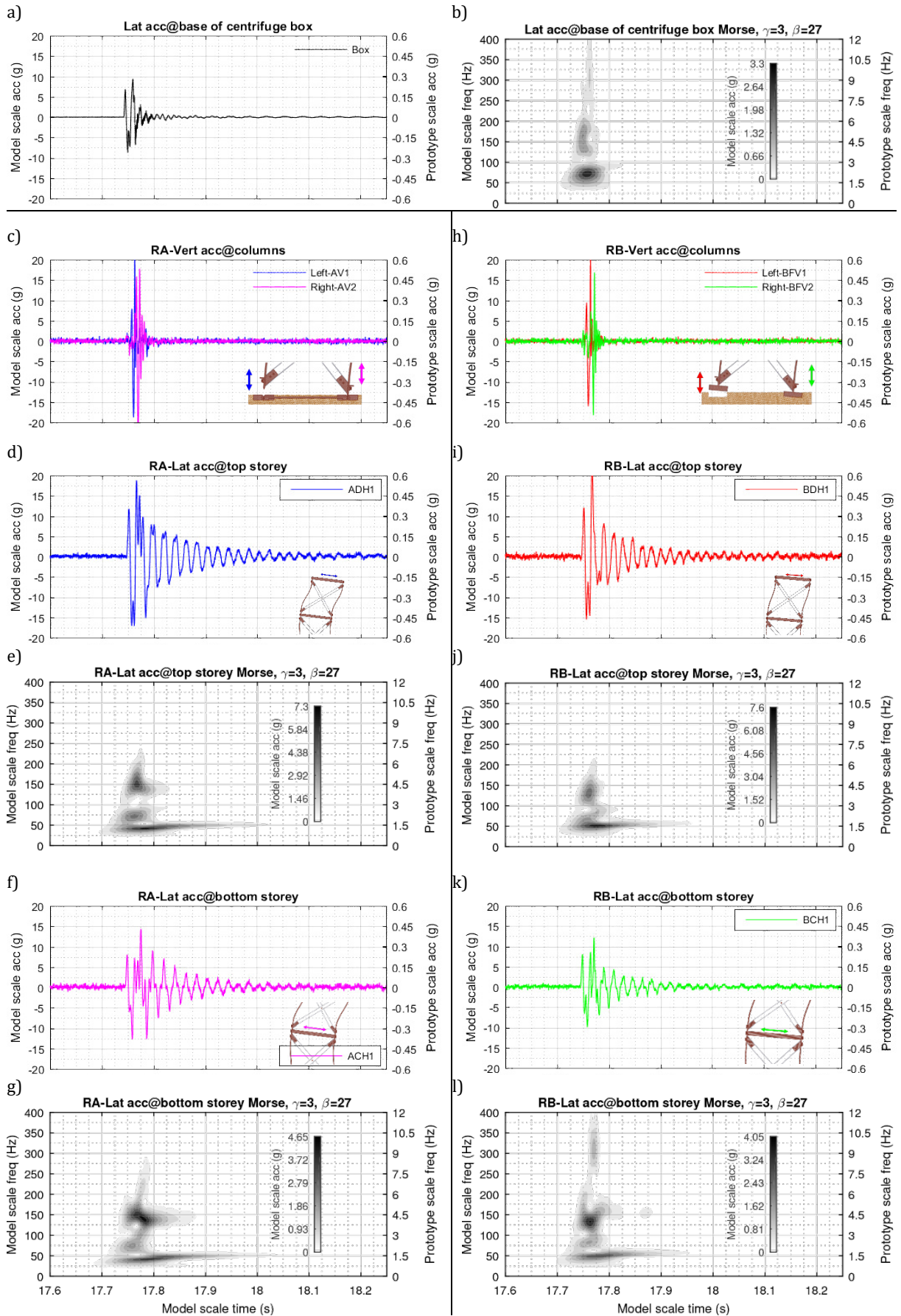


**Figure 10.9: Dense sand, Test-2 Eq-4: Top storey lateral acceleration response of model RA and time-frequency maps for different values of the  $\beta$ ,  $\gamma$  parameters of the Morse wavelet**

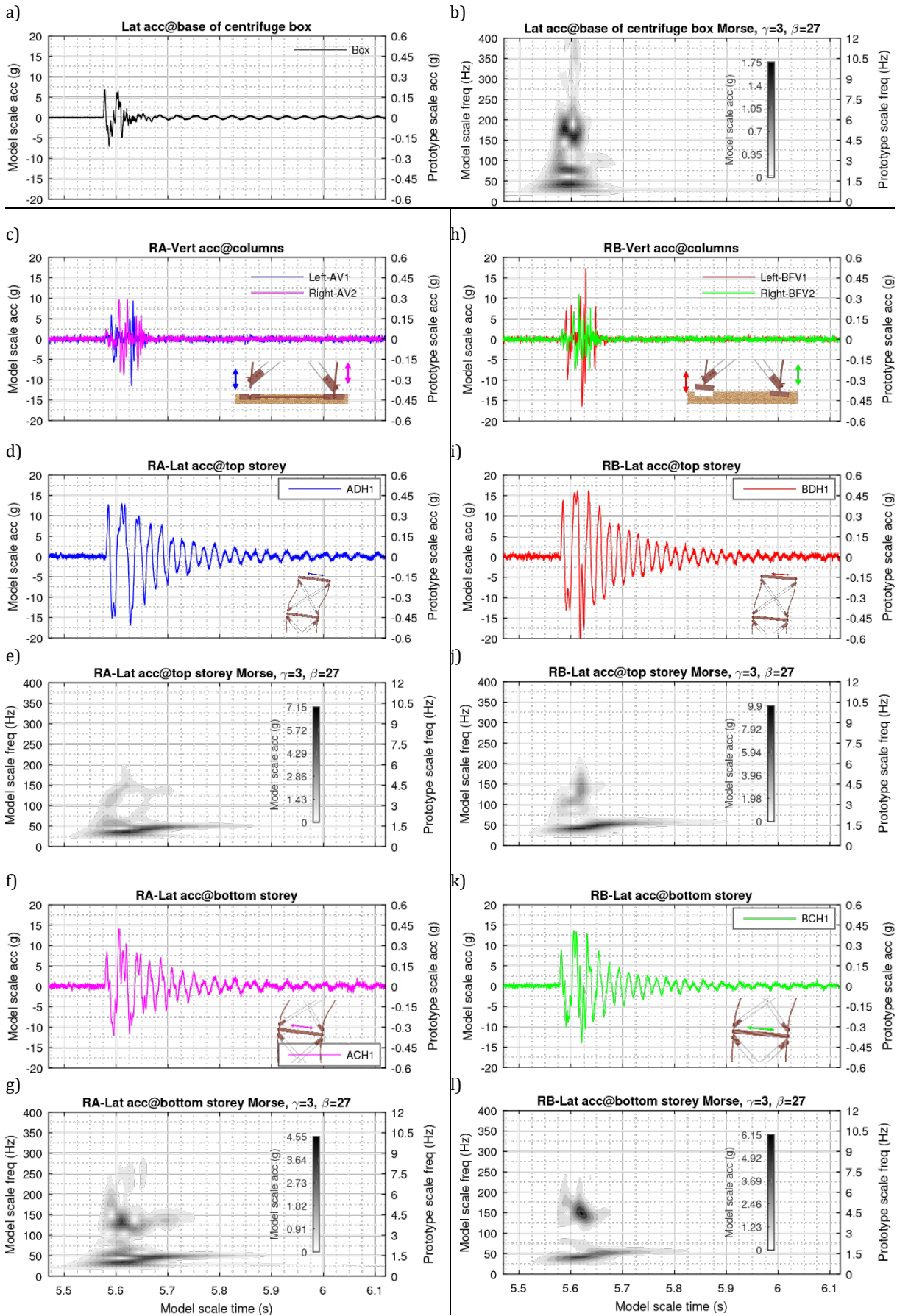
# Appendix F: Experimental responses



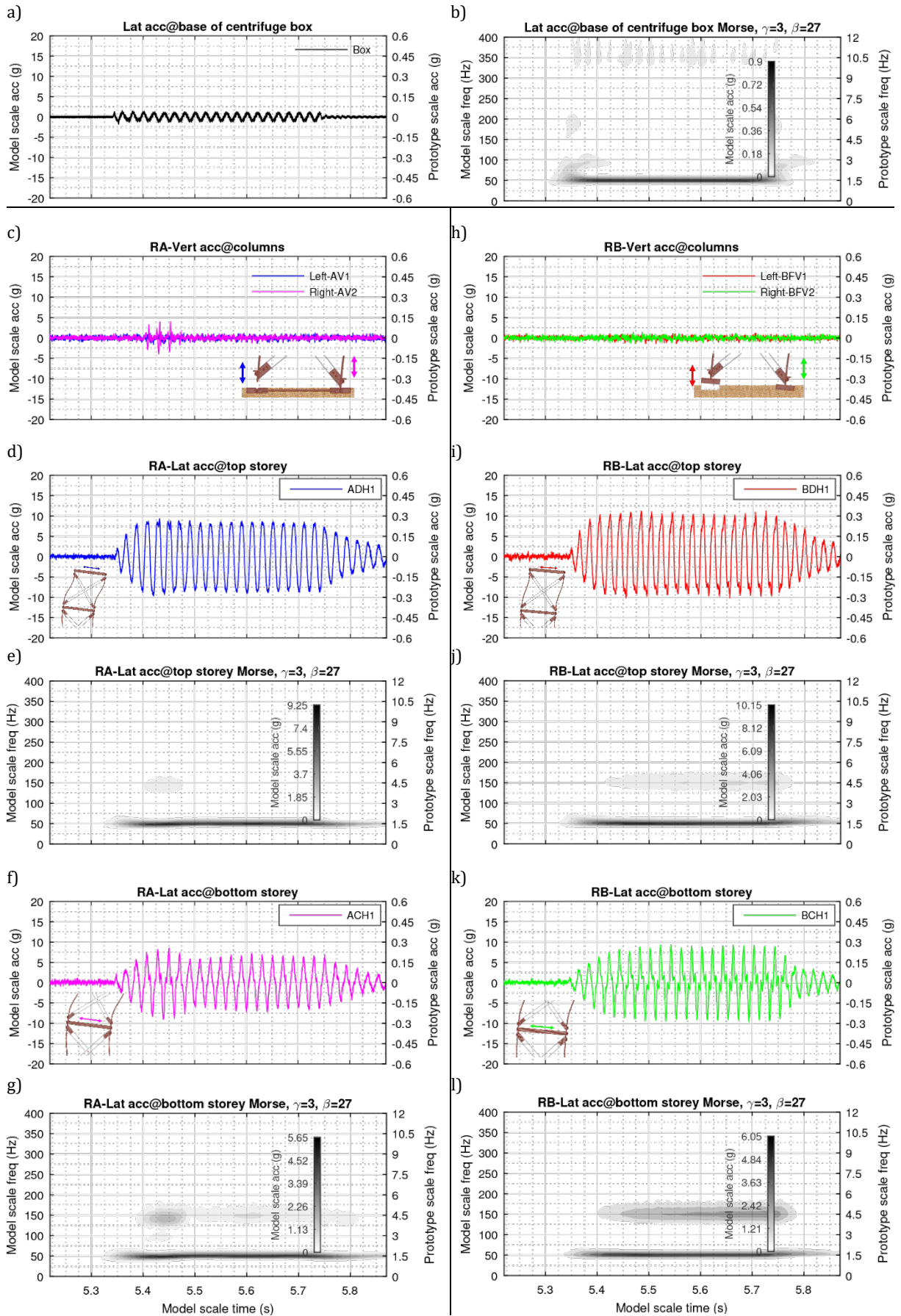
**Dense sand, Test-0 Eq-1: Excitation (a, b), vertical acceleration response of model RA (c), storeys' time-frequency response of model RA (d-g) and similarly for model RB (h-l)**



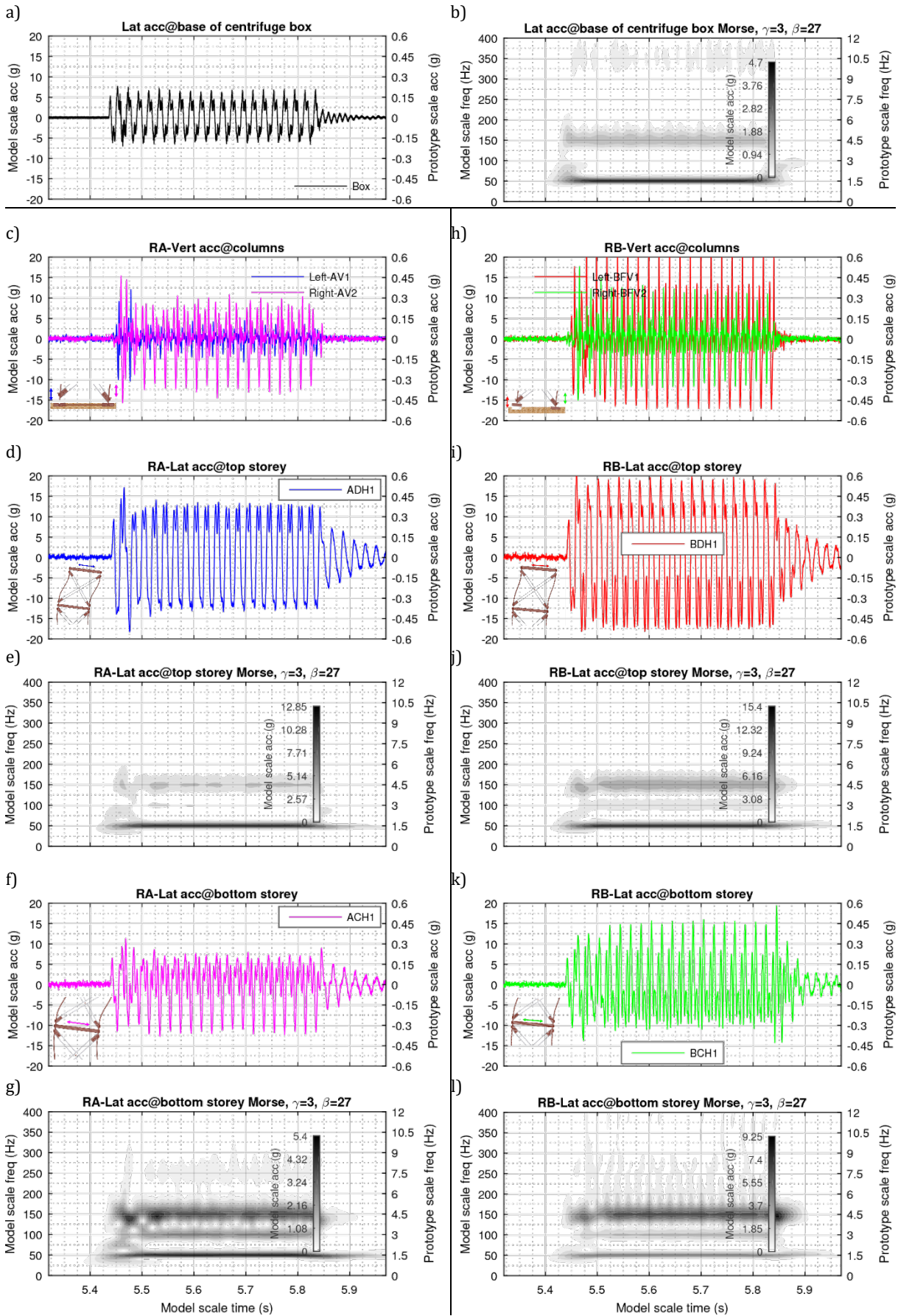
**Dense sand, Test-0 Eq-2: Excitation (a, b), vertical acceleration response of model RA (c), storeys' time-frequency response of model RA (d-g) and similarly for model RB (h-l)**



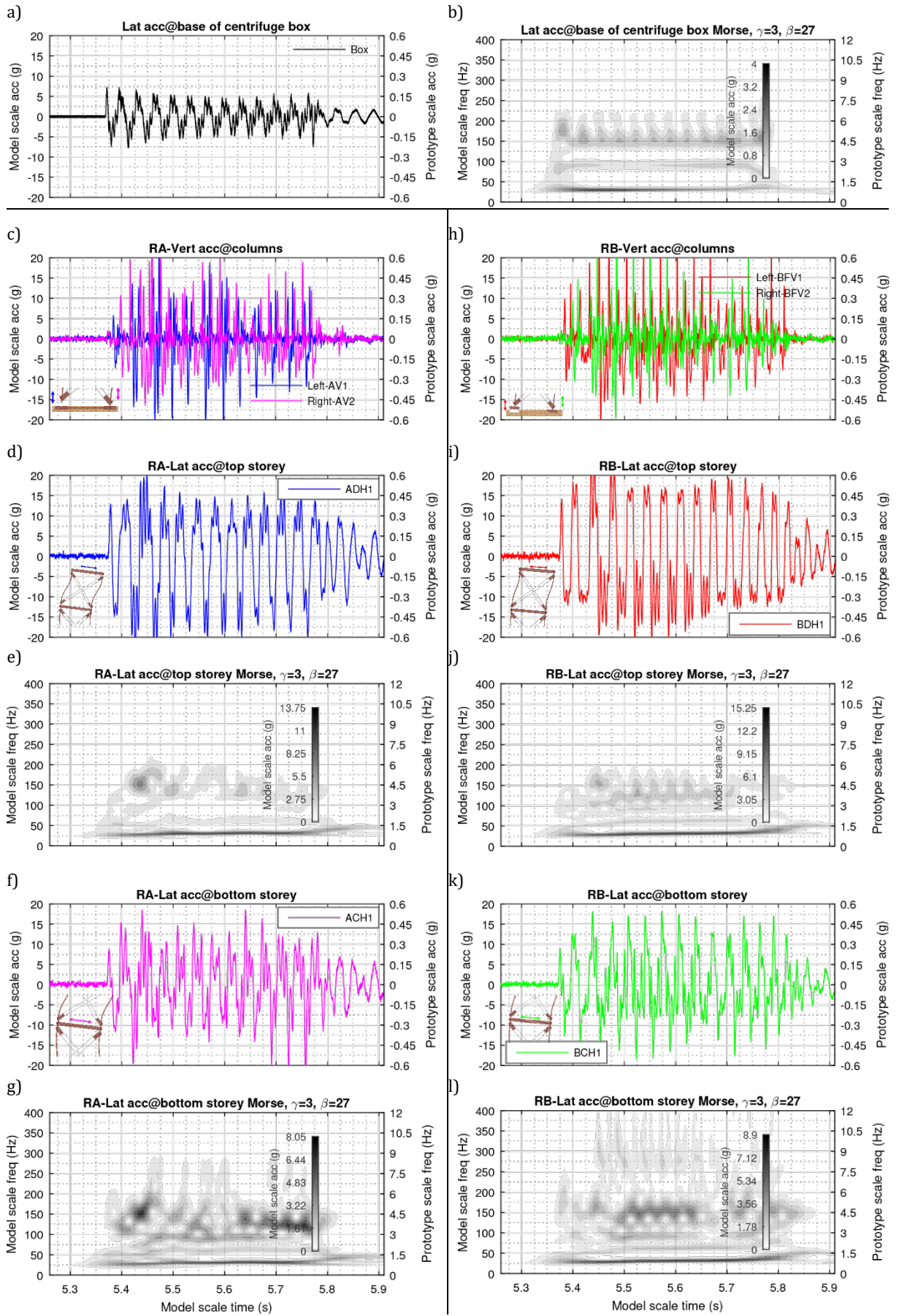
**Dense sand, Test-0 Eq-3: Excitation (a, b), vertical acceleration response of model RA (c), storeys' time-frequency response of model RA (d-g) and similarly for model RB (h-l)**



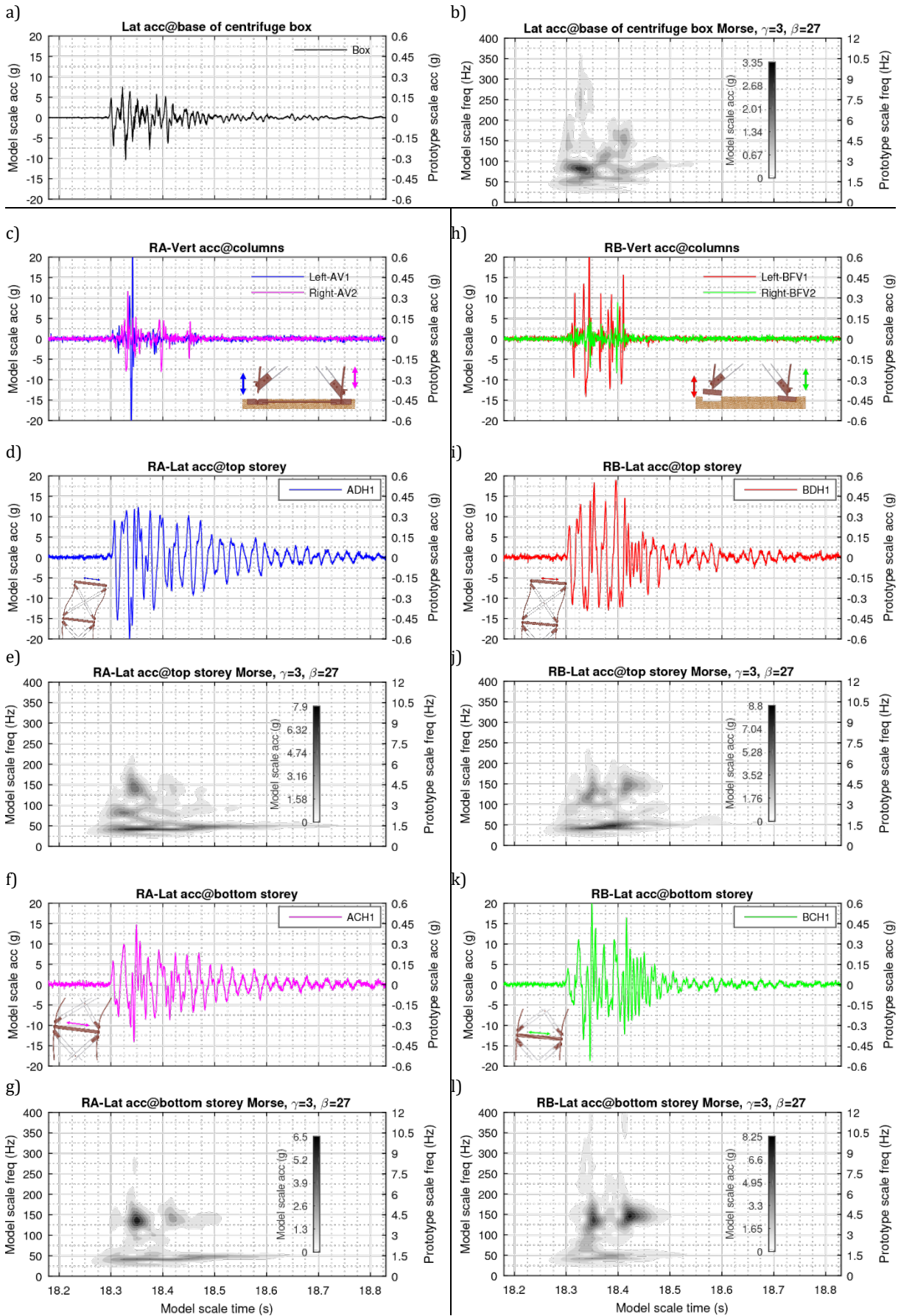
**Dense sand, Test-0 Eq-4: Excitation (a, b), vertical acceleration response of model RA (c), storeys' time-frequency response of model RA (d-g) and similarly for model RB (h-l)**



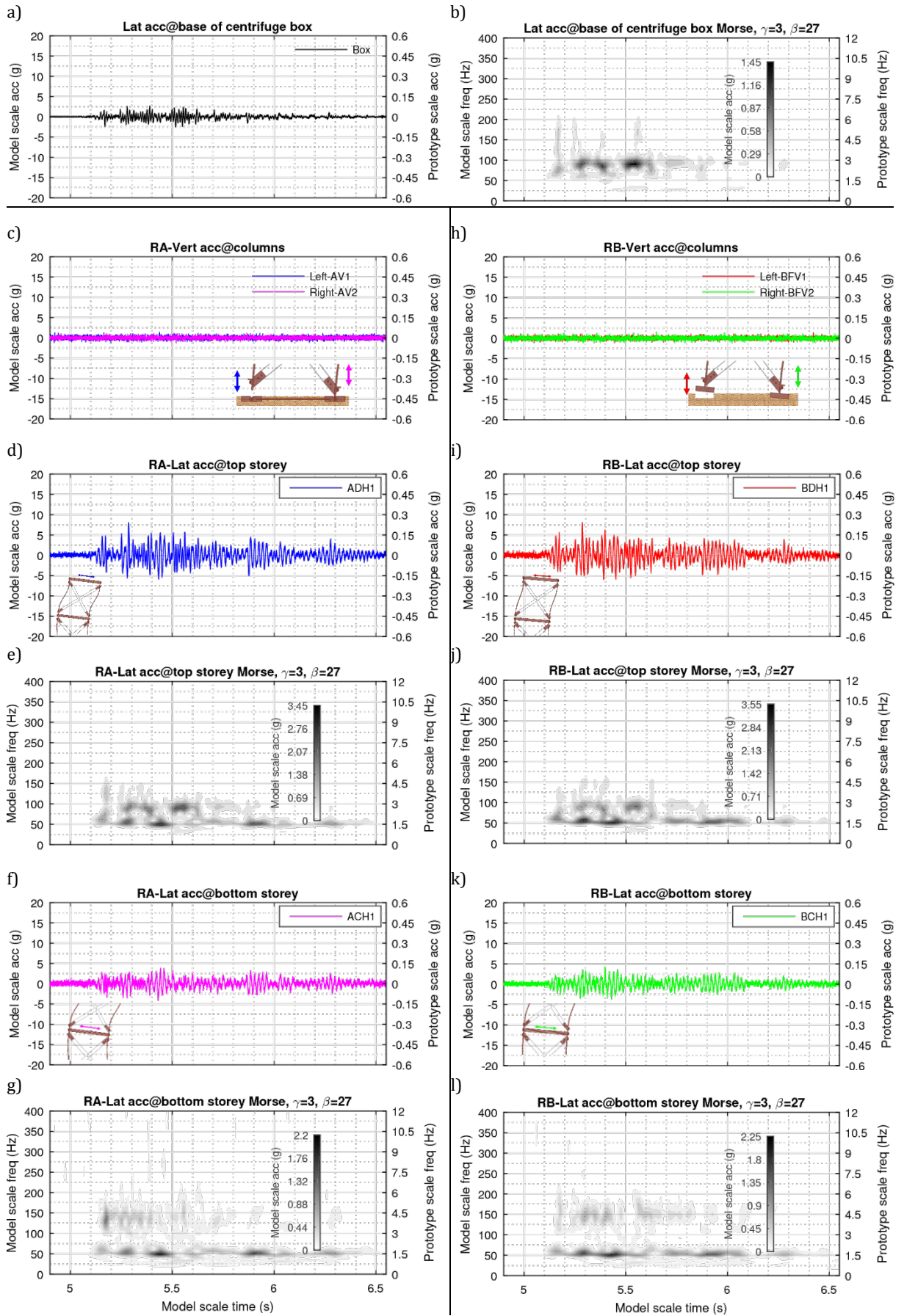
**Dense sand, Test-0 Eq-5: Excitation (a, b), vertical acceleration response of model RA (c), storeys' time-frequency response of model RA (d-g) and similarly for model RB (h-l)**



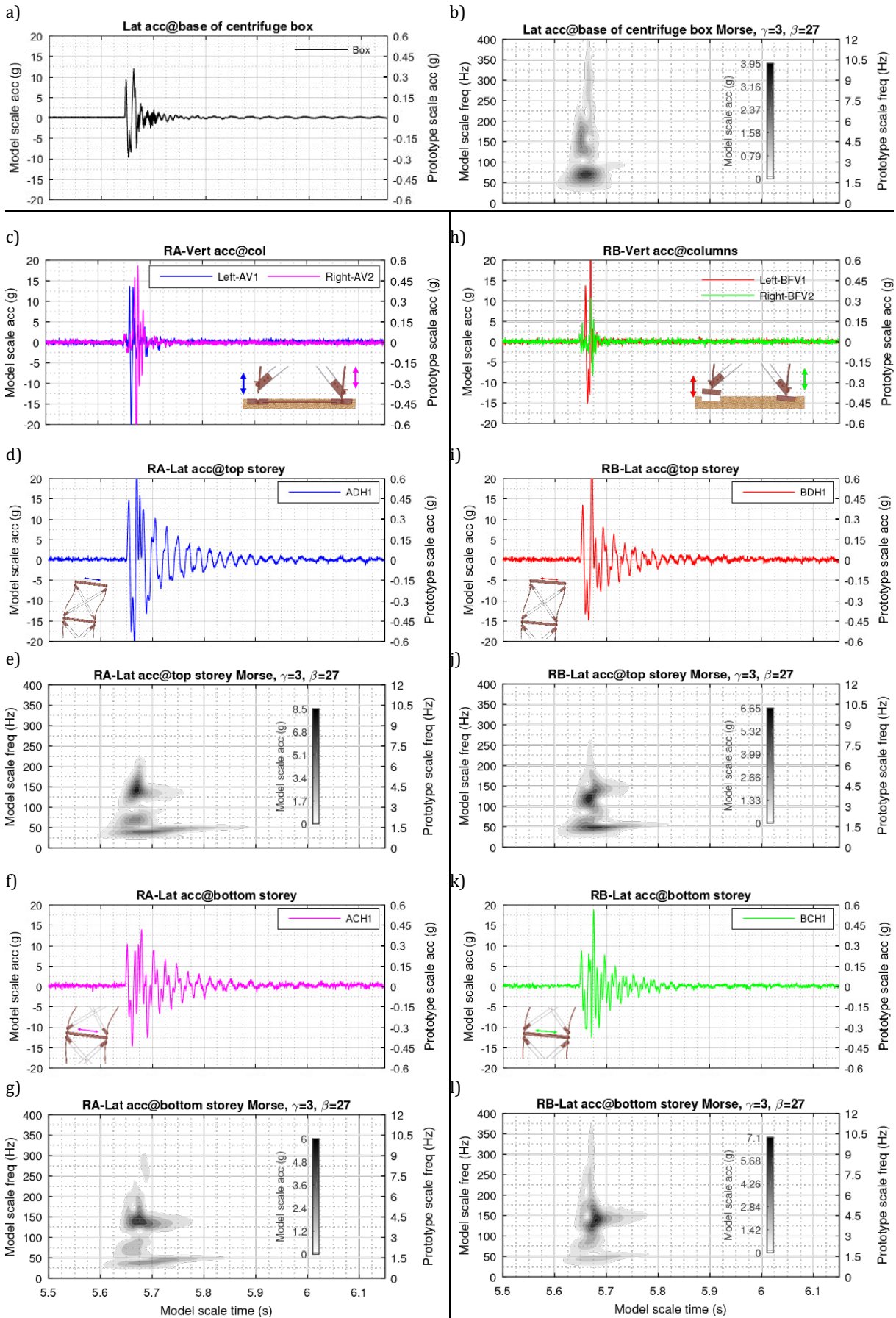
**Dense sand, Test-0 Eq-6: Excitation (a, b), vertical acceleration response of model RA (c), storeys' time-frequency response of model RA (d-g) and similarly for model RB (h-l)**



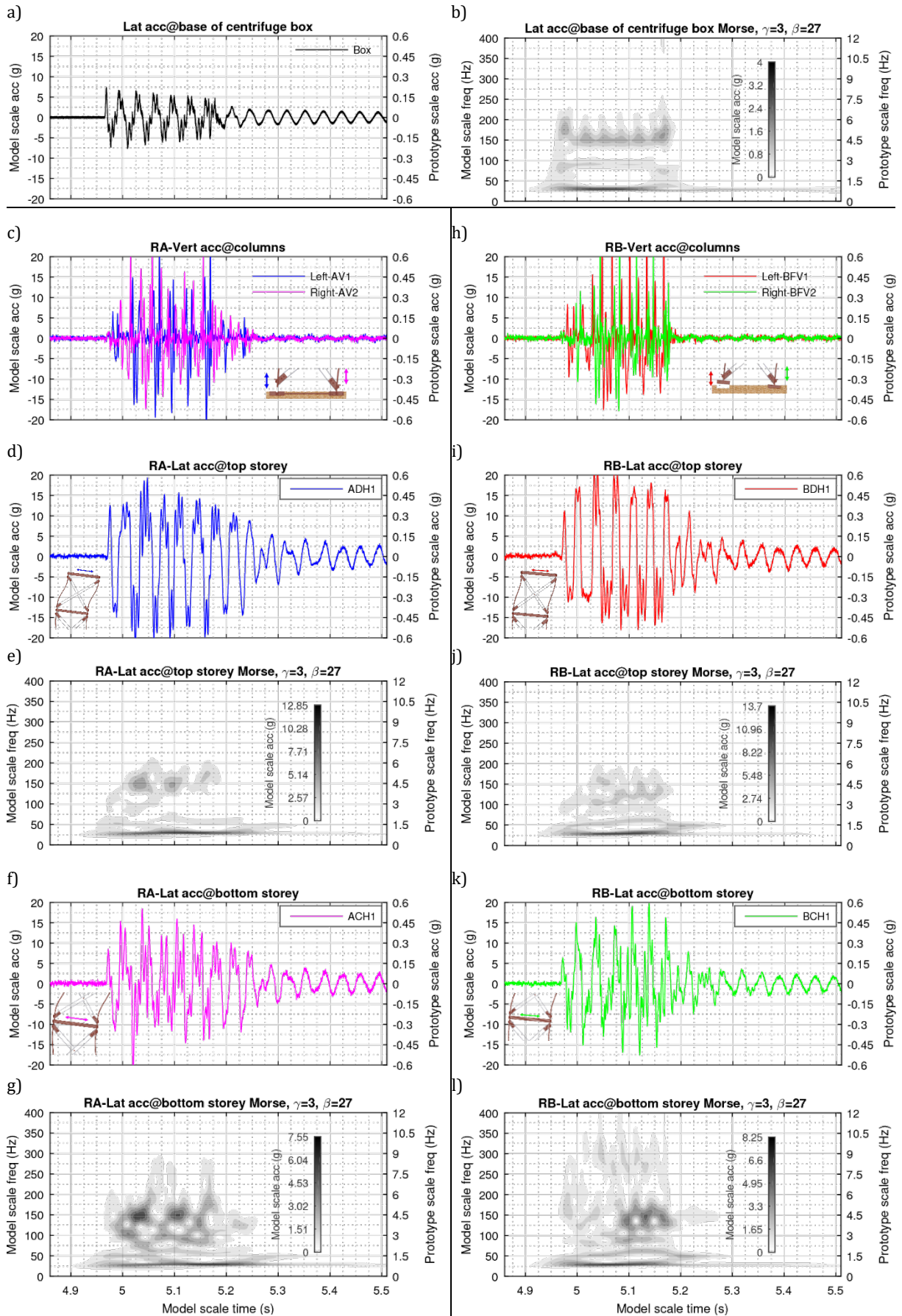
**Dense sand, Test-1 Eq-1: Excitation (a, b), vertical acceleration response of model RA (c), storeys' time-frequency response of model RA (d-g) and similarly for model RB (h-l)**



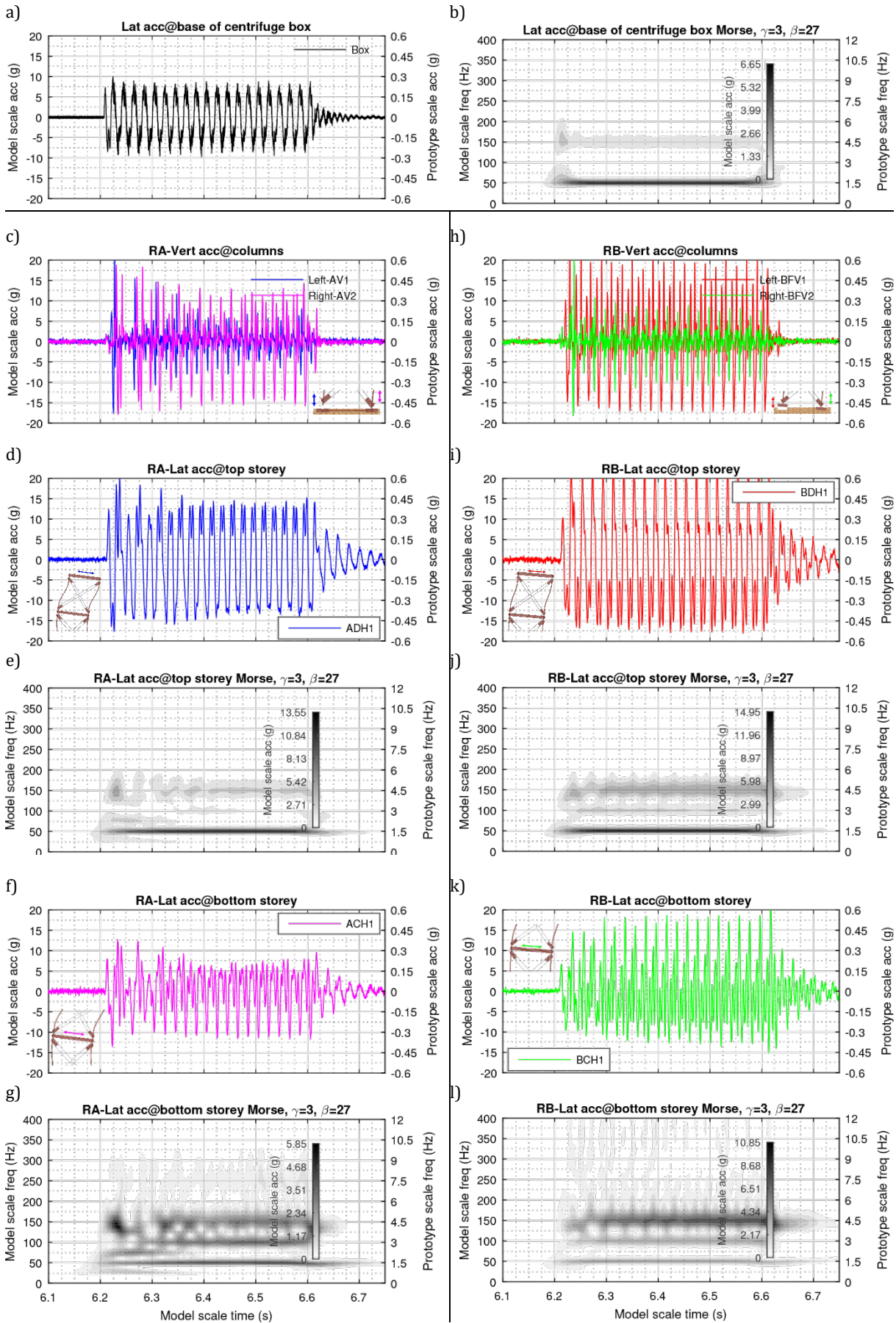
Dense sand, Test-1 Eq-2: Excitation (a, b), vertical acceleration response of model RA (c), storeys' time-frequency response of model RA (d-g) and similarly for model RB (h-l)



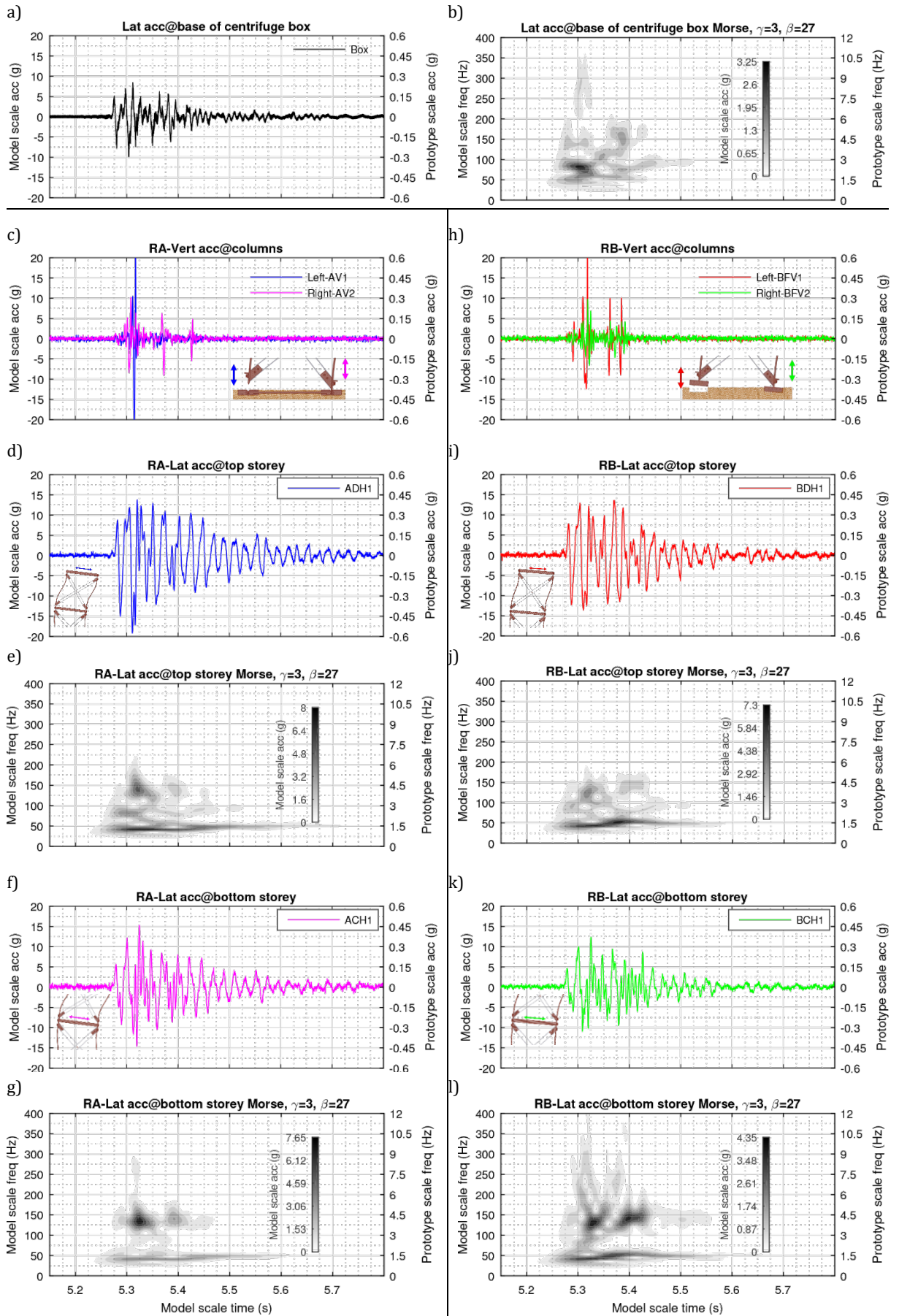
**Dense sand, Test-1 Eq-3: Excitation (a, b), vertical acceleration response of model RA (c), storeys' time-frequency response of model RA (d-g) and similarly for model RB (h-l)**



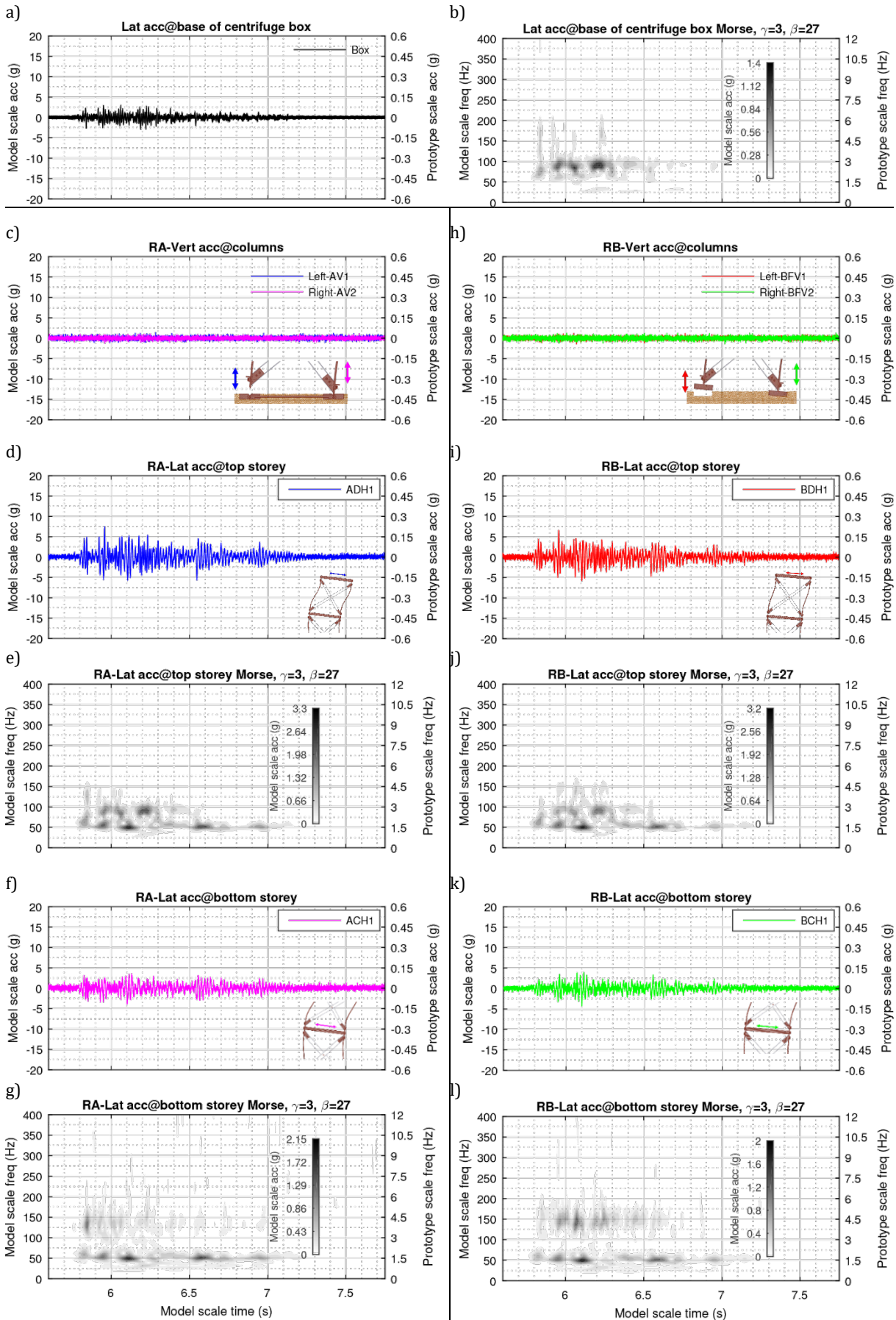
**Dense sand, Test-1 Eq-4: Excitation (a, b), vertical acceleration response of model RA (c), storeys' time-frequency response of model RA (d-g) and similarly for model RB (h-l)**



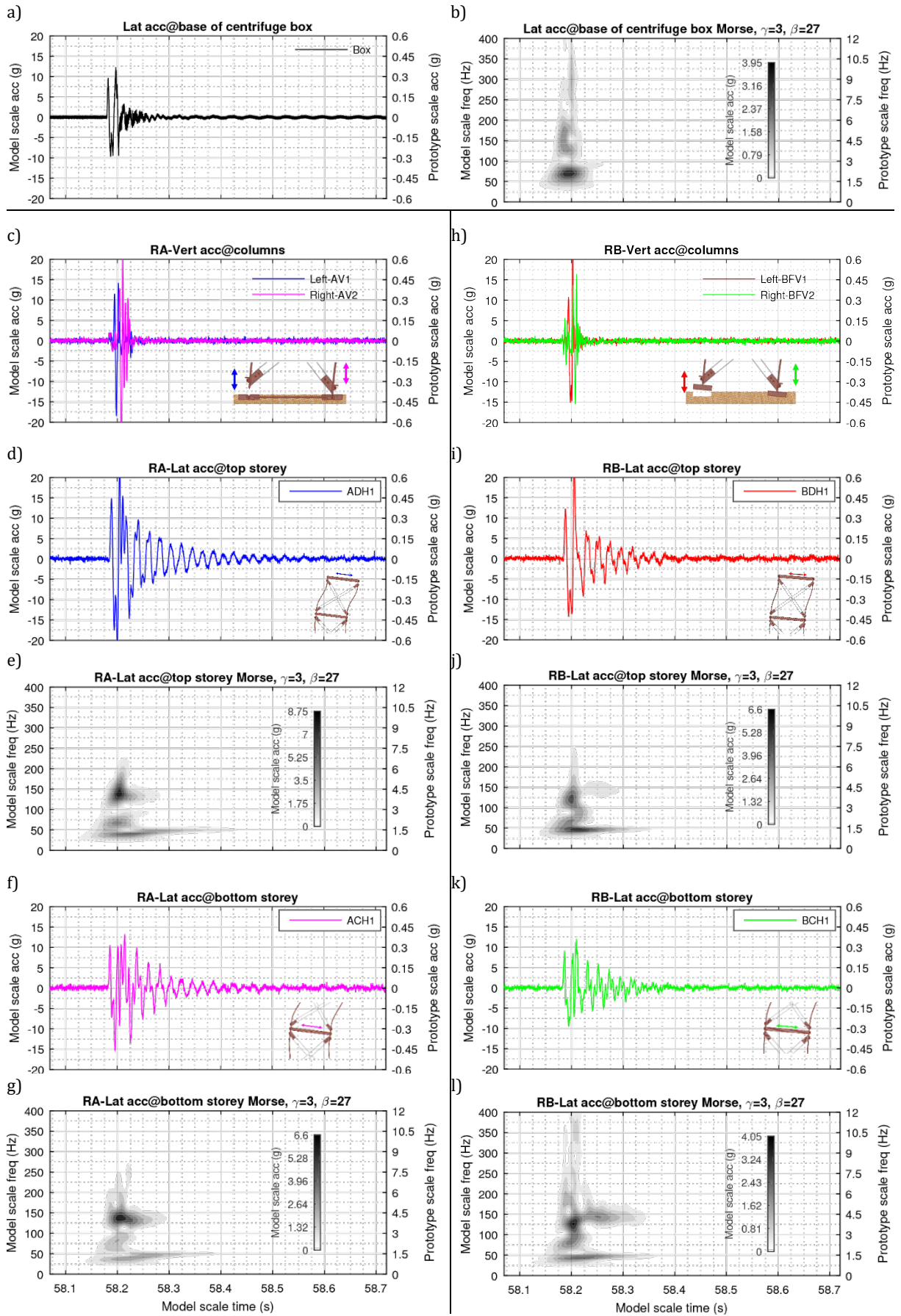
**Dense sand, Test-1 Eq-5: Excitation (a, b), vertical acceleration response of model RA (c), storeys' time-frequency response of model RA (d-g) and similarly for model RB (h-l)**



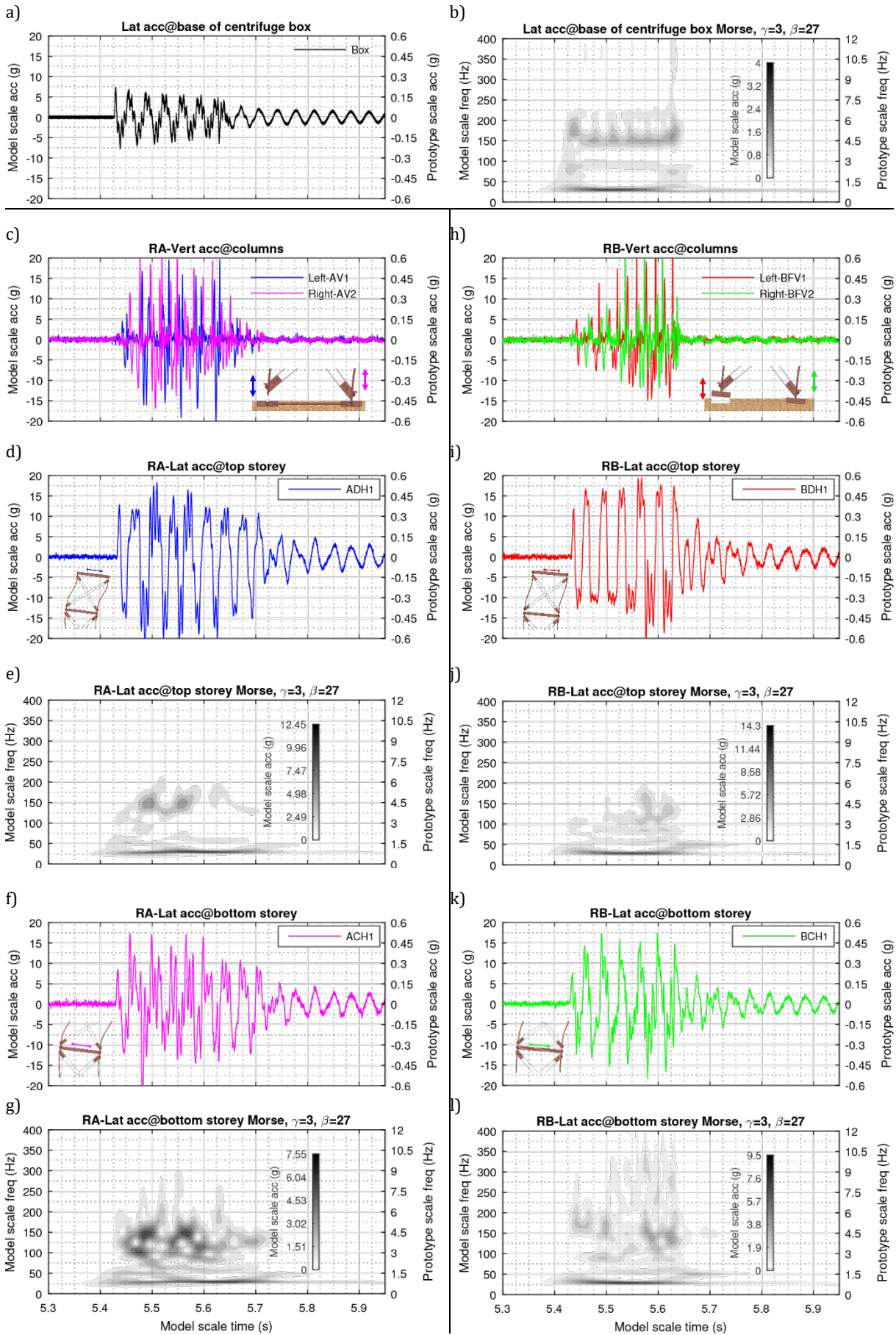
**Dense sand, Test-2 Eq-1: Excitation (a, b), vertical acceleration response of model RA (c), storeys' time-frequency response of model RA (d-g) and similarly for model RB (h-l)**



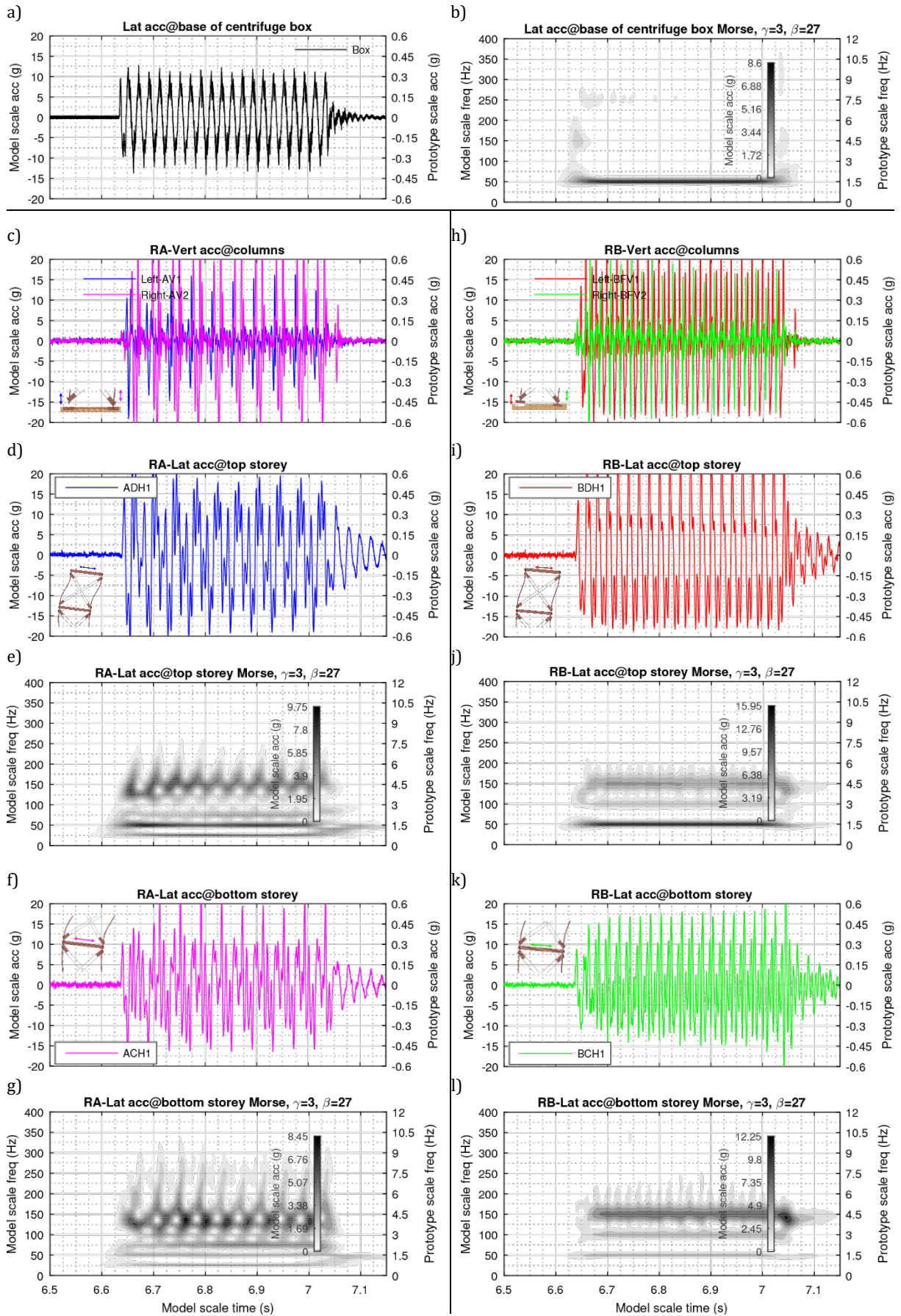
Dense sand, Test-2 Eq-2: Excitation (a, b), vertical acceleration response of model RA (c), storeys' time-frequency response of model RA (d-g) and similarly for model RB (h-l)



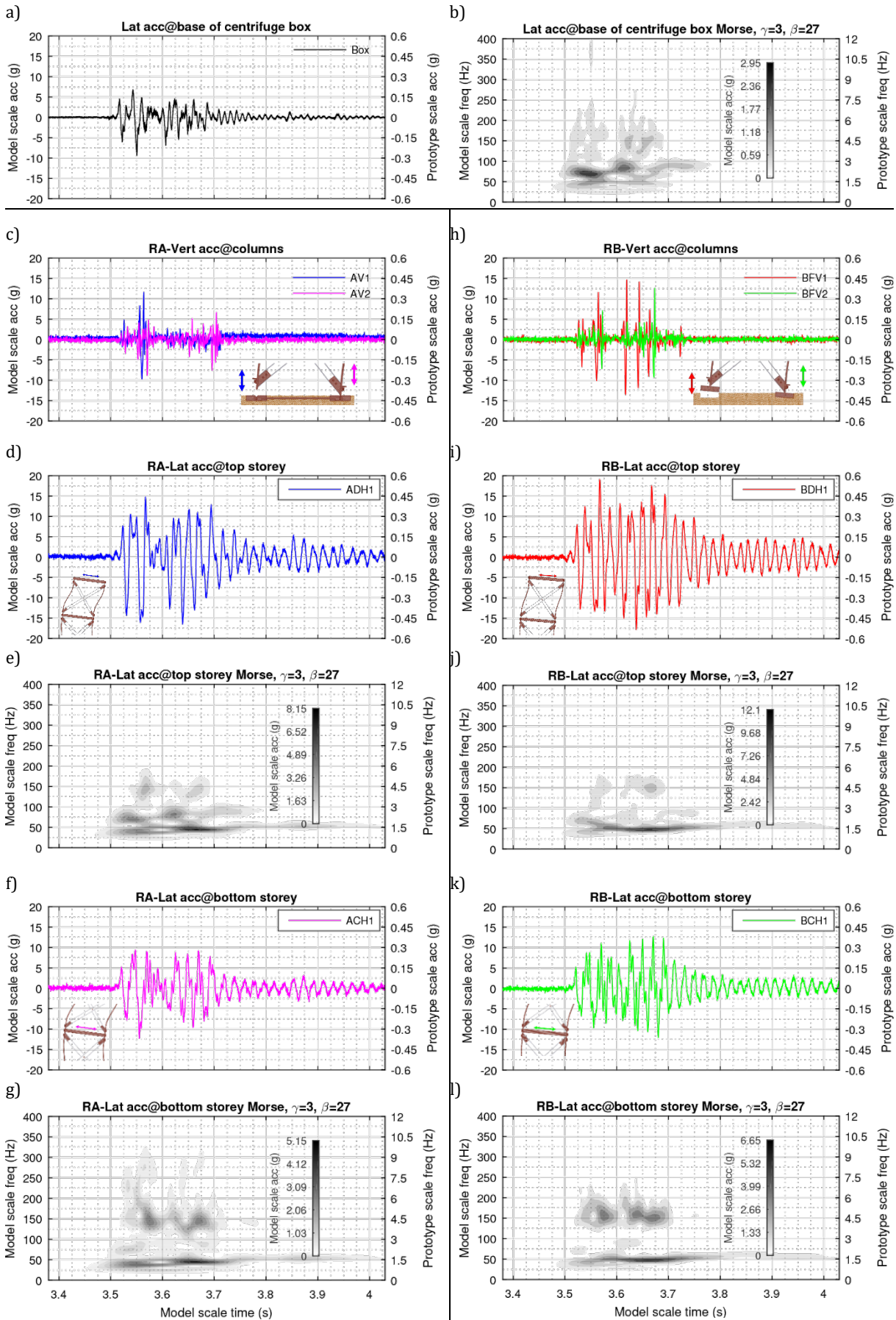
**Dense sand, Test-2 Eq-3: Excitation (a, b), vertical acceleration response of model RA (c), storeys' time-frequency response of model RA (d-g) and similarly for model RB (h-l)**



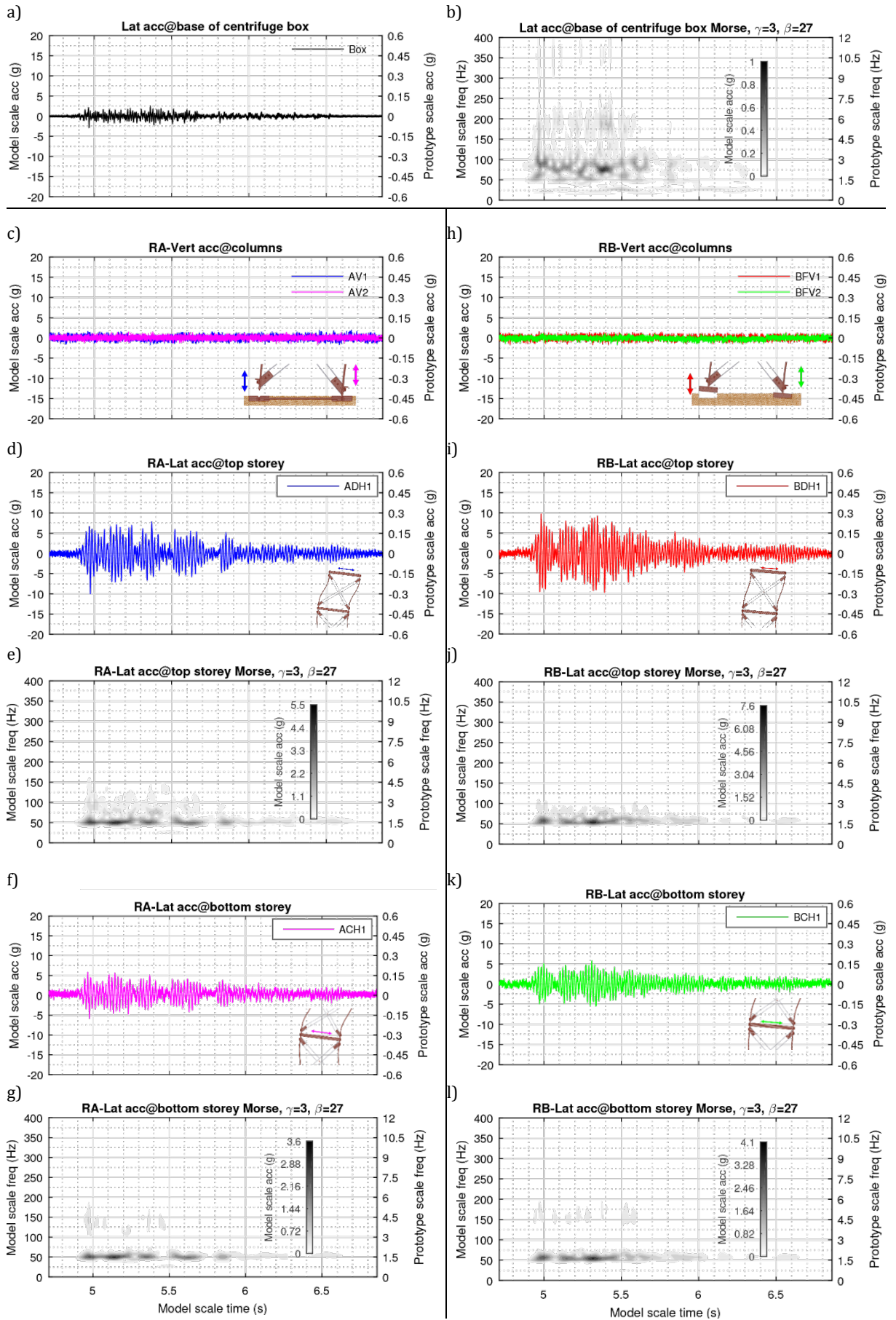
**Dense sand, Test-2 Eq-4: Excitation (a, b), vertical acceleration response of model RA (c), storeys' time-frequency response of model RA (d-g) and similarly for model RB (h-l)**



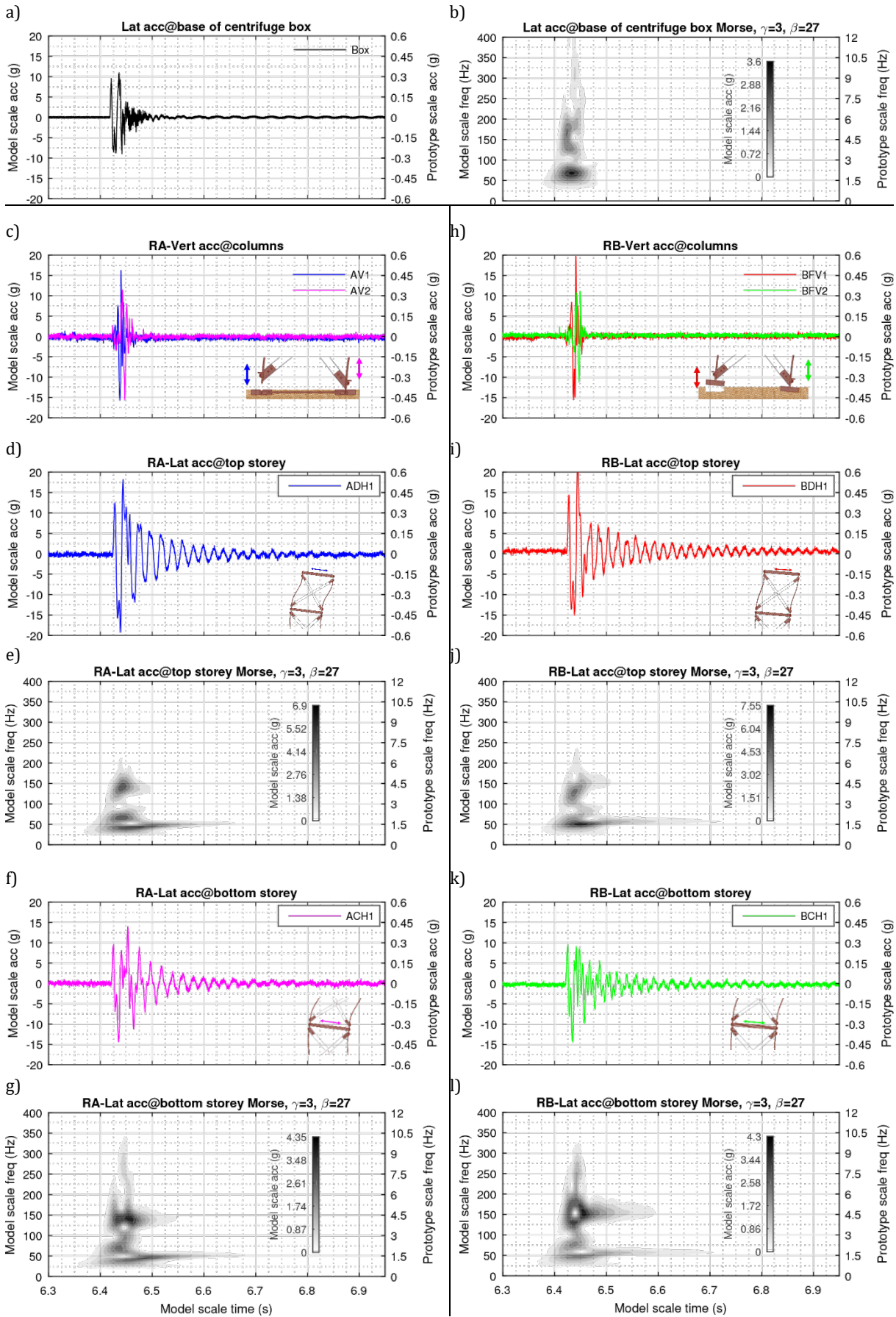
**Dense sand, Test-2 Eq-5: Excitation (a, b), vertical acceleration response of model RA (c), storeys' time-frequency response of model RA (d-g) and similarly for model RB (h-l)**



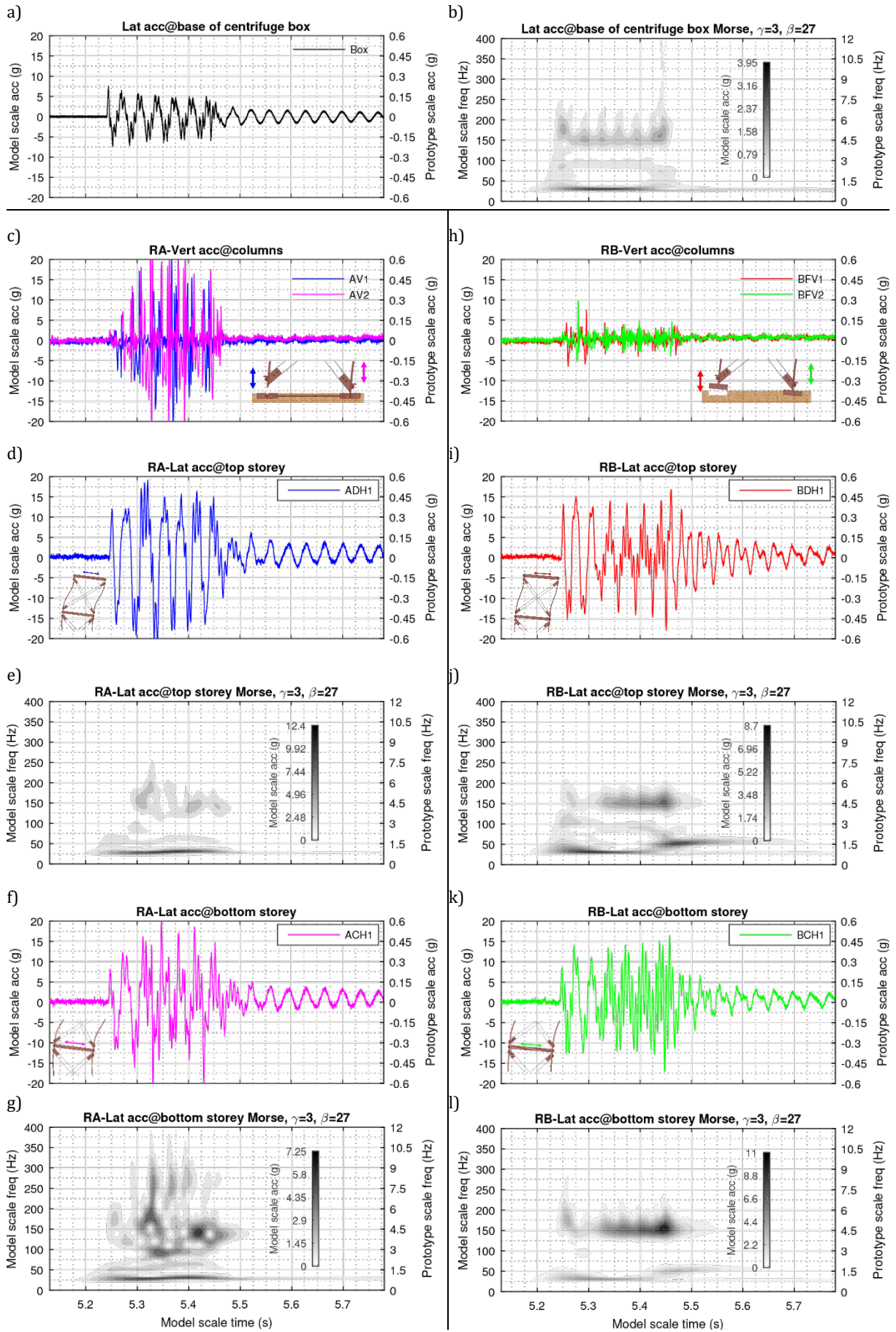
**Loose sand, Test-1 Eq-1: Excitation (a, b), vertical acceleration response of model RA (c), storeys' time-frequency response of model RA (d-g) and similarly for model RB (h-l)**



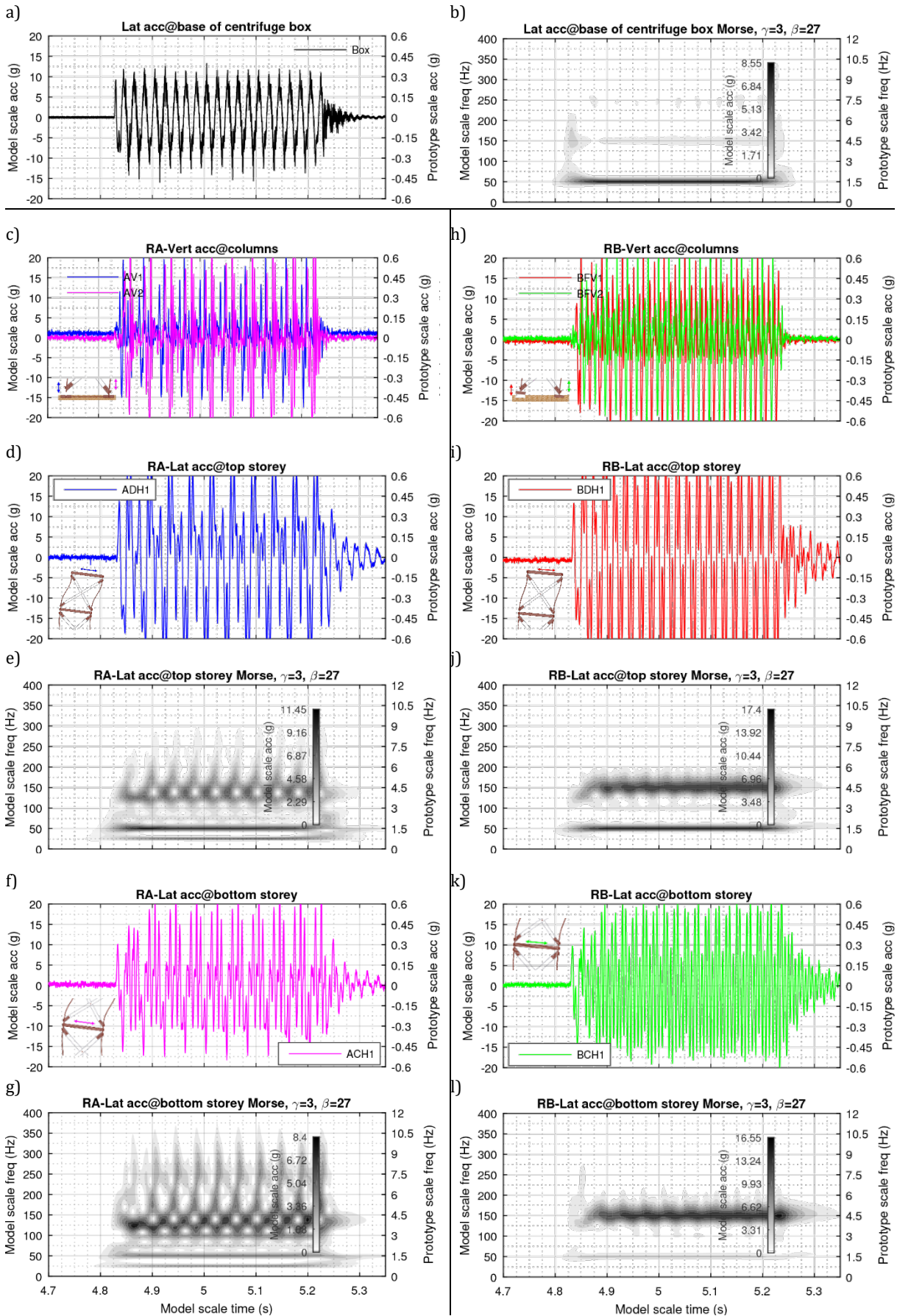
**Loose sand, Test-1 Eq-2: Excitation (a, b), vertical acceleration response of model RA (c), storeys' time-frequency response of model RA (d-g) and similarly for model RB (h-l)**



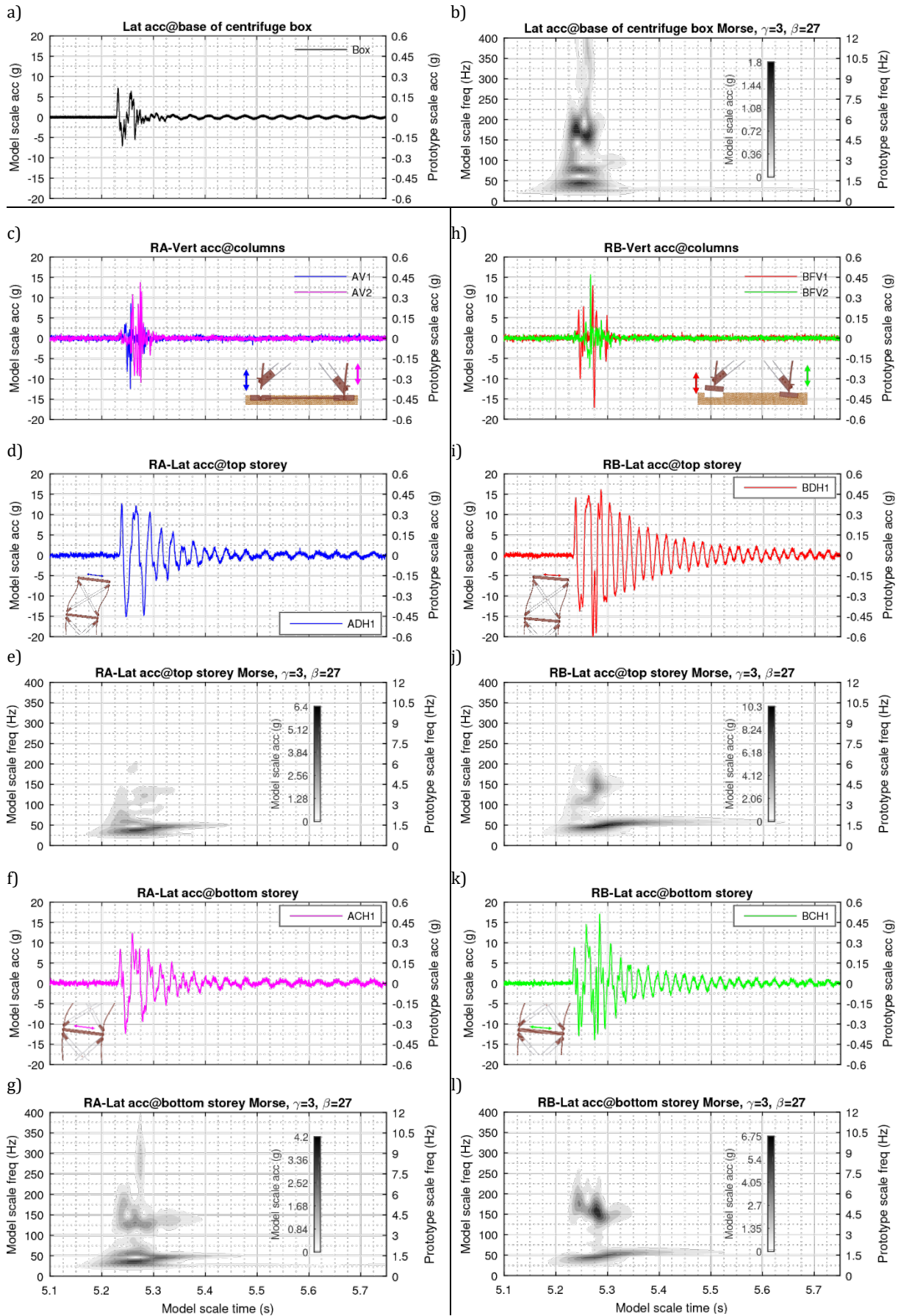
**Loose sand, Test-1 Eq-3: Excitation (a, b), vertical acceleration response of model RA (c), storeys' time-frequency response of model RA (d-g) and similarly for model RB (h-l)**



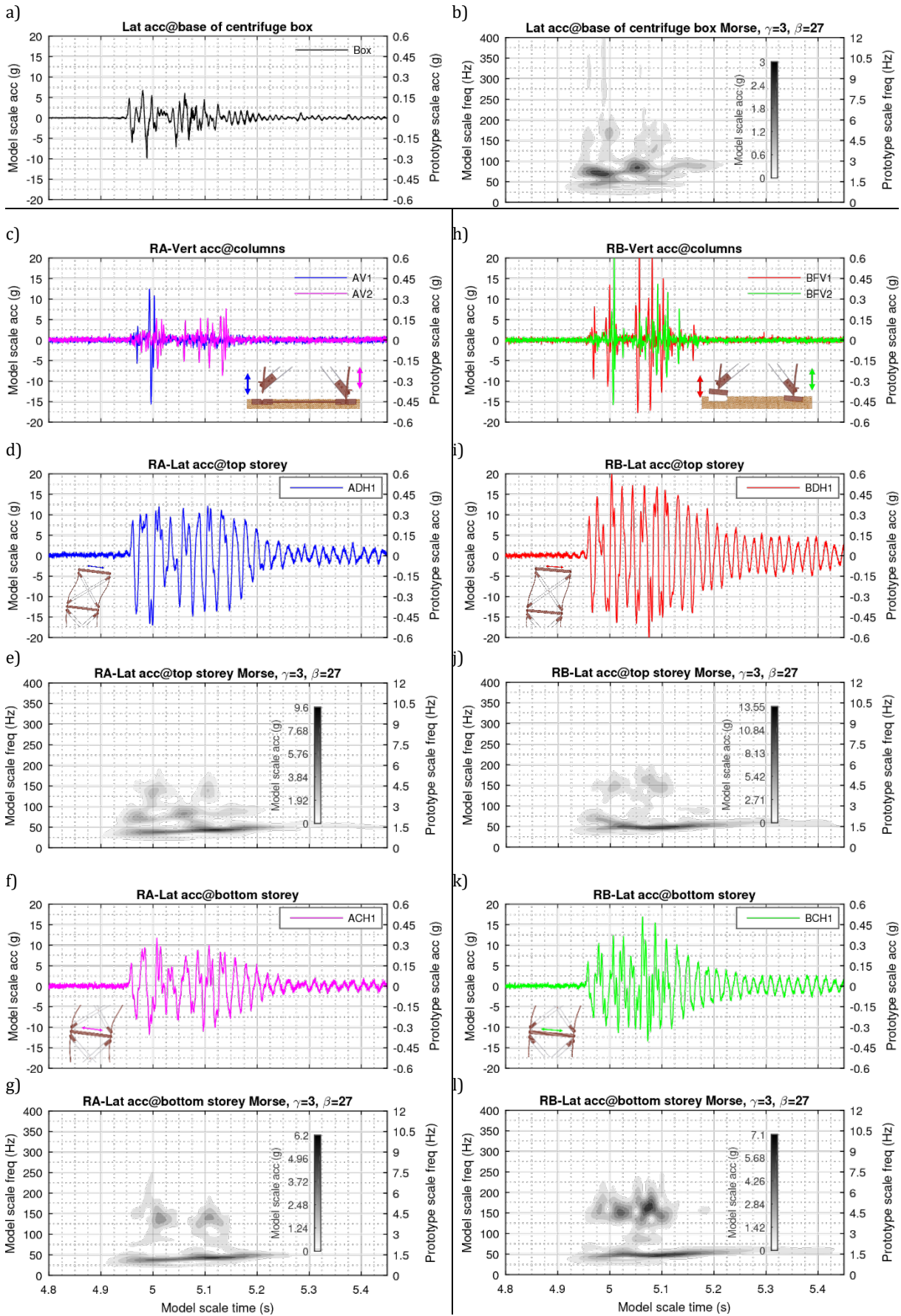
**Loose sand, Test-1 Eq-4: Excitation (a, b), vertical acceleration response of model RA (c), storeys' time-frequency response of model RA (d-g) and similarly for model RB (h-l)**



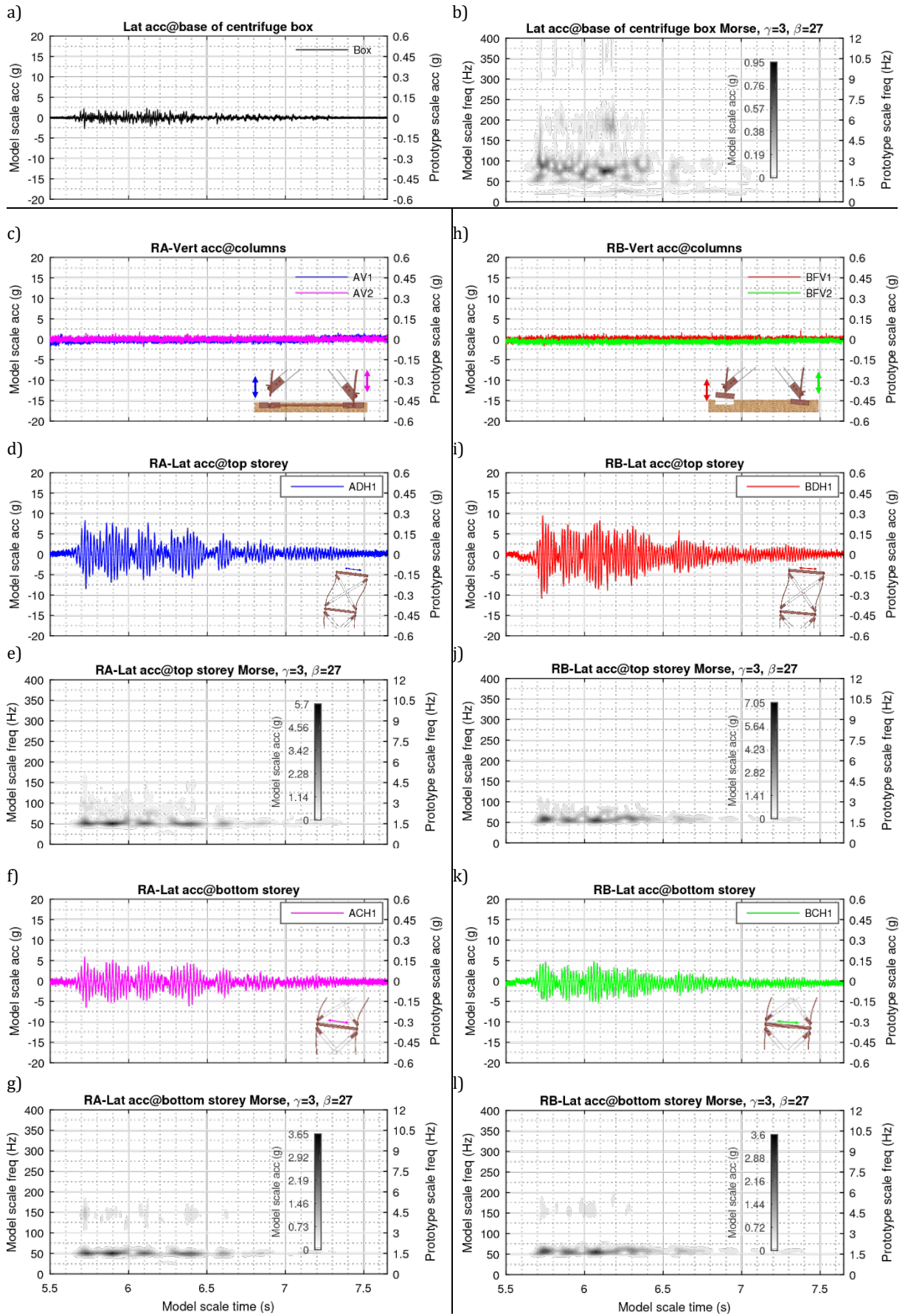
**Loose sand, Test-1 Eq-5: Excitation (a, b), vertical acceleration response of model RA (c), storeys' time-frequency response of model RA (d-g) and similarly for model RB (h-l)**



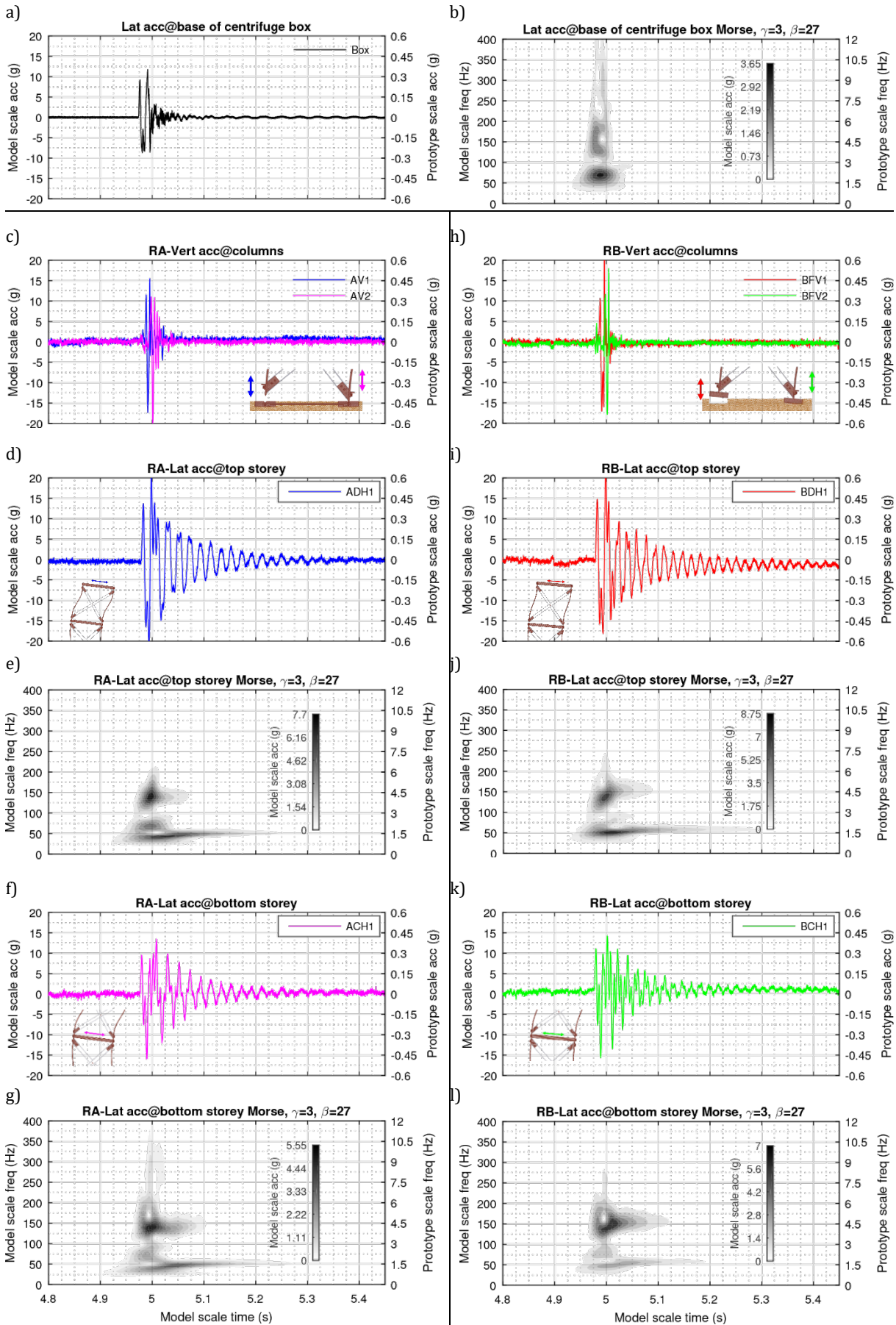
**Loose sand, Test-1 Eq-6: Excitation (a, b), vertical acceleration response of model RA (c), storeys' time-frequency response of model RA (d-g) and similarly for model RB (h-l)**



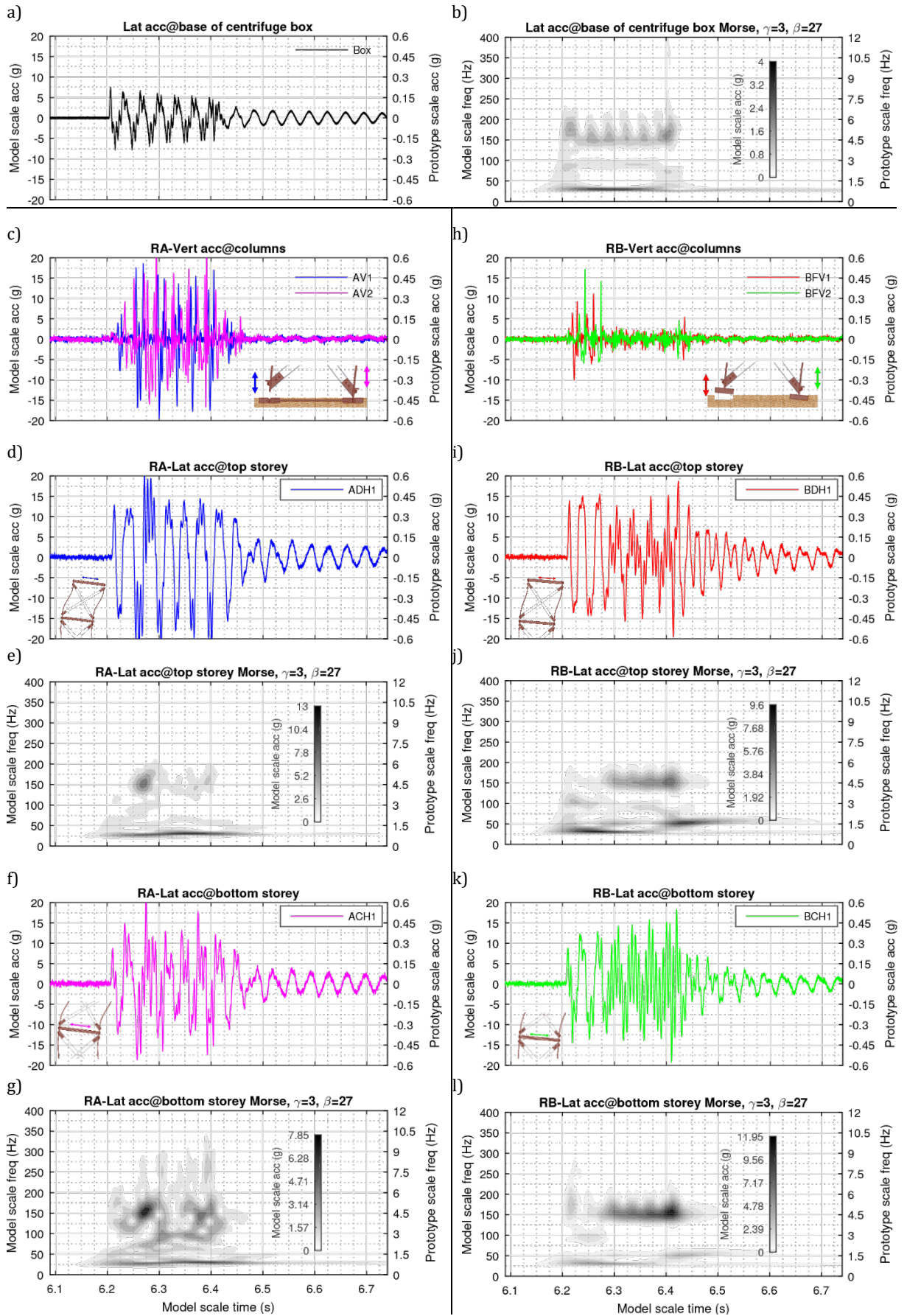
**Loose sand, Test-2 Eq-1: Excitation (a, b), vertical acceleration response of model RA (c), storeys' time-frequency response of model RA (d-g) and similarly for model RB (h-l)**



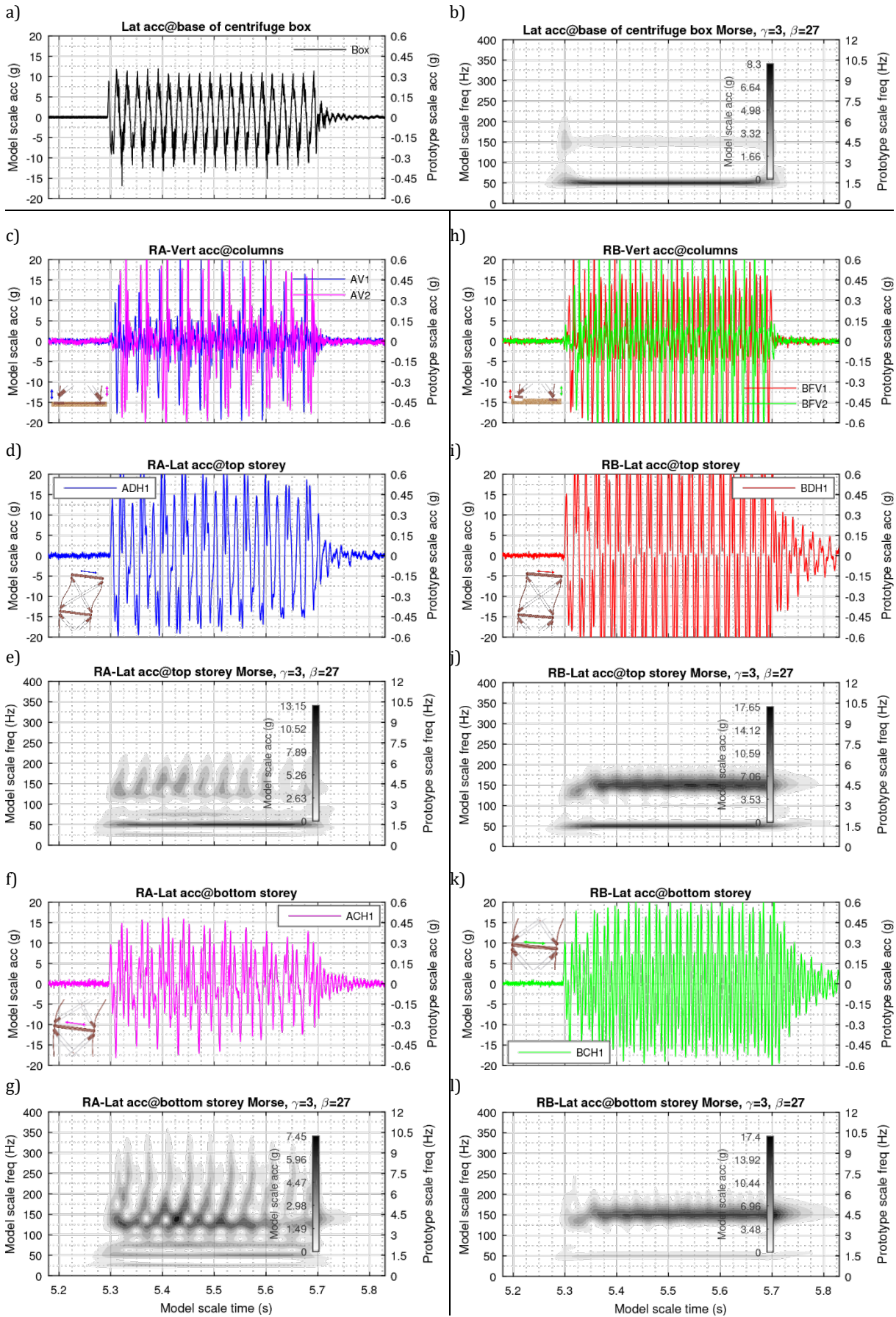
**Loose sand, Test-2 Eq-2: Excitation (a, b), vertical acceleration response of model RA (c), storeys' time-frequency response of model RA (d-g) and similarly for model RB (h-l)**



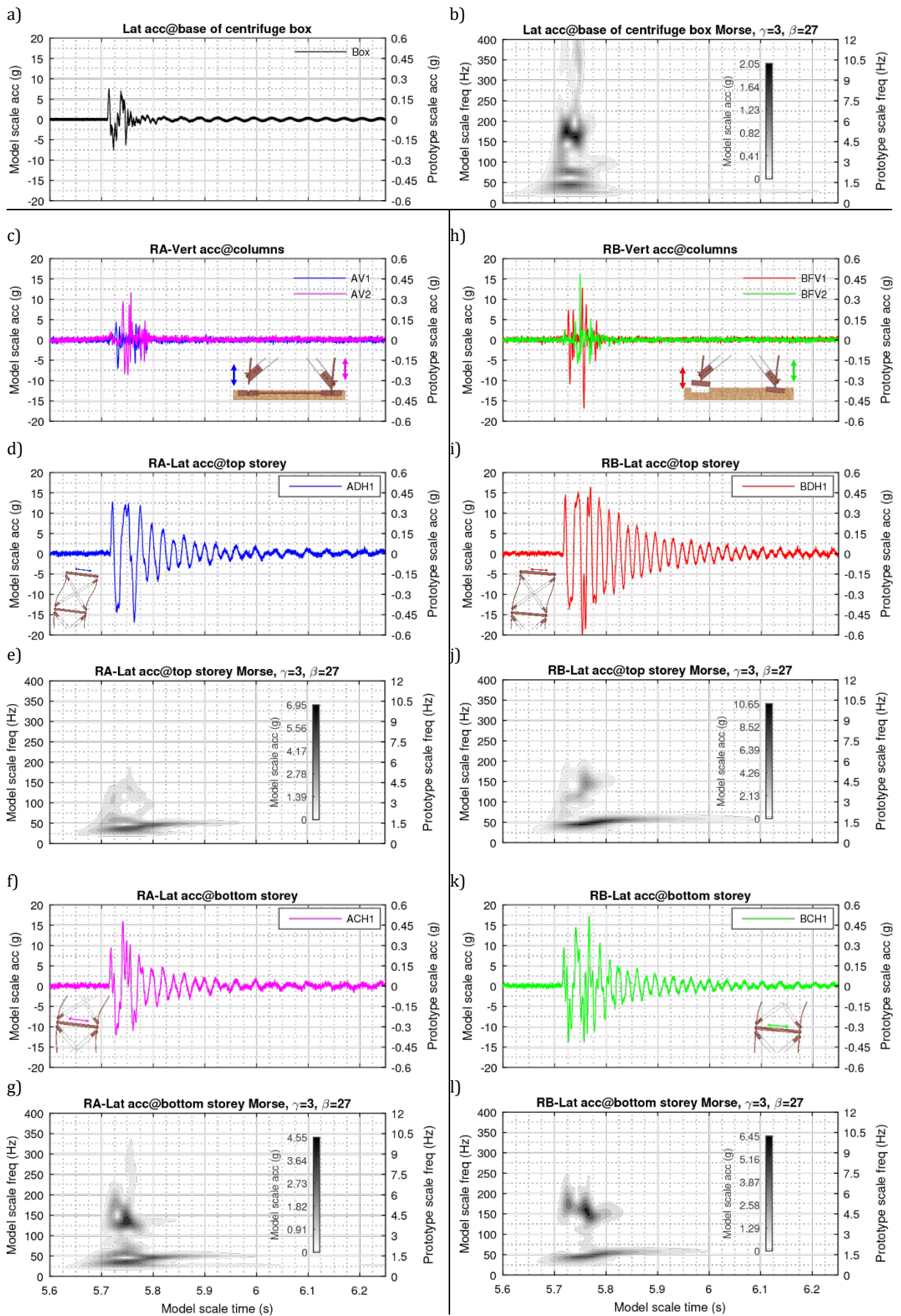
**Loose sand, Test-2 Eq-3: Excitation (a, b), vertical acceleration response of model RA (c), storeys' time-frequency response of model RA (d-g) and similarly for model RB (h-l)**



**Loose sand, Test-2 Eq-4: Excitation (a, b), vertical acceleration response of model RA (c), storeys' time-frequency response of model RA (d-g) and similarly for model RB (h-l)**

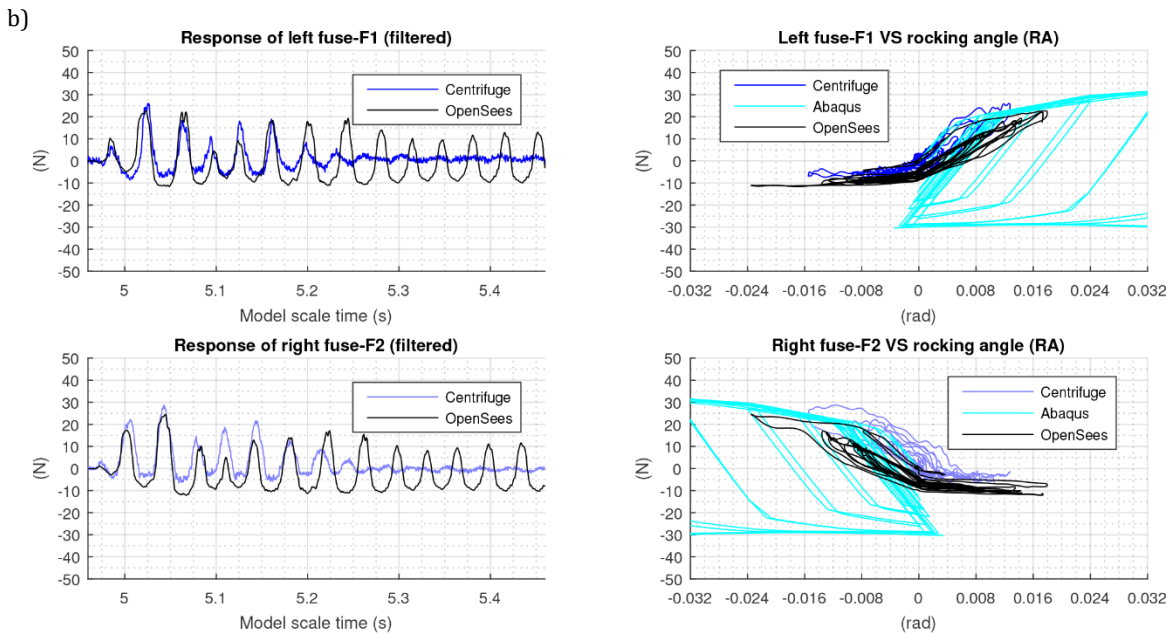
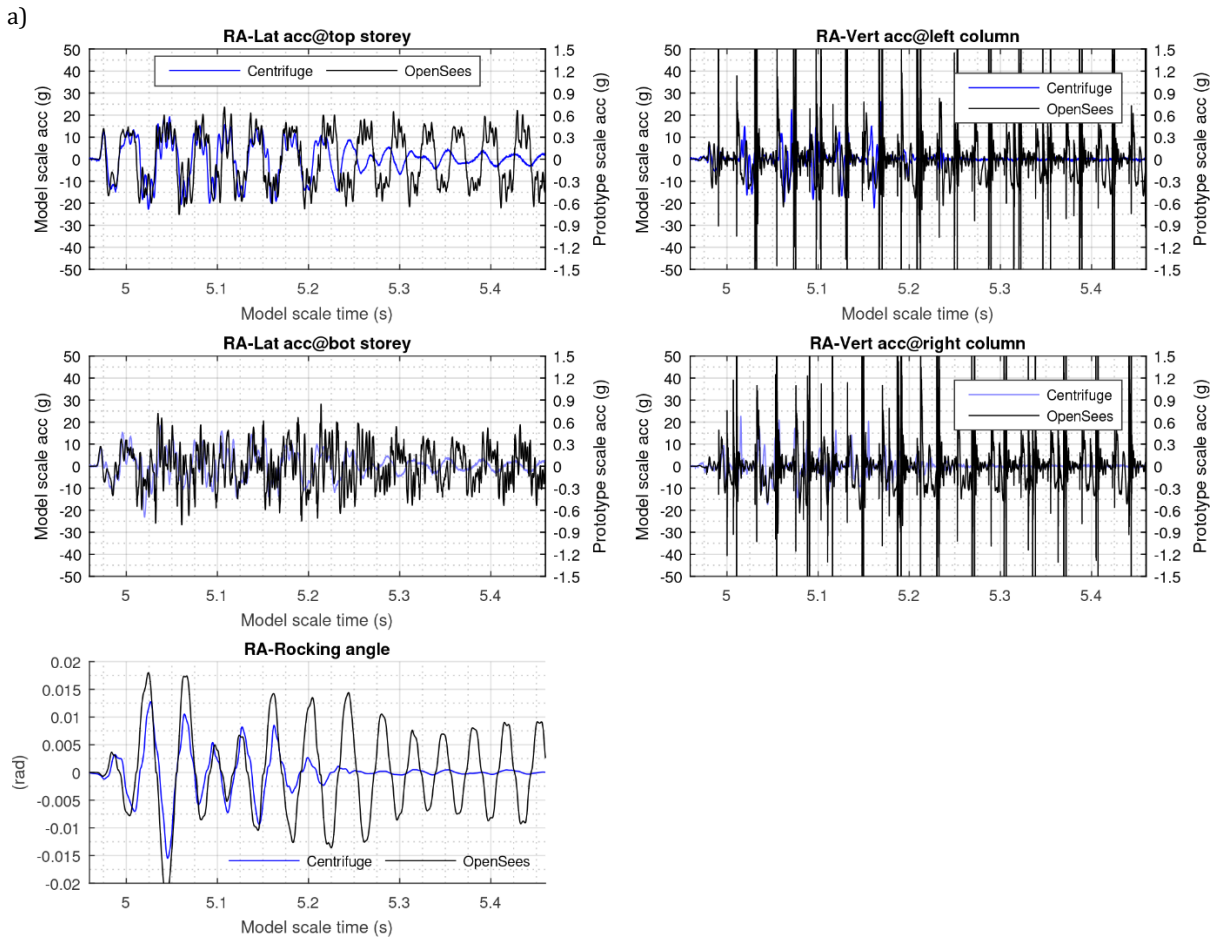


**Loose sand, Test-2 Eq-5: Excitation (a, b), vertical acceleration response of model RA (c), storeys' time-frequency response of model RA (d-g) and similarly for model RB (h-l)**



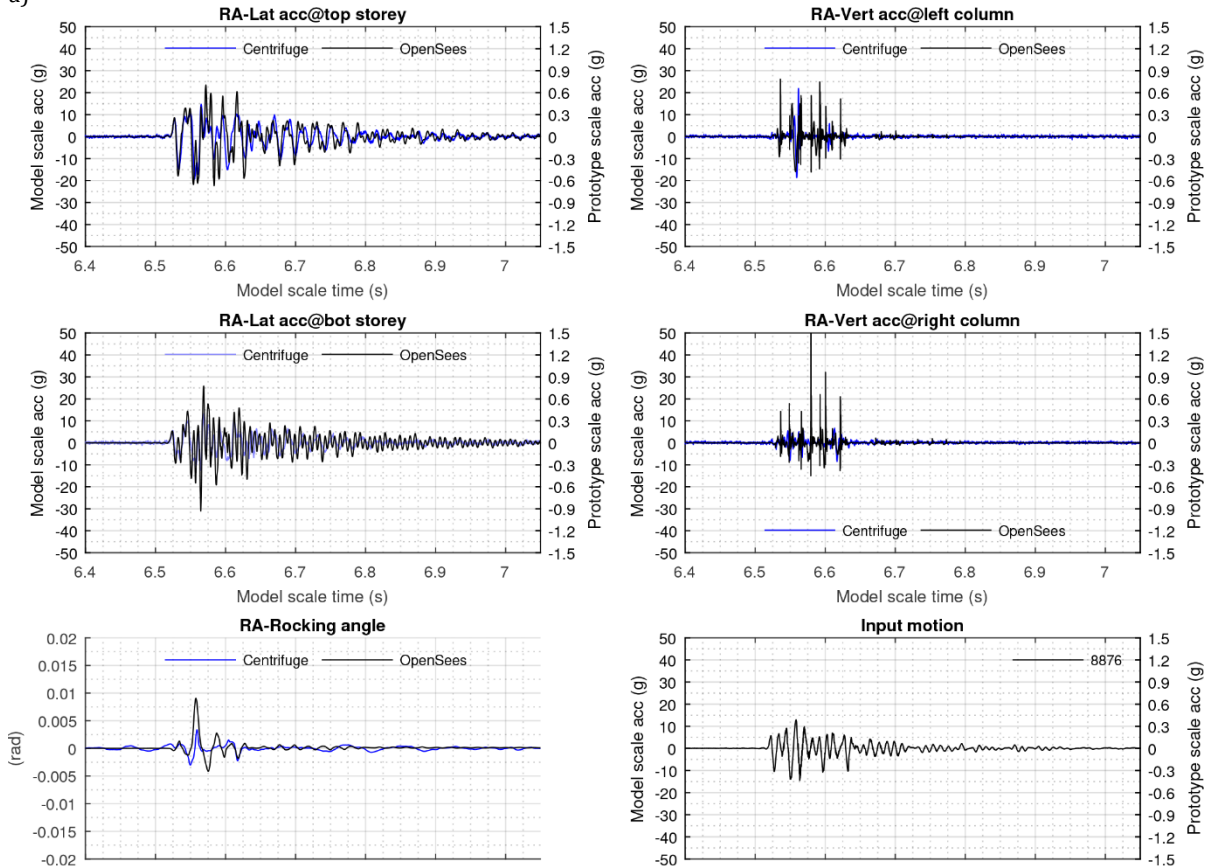
**Loose sand, Test-2 Eq-6: Excitation (a, b), vertical acceleration response of model RA (c), storeys' time-frequency response of model RA (d-g) and similarly for model RB (h-l)**

# Appendix G: Computational responses

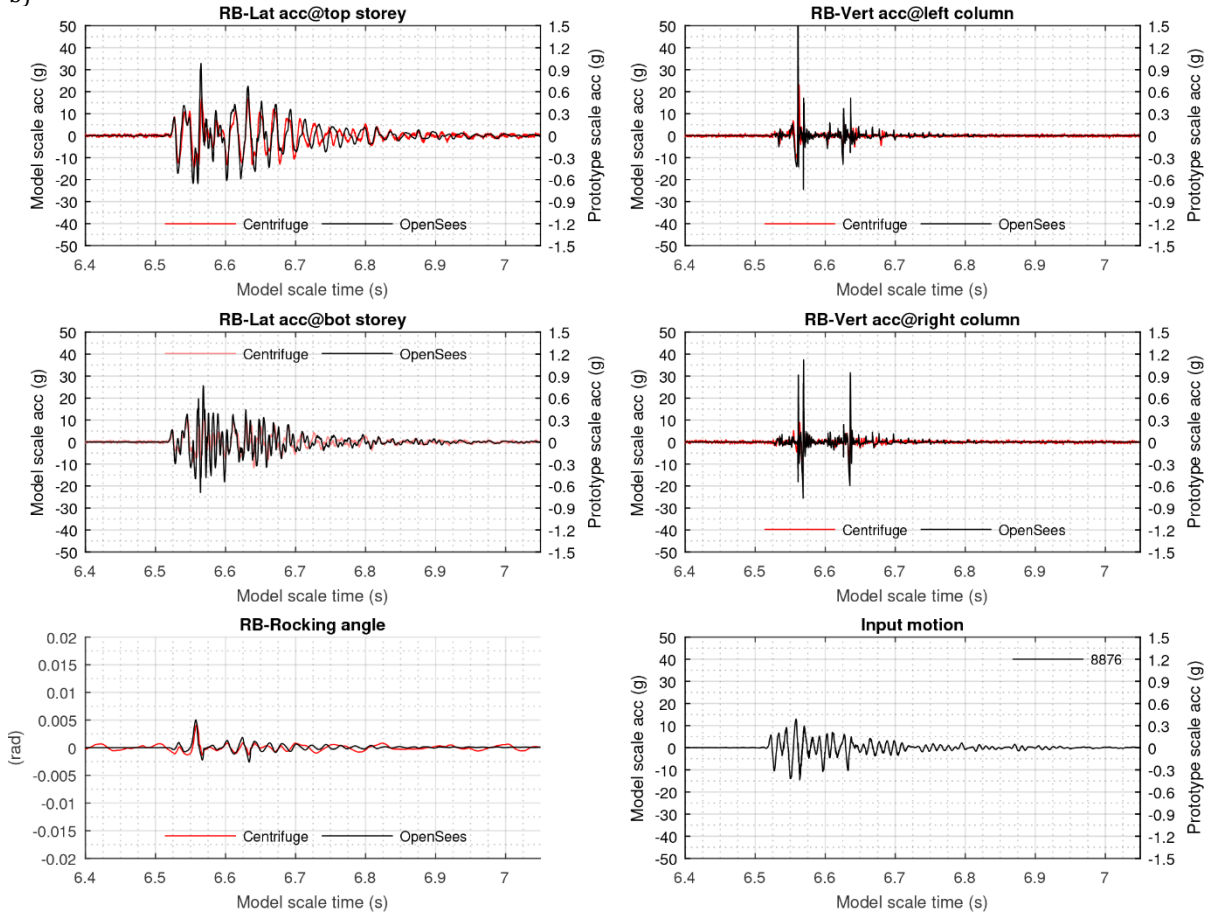


**Dense sand, Test-1 Eq-4: Lateral and vertical accelerations at storeys and columns respectively and rocking angle (a) and fuse time-history and force-rocking angle response (b)**

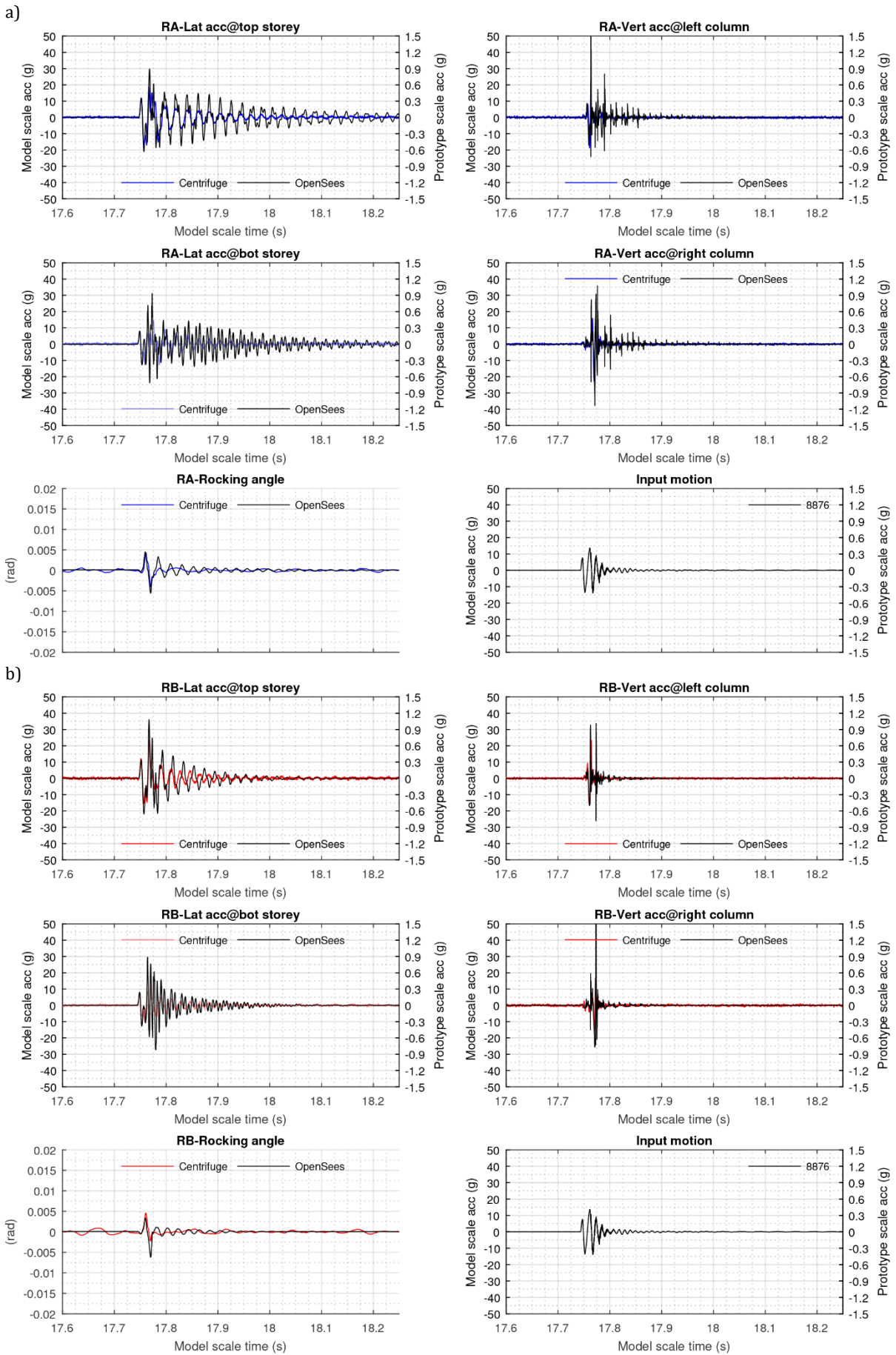
a)



b)

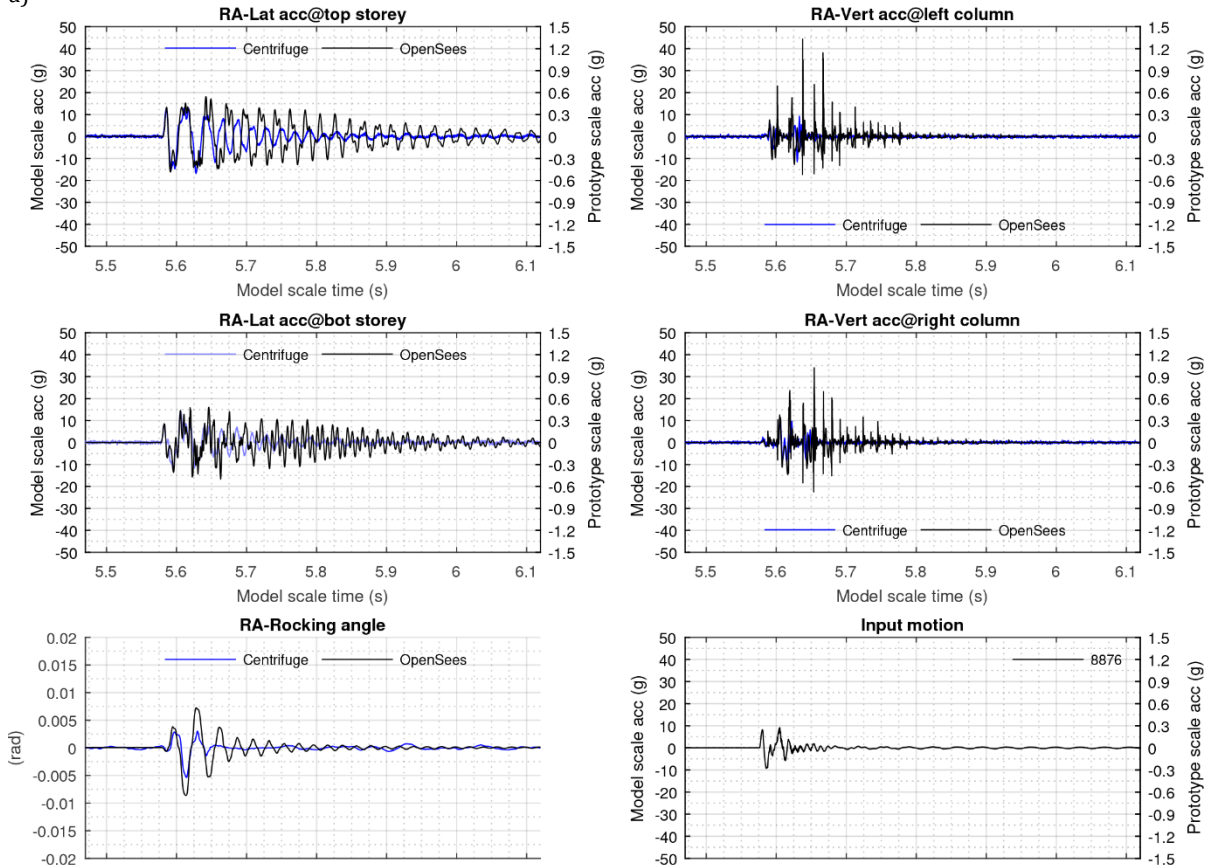


**Dense sand, Test-0 Eq-1: Lateral and vertical accelerations at storeys and columns respectively, rocking angle and input motion for model RA (a) and model RB (b)**

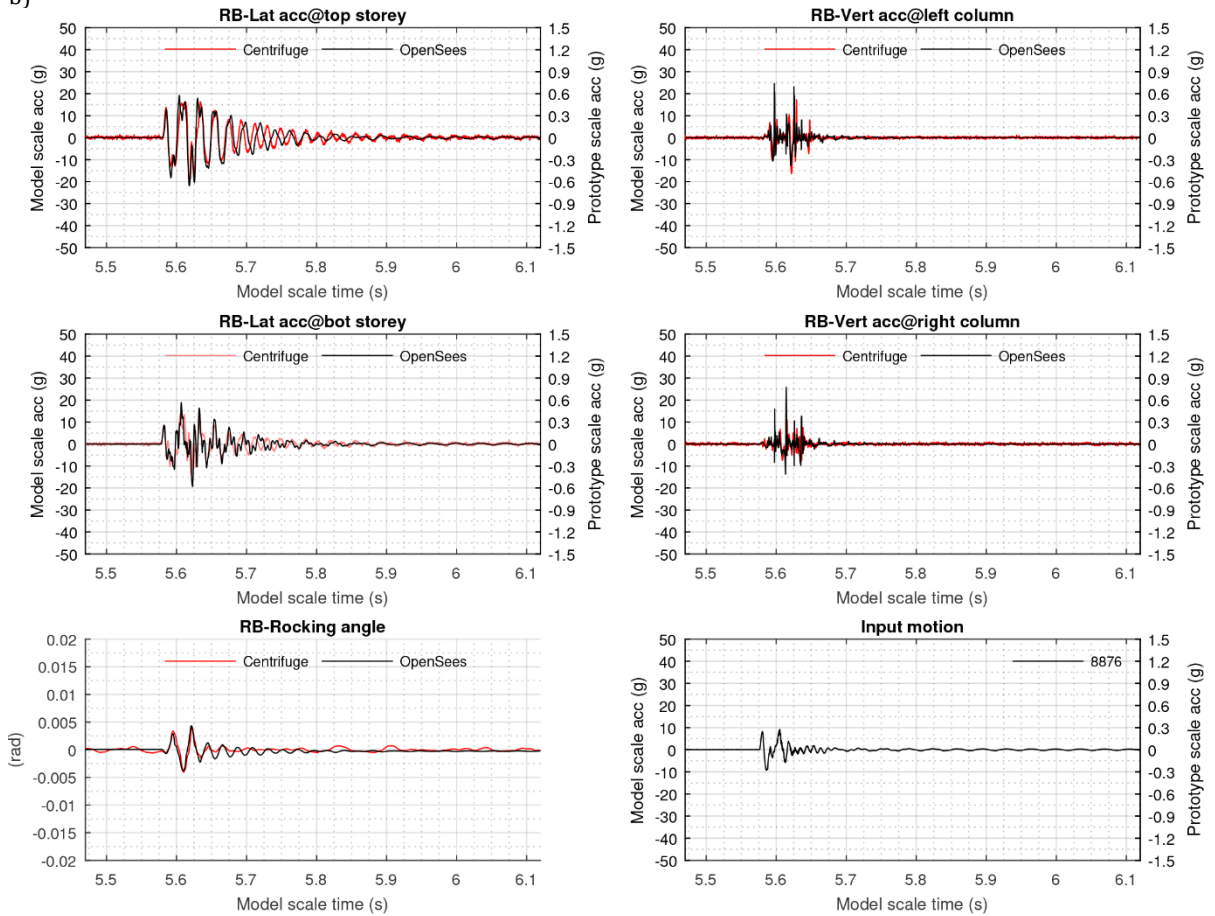


**Dense sand, Test-0 Eq-2: Lateral and vertical accelerations at storeys and columns respectively, rocking angle and input motion for model RA (a) and model RB (b)**

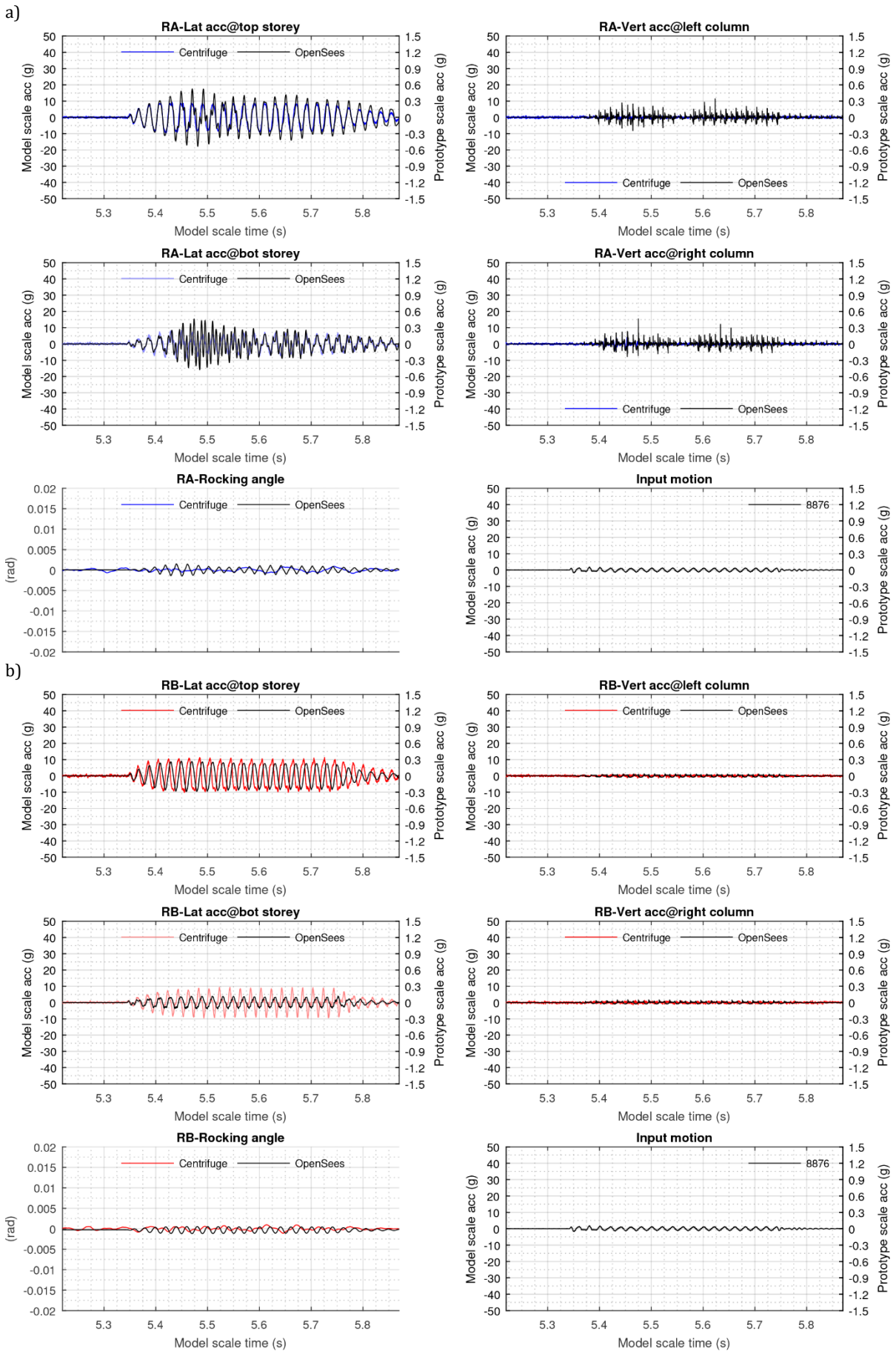
a)



b)

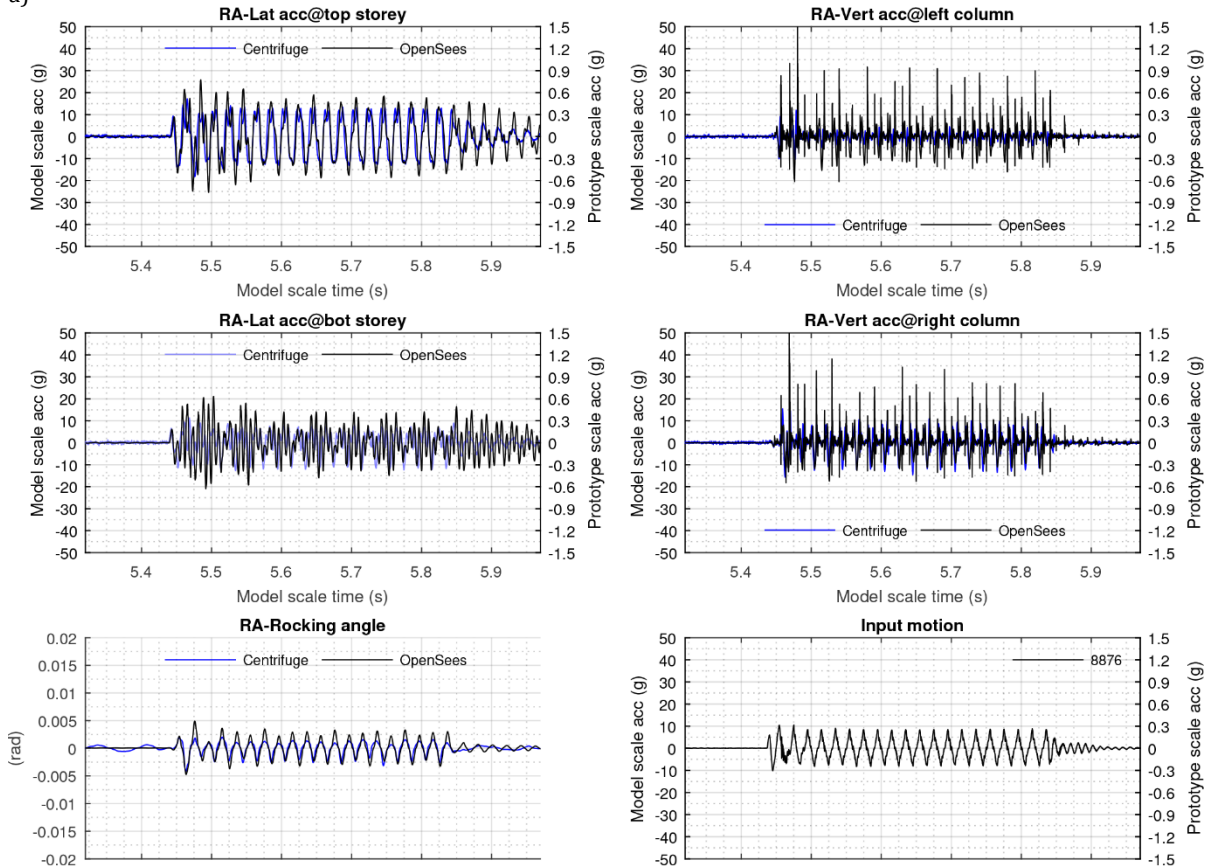


**Dense sand, Test-0 Eq-3: Lateral and vertical accelerations at storeys and columns respectively, rocking angle and input motion for model RA (a) and model RB (b)**

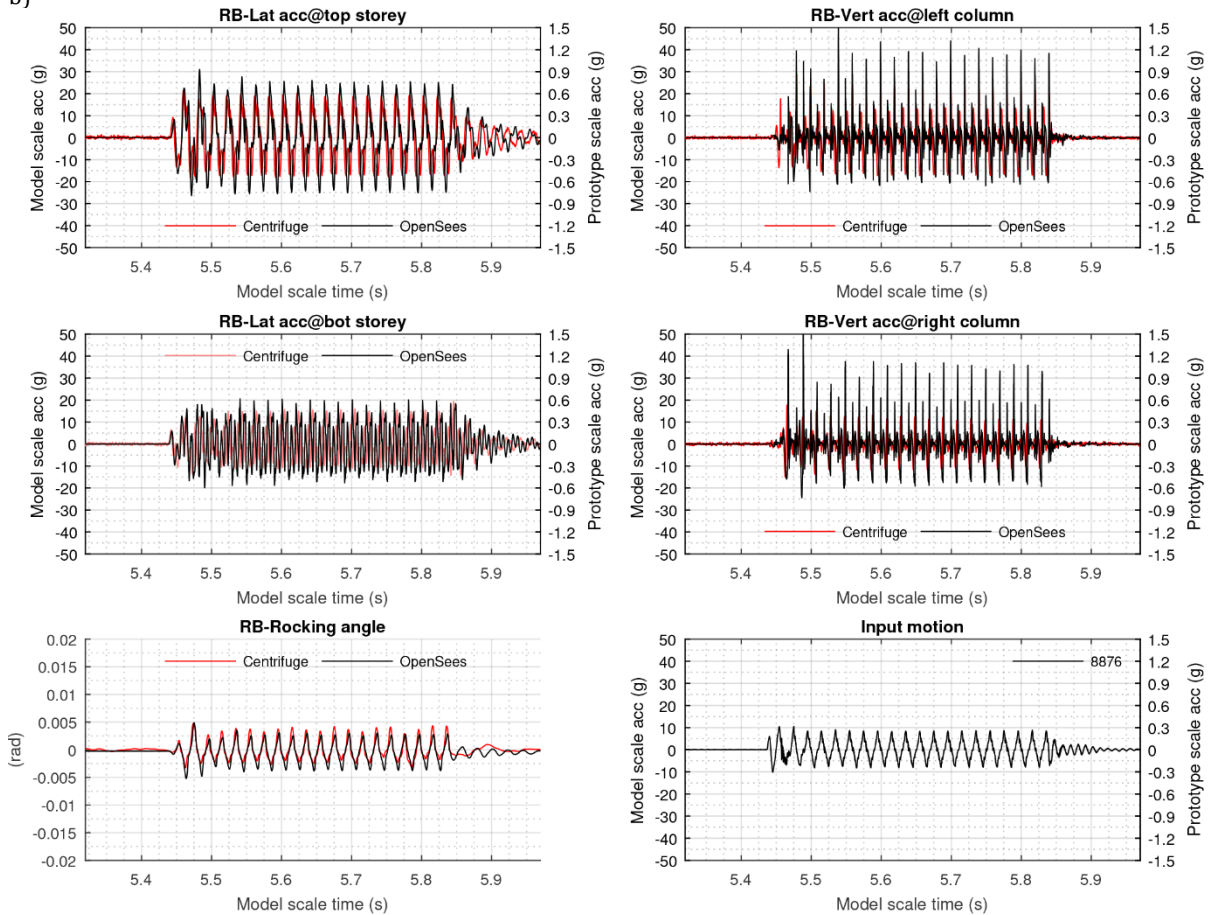


**Dense sand, Test-0 Eq-4: Lateral and vertical accelerations at storeys and columns respectively, rocking angle and input motion for model RA (a) and model RB (b)**

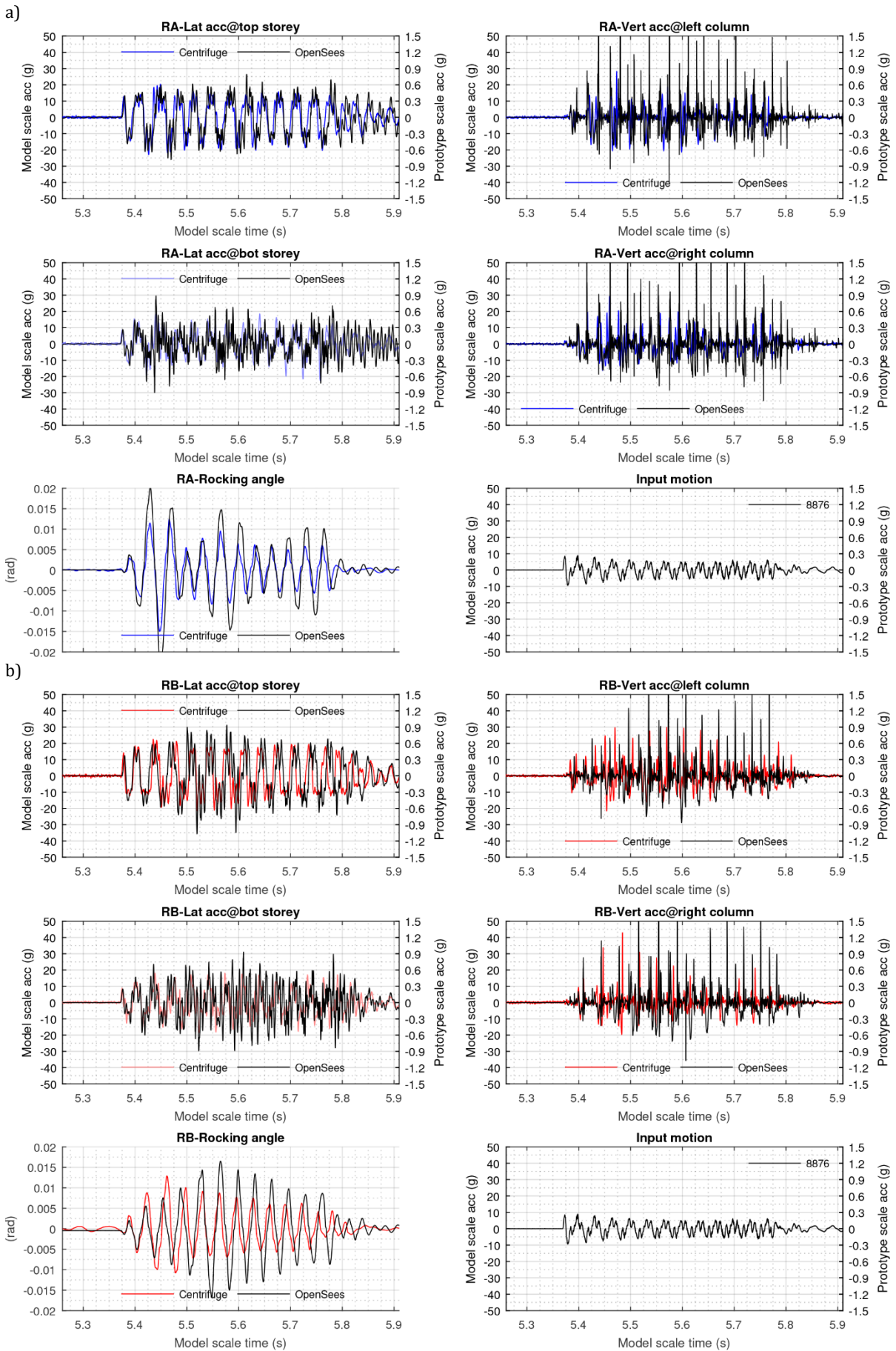
a)



b)

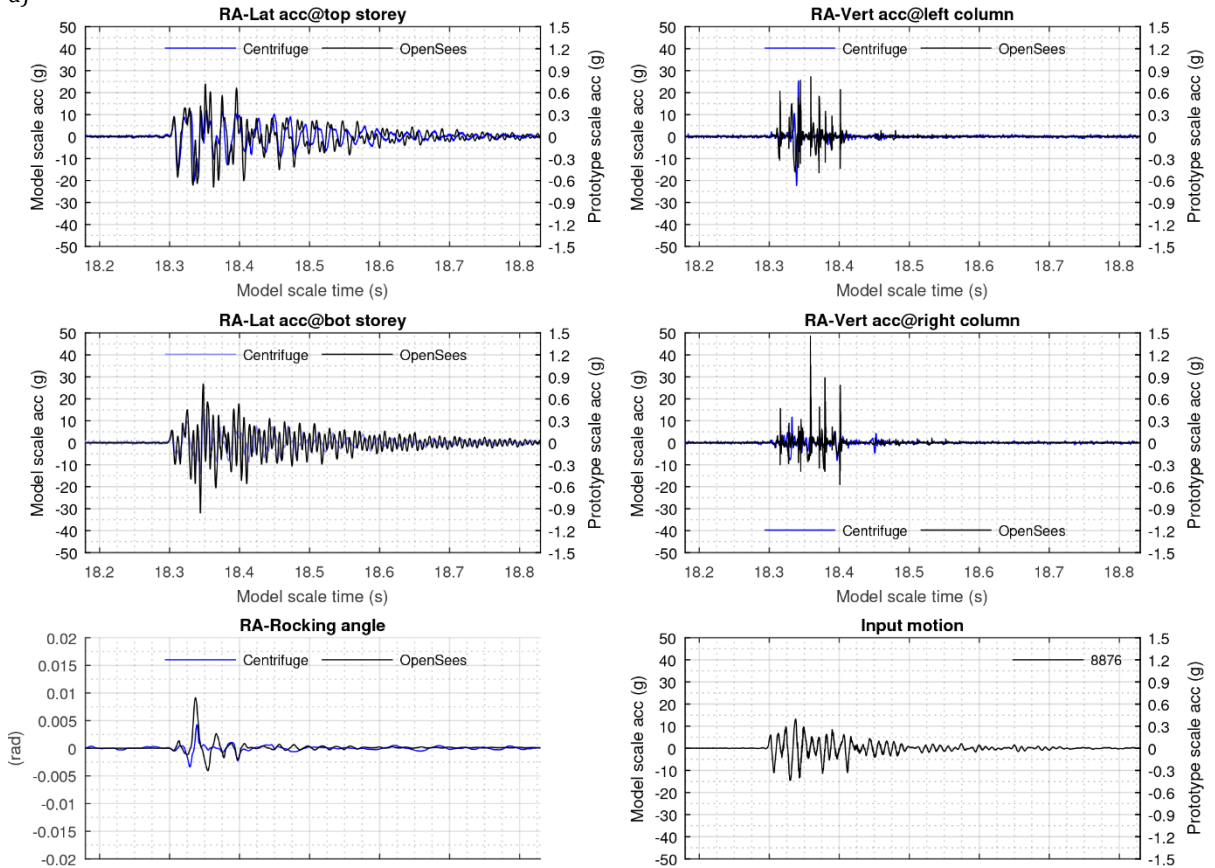


**Dense sand, Test-0 Eq-5: Lateral and vertical accelerations at storeys and columns respectively, rocking angle and input motion for model RA (a) and model RB (b)**

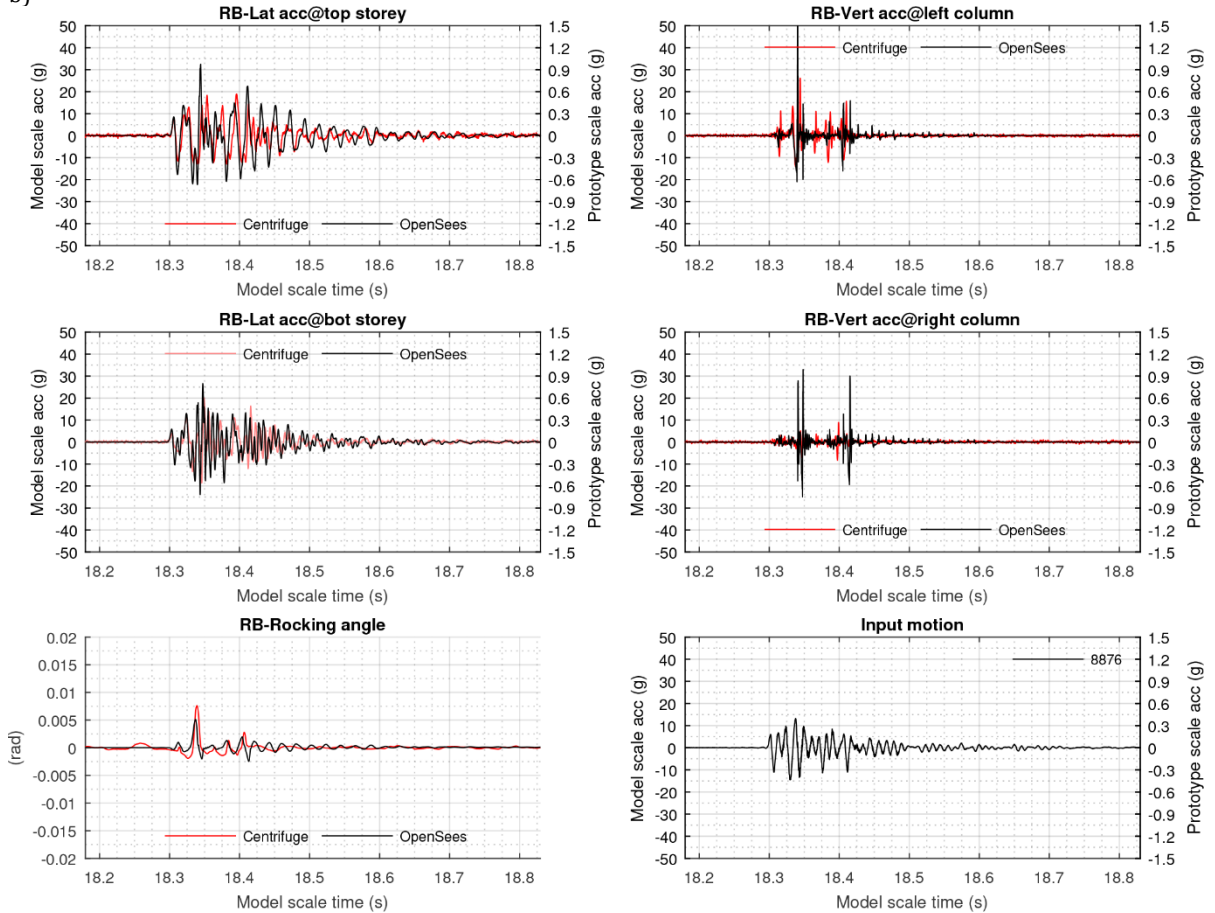


**Dense sand, Test-0 Eq-6: Lateral and vertical accelerations at storeys and columns respectively, rocking angle and input motion for model RA (a) and model RB (b)**

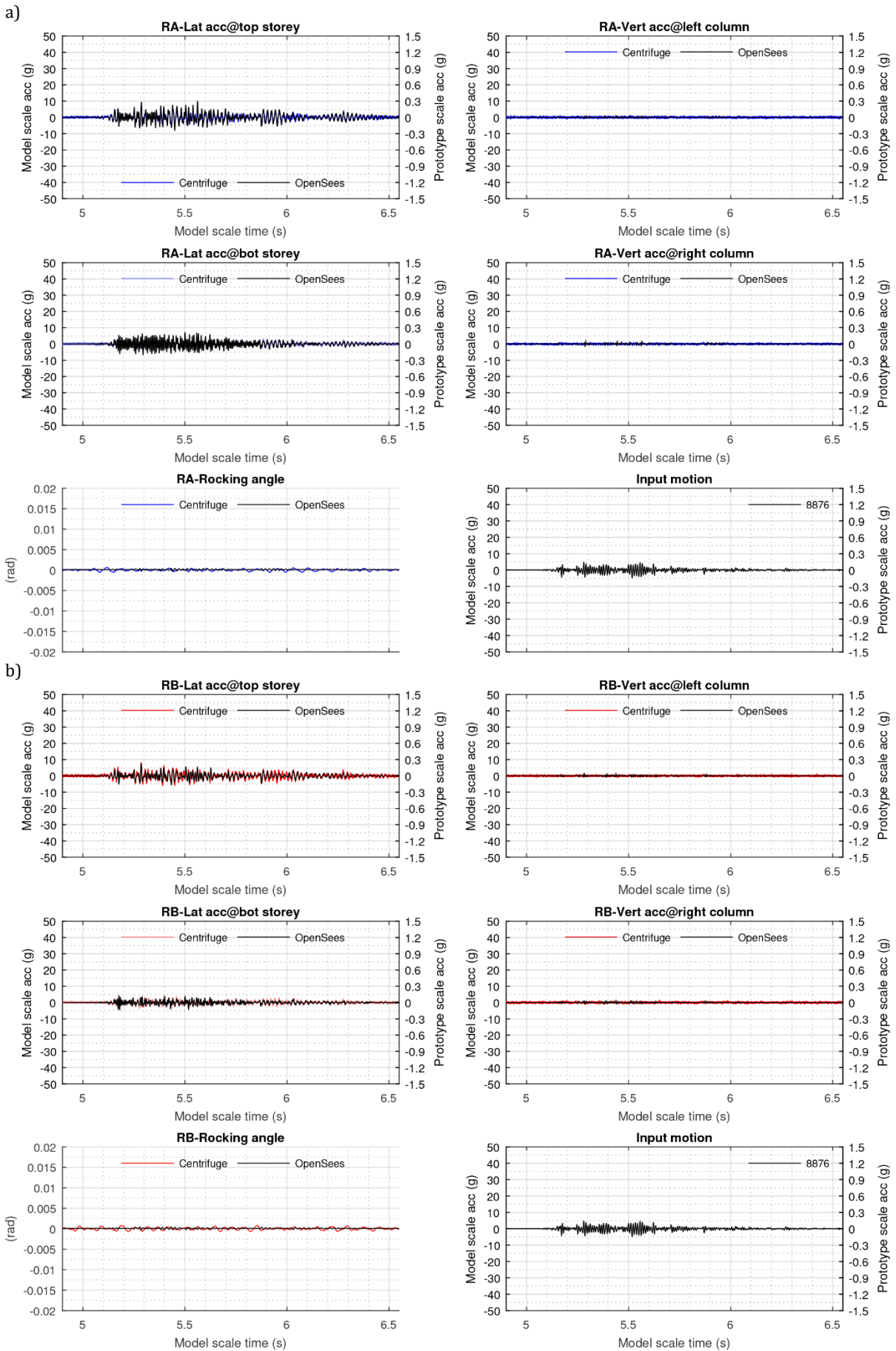
a)



b)

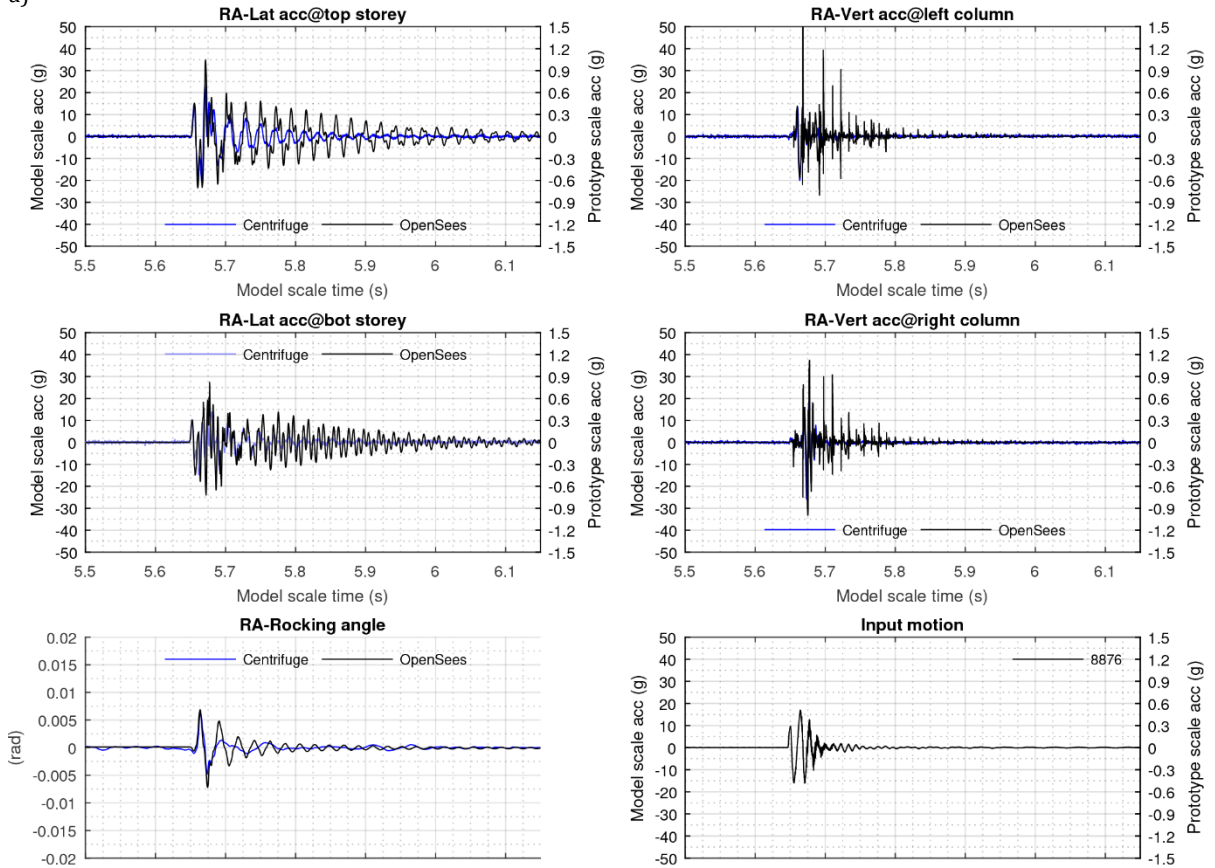


**Dense sand, Test-1 Eq-1: Lateral and vertical accelerations at storeys and columns respectively, rocking angle and input motion for model RA (a) and model RB (b)**

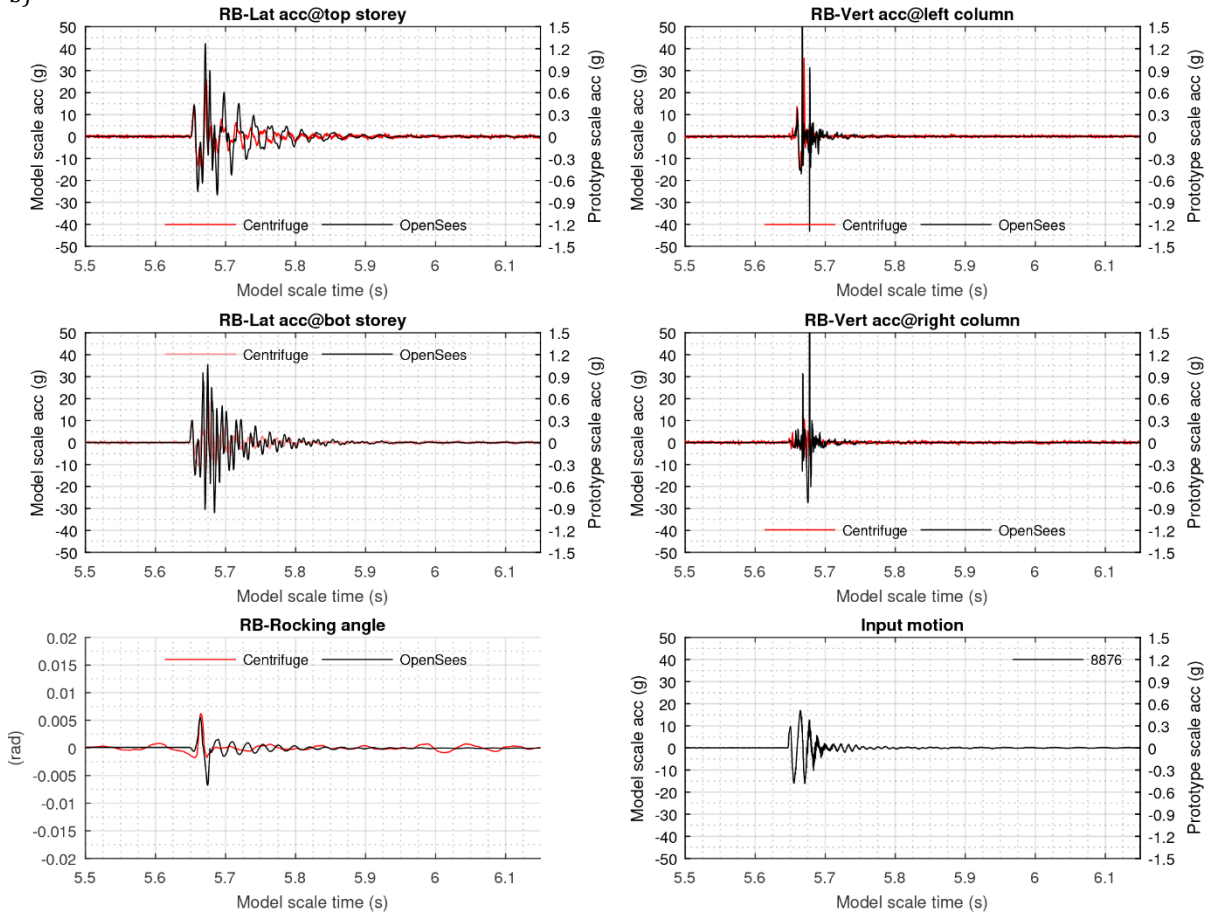


**Dense sand, Test-1 Eq-2: Lateral and vertical accelerations at storeys and columns respectively, rocking angle and input motion for model RA (a) and model RB (b)**

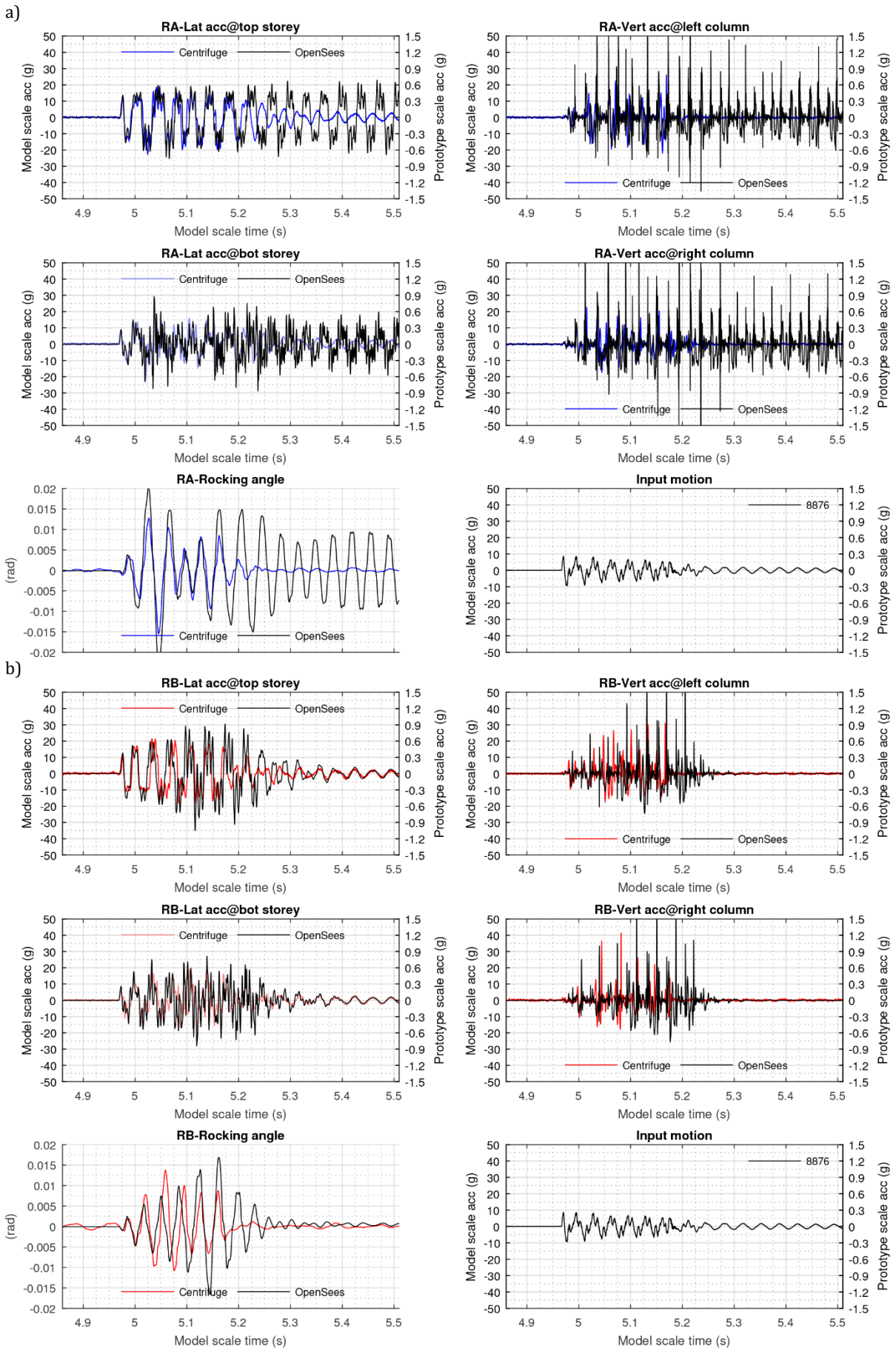
a)



b)

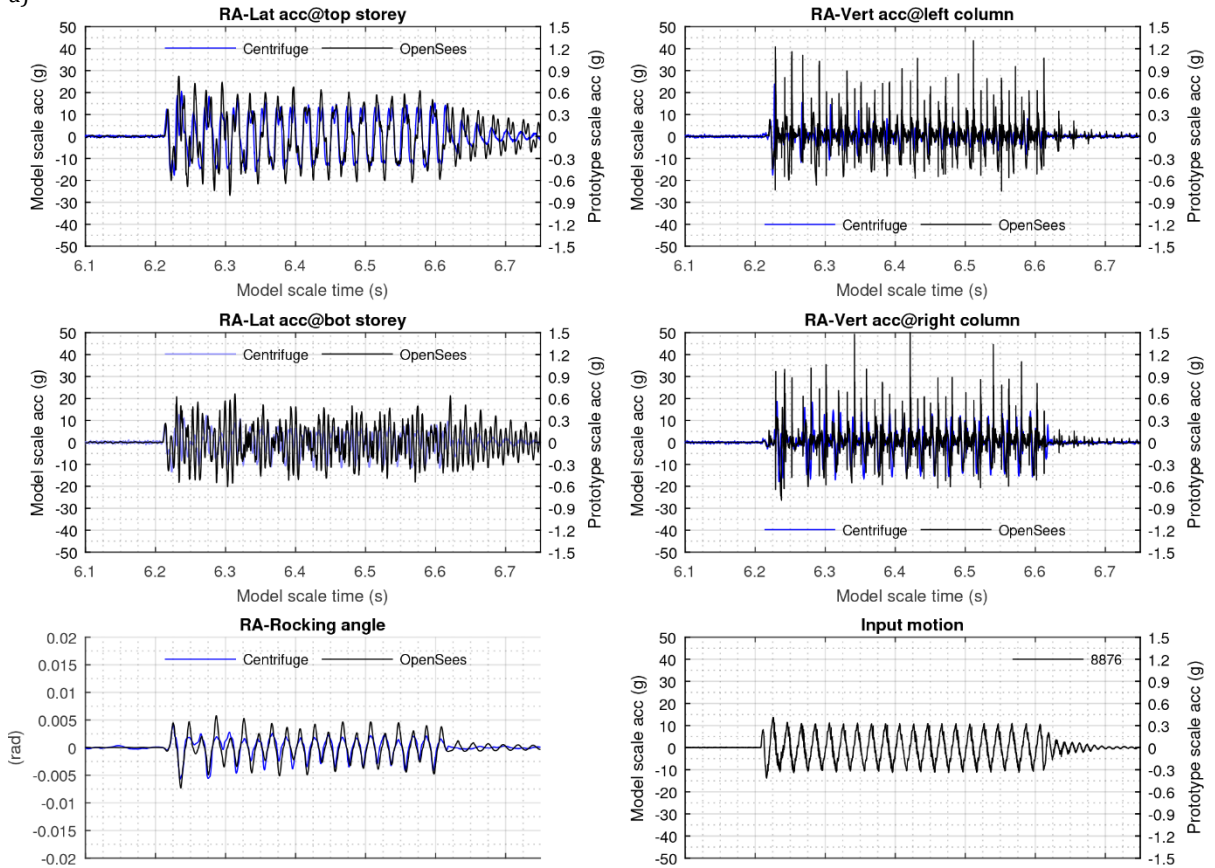


**Dense sand, Test-1 Eq-3: Lateral and vertical accelerations at storeys and columns respectively, rocking angle and input motion for model RA (a) and model RB (b)**

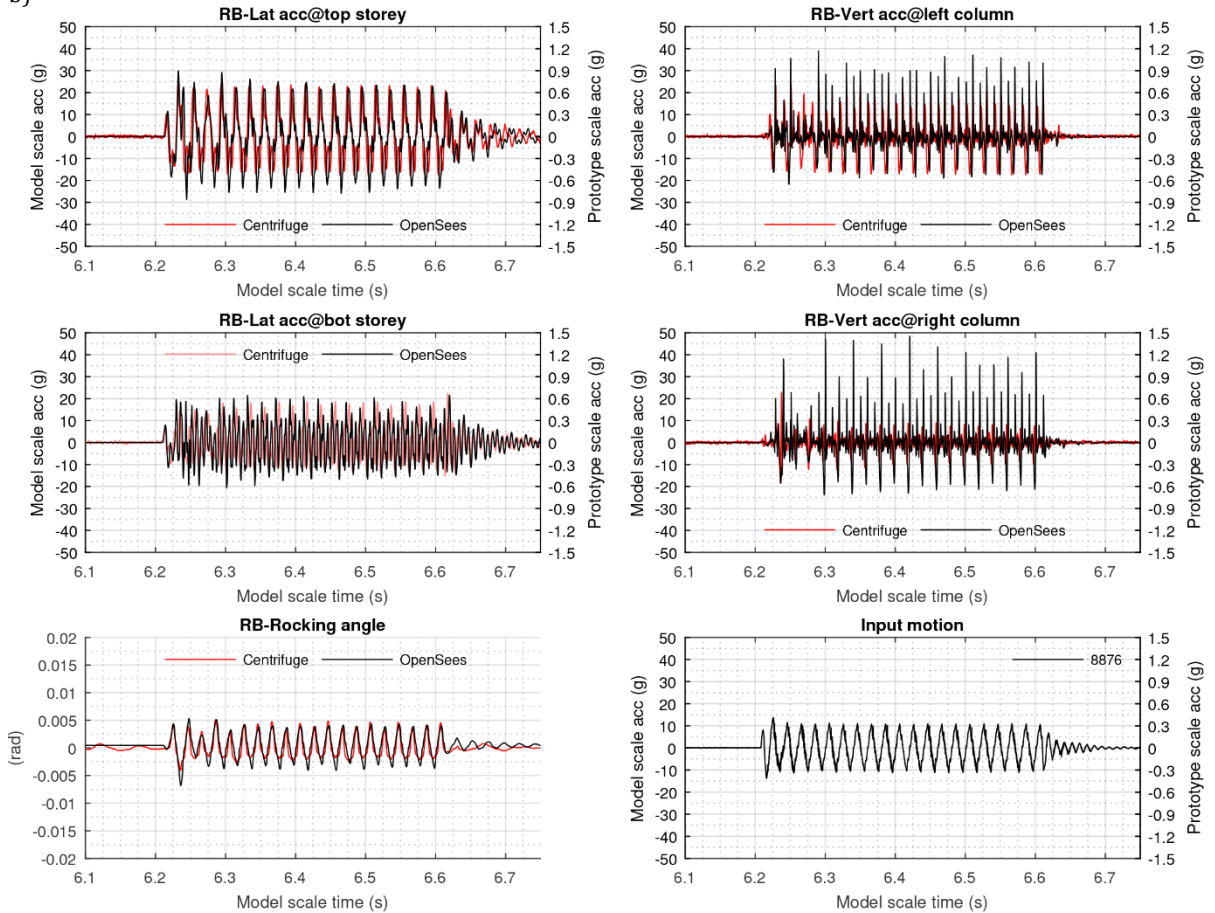


**Dense sand, Test-1 Eq-4: Lateral and vertical accelerations at storeys and columns respectively, rocking angle and input motion for model RA (a) and model RB (b)**

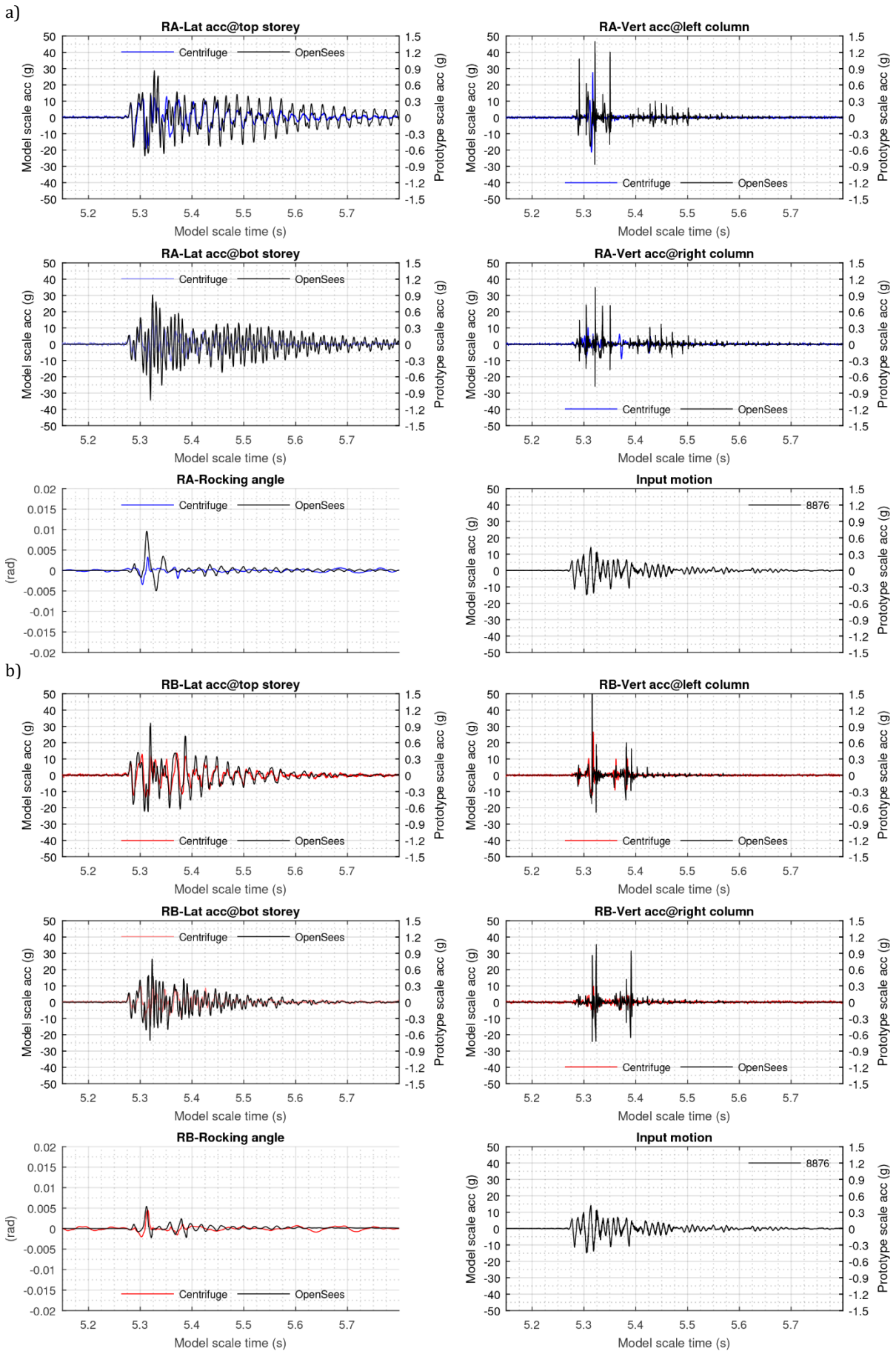
a)



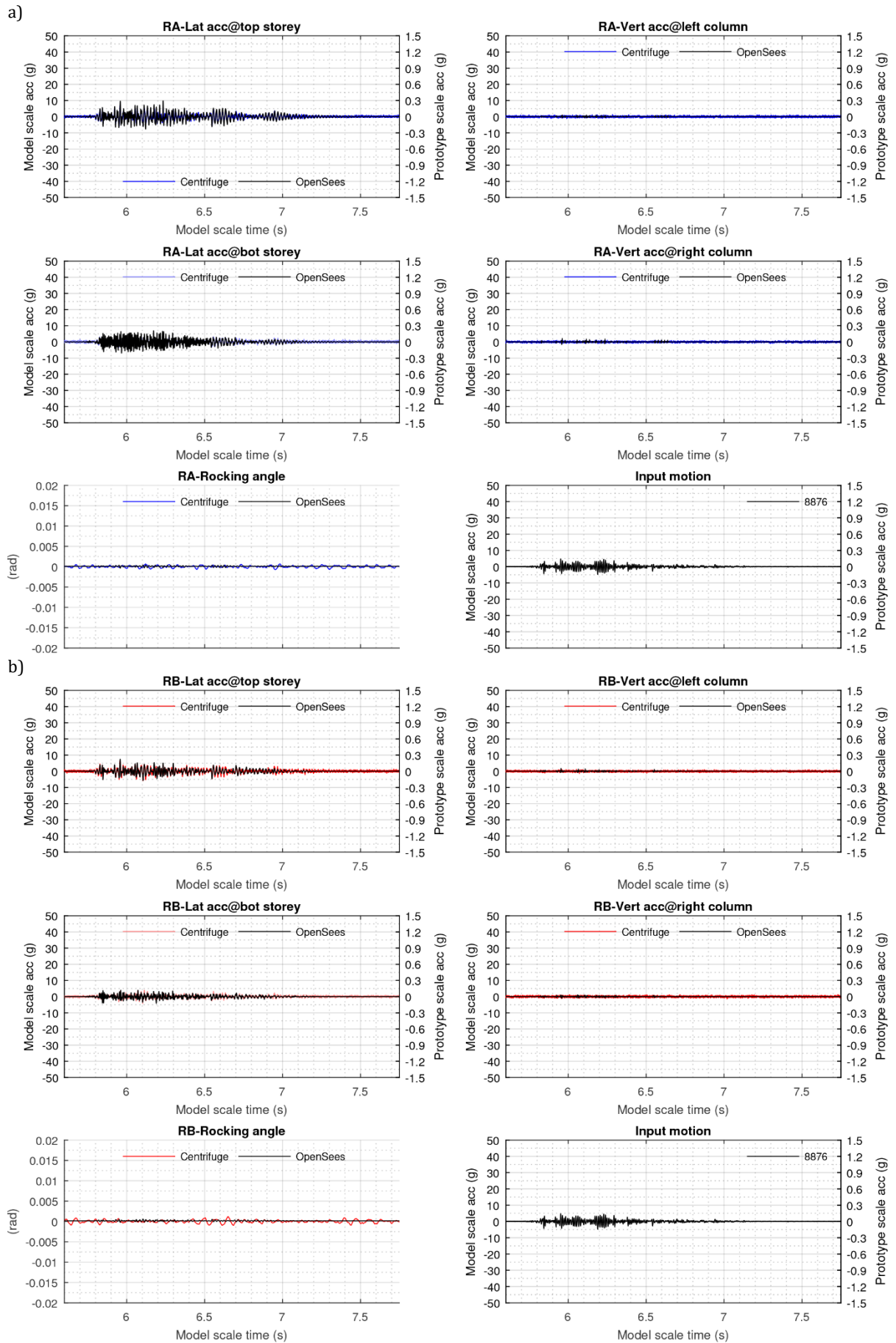
b)



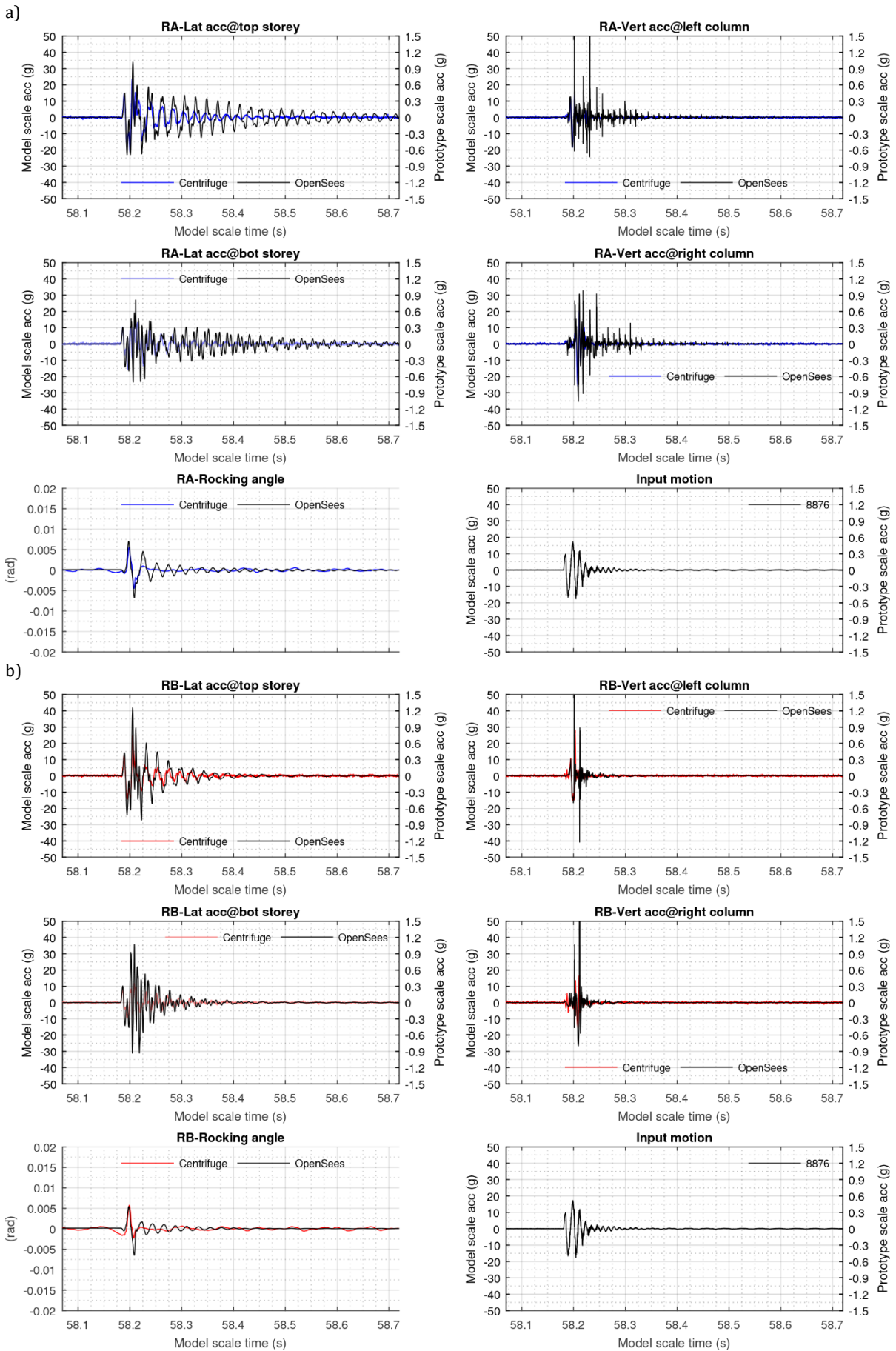
**Dense sand, Test-1 Eq-5: Lateral and vertical accelerations at storeys and columns respectively, rocking angle and input motion for model RA (a) and model RB (b)**



**Dense sand, Test-2 Eq-1: Lateral and vertical accelerations at storeys and columns respectively, rocking angle and input motion for model RA (a) and model RB (b)**

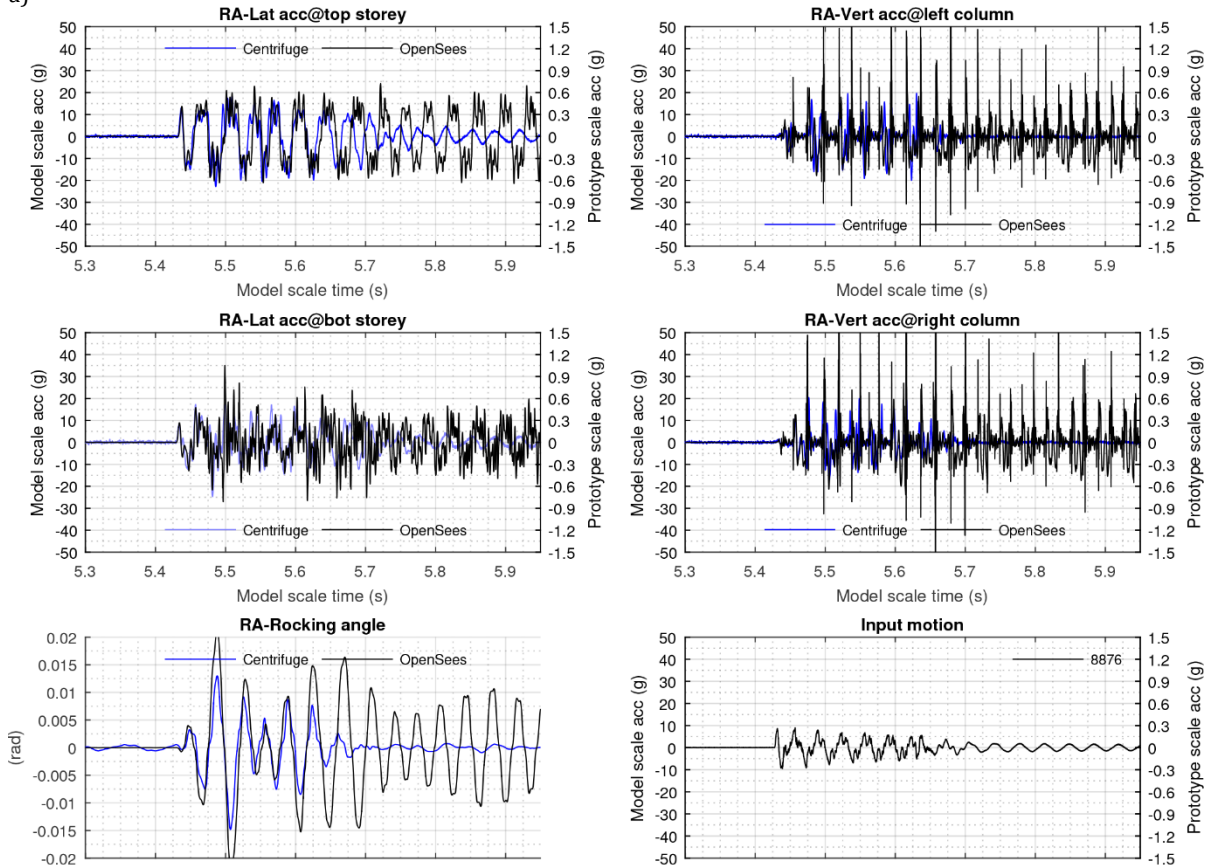


**Dense sand, Test-2 Eq-2: Lateral and vertical accelerations at storeys and columns respectively, rocking angle and input motion for model RA (a) and model RB (b)**

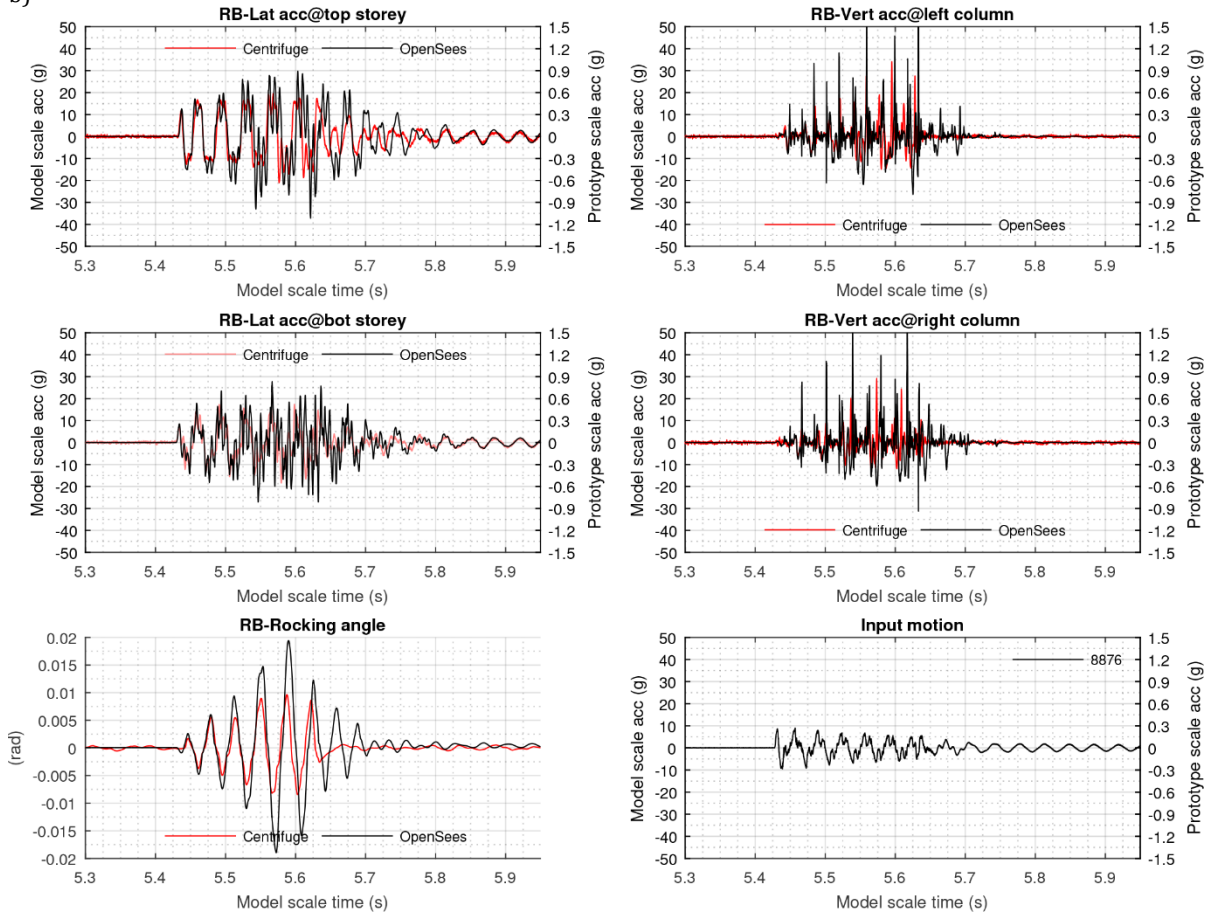


**Dense sand, Test-2 Eq-3: Lateral and vertical accelerations at storeys and columns respectively, rocking angle and input motion for model RA (a) and model RB (b)**

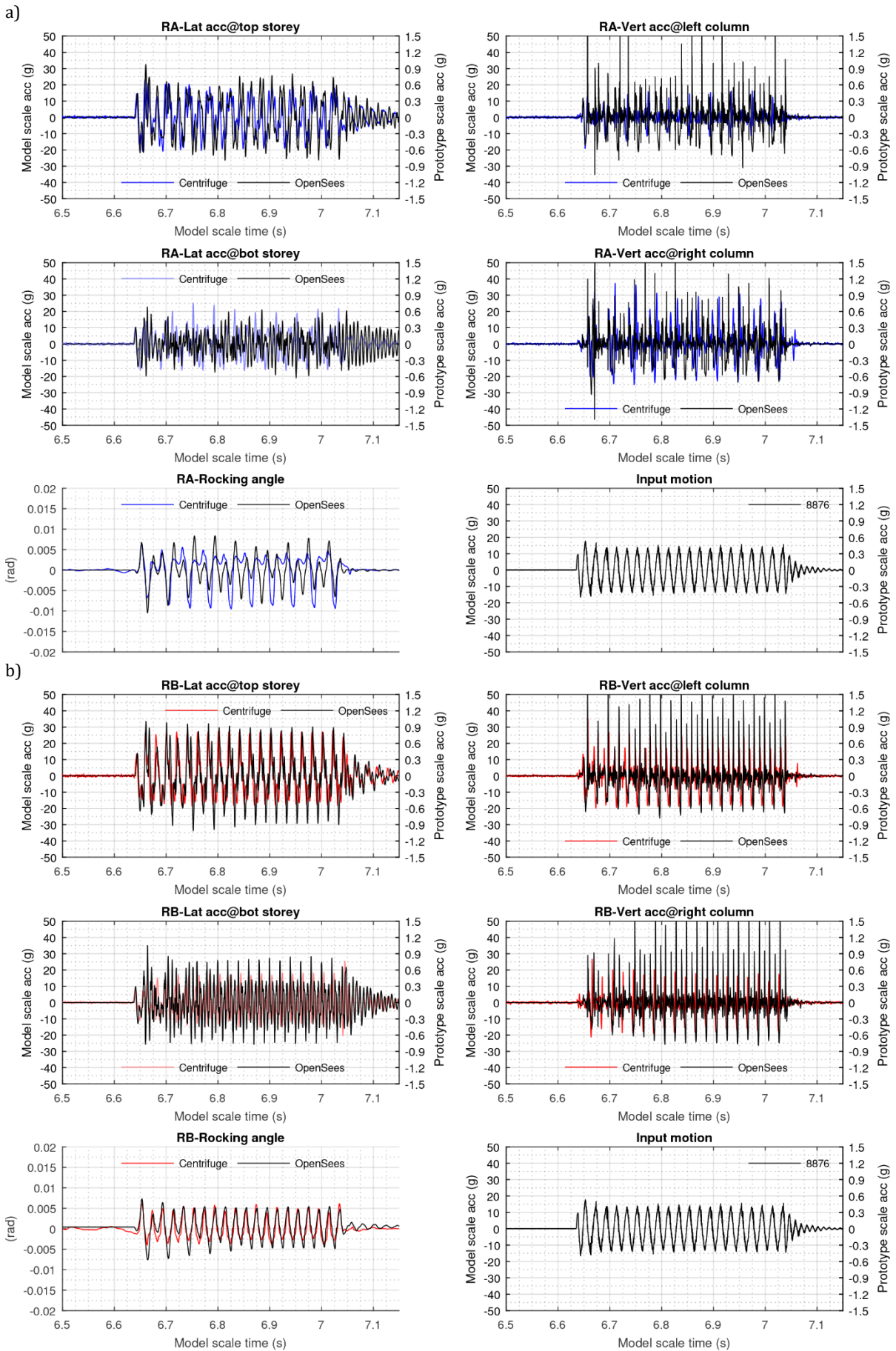
a)



b)

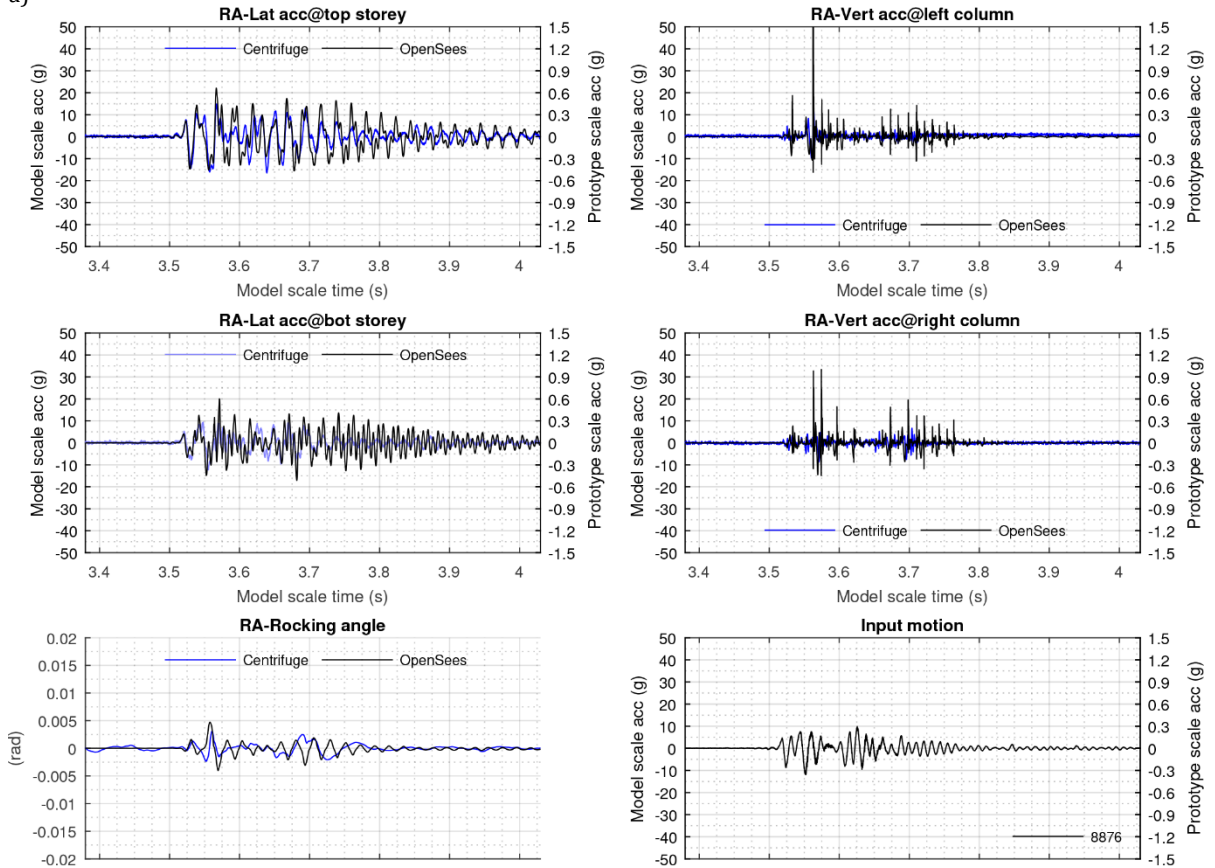


**Dense sand, Test-2 Eq-4: Lateral and vertical accelerations at storeys and columns respectively, rocking angle and input motion for model RA (a) and model RB (b)**

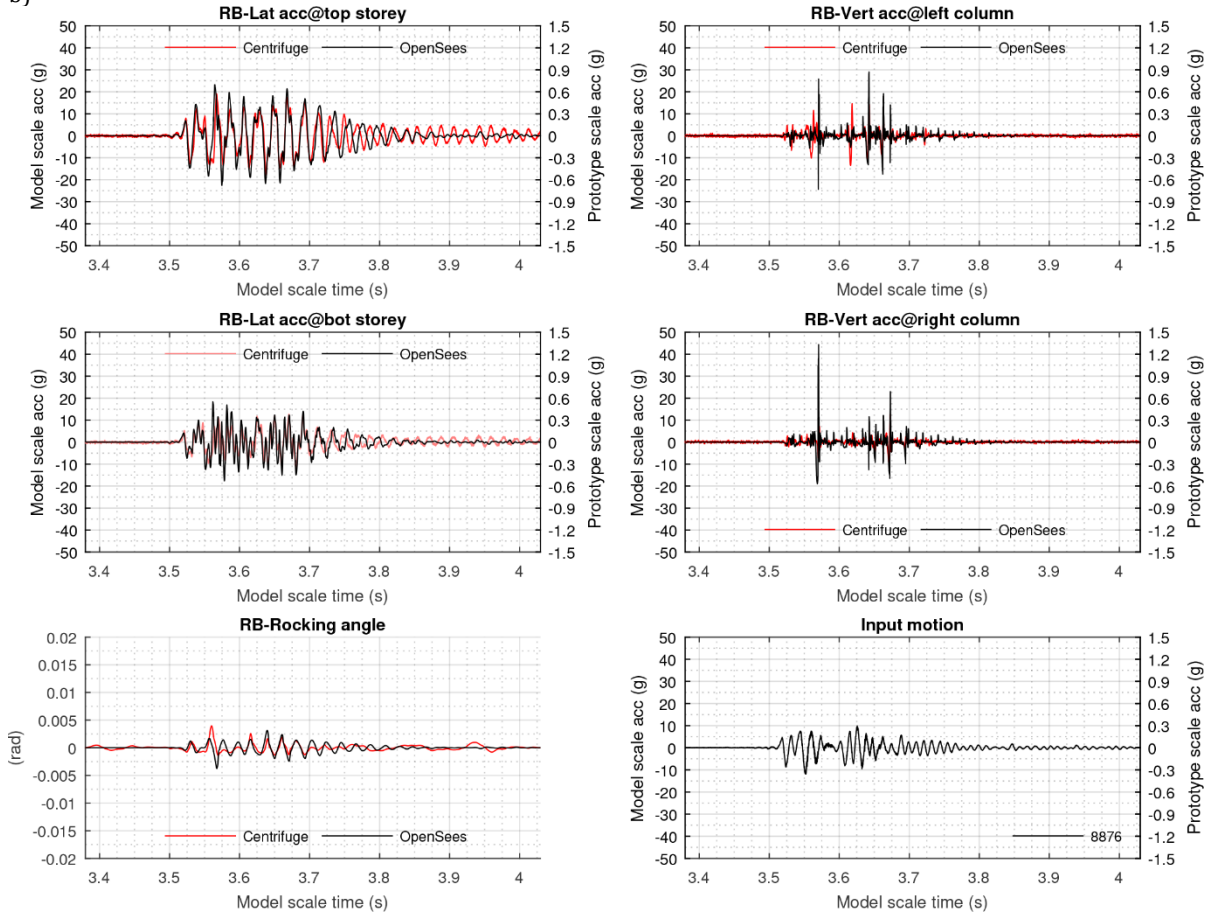


**Dense sand, Test-2 Eq-5: Lateral and vertical accelerations at storeys and columns respectively, rocking angle and input motion for model RA (a) and model RB (b)**

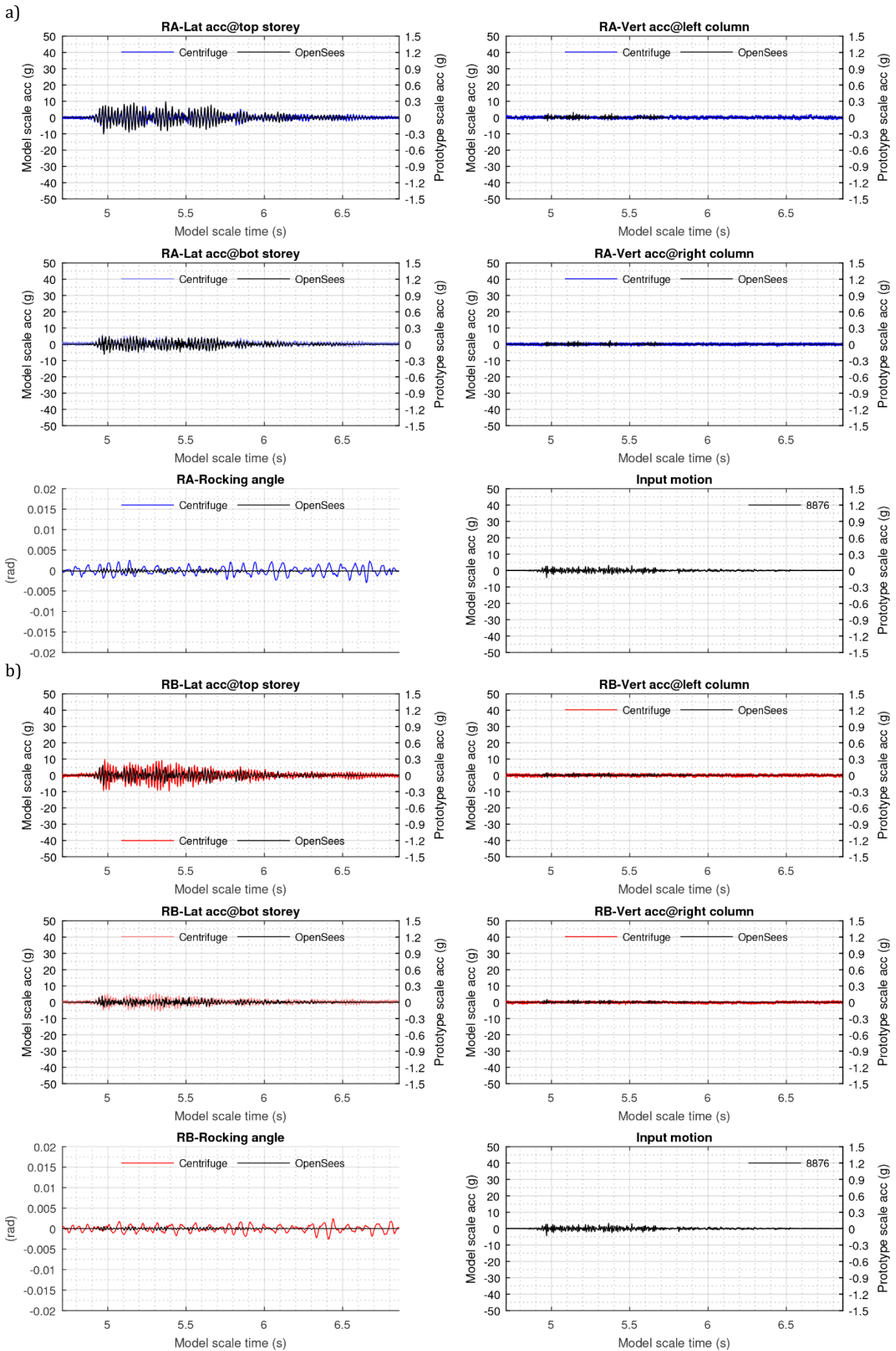
a)



b)

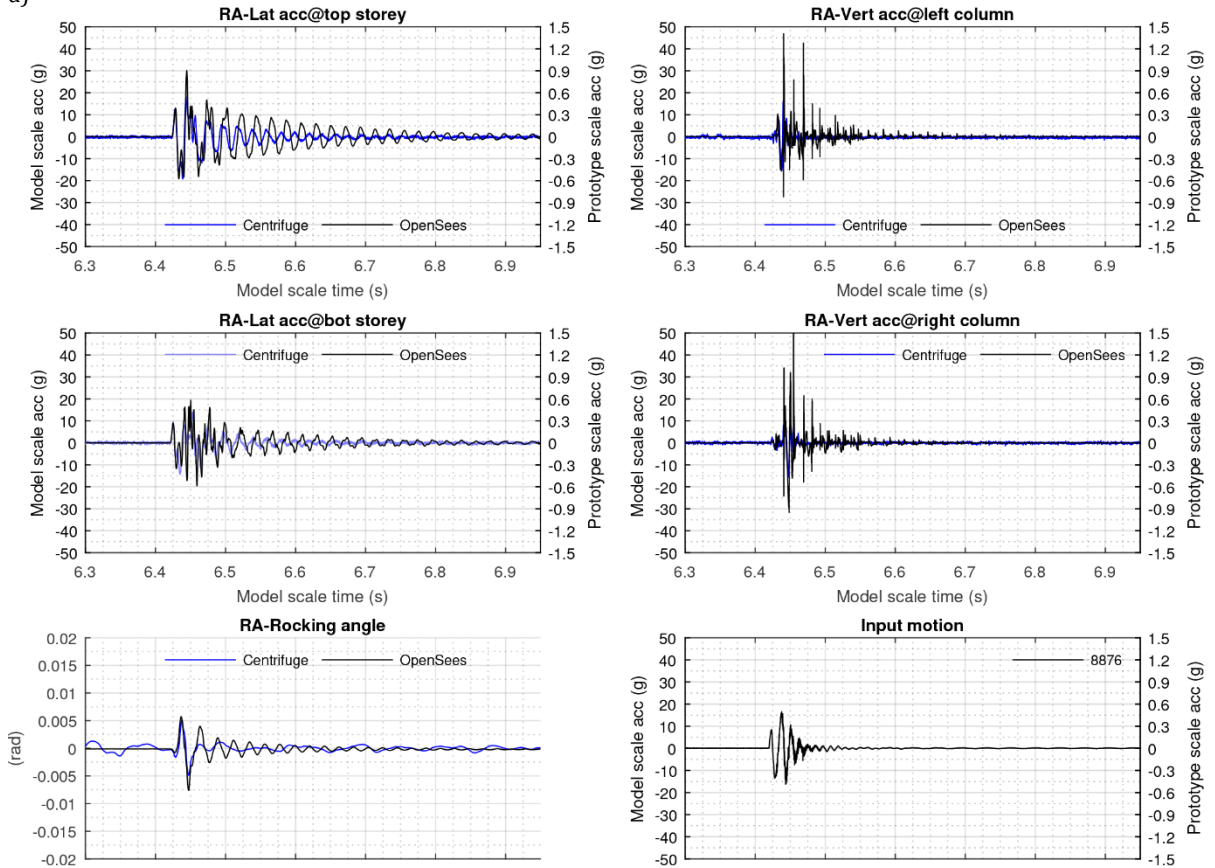


**Loose sand, Test-1 Eq-1: Lateral and vertical accelerations at storeys and columns respectively, rocking angle and input motion for model RA (a) and model RB (b)**

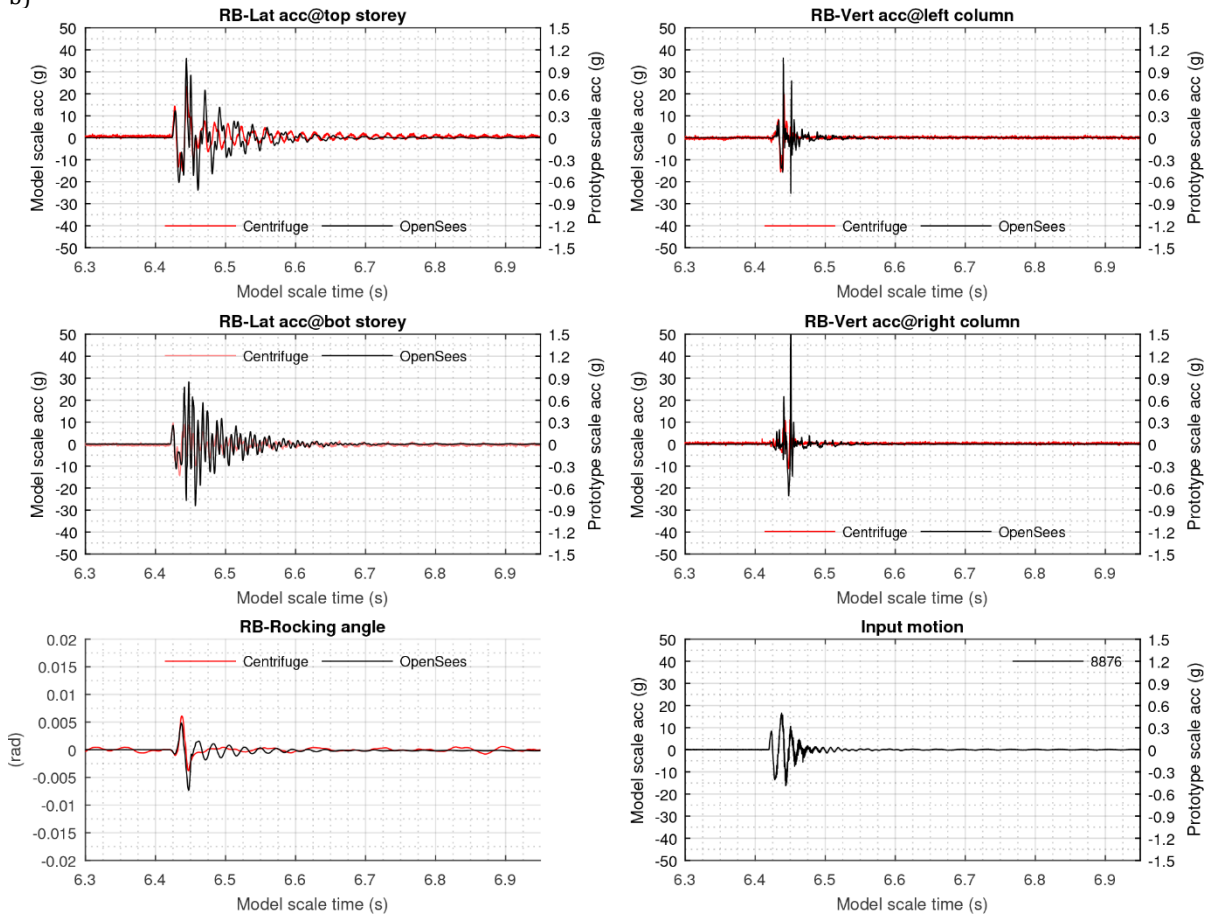


**Loose sand, Test-1 Eq-2: Lateral and vertical accelerations at storeys and columns respectively, rocking angle and input motion for model RA (a) and model RB (b)**

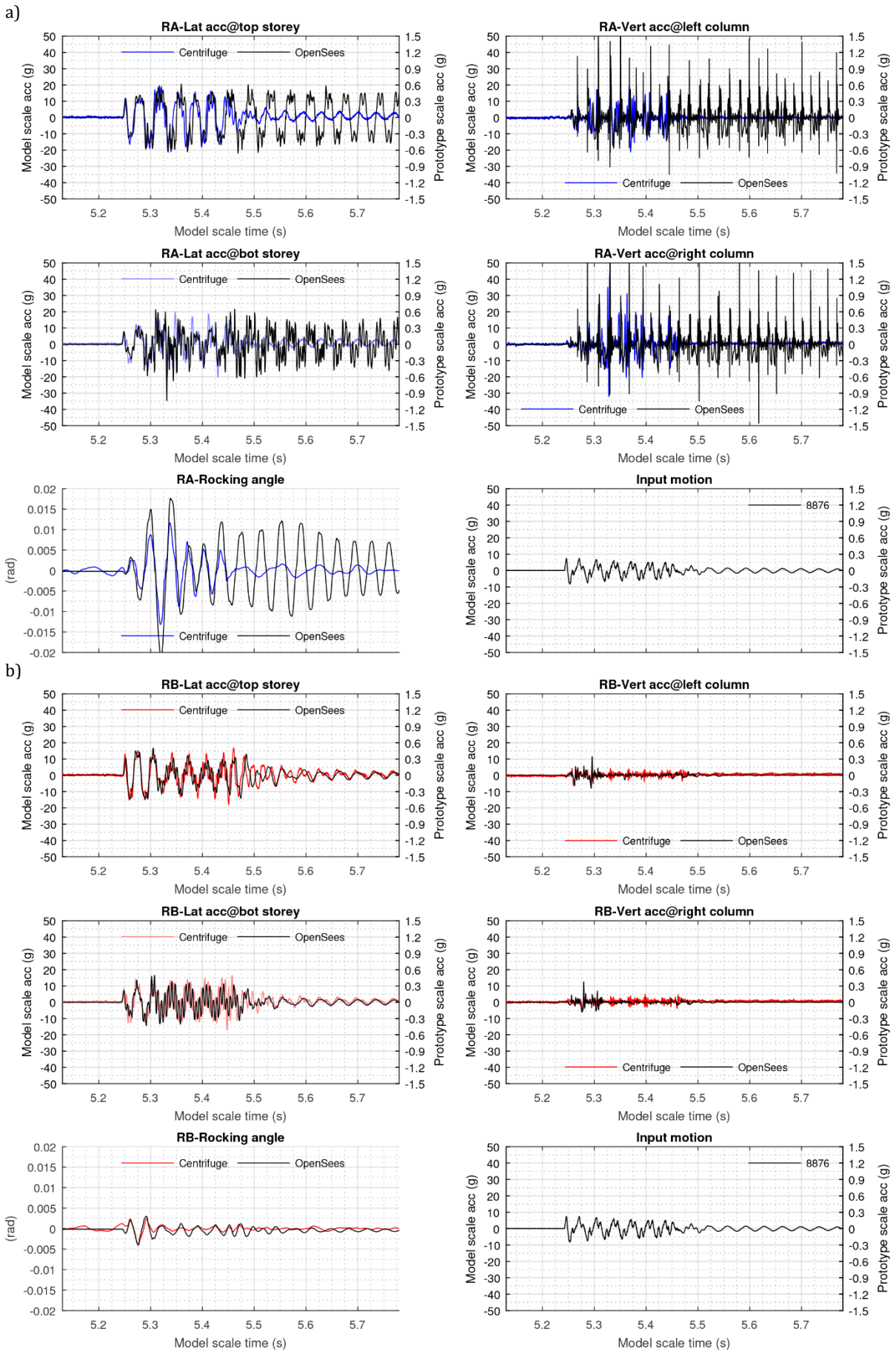
a)



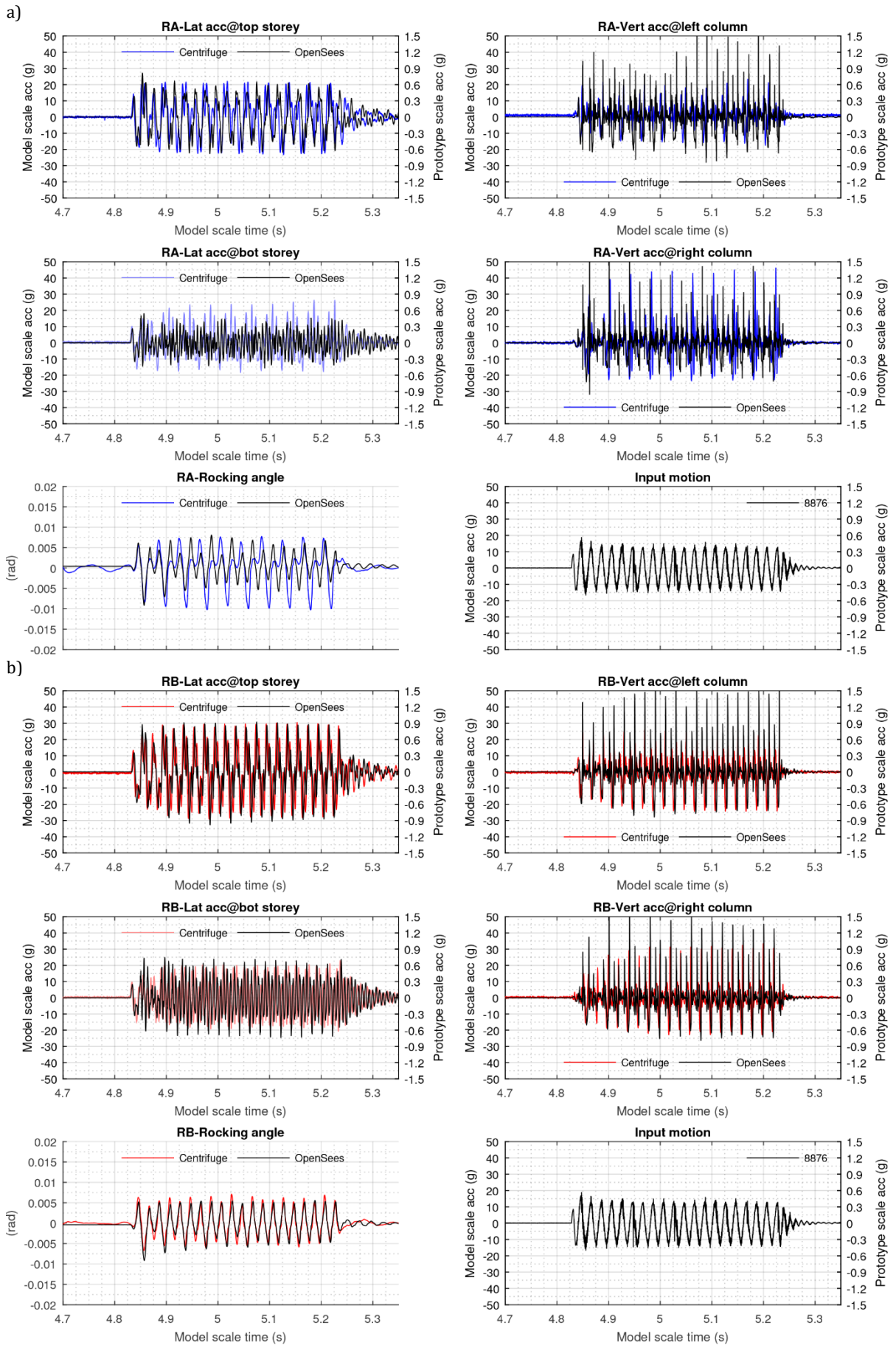
b)



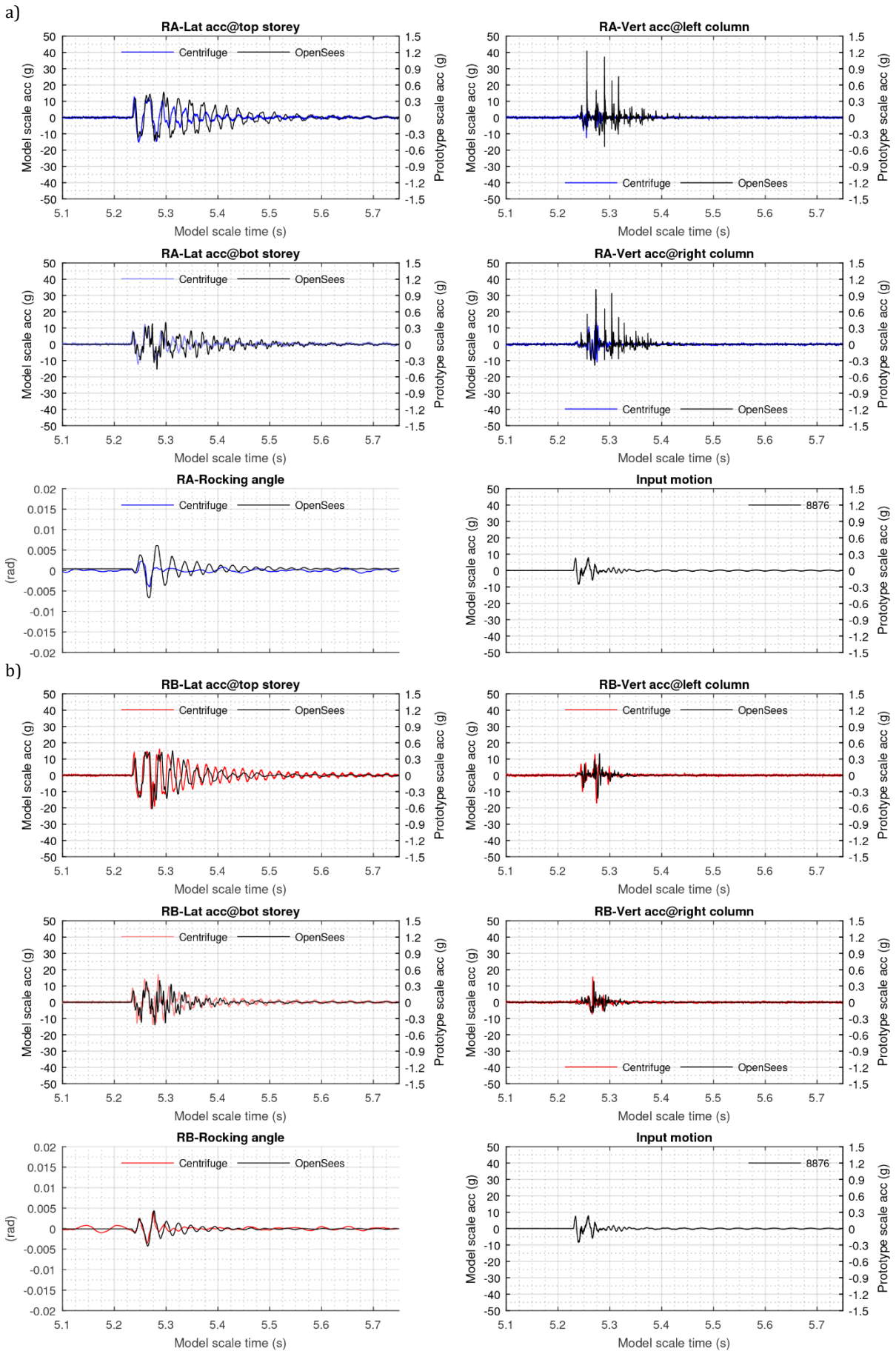
**Loose sand, Test-1 Eq-3: Lateral and vertical accelerations at storeys and columns respectively, rocking angle and input motion for model RA (a) and model RB (b)**



**Loose sand, Test-1 Eq-4: Lateral and vertical accelerations at storeys and columns respectively, rocking angle and input motion for model RA (a) and model RB (b)**

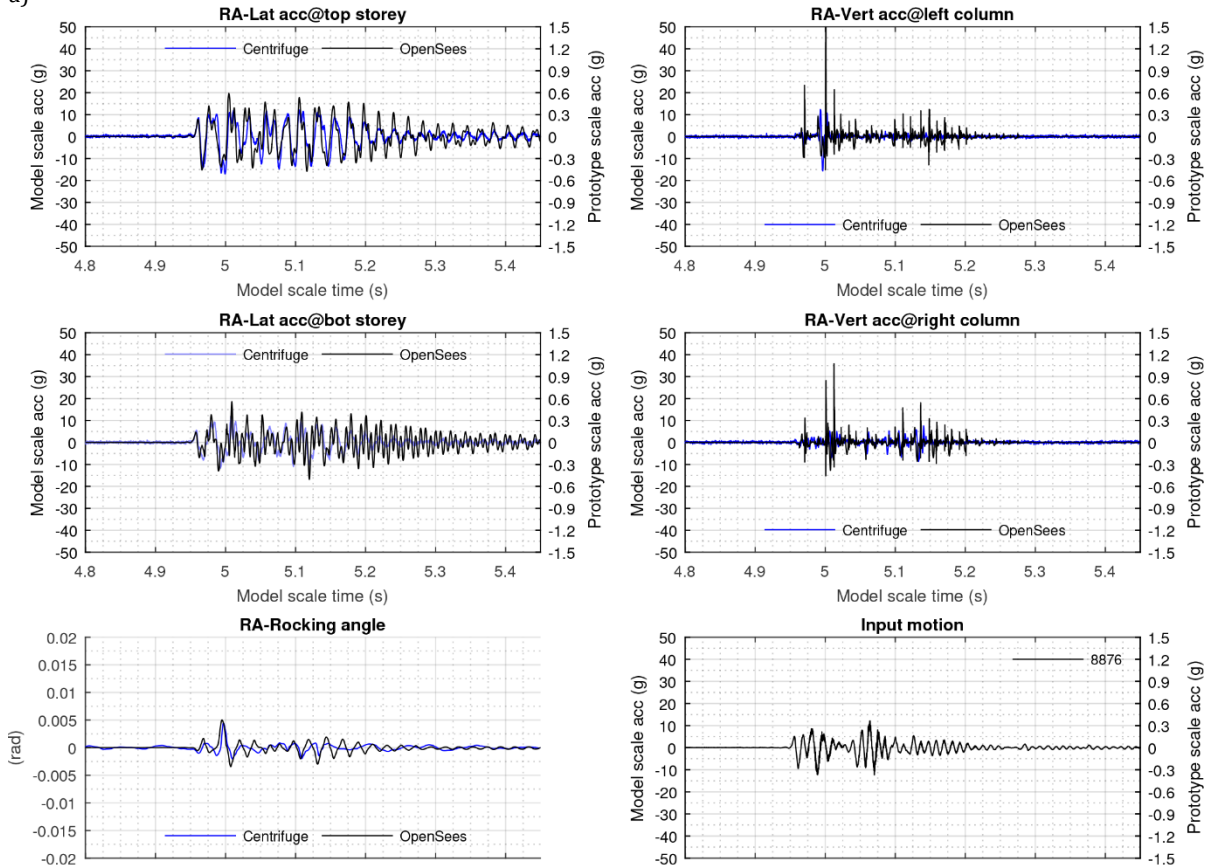


**Loose sand, Test-1 Eq-5: Lateral and vertical accelerations at storeys and columns respectively, rocking angle and input motion for model RA (a) and model RB (b)**

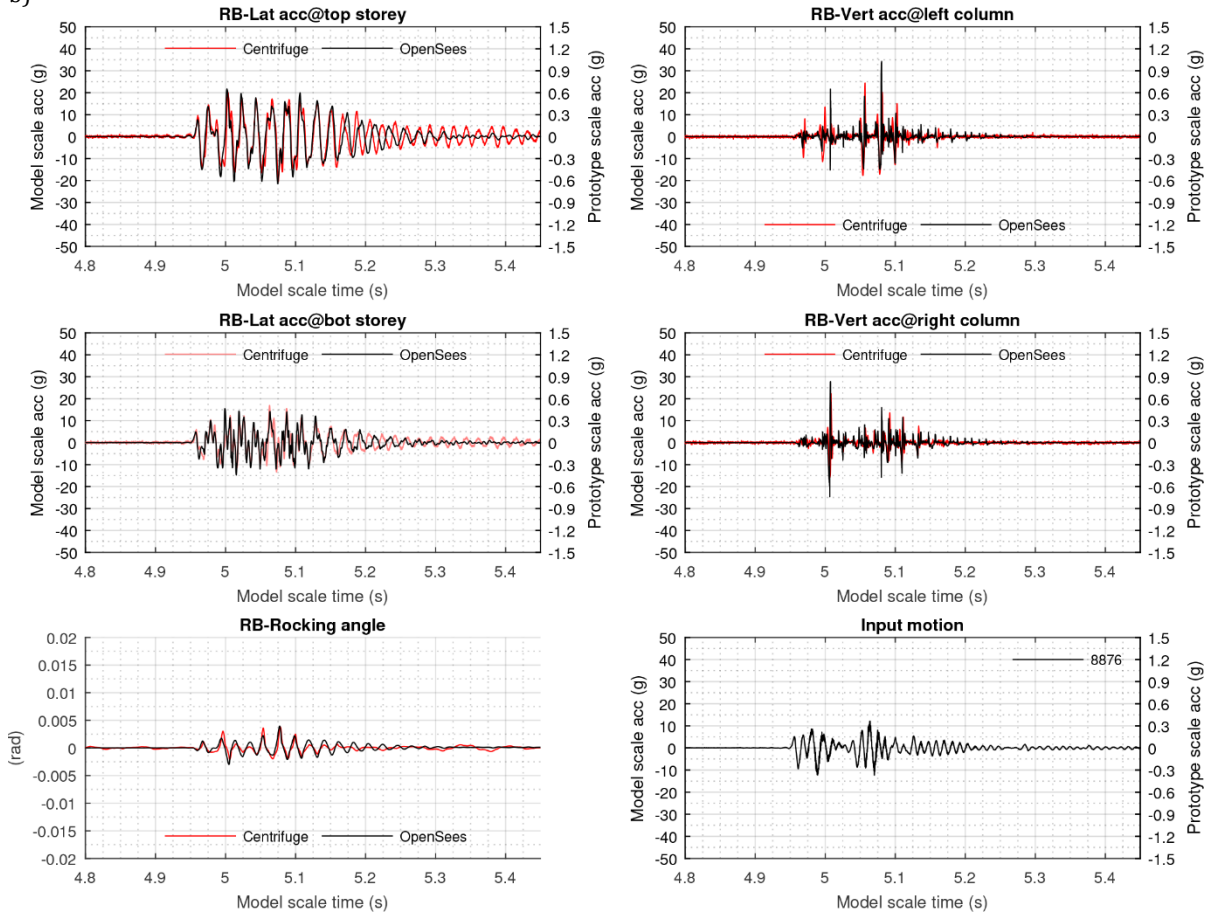


**Loose sand, Test-1 Eq-6: Lateral and vertical accelerations at storeys and columns respectively, rocking angle and input motion for model RA (a) and model RB (b)**

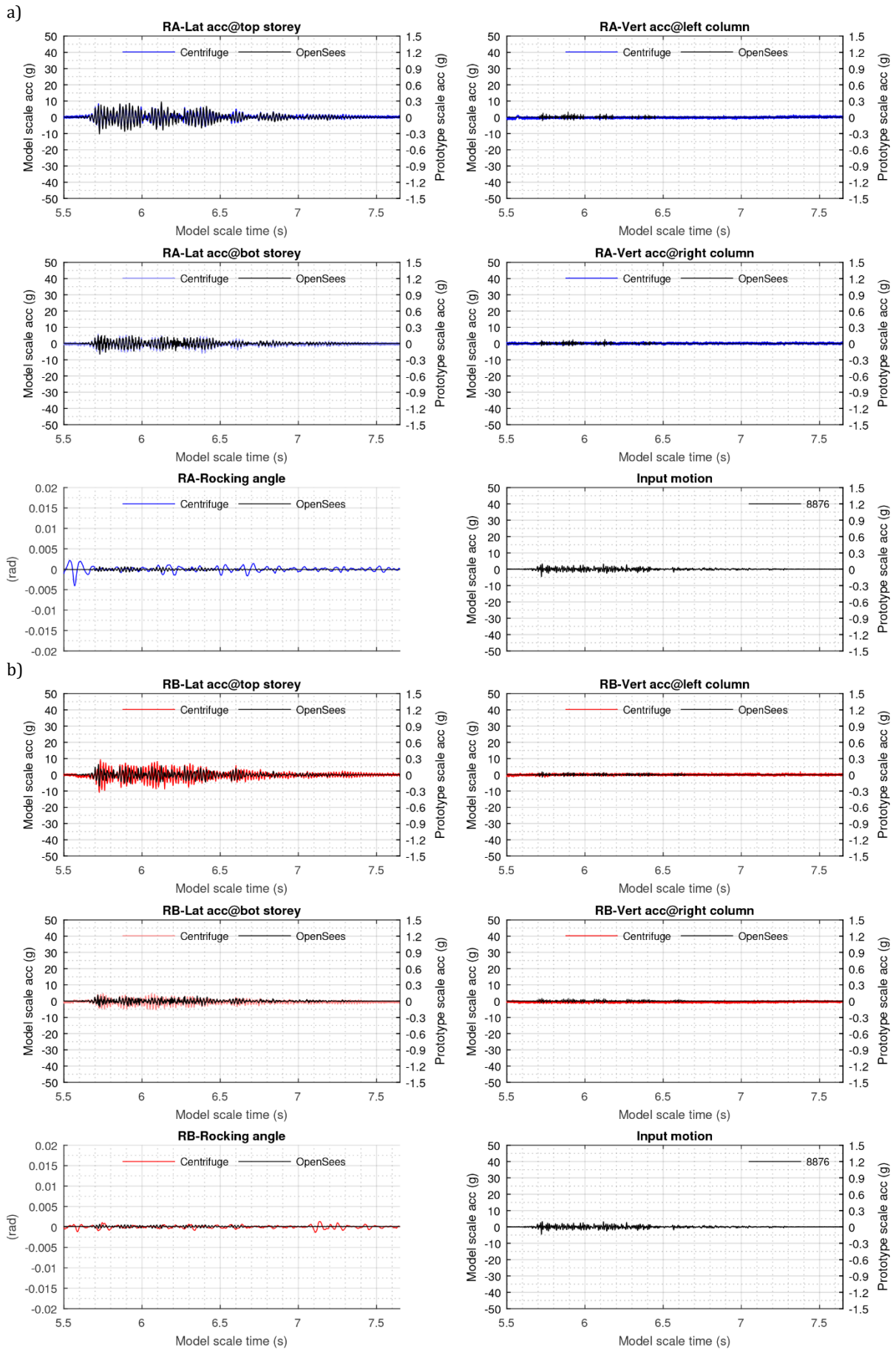
a)



b)

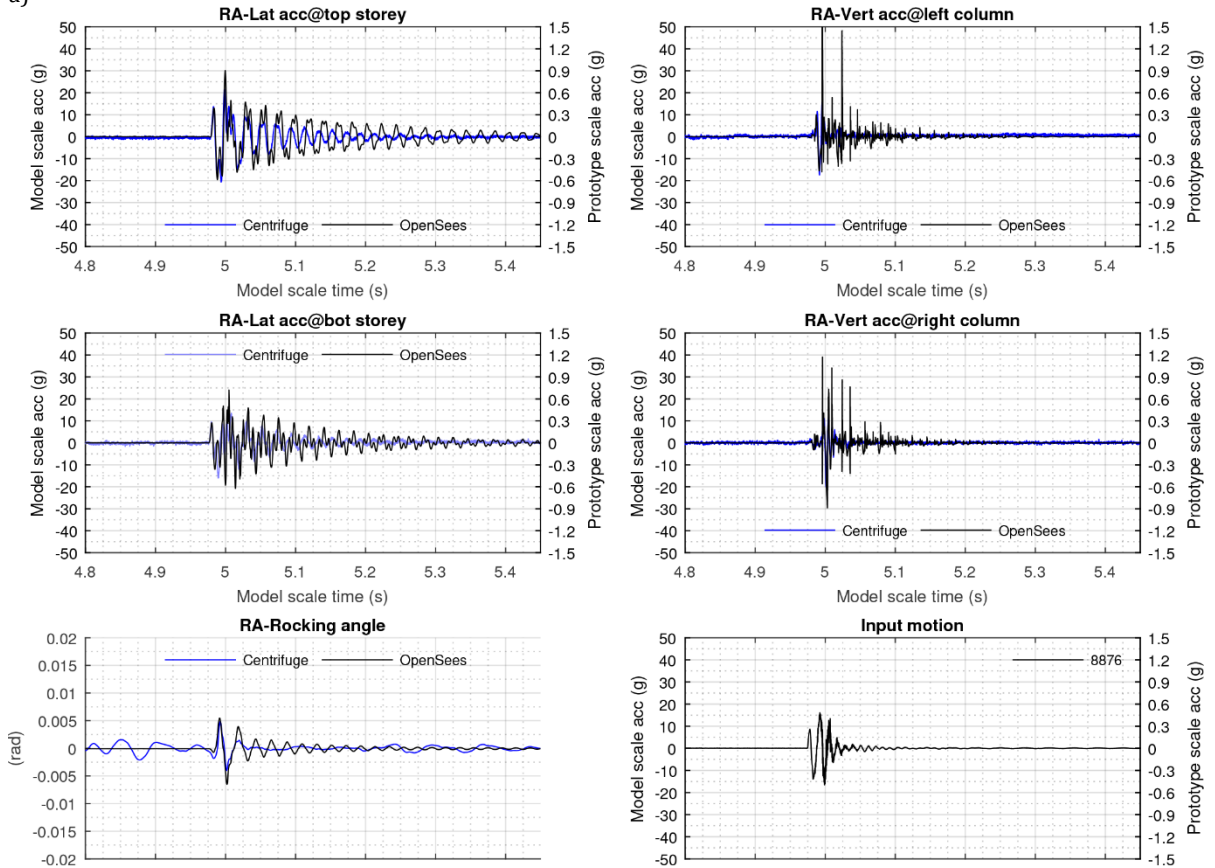


**Loose sand, Test-2 Eq-1: Lateral and vertical accelerations at storeys and columns respectively, rocking angle and input motion for model RA (a) and model RB (b)**

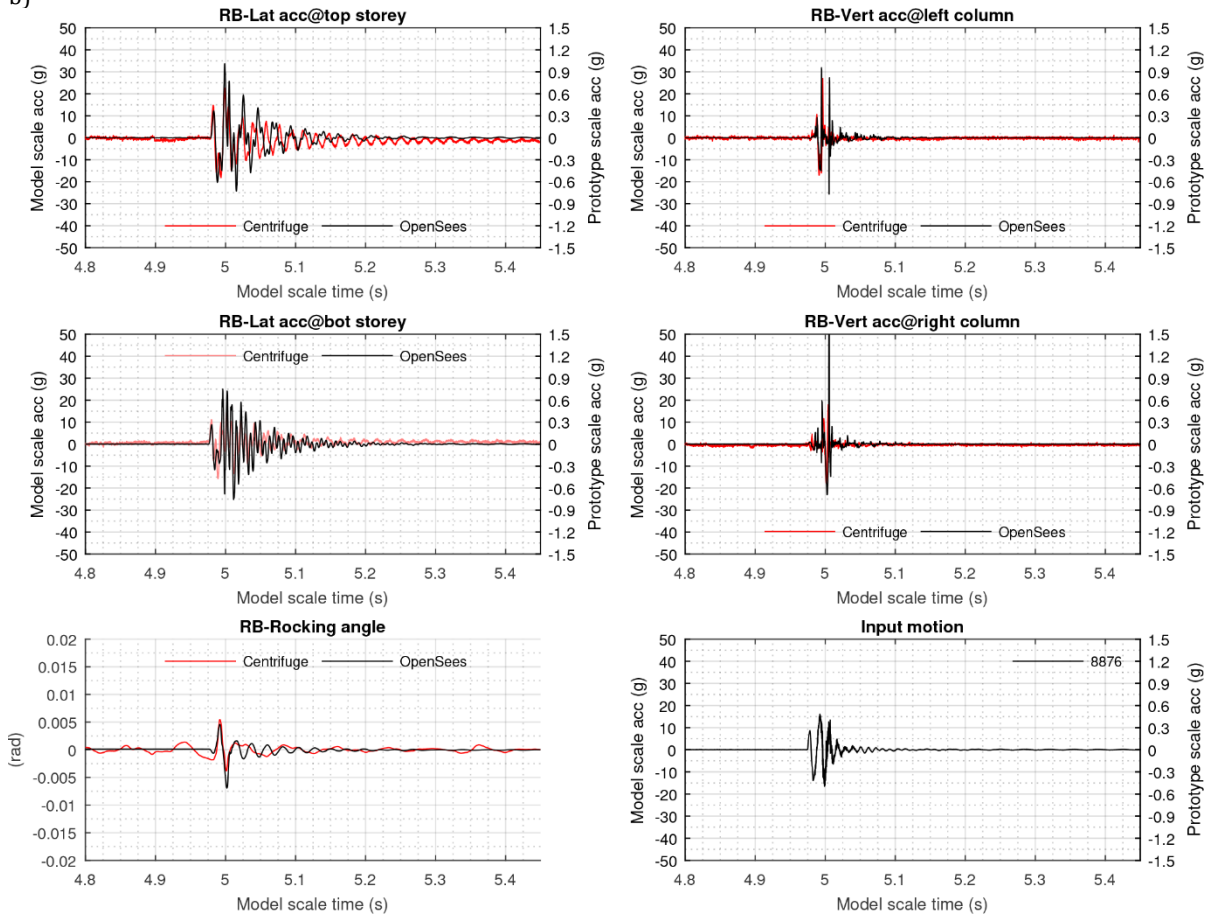


**Loose sand, Test-2 Eq-2: Lateral and vertical accelerations at storeys and columns respectively, rocking angle and input motion for model RA (a) and model RB (b)**

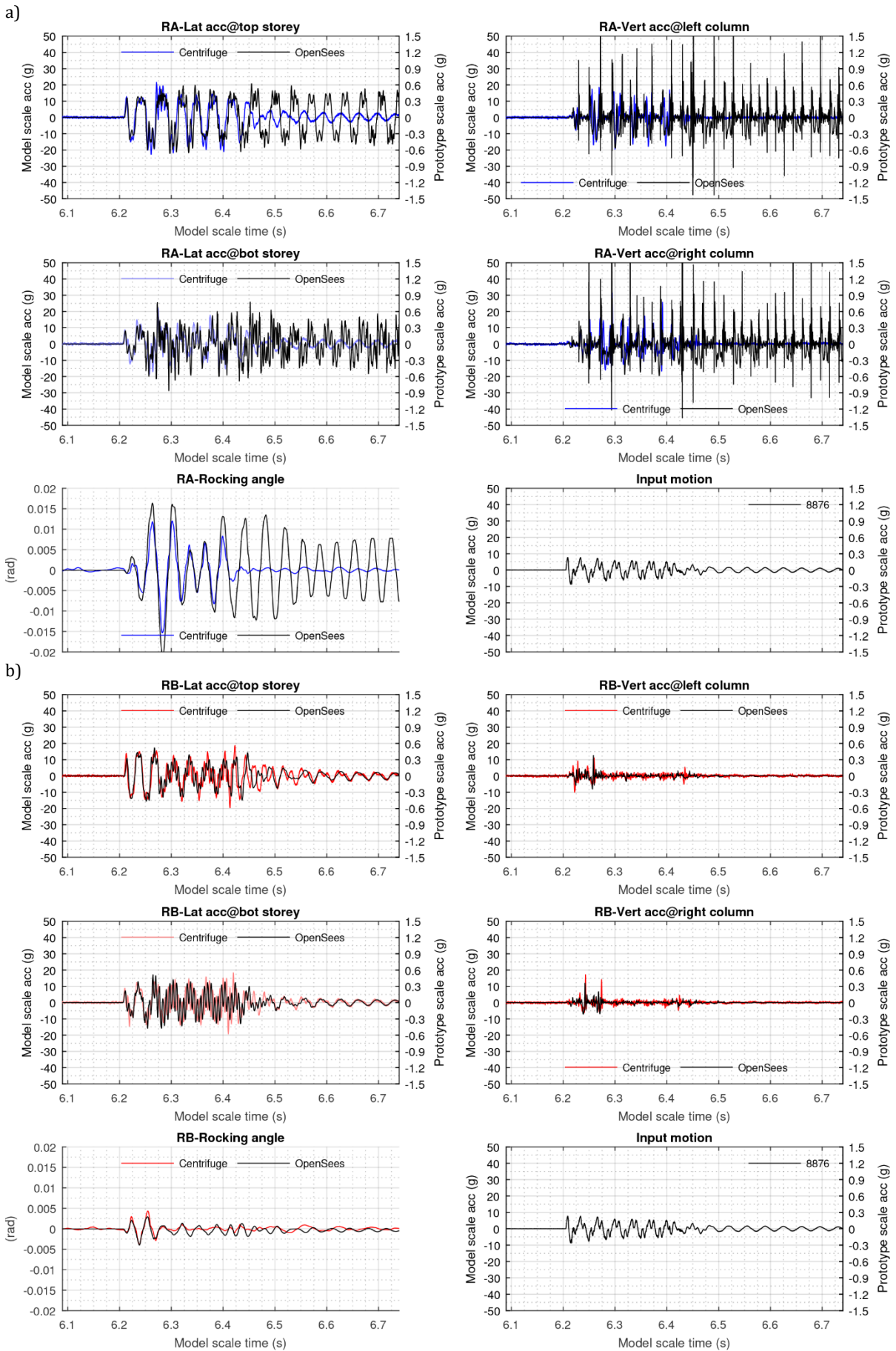
a)



b)

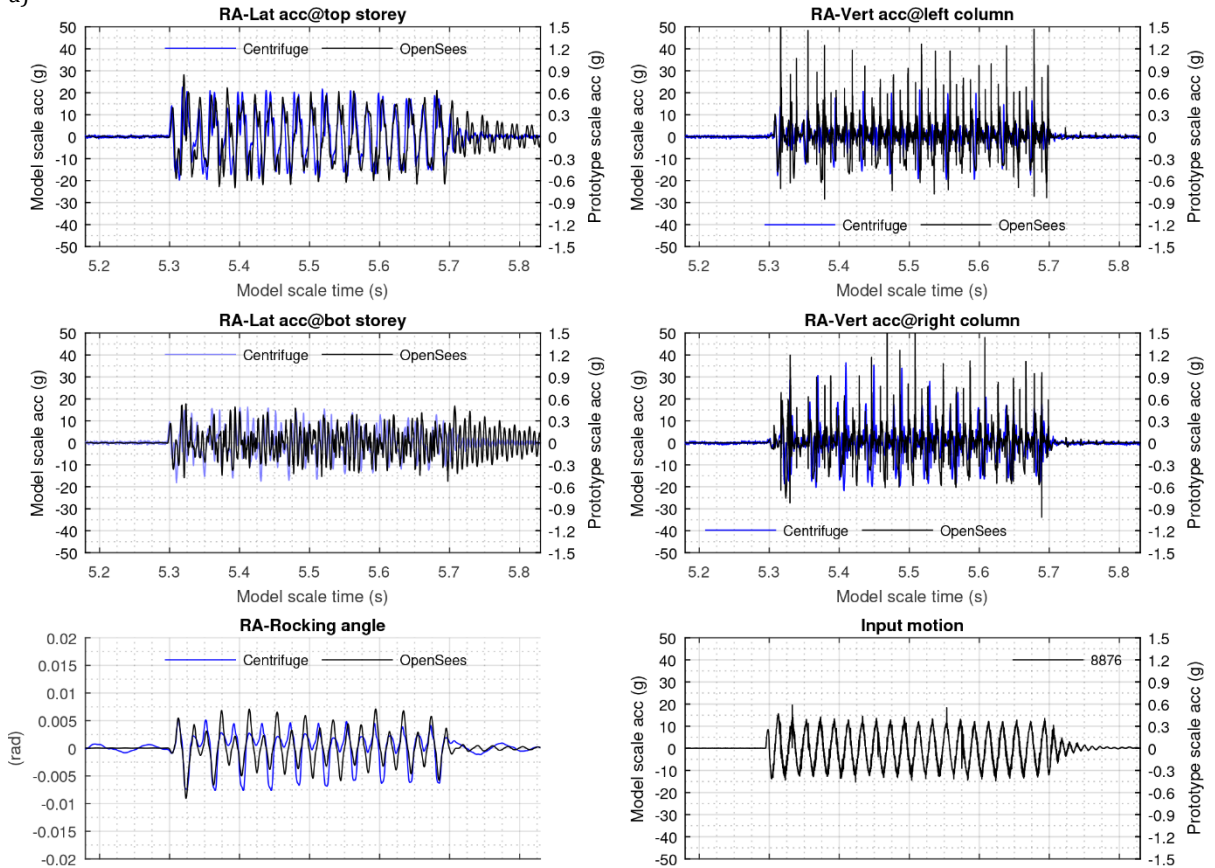


**Loose sand, Test-2 Eq-3: Lateral and vertical accelerations at storeys and columns respectively, rocking angle and input motion for model RA (a) and model RB (b)**

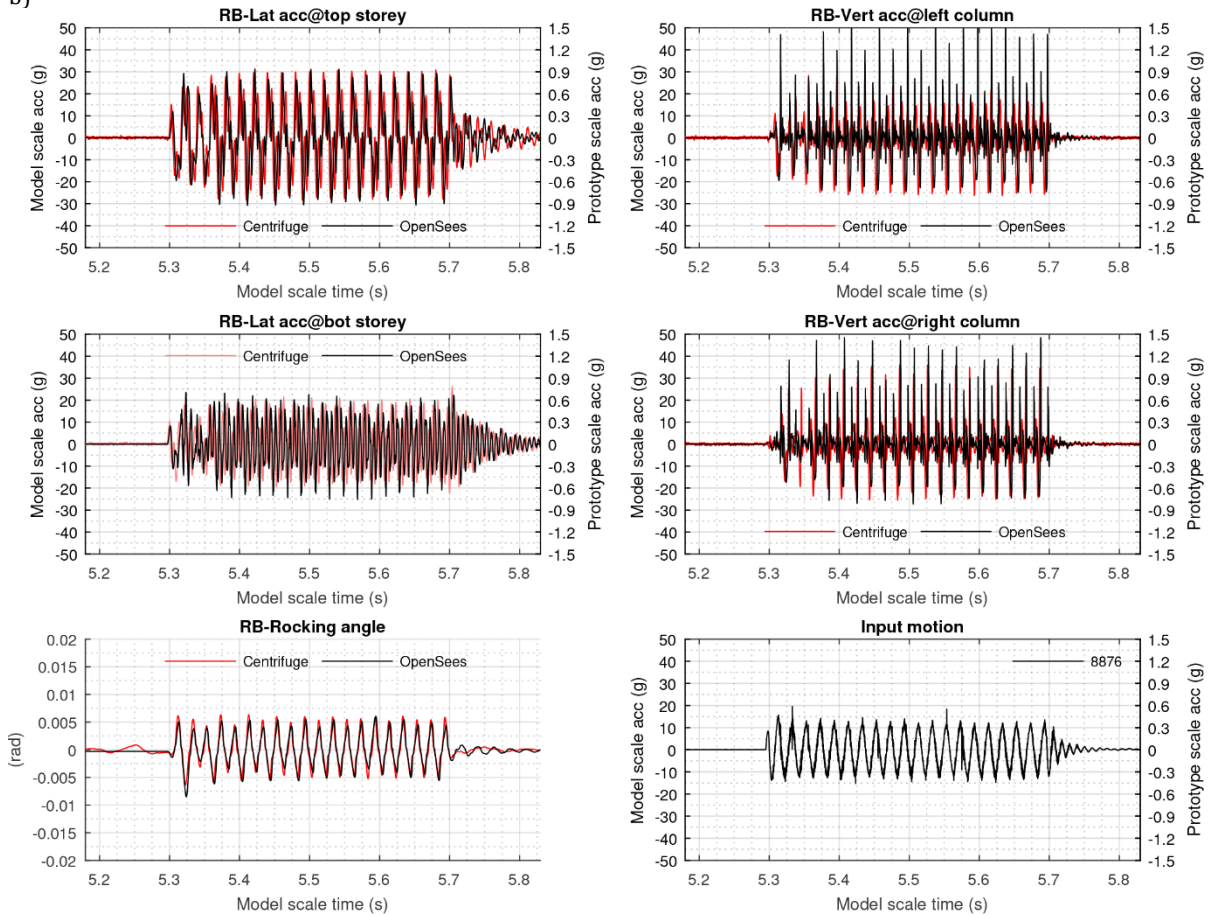


**Loose sand, Test-2 Eq-4: Lateral and vertical accelerations at storeys and columns respectively, rocking angle and input motion for model RA (a) and model RB (b)**

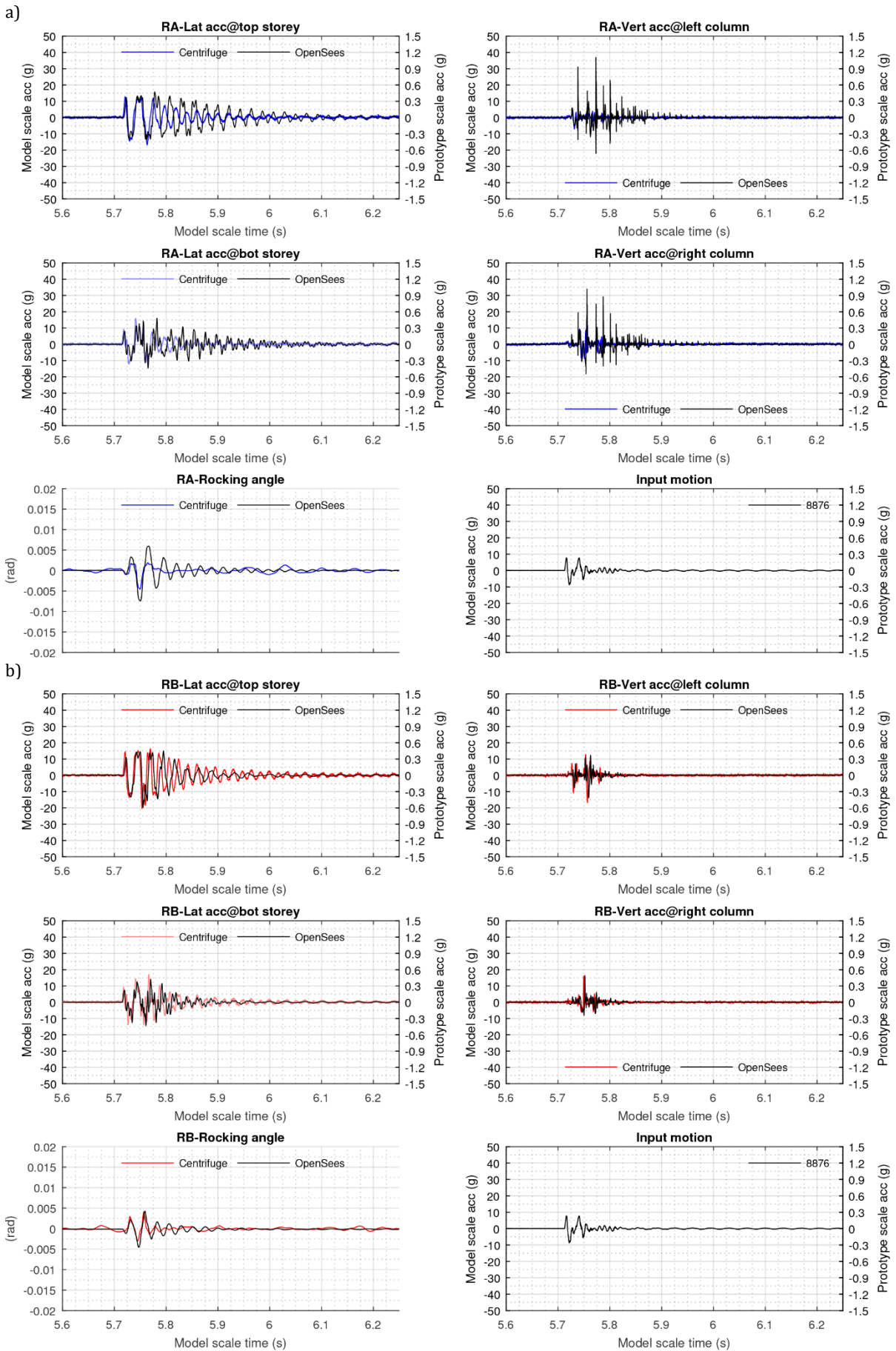
a)



b)



**Loose sand, Test-2 Eq-5: Lateral and vertical accelerations at storeys and columns respectively, rocking angle and input motion for model RA (a) and model RB (b)**



**Loose sand, Test-2 Eq-6: Lateral and vertical accelerations at storeys and columns respectively, rocking angle and input motion for model RA (a) and model RB (b)**